Developing Improved Earth-Abundant Electrocatalysts for the Reduction of Dioxygen through Mechanistic Insight

Emma N. Cook

B.S. Chemistry, University of North Carolina at Chapel Hill, 2019

A Dissertation presented to the Graduate Faculty of the University of Virginia in Candidacy for the Degree of Doctor of Philosophy

Department of Chemistry

University of Virginia

April, 2024

Prof. Charles W. Machan, Advisor

Abstract

The oxygen reduction reaction (ORR) is an attractive route to alternative energy sources as well as environmentally friendly industrial processes. Development of earth abundant catalysts is necessary for the ORR to be a sustainable option. Motivated by the lack of synthetic non-heme Fe centered catalysts for the ORR, we have studied two non-heme Fe systems containing N_3O ligand frameworks, $Fe(PMG)Cl_2$ and $Fe(tpy^{tbu}pho)Cl_2$. Mechanistic analyses revealed that both systems operated via a 2+2 mechanism, where H_2O_2 was a discrete intermediate during catalysis before further reduction to H_2O. Interestingly, the rate limiting step for $Fe(PMG)Cl_2$ was cleavage of an off-cycle dimer species, while O_2 binding to the reduced Fe center was rate limiting for $Fe(tpy^{tbu}pho)Cl_2$. Based on these results, a key factor in observed reactivity was the axial ligand *trans* to the O_2 binding site.

Mn-based systems for the ORR are much less widely studied in comparison to Fe and Co. Because of the prevalence of Mn in nature, we undertook a mechanistic study examining two Mn complexes containing N_2O_2 ligand frameworks to understand how secondary coordination sphere interactions could tune Mn-based ORR. Analysis of these complexes using an ammonium proton source revealed that incorporation of a –OMe pendent relay group could shift selectivity to preferably producing H_2O_2. Interestingly, without added conjugate base strong hydrogen bonding with the pendent –OMe group suppressed catalysis. However, in the presence of added base, this suppression is mitigated and there is an accessible dimeric pathway that is controlled by the pK_a of the Mn–H_2O_2 intermediate.

Redox-active organic molecules that are stable toward reactive oxygen species have drawn increasing attention for use as sustainable ORR catalysts. Here, two cationic organic molecules have been evaluated as ORR catalysts. First, an iminium-based compound was studied under both electrochemical and spectrochemical conditions with TFAH as a proton source and was shown to catalytically reduce O_2 under electrochemical and spectrochemical conditions. We observed a divergence in mechanism, where under spectrochemical conditions, outer-sphere O_2

reduction occurred to produce H_2O_2, whereas under electrochemical conditions in the presence of excess reduced catalyst, $O_2^{\bullet-}$ reacted via an inner-sphere mechanism to be further reduced to H_2O. Then, a substituted phenanthroline diium compound was evaluated for the ORR using acetic acid derivatives to understand the dependence of ORR on acid strength. It was found that activity and rate-determining step was dependent on acid strength. Additionally, under certain conditions an off-cycle dimeric species was observed to be kinetically relevant. A mechanistic understanding of the controlling factors of the ORR is imperative to the development of efficient earth-abundant catalysts.

Copyright Information

Chapters 1 - **6** are modified versions of published work that have been reproduced in accordance with the American Chemical Society Journal Publishing Agreement and Royal Society of Chemistry Publication Agreement. Proper citation for each chapter is given below and on the first page of each of the chapters within this thesis.

Chapter 1:
Cook, E. N. and Machan, C. W. Homogeneous catalysis of dioxygen reduction by molecular Mn complexes. *Chemical Communications* **2022**, 58, 11746-11761. doi: 10.1039/D2CC04628H.

Chapter 2:
Cook, E. N.; Dickie, D. A.; Machan, C. W. Catalytic Reduction of Dioxygen to Water by a Bioinspired Non-Heme Iron Complex via a 2+2 Mechanism *Journal of the American Chemical Society* **2021** 143, 40, 16411-16418. doi: 10.1021/jacs.1c04572.

Chapter 3:
Cook, E. N.[#]; Hooe, S. L.[#]; Dickie, D. A.; Machan, C. W. Homogeneous Catalytic Reduction of O_2 to H_2O by a Terpyridine-Based FeN_3O Complex. *Inorganic Chemistry* **2022**, 61, 8387-8392. doi: 10.1021/acs.inorgchem.2c00524.

Chapter 4:
Cook, E. N.; Courter, I. M.; Dickie, D. A.; Machan, C. W. Controlling product selectivity during dioxygen reduction with Mn complexes using pendent proton donor relays and added base. *Chemical Science* **2024**, 15, 4478-4488. doi: 10.1039/DS3C02611F

Chapter 5:
Cook, E. N.; Davis, A. E.; Hilinski, M. K.; Machan, C. W. Metal-Free Homogeneous O_2 Reduction by an Iminium-Based Electrocatalyst *Journal of the American Chemical Society*, **2024**, 146, 12, 7931-7935. doi: 10.1021/jacs.3c14549

Chapter 6:
Cook, E. N.; Flaxman, L. A.; Reid, A. G.; Dickie, D. A.; Machan, C. W. *Manuscript submitted for publication.*

Acknowledgements

I would not be where I am today without the guidance, support, encouragement, and love of so many people around me. I would first like to thank all of my teachers and mentors growing up, it was from them that I discovered a love of learning. Specifically, I would like to thank Mrs. Sowle, who was always there to support my love of art and science. She knew that I wanted to be a scientist from the beginning and was my cheerleader throughout high school. My first exposure to chemistry was in my high school chemistry class with Ms. Shields. It was in this class, and then AP Chemistry, that I first became interested in chemistry… and the rest is history.

If it weren't for my mentors at UNC, I would not have ended up in graduate school let alone at UVA. To Melody, thank you for guiding me and being patient with me. The skills and values I learned from you have been essential to my success and I couldn't have asked for a better graduate mentor. To Dr. Jill Dempsey, thank you for introducing me to research and the possibilities within and outside of the lab. To Dr. Kathleen Nevins, who suggested I try doing research in the first place – look where it got me! Having such strong leaders to look up to has shaped how I view my role as a scientist and motivated me to be a leader and mentor, as well.

The faculty and staff at UVA have been what make the Department of Chemistry the best at the University. I am grateful for everyone that works to make the Department great, working with you all has been a pleasure. And to my committee members, Dr. T. Brent Gunnoe, Dr. Sen Zhang, Dr. Ian Harrison, Dr. Jason Bates, and Dr. Robert Gilliard. Your assistance, feedback, and support during my time at UVA has been important to my success. I am so appreciative of your willingness to help and dedication to my graduate career.

To all my friends I met while in graduate school, you have made my time here at UVA incredible. Thank you to Joe, Seamus, Kim, and Hazel for being there from the beginning. It has been so much fun being able to do this journey together, even if we all ended up in separate places by the end. To Zoë and Hannah, thank you for always being down for anything, from

chatting in the hallway to trying a new restaurant. I am so proud of you all and I have had a blast over the years, and it makes me so happy to see you all thriving.

To the members of the Machan group (both past and present!), thank you for being the best people to work alongside. Shelby, I can't adequately explain how much your encouragement and support means to me. Thank you for always knowing how to calm me down when I'm on a downward spiral of overthinking, for teaching me how to be independent in lab, and how to know when too many things are going wrong and it would be best if I just left for the day. And Asa, working with you was a highlight of graduate school. Thanks for your support and always making us laugh in lab. To Juanjo, Connor, and Sameeta, thank you for teaching me so much, even if it is just to calm down and that everything will be okay. I have learned so much from you all, in and outside of lab. Your support and encouragement has been so important to me and helped me in explicable ways. Megan, thank you for always being there to watch ITYSL clips in the office (or watch Napoleon Dynamite), talk about anything, or just sit next to each other while we work. I can't adequately express how much it has meant to me to have you there next to me for the past three years – thanks for just getting me. Elizabeth, Mary Jo, and Mollie, working with you all has been so much fun from the vineyards to the lab. You all are amazing and those that come after you are so lucky to have you as mentors. I know you will all do incredible things and I am so excited to see you succeed. To James, Ian, Andy and Luke, thanks for being great undergraduate mentees. You have taught me so much and I have thoroughly enjoyed working with you all. I can't wait to watch you continue to succeed in everything you all do.

Deciding to join the Machan lab has been one of the best decisions I could have made. Charlie, your mentorship and constant support has meant so much to me and has made me the scientist and person that I am. I have learned so many things from you, from managing priorities and projects in the lab to learning how to prioritize my mental health. I am so fortunate to have been able to work with you. Thank you for always pushing me to do my best and believing in me. The time we spent with your family has been some of my most favorite memories. I always have

the best time being with you all, from reading with the kids to watching karaoke performances. Thank you and Amanda for welcoming me into your home.

My friends outside of the department have had a tremendous impact on my success. I couldn't have made it this far without their constant encouragement. To Kayla, Juli, and Olivia, our friendship means so much to me, thank you for always being down for anything – our time together brings me such joy. And to Grace, thank you for being there for the past 13 (!) years. I am so thankful for you and our friendship and I am so excited that we get to live in the same state again.

I wouldn't be anywhere close to where I am today without my family. They are my rock and my home base whenever I feel happy, stressed, sad and anything in between. Thank you to my parents for always being there for me when I call after a good or bad day to listen to me talk about however I feel, give me advice and guidance, and have a place ready for me to come home to. And to my siblings, the best friends I could ever ask for. I couldn't have done this without your support. Tillmon, I know I can always count on you for anything, whether it's pressure to run in a race or motivation to working on whatever I'm supposed to be working on. I'm so happy I've been able to go through all of school with you by my side. Angela, I'm so happy to have you as a sister (because even though you are married to my brother, you are my sister). Thank you for being my advocate, shopping partner, and one of my best friends, I'm so lucky you're in my life. Lillie, I can't thank you enough for all you've been to me. You are always there to talk to me about whatever it is I'm happy or sad about. You are my biggest champion, and I couldn't have done this without your encouragement. Garret, our time together is always a highlight and makes me so happy. Thank you for always making me laugh, being the best travel partner, and helping me forget how stressed I am. To my MawMaw, thank you for trying to understand what I do and trying to explain to other people what I do. Our car rides and lunches together are some of my favorite times and I hold them so close to my heart. Grandma and Grandpa, thank you for always answering when I call to chat, for all the help you've provided, your support, and for teaching me some of the most

important things in life. I'm also lucky to have support and encouragement from my aunts, uncles, and cousins, being together are always some of my favorite times.

To Michael, thank you for everything. From listening to me talk about anything and everything, to just being with me. I have loved every second of our adventures together and I am so excited to experience life with you. Your constant love, encouragement, and patience has meant so much to me and has helped me reach the finish line.

And, finally, to Amelia, I don't really know where to start… I guess our visitation weekend would be a good place! Who knew going back to my mom in the hotel room and telling her that I thought I made a friend would be the start of something incredible. Thank you for *always* being there for me, I couldn't ask for a better friend, lab mate, roommate, Galentine, soul sister (etc. etc. etc.). Your encouragement is what has gotten me through some really hard days (and really great ones, too), and I am forever grateful for our friendship. I am so very proud of you and there's no one else I would want to have done this with. I'm so glad you're in my life. Thank you for loving me more than I deserve. I truly could not have done this without you.

Dedication

This thesis is dedicated to my dad, Tim Cook, and my mom, Amy Cook. Thank you for your unwavering support, constant encouragement and always believing in me, even when I couldn't believe in myself.

I could not have done this without the both of you. I love you.

Table of Contents

List of Abbreviations

$Ac(X)^+$	9-(4-X-phenyl)-*N*-methylacridinium salts
AcOH	acetic acid
Ag	silver
Ar	argon
bpy	2,2'-bipyridine
Br	bromide
C	carbon
CEPT	concerted electron proton transfer
Cl	chloride
Cl_2AcOH	dichloroacetic acid
Cl_3AcOH	trichloroacetic acid
ClAcOH	chloroacetic acid
Co	cobalt
CO2	carbon dioxide
Cp*2Fe	decamethylferrocene
Cp2Co	cobaltocene
Cu	copper
CV	cyclic voltammetry
D	Diffusion coefficient
DFT	density functional theory
DI	deoionized
DIPEA	diisopropylamine
DIPEAHPF6	diisopropylammonium hexafluorophosphate
DMF	N,N'-dimethylformamide
DMSO	dimethylsulfoxide
E	potential of electrochemical cell
e^-	electron
EA	elemental analysis
E_p	peak potential
ESI-MS	electrospray ionization mass spectrometry
ET	electron transfer
F	Faraday's constant
F	fluoride
Fc	ferrocene

Fc^+	ferrocenium
Fe	iron
$Fe[TPP]^+$	iron tetraphenylporphyrin
FePc	iron phthalocynanine
$FePMGCl_2$	Fe(N,N′-bis(2-pyridylmethyl)glycine)$(Cl)_2$
FeTPc	iron-4,4',4",4'"-tetracarboxyphthalocyanine
ΔG	Gibb's free energy
H^+	proton
H	hydrogen
ΔH	enthalpy
h	Planck's constant
H_2bupa	bis[(N′-tert-butylurealy)-N-ethyl]-(6-pivalamido-2-pyridylmethyl)-aminato
H_2O	water
H_2O_2	hydrogen peroxide
H_2O_2RR	hydrogen peroxide reduction reaction
i_d	disk current
im^+	3,4-dihydro-2,4,4-trimethyl-1-(trifluoromethylisoquinolinium)
i_r	ring current
K_{AHA}	homoconjugation equilibrium constant
k_B	Boltzmann's constant
k_{cat}	catalytic rate constant
k_{ET}	electron transfer rate constant
k_{H2o2}	rate constant for H2O2 binding
k_{O2}	rate constant for O2 binding
L	axial ligand
LS^{2-}	2,2'-(2,2'-bypyridine-6,6'-diyl)bis(1,1-diphenylethanethiolate))
M	transition metal center
MCD	magnetic circular dichromism
^{Me8}CpFe	octamethylferrocene
MeCN	acetonitrile
MeOH	methanol
$MeSO_3H$	methanesulfonic acid
Mn	manganese
MV^{2+}	methyl viologen

N	nitrogen
N_2	nitrogen
NMR	nuclear magnetic resonance
O	oxygen
O_2	dioxygen
$O_2^{\bullet-}$	superoxide
OEC	Oxygen Evolving Complex
OER	oxygen evolution reaction
ORR	oxygen reduction reaction
PCET	proton coupled electron transfer
Ph_2Phen^{2+}	1,11-diphenyl-6,7-dihydro-5H-[1,4]diazepino[1,2,3,4-lmn][1,10]phenanthroline-4,8-diium bromide
PMG[H]	*N*-*N*′-bis(2-pyridylmethyl)glycine
PT	proton transfer
R	ideal gas law constant
RDE	rotating disk electrochemistry
RDS	rate determining step
RRDE	rotating ring disk electrode
RRDV	rotating ring disk voltammetry
ΔS	entropy
SCE	saturated calomel electrode
SHE	standard hydrogen electrode
T	temperature
TAML	tetraamido macrocyclic ligand
TATP	triacetone triperoxide
TBAAcO	tetrabutylammonium acetate
TBAPF6	tetrabutylammonium hexafluorophosphate
^{tbu}dhbpy[H]$_2$	6,6′-di(3,5-di-*tert*-butyl-2-hydroxybenzene)-2,2′-bipyridine
TEA	triethylamine
TEAHPF6	triethylammonium hexafluorophosphate
TFAH	trifluoroacetic acid
TFEOH	2,2,2-trifluoroethanol
TOF	turn over frequency
TPA	tris-(2-pyridylmethyl)amine
tpy	terpyridine

$tpy^{tbu}pho(H)$	2-([2,2':6',2''-terpyridin]-6-yl)-4,6-di-tert-butylphenol
TsOH	tosic acid
V	volts
ε	molar extinction coefficient
η	overpotential
υ	scan rate

List of Figures

Figure S2.5. CVs of $Fe(PMG)(Cl)_2$ obtained under Ar saturation conditions with (blue trace) and without (black trace) 0.525 M AcOH added.

Figure S2.6. (A) CVs of $Fe(PMG)(Cl)_2$ obtained under Ar saturation conditions with variable AcOH concentrations. (B) Plot of $E_{1/2}$ for $Fe(PMG)(Cl)_2$ against the log of [AcOH] showing the effect of increasing AcOH concentration of $E_{1/2}$.

Figure S2.7. (A) CVs of $[Fe(TPA)(Cl)_2][Cl]$ under Ar saturation conditions with variable AcOH concentration. (B) Plot of $E_{1/2}$ for $[Fe(PMG)(Cl)_2][Cl]$ against the log of [AcOH] showing the effect of increasing AcOH concentration of $E_{1/2}$.

Figure S2.8. (A) Variable scan rate CVs of $Fe(PMG)(Cl)_2$ at low scan rates ranging from 20 (black) to 100 (red) mV/s. (B) Linear fit of variable scan rate data from (A).

Figure S2.9. Rinse test of $Fe(PMG)(Cl)_2$ and AcOH to ensure the observed current response is not due to a species adsorbed to the electrode.

Figure S2.10. Determination of k_{O2} (**A**) CVs of $Fe(PMG)(Cl)_2$ under Ar saturation at 0.1 V/s (black) and O_2 saturation at varying scan rates (**B**) log(υ) vs. E_p-$E_{1/2}$ plot of variable scan rate data in A.

Figure S2.11. Determination of $k_{O2,H+}$ (**A**) CVs of $Fe(PMG)(Cl)_2$ in the presence of 0.525 M AcOH under Ar saturation at 0.1 V/s (black) and O_2 saturation at varying scan rates (**B**) log(υ) vs. E_p-$E_{1/2}$ plot of variable scan rate data in A.

Figure S2.12. Cyclic voltammograms of $Fe(PMG)(Cl)_2$ obtained under Ar saturation conditions with (red) and without (black) 0.1 M buffered TBA(AcO)/AcOH.

Figure S2.13. Linear Sweep Voltammograms of RRDE experiment with 0.5 mM ferrocene at various rotation rates under Ar saturation conditions; ring potential = +1.2 V vs. Ag/AgCl.

Figure S2.14. Linear Sweep Voltammograms of RRDE experiment with $Fe(PMG)(Cl)_2$ at various rotation rates with 0.5 mM $Fe(PMG)(Cl)_2$ and 0.35 M AcOH under Ar (**A**) and O_2 (**B**) saturation conditions; ring potential = 1.2 V vs Ag/AgCl.

Figure S2.15. Levich plots from data obtained from Linear Sweep Voltammograms of $Fe(PMG)(Cl)_2$ (0.5 mM) by RRDE with 0.35 M AcOH under Ar (**A**) and O_2 (**B**) saturation conditions at various rotation rates; ring potential = 1.2 V vs. Ag/AgCl.

Figure S2.16. Koutecky-Levich plots from data obtained from Linear Sweep Voltammograms of $Fe(PMG)(Cl)_2$ (0.5 mM) by RRDE with 0.35 M AcOH under Ar (**A**) and O_2 (**B**) saturation conditions at various rotation rates; ring potential = 1.2 V vs. Ag/AgCl.

Figure S2.17. Calibration curve of H_2O_2 quantification using a $Ti(O)SO_4$ colorimetric assay. (**A**) Serial dilution of urea•H_2O_2 in 50/50 MeCN/H_2O. using the above method. (**B**) Calibration made using a serial dilution of urea•H_2O_2 in 50/50 MeCN/H_2O.

Figure S2.18. H_2O_2 stability test in the presence of $Fe(PMG)(Cl)_2$. UV-vis spectra of $Fe(PMG)(Cl)_2$. (50 μM) and urea•H_2O_2 (1.12 mM) in the presence of 5 mM AcOH after 30 min before (black) and after (red) 0.1 mL $Ti(O)SO_4$ solution was added.

Figure S2.19. UV-vis spectrum of catalytic solution of $Fe(PMG)(Cl)_2$ before (black) and after (red) the addition of 0.1 mL $Ti(O)SO_4$ solution.

Figure S2.20. The calculated R_{fit}/n_{cat} values from stopped-flow spectrochemical experiments with AcOH, Cp^*_2Fe, O_2 with varying $Fe(PMG)(Cl)_2$ concentration.

Figure S2.21. The calculated R_{fit}/n_{cat} values from stopped-flow spectrochemical experiments with AcOH, O_2, and $Fe(PMG)(Cl)_2$ with varying Cp^*_2Fe concentration.

Figure S2.22. The calculated R_{fit}/n_{cat} values from stopped-flow spectrochemical experiments with O_2, Cp^*_2Fe, and $Fe(PMG)(Cl)_2$ with varying AcOH concentration.

Figure S2.23. The calculated R_{fit}/n_{cat} values from stopped-flow spectrochemical experiments with AcOH, Cp^*_2Fe, and $Fe(PMG)(Cl)_2$ with varying O_2 concentration.

Figure S2.24. The calculated R_{fit}/n_{cat} values from stopped-flow spectrochemical experiments with AcOH, Cp^*_2Fe, H_2O_2 with varying $Fe(PMG)(Cl)_2$ concentration.

Figure S2.25. The calculated R_{fit}/n_{cat} values from stopped-flow spectrochemical experiments with H_2O_2, Cp^*_2Fe, and $Fe(PMG)(Cl)_2$ with varying AcOH concentration.

Figure S2.26. The calculated R_{fit}/n_{cat} values from stopped-flow spectrochemical experiments with AcOH, H_2O_2, and $Fe(PMG)(Cl)_2$ with varying Cp^*_2Fe concentration.

Figure S2.27. The calculated R_{fit}/n_{cat} values from stopped-flow spectrochemical experiments with AcOH, Cp^*_2Fe, and $Fe(PMG)(Cl)_2$ with varying H_2O_2 concentration.

Figure S2.28. Example of UV-vis Stopped-Flow spectrochemical data (black) and the fit (red) used for this work. The data was fit with Kinetic Studio 4.0 to a double exponential (2Exp+Mx+C).

Figure S2.29. Spectral changes at 780 nm due to the formation of $[Cp^*_2Fe]^+$ over time with 35 mM AcOH, 4.05 mM O_2, 1.5 mM Cp^*_2Fe. Black: 50 μM $Fe(PMG)(Cl)_2$, red: control.

Figure S2.30. Representative spectral changes at 780 nm due to the formation of $[Cp^*2Fe]^+$ comparing $Fe(PMG)(Cl)_2$ under non-buffered (black) and buffered (red) conditions.

Figure S2.31. The calculated R_{fit}/n_{cat} values from stopped-flow spectrochemical experiments with AcOH, Cp^*_2Fe, O_2, and TBACl with varying $Fe(PMG)(Cl)_2$ concentration.

Figure S2.32. Eyring plot of the stopped-flow spectrochemical experiments with $Fe(PMG)(Cl)_2$ with AcOH.

Figure S2.33. Determination of k_{H2O2} (**A**) CVs of $Fe(PMG)(Cl)_2$ under Ar saturation with 5.4 mM urea•H_2O_2 at 0.1 V/s (black) and 1 V/s (red) at varying scan rates (**B**) log(υ) vs. E_p-$E_{1/2}$ plot of variable scan rate data in A.

Figure S2.34. (A) Spectral changes of $Fe(PMG)(Cl)_2$ (78 μM) with increasing concentrations of AcOH added. (B) Spectral changes of $Fe^{II}(PMG)Cl$ (50 μM) with increasing concentrations of AcOH.

Figure S2.35. Molar extinction plot of $Fe^{II}(PMG)Cl$ (black trace), $Fe^{II}(PMG)Cl$ and 0.58 M AcOH (red trace), and $Fe(PMG)(Cl)_2$ (blue trace) from Figure S2.31.

Figure S2.36. (A) Spectral changes of $Fe^{II}(PMG)Cl$ upon air exposure over time. (B) Change in absorbance at 420, 356, 315, and 255 nm upon air exposure.

Figure S2.37. (A) Spectral changes upon addition of increasing amounts of urea•H2O2 to a 50 μM solution of $Fe^{II}(PMG)Cl$ under N_2 in MeCN. (B) Plot of change in absorbance at 420 nm versus the ratio of [H2O2]:[$Fe^{II}(PMG)Cl$].

Figure S2.38. Spectral changes upon addition of increasing amounts of urea•H_2O_2 to 44 μM $Fe(PMG)(Cl)_2$ in MeCN.

Figure S2.39. ^{1}H-NMR spectrum of 3.2 mM [$Fe^{II}(PMG)Cl$] under N_2 in MeCN-d_3; 600 MHz, Varian.

Figure S2.40. ^{1}H-NMR spectrum of 3.2 mM [$Fe^{II}(PMG)Cl$] + 0.3 M AcOH under N_2 in MeCN-d_3; 600 MHz, Varian. Broad and less well-resolved resonances appear at 114.6 ppm, 107.3 ppm, and 85.5 ppm.

Figure S2.41. ^{1}H-NMR spectrum of 2.9 mM [$Fe(PMG)(Cl)_2$] in MeCN-d_3; 600 MHz, Varian.

Figure 3.1. Molecular structure of Fe(tpy^{tbu}pho)Cl_2 obtained from single-crystal X-ray diffraction studies. Blue = N, red = O, gray = C, green = Cl, orange = Fe; thermal ellipsoids at 50%; hydrogen atoms and non-coordinating solvent omitted for clarity; CCDC 2097186.

Figure 3.2. Comparison of CVs of Fe(tpy$^{\mathbf{tbu}}$pho)Cl_2 under Ar and O_2 saturation conditions with and without 0.0875 M AcOH.

Figure 3.3. The calculated R_{fit}/n_{cat} from stopped-flow spectrochemical experiments where the concentration of O_2 (**A**), Cp^*_2Fe (**B**), AcOH (**C**), and Fe(tpy^{tbu}pho)Cl_2 (**D**), and were each independently varied at 25.5°C in MeCN.

Figure S3.1. (A) UV-vis serial dilution absorbance data obtained from Fe(tpy^{tbu}pho)Cl_2 in a MeCN solution.

Figure S3.2. ESI-MS characterization of Fe(tpy^{tbu}pho)Cl_2.

Figure S3.3. (A) Variable scan rate CVs of Fe(tpy^{tbu}pho)Cl_2 at low scan rates ranging from 0.01 (red) to 0.1 (black) V/s. (B) Linear fit of variable scan rate data from (A).

Figure S3.4. Comparison of CVs of Fe(tpy^{tbu}pho)Cl_2 under Ar and conditions with (red) and without (red) 0.35 M AcOH.

Figure S3.5. Cyclic voltammograms of Fe(tpy^{tbu}pho)Cl_2 with (red) and without (black) TBACl and AcOH (blue) under Ar saturation conditions (A) and Fe(tpy^{tbu}pho)Cl_2 with TBACl (black) and increasing amounts of AcOH (B).

Figure S3.6. Linear sweep voltammograms of RRDE experiment with 0.5 mM Fe(tpy^{tbu}pho)Cl_2 and 0.1 M AcOH under Ar (A) and O_2 (B) saturation conditions; ring potential = 1.2 V vs Ag/AgCl.

Figure S3.7. Levich plots from data obtained from Linear Sweep Voltammograms of Fe(tpy^{tbu}pho)Cl_2 (0.5 mM) by RRDE with 0.1 M AcOH under Ar (A) and O_2 (B) saturation conditions at various rotation rates; ring potential = 1.2 V vs. Ag/AgCl.

Figure S3.8. Koutecky-Levich plots from data obtained from linear sweep voltammograms of Fe(tpy^{tbu}pho)Cl_2 (0.5 mM) by RRDE with 0.1 M AcOH under Ar (A) and O_2 (B) saturation conditions at various rotation rates; ring potential = 1.2 V vs. Ag/AgCl.

Figure S3.9. Representative spectral changes at 778 nm due to the formation of $[Cp^*_2Fe]^+$ comparing catalytic conditions with Fe(tpy^{tbu}pho)Cl_2 (red) versus identical conditions in the absence of Fe(tpy^{tbu}pho)Cl_2 as a control (black).

Figure S3.10. Eyring plot of the stopped-flow data spectrochemical experiments with Fe(tpy^{tbu}pho)Cl_2 in MeCN with AcOH.

Figure S3.11. (**A**) H_2O_2 selectivity testing under catalytic conditions with Fe(tpy^{tbu}pho)Cl_2 and **(B)** identical conditions in the absence of Fe(tpy^{tbu}pho)Cl_2.

Figure S3.12. UV-vis data analyzing the stability of Fe(tpy^{tbu}pho)Cl_2 in the presence of urea•H_2O_2. Conditions: quartz cell with 1 cm pathlength.

Figure S3.13. UV-vis spectral changes upon addition of increasing amounts of urea•H_2O_2 to 25 μM of Fe(tpy^{tbu}pho)Cl_2 in MeCN.

Figure S3.14. Representative spectral changes at 778 nm due to the formation of $[Cp^*_2Fe]^+$ comparing H_2O_2RR catalytic conditions with Fe(tpy^{tbu}pho)Cl_2 (red) versus identical conditions in the absence of Fe(tpy^{tbu}pho)Cl_2 as a control (black).

Figure S3.15. UV-vis data to determine the H2O2RR reaction stoichiometry described above.

Figure S3.16. The calculated R_{fit}/n_{cat} from stopped-flow spectrochemical experiments with Cp^*_2Fe, AcOH, urea•H_2O_2 with varying Fe(tpy^{tbu}pho)Cl_2 concentration at 25.5°C in MeCN.

Figure S3.17. The calculated R_{fit}/n_{cat} from stopped-flow spectrochemical experiments with Cp^*_2Fe, AcOH, Fe(tpy^{tbu}pho)Cl_2, with varying urea•H_2O_2 concentration at 25.5°C in MeCN.

Figure S3.18. The calculated R_{fit}/n_{cat} from stopped-flow experiments with Cp^*_2Fe, Fe(tpy^{tbu}pho)Cl_2, urea•H_2O_2 with varying AcOH concentration at 25.5°C in MeCN.

Figure S3.19. The calculated R_{fit}/n_{cat} from stopped-flow experiments with AcOH, Fe(tpy^{tbu}pho)Cl_2, urea•H_2O_2 with varying Cp^*_2Fe concentration at 25.5°C in MeCN.

Figure S3.20. Representative spectral changes at 778 nm due to the formation of $[Cp^*_2Fe]^+$ comparing Fe(tpy^{tbu}pho)Cl_2 under non-buffered (black) and buffered (red) conditions.

Figure S3.21. Sample variable O_2 concentration data under catalytic conditions. (A) Plots of the average of 5 injections across a series of variable O_2 concentration data under catalytic conditions. (B) Plot of data of all five injections at a single O_2 concentration (1.62×10^{-3} M), the average of those five injections (purple) and the second exponential linear fit of the average (grey).

Figure S3.22. CVs of 0.5 mM [Fe(tpy^{tbu}pho)][OTf]$_2$ under Ar saturation with (red and green traces) and without (black trace) the addition of 0.35 M AcOH.

Figure S3.23. UV-vis spectral changes of 50 μM Fe(tpy^{tbu}pho)Cl_2 upon addition of increasing amounts of AcOH in MeCN.

Figure S3.24. UV-vis spectral changes of 36 μM [Fe(tpy^{tbu}pho)][OTf]$_2$ upon addition of increasing amounts of AcOH in MeCN.

Figure S3.25. Molar extinction plot of Fe(tpy^{tbu}pho)Cl_2 and [Fe(tpy^{tbu}pho)][OTf]$_2$ upon exposure to 0.35 M AcOH in MeCN from **Figures S23** and **S24**.

Figure S3.26. (A) UV-vis spectral changes upon exposure of 36 μM [Fe^{II}(tpy^{tbu}pho)][OTf] to O_2 over the course of 1 h in MeCN (B) molar extinction plot of [Fe^{II}(tpy^{tbu}pho)][OTf] under N_2 and 1 h after O_2 exposure and [Fe(tpy^{tbu}pho)][OTf]$_2$

Figure S3.27. Overlaid 1H-NMR spectra of [Fe(tpy^{tbu}pho)][OTf]$_2$ (bottom, red), [Fe^{II}(tpy^{tbu}pho)][OTf] under N_2 (second from bottom, green) and exposed to O_2 after 2.5 h (third from bottom, cyan) and 18 h (top, purple). Varian, 600 MHz, MeCN-d_3.

Figure S3.28. Overlaid 1H-NMR spectra of 8.6 mM [Fe(tpy^{tbu}pho)][OTf]$_2$ (bottom, red) and 10.6 mM [Fe^{II}(tpy^{tbu}pho)][OTf] under N_2 (second from bottom, green) and exposed to O_2 after 2.5 h (third from bottom, cyan) and 18 h (top, purple) from 37 to 72 ppm. Varian, 600 MHz, MeCN-d_3.

Figure S3.29. Overlaid 1H-NMR spectra of 8.6 mM [Fe(tpy^{tbu}pho)][OTf]$_2$ (bottom, red), 10.6 mM [Fe^{II}(tpy^{tbu}pho)][OTf] under N_2 (second from bottom, green) and exposed to O_2 after 2.5 h (third from bottom, cyan) and 18 h (top, purple) from 10 to 30 ppm. Varian, 600 MHz, MeCN-d_3.

Figure 4.1. Summary of the work described here.

Figure 4.2. (A) Structure of **1** Mn($^{p\text{-}tbu}$dhbpy)Cl, (B) structure of **2** Mn(^{nPr}dhbpy)Cl, (C) Molecular structure of Mn(^{nPr}dhbpy)Cl **2** from single crystal X-ray diffraction studies showing the (D) dimeric solid-state species. Purple = Mn, red = O, green = Cl, gray = C; thermal ellipsoids 50%, H atoms and disordered atoms omitted for clarity. CCDC 2255849.

Figure 4.3. (A) CVs of Mn($^{p\text{-}tbu}$dhbpy)Cl **1** under Ar and O_2 with and without 10 mM DIPEAHPF_6/DIPEA present. (B) CVs of Mn(^{nPr}dhbpy)Cl **2** under Ar and O_2 with and without 10 mM DIPEAHPF_6/DIPEA present.

Figure 4.4. Change in absorbance at 780 nm over time as a result of the formation of $[Cp^*_2Fe]^+$ by ORR catalyzed by Mn($^{p\text{-}tbu}$dhbpy)Cl **1** (**A**) with $DIPEAHPF_6$ (red) and $DIPEAHPF_6$/DIPEA (blue) and Mn(^{nPr}dhbpy)Cl **2** (**B**) with $DIPEAHPF_6$ (red) and $DIPEAHPF_6$/DIPEA (blue). Black: buffered control.

Figure 4.5. Free energy diagram from DFT methods showing key thermodynamic intermediates in the production of H_2O_2 by complex **2**. Diagram considers the operating potential of catalysis to be –0.55 V vs $Fc^{+/0}$ and red indicates CEPT steps. DIPEA = A and $DIPEAH^+$ = HA^+.

Figure S4.1. (A) UV-vis serial dilution absorbance data from Mn($^{p\text{-}tbu}$dhbpy)Cl **1** in MeCN solution.

Figure S4.2. UV-vis serial dilution of Mn(^{nPr}dhbpy)Cl **2** in MeCN solution.

Figure S4.3. Molecular structure of $DIPEAHPF_6$ from single crystal X-ray diffraction studies. Blue = N, gray = C, white = H, green = F, orange; thermal ellipsoids at 50%, H atoms (except N–H) and disordered F atoms omitted for clarity. CCDC 2255850.

Figure S4.4. ^{1}H-NMR spectrum of $DIPEAHPF_6$ in MeCN-d_3; Varian 600 MHz.

Figure S4.5. $^{13}C\{^1H\}$-NMR spectrum of $DIPEAHPF_6$ in MeCN-d_3; Varian 150 MHz.

Figure S4.6. ^{1}H-NMR spectra of $DIPEAHPF_6$ (purple), DIPEA (blue), $TEAHPF_6$ (green), and TEA (red) used to estimate the pK_a of $DIPEAHPF_6$ in MeCN. MeCN-d_3; Varian 600 MHz.

Figure S4.7. ^{1}H NMR of titration of TEA into a 0.02 M solution of $DIPEAHPF_6$ for estimation of pK_a of $DIPEAHPF_6$ in MeCN. MeCN-d_3; Varian 600 MHz.

Figure S4.8. (A) CVs of Mn($^{p\text{-}tbu}$dhbpy)Cl **1** at variable scan rates ranging from 0.05 V/s (black) to 2 V/s (red) under Ar saturation conditions. (B) Linear fit data from A showing that Mn($^{p\text{-}tbu}$dhbpy)Cl is a diffusion-limited current response.

Figure S4.9. (A) CVs of Mn($^{p\text{-}tbu}$dhbpy)Cl **1** under Ar (black), O_2 (red) and with 10 mM $DIPEAHPF_6$ under Ar saturation (green). (B) CVs from A and catalytic trace shown (blue) with Mn($^{p\text{-}tbu}$dhbpy)Cl 1 and 10 mM $DIPEAHPF_6$ under O_2 saturation.

Figure S4.10. (A) CVs of Mn($^{p\text{-}tbu}$dhbpy)Cl **1** under Ar (black), O_2 (red) and with 10 mM buffer ($DIPEAHPF_6$/DIPEA) under Ar saturation (green). (B) CVs from A with catalytic trace shown (blue) with Mn($^{p\text{-}tbu}$dhbpy)Cl and 10 mM $DIPEAHPF_6$/DIPEA under O_2 saturation.

Figure S4.11. CVs of Mn($^{p\text{-}tbu}$dhbpy)Cl **1** with increasing $DIPEAHPF_6$ concentrations under Ar saturation conditions with 10 mM DIPEA.

Figure S4.12. Control CVs of Mn($^{p\text{-}tbu}$dhbpy)Cl **1** with and without the presence of 10 mM DIPEA.

Figure S4.13. CVs of Mn($^{p\text{-}tbu}$dhbpy)Cl **1** (black trace) in the presence of 0.1 M TBACl (red trace) with increasing concentrations of DIPEA added.

Figure S4.14. CVs of Mn($^{p\text{-}tbu}$dhbpy)Cl **1** (black trace) in the presence of 0.1 M TBACl (red trace) and 10 mM DIPEA with increasing concentrations of $DIPEAHPF_6$ under Ar saturation.

Figure S4.15. A) CVs of Mn(^{nPr}dhbpy)Cl **2** at variable scan rates ranging from 0.05 V/s (black) to 2 V/s (red) under Ar saturation conditions. (B) Linear fit data from A showing that Mn(^{nPr}dhbpy)Cl is a diffusion-limited current response.

Figure S4.16. CVs of Mn(^{nPr}dhbpy)Cl **2** under Ar (black), O_2 (red) and with 10 mM $DIPEAHPF_6$ under Ar saturation (green).

Figure S4.17. (A) CVs of Mn(^{nPr}dhbpy)Cl **2** under Ar with increasing amounts of $DIPEAHPF_6$ added.

Figure S4.18. (A) CVs of Mn(^{nPr}dhbpy)Cl **2** under Ar (black), O_2 (red) and with 10 mM $DIPEAHPF_6$/DIPEA under Ar saturation (green). (B) CVs from A with catalytic trace shown (blue) with Mn(^{nPr}dhbpy)Cl and 10 mM $DIPEAHPF_6$/DIPEA under O_2 saturation.

Figure S4.19. Comparison of electrocatalytic ORR by Mn(^{nPr}dhbpy)Cl **2** with 10 mM $DIPEAHPF_6$ with (red) and without (black) the presence of 10 mM DIPEA (traces from **Figure S16** and **S18** for black and red traces, respectively).

Figure S4.20. CVs of Mn(^{nPr}dhbpy)Cl **2** with increasing $DIPEAHPF_6$ concentrations under Ar saturation conditions with 10 mM DIPEA.

Figure S4.21. Control CVs of Mn(^{nPr}dhbpy)Cl **2** with and without the presence of 10 mM DIPEA.

Figure S4.22. CVs of Mn(^{nPr}dhbpy)Cl **2** (black trace) in the presence of 0.1 M TBACl (red trace) and DIPEA (green trace).

Figure S4.23. CVs of Mn(^{nPr}dhbpy)Cl **2** (black trace) in the presence of 0.1 M TBACl (red trace) and increasing amounts of $DIPEAHPF_6$.

Figure S4.24. (A) Control CVs of 24 mM $DIPEAHPF_6$ under Ar (black) and O_2 (red trace). (B) Control CVs of 24 mM $DIPEAHPF_6$ and 25 mM DIPEA under O_2.

Figure S4.25. Calibration curve of H_2O_2 quantification using a $Ti(O)SO_4$ colorimetric assay. (A) Serial dilution of urea•H_2O_2 using the method described above. (B) Calibration curve made from data in A.

Figure S4.26. H_2O_2 product quantification of ORR by Mn($^{p\text{-}tbu}$dhbpy)Cl **1** with $DIPEAHPF_6$. (A) UV-vis spectrum of extracted solution after 3 min of reaction time before (black) and after (red) 0.1 mL of 0.1 M $Ti(O)SO_4$ solution was added. (B) Corrected spectra (red – black trace from A).

Figure S4.27. H_2O_2 product quantification of ORR by Mn(^{nPr}dhbpy)Cl **2** with $DIPEAHPF_6$. (A) UV-vis spectrum of extracted solution before (black) and after (red) 0.1 mL of 0.1 M $Ti(O)SO_4$ solution was added, 20 min. (B) Corrected spectra (red – black trace from A).

Figure S4.28. Stability test of urea•H_2O_2 in the presence of Mn($^{p\text{-}tbu}$dhbpy)Cl **1**, $DIPEAHPF_6$, and O_2. (A) UV-vis spectra of an extracted sample after 12 minutes of reaction time before (black) and after (red) the addition of 0.1 mL of 0.1 M $Ti(O)SO_4$. (B) Corrected UV-vis spectra (red – black trace from A) of H_2O_2 only (black) and after 12 min (red).

Figure S4.29. Stability test of urea•H_2O_2 in the presence of Mn(^{nPr}dhbpy)Cl **1**, $DIPEAHPF_6$, and O_2. (A) UV-vis spectra of an extracted sample after 20 minutes of reaction time before (black) and after (red) the addition of 0.1 mL of 0.1 M $Ti(O)SO_4$. (B) Corrected UV-vis spectra (red – black traces from A) at 0 min (black trace) and after 20 min (red).

Figure S4.30. H_2O_2 product quantification of ORR by Mn($^{p\text{-}tbu}$dhbpy)Cl **1** with $DIPEAHPF_6$ and DIPEA. (A) UV-vis spectrum of extracted solution before (black) and after (red) 0.1 mL of 0.1 M $Ti(O)SO_4$ solution was added, 15 s. (B) Corrected spectra (red – black trace from A) for 15, 90, and 720 s aliquots.

Figure S4.31. H_2O_2 product quantification of ORR by Mn(^{nPr}dhbpy)Cl **2** with $DIPEAHPF_6$ and DIPEA. (A) UV-vis spectra of extracted solution before (black) and after (red) 0.1 mL of 0.1 M $Ti(O)SO_4$ solution was added, 15 s. (B) Corrected spectra (red – black trace from A) for 15, 120, and 720 s aliquots.

Figure S4.32. Stability test of urea•H_2O_2 in the presence of Mn($^{p\text{-}tbu}$dhbpy)Cl **1**, $DIPEAHPF_6$, DIPEA, and O_2. (A) UV-vis spectra before (black) and after (red) the addition of 0.1 mL of 0.1 M $Ti(O)SO_4$ to an extracted aliquot after 30 s. (B) Corrected UV-vis spectra (red – black traces) of H_2O_2 only (black) and after 30 (red) and 105 s (blue).

Figure S4.33. Stability test of urea•H_2O_2 in the presence of Mn(^{nPr}dhbpy)Cl **2**, DIPEAHPF$_6$, DIPEA, and O_2. (A) UV-vis spectra before (black) and after (red) the addition of 0.1 mL of 0.1 M Ti(O)SO_4 to an extracted aliquot after 15 s. (B) Corrected UV-vis spectra (red – black trace from A) of H_2O_2 only (black) and after 15 (red), 150 (green), and 540 s (blue).

Figure S4.34. Stability test of urea•H_2O_2 in the presence of Mn($^{p\text{-}tbu}$dhbpy)Cl **1**, DIPEAHPF$_6$, DIPEA, and FeCp*$_2$ (A) before (black trace) and after (red trace) the addition of 0.1 mL of 0.1 M Ti(O)SO_4 to an extracted aliquot after 30 s. (B) Corrected UV-vis spectra (red – black from A) after 30 s (black), 120 s (red), 600 s (green), and H_2O_2 only (blue).

Figure S4.35. Stability test of urea•H_2O_2 in the presence of Mn(^{nPr}dhbpy)Cl **2**, DIPEAHPF$_6$, DIPEA, and FeCp*$_2$ (A) before (black trace) and after (red trace) the addition of 0.1 mL of 0.1 M Ti(O)SO_4 to an extracted aliquot after 30 s. (B) Corrected UV-vis spectra (red – black from A) after 30 s (black), 120 s (red), 600 s (green), and H_2O_2 only (blue).

Figure S4.36. The calculated R_{fit}/n_{cat} values from stopped-flow spectrochemical experiments with DIPEAHPF$_6$, O_2, and Cp*$_2$Fe with varying Mn($^{p\text{-}tbu}$dhbpy)Cl **1** concentration.

Figure S4.37. The calculated R_{fit}/n_{cat} values from stopped-flow spectrochemical experiments with Mn($^{p\text{-}tbu}$dhbpy)Cl **1**, DIPEAHPF$_6$, and Cp*$_2$Fe with varying O_2 concentration.

Figure S4.38. The calculated R_{fit}/n_{cat} values from stopped-flow spectrochemical experiments with Mn($^{p\text{-}tbu}$dhbpy)Cl **1**, O_2, and Cp*$_2$Fe with varying DIPEAHPF6 concentration.

Figure S4.39. The calculated R_{fit}/n_{cat} values from stopped-flow spectrochemical experiments with Mn($^{p\text{-}tbu}$dhbpy)Cl **1**, O_2, and DIPEAHPF$_6$ with varying Cp*$_2$Fe concentration.

Figure S4.40. The calculated R_{fit}/n_{cat} values from stopped-flow spectrochemical experiments with DIPEAHPF$_6$, DIPEA, O_2, and Cp*$_2$Fe with varying Mn($^{p\text{-}tbu}$dhbpy)Cl **1** concentration.

Figure S4.41. The calculated R_{fit}/n_{cat} values from stopped-flow spectrochemical experiments with Mn($^{p\text{-}tbu}$dhbpy)Cl **1**, DIPEAHPF$_6$, DIPEA, and Cp*$_2$Fe with varying O_2 concentration.

Figure S4.42. The calculated R_{fit}/n_{cat} values from stopped-flow spectrochemical experiments with Mn($^{p\text{-}tbu}$dhbpy)Cl **1**, O_2, DIPEA, and Cp*$_2$Fe with varying DIPEAHPF$_6$:DIPEA ratio.

Figure S4.43. The calculated R_{fit}/n_{cat} values from stopped-flow spectrochemical experiments with Mn($^{p\text{-}tbu}$dhbpy)Cl **1**, O_2, and Cp*$_2$Fe with varying buffer (DIPEAHPF$_6$ and DIPEA, 1:1 ratio) concentration.

Figure S4.44. The calculated R_{fit}/n_{cat} values from stopped-flow spectrochemical experiments with Mn($^{p\text{-}tbu}$dhbpy)Cl **1**, DIPEAHPF$_6$, DIPEA, and O_2 with varying Cp*$_2$Fe concentration.

Figure S4.45. The calculated initial ORR rate from stopped-flow spectrochemical experiments with DIPEAHPF$_6$, O_2, Cp*$_2$Fe with varying Mn(^{nPr}dhbpy)Cl **2** concentration.

Figure S4.46. The calculated initial ORR rate from stopped-flow spectrochemical experiments with, Mn(^{nPr}dhbpy)Cl **2**, O_2, Cp*$_2$Fe with varying DIPEAHPF$_6$ concentration.

Figure S4.47. The calculated initial ORR rate from stopped-flow spectrochemical experiments with, Mn(^{nPr}dhbpy)Cl **2**, DIPEAHPF$_6$, O_2, with varying Cp*$_2$Fe concentration.

Figure S4.48. The calculated initial ORR rate from stopped-flow spectrochemical experiments with, Mn(^{nPr}dhbpy)Cl **2**, DIPEAHPF$_6$, Cp*$_2$Fe with varying O_2, concentration.

Figure S4.49. The calculated R_{fit}/n_{cat} values from stopped-flow spectrochemical experiments with DIPEAHPF$_6$, DIPEA, O_2, and Cp*$_2$Fe with varying Mn(^{nPr}dhbpy)Cl **2** concentration.

Figure S4.50. The calculated R_{fit}/n_{cat} values from stopped-flow spectrochemical experiments with Mn(^{nPr}dhbpy)Cl **2**, DIPEAHPF$_6$, DIPEA, and O_2 with varying Cp*$_2$Fe concentration.

Figure S4.51. The calculated R_{fit}/n_{cat} values from stopped-flow spectrochemical experiments with Mn(^{nPr}dhbpy)Cl **2**, O_2, and Cp^*_2Fe with varying buffer ($DIPEAHPF_6$ and DIPEA, 1:1 ratio) concentration.

Figure S4.52. The calculated R_{fit}/n_{cat} values from stopped-flow spectrochemical experiments with Mn(^{nPr}dhbpy)Cl **2**, O_2, and Cp^*_2Fe with varying $DIPEAHPF_6$:DIPEA ratio.

Figure S4.53. The calculated R_{fit}/n_{cat} values from stopped-flow spectrochemical experiments with Mn(^{nPr}dhbpy)Cl **2**, $DIPEAHPF_6$, DIPEA, and Cp^*_2Fe with varying O_2 concentration.

Figure S4.54. (A) Representative trace of time versus absorbance at 780 nm for ORR catalyzed by Mn($^{p\text{-}tbu}$dhbpy)Cl **1** with $DIPEAHPF_6$/DIPEA and (B) the 1Exp+Mx+C fit (red) and residual (blue) used for data analysis using the Kinetic Studio 4.0 software.

Figure S4.55. (A) Representative trace of time versus absorbance at 780 nm for ORR catalyzed by Mn(^{nPr}dhbpy)Cl **2** with $DIPEAHPF_6$/DIPEA and (B) the 1Exp+Mx+C fit (red) and residual (blue) used for data analysis using the Kinetic Studio 4.0 software.

Figure S4.56. (A) Representative trace of time versus absorbance at 780 nm for ORR catalyzed by Mn($^{p\text{-}tbu}$dhbpy)Cl **1** with $DIPEAHPF_6$ and (B) the 1Exp+Mx+C fit (red) and residual (blue) used for data analysis using the Kinetic Studio 4.0 software.

Figure S4.57. (A) Representative trace of time versus absorbance at 780 nm for ORR catalyzed by Mn(^{nPr}dhbpy)Cl **2** with $DIPEAHPF_6$ and (B) the initial Linear fit (red) and residual (blue) used for data analysis using the Kinetic Studio 4.0 software.

Figure S4.58. (A) UV-vis of spectra of 23 μM Mn($^{p\text{-}tbu}$dhbpy)Cl **1** with increasing amounts of DIPEA in MeCN (B) difference spectrum of the final titration point (blue – green traces).

Figure S4.59. (A) UV-vis of spectra of 26.8 μM Mn(^{nPr}dhbpy)Cl **2** with increasing amounts of DIPEA in MeCN (B) difference spectrum of the final titration point (blue – green traces).

Figure S4.60. UV-vis of spectra of 80 μM Mn($^{p\text{-}tbu}$dhbpy)Cl **1** with increasing amounts of $DIPEAHPF_6$.

Figure S4.61. (A) UV-vis spectra of 80 μM Mn(^{nPr}dhbpy)Cl **2** with increasing amounts of $DIPEAHPF_6$ in MeCN.

Figure S4.62. (A) UV-vis spectra of an 80 μM solution of Mn($^{p\text{-}tbu}$dhbpy)Cl **1** with increasing amounts of $CoCp_2$ in MeCN under N_2. (B) Absorbance at 515 nm versus equivalents of $CoCp_2$ relative to [**1**].

Figure S4.63. (A) UV-vis spectra of 80 μM solution of Mn($^{p\text{-}tbu}$dhbpy)Cl **1** in MeCN (black) under N_2 with 1.1 equiv of $CoCp_2$ (red) and after being exposed to air for 30 min (blue). (B) Time versus absorbance at 515 nm upon exposure of a 80 μM solution of Mn($^{p\text{-}tbu}$dhbpy)Cl with 1.1 equiv $CoCp_2$ to air.

Figure S4.64. (A) UV-vis spectra of 80 μM solution of Mn($^{p\text{-}tbu}$dhbpy)Cl **1** in MeCN (black) under N_2 with 1.1 equiv of $CoCp_2$ and 19.7 mM DIPEAHPF6/DIPEA (red) and after being exposed to air for 8 min (blue). (B) Time versus absorbance at 515 nm upon exposure of a 80 μM solution of Mn($^{p\text{-}tbu}$dhbpy)Cl with 1.1 equiv $CoCp_2$ and 19 mM $DIPEAHPF_6$/DIPEA to air.

Figure S4.65. (A) UV-vis spectra of 80 μM solution of Mn($^{p\text{-}tbu}$dhbpy)Cl **1** in MeCN (black) under N_2 with 1.1 equiv of $CoCp_2$ and 19.7 mM $DIPEAHPF_6$ (red) and after being exposed to air for 25 min (blue). (B) Time versus absorbance at 515 nm upon exposure of a 80 μM solution of Mn($^{p\text{-}tbu}$dhbpy)Cl with 1.1 equiv $CoCp_2$ and 19.7 mM $DIPEAHPF_6$ to air.

Figure S4.66. (A) UV-vis spectra of 80 μM solution of Mn($^{p\text{-}tbu}$dhbpy)Cl **1** in MeCN (black) under N_2 with 1.1 equiv of $CoCp_2$ and 19 mM DIPEA (red) and after being exposed to air for 15 min

(blue). (B) Time versus absorbance at 515 nm upon exposure of a 80 μM solution of Mn($^{p\text{-}tbu}$dhbpy)Cl with 1.1 equiv $CoCp_2$ and 19 mM DIPEA to air.

Figure S4.67. Overlay of data involving Mn($^{p\text{-}tbu}$dhbpy)Cl **1** from **Figs S63-S66** after samples were allowed to react with air completely.

Figure S4.68. UV-vis spectra of 80 μM Mn($^{p\text{-}tbu}$dhbpy)Cl **1** with (red) and without (black) 1 equiv TBAOH•30H_2O and with of 10 mM buffer (1:1 DIPEAHPF_6:DIPEA) in the presence of 1 equiv TBAOH•30H_2O (blue).

Figure S4.69. (A) UV-vis spectra of an 80 μM solution of Mn(^{nPr}dhbpy) **2** with increasing amounts of $CoCp_2$ in MeCN under N_2. (B) Absorbance at 515 nm versus equivalents of $CoCp_2$ relative to [**2**].

Figure S4.70. (A) UV-vis spectra of 80 μM solution of Mn(^{nPr}dhbpy)Cl **2** in MeCN (black) under N_2 with 1.1 equiv of $CoCp_2$ (red) and after being exposed to air for 70 min (blue). (B) Time versus absorbance at 515 nm upon exposure of an 80 μM solution of Mn(^{nPr}dhbpy)Cl with 1.1 equiv $CoCp_2$ to air.

Figure S4.71. (A) UV-vis spectra of 80 μM solution of Mn(^{nPr}dhbpy)Cl **2** in MeCN (black) under N_2 with 1.1 equiv of $CoCp_2$ and 10 mM DIPEAHPF_6/DIPEA (red) and after being exposed to air for 60 min (blue). (B) Time versus absorbance at 515 nm upon exposure of an 80 μM solution of Mn(^{nPr}dhbpy)Cl with 1.1 equiv $CoCp_2$ and 10 mM DIPEAHPF_6/DIPEA to air.

Figure S4.72. (A) UV-vis spectra of 80 μM solution of Mn(^{nPr}dhbpy)Cl **2** in MeCN (black) under N_2 with 1.1 equiv of $CoCp_2$ and 10 mM DIPEAHPF_6 (red) and after being exposed to air for 110 min (blue). (B) Time versus absorbance at 515 nm upon exposure of an 80 μM solution of Mn(^{nPr}dhbpy)Cl with 1.1 equiv $CoCp_2$ and 10 mM DIPEAHPF_6 to air.

Figure S4.73. (A) UV-vis spectra of 80 μM solution of Mn(^{nPr}dhbpy)Cl **2** in MeCN (black) under N_2 with 1.1 equiv of $CoCp_2$ and 10 mM DIPEA (red) and after being exposed to air for 60 min (blue). (B) Time versus absorbance at 515 nm upon exposure of an 80 μM solution of Mn(^{nPr}dhbpy)Cl with 1.1 equiv $CoCp_2$ and 10 mM DIPEA to air.

Figure S4.74. Overlay of data involving Mn(^{nPr}dhbpy)Cl **2** from **Figs S70-S73** after samples were allowed to react with air completely.

Figure S4.75. UV-vis spectra of 80 μM Mn(^{nPr}dhbpy)Cl **2** with (red) and without (black) 1 equiv TBAOH•30H_2O and with of 10 mM buffer (1:1 DIPEAHPF_6:DIPEA) in the presence of 1 equiv TBAOH•30H_2O (blue).

Figure S4.76. (A) UV-vis titration of [$CoCp_2$][PF_6] in MeCN. Conditions: [$CoCp_2$][PF_6] = 1.97 x 10^{-4}, 1.64 x 10^{-4}, 1.37 x 10^{-4}, 1.14 x 10^{-4}, 9.50 x 10^{-5}, 7.91 x 10^{-5}, 6.59 x 10^{-5}, 5.50 x 10^{-5} M; 1 cm pathlength cuvette.

Figure S4.77. Free energy diagram of ORR by Mn(^{nPr}dhbpy)Cl **2** to H_2O.

Figure 5.1. Summary of previously reported organic-based catalysts for the ORR and the catalyst (**im$^+$**) described here.

Figure 5.2. CVs of **im$^+$** under Ar and O_2 saturation conditions with and without acid. Conditions

Figure 5.3. Formation of [Cp^*_2Fe]$^+$ at 780 nm from ORR catalyzed by **im$^+$** (red trace) and control (black trace).

Figure S5.1. (A) CVs of **im$^+$** under Ar saturation at variable scan rates. (B) Logarithm of scan rate versus reduction peak potential from CVs in (A).

Figure S5.2. (A) CVs of **im$^+$** under Ar saturation at varying concentrations. (B) Logarithm of **im$^+$** concentration versus the reduction peak potential in (A).

Figure S5.3. (A) CVs of **im$^+$** under O_2 saturation at variable scan rates. (B) Logarithm of scan rate versus reduction peak potential from CVs in (A).

Figure S5.4. (A) CVs of **im$^+$** under O_2 saturation at varying concentrations. (B) Logarithm of im+ concentration versus the reduction peak potential in (A).

Figure S5.5. (A) CVs of **im$^+$** under Ar (black) and O_2 (red) saturation with 0.065 M TFAH added (green). (B) First derivative of current density of **im**$^+$ under Ar saturation (from black trace in A)

Figure S5.6. (A) CVs of **im$^+$** under Ar saturation in the presence of 0.261 M TFAH at variable scan rates. (B) Logarithm of scan rate versus reduction peak potential from CVs in (A).

Figure S5.7. (A) CVs of **im$^+$** under Ar saturation in the presence of 0.261 M TFAH at varying concentrations. (B) Logarithm of **im$^+$** concentration versus the reduction peak potential in (A).

Figure S5.8. Rinse test of **im$^+$** and TFAH. CV of TFAH under O_2 saturation (black trace), **im$^+$** under catalytic conditions (red trace), and rinse test (green trace).

Figure S5.9. CVs of **im$^+$** under catalytic conditions with variable **im$^+$** concentrations.

Figure S5.10. CVs of **im$^+$** under catalytic conditions with variable TFAH concentrations.

Figure S5.11. CVs of **im$^+$** under catalytic conditions with variable O_2 concentrations.

Figure S5.12. CVs of **im$^+$** with and without added 4.25 mM urea•H_2O_2 under Ar and O_2 saturation.

Figure S5.13. (A) CVs of **im$^+$** in the presence of 4.25 mM urea•H_2O_2 under Ar and O_2 saturation with added 0.261 M TFAH. (B) CVs of **im$^+$** in the presence of 4.25 mM urea•H_2O_2 with added 0.261 M TFAH under O_2 saturation.

Figure S5.14. Linear sweep voltammograms of RRDE experiment with 0.5 mM im+ and 0.1 M TFAH under Ar (A) and air (B) saturation conditions; ring potential = 1.2 V vs Ag/AgCl.

Figure S5.15. (A) Levich and Koutecky-Levich (B) plots from data obtained from linear sweep voltammograms of **im$^+$** (0.5 mM) by RRDE with 0.1 M TFAH under Ar saturation conditions at various rotation rates; ring potential = 1.2 V vs. Ag/AgCl.

Figure S5.16. (A) Levich and Koutecky-Levich (B) plots from data obtained from linear sweep voltammograms of **im$^+$** (0.5 mM) by RRDE with 0.1 M TFAH under air saturation conditions at various rotation rates; ring potential = 1.2 V vs. Ag/AgCl.

Figure S5.17. Change in absorbance at 780 nm over time as a result of the formation of $[Cp^*_2Fe]^+$ by ORR catalyzed by **im$^+$** with TFAH (black trace), example of 1Exp + Mx + C fit in Kinetic Studio 4.0 (red trace), and residual fit (blue trace).

Figure S5.18. Calculated R_{fit}/n_{cat} values from stopped-flow spectrochemical experiments with TFAH, O_2, and Cp^*_2Fe with varying **im$^+$** concentration.

Figure S5.19. Calculated R_{fit}/n_{cat} values from stopped-flow spectrochemical experiments with **im$^+$**, TFAH, Cp^*_2Fe with varying O_2 concentration.

Figure S5.20. Calculated R_{fit}/n_{cat} values from stopped-flow spectrochemical experiments with **im$^+$**, O_2, Cp^*_2Fe with varying TFAH concentration.

Figure S5.21. Calculated R_{fit}/n_{cat} values from stopped-flow spectrochemical experiments with **im$^+$**, TFAH, O_2 with varying Cp^*_2Fe concentration.

Figure S5.22. H_2O_2 product quantification of ORR by **im$^+$** with TFAH after 2 min. (A) UV-vis spectra of extracted solution before (black) and after (red) 0.1 mL of 0.1 M Ti(O)SO_4 solution was added. (B) Corrected spectra (red – black trace from A).

Figure S5.23. Stability test of urea•H_2O_2 in the presence of **im$^+$**, TFAH, and O_2 (A) before (black trace) and after (red trace) the addition of 0.1 mL of 0.1 M Ti(O)SO4 to an extracted aliquot. (B) Corrected UV-vis spectra (red – black from A) after 0 s (red) and 2 min (blue) with the H_2O_2 stock (black).

Figure S5.24. Stability test of urea•H_2O_2 in the presence of **im$^+$**, TFAH, and Cp^*_2Fe (A) before (black trace) and after (red trace) the addition of 0.1 mL of 0.1 M Ti(O)SO_4 to an extracted aliquot after 2 min. (B) Corrected UV-vis spectra (red – black from A) after 2 min (red) and H_2O_2 only (black).

Figure S5.25. (A) spin density plots (0.025 iso) and (B) Kohn-Sham Orbitals (0.05 iso) of the neutral radical **im^0** (S = ½) showing localization at C with contributions from N. Generated from the EPR calculation at the ωB97M-D4/def2-TZVPPD level of theory.

Figure S5.26. (A) spin density plots (0.025 iso) and (B) Kohn-Sham Orbitals (0.05 iso) of the neutral radical $C(CF_3)$–OH species (S = ½) showing localization at N. Generated from the EPR calculation at the ωB97M-D4/def2-TZVPPD level of theory.

Figure 6.1. Summary of the work described here, note that a simplified representation of the equilibrium dimerization reaction is depicted.

Figure 6.2. Molecular structure of **Ph_2Phen^{2+}** obtained from single-crystal X-ray diffraction studies.

Figure 6.3. CVs of **Ph_2Phen^{2+}** under catalytic conditions with ClAcOH (black), Cl_2AcOH (red), Cl_3AcOH (green), and TFAH (blue) as proton sources.

Figure 6.4. Change in absorbance at 780 nm over time as a result of the formation of $[Cp^*_2Fe]^+$ by ORR catalyzed by **Ph_2Phen^{2+}** with ClAcOH (red), TFAH (green), and TFAH control (black).

Figure 6.5. Proposed off-cycle dimer species implied by mechanistic data. A peroxo subunit bridges two equiv of **Ph_2Phen^{2+}** at the 4-position of a pyridine subunit.

Figure S6.1. (A) UV-vis serial dilution absorbance data from **Ph_2Phen^{2+}** in MeCN solution.

Figure S6.2. ^{1}H-NMR spectrum of Ph_2Phen^{2+} in MeOD-d_4; Varian 600 MHz.

Figure S6.3. $^{13}C\{^1H\}$ NMR of Ph_2Phen^{2+} in MeOD-d_4; Varian 150 MHz.

Figure S6.4. CV of **Ph_2Phen^{2+}** under Ar.

Figure 6.S5. (A) CVs of **Ph_2Phen^{2+}** under Ar saturation at various scan rates. (B) Square root of scan rate versus current density in (A).

Figure S6.6. (A) CVs of **Ph_2Phen^{2+}** under O_2 saturation at various scan rates. (B) Logarithm of the scan rate versus the reduction peak potential in (A).

Figure S6.7. (A) CVs of **Ph_2Phen^{2+}** under O_2 saturation at varying concentrations. (B) Logarithm of **Ph_2Phen^{2+}** concentration versus the reduction peak potential in (A).

Figure S6.8. CVs of Ph_2Phen^{2+} with and without added 6.7 mM urea•H_2O_2 under Ar and O_2 saturation.

Figure S6.9. (A) CVs of **Ph_2Phen^{2+}** under Ar (black), O_2 (red) and with 0.1 M TFAH under Ar saturation (green). (B) CVs from A and catalytic trace shown (blue) with Ph_2Phen^{2+} and 0.1 M TFAH under O_2 saturation.

Figure S6.10. CVs of **Ph_2Phen^{2+}** under catalytic conditions with 0.13 M TFAH at 0.1 V/s (black) and 0.8 V/s (red).

Figure S6.11. Rinse test of **Ph_2Phen^{2+}** and TFAH. Ph2Phen2+ under catalytic conditions (black trace), rinse test (red trace), and CV of TFAH under O_2 saturation (green trace).

Figure S6.12. (A) CVs of **Ph_2Phen^{2+}** under catalytic conditions with variable **Ph_2Phen^{2+}** concentrations. (B) Logarithm of **Ph_2Phen^{2+}** concentration versus the logarithm of current density from (A).

Figure S6.13. (A) CVs of **Ph_2Phen^{2+}** under catalytic conditions with variable TFAH concentrations. (B) Logarithm of TFAH concentration versus the logarithm of current density from (A).

Figure S6.14. (A) CVs of **Ph_2Phen^{2+}** under catalytic conditions with variable O_2 concentrations. (B) Logarithm of O_2 concentration versus the logarithm of current density from (A).

Figure S6.15. (A) CVs of **Ph_2Phen^{2+}** in the presence of 6.7 mM urea•H_2O_2 under Ar and O_2 saturation with added 0.11 M TFAH. (B) CVs of **Ph_2Phen^{2+}** in the presence of 6.7 mM urea•H_2O_2 with added 0.11 M TFAH under O_2 saturation.

Figure S6.16. Linear sweep voltammograms of RRDE experiment with 0.5 mM **Ph_2Phen^{2+}** and 0.1 M TFAH under air saturation conditions. (A) Uncorrected LSVs at 600 rpm. (B) Corrected LSVs at various rotation rates used for quantification of %H_2O_2.

Figure S6.17. (A) Levich and (B) Koutecky-Levich plots from data obtained from linear sweep voltammograms of **Ph_2Phen^{2+}** (0.5 mM) by RRDE with 0.1 M TFAH under air saturation conditions at various rotation rates (600, 1000, 1400, 1800, & 2200 rpm).

Figure S6.18. (A) CVs of **Ph_2Phen^{2+}** under Ar (black), O_2 (red) and with 0.1 M Cl_3AcOH under Ar saturation (green). (B) CVs from A and catalytic trace shown (blue) with **Ph_2Phen^{2+}** and 0.1 M Cl_3AcOH under O_2 saturation.

Figure S6.19. CVs of **Ph_2Phen^{2+}** under catalytic conditions with 0.1 M Cl_3AcOH at 0.1 V/s (black) and 1 V/s (red).

Figure S6.20. Rinse test of **Ph_2Phen^{2+}** and Cl_3AcOH. **Ph_2Phen^{2+}** under catalytic conditions (black trace), rinse test (red trace), and CV of Cl_3AcOH under O_2 saturation (green trace).

Figure S6.21. (A) CVs of **Ph_2Phen^{2+}** under catalytic conditions with variable **Ph_2Phen^{2+}** concentrations. (B) Logarithm of **Ph_2Phen^{2+}** concentration versus the logarithm of current density from (A).

Figure S6.22. CVs of **Ph_2Phen^{2+}** under catalytic conditions with variable Cl_3AcOH concentrations.

Figure S6.23. (A) CVs of Ph_2Phen_{2+} under catalytic conditions with variable O_2 concentrations. (B) Logarithm of O_2 concentration versus the logarithm of current density from (A).

Figure S6.24. (A) CVs of **Ph_2Phen^{2+}** in the presence of 5.7 mM urea•H_2O_2 under Ar and O_2 saturation with added 0.12 M Cl_3AcOH. (B) CVs of **Ph_2Phen^{2+}** in the presence of 5.7 mM urea•H_2O_2 with added 0.12 M Cl_3AcOH under O_2 saturation.

Figure S6.25. Linear sweep voltammograms of RRDE experiment with 0.5 mM **Ph_2Phen^{2+}** and 0.1 M Cl_3AcOH under air saturation conditions. (A) Uncorrected LSVs at 600 rpm. (B) Corrected LSVs at various rotation rates used for quantification of %H_2O_2.

Figure S6.26. (A) Levich and (B) Koutecky-Levich plots from data obtained from linear sweep voltammograms of **Ph_2Phen^{2+}** (0.5 mM) by RRDE with 0.1 M Cl_3AcOH under air saturation conditions at various rotation rates (600, 1000, 1400, 1800, & 2200 rpm).

Figure S6.27. (A) CVs of **Ph_2Phen^{2+}** under Ar (black), O_2 (red) and with 0.1 M Cl_2AcOH under Ar saturation (green). (B) CVs from A and catalytic trace shown (blue) with Ph_2Phen^{2+} and 0.1 M Cl_2AcOH under O_2 saturation.

Figure S6.28. CVs of **Ph_2Phen^{2+}** under catalytic conditions with 0.1 M Cl_2AcOH at 0.1 V/s (black) and 1 V/s (red).

Figure S6.29. Rinse test of **Ph_2Phen^{2+}** and Cl_2AcOH. **Ph_2Phen^{2+}** under catalytic conditions (black trace), rinse test (red trace), and CV of Cl_2AcOH under O_2 saturation (green trace).

Figure S6.30. CVs of **Ph_2Phen^{2+}** under catalytic conditions with variable **Ph_2Phen^{2+}** concentrations. (B) Logarithm of **Ph_2Phen^{2+}** concentration versus the logarithm of current density from (A).

Figure S6.31. (A) CVs of **Ph_2Phen^{2+}** under catalytic conditions with variable Cl_2AcOH concentrations. (B) Logarithm of Cl_2AcOH concentration versus the logarithm of current density from (A).

Figure S6.32. (A) CVs of **Ph_2Phen^{2+}** under catalytic conditions with variable O_2 concentrations. (B) Logarithm of O_2 concentration versus the logarithm of current density from (A).

Figure S6.33. (A) CVs of **Ph_2Phen^{2+}** in the presence of 5.5 mM urea•H_2O_2 under Ar and O_2 saturation with added 0.06 M Cl_2AcOH. (B) CVs of **Ph_2Phen^{2+}** in the presence of 5.7 mM urea•H_2O_2 with added 0.06 M Cl_2AcOH under O_2 saturation.

Figure S6.34. Linear sweep voltammograms of RRDE experiment with 0.5 mM **Ph_2Phen^{2+}** and 0.1 M Cl_2AcOH under air saturation conditions. (A) Uncorrected LSVs at 600 rpm. (B) Corrected LSVs at various rotation rates used for quantification of %H_2O_2.

Figure S6.35. (A) Levich and (B) Koutecky-Levich plots from data obtained from linear sweep voltammograms of **Ph_2Phen^{2+}** (0.5 mM) by RRDE with 0.1 M Cl_2AcOH under air saturation conditions at various rotation rates (600, 1000, 1400, 1800, & 2200 rpm).

Figure S6.36. (A) CVs of **Ph_2Phen^{2+}** under Ar (black), O_2 (red) and with 0.1 M ClAcOH under Ar saturation (green). (B) CVs from A and catalytic trace shown (blue) with **Ph_2Phen^{2+}** and 0.1 M ClAcOH under O_2 saturation.

Figure S6.37. CVs of **Ph_2Phen^{2+}** under catalytic conditions with 0.1 M ClAcOH at 0.1 V/s (black) and 1 V/s (red).

Figure S6.38. Rinse test of **Ph_2Phen^{2+}** and ClAcOH. **Ph_2Phen^{2+}** under catalytic conditions (black trace), rinse test (red trace), and CV of Cl_2AcOH under O_2 saturation (green trace).

Figure S6.39. CVs of **Ph_2Phen^{2+}** under catalytic conditions with variable **Ph_2Phen^{2+}** concentrations. (B) Logarithm of **Ph_2Phen^{2+}** concentration versus the logarithm of current density from (A).

Figure S6.40. (A) CVs of **Ph_2Phen^{2+}** under catalytic conditions with variable ClAcOH concentrations. (B) Logarithm of ClAcOH concentration versus the logarithm of current density from (A).

Figure S6.41. (A) CVs of **Ph_2Phen^{2+}** under catalytic conditions with variable O_2 concentrations. (B) Logarithm of O_2 concentration versus the logarithm of current density from (A).

Figure S6.42. (A) CVs of **Ph_2Phen^{2+}** in the presence of 5.7 mM urea•H_2O_2 under Ar and O_2 saturation with added 0.1 M ClAcOH. (B) CVs of **Ph_2Phen^{2+}** in the presence of 5.7 mM urea•H_2O_2 with added 0.1 M ClAcOH under O_2 saturation.

Figure S6.43. Linear sweep voltammogram of RRDE experiment with 0.5 mM **Ph_2Phen^{2+}** and 0.1 M ClAcOH under air saturation conditions at 200 rpm.

Figure S6.44. (A) Change in absorbance at 780 nm over time as a result of the formation of $[Cp^*_2Fe]^+$ by ORR catalyzed by **Ph_2Phen^{2+}** with TFAH (black trace), example of 2Exp + Mx + C fit in Kinetic Studio 4.0 (red trace), and residual fit (blue trace). (B) Black trace from (A) with TFAH only control (no **Ph_2Phen^{2+}** present).

Figure S6.45. Calculated R_{fit}/n_{cat} values from stopped-flow spectrochemical experiments with TFAH, O_2, and Cp^*_2Fe with varying **Ph_2Phen^{2+}** concentration.

Figure S6.46. Calculated R_{fit}/n_{cat} values from stopped-flow spectrochemical experiments with **$Ph2Phen^{2+}$**, O_2, and Cp^*_2Fe with varying TFAH concentration.

Figure S6.47. Calculated R_{fit}/n_{cat} values from stopped-flow spectrochemical experiments with **Ph_2Phen^{2+}**, TFAH, and Cp^*_2Fe with varying O_2 concentration.

Figure S6.48. Calculated R_{fit}/n_{cat} values from stopped-flow spectrochemical experiments with **Ph_2Phen^{2+}**, TFAH, and O_2 with varying Cp^*_2Fe concentration.

Figure S6.49. Change in absorbance at 780 nm over time as a result of the formation of $[Cp^*_2Fe]^+$ from the ORR (black trace) or H_2O_2RR (red trace) by **Ph_2Phen^{2+}** with TFAH.

Figure S6.50. Change in absorbance at 780 nm over time as a result of the formation of $[Cp^*_2Fe]^+$ by ORR catalyzed by **Ph_2Phen^{2+}** with Cl_3AcOH (black trace), example of 2Exp + Mx + C fit in Kinetic Studio 4.0 (red trace), and residual fit (blue trace). (B) Black trace from (A) with Cl_3AcOH only control (no **Ph_2Phen^{2+}** present).

Figure S6.51. Calculated R_{fit}/n_{cat} values from stopped-flow spectrochemical experiments with Cl_3AcOH, O_2, and Cp^*_2Fe with varying **Ph_2Phen^{2+}** concentration.

Figure S6.52. Calculated R_{fit}/n_{cat} values from stopped-flow spectrochemical experiments with **Ph_2Phen^{2+}**, O_2, and Cp^*_2Fe with varying Cl_3AcOH concentration.

Figure S6.53. Calculated R_{fit}/n_{cat} values from stopped-flow spectrochemical experiments with **Ph_2Phen^{2+}**, Cl_3AcOH, and Cp^*_2Fe with varying O_2 concentration.

Figure S6.54. Calculated R_{fit}/n_{cat} values from stopped-flow spectrochemical experiments with **Ph_2Phen^{2+}**, Cl_3AcOH, and O_2 with varying Cp^*_2Fe concentration.

Figure S6.55. Change in absorbance at 780 nm over time of $[Cp^*_2Fe]^+$ over time as a result of the formation of $[Cp^*_2Fe]^+$ from the ORR (black trace) or H_2O_2RR (red trace) by **Ph_2Phen^{2+}** with Cl_3AcOH.

Figure S6.56. (A) Change in absorbance at 780 nm over time as a result of the formation of $[Cp^*_2Fe]^+$ by ORR catalyzed by **Ph_2Phen^{2+}** with Cl_2AcOH (black trace), example of 2Exp + Mx + C fit in Kinetic Studio 4.0 (red trace), and residual fit (blue trace). (B) Black trace from (A) with Cl_2AcOH only control (no **Ph_2Phen^{2+}** present).

Figure S6.57. Calculated R_{fit}/n_{cat} values from stopped-flow spectrochemical experiments with Cl_2AcOH, O_2, and Cp^*_2Fe with varying **Ph_2Phen^{2+}** concentration.

Figure S6.58. Calculated Rfit/ncat values from stopped-flow spectrochemical experiments with **Ph_2Phen^{2+}**, O_2, and Cp^*_2Fe with varying Cl_2AcOH concentration.

Figure S6.59. Calculated R_{fit}/n_{cat} values from stopped-flow spectrochemical experiments with **Ph_2Phen^{2+}**, Cl_2AcOH, and Cp^*_2Fe with varying O_2 concentration.

Figure S6.60. Calculated R_{fit}/n_{cat} values from stopped-flow spectrochemical experiments with **Ph_2Phen^{2+}**, Cl_2AcOH, and O_2 with varying Cp^*_2Fe concentration.

Figure S6.61. Change in absorbance at 780 nm over time as a result of the formation of $[Cp^*_2Fe]^+$ from the ORR (black trace) or H_2O_2RR (red trace) by **Ph_2Phen^{2+}** with Cl_2AcOH.

Figure S6.62. Change in absorbance at 780 nm over time as a result of the formation of $[Cp^*_2Fe]^+$ by ORR catalyzed by **Ph_2Phen^{2+}** with ClAcOH (black trace), example of 2Exp + Mx + C fit in Kinetic Studio 4.0 (red trace), and residual fit (blue trace). (B) Black trace from (A) with ClAcOH only control (no **Ph_2Phen^{2+}** present).

Figure S6.63. Calculated R_{fit}/n_{cat} values from stopped-flow spectrochemical experiments with ClAcOH, O_2, and Cp^*_2Fe with varying **Ph_2Phen^{2+}** concentration.

Figure S6.64. Calculated R_{fit}/n_{cat} values from stopped-flow spectrochemical experiments with **Ph_2Phen^{2+}**, O_2, and Cp^*_2Fe with varying ClAcOH concentration.

Figure S6.65. Calculated R_{fit}/n_{cat} values from stopped-flow spectrochemical experiments with **Ph_2Phen^{2+}**, ClAcOH, and Cp^*_2Fe with varying O_2 concentration.

Figure S6.66. Calculated R_{fit}/n_{cat} values from stopped-flow spectrochemical experiments with **Ph_2Phen^{2+}**, ClAcOH, and O_2 with varying Cp^*_2Fe concentration.

Figure S6.67. Change in absorbance at 780 nm over time as a result of the formation of $[Cp^*_2Fe]^+$ from the ORR (black trace) or H_2O_2RR (red trace) by **Ph_2Phen^{2+}** with ClAcOH.

Figure S6.68. H_2O_2 product quantification of ORR by **Ph_2Phen^{2+}** with TFAH after 90 s. (A) UV-vis spectra of catalytic aliquot before (black) and after (red) 0.1 mL of 0.1 M $Ti(O)SO_4$ solution was added. (B) Corrected spectra (red – black trace from A).

Figure S6.69. H_2O_2 product quantification of ORR by **Ph_2Phen^{2+}** with Cl_3AcOH after 90 s. (A) UV-vis spectra of catalytic aliquot before (black) and after (red) 0.1 mL of 0.1 M $Ti(O)SO_4$ solution was added. (B) Corrected spectra (red – black trace from A).

Figure S6.70. H_2O_2 product quantification of ORR by **Ph_2Phen_{2+}** with Cl_2AcOH after 2 min. (A) UV-vis spectra of catalytic aliquot before (black) and after (red) 0.1 mL of 0.1 M $Ti(O)SO_4$ solution was added. (B) Corrected spectra (red – black trace from A).

Figure S6.71. H_2O_2 product quantification of ORR by **Ph_2Phen^{2+}** with ClAcOH after 3 min. (A) UV-vis spectra of catalytic aliquot before (black) and after (red) 0.1 mL of 0.1 M $Ti(O)SO_4$ solution was added. (B) Corrected spectra (red – black trace from A).

Figure S6.72. H_2O_2 product quantification of ORR by **Ph_2Phen^{2+}** with ClAcOH after 30 s, 2 min, and 5 min. (A) UV-vis spectra of catalytic aliquot before (black) and after (red) 0.1 mL of 0.1 M $Ti(O)SO_4$ solution was added after 30 s. (B) Corrected spectra (red – black trace from A) after 30 s, 2 min, and 5 min.

Figure S6.73. Stability test of urea•H_2O_2 in the presence of **Ph_2Phen^{2+}**, TFAH, and O_2 (A) before (black trace) and after (red trace) the addition of 0.1 mL of 0.1 M $Ti(O)SO_4$ to an aliquot. (B) Corrected UV-vis spectra (red – black from A) of each trial after 90 s with the H_2O_2 stock (black).

Figure S6.74. Stability test of urea•H_2O_2 in the presence of **Ph_2Phen^{2+}**, Cl_3AcOH, and O_2 (A) before (black trace) and after (red trace) the addition of 0.1 mL of 0.1 M Ti(O)SO4 to an aliquot. (B) Corrected UV-vis spectra (red – black from A) of each trial after 90 s with the H_2O_2 stock (black).

Figure S6.75. Stability test of urea•H_2O_2 in the presence of **Ph_2Phen^{2+}**, Cl_2AcOH, and O_2 (A) before (black trace) and after (red trace) the addition of 0.1 mL of 0.1 M $Ti(O)SO_4$ to an aliquot. (B) Corrected UV-vis spectra (red – black from A) of each trial after 2 min with the H_2O_2 stock (black).

List of Schemes

List of Tables

Table 4.1. Summary of ORR selectivity under spectrochemical conditions of 1 and 2 under unbuffered and buffered conditions.

Table S4.1. Summary of Evans' Method Data from Mn($^{p\text{-}tbu}$dhbpy)Cl **1** in *N,N′*-DMF (chosen for solubility reasons) supporting a high-spin d^4 complex.

Table S4.2. Table of Evans' Method data from Mn(^{nPr}dhbpy)Cl **2** in *N,N′*-DMF (chosen for solubility reasons) supporting a high spin d^4 complex.

Table S4.3. Summary of the chemical shifts for the estimation of DIPEAHPF$_6$ pK_a.

Table S4.4. Summary of H_2O_2 selectivity of ORR by Mn($^{p\text{-}tbu}$dhbpy)Cl **1** with 10 mM DIPEAHPF$_6$ (**Figure S4.26**).

Table S4.5. Summary of H_2O_2 selectivity of ORR by Mn(^{nPr}dhbpy)Cl **2** with 10 mM DIPEAHPF$_6$ (**Figure S4.27**).

Table S4.6. Summary of H_2O_2 disproportionation by Mn($^{p\text{-}tbu}$dhbpy)Cl **1** with 10 mM DIPEAHPF$_6$ (**Figure S4.28**) relative to 0.87 mM H_2O_2 stock solution.

Table S4.7. Summary of H_2O_2 disproportionation by Mn(^{nPr}dhbpy)Cl **2** with 10 mM DIPEAHPF$_6$ (**Figure S4.29**) relative to 0 min with 0.80 mM H_2O_2.

Table S4.8. Summary of H_2O_2 selectivity over the course of catalytic ORR by Mn($^{p\text{-}tbu}$dhbpy)Cl **1** with 10 mM DIPEAHPF$_6$/DIPEA (**Figure S4.30**).

Table S4.9. Summary of H_2O_2 selectivity over the course of catalytic ORR by Mn(^{nPr}dhbpy)Cl **2** with 10 mM DIPEAHPF$_6$/DIPEA (**Figure S4.31**).

Table S4.10. Summary of H_2O_2 disproportionation by Mn($^{p\text{-}tbu}$dhbpy)Cl **1** with 10 mM DIPEAHPF$_6$/DIPEA (**Figure S4.32**) relative to 1.49 mM H_2O_2 stock solution.

Table S4.11. Summary of H_2O_2 disproportionation by Mn(^{nPr}dhbpy)Cl **2** with 10 mM DIPEAHPF$_6$/DIPEA (**Figure S4.33**) relative to 0.89 mM H_2O_2 stock solution.

Table S4.12. Summary of H_2O_2RR by Mn($^{p\text{-}tbu}$dhbpy)Cl **1** with 10 mM DIPEAHPF$_6$/DIPEA and 1 mM FeCp*$_2$ (**Figure S4.34**) relative to 2.3 mM H_2O_2 stock solution.

Table S4.13. Summary of H_2O_2RR by Mn(^{nPr}dhbpy)Cl **2** with 10 mM DIPEAHPF$_6$/DIPEA and 1 mM FeCp*$_2$ (**Figure S4.35**) relative to 2.3 mM H_2O_2 stock solution.

Table S4.14. Crystallographic details for Mn(^{nPr}dhbpy)Cl **2** and DIPEAHPF$_6$

Table 6.1. Summary of spectrochemical activity and selectivity of ORR by **Ph$_2$Phen^{2+}** with each proton donor.

Table S6.1. Summary of calculated pK_a values in MeCN.

Table S6.2. Summary of ORR selectivity by **Ph$_2$Phen^{2+}** with each acid.

Table S6.3. Summary of ORR selectivity of **Ph$_2$Phen^{2+}** with ClAcOH at various time points from **Figure S6.73**.

Table S6.4. Summary of H_2O_2 Recovery for Stability Control Studies by **Ph$_2$Phen^{2+}** with each acid.

Table S6.5. Crystal data and structure refinement for **Ph$_2$Phen^{2+}**

Chapter 1:

Introduction

Portions of this chapter published as:

Cook, E.N. & Machan, C.W. *Chemical Communications,* **2022**, 58, 11746-11761.

1.1 Utilization of O_2 to Meet the Energy Demand

Since the industrial revolution, there has been a drastic increase in global atmospheric carbon dioxide (CO_2) concentration due to the burning of petroleum sources to generate the energy required to power transportation and industrial processes.[1,2] The accumulation of greenhouse gases, gases that trap heat in the atmosphere,[3] from anthropogenic processes has resulted in a number of environmental impacts, including global warming and climate change. Therefore, the development of alternative and renewable energy sources is crucial to limiting changes to Earth's climate. There has been work toward renewable energy sources like solar and wind energy; however, there are important challenges in the large-scale implementation and utilization of the intermittent energy produced from these sources. Specifically, current energy storage capabilities from these sources is not suitable for long term use. Thus, alternative strategies to generate and store clean energy and/or reduce energy requirements of industrial processes are necessary. One approach is to electrochemically activate abundant small molecules, such as CO_2, hydrogen (H_2), water (H_2O) and dioxygen (O_2), through the addition of protons (H^+) and electrons (e^-) in order to convert them into useful products using renewable energy.

The utilization of O_2 in synthetic and catalytic processes has long been inspired by its life-sustaining roles in nature, where it is essential for energy utilization, the degradation of harmful substances, metabolism, and the synthesis of important biomolecules.[4-8] Due to its natural abundance, researchers have been working to utilize the oxidative power of O_2 as an alternative oxidant in capital- and energy-intensive processes. Industrial production of commodity chemicals, complex organic molecules, and fuels from petrochemical feedstock relies on selective C–H bond activation and oxidation, where current processes often require the use of a stoichiometric oxidant and have poor selectivity and toxic byproducts.[9] Selective electrochemical utilization of O_2 in these processes would provide an affordable and abundant alternative with low toxicity (**Figure 1.1**).

The oxygen reduction reaction (ORR) is also of interest for alternative energy and fuel cell applications (**Figure 1.1**). Polymer electrolyte membrane fuel cells are the most promising

alternative for automotive power generation, with the advantage of high energy output and low emission profile.[10] These fuel cells function through the oxidation of molecular hydrogen into protons and electrons, coupled with the proton-dependent reduction of O_2 to water (H_2O). The alternative ORR product, hydrogen peroxide (H_2O_2) is used in a wide range of industrial processes including paper bleaching, wastewater treatment, and as a 'green' oxidant in chemical industry.[11,12] The current industrial anthraquinone process for the production of H_2O_2 is capital intensive and uses fossil fuel-derived H_2 (**Figure 1.1**). Further, H_2O_2-based fuel cells are becoming increasingly attractive as an alternative energy device.[13] With the increasing global energy demand, depletion of non-renewable fuel sources, and the environmental impact of current capital-intensive industrial processes, affordable and 'green' alternatives are crucial moving forward, however, expensive and platinum-based catalysts are commonly used for mediating the ORR and new fundamental understanding is required to develop replacements.

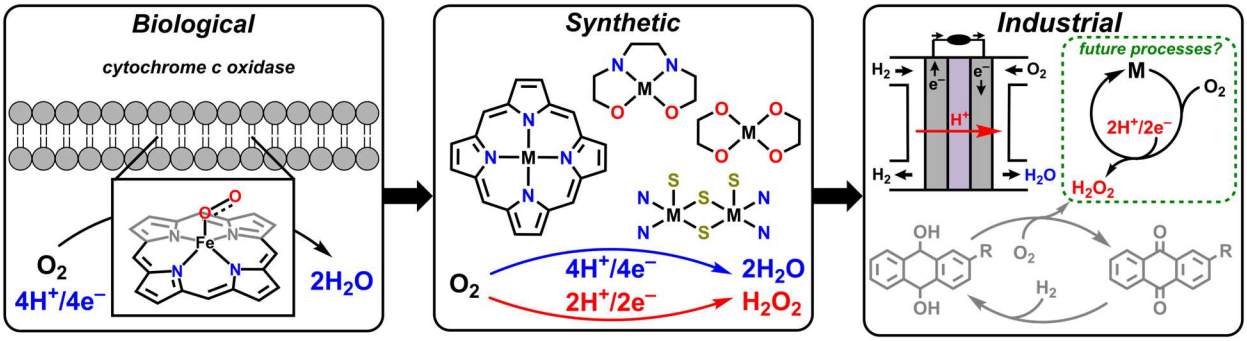

Figure 1.1. Summary of relevant O_2 reduction in biological, synthetic, and industrial chemistry. M = transition metal.

One challenge in the activation and reduction of O_2 is its triplet ground state, which inhibits reactivity with singlet organic substrates with limited spin polarization.[14] Nature has overcome this by employing open-shell transition metal centers that favorably react with O_2. Iron (Fe), copper (Cu), and manganese (Mn) are most commonly found in enzymatic active sites that activate O_2 due to their redox flexibility and their natural abundance. Some notable examples of these include hemoglobin, dioxygenases, lipoxygenases, monooxygenases, and superoxide dismutase, among many others.[4,5,15-21] These bioinorganic systems have inspired the development of a variety of

synthetic compounds for O_2 activation.[22] The prevalence of earth-abundant first-row transition metals for O_2 reduction in nature has led to of the development of homogeneous ORR catalysts based on manganese, iron, cobalt, and copper active sites.[7,23]

1.2. O_2 Activation and Reduction at Transition Metals

The molecular orbital description of O_2 gives essential context about its ground state and reactivity. O_2 exists in a triplet ground state where the highest occupied molecular orbitals are singly occupied degenerate π^* orbitals, giving the molecule an overall bond order of 2. A single reduction of O_2 to a superoxo ($O_2^{\bullet-}$) reduces the bond order to 1.5, with a formal $2e^-$ reduction to a peroxo (O_2^{2-}) species cleaving the O–O π-bond entirely.[24] Oxidation reactions involving O_2 are often thermodynamically favorable; however, there is often a significant kinetic barrier due in part to its triplet ground state, which makes reactivity with closed shell substrates a formally spin-forbidden process and therefore slow, under the assumption that the substrate experiences a minimum of spin polarization in its ground state.[14]

Conversely, O_2 activation by open-shell transition metals can be highly favorable (**Figure 1.2**). O_2 activation at a metal center results in the formation of reduced O_2 intermediates, known as reactive oxygen species (ROS), whose stability is crucial in determining reaction pathways. The binding mode of O_2 to a single metal center is dependent both on *d*-electron count and spin configuration of the metal, as well as the steric properties enforced by the supporting ligand framework. O_2 can bind in an end-on (**2A**) or side-on fashion (to either one (**2B)** or two (**2D**) metal centers), and this interaction typically results in formal oxidation of the metal center and reduction of O_2 to generate metal superoxo ($O_2^{\bullet-}$) or peroxo (O_2^{2-}) species. In addition to the σ-symmetric interactions possible with the lone pairs on each O atom, the π bond can also act as a σ donor. The propensity to reduction upon binding is in part due to another aspect of the frontier orbital structure of O_2, specifically, the partially occupied degenerate π^*-symmetric SOMOs. Upon

coordination with a metal center, these energetically accessible orbitals can act as a *π*-acid and accept electron density through a *π*-backbonding interaction, lowering bonding character.

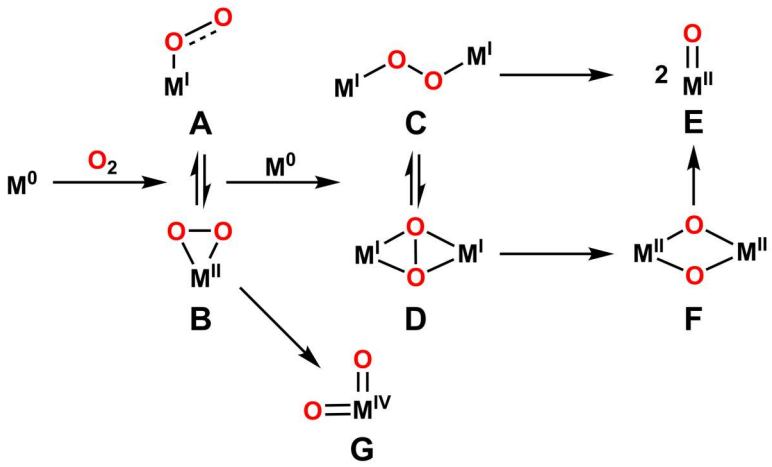

Figure 1.2. Summary of possible reaction pathways for aprotic O_2 activation in mono- and dinuclear configurations.

Generally, the end-on binding mode of metal superoxide is bent (**2A)** rather than linear. This is because the *σ* bond with the metal center arises from a fully occupied *π** orbital (generated through the formal one electron reduction of O_2) acting as a Lewis base and donating electron density into the d_z^2 acceptor orbital of the metal. Depending on the oxidation state of the metal, an additional *π*-interaction from partially filled d_π metal orbitals into the remaining singly occupied *π** orbital of O_2 is possible; strong coupling between these orbitals is responsible for the diamagnetic structure of Fe(III)-superoxides in porphyrinic frameworks.[23,25] In a side-on binding mode, the σ bond originates from a *σ*-symmetric interaction involving donation from the *π*-orbital of O_2 into the d_z^2 orbital of the metal, with π-backbonding from the metal's filled d_π orbitals into the partially occupied π* orbitals of O_2. O_2 can also act as a bridging ligand between two metal centers in a μ-η^1:η^1 (**2C**) or μ-η^2:η^2 fashion (**2D**) with each metal providing an electron to achieve an overall two-electron reduction to an O_2^{2-} configuration. One strategy to tune O_2 binding is modifying the supporting ligand framework, where ligand structure can be used to modulate the character of the frontier *d* orbitals, as well as inhibit specific binding modes through control of the stereochemical profile.[7,26,27]

During the electrocatalytic reduction of O_2, product selectivity is controlled, in part, by the nature of O_2 binding to the active site, which dictates the extent of ROS stabilization and the nature of the reactivity for intermediates formed through the mechanistic cycle. In protic media, there are two primary pathways for the ORR: a $2H^+/2e^-$ transformation to make H_2O_2 or a $4H^+/4e^-$ process to form two equivalents of H_2O. Generally, ORR to both H_2O_2 and H_2O mediated by *mononuclear* catalysts is initiated by electron transfer from a metal active site to O_2 to form a metal-bound $O_2^{\bullet-}$ as described above (**Figure 1.3**, ***iii***).[7,11,28] From here, a proton and electron transfer can occur in either a stepwise or concerted fashion to form a hydroperoxo intermediate (OOH^-), (**Figure 1.3**, ***iv***). Formation of H_2O_2 arises from favorable net reduction of the complex and protonation of the proximal oxygen based on the adsorption strength of the OOH^- species to the metal center and its consequences for the basicity of the M–O bond. The mechanistic pathway to H_2O formation commonly arises from protonation of the M–OOH adduct at the distal O atom, assisted by electron transfer from the metal center, leading to cleavage of the O–O bond, release of one equivalent of H_2O and the formation of a high valent metal oxo (O^{2-}) species (**Figure 1.3**, ***v***). Subsequent transfer of $2e^-$ to the metal and $2H^+$ to O^{2-} releases the second equivalent of H_2O. ORR to generate H_2O can also proceed via a 2+2 mechanism, where H_2O_2 produced during catalysis can be further reduced to two equivalents of water by the catalyst. There are a number of factors that govern mechanistic pathways and favorable formation and stability of reactive intermediates. For catalysts which form dinuclear species on the catalytic cycle, superoxide formation is generally avoided in favor of peroxo intermediates which can undergo aprotic or proton assisted cleavage to generate μ-oxo or -hydroxo species prior to further reduction and protonation to release H_2O.

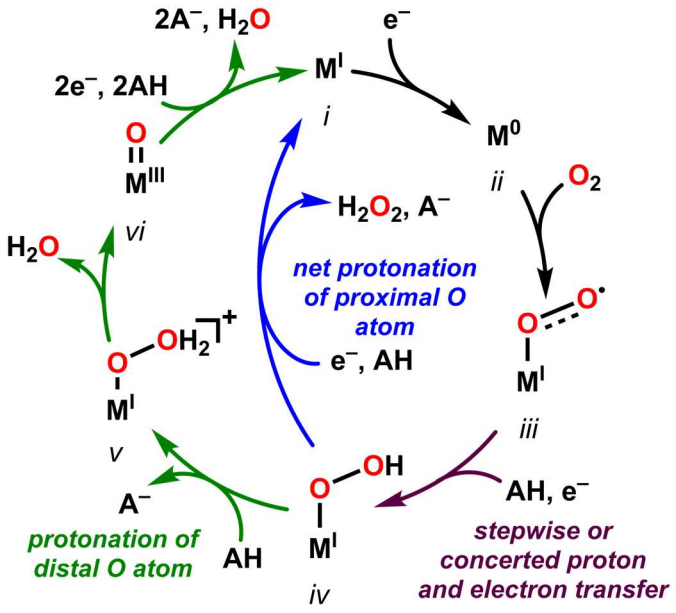

Figure 1.3. Generalized mechanism for the ORR at mononuclear active sites.

In fuel cells, the ORR to H_2O is preferred due to its higher free energy release as well as it being non-destructive to these devices.[7] The standard redox potential of O_2 reduction to H_2O is +1.229 V vs. SHE. By comparison, the $2e^-/2H^+$ reduction of O_2 to H_2O_2 is less thermodynamically favorable, with a more negative standard reduction potential of +0.68 V vs SHE.[28] However, further reduction of H_2O_2 by $2e^-/2H^+$ to two equivalents of water is very favorable, with a standard reduction potential of +1.77 V vs SHE.[28] When comparing electrocatalysts, overpotential (η) and turnover frequency (TOF) are common metrics that assess efficiency and activity. As described above, η describes the thermodynamic comparison of catalyst operating potential with the minimum reduction potential required under operating conditions.[7] TOF is given in reaction rate per unit time, reflecting how rapidly product is generated under catalytic conditions. An effective catalyst minimizes overpotential while maximizing TOF. The essential challenge to developing better electrocatalysts for O_2 reduction (and indeed any catalyst) is how to prevent the release of reactive intermediates during catalysis to prevent side reactions and catalyst deactivation, which can limit catalyst activity. Moduli of control in the testing and regulation of the possible reaction

pathways include the redox potential of the catalyst and the electronic and steric effects imparted by the primary and secondary coordination spheres.

1.3. Catalytic O_2 Reduction Mediated by Fe

1.3.1. Porphyrinic Systems

Fe is a common transition metal utilized by nature to assist in the activation and reduction of O_2. One of the most notable biological structures, the heme active site, plays crucial roles in the binding, transport, and storage of O_2. Heme cofactors are also important in O_2 activation and utilization as well as peroxide management and degradation.[29,30] This active site contains an Fe metal center supported by a porphyrinic ligand framework. Importantly, while the Fe center remains the same in a number of enzymes, its function is carefully tuned to achieve specific reactivity through primary and secondary coordination sphere effects.[29] Because of its versatility and importance in nature, Fe-based molecular ORR catalysis has been dominated by porphyrinic complexes such as porphyrins, corroles, and phthalocyanines, summarized in **Figure 1.4**.[29]

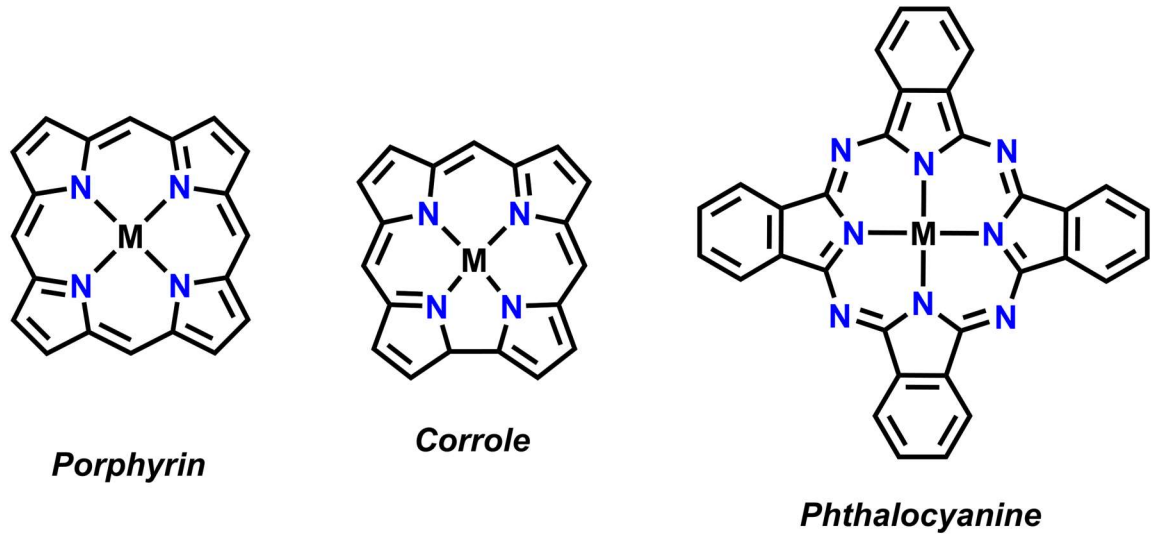

Figure 1.4. Generalized structure of porphyrin (left), corrole (middle) and phthalocyanine (right), where M = Fe.

1.3.1.1. Fe Porphyrins

As mentioned above, inspiration from nature has resulted in the development and extensive study of Fe-based porphyrin systems, particularly iron *meso*-tetraphenylporphyrin ($[Fe(TPP)]^+$) (**Figure 1.5**).

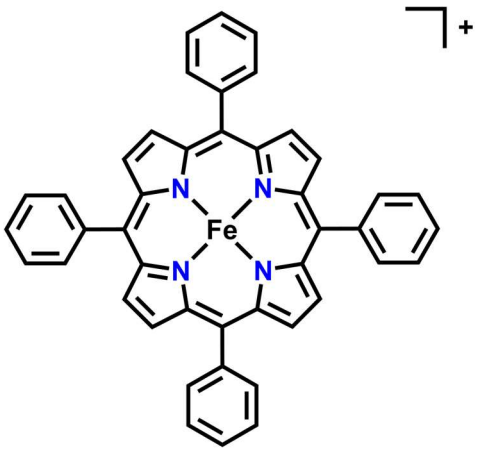

Figure 1.5. Structure of $[Fe(TPP)]^+$.

Since the first report by Fukuzumi and co-workers in 1989,[31,32] there have been a number of studies that describe reactivity of $[Fe(TPP)]^+$ as well as substituted analogues[7,33,34], a few of which will be discussed here. The Mayer group has published a series of mechanistic studies elucidating the full mechanism of the $4H^+/4e^-$ reduction of O_2 by $[Fe(TPP)]^+$ (**Figure 1.6**).[35-37] It was found that under both electrochemical and spectrochemical conditions with Cp^*_2Fe as a chemical reductant, there is a first-order dependence on the concentration of $[Fe(TPP)]^+$, tosic acid (TsOH), and O_2.[35] It is proposed that rapid reduction of $[Fe^{III}(TPP)]^+$ to $[Fe^{II}(TPP)]^0$ triggers reversible pre-equilbrium O_2 binding to form $[Fe^{III}(TPP)(O_2^{\bullet-})]^0$, followed by the rate-determining protonation to form $[Fe^{III}(TPP)(O_2H^{\bullet})]^+$. This species is rapidly reduced and protonated to eventually form two equiv of H_2O. Interestingly, Pegis *et al.* propose that over the course of the catalytic reaction, the resting state of the catalyst shifts to $[Fe^{III}(TPP)]^+$ as substrates are consumed.[35]

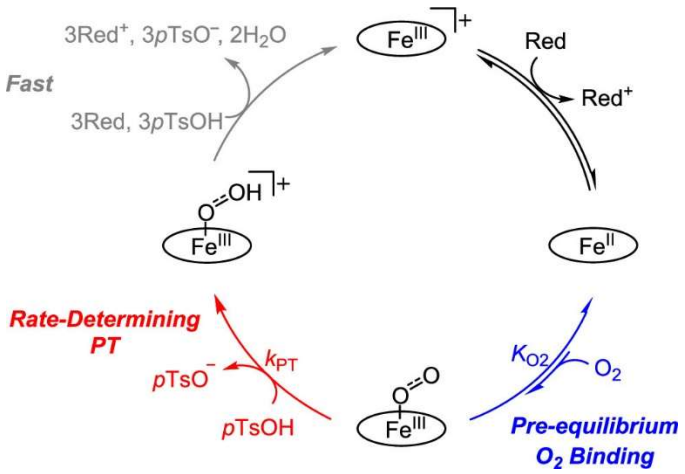

Figure 1.6. Proposed mechanism for oxygen reduction catalyzed by $[Fe(TPP)]^+$, with TPP abbreviated as an oval. Red = Cp^*_2Fe or electrode.[35] Reprinted with permission from ref 34. Copyright 2019, American Chemical Society, Washington, DC.

Incorporating functional groups in the phenyl substituent of the TPP ligand framework has provided information on secondary sphere effects during catalysis.[33] The Collman group has contributed significantly to the development of functional models of cytochrome *c* oxidase, hemoglobin, and myoglobin and the incorporation of secondary sphere substituents to understand O_2 reactivity and reduction.[30,38,39] Based on the role of secondary sphere interactions with important catalytic intermediates, the Mayer group also studied how incorporation of proton relays could affect ORR.[40] They incorporated carboxylic acid functional groups in either the *ortho* (**Figure 1.7**, complex 1) or *para* (**Figure 1.7**, complex 2) positions on the phenyl substituent, where the ortho-substituted analogue were poised to act as pendent proton relay.[40] The presence of the pendent proton relay both enhanced catalysis and shifted selectivity to exclusively producing H_2O.

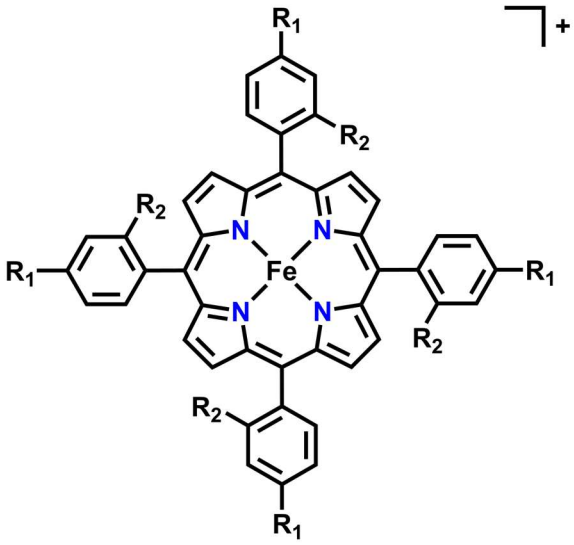

1: R_1 = -H, R_2 = -COOH
2: R_1 = -COOH, R_2 = -H

Mayer and co-workers, 2012

Figure 1.7. Carboxylic acid substituted $[Fe(TPP)]^+$ derivatives studied by Mayer and co-workers to analyze the role of pendent proton relays during the ORR.[40]

In addition to secondary coordination sphere modifications that interact with reactive intermediates during catalysis, synthetic modulation can be used to tune the reduction potential of the metal center, and therefore the overpotential (η) of the system. Mayer and co-workers reported a series of substituted $[Fe(TPP)]^+$s and observed a Tafel scaling relationship, where the rate of catalytic ORR correlates directly with the overpotential of the system, suggesting that tuning the operating potential of the system can be used to systematically alter the activity.[37]

Interestingly, derivatives used in this study were also expected to act as pendent proton relays during catalysis. However, they found that under the conditions examined ($DMF\text{-}H^+$ as a proton source), the pendent relays are at a mismatch and too weak of proton donors to directly protonate the $Fe\text{-}OO^{\bullet-}$ intermediate and protonation must occur from the added acid.[37]

More recently, Dey and co-workers have undertaken a number of studies focusing on secondary sphere effects in ORR by $[Fe(TPP)]^+$.[41-44] In 2020, they explored the role of amines as H-bond donors and acceptors during catalytic ORR by a substituted $[Fe(TPP)]^+$, finding that there was a “push-pull” effect by the secondary sphere functional groups that was dependent on

solution pH.[41] They determined that at low pHs there was a “pull” effect from the H-bond donation by the substituent that activates the O–O bond and results in H_2O production. However, at basic pHs there was a “push” effect from the deprotonation of the axial H_2O ligand, which increases the pK_a of the -OOH intermediate and ultimately produces H_2O_2 as a product.[41] In follow up work, the Dey group analyzed the role of the 1,10-phenanthroline moiety and axial H_2O ligand at different pHs in the mechanism of ORR.[43] They found that at neutral pH, H_2O binding to the Fe center is high, inhibiting O_2 binding. However, at acidic pHs, the phenanthroline is protonated and acts as a H-bond donor, weakening H_2O binding to the Fe center, significantly increasing the rate of O_2 binding. Additionally, at basic pHs, the axial ligand becomes $^{-}$OH, which also renders the *trans* H_2O more labile and increases the rate of O_2 binding (**Figure 1.8**).

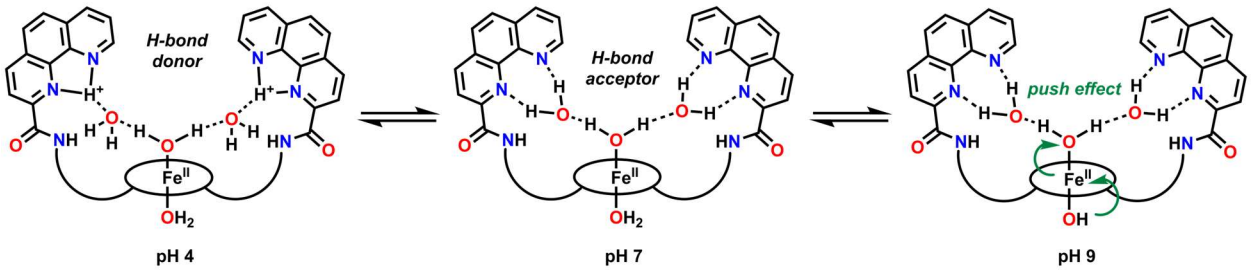

Figure 1.8. Schematic representation of 6-coordinated H_2O bound Fe^{II}-Bisphen showing the influence of push and pull effects during O_2 reduction at different pHs. Modified from ref. 42.[42]

The Dey group has also introduced amine groups in the secondary coordination sphere of $[Fe(TPP)]^+$ (**Figure 1.9**).[44] When these amine groups are protonated, there is a slight positive potential shift in the $Fe^{III/II}$ reduction potential without a significant change in the catalytic ORR rates. They found that the positively charged amines enhanced both O–O bond cleavage as well as O_2 binding to the reduced metal center. However, there was no observed correlation between the turnover frequency (TOF) and the η, as the amine moieties played a stronger role in the rate determining step rather than controlling the reduction potential of the metal center.[44]

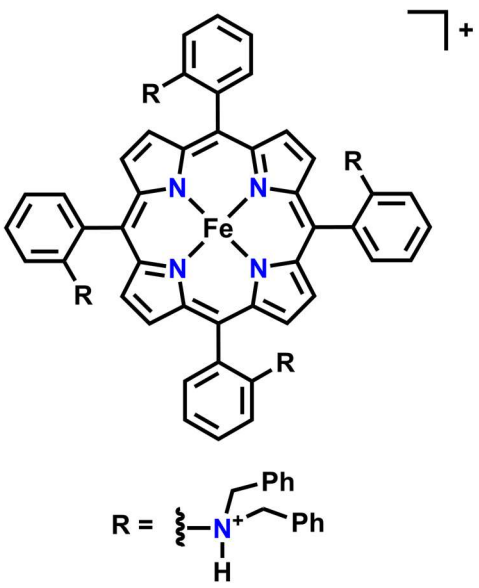

Dey and co-workers, 2023

Figure 1.9. [Fe(TPP)]$^+$ substituted with tertiary amine groups capable of tuning the rate determining step during ORR analyzed by Dey and co-workers in 2023.[44]

The extensive work focused on [Fe(TPP)]$^+$ and its substituted derivatives has contributed greatly to the development of efficient electrocatalysts for the ORR. Taken together, there are a number of strategies to be employed in order to tune O_2 reactivity at the Fe metal center. Importantly, [Fe(TPP)]$^+$ has been an excellent model compound to interrogate the ability of various functional groups to tune activity and selectivity during the ORR.

1.3.1.2. Fe Corroles & Phthalocyanines

In comparison to porphyrin ligand frameworks, corroles have been much less-widely studied. While similar to porphyrins, corroles are trianionic ligands and are able to stabilize higher metal oxidation states than porphyrins, thanks to a contracted ring structure.[29,45] Phthalocyanines are also similar to the porphyrins, retaining a comparable inner-coordination sphere and dianionic character. However, the prevalence of Fe corroles and phthalocyanines as homogeneous ORR catalysts is sparse, as Co and immobilized systems dominate the field.[29] In 2005, Collman and co-workers reported a series of metal corroles containing Fe, Mn, and Co metal centers adsorbed to an edge plane graphite (EPG) electrode for catalytic ORR. It was found that free-base, Mn and Co-corroles catalyze the $2H^+/2e^-$ reduction of O_2, while Fe preferably produced H_2O.[45]

Interestingly, for Fe and Co-based systems, ORR began at much more positive potentials than the $M^{III/II}$ redox event. It was reasoned that the active state of the catalyst is M^{II} that results from a corrole-to-metal electron transfer, followed by O_2 binding to the reduced metal center. In 1985, Kobayashi and Nishiyama reported a study of ORR by 4,4',4'',4'''-tetracarboxyphthalocynanine with an Fe (FeTPc) metal center under aqueous conditions.[46] They found that FeTPc catalytically reduced O_2 to H_2O via a 2+2 mechanism, where H_2O_2 is an intermediate. They also observed a low-spin Fe(II) intermediate by UV-vis spectroscopy and magnetic circular dichromism (MCD). Park and co-workers reported Fe phthalocyanine (FePc) as a co-catalyst in a chemically regenerative redox fuel cell, where Fe^{3+} is reduced to Fe^{2+} at a carbon felt electrode.[47] Fe^{3+} was catalytically regenerated using the ORR to H_2O by FePc and Fe^{2+} as the reductant. However, many reports focus on the catalytic behavior of immobilized Fe phthalocyanines for the ORR.[48-50]

The prevalence of heme-like frameworks for the study of the ORR is in part the result of the biological relevance of heme active sites and a desire to model them. Mechanistic studies and synthetic modifications have been successfully used to elucidate the reaction mechanism of ORR as well as understand the underlying structure-function relationships. These advancements have contributed to the development of new types of electrocatalysts for the ORR, as well as provided fundamental information about the behavior of structurally related dioxygen-dependent bioinorganic cofactors. However, there remains a gap in knowledge of developing non-porphyrinic ORR systems, despite their ubiquity in biology.

1.3.2. Non-Porphyrinic Systems

Despite the prevalence of non-heme, or non-porphyrinic, active sites in nature, there has been significantly less focus on the development of non-heme Fe catalysts for the ORR, with only two non-heme systems reported prior to our two disclosed systems (*vide infra*).[19,51-55] In 2019, Duboc and coworkers studied a dinuclear Fe(II) thiolate complex, $[Fe^{II}_2(LS)(LSH)]^+$ (LS^{2-} = 2,2'-(2,2'-bypyridine-6,6'-diyl)bis(1,1-diphenylethanethiolate)) (**Figure 1.10**) for the catalytic reduction of O_2 under both electrochemical and spectrochemical conditions.[51] They found that selectivity

was dependent upon the method of electron delivery: under electrochemical conditions the system was selective for H_2O and with a chemical reductant the system selectively produced H_2O_2. It was hypothesized that the difference in selectivity was the capability of the $[Fe_2^{OO/SH}]^+$ or $[Fe_2^{OOH}]^+$ intermediate formed being immediately reduced at the electrode before being able to react with an additional H^+, whereas under chemical conditions, a second protonation that leads to H_2O_2 release is favorable.[51]

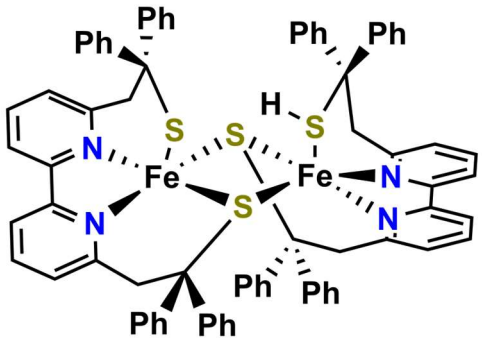

Duboc and coworkers, 2019

Figure 1.10. Structure of $[Fe^{II}_2(LS)(LSH)]^+$ reported by Duboc and coworkers.[51]

Soon after, Fukuzumi and coworkers reported an Fe(III)TAML (TAML = tetraamido macrocyclic ligand) (**Figure 1.11**) that catalytically reduced O_2 to H_2O by a chemical reductant (decamethylferrocene Cp^*_2Fe and octamethylferrocene $^{Me8}CpFe$) with acetic acid (AcOH) as a proton source in the presence of aerated acetone.[52] They found that a key reaction intermediate was the formation of an $Fe^V(O)$ species by an oxygenation reaction involving triacetone triperoxide (TATP), which is an autocatalytically formed intermediate under reaction conditions. $Fe^V(O)$ was then reduced followed by rapid protonation and reduction to release H_2O.[52]

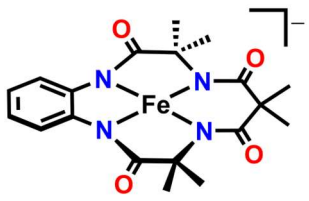

Fukuzumi and coworkers, 2020

Figure 1.11. Structure of Fe^{III}TAML, ORR catalyst reported by Fukuzumi and co-workers in 2020.[52]

In 2023, Zhang *et al.* demonstrated the importance of bimetallic cooperativity to facilitate the production of water in a nonheme CuFe-OAc system, comparing results to analogous CuCu-OAc and FeFe-OAc systems.[56] The CuFe analogue reached a turnover frequency (TOF) of 2.4 x 10^3 s^{-1} for H_2O with TEA•HCl as a proton source compared to TOF of 2.7 s^{-1} for H_2O_2 of the CuCu system and an inactive FeFe system. The key difference in activity and selectivity was found to be the M_2-O_2 intermediates that are accessible during catalysis, where through computational and mechanistic analyses it was shown that collaboration between Fe and Cu promotes O–O bond cleavage through a key $Cu^{II}(\mu\text{-}\eta^1\text{:}\eta^2\text{-}O_2)Fe^{III}$ (**Figure 1.12**, left). In comparison, the CuCu system was only able to form a bridging peroxo intermediate between the two Cu sites ($Cu^{II}(\mu\text{-}\eta^1\text{:}\eta^1\text{-}O_2)Cu^{II}$, **Figure 1.12**, right). Importantly, reduction and O–O bond cleavage $Cu^{II}(\mu\text{-}\eta^1\text{:}\eta^2\text{-}O_2)Fe^{III}$ was found to be more favorable, contrasting to $Cu^{II}(\mu\text{-}\eta^1\text{:}\eta^1\text{-}O_2)Cu^{II}$, where the protonation of the peroxo intermediate to release H_2O_2 was more favorable. These data are important in emphasizing the value of bimetallic cooperativity during the ORR in controlling activity and selectivity, particularly for key reactive intermediates during catalysis.

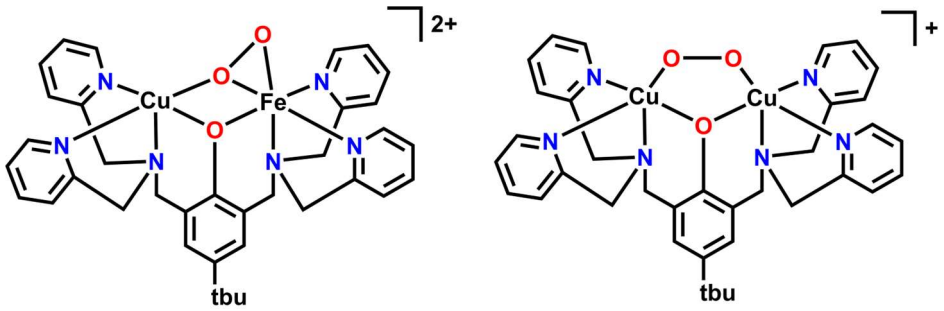

$Cu^{II}(\mu\text{-}\eta^1\text{:}\eta^2\text{-}O_2)Fe^{III}$ $Cu^{II}(\mu\text{-}\eta^1\text{:}\eta^1\text{-}O_2)Cu^{II}$

Figure 1.12. Relevant O_2 intermediates of dinuclear CuFe and CuCu complexes during ORR where CuFe (left) makes H_2O and CuCu (right) makes H_2O_2.[56]

More recently, Paria and co-workers reported an Fe^{III} catalyst containing a monoanionic bispyridine-dioxime ligand $Fe^{III}(HL)(CH_3CN)_2$, (**Figure 1.13**).[57] Interestingly, they found the role of the oxime protons were essential to catalytic reduction of O_2 to water, where exchanging the oxime protons with either methyl groups or a bridging $–BPh_2$ moiety suppresses catalytic activity.

Under both electrochemical and chemical conditions using Cp^*_2Fe as a reductant and trifluoroacetic acid (TFAH) as a proton source, $Fe^{III}(HL)(CH_3CN)_2$ was active for ORR, where the rate of catalysis showed a first-order dependence on catalyst, acid, and O_2 concentrations. Through mechanistic analyses, they propose that the rate-determining step of the catalytic cycle is intramolecular proton transfer to the distal O atom of the intermediate Fe–OOH species by the oxime backbone to promote O–O bond cleavage and release H_2O. While the $–BPh_2$ substituted derivative is active under chemical conditions, albeit much slower, H_2O is also the primary product. The suppression of catalysis emphasizes the importance of the secondary coordination sphere containing the proton relay in directing the proton donor co-substrate to the active site.

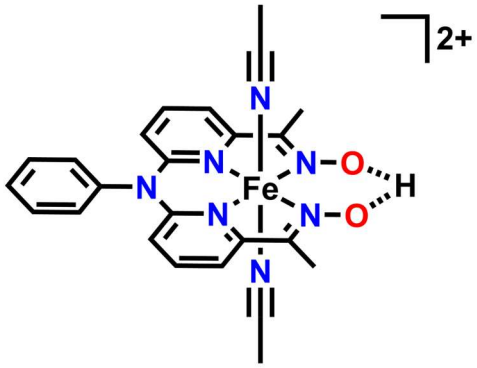

Paria and co-workers, 2024

Figure 1.13. Non-heme Fe complex containing oxime protons found to be the most active ORR catalyst studied by Paria and co-workers.[57]

Despite the extensive work that has focused on Fe-based systems for the ORR, there remains a disparity in the understanding of non-heme Fe systems. Taken together, the limited work on non-heme Fe systems for ORR has shown strategies to enhance and tune catalysis including the use of dinuclear active sites as well as tuning the primary and secondary coordination sphere. Elucidation of the controlling factors that tune electronic, steric, and secondary sphere interactions that can tune ORR at Fe metal centers is crucial for the development of optimized systems and provide a foundation for understanding the underlying structure-function relationships of their ORR response.

1.4. Catalytic O_2 Reduction Mediated by Mn

While Fe is a common metal center in the active sites of several enzymes, there are a number of Mn-based enzymatic active sites that activate O_2 and play crucial roles in nature, including superoxide dismutase, ribonucleotide reductase, and Mn catalases.[18,58] Mn is also found in the only enzyme active site which oxidizes water during photosynthesis (the oxygen evolution reaction, OER), which is the reverse reaction of the $4H^+/4e^-$ ORR. The Oxygen Evolving Complex (OEC) in Photosystem II contains a Mn_4CaO_5 cluster, and the Mn atoms are thought to be the key active sites for O–O bond formation.[59,60] The OEC has inspired an expanding field of Mn-based electrocatalysts for the OER.[29,61,62] However, despite the prevalence of Mn-centered enzymatic active sites for O_2 activation and reduction,[22] there remains a lack of synthetic Mn-based electrocatalysts for the ORR in comparison to iron and cobalt.

It is challenging to assess an exact first example of Mn-based ORR, given that O_2 consumption in aerobic reactions can be of secondary importance to the oxidative conversion of interest. One of the first examples of catalytic ORR by a molecular Mn system was disclosed by Hamilton and Revesz in 1966 (**Figure 1.14**).[63] Interest in developing models to understand the function of amine oxidases led to studies on an amine oxidase mimic based on catalytic amounts of pyridoxal and Mn. Amine oxidases use O_2 to convert alkylamines into aldehydes with ammonia as a co-product, producing H_2O_2 as the result of simultaneous ORR.[64] Hamilton and Revesz found that under slightly basic conditions (pH 9.1), alanine could be catalytically decomposed to pyruvate and ammonia. Reaction stoichiometry implied that H_2O_2 was produced as a co-product from O_2, although it was not observed during the reaction. However, control testing showed that H_2O_2 is rapidly consumed under reaction conditions, consistent with previous reports on the aqueous chemistry of Mn(III) ions with H_2O_2.[65] It was proposed that pyridoxal and the alanine substrate undergo a condensation reaction under catalytic conditions to form a transient imine-containing active species with the Mn ion. It is this Schiff base-type species (**Figure 1.14**), which was proposed to bind O_2 and facilitate the oxidation reaction.

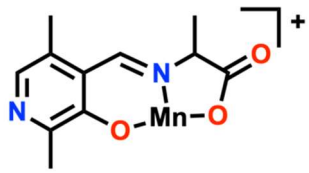

Hamilton and Revesz, 1966

Figure 1.14. Catalytically relevant intermediate in amine oxidation activity, the condensation product of pyridoxal and glycine in the presence of Mn(III).[63]

Following this report, Bettelheim *et al.* reported the electrochemical properties of Mn(III) 5,10,15,20-tetrakis-(4-*N*,*N*′,*N*″-trimethylanilinium)porphyrin pentachloride (**Figure 1.15A**) under aqueous conditions, including in the electrocatalytic reduction of O_2, in 1983.[66] In phosphate buffer with added NaCl (pH = 8), adsorption was observed (equilibration time <5 min), and the electrode was determined to have monolayer coverage of the Mn-based porphyrin complex. Analysis of the voltammetric response with respect to scan rate under catalytic conditions was used to propose that H_2O_2 was the major product. The authors did not describe whether a significant difference in activity was observed when comparing solutions of the Mn-based porphyrin complex with electrodes covered by a molecular monolayer, mentioning only that a positive shift in the catalyst standard potential was observed, which is consistent with favorable O_2 binding following the Mn(III)/(II) reduction. Subsequently in 1985, Nagao *et al.* conducted a study on electrocatalytic ORR mediated by Mn(III) 5,10,15,20-tetrakis-(1-methylpyridinium-4-yl)porphyrin pentachloride under aqueous conditions (**Figure 1.15B**).[67] Although variable scan rate data suggested a homogeneous response under inert atmosphere, exposure to solutions with >1 mM concentrations of the porphyrin was found to result in adsorption and the voltammetric response was noted to be similar for the modified electrode in a blank solution and the prepared Mn porphyrin solutions at concentrations of 57-65 micromolar. However, the stability of the adsorbed Mn porphyrin was found to be limited during ORR, where H_2O_2 was the major product, suggesting incompatibility between adsorbed catalyst and reaction product. Based on rotating ring-disk voltammetry (RRDV), a second-order rate constant of 1.1 x 10^6 $M^{-1}s^{-1}$ was determined for the

ORR to H_2O_2. Analogous adsorption phenomena for the analogous Fe-based porphyrin have been described more recently.[68]

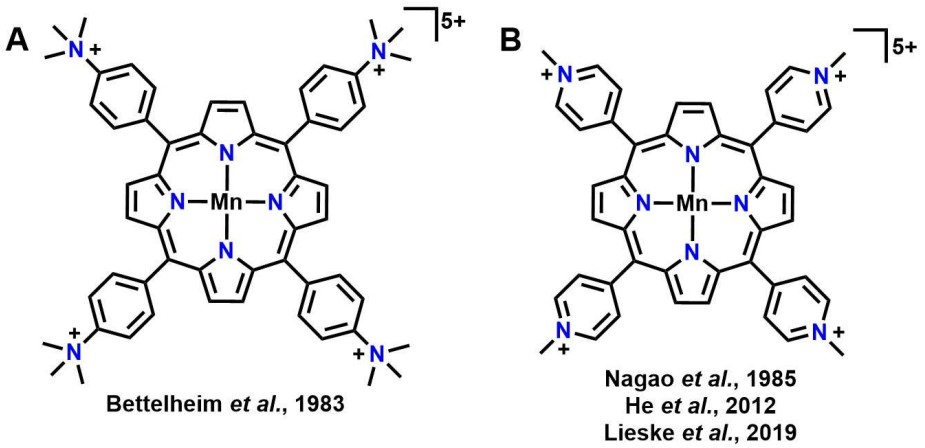

Figure 1.15. Structures of charged Mn(porphyrin) derivatives examined for ORR under aqueous conditions: (**A**) Mn(III) 5,10,15,20-tetrakis-(4-*N*,*N*′,*N*″-trimethylanilinium)-porphyrin and (**B**) Mn(III) 5,10,15,20-tetrakis-(1-methylpyridinium-4-yl)porphyrin.[66]

Concurrent with the report by Nagao *et al.*,[67] Evans and Sheriff disclosed the production of H_2O_2 during ORR in a pH range of 7.5-8.6 by combining Mn(II) with 4,5-dihydroxybenzene-1,3-disulfonate as a catalyst (**Figure 1.16**).[69] Solutions of hydroxylamine provided the electrons and protons necessary to drive the reaction with turnover numbers observed in excess of 10^4. A follow-up study in 1992 by Sheriff showed that substituted catechol moieties were also active toward ORR, although none of these combinations demonstrated better activity than the original sulfonated derivative.[70] Hydrazine was also determined to be a suitable reductant when substituted for hydroxylamine. Notably, activity with Co, Cu, or Fe ions substituted for Mn produced significantly lower activity. It was proposed that a bis(catecholate) Mn complex was the active species under reaction conditions and that the O atoms coordinated to Mn played a key role in supporting the binding of the monodeprotonated hydroxylamine reductant through a hydrogen bonding interaction, prior to an electron transfer to O_2.

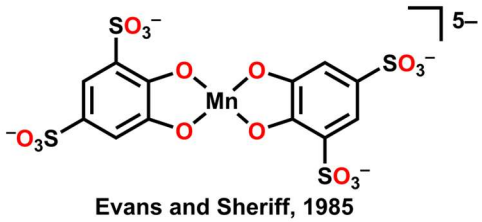

Figure 1.16. Mn(III) bis(catecholate) complex proposed as the active species for the most active catalytic system reported by Evans and Sheriff.[69]

In 1989, Fukuzumi and co-workers reported a pair of studies on the use of ferrocene derivatives as chemical reductants in the ORR mediated by metallotetraphenylporphyrins.[31,32] In both studies, Mn (**Figure 1.17**) was compared to Co and Fe in MeCN solution with perchloric acid as the proton donor. The reaction product was not directly characterized for Mn; the Co-based analogue was proposed to generate water via a 2+2 mechanism where the production of H_2O_2 was mediated by Co and H_2O_2 was reduced by the presence of excess ferrocene derivatives. Despite having a standard reduction potential 0.5 V more negative than Co, the Mn derivative had a lower catalytic second order rate constant of 1.4 x 10^5 $M^{-1}s^{-1}$, compared to 1.1 x 10^6 $M^{-1}s^{-1}$ for Co under the same conditions when decamethylferrocene was used as the reductant. Unlike ferrocene, the decamethylferrocene derivative has a reduction potential which is more negative than both catalyst standard potentials.[71]

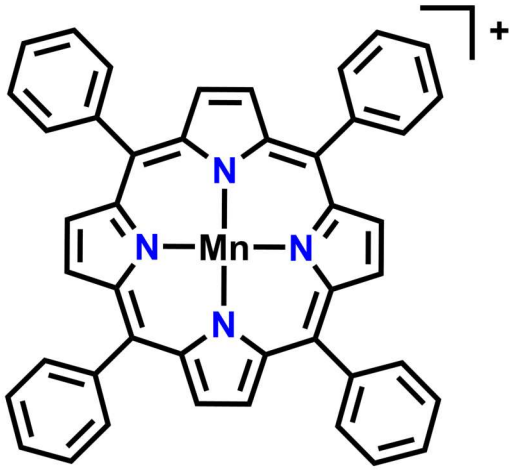

Fukuzumi and co-workers, 1989

Figure 1.17. Mn(III) 5,10,15,20-tetrakisphenylporphyrin reported as an ORR catalyst by Fukuzumi and co-workers in 1989.[31,32]

The next example of catalytic O_2 reduction by a homogeneous Mn complex was a non-porphyrinic system reported by Borovik and co-workers in 2011.[72] The supporting ligand framework, bis[(N′-tert-butylurealy)-N-ethyl]-(6-pivalamido-2-pyridylmethyl)-aminato, contains two N-coordinated monodeprotonated urea moieties and a carboxyamido group which is O-coordinated to Mn(II) for steric reasons as part of an overall $[N_4O]^{3-}$ primary coordination sphere ($[Mn(H_2bupa)]^-$; **Figure 1.18**). Exposure to O_2 rapidly produced an intermediate end-on Mn(III) peroxo species in the presence of diphenylhydrazine (or hydrazine), with net proton and electron transfer occurring to the N atom of the O-coordinated carboxyamido group and O_2, respectively. Over the course of five hours, the Mn(III) peroxo species converted to a terminal Mn(III)–O species stabilized by significant proton donation from the carboxyamide arm, resulting in structural character that is intermediate between oxo and hydroxo end states. This intermediate Mn(III) oxo/hydroxo could be converted back to the starting Mn(II) state with water release in the presence of diphenylhydrazine (overall two-electron/two-proton reduction reaction). Since the formation of the Mn(III) oxo/hydroxo intermediate also required an overall two-electron/two-proton reduction with water release, this system became catalytic when an excess of diphenylhydrazine and O_2 were present in solution. Turnover numbers as high as 200 could be observed, with the elevated concentrations of the water product degrading the catalyst beyond this point. The authors proposed that a key mechanistic aspect was the participation of two different types of hydrogen bond donors with different pK_as and steric geometries, which could stabilize intermediates and participate in formal transfers with different parameters. The development of biologically inspired secondary coordination spheres which participate in the reaction has become increasingly important in the development of active and selective molecular catalysts for a variety of redox-based transformations.[73-82]

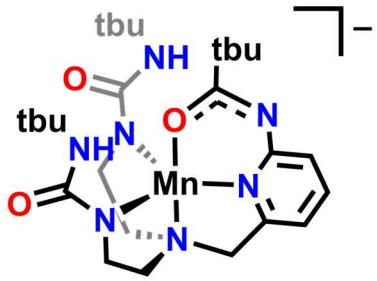

Borovik and co-workers, 2011

Figure 1.18. Mn-based $[Mn(H_2bupa)]^-$ catalyst with secondary-sphere moieties capable of hydrogen bonding with and proton transfer to O_2 and ROSs reported by Borovik and co-workers.[72]

He *et al.* also studied the electrocatalytic performance of Mn(III) 5,10,15,20-tetrakis-(1-methylpyridinium-4-yl)porphyrin pentachloride in aqueous conditions (**Figure 1.15B**), using 0.1 M aqueous solutions of trifluoromethanesulfonic acid as the supporting electrolyte.[83] Although not directly measured, trifluoromethanesulfonic acid is expected to fully dissociate and generate a working solution with a pH = 1.[84] Under these conditions, the Mn porphyrin produced H_2O_2 as the primary product, with a comparable second order rate constant (10^4 $M^{-1}s^{-1}$) to the Co analogue which produced the same majority product, despite the standard potential for Mn being measured to be 0.2 V more reducing under reaction conditions. Adsorption of the complex was not observed and catalyst degradation was not described, although Bettelheim *et al.* had observed instability below pH < 3.6 for the related Mn(III) 5,10,15,20-tetrakis-(4-*N*,*N*′,*N*″-trimethylanilinium)porphyrin pentachloride complex **(Figure 1.15A)**.[66] In our own report on Mn(III) 5,10,15,20-tetrakis-(1-methylpyridinium-4-yl)porphyrin pentachloride, we noted an instability at pH ≤ 3 in the Mn(II) state during spectroelectrochemical experiments using Britton-Robinson Buffer, *vide infra*.[85]

Abu-Omar, Fukuzumi and co-workers disclosed in 2015 that Mn(III) corroles could catalyze the two-electron reduction of O_2 using octamethylferrocene as a sacrificial electron source and trifluoroacetic acid as the proton donor (**Figure 1.19**).[86] Unlike the known examples with porphyrins, this system is proposed to have a Mn(III) active state which can react with O_2 to produce a Mn(IV) superoxide intermediate. Mechanistic studies showed that the reaction rate had a first-order dependence on the concentrations of the catalyst and O_2 (and was independent of

the concentrations of trifluoroacetic acid and octamethylferrocene), which the authors ascribed to a catalytic cycle with O_2 binding and reduction by one-electron as the rate-determining step. Product analysis suggested that H_2O_2 was the nearly exclusive product. Unlike the previous studies by Fukuzumi and co-workers,[31] no reduction of the H_2O_2 product by octamethylferrocene was observed, which can likely be attributed to the use of the relatively weaker trifluoroacetic acid as a proton donor instead of perchloric acid. Although a Mn(V) arylimido was the catalyst precursor, the following reduction and protonation to release a primary arylamine in the catalytic reaction only required Mn(IV)/(III) cycling for ORR to occur.

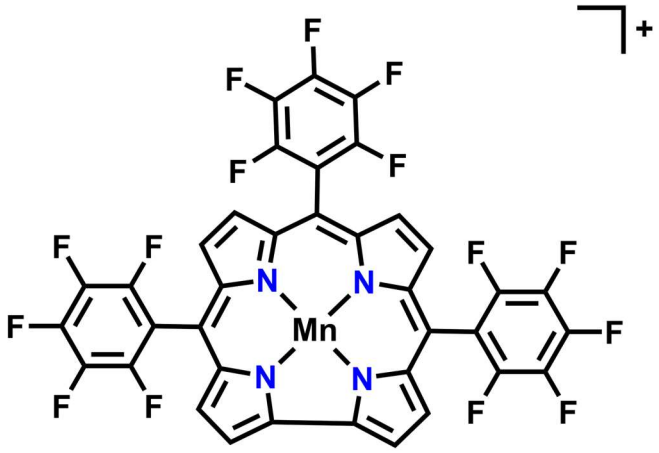

Abu-Omar, Fukuzumi and coworkers, 2015

Figure 1.19. The resting state of the catalytic cycle proposed by Abu-Omar, Fukuzumi and co-workers: Mn(III) 5,10,15-tris(pentafluorophenyl)corrole.[86]

Duboc and co-workers then published a unique example of a dinuclear Mn catalyst based on a dithiolate-modified 2,2'-bipyridine ligand (**Figure 1.20**).[87] When the dipotassium salt of the ligand was exposed to a stoichiometric amount of manganese, a dinuclear Mn complex with a single thiol ligand was isolated (*N.B.* both Mn centers retained the divalent oxidation state of the precursor perchlorate salt). We note that the stoichiometric chemistry of Mn complexes with thiolate containing ligands and O_2 has been explored extensively by Kovacs and co-workers.[88-92] Upon exposure to dry air, both centers were oxidized by a single electron and a bridging hydroxide species was recovered. Mechanistic studies established that the dinuclear monothiol species

united two separate reaction cycles, where either H_2O_2 or H_2O production was favored. The isolated μ_2-hydroxo species is situated on a stoichiometric reaction cycle, which produces water in the presence of sufficient acid. Although the dinuclear monothiol Mn(II) complex can be regenerated electrochemically, only 35% of the material is recovered following electrolysis. Conversely, octamethyl- and decamethylferrocene can be used to establish a catalytic cycle for ORR in the presence of 2,6-lutidinium tetrafluoroborate as an acid with H_2O_2 as the primary reaction product. The authors ascribed the product differentiation as a consequence of the relative concentrations of acid to the dinuclear Mn complex under catalytic and stoichiometric conditions: high acid concentrations favor protonation of the M–O bond while at low concentrations O–O bond scission can occur. Interestingly, the Fe-based analogue of this Mn system was later shown to have a product dependence based on whether an electrode or soluble chemical reductant was used: under electrochemical conditions the electrode was capable of reducing key intermediates and favoring O–O bond cleavage to produce water, while the diffusion-limited process of reduction by dissolved ferrocene derivatives instead favored H_2O_2 release through M–O bond protonation.[51]

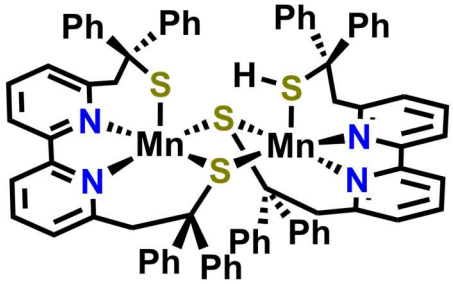

Duboc and co-workers, 2015

Figure 1.20. Dinuclear catalyst developed by Duboc and co-workers based on a dithiolate-modified 2,2′-bipyridine ligand.[87]

Noting the relatively limited examples of electrochemical ORR mediated by Mn complexes, we became interested in identifying strictly homogeneous electrocatalysts (adsorption equilibria with the electrode surface were not observed or implied). We noted that a feature of many general synthetic preparations for Mn complexes is to begin with a Mn(II) precursor and ligand under aerobic conditions and isolate a Mn(III) complex.[93] Curious about the generality of this observation

for salen- and salophen-type ligand frameworks,[94] we were interested in related ligand frameworks which did not contain potentially reactive imine bonds.[95] Based on prior studies conducted by Arora et al.,[96] we developed an alternative Pd-catalyzed method for isolating the 6,6′-di(3,5-di-*tert*-butyl-2-hydroxybenzene)-2,2′-bipyridine (^{tbu}dhbpy(H)$_2$) ligand in high-yield.[97] Exposure to a suitable base and Mn(II) precursor under aerobic conditions allowed us to isolate the Mn(III) complex Mn(^{tbu}dhbpy)Cl (**Figure 1.21**).[97] In MeCN solvent with 2,2,2-trifluoroethanol present as a weak acid, this compound was found to be ca. 80% selective for H_2O_2 production during the electrocatalytic ORR using rotating ring-disk voltammetry (RRDV) methods.

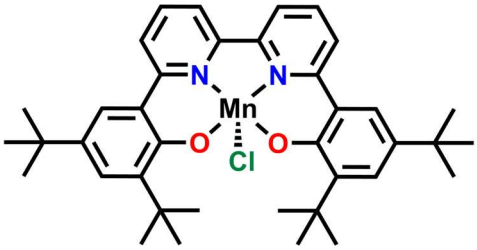

Machan and co-workers, 2018

Figure 1.21. Mn(^{tbu}dhbpy)Cl catalyst developed in our group.[97]

Under electrochemical conditions, our mechanistic testing revealed a catalytic reaction mediated by Mn(^{tbu}dhbpy)Cl which showed first-order dependence on the concentrations of catalyst, O_2, and proton donor. Further, the Mn(III)/(II) reduction couple showed a sensitivity to the concentration of the added proton donor that was independent of a Cl^- ion loss equilibria. This was ascribed to a protonation continuum involving the Mn-bound O atoms of the ligand in the Mn(II) state, as established through the use of a potential-pK_a diagram.[98] Control testing suggested that the less-than-quantitative production of H_2O_2 was the result of a Mn-mediated disproportionation reaction. On the basis of these data, we proposed a catalytic cycle where the reduction and protonation of a Mn(III) superoxide intermediate was the rate-limiting step in the reaction, k_3 in **Figure 1.22**.[99]

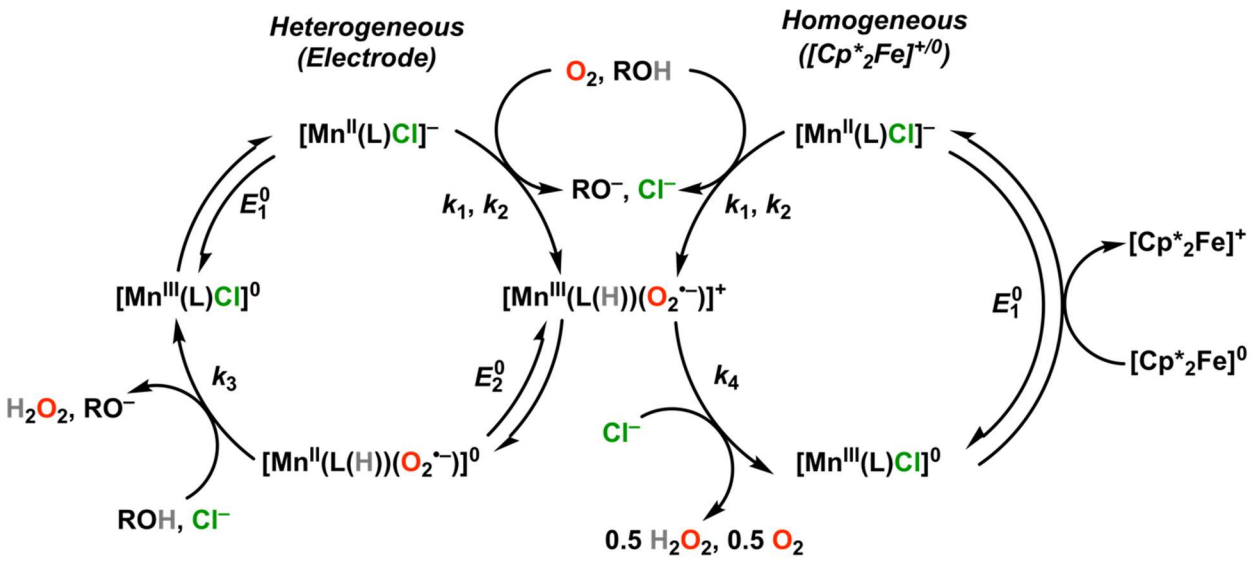

Figure 1.22. Electrocatalytic and electrochemical catalytic cycles for Mn(^{tbu}dhbpy)Cl; L(H) indicates monoprotonation of the phenolate groups of the ligand framework.[99] Reprinted with permission from *J. Am. Chem. Soc.* **2019**, *141*, 4379–4387. Copyright 2019 American Chemical Society.

Subsequently, we became interested in using thermodynamic reaction control[7,100] to decrease the overpotential for H_2O_2 formation.[99] At overpotentials (η) as low as 20 mV, electrocatalytic turnover frequencies of 7.82 s^{-1} were observed. Under electrochemical conditions with buffered proton donors (equivalent amounts of proton donor and its conjugate base), a strong dependence on acid pK_a was observed and no catalytic activity occurred when the system was placed under counterthermodynamic conditions with respect to the standard potential of H_2O_2 production (catalyst standard reduction potential was positive of the reaction standard potential). However, replacing the electrode with decamethylferrocene as a source of electron equivalents resulted in identical rates for the electrochemical ORR using same set of buffered acids with Mn(^{tbu}dhbpy)Cl, implying a mechanistic change had occurred. Under chemical reduction conditions, we proposed that the Mn(III) superoxide intermediate proposed from electrochemical studies is a branching point between two overlapping catalytic cycles. At low proton donor activity and concentration, the catalytic wave contains two distinct features, which we assigned to the Mn(III)/(II) reduction that triggers O_2 binding, and the proton-dependent reduction of the resultant Mn(III) superoxide. In other words, the second electron transfer requires slightly more reducing

conditions. Since the reducing power of the decamethylferrocene chemical reductant is fixed, the driving force for the second electron transfer decreases, allowing a disproportionation reaction to occur whereby H_2O_2 and O_2 are generated in equal amounts.

Following our initial report on Mn(^{tbu}dhbpy)Cl,[97] Nocera and co-workers reported a study on the electrocatalytic behavior of manganese porphyrins in MeCN solvent, comparing the effects of including a pendent proton donor in the secondary coordination sphere (**Figure 1.23**).[101] For Mn(III) 5,10,15,20-tetrakis-phenylporphyrin chloride, H_2O was observed as the majority product across a range of pK_as and the rate law showed a first-order dependence on Mn and O_2 concentration, with a second-order dependence on acid concentration, leading the authors to propose that hydrogen bond-assisted stabilization of a Mn(III) superoxide intermediate was important, prior to further reduction. The rate-limiting step was proposed to be a proton transfer-assisted O–O bond cleavage to generate a Mn(V) oxo intermediate which is rapidly reduced and protonated to release water under experimental conditions. Consistent with this, the use of the pendent proton donor changed the rate dependence on [acid]: at low concentrations of added acid, the system showed a first-order dependence, reflecting the participation of the pendent proton donor in stabilizing the peroxide intermediate (**Figure 1.23**). A shallow Brønsted slope was obtained in the comparison of proton donor pK_a with the catalytic rate constant, which was ascribed to the role of the two equivalents of acid in driving an electron transfer that is not rate determining to generate the pre-catalytic Mn(III) peroxide state. It was also noted that the use of strong acids promoted demetallation at sufficient concentrations under experimental conditions in MeCN, which was determined by the appearance of a new redox wave that matched the response of the free base porphyrin ligand.

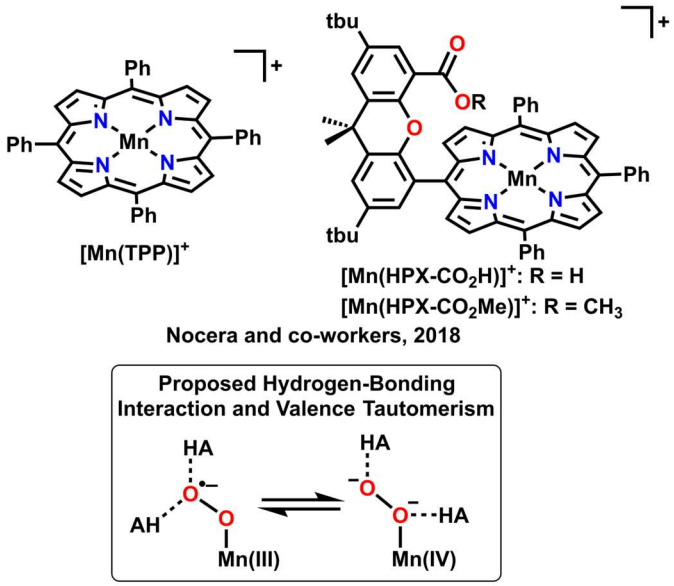

Figure 1.23. Mn(porphyrin)-based catalysts examined by Nocera and co-workers. Non-covalent interactions with hydrogen bond donors were proposed to impact the equilibrium resonance structure of the Mn–O_2 adduct. The inclusion of pendent proton sources in the hangman ligand framework was reflected in changes in the observed rate law at low acid concentrations; HA indicates added Brøntsed acid or pendent proton donor.[101]

Motivated by these precedents, we re-examined the reported behavior[67,83] of Mn(III) 5,10,15,20-tetrakis-(1-methylpyridinium-4-yl)porphyrin pentachloride under aqueous conditions (**Figure 1.15B**).[85] Contrary to these previous reports, which showed selectivity for H_2O_2 using phosphate buffer (pH = 7) and 0.1 M trifluoromethanesulfonic acid (pH = 1) in indirect product analyses based on rotating disc electrochemistry (RDE), we found selectivity ranging between 82-93% for H_2O across a pH range of 3-6 with pH-adjusted Britton-Robinson buffer. Measurements at lower pH were precluded by the demetallation of the Mn complex, as had been reported previously under strongly acidic conditions,[66,101-103] and at higher pH because of a significant background ORR response by the electrode. Control experiments showed that the selectivity for H_2O is not likely to be the result of a 2+2 mechanism in the pH range of 3-6, as expected from previous reports.[104,105] Using potential-pH analysis and UV-vis spectroelectrochemistry, we proposed that the active Mn(II) species was five-coordinate, with an axial water ligand opposite the site of O_2 binding.[106-108]

More recently, we returned to our Mn(^{tbu}dhbpy)Cl catalyst to develop a method to shift selectivity from H_2O_2 to H_2O (**Figure 1.24**).[109] Anson and Stahl had demonstrated that the combination of Co(salophen) and *p*-hydroquinone resulted in a co-electrocatalytic system for the ORR.[110] Based on prior mechanistic studies,[111] they showed that electrogeneration of *p*-hydroquinone occurs under conditions where Co(salophen) binds and activates O_2 through a single electron transfer. The resultant Co(III) superoxide is rapidly reduced by sequential HAT and proton-coupled electron transfer reactions from the electrogenerated *p*-hydroquinone, resulting in a product selectivity shift from H_2O_2 (without *p*-hydroquinone) to H_2O (with *p*-hydroquinone). Given that our Mn-based complex is also proposed to have an important intermediate peroxide,[97,99] we reasoned that redox mediators which transfer proton and electron equivalents to the catalytically active site could also be used to enhance its activity and shift product selectivity. In contrast to the work of Anson and Stahl, we elected to use a much weaker acid that should only monoprotonate the electrogenerated *p*-benzoquinone dianion under the conditions of the reaction.[112-121] The non-ideal solvent mixture of MeCN with molar concentrations of 2,2,2-trifluoroethanol resulted in the favorable solvation of the dianion by 5-6 equivalents of the proton donor (K_{eq} = 2.31 x 10^6 with 2.5 mM *p*-benzoquinone and 1.37 M 2,2,2-trifluoroethanol).[109] In this non-ideal solvation environment, two proton transfers became thermodynamically feasible, although trifluoroethoxide base is assumed to remain strongly associated in solution and oxidation of the reduced quinone core was expected to favor proton transfer back to 2,2,2-trifluoroethanol.[113,122,123] Interestingly, the non-covalent assembly of weak proton donors with the reduced quinone was found to be more reactive than *p*-hydroquinone[110]; however, it did not have intrinsic ORR activity and similarly shifted product selectivity from H_2O_2 to H_2O (96%) while increasing the observed activity (**Figure 1.24**). Based on our studies, we proposed that the observation of a product selectivity change could be attributed to the reduced and hydrogen bond-stabilized quinone mediator transferring one proton and two electrons to the Mn(III) superoxide intermediate as part of a new co-catalytic mechanism.

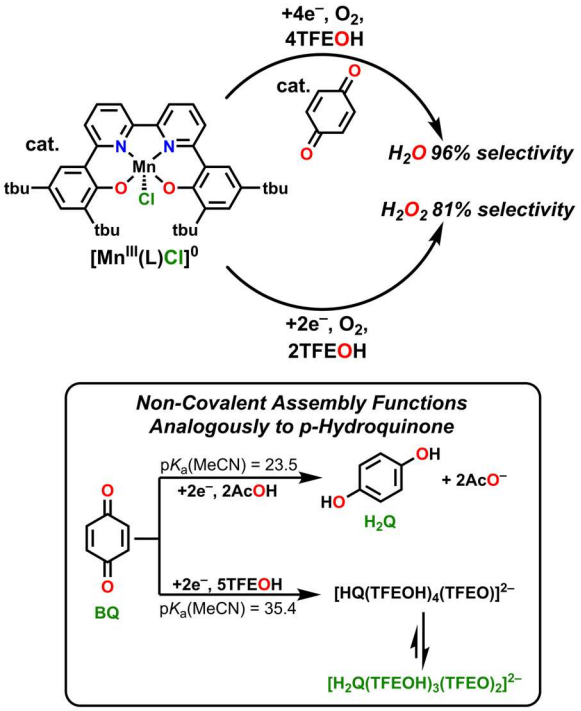

Figure 1.24. A product selectivity switch from H_2O_2 to H_2O is observed upon the inclusion of a p-benzoquinone (BQ) as a redox mediator in the presence of excess weak acid, TFEOH.[109] Adapted with permission from *Chem. Sci.* **2021**, *12*, 9733–9741. Copyright 2021 Royal Society of Chemistry.

1.5. Analysis of O_2 Adduct Structure in Mn/Co/Fe

Clearly, there is a large disparity in the available information on Mn-centered systems relative to Fe and Co-based ones. However, comparing Mn to Fe and Co is informative to the development of better catalysts. First, we must consider the ability of different metal centers to bind O_2 based on frontier orbital configuration and reduction potential.[124] Based on the limiting approximation of the Sabatier Principle, for ORR to occur the catalytic metal center must not bind any intermediate species, such as $O_2^{\bullet-}$, OOH, and OH, too weakly or too strongly. [125] It is worth emphasizing that many different scaling relationships are possible with molecular systems, but that within catalyst families, intrinsic parameters like reduction potential can scale proportionately with activity because of a relatively uniform relationship to the stability of intermediates and/or the energy of the rate-determining transition state.[37,126]

A 2014 study by Flyagina *et al.* used single-hybrid DFT functional methods to examine the primary differences in the ORR catalyzed by Mn, Fe and Co in four different macrocyclic ligand frameworks.[127] They found that while O_2 binding was dependent on the nature of the metal center and the macrocycle structure, binding to Mn was the strongest in all frameworks, with the side-on configuration preferred. The binding interaction between Co and O_2 was found to be the weakest and only occurred in an end-on fashion. The behavior of Fe was intermediate to these two extremes, binding O_2 in both end-on and side-on configurations. Next, the complete catalytic cycles were assessed for model systems of the ligand frameworks with each metal center by including an OH^- group *trans* to the site of O_2 binding. Given the relatively lower catalytic response predicted for Mn in this class of active site in comparison to Fe and Co, the authors proposed that its O_2 binding strength impedes the kinetics of subsequent reaction steps. The Fe macrocycle was predicted to be the most active of the three and catalyzes the ORR via a concerted $4e^-/4H^+$ pathway. In comparison, although both pathways were feasible, Mn was able to catalyze the $2e^-/2H^+$ pathway faster than the $4e^-/4H^+$ due to the unfavorable second protonation of the distal O atom during catalysis.[127] Further, in comparison to Fe and Co, the protonation of the intermediate bis(hydroxide) species during the $4e^-/4H^+$ pathway to generate an equivalent of water bound to the metal center was significantly less favorable for Mn, indicative of greater thermodynamic stability. Qualitatively speaking, this has been observed experimentally by Fukuzumi and co-workers, who found that Mn-based catalysts were the slowest of the three under otherwise identical reaction conditions.[31,32]

A parallel study by Baran *et al.* disclosed a computational analysis on electrochemical ORR mediated by porphyrinic first row transition metal complexes which included an assessment of the role of secondary coordination sphere interactions on catalysis using a gradient-corrected DFT functional.[128] This study found that the binding energy of metal-bound –OH, –O, and –OOH intermediates decreased moving from left to right on the periodic table, meaning again that Mn binds these intermediates more strongly than Fe and Co. Interestingly, the difference between the

M–OH and M–OOH binding energies remains constant across the first row transition metals, suggestive of an intrinsic scaling relationship between these intermediates. A comparison of the base metal macrocycle with a comparable 'hangman' scaffold containing a carboxylic acid provided adequate conformational flexibility to stabilize the M–O intermediate through a hydrogen bonding interaction (see **Figure 1.23** for an example of a 'hangman' ligand). The study found that substituting sulfonic acid for the carboxylic further stabilized the M–O intermediate, which was attributed to its decreased pK_a.[128] Overall, they found that the higher activity of the hangman metalloporphyrins relative to the unfunctionalized porphyrin arises from a combination of the destabilization of M–OH and M–OOH intermediates due to the inclusion of electron-withdrawing groups at the *meso* positions of the porphyrin in addition to the stabilization of M–O intermediates by the hangman carboxylic acid group.[128]

Explaining why Mn binds O_2 and its reduced intermediates more strongly than Fe and Co is not trivial, but there are several important factors to consider. It is generally accepted that the Fe(II) in porphyrinic frameworks binds O_2 in an end-on fashion after reducing it by one electron and that the primary bonding interactions arise from an interaction between the vacant d_z^2 of the low-spin Fe(III) center and the fully occupied π^* orbital of $O_2^{\bullet-}$, antiferromagnetically coupled as ^{2}Fe(III)-$^2O_2^{\bullet-}$, **Figure 1.25**.[129] In comparison, Mn has been shown to prefer to bind O_2 in a side-on configuration in porphyrinic frameworks and prefers to be in a high-spin state.[26,130] In this geometry, calculations performed using second-order perturbation theory indicate that the major resonance contributor is the ^{4}Mn(IV)-$^1O_2^{2-}$ resonance form (minor ^{3}Mn(III)-$^2O_2^-$), where two electrons have been formally donated from the Mn center to O_2 (**Figure 1.25**).[131] The obvious difference is that the Fe center prefers a low-spin configuration upon O_2 binding and a single electron transfer while the Mn center prefers a high-spin one, with a final electronic state which is a resonance-averaged electron transfer greater than one but less than two. Mn(II) has a high spin-pairing energy relative to later first row transition metals and strong ligand fields are required to achieve low-spin configurations in octahedral environments.[27] Low-spin states become slightly

more accessible for Mn(III), which is also prone to Jahn-Teller distortion, but the preference is still for a high-spin configuration. Consistent with the trend for the divalent and trivalent formal oxidation states, the d^3 configuration of Mn(IV) prefers an open-shell configuration.

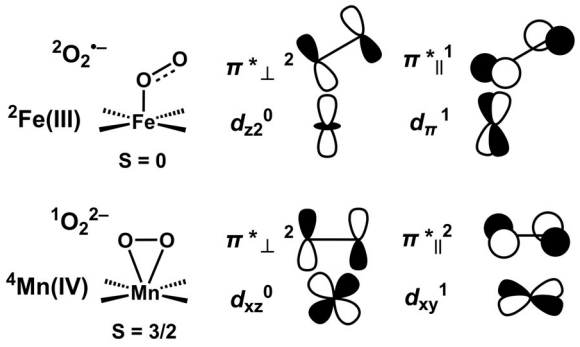

Figure 1.25. Comparison of the electronic structures proposed for O_2 adducts formed upon exposure to Mn(II) and Fe(II) porphyrins.

Phung and Pierloot have proposed that O_2 binding to Mn(II) in the porphyrinic framework occurs through sequential electron transfer events.[131] The relatively slow step is the initial electron transfer from Mn(II) center occurring between its singly occupied d_{xz} orbital and the π^* orbital perpendicular to the metal- O_2 bonding axis, forming a π-symmetric bonding interaction. The resultant adduct is in a formally quartet spin manifold, which crosses into a different quartet spin manifold as the distance between Mn and O_2 shortens during bond formation. At the minimum energy crossing point between these two different quartet spin manifolds, a second electron transfers from Mn $d_{x2\text{-}y2}$ into the π^* orbital parallel to the M–O_2 bond axis. The resultant fully occupied π^* orbital is δ symmetric with respect to the Mn d_{xy} orbital (**Figure 1.25**), resulting in a weak interaction which primarily resembles the parallel π^* orbital on O_2^{2-}. This means that the singly occupied d_{xy} orbital is formally antibonding with respect to this δ-symmetric interaction and the singly occupied d_{yz} and d_{z2} orbitals form negligible interactions with O_2^{2-}. It is reasonable to speculate that the relative inflexibility of the Mn spin manifold which manifests in this preference for side-on binding is also a contributor to the observed ORR activity and selectivity. Relative to an end-on superoxide adduct with distal and proximal O sites, a side-on peroxide adduct will have symmetric O atoms that are relatively less basic thanks to interactions with the high-valent Mn

center. For formal cleavage of the O–O bonding interaction to occur in the mononuclear side-on peroxide adduct, adjacent oxo/hydroxo species need to form (**Figure 1.2G**), which isn't sterically accessible within a rigid macrocyclic ligand framework. In the event that the formation of a bridging dinuclear Mn peroxide adduct is sterically accessible, the O atoms are again likely to be less basic and formal O–O bond cleavage would result in the possibility of strong electronic coupling between the unpaired spin of the Mn centers in the resultant Mn_2O_2 core (**Figure 1.2D** and **F**).[58,91]

As described here, there are several factors that contribute to the differences in reactivity of O_2 at transition metal centers. Work to understand how to effectively tune and control reactivity and selectivity in catalytic ORR at transition metal active sites is ongoing and expansive. While first row transition metals are a sustainable alternative to traditionally used Pt catalysts, there are alternative strategies to be employed to further develop the field of ORR.

1.6. Metal-Free Homogeneous O_2 Reduction Catalysis

As broadly summarized above, transition metal-centered catalysts have been the primary focus of the field of ORR. Organic molecules are generally ineffective catalysts, given that the highly reactive nature of ROS that are formed as a result of O_2 reduction can degrade organic molecules. However, provided that an organic molecule can undergo redox processes to form a stable electrogenerated species at a reduction potential more positive than that of $O_2/O_2^{\bullet-}$, ET to O_2 can occur and catalytic turnover is possible.[7,132] While the overall number is limited, there have been a few reports on organic molecules that have the ability to catalytically reduce O_2.[133] Although not described in detail here, there have also been reports of metal-free macrocycles for the outer-sphere reduction of O_2, as well as doped graphene-based materials.[133,134]

1.6.1. Reduction of O_2 by Organocatalysts via Outer-Sphere Mechanisms

Upon reduction of O_2 to $O_2^{\bullet-}$, there are a number of accessible pathways (**Figure 1.26**) to form H_2O_2, via an outer-sphere mechanism initiated by a redox-active organic molecule. $O_2^{\bullet-}$ can be protonated to form a $HO_2^{\bullet}$, which can be further reduced by one e^- or by an equivalent of $O_2^{\bullet-}$

to form HO_2^-, followed by protonation to form H_2O_2. Alternatively, two equiv of $HO_2^\bullet$ can disproportionate into an equivalent of H_2O_2 and O_2.

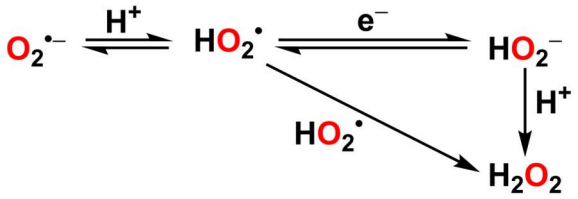

Figure 1.26. Possible reaction pathways of superoxide ($O_2^{\bullet-}$) formed via an outer-sphere electron transfer.

One of the first reports of metal-free ORR by a homogeneous organic molecule was in 1985 when Savéant and co-workers reported methyl viologen (MV^{2+}, **Figure 1.27**) as an efficient catalyst for outer-sphere O_2 reduction in acidic dimethylsulfoxide (DMSO).[132] In the presence of acetic (AcOH) and chloroacetic acid (ClAcOH), MV^{2+} operated under total catalysis conditions to form H_2O_2.[132] It was proposed that ORR by MV^{2+} was an outer-sphere mechanism, where an ET from $MV^{\bullet+}$ to O_2 forms $O_2^{\bullet-}$, which is protonated to form $HO_2^\bullet$. An additional outer-sphere ET from $MV^{\bullet+}$ occurs to form HO_2^- and is protonated to make H_2O_2.

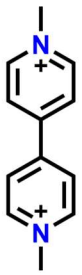

Savéant and co-workers, 1985

Figure 1.27. Methyl viologen studied by Savéant and co-workers for ORR in DMSO with AcOH and ClAcOH as proton sources.[132]

Following this, Audebert and Hapiot reported a series of 9-(4-X-phenyl)-*N*-methylacridinium salts ($Ac(X)^+$ where X = H, F, Cl; **Figure 1.28**) in DMSO with ClAcOH as a proton source that were also active for the ORR toward H_2O_2 (**Figure 1.28**). They found that at low O_2 concentrations, total catalysis was achieved, with the recovery of the reversible $Ac(H)^+/Ac(H)^\bullet$ at –0.503 V vs. SCE for X = H. The substituents had little effect on catalysis, where the kinetic rate constant of ET (k_{ET}) from $Ac(X)^\bullet$ to O_2 was dependent on the reduction potential of $Ac(X)^+$ and a more negative

reduction potential lead to an increase in k_{ET}. The unsubstituted Ac(H)$^+$ had the most negative reduction potential of –0.503 V vs. SCE, followed by Ac(F)$^+$ of –0.490 V vs. SCE and Ac(Cl)$^+$ of –0.480 V vs. SCE with observed k_{ET} of 5 x 10^{-5} $M^{-1}{\cdot}s^{-1}$, 5 x 10^{-5} $M^{-1}{\cdot}s^{-1}$, and 1.5 x 10^{-5} $M^{-1}{\cdot}s^{-1}$, respectively. They proposed that the operational mechanism was similar to that was previously reported by Savéant (described above), where H_2O_2 was formed via an outer-sphere mechanism.

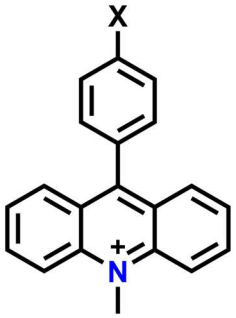

X = H, F, Cl

Audebert and Hapiot, 1993

Figure 1.28. Substituted 9-(4-X-phenyl)-N-methylacridinium salts that are active for ORR in DMSO with ClAcOH as a proton source.[135]

1.6.2. Reduction of O_2 by Organocatalysts via Inner-Sphere Mechanisms

There are fewer examples of organocatalysts that operate through an inner-sphere mechanism, where O_2 binds to an active site during catalysis. In 2020, Gabbai and co-workers analyzed a series of xanthylium-based molecules (**Figure 1.29**) that catalytically reduced O_2 to H_2O_2 with Cp^*_2Fe as a chemical reductant and methanesulfonic acid ($MeSO_3H$) as a proton source in MeCN solution.[136] It was found that [4]$^{2+}$ was the most active catalyst under these conditions with a first-order dependence on catalyst and acid concentrations and a second-order catalytic rate constant (k_{cat}) of 367 ± 6 M^{-1} s^{-1}, followed by **[3]$^{2+}$**, **[2]$^{2+}$**, and **[1]$^+$**.[136] They proposed that after formation and protonation of a bridging peroxo species between the two carbenium atoms, protonation of the key hydroperoxo intermediate to release H_2O_2 was rate-limiting. They the higher catalytic activity to the rigid dimethylxanthine backbone containing an O atom, which destabilizes C–O–O–C moiety during catalysis, making protonation more favorable. Interestingly,

these results emphasized the importance of linkers in catalyst activity as well as the role of the bifunctional carbenium groups.

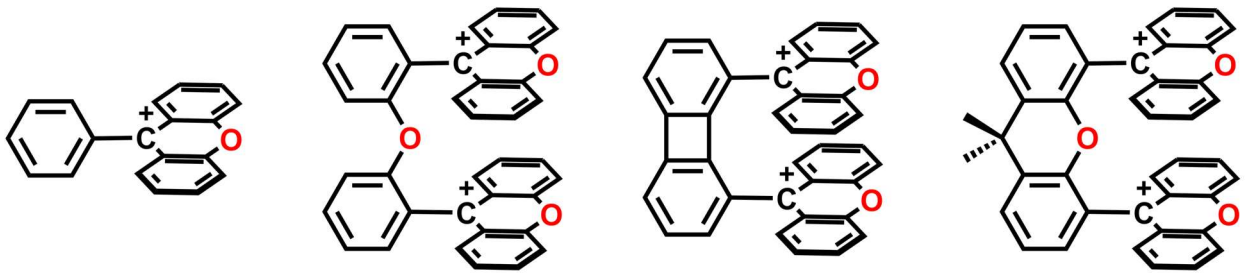

Gabbai and co-workers, 2020

Figure 1.29. Series of xanthylium compounds that were analyzed for catalytic O_2 reduction by Gabbai and co-workers.[136]

More recently, Kiatisevi and co-workers reported substituted imidazole-benzimidazole catalysts for the ORR in neutral and alkaline aqueous solution (**Figure 1.30**).[137] Substituting the imidazole moiety to tune the electronic properties of the catalyst showed a shift in selectivity. It was reported that incorporation of electron-withdrawing $–NO_2$ showed high selectivity for H_2O in a neutral aqueous solution. However, unsubstituted catalysts (where R = H, **Figure 1.30**) had the highest selectivity for H_2O_2 in alkaline conditions and achieved the highest TOFs in both neutral and alkaline conditions. Based on DFT calculations, they propose that an inner-sphere reaction occurs between the imidazole-benzimidazole to O_2, initiating formal reduction to a carbon-bound $O_2^{\bullet-}$ moiety, which is reduced and protonated to release H_2O_2.[137]

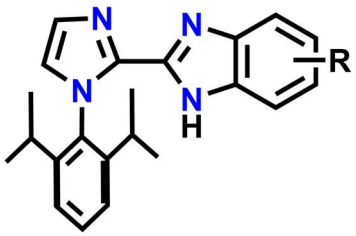

R = H, NO_2, OCH_3

Kiatisevi and co-workers, 2023

Figure 1.30. Substituted imidazole-benzimidazole catalysts for the ORR in neutral and alkaline aqueous solution.[137]

1.7. Outline of Research Chapters

Motivated by an interest in earth abundant systems for the ORR which include non-heme Fe and Mn complexes, as well as by the possibilities offered by organoelectrocatalysts, several studies have been undertaken to elucidate the reactivity of O_2 at these active sites. First, in Chapter 2 we have examined a bioinspired non-heme Fe catalyst containing an $[N_3O]^-$ ligand framework for the ORR using acetic acid (AcOH) as a proton source under spectroscopic conditions using Cp^*_2Fe as a chemical reductant. Following this, Chapter 3 describes an additional non-heme Fe-based system for the ORR containing a terpyridine $[N_3O]^-$ ligand framework with AcOH again as a proton source. Interestingly, both Fe catalysts operate via a 2+2 mechanism, where H_2O_2 produced during catalysis is reduced by $2H^+/2e^-$ to H_2O. We found that with using a more flexible ligand framework dimerization was favorable due to the axial ligand *trans* to the O_2 binding site. Interested in expanding the understanding of O_2 reactivity at Mn metal centers, we analyzed the incorporation of –OMe pendent groups in the secondary coordination sphere of bipyridine based ligand frameworks in Mn catalysts, described in Chapter 4. We found that introduction of a pendent relay shifts selectivity to H_2O_2 and through the addition of added base, we can tune the accessible reaction pathways. In an attempt to move toward more sustainable catalysts, Chapter 5 describes catalytic ORR under both electrochemical and spectrochemical conditions by an iminium-based organic electrocatalyst, revealing a change in accessible reaction pathways depending on the electron source. Under electrochemical conditions, an inner sphere mechanism occurs where reduced catalyst can bind $O_2^{\bullet-}$ and reduce it to water, whereas under spectrochemical conditions an outer-sphere mechanism occurs where initial O_2 reduction to $O_2^{\bullet-}$ is followed by H_2O_2 production. We attribute this difference in reactivity to the availability of reduced catalyst in the solution. In an extension of Chapter 5, Chapter 6 explores the use of a substituted phenanthroline diium complex for the reduction of O_2 and how changing acid pK_a can affect ORR. We found that an off-cycle dimer species forms during

catalysis and use of a sufficiently strong acid can mitigate its affect under certain conditions.

Finally, Chapter 7 summarizes the conclusions and outlook of the work described here.

1.8. References

(1) Solomon, S.; Plattner, G.-K.; Knutti, R.; Friedlingstein, P. Irreversible climate change due to carbon dioxide emissions. *Proc. Natl. Acad. Sci.* **2009**, *106* (6), 1704-1709. DOI: 10.1073/pnas.0812721106.

(2) *BP Statistical Review of World Energy, 71st Edition*; BP p.l.c., 2022.

(3) *Overview of Greenhouse Gases*. United States Environmental Protection Agency, 2024. https://www.epa.gov/ghgemissions/overview-greenhouse-gases (accessed.

(4) Kovaleva, E. G.; Lipscomb, J. D. Versatility of biological non-heme Fe(II) centers in oxygen activation reactions. *Nat. Chem. Biol.* **2008**, *4* (3), 186-193. DOI: 10.1038/nchembio.71.

(5) Blomberg, M. R. A. Mechanism of Oxygen Reduction in Cytochrome c Oxidase and the Role of the Active Site Tyrosine. *Biochem.* **2016**, *55* (3), 489-500. DOI: 10.1021/acs.biochem.5b01205.

(6) Denisov, I. G.; Makris, T. M.; Sligar, S. G.; Schlichting, I. Structure and Chemistry of Cytochrome P450. *Chem. Rev.* **2005**, *105* (6), 2253-2278. DOI: 10.1021/cr0307143.

(7) Pegis, M. L.; Wise, C. F.; Martin, D. J.; Mayer, J. M. Oxygen Reduction by Homogeneous Molecular Catalysts and Electrocatalysts. *Chem. Rev.* **2018**, *118* (5), 2340-2391. DOI: 10.1021/acs.chemrev.7b00542.

(8) Yoshikawa, S.; Shimada, A. Reaction mechanism of cytochrome c oxidase. *Chem. Rev.* **2015**, *115* (4), 1936-1989. DOI: 10.1021/cr500266a.

(9) Campbell, A. N.; Stahl, S. S. Overcoming the “Oxidant Problem”: Strategies to Use O2 as the Oxidant in Organometallic C–H Oxidation Reactions Catalyzed by Pd (and Cu). *Acc. Chem. Res.* **2012**, *45* (6), 851-863. DOI: 10.1021/ar2002045.

(10) Kiani, M.; Tian, X. Q.; Zhang, W. Non-precious metal electrocatalysts design for oxygen reduction reaction in polymer electrolyte membrane fuel cells: Recent advances, challenges and future perspectives. *Coord. Chem. Rev.* **2021**, *441*, 213954. DOI: 10.1016/j.ccr.2021.213954.

(11) Wang, Y.; Waterhouse, G. I. N.; Shang, L.; Zhang, T. Electrocatalytic Oxygen Reduction to Hydrogen Peroxide: From Homogeneous to Heterogeneous Electrocatalysis. *Adv. Energy Mater.* **2021**, *11* (15), 2003323. DOI: 10.1002/aenm.202003323.

(12) Campos-Martin, J. M.; Blanco-Brieva, G.; Fierro, J. L. G. Hydrogen peroxide synthesis: An outlook beyond the anthraquinone process. *Angew. Chem. Int. Ed.* **2006**, *45* (42), 6962-6984. DOI: 10.1002/anie.200503779.

(13) Fukuzumi, S.; Yamada, Y.; Karlin, K. D. Hydrogen peroxide as a sustainable energy carrier: Electrocatalytic production of hydrogen peroxide and the fuel cell. *Electrochim. Acta* **2012**, *82*, 493-511. DOI: 10.1016/j.electacta.2012.03.132.

(14) Saouma, C. T.; Mayer, J. M. Do spin state and spin density affect hydrogen atom transfer reactivity? *Chem. Sci.* **2014**, *5* (1), 21-31, 10.1039/C3SC52664J. DOI: 10.1039/C3SC52664J.

(15) Solomon, E. I.; Goudarzi, S.; Sutherlin, K. D. O2 Activation by Non-Heme Iron Enzymes. *Biochem.* **2016**, *55* (46), 6363-6374. DOI: 10.1021/acs.biochem.6b00635.

(16) Rittle, J.; Green, M. T. Cytochrome P450 Compound I: Capture, Ch. *Science* **2010**, *330* (6006), 933-937. DOI: 10.1126/science.1193478.

(17) Andreou, A.; Feussner, I. Lipoxygenases - Structure and reaction mechanism. *Phytochem.* **2009**, *70* (13-14), 1504-1510. DOI: 10.1016/j.phytochem.2009.05.008.

(18) Sheng, Y.; Abreu, I. A.; Cabelli, D. E.; Maroney, M. J.; Miller, A. F.; Teixeira, M.; Valentine, J. S. Superoxide dismutases and superoxide reductases. *Chem. Rev.* **2014**, *114* (7), 3854-3918. DOI: 10.1021/cr4005296.

(19) Costas, M.; Mehn, M. P.; Jensen, M. P.; Que, L. Dioxygen Activation at Mononuclear Nonheme Iron Active Sites: Enzymes, Models, and Intermediates. *Chem. Rev.* **2004**, *104* (2), 939-986. DOI: 10.1021/cr020628n.

(20) Decker, A.; Solomon, E. I. Dioxygen activation by copper, heme and non-heme iron enzymes: Comparison of electronic structures and reactivities. *Curr. Opin. Chem. Biol.* **2005**, *9* (2), 152-163. DOI: 10.1016/j.cbpa.2005.02.012.

(21) Kovaleva, E. G.; Neibergall, M. B.; Chakrabarty, S.; Lipscomb, J. D. Finding Intermediates in the O2 Activation Pathways of Non-Heme Iron Oxygenases. *Acc. Chem. Res.* **2007**, *40* (7), 475-483. DOI: 10.1021/ar700052v.

(22) Cook, E. N.; Machan, C. W. Bioinspired mononuclear Mn complexes for O2 activation and biologically relevant reactions. *Dalton Trans.* **2021**, *50* (46), 16871-16886, 10.1039/D1DT03178C. DOI: 10.1039/D1DT03178C.

(23) Machan, C. W. Advances in the Molecular Catalysis of Dioxygen Reduction. *ACS Catal.* **2020**, *10* (4), 2640-2655. DOI: 10.1021/acscatal.9b04477.

(24) Niederhoffer, E. C.; Timmons, J. H.; Martell, A. E. Thermodynamics of oxygen binding in natural and synthetic dioxygen complexes. *Chem. Rev.* **1984**, *84* (2), 137-203. DOI: 10.1021/cr00060a003.

(25) Degtyarenko, I.; Nieminen, R. M.; Rovira, C. Structure and Dynamics of Dioxygen Bound to Cobalt and Iron Heme. *Biophys. J.* **2006**, *91* (6), 2024-2034. DOI: 10.1529/biophysj.106.083048 (acccessed 2022/08/12).

(26) Zaragoza, J. P. T.; Goldberg, D. P. CHAPTER 1 Dioxygen Binding and Activation Mediated by Transition Metal Porphyrinoid Complexes. In *Dioxygen-dependent Heme Enzymes*, The Royal Society of Chemistry, 2019; pp 1-36.

(27) F. Albert Cotton, G. W., Carlos A. Murillo, Manfred Bochmann. *Advanced Inorganic Chemistry, 6th Edition*; Wiley, 1999.

(28) Fukuzumi, S.; Lee, Y. M.; Nam, W. Mechanisms of Two-Electron versus Four-Electron Reduction of Dioxygen Catalyzed by Earth-Abundant Metal Complexes. *ChemCatChem* **2018**, *10* (1), 9-28. DOI: 10.1002/cctc.201701064.

(29) Zhang, W.; Lai, W.; Cao, R. Energy-Related Small Molecule Activation Reactions: Oxygen Reduction and Hydrogen and Oxygen Evolution Reactions Catalyzed by Porphyrin- and Corrole-Based Systems. *Chem. Rev.* **2017**, *117* (4), 3717-3797. DOI: 10.1021/acs.chemrev.6b00299.

(30) Collman, J. P.; Boulatov, R.; Sunderland, C. J.; Fu, L. Functional Analogues of Cytochrome c Oxidase, Myoglobin, and Hemoglobin. *Chem. Rev.* **2004**, *104* (2), 561-588. DOI: 10.1021/cr0206059.

(31) Fukuzumi, S.; Mochizuki, S.; Tanaka, T. Metalloporphyrin-Catalyzed Reduction of Dioxygen by Ferrocene Derivatives. *Chem. Lett.* **1989**, *18* (1), 27-30. DOI: 10.1246/cl.1989.27 (acccessed 2022/04/21).

(32) Fukuzumi, S.; Mochizuki, S.; Tanaka, T. Efficient reduction of dioxygen with ferrocene derivatives, catalyzed by metalloporphyrins in the presence of perchloric acid. *Inorg. Chem.* **1989**, *28* (12), 2459-2465. DOI: 10.1021/ic00311a042.

(33) Bhunia, S.; Ghatak, A.; Dey, A. Second Sphere Effects on Oxygen Reduction and Peroxide Activation by Mononuclear Iron Porphyrins and Related Systems. *Chem. Rev.* **2022**, *122* (14), 12370-12426. DOI: 10.1021/acs.chemrev.1c01021.

(34) Brezny, A. C.; Nedzbala, H. S.; Mayer, J. M. Multiple selectivity-determining mechanisms of H2O2 formation in iron porphyrin-catalysed oxygen reduction. *Chem. Commun.* **2021**, *57* (10), 1202-1205, 10.1039/D0CC06701F. DOI: 10.1039/D0CC06701F.

(35) Pegis, M. L.; Martin, D. J.; Wise, C. F.; Brezny, A. C.; Johnson, S. I.; Johnson, L. E.; Kumar, N.; Raugei, S.; Mayer, J. M. Mechanism of Catalytic O2 Reduction by Iron Tetraphenylporphyrin. *J. Am. Chem. Soc.* **2019**, *141* (20), 8315-8326. DOI: 10.1021/jacs.9b02640.

(36) Wasylenko, D. J.; Rodríguez, C.; Pegis, M. L.; Mayer, J. M. Direct Comparison of Electrochemical and Spectrochemical Kinetics for Catalytic Oxygen Reduction. *J. Am. Chem. Soc.* **2014**, *136* (36), 12544-12547. DOI: 10.1021/ja505667t.

(37) Pegis, M. L.; McKeown, B. A.; Kumar, N.; Lang, K.; Wasylenko, D. J.; Zhang, X. P.; Raugei, S.; Mayer, J. M. Homogenous electrocatalytic oxygen reduction rates correlate with reaction overpotential in acidic organic solutions. *ACS Cent. Sci.* **2016**, *2* (11), 850-856. DOI: 10.1021/acscentsci.6b00261.

(38) Collman, J. P.; Fu, L. Synthetic Models for Hemoglobin and Myoglobin. *Acc. Chem. Res.* **1999**, *32* (6), 455-463. DOI: 10.1021/ar9603064.

(39) Collman, J. P. Synthetic models for the oxygen-binding hemoproteins. *Acc. Chem. Res.* **1977**, *10* (7), 265-272. DOI: 10.1021/ar50115a006.

(40) Carver, C. T.; Matson, B. D.; Mayer, J. M. Electrocatalytic Oxygen Reduction by Iron Tetra-arylporphyrins Bearing Pendant Proton Relays. *J. Am. Chem. Soc.* **2012**, *134* (12), 5444-5447. DOI: 10.1021/ja211987f.

(41) Mukherjee, S.; Nayek, A.; Bhunia, S.; Dey, S. G.; Dey, A. A Single Iron Porphyrin Shows pH Dependent Switch between “Push” and “Pull” Effects in Electrochemical Oxygen Reduction. *Inorg. Chem.* **2020**, *59* (19), 14564-14576. DOI: 10.1021/acs.inorgchem.0c02408.

(42) Bhunia, S.; Rana, A.; Roy, P.; Martin, D. J.; Pegis, M. L.; Roy, B.; Dey, A. Rational Design of Mononuclear Iron Porphyrins for Facile and Selective 4e–/4H+ O2 Reduction: Activation of O–O Bond by 2nd Sphere Hydrogen Bonding. *J. Am. Chem. Soc.* **2018**, *140* (30), 9444-9457. DOI: 10.1021/jacs.8b02983.

(43) Ghatak, A.; Samanta, S.; Nayek, A.; Mukherjee, S.; Dey, S. G.; Dey, A. Second-Sphere Hydrogen-Bond Donors and Acceptors Affect the Rate and Selectivity of Electrochemical Oxygen Reduction by Iron Porphyrins Differently. *Inorg. Chem.* **2022**, *61* (33), 12931-12947. DOI: 10.1021/acs.inorgchem.2c02170.

(44) Bhunia, S.; Ghatak, A.; Rana, A.; Dey, A. Amine Groups in the Second Sphere of Iron Porphyrins Allow for Higher and Selective 4e–/4H+ Oxygen Reduction Rates at Lower Overpotentials. *J. Am. Chem. Soc.* **2023**, *145* (6), 3812-3825. DOI: 10.1021/jacs.2c13552.

(45) Collman, J. P.; Kaplun, M.; Decréau, R. A. Metal corroles as electrocatalysts for oxygen reduction. *Dalton Trans.* **2006**, (4), 554-559, 10.1039/B512982F. DOI: 10.1039/B512982F.

(46) Kobayashi, N.; Nishiyama, Y. Catalytic electroreduction of molecular oxygen using iron or cobalt 4,4',4",4'"-tetracarboxyphthalocyanine. *J. Phys. Chem.* **1985**, *89* (7), 1167-1170. DOI: 10.1021/j100253a023.

(47) Han, S.-B.; Kwak, D.-H.; Park, H. S.; Choi, I.-A.; Park, J.-Y.; Ma, K.-B.; Won, J.-E.; Kim, D.-H.; Kim, S.-J.; Kim, M.-C.; et al. Chemically Regenerative Redox Fuel Cells Using Iron Redox Couples as a Liquid Catalyst with Cocatalysts. *ACS Catal.* **2016**, *6* (8), 5302-5306. DOI: 10.1021/acscatal.6b01388.

(48) Chen, K.; Liu, K.; An, P.; Li, H.; Lin, Y.; Hu, J.; Jia, C.; Fu, J.; Li, H.; Liu, H.; et al. Iron phthalocyanine with coordination induced electronic localization to boost oxygen reduction reaction. *Nat. Commun.* **2020**, *11* (1), 4173. DOI: 10.1038/s41467-020-18062-y.

(49) Cao, R.; Thapa, R.; Kim, H.; Xu, X.; Gyu Kim, M.; Li, Q.; Park, N.; Liu, M.; Cho, J. Promotion of oxygen reduction by a bio-inspired tethered iron phthalocyanine carbon nanotube-based catalyst. *Nat. Commun.* **2013**, *4* (1), 2076. DOI: 10.1038/ncomms3076.

(50) Van Den Brink, F.; Visscher, W.; Barendrecht, E. Electrocatalysis of cathodic oxygen reduction by metal phthalocyanines: Part III. Iron phthalocyanine as electrocatalyst: experimental part. *J. Electroanal. Chem. Interf. Electrochem.* **1984**, *172* (1), 301-325. DOI: 10.1016/0022-0728(84)80194-1.

(51) Wang, L.; Gennari, M.; Cantú Reinhard, F. G.; Gutiérrez, J.; Morozan, A.; Philouze, C.; Demeshko, S.; Artero, V.; Meyer, F.; de Visser, S. P.; et al. A Non-Heme Diiron Complex for (Electro)catalytic Reduction of Dioxygen: Tuning the Selectivity through Electron Delivery. *J. Am. Chem. Soc.* **2019**, *141* (20), 8244-8253. DOI: 10.1021/jacs.9b02011.

(52) Lu, X.; Lee, Y. M.; Sankaralingam, M.; Fukuzumi, S.; Nam, W. Catalytic Four-Electron Reduction of Dioxygen by Ferrocene Derivatives with a Nonheme Iron(III) TAML Complex. *Inorg. Chem.* **2020**, *59* (24), 18010-18017. DOI: 10.1021/acs.inorgchem.0c02400.

(53) Cook, E. N.; Dickie, D. A.; Machan, C. W. Catalytic Reduction of Dioxygen to Water by a Bioinspired Non-Heme Iron Complex via a 2+2 Mechanism. *J. Am. Chem. Soc.* **2021**, *143* (40), 16411-16418. DOI: 10.1021/jacs.1c04572.

(54) Cook, E. N.; Hooe, S. L.; Dickie, D. A.; Machan, C. W. Homogeneous Catalytic Reduction of O2 to H2O by a Terpyridine-Based FeN3O Complex. *Inorg. Chem.* **2022**, *61* (22), 8387-8392. DOI: 10.1021/acs.inorgchem.2c00524.

(55) Sahu, S.; Goldberg, D. P. Activation of Dioxygen by Iron and Manganese Complexes: A Heme and Nonheme Perspective. *J. Am. Chem. Soc.* **2016**, *138* (36), 11410-11428. DOI: 10.1021/jacs.6b05251.

(56) Zhang, H.-T.; Xie, F.; Guo, Y.-H.; Xiao, Y.; Zhang, M.-T. Selective Four-Electron Reduction of Oxygen by a Nonheme Heterobimetallic CuFe Complex. *Angew. Chem. Int. Ed.* **2023**, *62* (48), e202310775. DOI: 10.1002/anie.202310775 (acccessed 2024/02/06).

(57) Santra, A.; Das, A.; Kaur, S.; Jain, P.; Ingole, P. P.; Paria, S. Catalytic reduction of oxygen to water by non-heme iron complexes: exploring the effect of the secondary coordination sphere proton exchanging site. *Chem. Sci.* **2024**, 10.1039/D3SC06753J. DOI: 10.1039/D3SC06753J.

(58) Pecoraro, V. L.; Baldwin, M. J.; Gelasco, A. Interaction of Manganese with Dioxygen and Its Reduced Derivatives. *Chem. Rev.* **1994**, *94* (3), 807-826. DOI: 10.1021/cr00027a012.

(59) Yano, J.; Yachandra, V. Mn4Ca Cluster in Photosynthesis: Where and How Water is Oxidized to Dioxygen. *Chem. Rev.* **2014**, *114* (8), 4175-4205. DOI: 10.1021/cr4004874.

(60) Umena, Y.; Kawakami, K.; Shen, J.-R.; Kamiya, N. Crystal structure of oxygen-evolving photosystem II at a resolution of 1.9 Å. *Nature* **2011**, *473* (7345), 55-60. DOI: 10.1038/nature09913.

(61) Li, X.; Lei, H.; Xie, L.; Wang, N.; Zhang, W.; Cao, R. Metalloporphyrins as Catalytic Models for Studying Hydrogen and Oxygen Evolution and Oxygen Reduction Reactions. *Acc. Chem. Res.* **2022**, *55* (6), 878-892. DOI: 10.1021/acs.accounts.1c00753.

(62) Paul, S.; Neese, F.; Pantazis, D. A. Structural models of the biological oxygen-evolving complex: achievements, insights, and challenges for biomimicry. *Green Chemistry* **2017**, *19* (10), 2309-2325, 10.1039/C7GC00425G. DOI: 10.1039/C7GC00425G.

(63) Hamilton, G. A.; Revesz, A. Oxidation by Molecular Oxygen. IV. A Possible Model Reaction for Some Amine Oxidases1-3. *J. Am. Chem. Soc.* **1966**, *88* (9), 2069-2070. DOI: 10.1021/ja00961a054.

(64) Mondovì, B.; Agrò, A. F. Structure and Function of Amine Oxidases. In *Structure and Function Relationships in Biochemical Systems*, Bossa, F., Chiancone, E., Finazzi-Agrò, A., Strom, R. Eds.; Springer US, 1982; pp 141-153.

(65) Davies, G. Some aspects of the chemistry of manganese(III) in aqueous solution. *Coord. Chem. Rev.* **1969**, *4* (2), 199-224. DOI: 10.1016/S0010-8545(00)80086-7.

(66) Bettelheim, A.; Ozer, D.; Parash, R. Electrochemical and spectroscopic properties of manganese tetra(4-NN′N″-trimethylanilinium)porphyrin. *J. Chem. Soc., Faraday Trans. 1* **1983**, *79* (7), 1555-1564. DOI: 10.1039/F19837901555.

(67) Nagao, K.; Hiroshi, S.; Tetsuo, O. Catalytic Electroreduction of Molecular Oxygen Using [5,10,15,20-tetrakis-(1-methylpyridinium-4-yl)porphinato]manganese. *Chem. Lett.* **1985**, *14* (12), 1917-1920. DOI: 10.1246/cl.1985.1917.

(68) Costentin, C.; Dridi, H.; Savéant, J.-M. Molecular Catalysis of O2 Reduction by Iron Porphyrins in Water: Heterogeneous versus Homogeneous Pathways. *J. Am. Chem. Soc.* **2015**, *137* (42), 13535-13544. DOI: 10.1021/jacs.5b06834.

(69) Evans, D. F.; Sheriff, T. S. The production of hydrogen peroxide from dioxygen and hydroxylamine catalysed by manganese complexes. *J. Chem. Soc., Chem. Commun.* **1985**, (20), 1407-1408, 10.1039/C39850001407. DOI: 10.1039/C39850001407.

(70) Sheriff, T. S. Production of hydrogen peroxide from dioxygen and hydroxylamine or hydrazine catalysed by manganese complexes. *J. Chem. Soc., Dalton Trans.* **1992**, (6), 1051-1058, 10.1039/DT9920001051. DOI: 10.1039/DT9920001051.

(71) Noviandri, I.; Brown, K. N.; Fleming, D. S.; Gulyas, P. T.; Lay, P. A.; Masters, A. F.; Phillips, L. The Decamethylferrocenium/Decamethylferrocene Redox Couple: A Superior Redox Standard to the Ferrocenium/Ferrocene Redox Couple for Studying Solvent Effects on the Thermodynamics of Electron Transfer. *The J. Phys. Chem. B* **1999**, *103* (32), 6713-6722. DOI: 10.1021/jp991381+.

(72) Shook, R. L.; Peterson, S. M.; Greaves, J.; Moore, C.; Rheingold, A. L.; Borovik, A. S. Catalytic Reduction of Dioxygen to Water with a Monomeric Manganese Complex at Room Temperature. *J. Am. Chem. Soc.* **2011**, *133* (15), 5810-5817. DOI: 10.1021/ja106564a.

(73) Costentin, C.; Drouet, S.; Robert, M.; Savéant, J.-M. A Local Proton Source Enhances CO2 Electroreduction to CO by a Molecular Fe Catalyst. *Science* **2012**, *338* (6103), 90–94. DOI: 10.1126/science.1224581.

(74) Azcarate, I.; Costentin, C.; Robert, M.; Savéant, J.-M. Through-Space Charge Interaction Substituent Effects in Molecular Catalysis Leading to the Design of the Most Efficient Catalyst of CO2-to-CO Electrochemical Conversion. *J. Am. Chem. Soc.* **2016**, *138* (51), 16639-16644. DOI: 10.1021/jacs.6b07014.

(75) Nichols, A. W.; Machan, C. W. Secondary-Sphere Effects in Molecular Electrocatalytic CO2 Reduction. *Front. Chem.* **2019**, *7*. DOI: 10.3389/fchem.2019.00397.

(76) Nichols, A. W.; Cook, E. N.; Gan, Y. J.; Miedaner, P. R.; Dressel, J. M.; Dickie, D. A.; Shafaat, H. S.; Machan, C. W. Pendent Relay Enhances H_2O_2 Selectivity during Dioxygen Reduction Mediated by Bipyridine-Based Co–N_2O_2 Complexes. *J. Am. Chem. Soc.* **2021**, *143* (33), 13065-13073. DOI: 10.1021/jacs.1c03381.

(77) Nichols, Eva M.; Derrick, J. S.; Nistanaki, S. K.; Smith, P. T.; Chang, C. J. Positional effects of second-sphere amide pendants on electrochemical CO2 reduction catalyzed by iron porphyrins. *Chem. Sci.* **2018**, *9* (11), 2952-2960, 10.1039/C7SC04682K. DOI: 10.1039/C7SC04682K.

(78) Gotico, P.; Boitrel, B.; Guillot, R.; Sircoglou, M.; Quaranta, A.; Halime, Z.; Leibl, W.; Aukauloo, A. Second-Sphere Biomimetic Multipoint Hydrogen-Bonding Patterns to Boost CO2 Reduction of Iron Porphyrins. *Angew. Chem. Int. Ed.* **2019**, *58* (14), 4504-4509. DOI: 10.1002/anie.201814339.

(79) Gotico, P.; Roupnel, L.; Guillot, R.; Sircoglou, M.; Leibl, W.; Halime, Z.; Aukauloo, A. Atropisomeric Hydrogen Bonding Control for CO2 Binding and Enhancement of Electrocatalytic Reduction at Iron Porphyrins. *Angew. Chem. Int. Ed.* **2020**, *59* (50), 22451-22455. DOI: 10.1002/anie.202010859 (acccessed 2022/06/14).

(80) Rakowski Dubois, M.; Dubois, D. L. Development of Molecular Electrocatalysts for CO2 Reduction and H2 Production/Oxidation. *Acc. Chem. Res.* **2009**, *42* (12), 1974-1982, 10.1021/ar900110c. DOI: 10.1021/ar900110c.

(81) DuBois, D. L. Development of Molecular Electrocatalysts for Energy Storage. *Inorg. Chem.* **2014**, *53* (8), 3935-3960. DOI: 10.1021/ic4026969.

(82) Shaw, W. J. The Outer-Coordination Sphere: Incorporating Amino Acids and Peptides as Ligands for Homogeneous Catalysts to Mimic Enzyme Function. *Catal. Rev. - Sci. Eng.* **2012**, *54* (4), 489-550. DOI: 10.1080/01614940.2012.679453.

(83) He, Q.; Mugadza, T.; Hwang, G.; Nyokong, T. Mechanisms of Electrocatalysis of Oxygen Reduction by Metal Porphyrins in Trifluoromethane Sulfonic Acid Solution *Int J Electrochem Sc* **2012**, *7* (8), 7045 - 7064.

(84) Trummal, A.; Lipping, L.; Kaljurand, I.; Koppel, I. A.; Leito, I. Acidity of Strong Acids in Water and Dimethyl Sulfoxide. *J. Phys. Chem. A* **2016**, *120* (20), 3663-3669. DOI: 10.1021/acs.jpca.6b02253.

(85) Lieske, L. E.; Hooe, S. L.; Nichols, A. W.; Machan, C. W. Electrocatalytic reduction of dioxygen by Mn(iii) meso-tetra(N-methylpyridinium-4-yl)porphyrin in universal buffer. *Dalton Trans.* **2019**, *48*, 8633-8641, 10.1039/C9DT01436E. DOI: 10.1039/C9DT01436E.

(86) Winkler, J. R.; Gray, H. B. Electronic Structures of Oxo-Metal Ions. In *Molecular Electronic Structures of Transition Metal Complexes I*, Mingos, D. M. P., Day, P., Dahl, J. P. Eds.; Structure and Bonding, Vol. 142; Springer, 2011; pp 17-28.

(87) Gennari, M.; Brazzolotto, D.; Pécaut, J.; Cherrier, M. V.; Pollock, C. J.; Debeer, S.; Retegan, M.; Pantazis, D. A.; Neese, F.; Rouzières, M.; et al. Dioxygen Activation and Catalytic Reduction to Hydrogen Peroxide by a Thiolate-Bridged Dimanganese(II) Complex with a Pendant Thiol. *J. Am. Chem. Soc.* **2015**, *137* (26), 8644-8653. DOI: 10.1021/jacs.5b04917.

(88) Coggins, M. K.; Toledo, S.; Shaffer, E.; Kaminsky, W.; Shearer, J.; Kovacs, J. A. Characterization and dioxygen reactivity of a new series of coordinatively unsaturated thiolate-ligated manganese(II) complexes. *Inorg. Chem.* **2012**, *51* (12), 6633-6644. DOI: 10.1021/ic300192q.

(89) Coggins, M. K.; Sun, X.; Kwak, Y.; Solomon, E. I.; Rybak-Akimova, E.; Kovacs, J. A. Characterization of Metastable Intermediates Formed in the Reaction between a Mn(II) Complex and Dioxygen, Including a Crystallographic Structure of a Binuclear Mn(III)–Peroxo Species. *J. Am. Chem. Soc.* **2013**, *135* (15), 5631-5640. DOI: 10.1021/ja311166u.

(90) Kovacs, J. A. Tuning the Relative Stability and Reactivity of Manganese Dioxygen and Peroxo Intermediates via Systematic Ligand Modification. *Acc. Chem. Res.* **2015**, *48* (10), 2744-2753. DOI: 10.1021/acs.accounts.5b00260.

(91) Chaau Yan Poon, P.; Dedushko, M. A.; Sun, X.; Yang, G.; Toledo, S.; Hayes, E. C.; Johansen, A.; Piquette, M. C.; Rees, J. A.; Stoll, S.; et al. How Metal Ion Lewis Acidity and Steric Properties Influence the Barrier to Dioxygen Binding, Peroxo O-O Bond Cleavage, and Reactivity. *J. Am. Chem. Soc.* **2019**, *141*, 15046-15057. DOI: 10.1021/jacs.9b04729.

(92) Downing, A. N.; Coggins, M. K.; Poon, P. C. Y.; Kovacs, J. A. Influence of Thiolate versus Alkoxide Ligands on the Stability of Crystallographically Characterized Mn(III)-Alkylperoxo Complexes. *J. Am. Chem. Soc.* **2021**, *143* (16), 6104-6113. DOI: 10.1021/jacs.0c13001.

(93) Hanson, J. Synthesis and Use of Jacobsen's Catalyst: Enantioselective Epoxidation in the Introductory Organic Laboratory. *J. Chem. Ed.* **2001**, *78* (9), 1266. DOI: 10.1021/ed078p1266.

(94) Cozzi, P. G. Metal-Salen Schiff base complexes in catalysis: practical aspects. *Chem. Soc. Rev.* **2004**, *33* (7), 410-421, 10.1039/B307853C. DOI: 10.1039/B307853C.

(95) Machan, C. W.; Chabolla, S. A.; Kubiak, C. P. Reductive Disproportionation of Carbon Dioxide by an Alkyl-Functionalized Pyridine Monoimine Re(I) fac-Tricarbonyl Electrocatalyst. *Organometallics* **2015**, *34* (19), 4678–4683. DOI: 10.1021/acs.organomet.5b00406.

(96) Arora, H.; Philouze, C.; Jarjayes, O.; Thomas, F. CoII, NiII, CuII and ZnII complexes of a bipyridine bis-phenol conjugate: Generation and properties of coordinated radical species. *Dalton Trans.* **2010**, *39* (42), 10088–10098, 10.1039/C0DT00342E. DOI: 10.1039/C0DT00342E.

(97) Hooe, S. L.; Rheingold, A. L.; Machan, C. W. Electrocatalytic Reduction of Dioxygen to Hydrogen Peroxide by a Molecular Manganese Complex with a Bipyridine-Containing Schiff Base Ligand. *J. Am. Chem. Soc.* **2018**, *140* (9), 3232-3241. DOI: 10.1021/jacs.7b09027.

(98) McCarthy, B. D.; Dempsey, J. L. Decoding Proton-Coupled Electron Transfer with Potential-pKa Diagrams. *Inorg. Chem.* **2017**, *56* (3), 1225-1231. DOI: 10.1021/acs.inorgchem.6b02325.

(99) Hooe, S. L.; Machan, C. W. Dioxygen Reduction to Hydrogen Peroxide by a Molecular Mn Complex: Mechanistic Divergence between Homogeneous and Heterogeneous Reductants. *J. Am. Chem. Soc.* **2019**, *141* (10), 4379-4387. DOI: 10.1021/jacs.8b13373.

(100) Pegis, M. L.; Roberts, J. A. S.; Wasylenko, D. J.; Mader, E. A.; Appel, A. M.; Mayer, J. M. Standard Reduction Potentials for Oxygen and Carbon Dioxide Couples in Acetonitrile and N,N-Dimethylformamide. *Inorg. Chem.* **2015**, *54* (24), 11883-11888. DOI: 10.1021/acs.inorgchem.5b02136.

(101) Passard, G.; Dogutan, D. K.; Qiu, M.; Costentin, C.; Nocera, D. G. Oxygen Reduction Reaction Promoted by Manganese Porphyrins. *ACS Catal.* **2018**, *8* (9), 8671-8679. DOI: 10.1021/acscatal.8b01944.

(102) Weitner, T.; Budimir, A.; Kos, I.; Batinić-Haberle, I.; Biruš, M. Acid–base and electrochemical properties of manganese meso(ortho- and meta-N-ethylpyridyl)porphyrins: potentiometric, spectrophotometric and spectroelectrochemical study of protolytic and redox equilibria. *Dalton Trans.* **2010**, *39* (48), 11568-11576, 10.1039/C0DT00585A. DOI: 10.1039/C0DT00585A.

(103) Weitner, T.; Kos, I.; Mandić, Z.; Batinić-Haberle, I.; Biruš, M. Acid–base and electrochemical properties of manganese meso(ortho- and meta-N-ethylpyridyl)porphyrins: voltammetric and chronocoulometric study of protolytic and redox equilibria. *Dalton Trans.* **2013**, *42* (41), 14757-14765, 10.1039/C3DT50767J. DOI: 10.1039/C3DT50767J.

(104) Naruta, Y.; Sasayama, M.-A. Importance of Mn–Mn separation and their relative arrangement on the development of high catalase activity in manganese porphyrin dimer catalysts. *J. Chem. Soc., Chem. Comm.* **1994**, (23), 2667-2668, 10.1039/C39940002667. DOI: 10.1039/C39940002667.

(105) Balasubramanian, P. N.; Schmidt, E. S.; Bruice, T. C. Catalase modeling. 2. Dynamics of reaction of a water-soluble and non .mu.-oxo dimer forming manganese(III) porphyrin with hydrogen peroxide. *J. Am. Chem. Soc.* **1987**, *109* (25), 7865-7873. DOI: 10.1021/ja00259a040.

(106) Carnieri, N.; Harriman, A.; Porter, G. Photochemistry of manganese porphyrins. Part 6. Oxidation–reduction equilibria of manganese(III) porphyrins in aqueous solution. *J. Chem. Soc., Dalton Trans.* **1982**, (5), 931-938, 10.1039/DT9820000931. DOI: 10.1039/DT9820000931.

(107) Harriman, A. Photochemistry of manganese porphyrins. Part 8. Electrochemistry. *J. Chem. Soc., Dalton Trans.* **1984**, (2), 141-146, 10.1039/DT9840000141. DOI: 10.1039/DT9840000141.

(108) Harriman, A.; Porter, G. Photochemistry of manganese porphyrins. Part 1.—Characterisation of some water soluble complexes. *J. Chem. Soc., Faraday Trans. 2* **1979**, *75* (0), 1532-1542, 10.1039/F29797501532. DOI: 10.1039/F29797501532.

(109) Hooe, S. L.; Cook, E. N.; Reid, A. G.; Machan, C. W. Non-covalent assembly of proton donors and p- benzoquinone anions for co-electrocatalytic reduction of dioxygen. *Chem. Sci.* **2021**, *12* (28), 9733-9741. DOI: 10.1039/d1sc01271a.

(110) Anson, C. W.; Stahl, S. S. Cooperative Electrocatalytic O2 Reduction Involving Co(salophen) with p-Hydroquinone as an Electron–Proton Transfer Mediator. *J. Am. Chem. Soc.* **2017**, *139* (51), 18472-18475. DOI: 10.1021/jacs.7b11362.

(111) Anson, C. W.; Ghosh, S.; Hammes-Schiffer, S.; Stahl, S. S. Co(salophen)-Catalyzed Aerobic Oxidation of p-Hydroquinone: Mechanism and Implications for Aerobic Oxidation Catalysis. *J. Am. Chem. Soc.* **2016**, *138* (12), 4186-4193. DOI: 10.1021/jacs.6b00254.

(112) Huynh, M. T.; Anson, C. W.; Cavell, A. C.; Stahl, S. S.; Hammes-Schiffer, S. Quinone 1 e– and 2 e–/2 H+ Reduction Potentials: Identification and Analysis of Deviations from Systematic Scaling Relationships. *J. Am. Chem. Soc.* **2016**, *138* (49), 15903-15910. DOI: 10.1021/jacs.6b05797.

(113) Gupta, N.; Linschitz, H. Hydrogen-Bonding and Protonation Effects in Electrochemistry of Quinones in Aprotic Solvents. *J. Am. Chem. Soc.* **1997**, *119* (27), 6384-6391. DOI: 10.1021/ja970028j.

(114) Costentin, C. Electrochemical Approach to the Mechanistic Study of Proton-Coupled Electron Transfer. *Chem. Rev.* **2008**, *108* (7), 2145-2179. DOI: 10.1021/cr068065t.

(115) Quan, M.; Sanchez, D.; Wasylkiw, M. F.; Smith, D. K. Voltammetry of Quinones in Unbuffered Aqueous Solution: Reassessing the Roles of Proton Transfer and Hydrogen Bonding in the Aqueous Electrochemistry of Quinones. *J. Am. Chem. Soc.* **2007**, *129* (42), 12847-12856. DOI: 10.1021/ja0743083.

(116) Staley, P. A.; Lopez, E. M.; Clare, L. A.; Smith, D. K. Kinetic Stabilization of Quinone Dianions via Hydrogen Bonding by Water in Aprotic Solvents. *J. Phys. Chem. C* **2015**, *119* (35), 20319-20327. DOI: 10.1021/acs.jpcc.5b06323.

(117) Evans, D. H. One-Electron and Two-Electron Transfers in Electrochemistry and Homogeneous Solution Reactions. *Chem. Rev.* **2008**, *108* (7), 2113-2144. DOI: 10.1021/cr068066l.

(118) Astudillo, P. D.; Tiburcio, J.; González, F. J. The role of acids and bases on the electrochemical oxidation of hydroquinone: Hydrogen bonding interactions in acetonitrile. *J. Electroanal. Chem.* **2007**, *604* (1), 57-64. DOI: 10.1016/j.jelechem.2007.02.031.

(119) Astudillo, P. D.; Valencia, D. P.; González-Fuentes, M. A.; Díaz-Sánchez, B. R.; Frontana, C.; González, F. J. Electrochemical and chemical formation of a low-barrier proton transfer complex between the quinone dianion and hydroquinone. *Electrochim. Acta* **2012**, *81*, 197-204. DOI: 10.1016/j.electacta.2012.07.078.

(120) Alligrant, T. M.; Hackett, J. C.; Alvarez, J. C. Acid/base and hydrogen bonding effects on the proton-coupled electron transfer of quinones and hydroquinones in acetonitrile: Mechanistic investigation by voltammetry, 1H NMR and computation. *Electrochim. Acta* **2010**, *55* (22), 6507-6516. DOI: 10.1016/j.electacta.2010.06.029.

(121) Lam, Y. C.; Nielsen, R. J.; Gray, H. B.; Goddard, W. A. A Mn Bipyrimidine Catalyst Predicted To Reduce CO2 at Lower Overpotential. *ACS Catal.* **2015**, *5* (4), 2521-2528. DOI: 10.1021/cs501963v.

(122) Macías-Ruvalcaba, N. A.; Okumura, N.; Evans, D. H. Change in Reaction Pathway in the Reduction of 3,5-Di-tert-butyl-1,2-benzoquinone with Increasing Concentrations of 2,2,2-Trifluoroethanol. *J. Phys. Chem. B* **2006**, *110* (43), 22043-22047. DOI: 10.1021/jp064003v.

(123) Evans, D. H.; René, A. Reinvestigation of a former concerted proton-electron transfer (CPET), the reduction of a hydrogen-bonded complex between a proton donor and the anion radical of 3,5-di-tert-butyl-1,2-benzoquinone. *Phys. Chem. Chem. Phys.* **2012**, *14* (14), 4844-4848, 10.1039/C2CP00021K. DOI: 10.1039/C2CP00021K.

(124) Zagal, J. H.; Koper, M. T. M. Reactivity Descriptors for the Activity of Molecular MN4 Catalysts for the Oxygen Reduction Reaction. *Angew. Chem. Int. Ed.* **2016**, *55* (47), 14510-14521. DOI: 10.1002/anie.201604311.

(125) Sabatier, P. Hydrogénations et déshydrogénations par catalyse. *Ber. Dtsch. Chem. Ges.* **1911**, *44* (3), 1984-2001. DOI: 10.1002/cber.19110440303.

(126) Costentin, C.; Savéant, J.-M. Homogeneous Molecular Catalysis of Electrochemical Reactions: Manipulating Intrinsic and Operational Factors for Catalyst Improvement. *J. Am. Chem. Soc.* **2018**, *140* (48), 16669-16675. DOI: 10.1021/jacs.8b09154.

(127) Flyagina, I. S.; Hughes, K. J.; Pourkashanian, M.; Ingham, D. B. DFT study of the oxygen reduction reaction on iron, cobalt and manganese macrocycle active sites. *Int. J. Hydrogen Energy* **2014**, *39* (36), 21538-21546. DOI: 10.1016/j.ijhydene.2014.09.075.

(128) Baran, J. D.; Grönbeck, H.; Hellman, A. Analysis of Porphyrines as Catalysts for Electrochemical Reduction of O2 and Oxidation of H2O. *J. Am. Chem. Soc.* **2014**, *136* (4), 1320-1326. DOI: 10.1021/ja4060299.

(129) Chen, H.; Ikeda-Saito, M.; Shaik, S. Nature of the Fe−O2 Bonding in Oxy-Myoglobin: Effect of the Protein. *J. Am. Chem. Soc.* **2008**, *130* (44), 14778-14790. DOI: 10.1021/ja805434m.

(130) VanAtta, R. B.; Strouse, C. E.; Hanson, L. K.; Valentine, J. S. Peroxo(tetraphenylporphinato)manganese(III) and chloro(tetraphenylporphinato)manganese(II) anions. Synthesis, crystal structures, and electronic structures. *J. Am. Chem. Soc.* **1987**, *109* (5), 1425-1434. DOI: 10.1021/ja00239a024.

(131) Phung, Q. M.; Pierloot, K. The dioxygen adducts of iron and manganese porphyrins: electronic structure and binding energy. *Phys. Chem. Chem. Phys.* **2018**, *20* (25), 17009-17019, 10.1039/C8CP03078B. DOI: 10.1039/C8CP03078B.

(132) Andrieux, C. P.; Hapiot, P.; Sa Véant, J. M. Electron transfer coupling of diffusional pathways. Homogeneous redox catalysis of dioxygen reduction by the methylviologen cation radical in acidic dimethylsulfoxide. *J. Electroanal. Chem. Interf. Electrochem.* **1985**, *189* (1), 121-133. DOI: 10.1016/0368-1874(85)85630-6.

(133) Dai, L.; Xue, Y.; Qu, L.; Choi, H.-J.; Baek, J.-B. Metal-Free Catalysts for Oxygen Reduction Reaction. *Chem. Rev.* **2015**, *115* (11), 4823-4892. DOI: 10.1021/cr5003563.

(134) Kahan, R. J.; Hirunpinyopas, W.; Cid, J.; Ingleson, M. J.; Dryfe, R. A. W. Well-Defined Boron/Nitrogen-Doped Polycyclic Aromatic Hydrocarbons Are Active Electrocatalysts for the Oxygen Reduction Reaction. *Chem. Mater.* **2019**, *31* (6), 1891-1898. DOI: 10.1021/acs.chemmater.8b04027.

(135) Audebert, P.; Hapiot, P. Preparation and electrochemistry of several substituted 9-(4-R-phenyl)-N-methylacridinium salts.: Kinetic analysis of the O2 catalytic reduction in acidic dimethylsulfoxide and in hydrophobic Nafion® gels. *J. Electroanal. Chem.* **1993**, *361* (1), 177-183. DOI: 10.1016/0022-0728(93)87052-W.

(136) Karimi, M.; Borthakur, R.; Dorsey, C. L.; Chen, C.-H.; Lajeune, S.; Gabbaï, F. P. Bifunctional Carbenium Dications as Metal-Free Catalysts for the Reduction of Oxygen. *J. Am. Chem. Soc.* **2020**, *142* (32), 13651-13656. DOI: 10.1021/jacs.0c04841.

(137) Tanjedrew, N.; Thammanatpong, K.; Surawatanawong, P.; Chakthranont, P.; Chantarojsiri, T.; Unjarern, T.; Kiatisevi, S. Tunable Metal-free Imidazole-Benzimidazole Electrocatalysts for Oxygen Reduction in Aqueous Solutions. *Chem. Eur. J.* **2023**, *30* (5), e202302854. DOI: 10.1002/chem.202302854.

Chapter 2:

Catalytic Reduction of Dioxygen to Water by a Bioinspired Non-Heme Iron Complex via a 2+2 Mechanism

Published as:

Cook, E. N.; Dickie, D. A.; Machan, C. W.*, *Journal of the American Chemical Society* **2021** 143, 40, 16411-16418. doi: 10.1021/jacs.1c04572.

2.1. Abstract

We report a bioinspired non-heme Fe complex with a tripodal $[N_3O]^-$ ligand framework ($Fe(PMG)(Cl)_2$) that is electrocatalytically active toward dioxygen reduction with acetic acid as a proton source in acetonitrile solution. Under electrochemical and chemical conditions, $Fe(PMG)(Cl)_2$ selectively produces water via a 2+2 mechanism, where H_2O_2 is generated as a discrete intermediate species before further reduction to two equivalents of H_2O. Mechanistic studies support a catalytic cycle for dioxygen reduction where an off-cycle peroxo dimer species is the resting state of the catalyst. Spectroscopic analysis of the reduced complex $Fe^{II}(PMG)Cl$ shows the stoichiometric formation of an Fe(III)-hydroxide species following exposure to H_2O_2; no catalytic activity for H_2O_2 disproportionation is observed, although the complex is electrochemically active for H_2O_2 reduction to H_2O. Electrochemical studies, spectrochemical experiments, and DFT calculations suggest that the carboxylate moiety of the ligand is sensitive to hydrogen-bonding interactions with the acetic acid proton donor upon reduction from Fe(III)/(II), favoring chloride loss *trans* to the tris-alkyl amine moiety of the ligand framework. These results offer insight into how mononuclear non-heme Fe active sites in metalloproteins distribute added charge and poise proton donors during reactions with dioxygen.

2.2. Introduction

The oxygen reduction reaction (ORR) plays important roles in both biological energy conversion and next-generation energy technologies.[1-6] Selectivity for the two proton-two electron ($2H^+/2e^-$) product, H_2O_2, is attractive as a direct route to an important chemical oxidant.[1, 7] The alternative $4H^+/4e^-$ product, H_2O, is an ideal half-reaction for fuel cell applications, where it enables the coupled electrochemical oxidation of energy-rich fuels.[1] This is analogous to the use of O_2 in many bioinorganic systems, where O_2 reduction drives chemical oxidation reactions. Additionally, the ORR can proceed via a 2+2 mechanism, where the $2H^+/2e^-$ reduction of O_2 to H_2O_2 is further reduced by an additional $2H^+$ and $2e^-$ to H_2O.[1] An understanding of what controls O_2 activation, reduction, and ORR selectivity at well-defined metal active sites remains an important question.

Platinum has traditionally been the best catalyst for the ORR, but due to its high cost and limited reserves, low-cost and earth-abundant transition metal catalysts are needed. [5] Stemming from continuous efforts to mimic biological active sites for O_2 storage, transport, and activation, macrocyclic N_4 complexes with iron,[8,9] cobalt,[10,11] and manganese[12,13] active sites have been studied extensively as molecular catalysts for the ORR.[1,14-18] Non-macrocyclic ligand frameworks have been relatively less explored, with limited reports on cobalt-,[19,20] copper-,[21,22] and manganese-based[23-25] systems.[1] To the best of our knowledge, there has only been one previously reported non-macrocyclic iron system shown to be a competent catalyst for the ORR.[26] In 2019, Wang *et al.* reported an iron(II) thiolate dinuclear complex that was an efficient ORR catalyst whose selectivity shifted from H_2O_2 (~95%) under chemical conditions to H_2O (less than ~10% H_2O_2) under electrochemical conditions.[26] It is also worth noting that an electrode-deposited molecular non-heme iron catalyst for the ORR has been reported previously.[27]

Despite the focus on Fe heme-based molecular ORR catalysts, there are abundant examples of non-heme Fe metalloenzymes that activate dioxygen.[28-32] For example, iron dioxygenases catalyze the oxidative cleavage of catechols during the degradation of natural aromatics.[29] The

inner coordination sphere of this active site contains histidine residues and an anionic carboxylate moiety.[29,33,34] Synthetic models of dioxygenase active sites have been developed using a variety of tripodal ligand frameworks to study O_2 activation and reactivity with catechol.[29,35-39] However, we are unaware of demonstrated catalytic activity toward the ORR with these activity and structural models. Interestingly, homologous mononuclear Fe active sites are also observed in Fe superoxide dismutase, lipoxygenase, pterin-dependent hydroxylases, α-keto acid dependent enzymes, and isopenicillin N synthase.[29,40]

A $[N_3O]^-$ tripodal ligand framework provides an anionic O group in the inner-coordination sphere, which can act as a Lewis base, and two open coordination sites in the axial and equatorial positions that allow for substrate binding.[38] Using a $[N_3O]^-$ ligand that mimics the inner-coordination sphere of the metalloenzymes described above, we show that the non-heme Fe(III) complex $Fe(PMG)(Cl)_2$ electrocatalytically reduces O_2 to water through a 2+2 mechanism with quantitative efficiency. Further, a component of catalyst activation during reduction is a noncovalent interaction between acetic acid and the carboxylate moiety, suggesting that distribution of added charge and proton equivalents between the metal center and ligand framework is essential to the observed activity.

2.3. Results

2.3.1. Synthesis and Characterization

N-*N*′-bis(2-pyridylmethyl)glycine (PMG(H)) was synthesized using previously reported procedures.[41] Under basic conditions, a solution of glycine and two equivalents of 2-(chloromethyl)pyridine hydrochloride was allowed to stir at room temperature for five days. Metalation of PMG(H) to generate Fe(N,N′-bis(2-pyridylmethyl)glycine)$(Cl)_2$ ($Fe(PMG)(Cl)_2$) was achieved after 24 h under reflux conditions in ethanol with a stoichiometric amount of iron(III) chloride hexahydrate. UV-vis and NMR spectroscopies, as well as ESI-MS and microanalysis (See SI), are consistent with the crystallographically determined structure of the Fe complex

shown in **Figure 2.1**. Evans' method measurements in methanol (MeOH) exhibited a μ_{eff} of 5.64 ± 0.05, consistent with a high spin d^5 Fe(III) complex.[42,43]

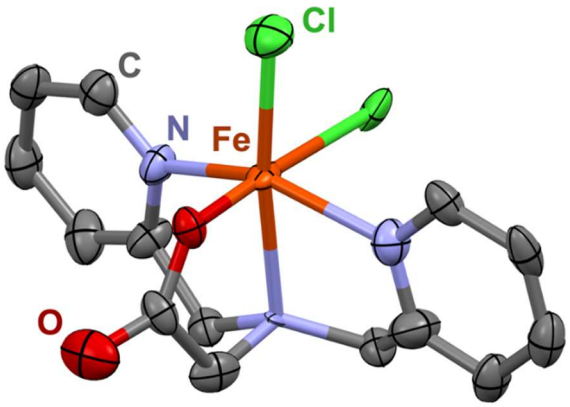

Figure 2.1. Molecular structure of Fe(PMG)$(Cl)_2$ from single crystal X-ray diffraction studies. Orange = Fe, green = Cl, red = O, blue = N, gray = C; H atoms omitted for clarity; ellipsoids at 50%.

2.3.2. Electrochemical Studies with O_2.

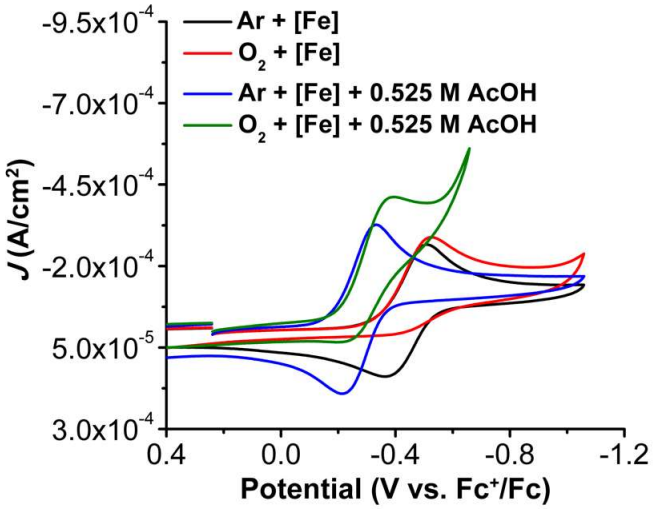

Figure 2.2. CVs of Fe(PMG)$(Cl)_2$ under Ar (black) saturation with 0.525 M AcOH (blue) and O_2 (red) saturation with 0.525 M AcOH (green). Conditions: 1 mM Fe(PMG)$(Cl)_2$, 0.1 M $TBAPF_6$ in MeCN; glassy carbon working electrode; Ag/AgCl pseudoreference electrode; scan rate 100 mV/s; referenced to internal ferrocene standard.

Cyclic voltammetry (CV) experiments were performed on Fe(PMG)$(Cl)_2$ in a solution of 0.1 M tetrabutylammonium hexafluorophosphate ($TBAPF_6$) in acetonitrile (MeCN). A single quasi-reversible feature is observed at $E_{1/2}$ = –0.44 V vs. Fc^+/Fc (**Figure 2.2**, black trace), which is attributed to the Fe(III)/(II) reduction. This reduction feature shows a proton donor-dependent

voltage response where titrating acetic acid (AcOH) into solution shows a shift to more positive potentials (**Figure 2.2**, blue trace). Plotting the $E_{1/2}$ values against log[AcOH] exhibits a 127 mV/log [AcOH] dependence (**Figure S2.6**). Although Nernstian responses can be consistent with a proton-coupled electron transfer (PCET) process,[23,44,45] control studies suggest that formal proton transfer does not occur under these conditions. We conducted analogous electroanalytic studies with a control complex containing a neutral ligand framework (tris-pyridylamine = TPA), [Fe(TPA)$(Cl)_2$][Cl], whose structure is similar to a previously reported Fe(II) complex.[46] In MeCN solution, a reversible Fe(III)/(II) redox feature at −0.20 V vs Fc^+/Fc is observed under Ar saturation conditions, which shows a proton donor-dependent voltage response: titrating AcOH shows a 91 mV/log [AcOH] dependence (**Figure S2.7**). These data suggest that addition of AcOH aids in Cl^- dissociation. However, the steeper voltage dependence of Fe(PMG)$(Cl)_2$ on [AcOH] is suggestive of additional interactions, which we propose involve hydrogen-bonding interactions with the anionic carboxylate group, *vide infra*.

Under O_2 saturation conditions the Fe(III)/(II) reduction feature of complex **1** becomes completely irreversible (**Figure 2.2**, red trace), indicative of O_2 binding to the reduced metal center via an *EC* mechanism.[47,48] To ensure that the observed loss of reversibility was not attributed to delayed Cl^- loss, variable scan rate studies were performed from 20-100 mV/s under Ar saturation conditions (**Figure S2.8**). These data suggest chloride-loss kinetics are slow on the CV timescale and that irreversibility is driven by thermodynamically favorable O_2 binding to Fe(II). In the presence of AcOH as an added proton donor, there is an increase in current at the Fe(III)/(II) reduction feature, consistent with electrochemical activity toward O_2 reduction (**Figure 2.2**, green trace). Subsequently, second-order rate constants for O_2 binding under aprotic (k_{O2}) and protic ($k_{O2,H+}$) conditions were determined using the evolution of the observed peak potential with respect to changes in scan rate, as previously described by Dempsey and co-workers.[49,50] The rate constant, k_{O2}, was determined to be 18.6 ± 4.6 $M^{-1}s^{-1}$ and $k_{O2,H+}$ = 7.88 ± 1.2 $M^{-1}s^{-1}$ with 0.525 M AcOH (See SI). The decrease from aprotic to protic conditions indicates that O_2 binding is

sensitive to the reducing power of the Fe center in a Tafel-dependent manner. Rotating ring-disk electrode methods were used to determine that $Fe(PMG)(Cl)_2$ demonstrated 25 ± 10% selectivity for H_2O_2 under electrochemical ORR conditions with 0.525 M AcOH present (See SI).

To analyze the proton-donor dependence and take into account homoconjugation of AcOH in MeCN ($\log(K_{AHA}) = 3.9$), CVs were subsequently taken under buffered conditions. [51] Addition of 1:1 tetrabutylammonium acetate (TBAAcO):AcOH resulted in a negative potential shift of 190 mV in the Fe(III)/(II) reduction feature (**Figure S2.12**), indicative of acetate binding as a ligand to the Fe metal center and implying the formation of a new Fe(III) species. Spectrochemical evaluation of ORR catalysis under buffered conditions showed a significantly slower rate in comparison to non-buffered conditions, reflecting the shift to a more negative potential (**Figure S2.30**). We propose that the observed decrease in activity is the result of superior binding of acetate to the Fe center following reduction to the formally Fe(II) state. As a result of this inhibition, although the effective overpotentials given below are corrected using the reported homoconjugation value for AcOH in MeCN, this value should still be considered as a lower limit estimation (See SI).[52]

2.3.3. Spectrochemical Studies with O_2.

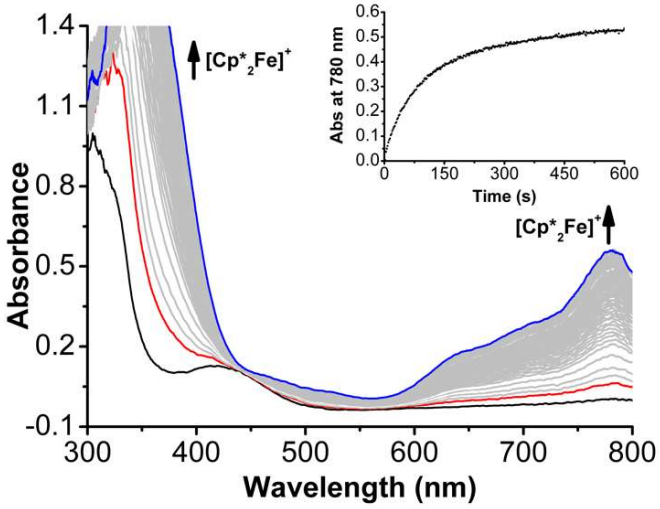

Figure 2.3. Representative UV-vis spectral changes under catalytic conditions in MeCN over 15 min. Concentrations: 50 μM $Fe(PMG)(Cl)_2$, 35 mM AcOH, 4.05 mM O_2, and 1.5 mM Cp^*_2Fe. Inset: Absorbance changes at 780 nm arise from the formation of $[Cp^*_2Fe]^+$.

Catalytic ORR experiments with $Fe(PMG)(Cl)_2$ were run under spectrochemical conditions using decamethylferrocene (Cp^*_2Fe) as a chemical reductant. UV-vis stopped-flow spectroscopy was used to determine the kinetic parameters of the ORR based on the rate of $[Cp^*_2Fe]^+$ appearance under O_2 saturation conditions with AcOH present in MeCN (**Eq. 2.1**, **Figure 2.3**), where under the same reaction conditions without $Fe(PMG)(Cl)_2$, the system shows negligible background reactivity (**Figure S2.29**). Variable concentration studies were used to elucidate the catalytic rate law of the ORR by $Fe(PMG)(Cl)_2$, which showed zero-order dependencies on [AcOH], $[Cp^*_2Fe]$, and $[O_2]$. Conversely, a half-order dependence was observed on $[Fe(PMG)(Cl)_2]$ (**Eq. 2.2**, **Figures S2.20-S2.23**). The turnover frequency (TOF) was determined to be 0.92 s^{-1} with 35 mM AcOH (overpotential (η) = 0.15 V, see SI). As mentioned above, the lack of activity under buffered conditions precludes us from being able to accurately calculate overpotential. We have corrected the reported standard reduction potentials for the ORR, as outlined in the **SI**, to take into account the pK_a (23.5) and log(K_{AHA}) (3.9) values for AcOH in MeCN. [1, 51, 52] We emphasize here that our calculation of overpotential is a *lower-limit approximation*.

$$O_2 + 4Cp^*_2Fe + 4AcOH \xrightarrow{\boldsymbol{Fe}} 2H_2O + 4Cp^*_2Fe^+ + 4AcO^- \qquad (\mathbf{2.1})$$

$$rate = k_{cat}[Fe]^{0.5}[AcOH]^0[O_2]^0[Cp^*_2Fe]^0 \qquad (\mathbf{2.2})$$

Selectivity for the ORR determined via a $Ti(O)SO_4$-based colorimetric assay showed the system had H_2O_2 selectivity of only 1.1 ± 2%, which is less than the 25% H_2O_2 selectivity under electrochemical conditions. [53] Notably, control experiments indicated that no H_2O_2 disproportionation occurred over the course of 30 minutes when $Fe(PMG)(Cl)_2$, AcOH, and urea•H_2O_2 were combined under Ar gas saturation conditions (**Figure S2.18**). However, placing $Fe(PMG)(Cl)_2$ under anaerobic conditions with Cp^*_2Fe in addition to added acid and urea•H_2O_2 showed rapid reduction of H_2O_2 to H_2O with quantitative efficiency. We attribute the difference in observed selectivity under electrochemical and spectrochemical conditions to the timescale of each experiment. In a typical spectrochemical product quantification experiment, the reaction is

run to completion with respect to the amount of O_2 present (~15 minutes) in the presence of excess Cp^*_2Fe and AcOH, which allows for any H_2O_2 produced during catalysis to be further reduced by $Fe(PMG)(Cl)_2$. However, in a typical RRDE experiment, catalysis occurs at the glassy carbon disk and H_2O_2 produced during catalysis is rapidly (~1 second) swept away from where catalytically active Fe(II) is generated, preventing further reduction. Consistent with this, control experiments show no catalytic activity for disproportionation of H_2O_2 mediated by $Fe(PMG)(Cl)_2$ (**Figure S2.18**), although stoichiometric oxidation of the singly reduced $Fe^{II}(PMG)Cl$ complex is observed, *vide infra*. Overall, these data support a ~99% selectivity toward water corresponding to the consumption of n_{cat} = 3.98 electrons per catalyst turnover and implicate a 2+2 mechanism, where H_2O_2 is a discrete intermediate. Variable-temperature stopped-flow spectroscopic data was used for Eyring analysis of the ORR catalyzed by $Fe(PMG)(Cl)_2$ (**Table 2.1**, **Figure S2.32**), which revealed a barrier for the rate-determining step (RDS) at 298 K of 20.5 kcal mol^{-1}, which is consistent with the observed TOF of 0.92 s^{-1}.

Table 2.2. Eyring Parameters of O_2 Reduction with $Fe(PMG)(Cl)_2$ from Variable-Temperature Spectrochemical Experiments.

$\Delta H^{\ddagger}$	4.82 kcal mol^{-1}
$\Delta S^{\ddagger}$	-52.5 cal mol^{-1} K^{-1}
$\Delta G^{\ddagger}_{298K}$	20.5 kcal mol^{-1}

The reduction of H_2O_2 to H_2O under spectrochemical conditions was also studied using UV-vis stopped-flow spectroscopy, revealing relatively faster rates than the ORR catalyzed by $Fe(PMG)(Cl)_2$ (**Eq. 2.3**, **Figure 2.4**). Variable concentration studies under anerobic conditions revealed a rate of H_2O_2 reduction that has first-order dependencies on $[Fe(PMG)(Cl)_2]$ and [AcOH]. Conversely, zero-order dependencies on $[Cp^*_2Fe]$ and $[H_2O_2]$ are observed under the same conditions (Eq. 4, **Figures S2.24-S2.27**) and the TOF was determined to be 2.9 x 10^3 s^{-1} (η = 0.49 V, see **SI**). Interestingly, the Cp^*_2Fe is required to be present in solution for any consumption of H_2O_2 to occur (**Figure S2.18**). As before, this overpotential is determined by

correcting the standard potential for the homoconjugation of AcOH and is a *lower-limit approximation*.

$$H_2O_2 + 2Cp^*_2Fe + 2AcOH \xrightarrow{Fe} 2H_2O + 2Cp^*_2Fe^+ + 2AcO^- \quad (\mathbf{2.3})$$

$$rate = k_{cat}[Fe]^1[AcOH]^1[H_2O_2]^0[Cp^*_2Fe]^0 \quad (\mathbf{2.4})$$

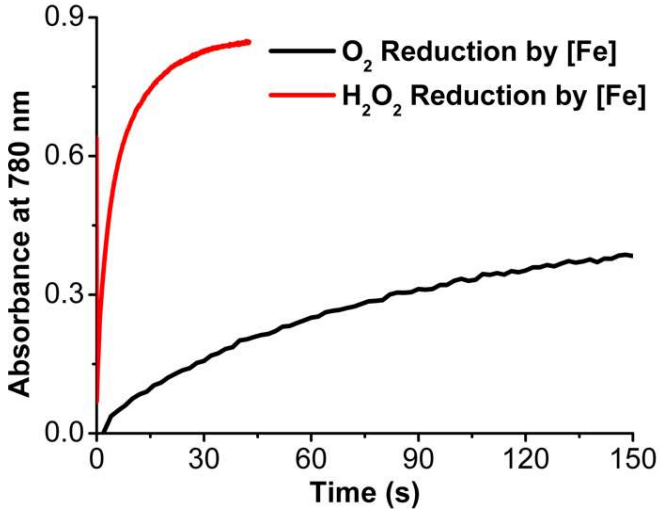

Figure 2.4. Absorbance changes at 780 nm due to the formation of $[Cp^*_2Fe]^+$ during O_2 (black) and H_2O_2 (red) reduction catalyzed be $Fe(PMG)(Cl)_2$. Conditions: (black) 50 μM $[Fe(PMG)(Cl)_2]$, 35 mM [AcOH], 1.50 mM $[Cp^*_2Fe]$, 4.05 mM O_2 (red) 50 μM $[Fe(PMG)(Cl)_2$, 35 mM [AcOH], 1.53 mM Cp^*_2Fe, 4 mM urea•H_2O_2.

2.3.4. Electrochemical Studies with H_2O_2.

CV studies were also performed with $Fe(PMG)(Cl)_2$ in the presence of H_2O_2 with AcOH under an inert atmosphere (Ar). Addition of urea•H_2O_2 to a solution of $Fe(PMG)(Cl)_2$ resulted in the loss of reversibility of the Fe(III)/(II) feature, indicative of the formation of an irreversible reaction between Fe(II) via a non-catalytic *EC* mechanism (**Figure 2.5**, red trace).[48,49] The evolution of observed peak potential with respect to changes in scan rate was used to determine the second-order rate constant for H_2O_2 binding, as previously described.[49,50] The rate constant, k_{H2O2} was determined to be 1.52 ± 0.16 x 10^3 $M^{-1}s^{-1}$ (See **SI**) and is consistent with the difference in O_2 and H_2O_2 reduction rates observed under spectrochemical conditions (**Figure 2.4**).Spectroscopic studies described below indicate that the primary product of this stoichiometric *EC* reaction is an Fe(III)-OH species. However, complex **1** is electrocatalytically active toward H_2O_2 reduction in the

presence of AcOH, with an appreciable increase in current density at the Fe(III)/(II) redox feature (**Figure 2.5,** green trace) consistent with the spectrochemical data discussed above. Overall, the spectrochemical and electrochemical data suggest that the Fe(III) state of the pre-catalyst $Fe(PMG)(Cl)_2$ does not appreciably react with H_2O_2.

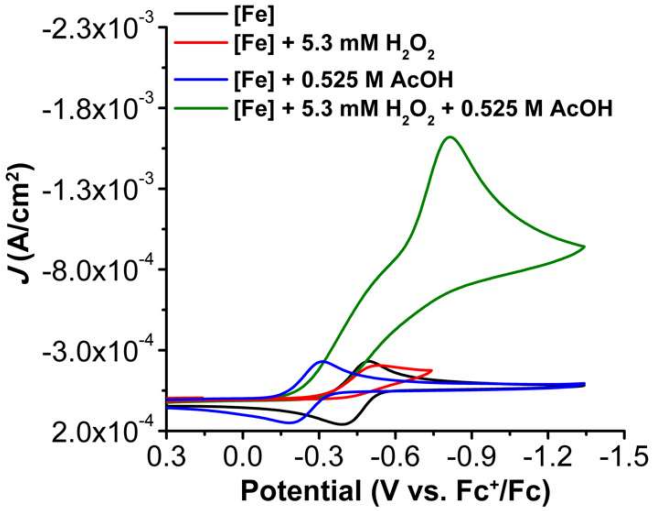

Figure 2.5. CVs of $Fe(PMG)(Cl)_2$ under Ar (black) saturation with 5.3 mM urea•H_2O_2 (red), 0.525 M AcOH (blue) and 0.525 M AcOH in the presence of 5.3 mM urea•H_2O_2 (green). Conditions: 1 mM $Fe(PMG)(Cl)_2$, 0.1 M $TBAPF_6$ in MeCN; glassy carbon working electrode; Ag/AgCl pseudoreference electrode; scan rate 100 mV/s; referenced to internal ferrocene standard.

2.3.5. Spectroscopic Studies with $Fe^{II}(PMG)Cl$

To better probe reaction intermediates, we directly prepared the catalytically active Fe(II) species ($Fe^{II}(PMG)Cl$) under anaerobic conditions and undertook UV-vis and ^{1}H-NMR spectroscopic studies in MeCN in the presence of O_2, H_2O_2, and AcOH. First, we analyzed the role of the reduced Fe(II) in hydrogen-bonding with AcOH during catalysis. Titrating increasing amounts of AcOH to a sample of $Fe(PMG)(Cl)_2$ shows minimal spectral changes, whereas adding AcOH to $Fe^{II}(PMG)Cl$ shows distinct increases in absorbance at 260, 325, and 365 nm, indicative of an interaction between AcOH and $Fe^{II}(PMG)Cl$ (**Figure S2.34**). UV-vis spectroscopic studies revealed that exposure of $Fe^{II}(PMG)Cl$ to O_2 at room temperature resulted in the formation of a new stable species after 8 minutes (**Figure S2.36**). To assess if this species corresponded to the proposed dimeric Fe species, we next titrated increasing amounts of urea•H_2O_2 to a 50 μM

solution of Fe^{II}(PMG)Cl; clean isosbestic points were observed and changes in the UV-vis spectrum associated with the Fe(II) complex saturated at a 1:1 ratio of Fe^{II}(PMG)Cl to H_2O_2 (**Figure S2.37**). During this titration a band of relatively low absorptivity at 409 nm decreases in intensity, accompanied by the appearance of a new feature at 365 nm, with corresponding increases in absorbance features at 327 and 259 nm (**Figure 2.6**).

Molar absorptivity plots comparing the species produced when Fe^{II}(PMG)Cl exposed to O_2 and H_2O_2 with Fe(PMG)$(Cl)_2$ indicate a loss of all Fe(II) features are lost with O_2 and H_2O_2 (**Figure 2.6**). These data suggest formation of a Fe(III) species, however, the spectral features following O_2 and H_2O_2 exposure do match those of an authentic sample of Fe(PMG)$(Cl)_2$, which we propose is consistent with the absence of one of the chloride ligands. To assess alternate possibilities for the primary coordination environments in the Fe(III) species that is formed, we exposed a sample of Fe(PMG)$(Cl)_2$ to tetrabutylammonium hydroxide (TBAOH). Overlay of Fe(PMG)Cl_2 with and without added TBAOH with Fe^{II}(PMG)Cl exposed to O_2 and H_2O_2 show good agreement, indicating that the product mixture likely contains stable Fe(III)-OH species (**Figure 2.6**). Since the kinetic data obtained in the mechanistic experiments imply the existence of an off-cycle dimer species, the formation of the same Fe(III)-OH species obtained from these two reactions suggest that the presumptive diiron peroxo dimer intermediate is reactive under experimental conditions, scavenging adventitious protons or H atom equivalents.

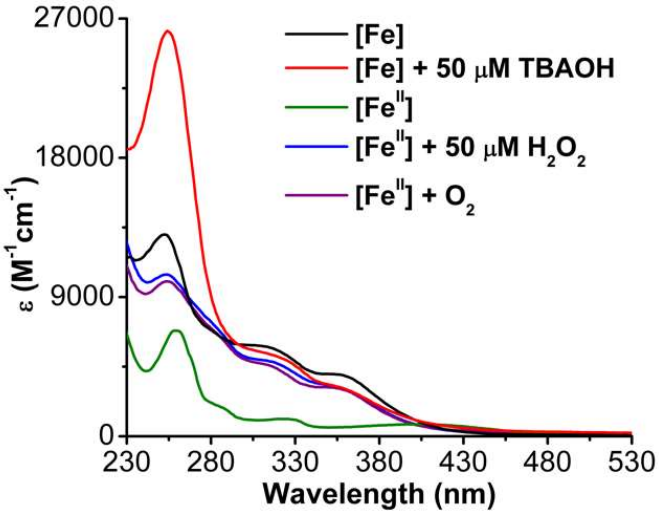

Figure 2.6. Molar extinction plot of 50 μM $Fe(PMG)(Cl)_2$ (black trace) exposed to 50 μM TBAOH and 50 μM $Fe^{II}(PMG)Cl$ (green trace) exposed to 50 μM urea•H_2O_2 (blue trace) and O_2 (purple trace) in MeCN.

To supplement these data, we next analyzed the reactivity of $Fe^{II}(PMG)Cl$ with AcOH using ^{1}H-NMR spectroscopy. The paramagnetic ^{1}H-NMR spectrum of $Fe^{II}(PMG)Cl$ under N_2 showed six well-resolved broad resonances, indicative of a complex with a plane of internal symmetry (**Figure S2.39).** The addition of 0.3 M AcOH under N_2 showed changes consistent with the loss of the initial symmetry of $Fe^{II}(PMG)Cl$ with ten total paramagnetic resonances observed (**Figure S2.40**), which we ascribe to a hydrogen-bonded adduct of AcOH and the Fe(II) complex, as was previously demonstrated by comparable UV-vis (**Figure S2.34**) and electrochemical data (**Figure 2.2**). Exposure of $Fe^{II}(PMG)Cl$ to H_2O_2 and O_2 showed a loss of all resolved paramagnetic features, precluding us from being able to characterize the Fe(III)-OH species via ^{1}H-NMR.

2.3.6. DFT Calculations

To better understand the role of non-covalent interactions in facilitating chloride loss and the observed shift in the Fe(III)/(II) redox couple, we examined the thermodynamic positioning of reaction pathways involving $Fe(PMG)(Cl)_2$ (complex **1**) AcOH, MeCN, and the chloride anion before and after one-electron reduction using DFT methods (See **SI**). Note that this level of theory accurately replicated the sextet ground state of the complex observed experimentally; for brevity

only the lowest energy spin configuration will be discussed, although alternative pathways have also been computed (See Computational Coordinates). From complex **1**, chloride loss is endergonic: *trans* to the tri-alkyl amine fragment of the ligand +13.8 kcal/mol, *trans* to the carboxylate +10.1 kcal/mol. Subsequent binding of MeCN is exergonic in both cases, however, the net displacement of chloride by MeCN is at least 8.0 kcal/mol endergonic (**Figure 2.7**). The introduction of AcOH in a non-covalent interaction with the Fe-bound carboxylate is at least 4 kcal/mol endergonic in both cases. Alternative mechanistic pathways for the ordering of these three reaction steps were all higher in energy.

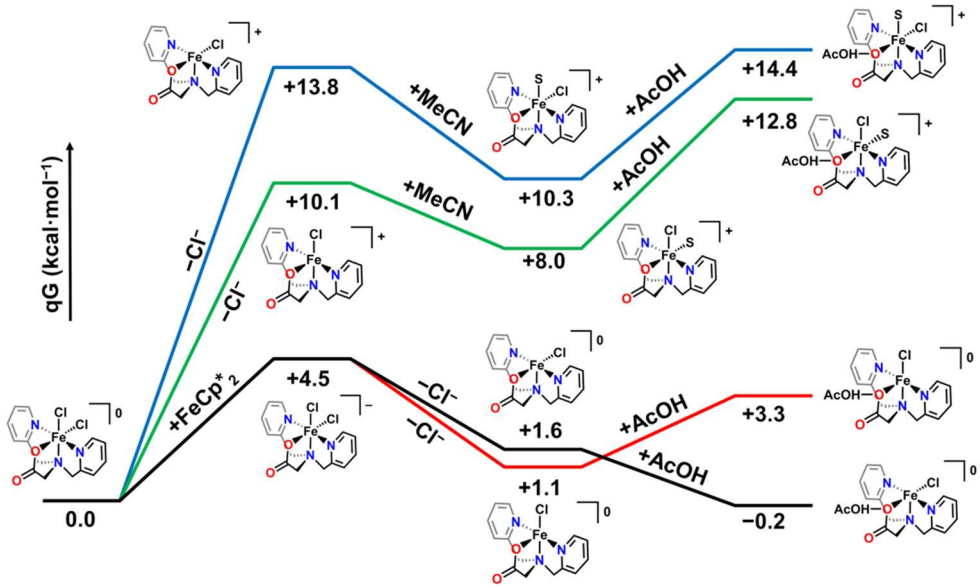

Figure 2.7. Computed reaction pathways comparing the effects of reduction and AcOH on chloride loss and MeCN binding. All Fe(III) species are S = 5/2; all Fe(II) species are S = 2; alternative spin configurations were higher in energy.

Alternatively, a much lower pathway exists when complex **1** first undergoes a redox reaction with the Cp^*_2Fe reductant in solution (+4.5 kcal/mol). This reduction produces a formally Fe(II) species, which is most stable in the S = 2 spin manifold; alternate spin configurations were higher in energy. Chloride loss then becomes exergonic at both the possible positions (**Figure 2.7**, red and black, however AcOH binding is only favorable when chloride loss occurs in the position *trans* to the tri-alkylamine moiety of the ligand framework (**Figure 2.7**, black). For both of the reduction-

first pathways, MeCN binding is slightly endergonic (+2.7 kcal/mol from the final species in the black pathway, **Figure 2.7**; +0.6 kcal/mol for the red). Formal protonation instead of MeCN binding is also thermodynamically disfavored in these non-covalent adducts by at least 4.2 kcal/mol and solvento speciation does not help the favorability of the formal protonation reaction. Therefore, the lowest energy species in solution following one-electron reduction is five-coordinate, with a vacant coordination site opposite the tri-alkylamine. Non-covalent interactions between the five-coordinate neutral Fe species and AcOH increase the thermodynamic favorability of the chloride-loss reaction. Alternative sequences for reduction, chloride loss, and AcOH binding all produced higher-energy pathways.

2.4. Discussion

Based on combined electrochemical and spectrochemical data, we can propose a mechanism for the ORR catalyzed by $Fe(PMG)(Cl)_2$, **Scheme 2.1**. Starting from **1**, a thermodynamically favorable non-covalent interaction between the anionic carboxylate group of the ligand in the inner coordination sphere and AcOH drives Cl loss following the formal reduction of the Fe(III) metal center to an Fe(II) species to form intermediate **2**. This proposal is supported indirectly by the sensitivity of the Fe(III)/(II) redox feature to added AcOH and directly by UV-vis spectroscopic data obtained during the titration of AcOH into solutions with $Fe(PMG)(Cl)_2$ and $Fe^{II}(PMG)Cl$, showing a distinct interaction for the Fe(II) complex (**Figure S2.34**). Consistent with this interpretation, paramagnetic ^1H NMR data show a loss of internal symmetry for the Fe(II) species, $Fe^{II}(PMG)Cl$, when AcOH is added (**Figure S2.40**). These experimental data are supported by DFT studies, which suggest chloride loss occurs opposite the tri-alkyl amine fragment of the ligand.

Scheme 2.1. Proposed catalytic cycle for the ORR catalyzed by $Fe(PMG)(Cl)_2$.

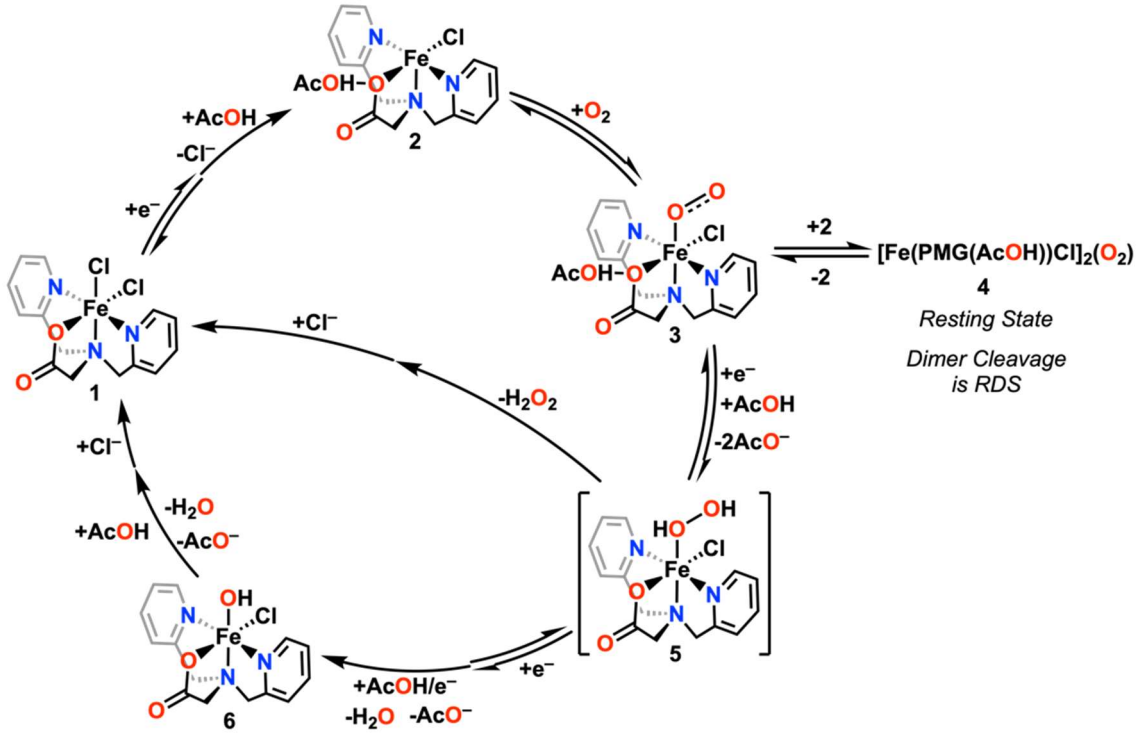

From this five-coordinate neutral species, we propose that O_2 binds to the Fe(II) metal center to form a mononuclear superoxo species, **3**. Using variable-scan rate electrochemical experiments, a second-order rate constant of $k_{O2,H+}$ = 7.88 ± 1.2 $M^{-1}s^{-1}$ is obtained with AcOH present for this reaction. From this intermediate it is likely a second equivalent of **2** reacts with an equivalent of **3** to form a bridging peroxo species, **4**, which we propose to be the resting state of the catalyst in solution. This assignment of an off-cycle dimer is based on the mechanistic kinetic analysis of this catalyst system described above, where the reaction has a half-order concentration dependence on the Fe-based catalyst precursor, **Eq. 2.2**. Off-cycle dimers have been previously reported for other systems and were likewise observed to have a half order concentration dependence with respect to catalyst.[54,55] Based on literature precedent, we speculate that a μ_2-1,2-peroxo coordination mode is a likely possibility, although we note the reactivity of this species has precluded direct characterization.[56-58] As described above, the only stable product observed in exposing $Fe^{II}(PMG)Cl$ to O_2 is a Fe(III)-OH species, suggesting the proposed intermediate O_2 dimer decomposes (**Figure 2.6**).

The rate-determining step of the catalytic cycle is proposed to be the cleavage of an Fe(III)-O bond to reform an equivalent of **3** and an equivalent of **2**. Complex **3** can then undergo further reduction and coupled protonation to form an unobserved hydroperoxo intermediate, **5**. To explore an alternative on-cycle dimer cleavage pathway, a kinetic study under standard ORR conditions varying [Fe(PMG)Cl_2] concentration in the presence of 1 mM tetrabutylammonium chloride (TBACl) was conducted, to probe the possibility chloride coordination accelerating peroxo dimer cleavage (**Figure S2.31**). However, the observed R_{fit}/n_{cat} dependence is slightly shallower than data obtained without TBACl present, indicating a slight inhibition of the catalytic response. These data are not consistent with Cl^- association mediating rate-limiting dimer cleavage.

Unobserved intermediate **5** can then release of H_2O_2. UV-vis experiments with complex **1** show no interaction between H_2O_2 and Fe(III) oxidation state (**Figure S2.38**). This is consistent with the increased amount of H_2O_2 production observed by RRDE under electrochemical conditions, since the two-electron/two-proton intermediate has time to diffuse away from the electrode where Fe(II) species capable of H_2O_2 reduction are generated. Alternatively, **5** can undergo a 2 e^- reduction and protonation of the distal O leading to the release of water and formation of the stable Fe(III)-OH species, **6**. Stoichiometric experiments with Fe^{II}(PMG)Cl quantitative oxidation by H_2O_2 to Fe(III) (**Figure S2.37**), which is supported by supplemental control studies with Fe(PMG)$(Cl)_2$ with added TBAOH (**Figure 2.6**). UV-vis data suggest that exposure of Fe^{II}(PMG)Cl to O_2 also leads to the formation of **6**; overlays of the product generated from Fe^{II}(PMG)Cl following exposure to O_2 or H_2O_2 show almost identical spectra (**Figure 2.6**). We propose that the dimer species decomposes to form species **6** under non-catalytic conditions by scavenging protons and H atom equivalents from solution. Following one-electron reduction, the terminal hydroxide ligand in complex **6** is then protonated to release one equivalent of water and complete the catalytic cycle.

Mechanistic studies with H_2O_2 demonstrate rapid catalytic reduction to H_2O occurs under these conditions with sufficient Cp^*_2Fe present. The catalytic rate law implies a Fe(III)-OH resting

state with first-order dependencies on [Fe(PMG)$(Cl)_2$] and [AcOH]. Based on spectroscopic analysis, we propose that H_2O_2 rapidly binds to complex **2**, which releases 1 equivalent of water to form the oxidized **6**, the resting state during H_2O_2RR. Consistent with the greater rates observed for H_2O_2RR than ORR spectrochemically, the electrochemically determined second-order rate constant for H_2O_2 binding, k_{H2O2} = 1.52 ± 0.16 x 10^3 $M^{-1}s^{-1}$ is two orders of magnitude greater than that for O2 binding with AcOH present, $k_{O2,H+}$ = 7.88 ± 1.2 $M^{-1}s^{-1}$. Overall, the electrochemical and spectrochemical product analysis and mechanistic studies described above imply a 2+2 mechanistic pathway, where H_2O_2 is a viable intermediate in the catalytic cycle that is rapidly reduced to H_2O under reducing conditions.

2.5. Conclusions

These data suggest that the bioinspired Fe(PMG)$(Cl)_2$ complex is an active and selective molecular catalyst for the reduction of O_2 to H_2O. Mechanistic studies support the existence of an off-cycle bridging diiron peroxo dimer, whose cleavage is rate-limiting. Additionally, the Fe(PMG)$(Cl)_2$ complex is also active for the catalytic reduction of H_2O_2, suggesting that the observed selectivity for water arises from an overall 2+2 mechanistic pathway. This proposal is supported by the observation of higher H_2O_2 efficiencies by RRDE, where hydrodynamic conditions push the two-electron/two-proton product away from sufficiently reducing conditions. The kinetic parameters of H_2O_2 reduction are consistent with a Fe(III)-hydroxide resting state, which was spectroscopically observed, indicating that this system could serve as a viable reactivity model for the O_2-driven oxidation reactions non-heme Fe metalloenzymes. Further, the observation of non-covalent interactions with the AcOH proton donor tuning the second-order rate constant of O_2 binding suggests that the electronic structure of the activated can be tuned via the carboxylate moiety. The role of anionic residues and their protonation state in regulating the reduction potentials at active sites has clear implications for a wide range of bioinorganic catalytic processes. Studies investigating the consequences of this ORR behavior on catalytic oxidation

reactions and improving the ligand framework through synthetic modifications are currently underway.

2.6. Supplementary Information for Chapter 2

General Considerations.

All chemicals and solvents were commercially available and used as received unless otherwise stated. Tetrabutylammonium hydroxide was added as a hydrate salt, with the formula $(CH_3CH_2CH_2CH_2)_4N(OH)•30H_2O$. All experiments were performed under light-free conditions, note that *Fe(PMG)(Cl)$_2$* was found to be specifically light-sensitive in both solid and solution states. For air-sensitive reactions, electrochemical, and spectrochemical experiments, solvents were obtained as anhydrous and air-free from a PPT Glass Contour Solvent Purification System. Gas cylinders were obtained from Praxair (Ar as 5.0; O_2 as 4.0). NMR spectra were obtained on a Varian 600 MHz instrument and referenced to the residual solvent signal. UV-vis absorbance spectra were recorded on a Cary 60 from Agilent. Stopped-flow data were collected as single-mixing experiments on a CSF-61DX2 Stopped-Flow System from Hi-Tech Scientific. The temperature was controlled using a VWT refrigerated circulator with an ethylene glycol and water mixture. The concentration of O_2 saturation in MeCN is reported to be 8.1 mM and the saturation concentration in MeCN with added electrolyte to be 6.3 mM.[59]

Experimental Methods.

Synthesis of N,N'-bis(2-pyridylmethyl)glycine (PMG(H)).

PMG(H) was prepared according to a reported literature procedure.[41]To a solution of water (30 mL) in a single neck round bottom flask, 2-(chloromethyl)pyridine hydrochloride (3.61 g, 22 mmol) and glycine (0.826 g, 11 mmol) were added. A solution of 5 M NaOH was added gradually until the reaction mixture reached a pH of 10. During the gradual addition of NaOH solution, the solution turned from colorless, to pink, to dark red and it was allowed to stir at room temperature for 5 days. During this time, the pH was evaluated and additional NaOH solution was added to maintain a pH of 8-10 over the course of the reaction. The final dark red solution was extracted

with ethyl acetate (3 x 50 mL). The aqueous layer of the biphasic solution was separated and titrated with concentrated HCl to a pH of 6, before extraction with dichloromethane (3 x 50 mL). The combined organic layers were dried with $MgSO_4$ and the solvent was reduced via rotary evaporation. The final red oil was recrystallized in a minimal amount of methanol and diethyl ether to yield 1.95 g (70 % yield) of a faint brown solid. ^{1}H-NMR (d_4-CD_3OD, 600 MHz Varian): δ 8.53 (d, 2H), 7.86(t, 2H), 7.60 (d, 2H), 7.32 (t, 2H), 4.38 (s, 4H), 3.63 (s, 2H). $^{13}C\{^{1}H\}$-NMR (d_4-CD_3OD, 150 MHz Varian): δ 171.53, 154.83, 148.38, 137.74, 123.64, 123.65, 58.41, 55.82. X-ray suitable crystals were obtained by slow diffusion of diethyl ether into a solution of PMG in methanol at 0 °C. Elemental analysis calculated for $C_{14}H_{14}N_3O_2$: C, 65.36; H, 5.88; N, 16.33. Found: C, 65.13; H, 5.92; N, 16.08.

Computational Methods.

DFT calculations were performed on the Rivanna High-Performance Computing Cluster at the University of Virginia using the Gaussian 16 program, Rev B.01(1).[60] The hybrid functional B3LYP[61-64] (2-5) and the def2-SVP basis set for all atoms[65,66] were used for all calculations. Energies were refined by means of single point calculations with the larger def2-TZVP basis set. Unrestricted geometry optimizations were carried out without geometry constraints and dispersion effects were accounted for by using Grimme's D3 parameter set with Becke-Johnson (BJ) damping.[67] Bulk solvent effects (MeCN) were included at the optimization stage with the SMD continuum model.[68] The stationary points and their nature as minima were characterized by vibrational analysis, which also produced enthalpy (H), entropy (S) and Gibbs energy (G) data at 298.15 K. Free energies were corrected to account for concentration effects and for errors associated with the harmonic oscillator approximation. Thus, according to Truhlars's quasi-harmonic approximation, all vibrational frequencies below 100 cm^{-1} were set to this value.[69] All anharmonic and concentration corrections were calculated with the Goodvibes 3.0.1 code,[70] the entropic quasi-harmonic treatment used a mixture of RRHO and Free-rotor vibrational entropies[71] and the enthalpic quasi-harmonic treatment used the RRHO treatment with an approximation

term for vibrational energy.[72] The concentration corrections for all species under representative catalytic conditions were set to 40 micromolar, with the exception of [MeCN] = 18.9 M, [O_2] = 4.0 mM, [AcOH] = 35 mM, [$FeCp^*_2$] = 1 mM.

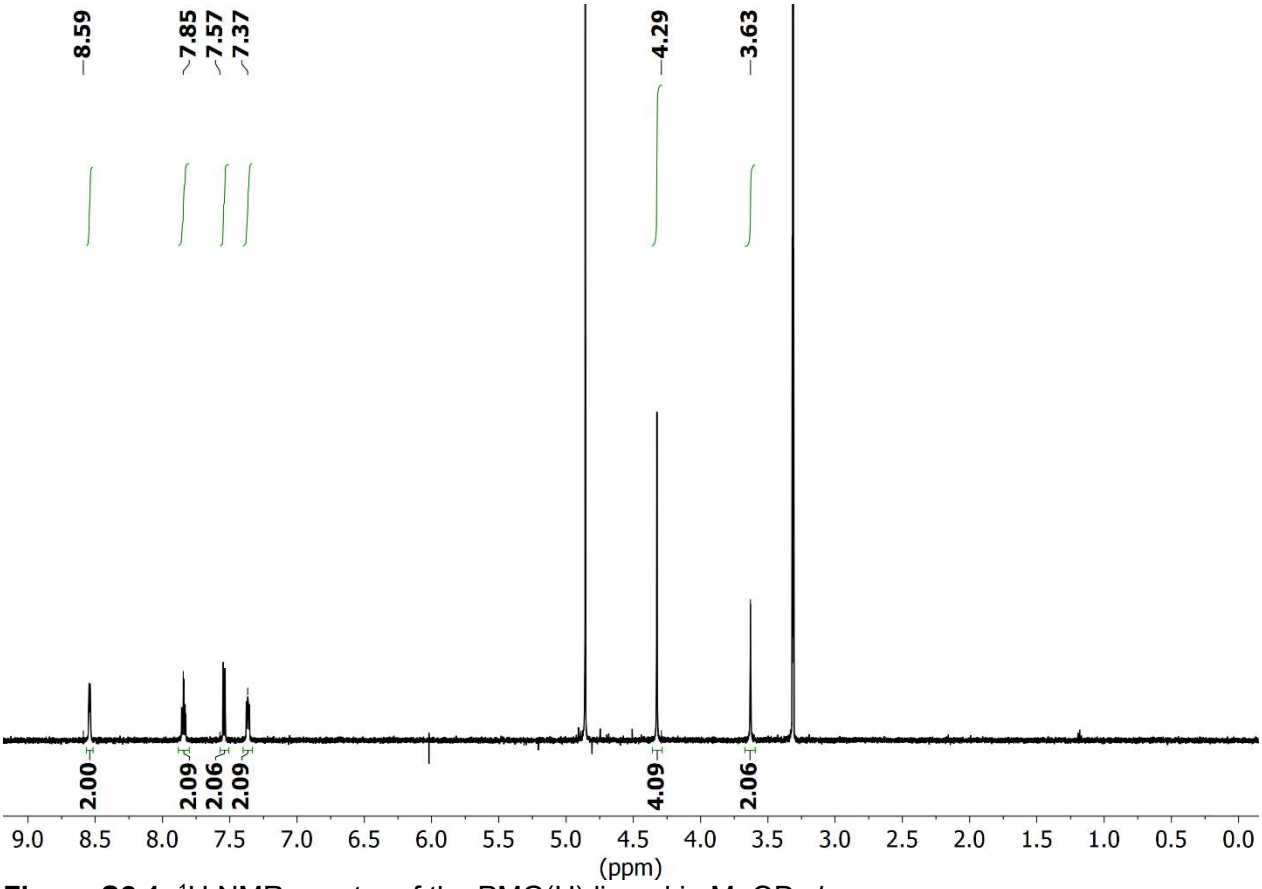

Figure S2.1. ^{1}H NMR spectra of the PMG(H) ligand in MeOD-d_4

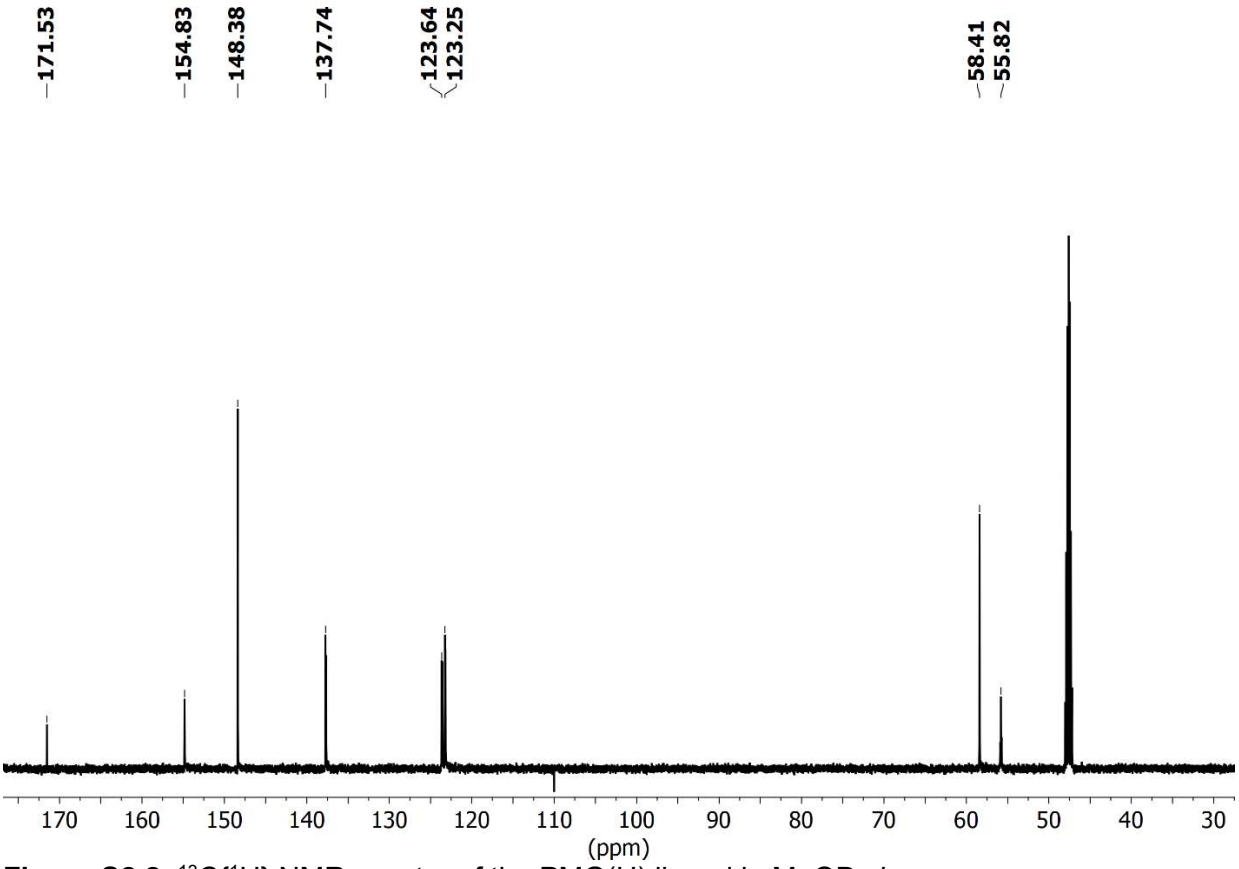

Figure S2.2. $^{13}C\{^{1}H\}$ NMR spectra of the PMG(H) ligand in MeOD-d_4.

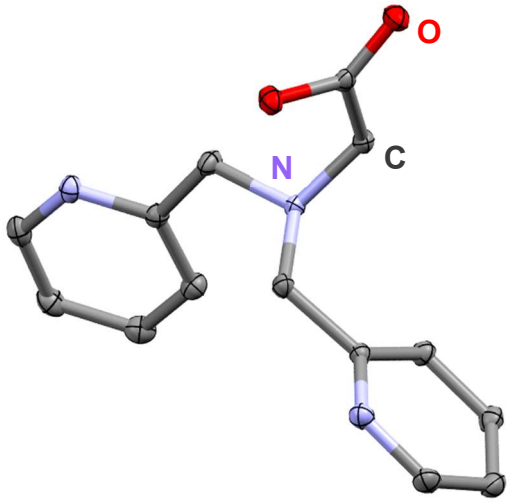

Figure S2.3. Molecular structure of PMG(H) obtained from single-crystal X-ray diffraction studies. Blue = N, red = O, gray = C; thermal ellipsoids at 50%, H atoms omitted for clarity.

Synthesis of Fe(N,N'-bis(2-pyridylmethyl)glycine)Cl_2 (Fe(PMG)$(Cl)_2$).

Fe(PMG)$(Cl)_2$ was prepared according to a reported literature procedure.[15] PMG(H) ligand (0.2 g, 0.78 mmol) and $FeCl_3 \cdot (6H_2O)$ (0.21 g, 0.78 mmol) were dissolved in ethanol and brought to reflux. The reaction was allowed to stir under air for 6 hours. The resulting yellow precipitate was filtered and washed with hexanes to yield 0.182 g (67.4% yield). X-ray suitable yellow needles were obtained by slow cooling of hot methanol. Three characteristic absorbances with λ_{max} at 252 nm, 311 nm, and 357 nm with molar absorptivities of 9.33 x 10^3, 4.15 x 10^3, and 2.94 x 10^3 M^{-1} cm^{-1}, respectively. Elemental analysis calculated for $C_{14}H_{14}Cl_2FeN_3O_2$: C, 43.90; H, 3.68; N, 10.97. Found: C, 44.04; H, 3.57; N, 10.76. Evans' method was completed in methanol using capillary tube inserts containing a 50/50 mixture of deuterated and non-deuterated methanol.

Synthesis of Fe(N,N'-bis(2-pyridylmethyl)glycine)Cl ([Fe(TPA)$(Cl)_2$][Cl]).

[Fe(TPA)Cl][Cl] was prepared according to previously reported methods.[35] Under anaerobic conditions, tris-(2-pyridylmethyl)amine (0.145 g, 0.5 mmol) and anhydrous $FeCl_3$ (0.0811 g, 0.5 mmol) were allowed to stir in methanol at room temperature overnight. The solvent was reduced under pressure and the product was recrystallized in a minimal amount of methanol and diethyl ether to yield a yellow powder (0.115 g, 50.8% yield). Suitable yellow needles for X-ray diffraction

were obtained by slow evaporation of a solution of the complex in DCM-d_2. Elemental analysis calculated for $C_{16}H_{16}Cl_3FeN_4$•1/2CH_2Cl_2: C, 44.89; H, 3.87; N, 11.32. Found: C, 45.15; H, 4.13; N, 11.58. Evans' method was completed in acetonitrile using capillary tube inserts containing a 50/50 mixture of deuterated and non-deuterated acetonitrile.

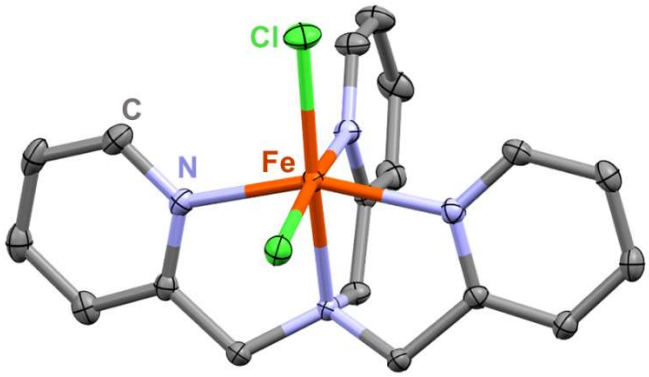

Figure S2.4. Molecular structure of [Fe(TPA)$(Cl)_2$][Cl]obtained from single-crystal X-ray diffraction studies. Orange = Fe, Green = Cl, Blue = N, gray = C; thermal ellipsoids at 50%, H atoms, counter Cl ion, and solvent omitted for clarity. This structure is similar to the previously reported structure by Mandon *et al.*[46]

Synthesis of Fe^{II}(N-N'-bis(2-pyridylmethyl)glycine)Cl (Fe^{II}(PMG)Cl).

Fe^{II}(PMG)Cl was synthesized according to a modified procedure.[73] Under anaerobic conditions PMGH (0.07 g, 0.27 mmol) and K_2CO_3 (0.037 g, 0.27 mmol) were allowed to stir in acetonitrile solution for 1 h. Then, $FeCl_2$ (0.034 g, 0.27 mmol) was added and the mixture left to stir overnight. The resultant yellow precipitate was filtered, redissolved in dichloromethane, passed through a syringe filter, and the solvent was reduced under pressure to yield a yellow-orange powder. Elemental analysis calculated for $C_{14}H_{14}ClFeN_3O_2$•3/2C_4H_8O: C, 52.71; H, 5.75; N, 9.22. Found: C, 53.21; H, 5.28; N, 8.82.

Electrochemistry with O_2

All electroanalytical experiments were performed using a Metrohm Autolab PGSTAT302N potentiostat. Glassy carbon working and nonaqueous silver/silver chloride pseudoreference electrodes behind PTFE tips were obtained from CH Instruments. The pseudoreference electrodes were obtained by depositing chloride on a bare silver wire in 10% HCl at oxidizing

potentials and stored in a 0.1 M tetrabutylammonium hexafluorophosphate/acetonitrile solution in the dark prior to use. The counter electrode was a glassy carbon rod. All CV experiments were performed in a modified scintillation vial (20 mL volume) as a single-chamber cell covered with aluminum foil with a cap modified with ports for all electrodes and a sparging needle. Tetrabutylammonium hexafluorophosphate was purified by recrystallization from ethanol and dried in a vacuum oven before being stored in a desiccator. In a typical experiment, potentials were initially swept in the negative direction. All data were referenced to an internal ferrocene standard (ferrocenium/ferrocene reduction potential under stated conditions) unless otherwise specified.

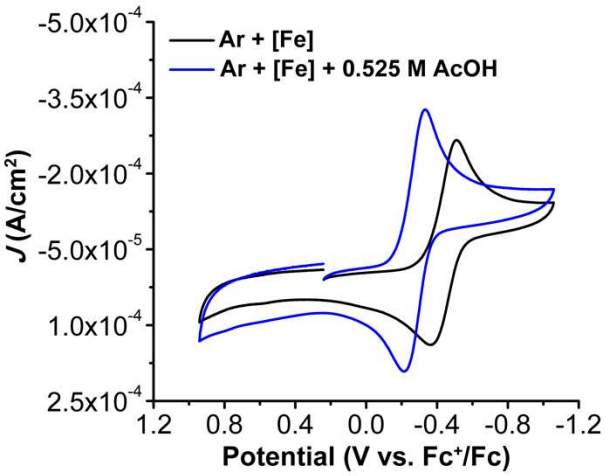

Figure S2.5. CVs of $Fe(PMG)(Cl)_2$ obtained under Ar saturation conditions with (blue trace) and without (black trace) 0.525 M AcOH added. Conditions: 1 mM $Fe(PMG)(Cl)_2$, 0.1 M $TBAPF_6$ in MeCN; glassy carbon working electrode; Ag/AgCl pseudoreference electrode; scan rate 100 mV/s; referenced to internal ferrocene standard.

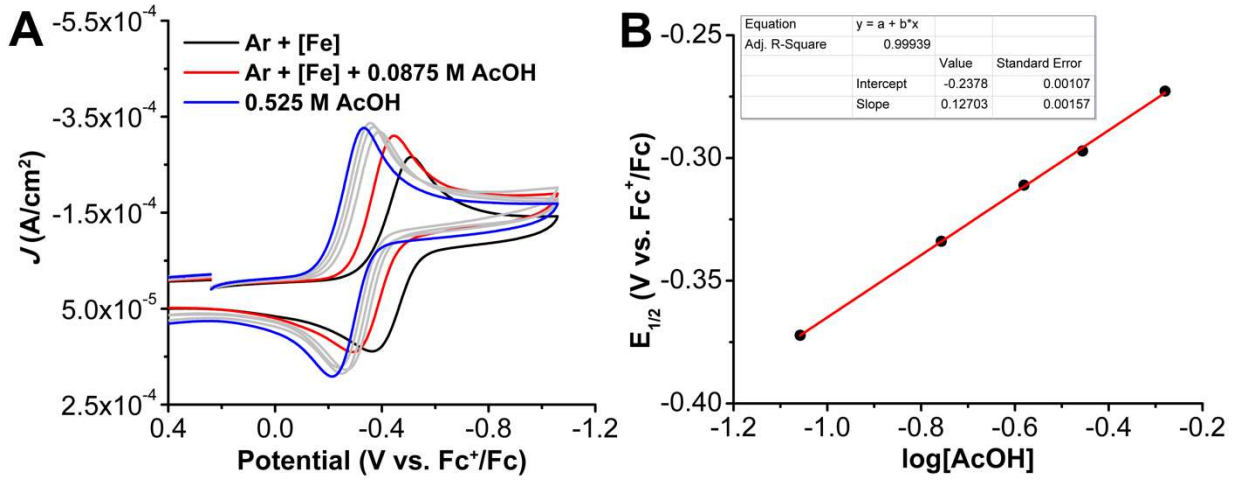

Figure S2.6. (A) CVs of $Fe(PMG)(Cl)_2$ obtained under Ar saturation conditions with variable AcOH concentrations. (B) Plot of $E_{1/2}$ for $Fe(PMG)(Cl)_2$ against the log of [AcOH] showing the effect of increasing AcOH concentration of $E_{1/2}$. Conditions: 1 mM $Fe(PMG)(Cl)_2$, 0.1 M $TBAPF_6$ in MeCN; glassy carbon working electrode; Ag/AgCl pseudoreference electrode; scan rate 100 mV/s; referenced to internal ferrocene standard.

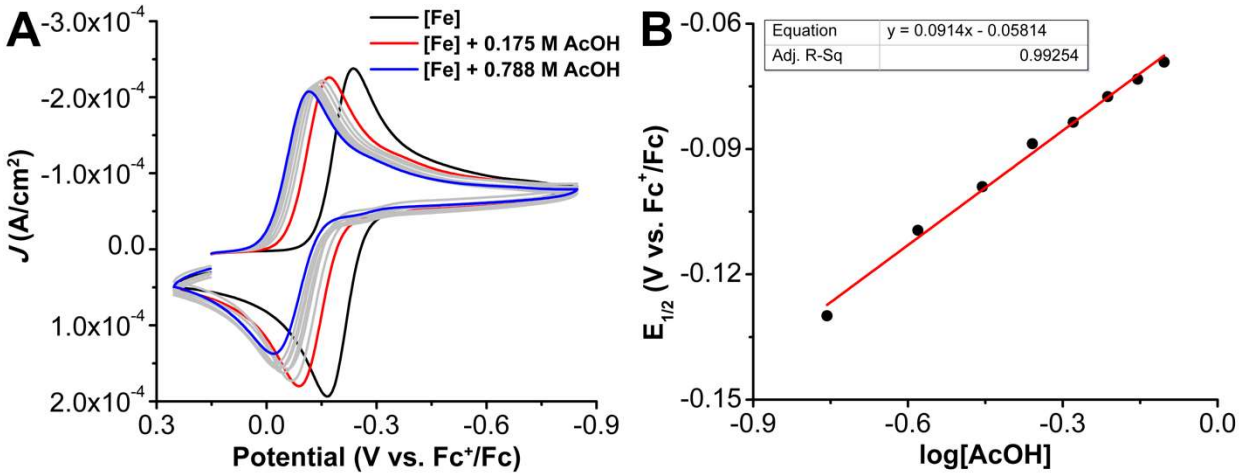

Figure S2.7. (A) CVs of $[Fe(TPA)(Cl)_2][Cl]$ under Ar saturation conditions with variable AcOH concentration. (B) Plot of $E_{1/2}$ for $[Fe(PMG)(Cl)_2][Cl]$ against the log of [AcOH] showing the effect of increasing AcOH concentration of $E_{1/2}$. Conditions: 1 mM $[Fe(TPA)(Cl)_2][Cl]$, 0.1 M $TBAPF_6$ in MeCN; glassy carbon working electrode; Ag/AgCl pseudoreference electrode; scan rate 100 mV/s; referenced to ferrocene standard.

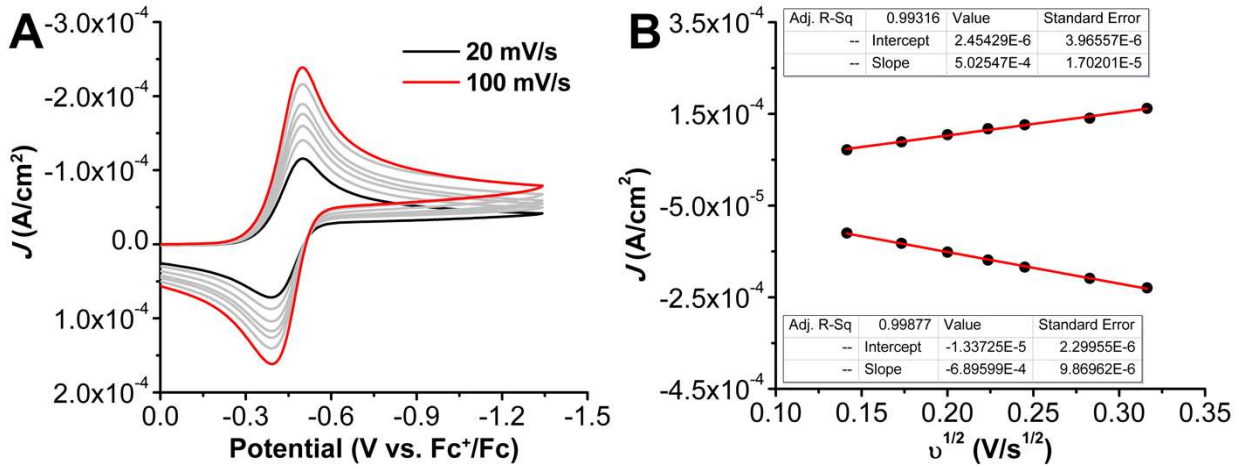

Figure S2.8. (A) Variable scan rate CVs of $Fe(PMG)(Cl)_2$ at low scan rates ranging from 20 (black) to 100 (red) mV/s. (B) Linear fit of variable scan rate data from (A). Conditions: 1 mM $Fe(PMG)(Cl)_2$, 0.1 M $TBAPF_6$/MeCN; glassy carbon working electrode, glassy carbon counter electrode, Ag/AgCl pseudoreference electrode; scan rates: 20, 30, 40, 50, 60, 80, and 100 mV/s; referenced to internal ferrocene standard.

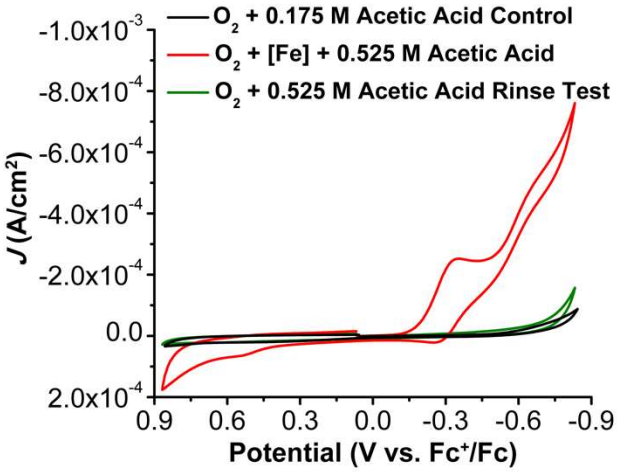

Figure S2.9. Rinse test of $Fe(PMG)(Cl)_2$ and AcOH to ensure the observed current response is not due to a species adsorbed to the electrode. Conditions: 1 mM $Fe(PMG)(Cl)_2$, 0.1 M $TBAPF_6$ in MeCN; glassy carbon working electrode; Ag/AgCl pseudoreference electrode; scan rate 100 mV/s; referenced to internal ferrocene standard.

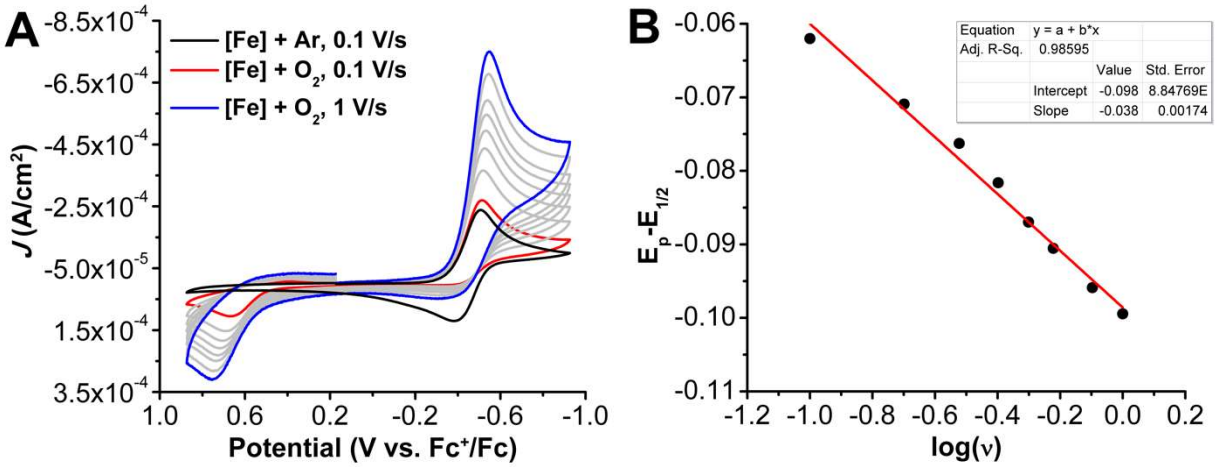

Figure S2.10. Determination of k_{O2} (**A**) CVs of Fe(PMG)$(Cl)_2$ under Ar saturation at 0.1 V/s (black) and O_2 saturation at varying scan rates (**B**) log(υ) vs. E_p-$E_{1/2}$ plot of variable scan rate data in A. Conditions: 1 mM Fe(PMG)$(Cl)_2$, 0.1 M $TBAPF_6$ in MeCN; glassy carbon working electrode; Ag/AgCl pseudoreference electrode; referenced to internal ferrocene standard; scan rates: 0.1, 0.2, 0.3, 0.4, 0.5, 0.6, 0.8, 1 V/s.

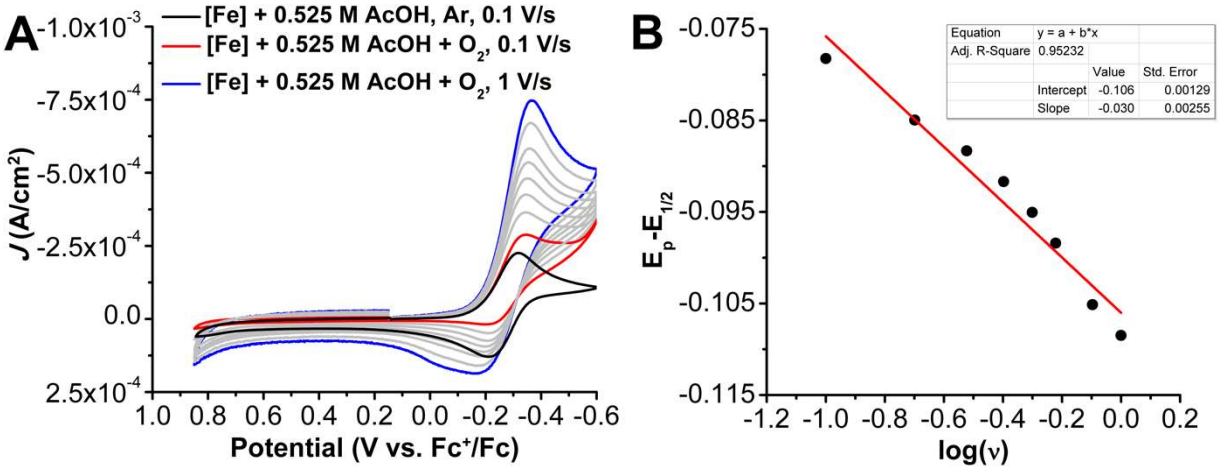

Figure S2.11. Determination of $k_{O2,H+}$ (**A**) CVs of Fe(PMG)$(Cl)_2$ in the presence of 0.525 M AcOH under Ar saturation at 0.1 V/s (black) and O_2 saturation at varying scan rates (**B**) log(υ) vs. E_p-$E_{1/2}$ plot of variable scan rate data in A. Conditions: 1 mM Fe(PMG)$(Cl)_2$, 0.1 M $TBAPF_6$ with 0.525 M AcOH in MeCN; glassy carbon working electrode; Ag/AgCl pseudoreference electrode; referenced to internal ferrocene standard; scan rates: 0.1, 0.2, 0.3, 0.4, 0.5, 0.6, 0.8, 1 V/s.

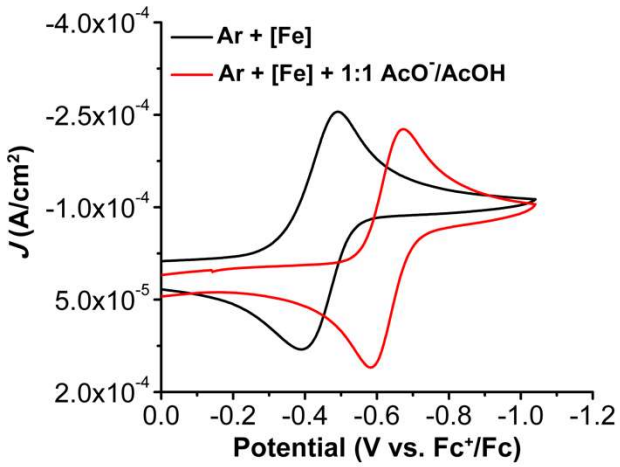

Figure S2.12. Cyclic voltammograms of $Fe(PMG)(Cl)_2$ obtained under Ar saturation conditions with (red) and without (black) 0.1 M buffered TBA(AcO)/AcOH. Conditions: 1 mM $Fe(PMG)(Cl)_2$, 0.1 M $TBAPF_6$ in MeCN; glassy carbon working electrode; Ag/AgCl pseudoreference electrode; scan rate 100 mV/s; referenced to internal ferrocene standard.

RRDE Experiments for Electrochemical Determination of ORR selectivity of $Fe(PMG)(Cl)_2$.

Description of RRDE Collection Efficiency. The collection efficiency was determined as previously reported.[23] Conditions: Ar saturation, 0.1 M $TFAPF_6$, 0.5 mM ferrocene in MeCN (50 mL), glassy carbon disk electrode (5 mm), Pt ring electrode, glassy carbon rod counter electrode, Ag/AgCl pseudoreference electrode; scan rate 0.01 V/s. To calculate the collection efficiency of the RRDE, the ratio of the ring current (i_r) to the disk current (i_d) at each rotation rate was used to determine $N_{empirical}$ (**Eq. S2.1**). The $N_{empirical}$ value at each rotation rate was multiplied by a factor of 100 to determine the collection efficiency % at each rotation rate (~27%).

$$N_{empirical} = \frac{i_{\text{ring corrected}}}{i_{disk\ corrected}} \qquad \textbf{(S2.1)}$$

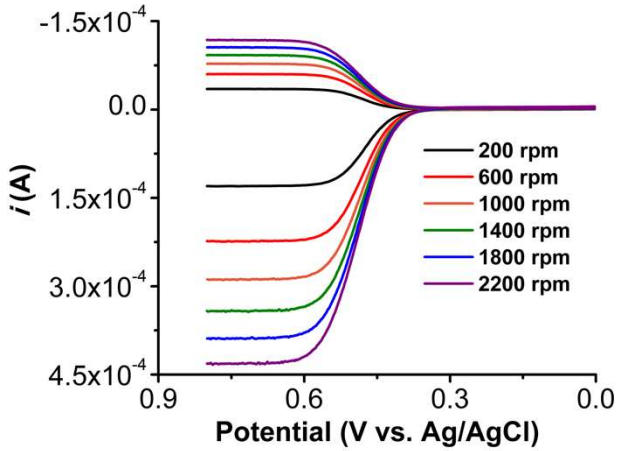

Figure S2.13. Linear Sweep Voltammograms of RRDE experiment with 0.5 mM ferrocene at various rotation rates under Ar saturation conditions; ring potential = +1.2 V vs. Ag/AgCl. Conditions: glassy carbon working electrode/Pt ring working electrode, glassy carbon rod counter electrode, Ag/AgCl pseudoreference electrode; scan rate 0.01 V/s.

RRDE Experiments. Conditions: Performed under both Ar and O_2 saturation conditions, 0.1 M $TBAPF_6$, 0.5 mM $Fe(PMG)(Cl)_2$, 0.35 M AcOH, MeCN (50 mL), glassy carbon disk electrode (5 mm diameter), Pt ring electrode, glassy carbon rod counter electrode, Ag/AgCl pseudoreference electrode; scan rate 0.01 V/s.

The solution was sparged with Ar until saturation was achieved. The analyte (0.5 mM) was dissolved in solution and 0.35 M AcOH was added. A standard CV was taken of the solution to confirm the potential window to be used for the experiment (0.5 to –0.1 V). The Pt ring was set to +1.2 V. LSVs were obtained for various rotation rates (between 200 and 2200 rpm) under the described conditions. Between each LSV, the electrode was polished on alumina and rinsed with ethanol. The cleaning procedure for the electrode was standardized by taking repeated LSVs at the same rotation rates to confirm repeated scans at the same rotation rate were exact overlays of one another. This same procedure was repeated for O_2 saturation conditions, which were achieved by sparging the solution with O_2.

The arithmetic mean of the number of electrons received by O_2 (n_{cat}) during the ORR was calculated from the disk current (i_d) and ring current (i_r) according to **Eq. S2.2**[74]:

$$n_{\mathrm{cat}} = 4 \times \frac{i_{\mathrm{d}}}{i_{\mathrm{d}} + \frac{i_{\mathrm{r}}}{N_{\mathrm{empirical}}}} \qquad \textbf{(S2.2)}$$

The H_2O_2 ratio (p) is defined as the fraction of O_2 reduced to H_2O_2 and relates to n_{cat} by **Eq. S2.3**[74]:

$$n_{\mathrm{cat}} = 4 - 2p \qquad \textbf{(S2.3)}$$

Multiplying p by 100% provides the % H_2O_2 selectivity of the ORR.

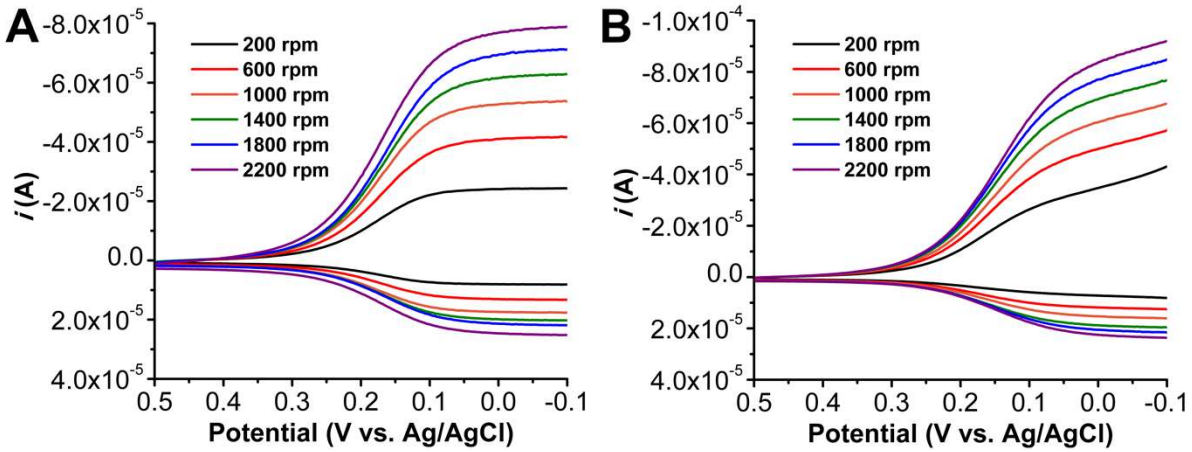

Figure S2.14. Linear Sweep Voltammograms of RRDE experiment with $Fe(PMG)(Cl)_2$ at various rotation rates with 0.5 mM $Fe(PMG)(Cl)_2$ and 0.35 M AcOH under Ar (**A**) and O_2 (**B**) saturation conditions; ring potential = 1.2 V vs Ag/AgCl. Conditions: 0.5 mM analyte; glassy carbon working electrode/Pt ring working electrode, glassy carbon counter electrode, Ag/AgCl pseudoreference electrode; scan rate 0.01 V/s.

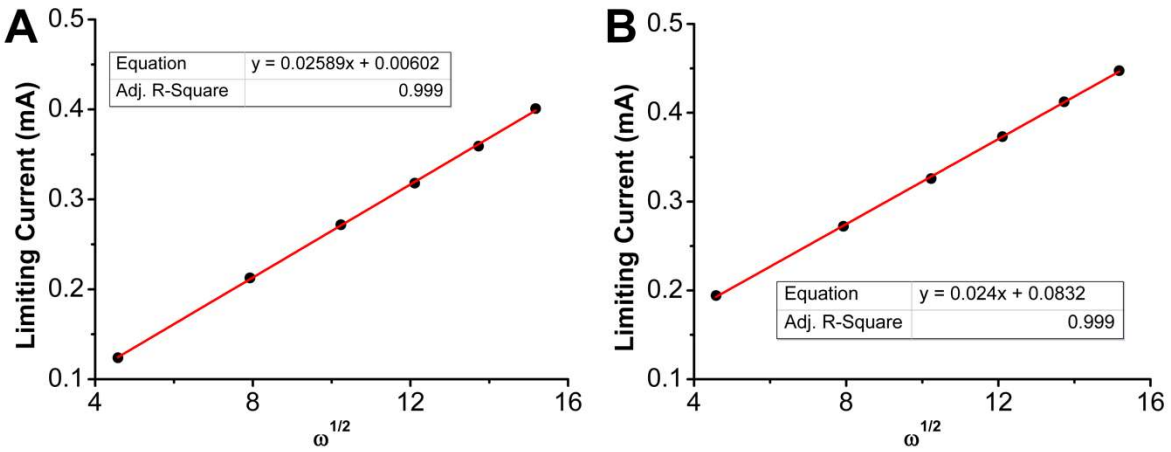

Figure S2.15. Levich plots from data obtained from Linear Sweep Voltammograms of $Fe(PMG)(Cl)_2$ (0.5 mM) by RRDE with 0.35 M AcOH under Ar (**A**) and O_2 (**B**) saturation conditions at various rotation rates; ring potential = 1.2 V vs. Ag/AgCl.

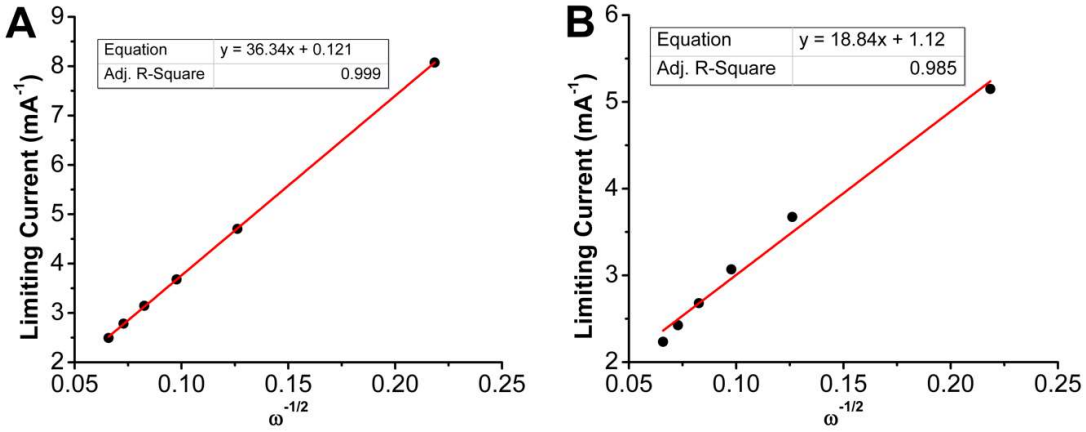

Figure S2.16. Koutecky-Levich plots from data obtained from Linear Sweep Voltammograms of $Fe(PMG)(Cl)_2$ (0.5 mM) by RRDE with 0.35 M AcOH under Ar (**A**) and O_2 (**B**) saturation conditions at various rotation rates; ring potential = 1.2 V vs. Ag/AgCl.

Spectroscopic Determination of Product Selectivity for ORR with $Ti(O)SO_4$ Colorimetric Assay.

The concentration of catalytically produced H_2O_2 was determined by $Ti(O)SO_4$ as previously reported.[53]

Preparation of 0.1 M $Ti(O)SO_4$ solution. In a modified procedure,[75] $Ti(O)SO_4$ (3.998 g, 25 mmol) was added to a 2.0 M solution of sulfuric acid (26.65 mL of H_2SO_4 in 250 mL of DI water). The $Ti(O)SO_4$ was gently heated to completely dissolve all the solid.

A calibration curve (**Figure S2.17**) was obtained through a serial dilution of a stock solution of urea•H_2O_2 in MeCN while monitoring the absorbance at 408 nm. For each UV-vis sample, 1.5 mL of the stock solution was added to an equal volume of DI water. An initial UV-vis spectrum was collected to ensure no background absorbance occurred, then 0.1 mL of the $Ti(O)SO_4$ solution was added.

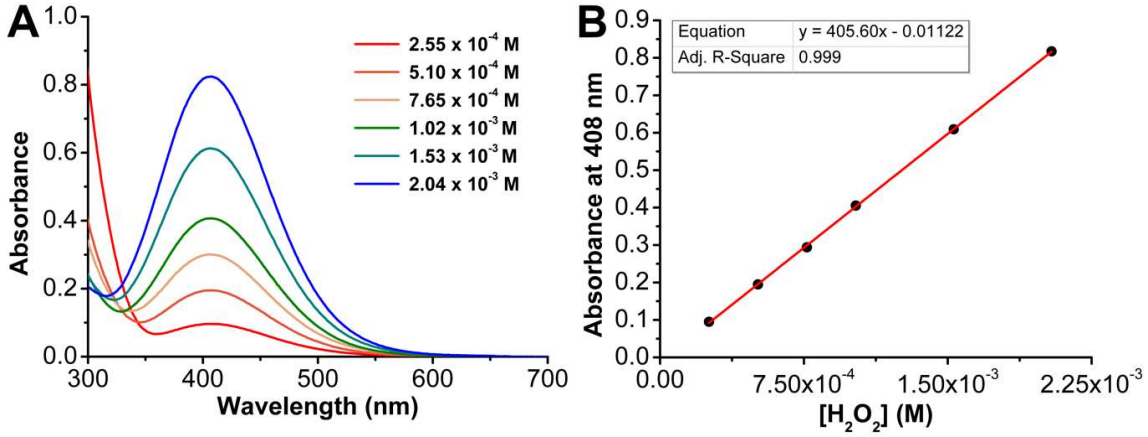

Figure S2.17. Calibration curve of H_2O_2 quantification using a $Ti(O)SO_4$ colorimetric assay. (**A**) Serial dilution of urea•H_2O_2 in 50/50 MeCN/H_2O. using the above method. (**B**) Calibration made using a serial dilution of urea•H_2O_2 in 50/50 MeCN/H_2O.

To ensure $Fe(PMG)(Cl)_2$ does not facilitate H_2O_2 disproportionation or interfere with the $Ti(O)SO_4$ calorimetric assay, a known amount of urea•H_2O_2 in MeCN (1.12 mM final concentration) was added to $Fe(PMG)(Cl)_2$ (50 μM final concentration) with AcOH (5 mM final concentration) that had

been saturated with O_2. An aliquot was removed from the solution and a UV-vis spectrum was taken at 0 min (before and after $Ti(O)SO_4$ addition, as described above), and the solution was allowed to react for the full reaction time of a catalytic run (30 min) and another UV-vis spectrum was taken. The difference between the final and initial traces was taken at 408 nm for both 0 min and 30 min and used to quantify the final H_2O_2. After 30 min, no H_2O_2 degradation was apparent (101 ± 5% H_2O_2 recovered).

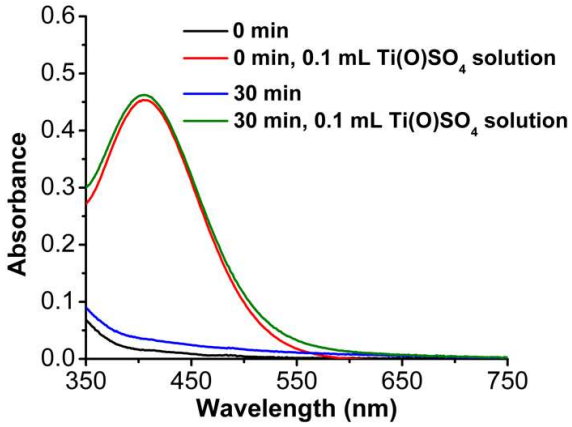

Figure S2.18. H_2O_2 stability test in the presence of $Fe(PMG)(Cl)_2$. UV-vis spectra of $Fe(PMG)(Cl)_2$. (50 μM) and urea•H_2O_2 (1.12 mM) in the presence of 5 mM AcOH after 30 min before (black) and after (red) 0.1 mL $Ti(O)SO_4$ solution was added.

The selectivity of $Fe(PMG)(Cl)_2$ for the ORR was determined according to **Eqs. S2.4-S2.6**. Catalytic reaction mixtures (50 μM $Fe(PMG)(Cl)_2$, 5 mM AcOH, 1.5 mM Cp^*_2Fe, 4.05 mM O_2) were allowed to run to completion (30 min). Aliquots (1.5 mL) were diluted in 1.5 mL DI H_2O. Upon exposure to water, the solution became cloudy and was filtered through a pipette filter containing glass wool. A UV-vis spectrum was obtained before and after 0.1 mL $Ti(O)SO_4$ was added. Aliquots were withdrawn and analyzed with and without $Ti(O)SO_4$ (red and black traces, respectively in **Figure S2.14**, **Eq. S2.4**). The experimental H_2O_2 yield was then converted to % selectivity according to **Eqs. S2.4 & S2.6**.

$$O_2 + 2Cp^*_2Fe\ (1.5\ mM) + 2AcOH \xrightarrow{cat.[Fe]} H_2O_2(0.75\ mM) + 2Cp^*_2Fe^+ + 2AcO^- \quad \textbf{(S2.4)}$$

Abs@408 nm (red trace, **Figure S2.19**) – Abs@408 nm (black trace, **Figure S2.19**)

= 405.60$[H_2O_2]_{exp}$ – 0.01122 (**Figure S2.17**) **(S2.5)**

$$\frac{[H_2O_2]_{exp}}{0.75\ mM\ H_2O_2} \times 100 = \%\ H_2O_2\ selectivity \quad \textbf{(S2.6)}$$

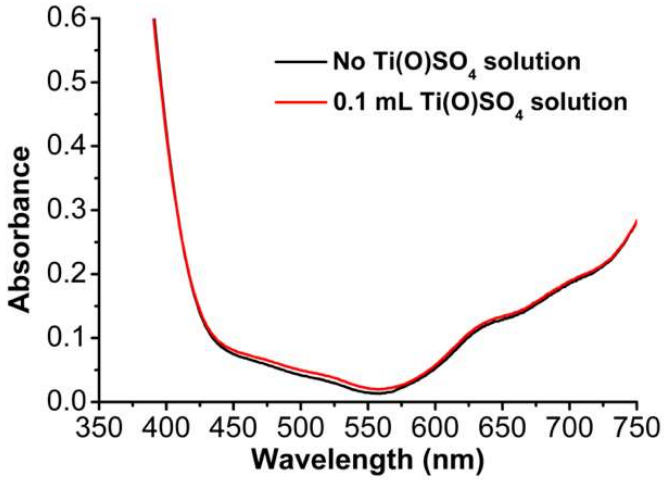

Figure S2.19. UV-vis spectrum of catalytic solution of Fe(PMG)$(Cl)_2$ before (black) and after (red) the addition of 0.1 mL Ti(O)SO_4 solution.

The stoichiometry of the H_2O_2 reduction reaction (**Eq. S2.7**) was confirmed by quantifying the amount of oxidized decamethylferrocenium ($[Cp^*_2Fe]^+$) formed under anaerobic catalytic conditions limited with respect to [urea•H_2O_2] substrate. Catalytic reaction mixtures (50 μM Fe(PMG)$(Cl)_2$, 35 mM AcOH, 1.5 mM Cp^*_2Fe, and 0.42 mM urea•H_2O_2) were allowed to run to completion (5 min). Aliquots were (0.3 mL) diluted in 2.7 mL MeCN and a UV-vis spectrum was obtained. The amount of $[Cp^*_2Fe]^+$ was quantified using the molar extinction coefficient at 780 nm (ε = 461 M^{-1} cm^{-1} as determind by serial dilution of a chemically prepared sample of $[Cp^*_2Fe][BF_4]$). The concentration of urea•H_2O_2 in the catalytic solutions was confirmed by Ti(O)SO_4 as described above. The number of equiv. of Cp^*_2Fe consumed per equiv. H_2O_2 was determined by Eq. **S2.8**:

$$H_2O_2 + 2Cp^*_2Fe + 2AcOH \xrightarrow{cat.\ Fe} 2H_2O + 2Cp^*_2Fe^+ + 2AcO^- \qquad \textbf{(S2.7)}$$

$$\frac{[[Cp^*_2Fe]^+]_{exp}}{[H_2O_2]} = Eq.\ Cp^*_2Fe\ consumed\ per\ H_2O_2 \qquad \textbf{(S2.8)}$$

It was determined that 2.1 +/- 0.07 equiv of Cp^*_2Fe were consumed per equivalent of H_2O_2, confirming the $2e^-$ stoichiometry for the reduction of H_2O_2. The slight excess of $[Cp^*_2Fe]^+$ in solution is attributed to a redox equilibrium between Cp^*_2Fe and $Fe(PMG)(Cl)_2$.**Stopped-Flow Spectrochemical Methods.**

Stopped-flow spectrochemical kinetics studies were performed with a CSF-61DX2 Stopped-Flow System from Hi-Tech Scientific. Kinetic Studio Software was used to monitor a single wavelength and Integrated CCD Software was used to monitor the entire visible spectrum. All data fits were performed within the Kinetic Studio 4.0 Software Suite. Prior to experiments, dried and degassed MeCN was passed through syringes and the cell block before reagents were loaded. In a typical experiment, syringes would be charged with known concentrations of reagent. All reagent solutions were prepared immediately before use.

Determination of the Catalytic Rate Law for ORR by $Fe(PMG)(Cl)_2$.

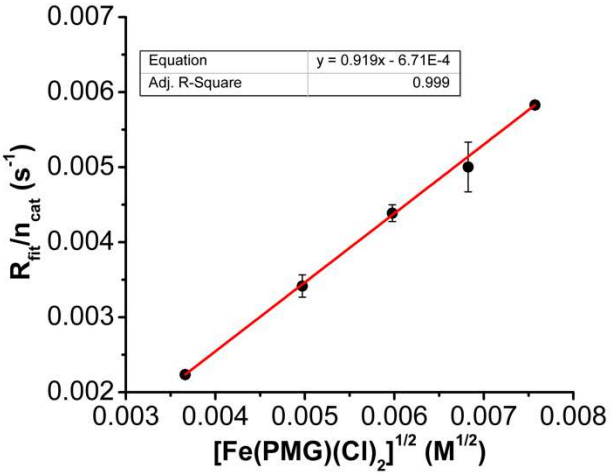

Figure S2.20. The calculated R_{fit}/n_{cat} values from stopped-flow spectrochemical experiments with AcOH, Cp^*_2Fe, O_2 with varying $Fe(PMG)(Cl)_2$ concentration. Data were fit using Kinetic Studio 4.0 (2Exp+Mx+C). Concentrations: AcOH = 0.035 M, Cp^*_2Fe = 1.5 mM, O_2 = 4.05 mM.

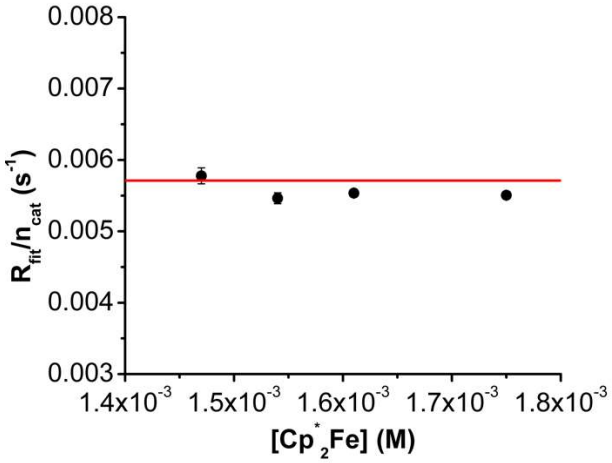

Figure S2.21. The calculated R_{fit}/n_{cat} values from stopped-flow spectrochemical experiments with AcOH, O_2, and Fe(PMG)$(Cl)_2$ with varying Cp^*_2Fe concentration. The horizontal line represents the global average rate observed across all experiments for variable [Cp^*_2Fe]. Data were fit using Kinetic Studio 4.0 (2Exp+Mx+C). Concentrations: AcOH = 0.035 M, O_2 = 4.05 mM, Fe(PMG)$(Cl)_2$ = 50 µM.

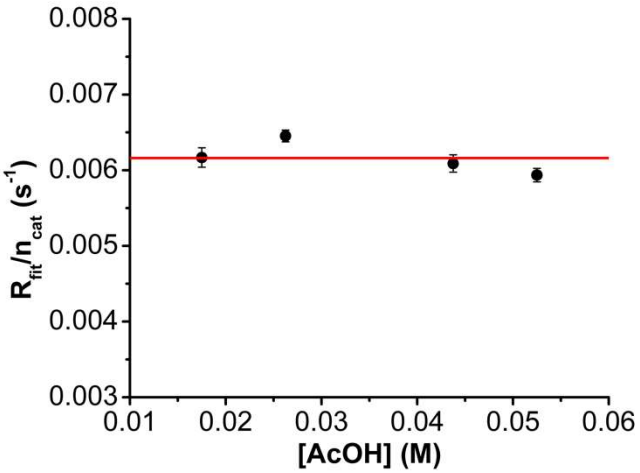

Figure S2.22. The calculated R_{fit}/n_{cat} values from stopped-flow spectrochemical experiments with O_2, Cp^*_2Fe, and Fe(PMG)$(Cl)_2$ with varying AcOH concentration. The horizontal line represents the global average rate observed across all experiments for variable [AcOH]. Data were fit using Kinetic Studio 4.0 (2Exp+Mx+C). Concentrations: O_2 = 4.05 mM, Cp^*_2Fe = 1.5 mM, Fe(PMG)$(Cl)_2$ = 50 µM.

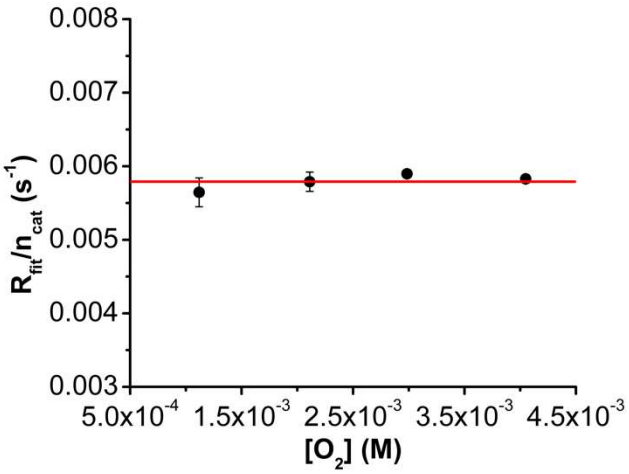

Figure S2.23. The calculated R_{fit}/n_{cat} values from stopped-flow spectrochemical experiments with AcOH, Cp^*_2Fe, and $Fe(PMG)(Cl)_2$ with varying O_2 concentration. The horizontal line represents the global average rate observed across all experiments for variable $[O_2]$. Data were fit using Kinetic Studio 4.0 (2Exp+Mx+C). Concentrations: AcOH = 0.035 M, Cp^*_2Fe = 1.5 mM, $Fe(PMG)(Cl)_2$ = 50 μM.

Determination of the Catalytic Rate Law for H_2O_2RR by $Fe(PMG)(Cl)_2$.

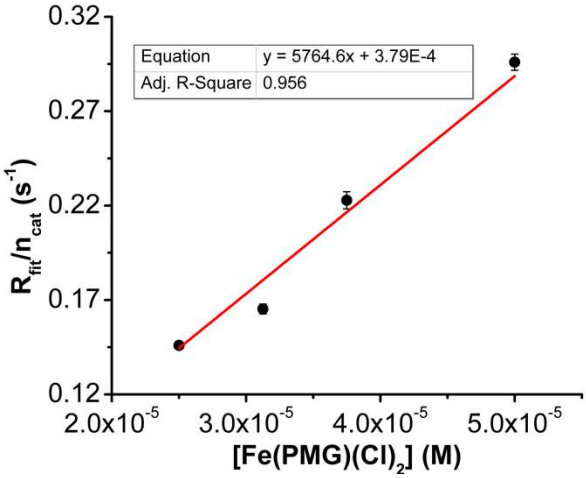

Figure S2.24. The calculated R_{fit}/n_{cat} values from stopped-flow spectrochemical experiments with AcOH, Cp^*_2Fe, H_2O_2 with varying $Fe(PMG)(Cl)_2$ concentration. Data were fit using Kinetic Studio 4.0 (2Exp+Mx+C). Concentrations: AcOH = 0.035 M, Cp^*_2Fe = 1.5 mM, H_2O_2 = 4.0 mM.

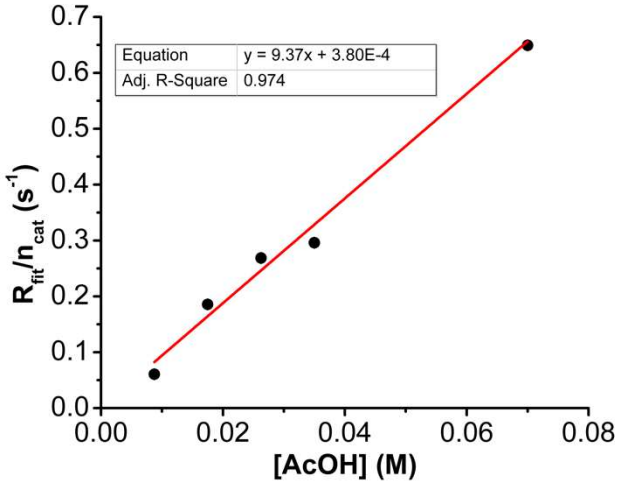

Figure S2.25. The calculated R_{fit}/n_{cat} values from stopped-flow spectrochemical experiments with H_2O_2, Cp^*_2Fe, and $Fe(PMG)(Cl)_2$ with varying AcOH concentration. Data were fit using Kinetic Studio 4.0 (2Exp+Mx+C). Concentrations: H_2O_2 = 4.0 mM, Cp^*_2Fe = 1.5 mM, $Fe(PMG)(Cl)_2$ = 50 μM.

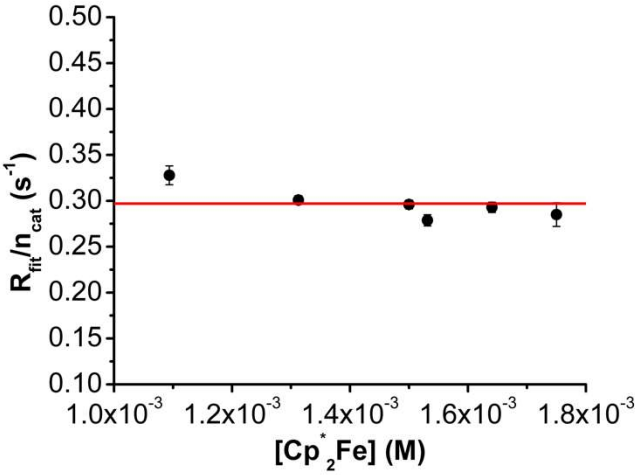

Figure S2.26. The calculated R_{fit}/n_{cat} values from stopped-flow spectrochemical experiments with AcOH, H_2O_2, and $Fe(PMG)(Cl)_2$ with varying Cp^*_2Fe concentration. The horizontal line represents the global average rate observed across all experiments for variable [Cp^*_2Fe]. Data were fit using Kinetic Studio 4.0 (2Exp+Mx+C). Concentrations: AcOH = 0.035 M, H_2O_2 = 4.0 mM, $Fe(PMG)(Cl)_2$ = 50 μM.

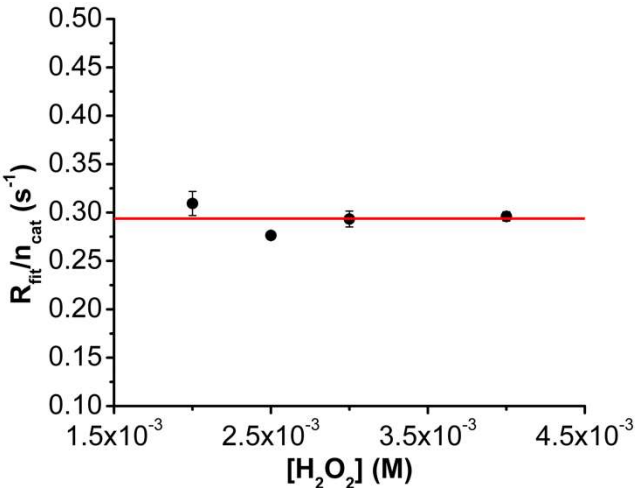

Figure S2.27. The calculated R_{fit}/n_{cat} values from stopped-flow spectrochemical experiments with AcOH, Cp^*_2Fe, and $Fe(PMG)(Cl)_2$ with varying H_2O_2 concentration. The horizontal line represents the global average rate observed across all experiments for variable [H_2O_2]. Data were fit using Kinetic Studio 4.0 (2Exp + Mx + C). Concentrations: AcOH = 0.035 M, Cp^*_2Fe = 1.5 mM, $Fe(PMG)(Cl)_2$ = 50 μM.

R_{fit} values (as R_1 in fitting function) were obtained by fitting the data in the Kinetic Studio 4.0 Software to a double exponential (2Exp+Mx+C) to achieve an R^2 value of 0.999. The R_{fit} values were corrected for the number of electrons passed during catalysis (n_{cat} = 3.98) and plotted against variable concentrations to obtain the experimental rate law (**Eq. 2.2**, main text). The turnover frequency can be defined by the slope of the variable [$Fe(PMG)(Cl)_2$] plot (**Figure S2.16** and **Eq. S2.9**).

$$\frac{R_{fit}}{n_{cat}} = k_{cat}[Fe(PMG)(Cl)_2]^{0.5} \qquad \textbf{(S2.9)}$$

$$TOF_{ORR} = 0.92\ s^{-1}$$

For H_2O_2RR, the slope of both the variable [$Fe(PMG)(Cl)_2$] and [AcOH] were used to determine the TOF according to **Eq. S2.10** and averaged (**Figure S2.21** and **S2.22**). For this analysis, n_{cat} = 2 was used.

$$\frac{R_{fit}}{n_{cat}} = k_{cat}[Fe(PMG)(Cl)_2]^1[AcOH]^1 \qquad \textbf{(S2.10)}$$

$$TOF_{H2O2RR} = 2.9 \times 10^3\ s^{-1}$$

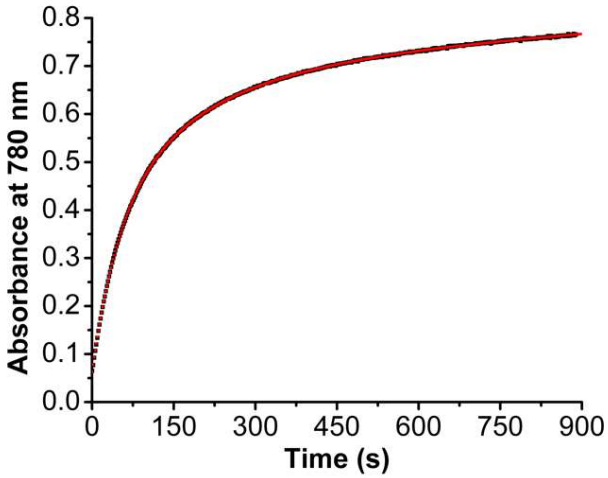

Figure S2.28. Example of UV-vis Stopped-Flow spectrochemical data (black) and the fit (red) used for this work. The data was fit with Kinetic Studio 4.0 to a double exponential (2Exp+Mx+C).

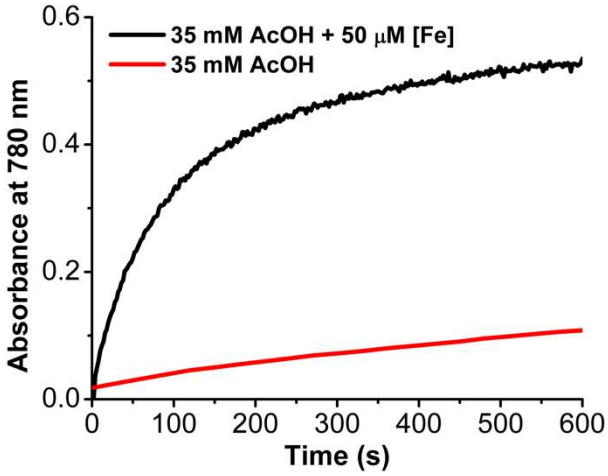

Figure S2.29. Spectral changes at 780 nm due to the formation of $[Cp^*_2Fe]^+$ over time with 35 mM AcOH, 4.05 mM O_2, 1.5 mM Cp^*_2Fe. Black: 50 μM $Fe(PMG)(Cl)_2$, red: control.

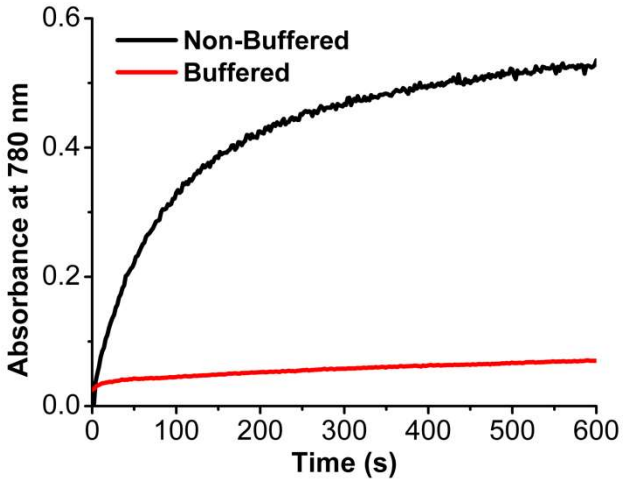

Figure S2.30. Representative spectral changes at 780 nm due to the formation of $[Cp^*2Fe]^+$ comparing $Fe(PMG)(Cl)_2$ under non-buffered (black) and buffered *(red) conditions.* Concentrations: 50 μM $Fe(PMG)(Cl)_2$, 35 mM TBAAcO/AcOH, 4.05 mM O_2, and 1.5 mM Cp^*_2Fe.

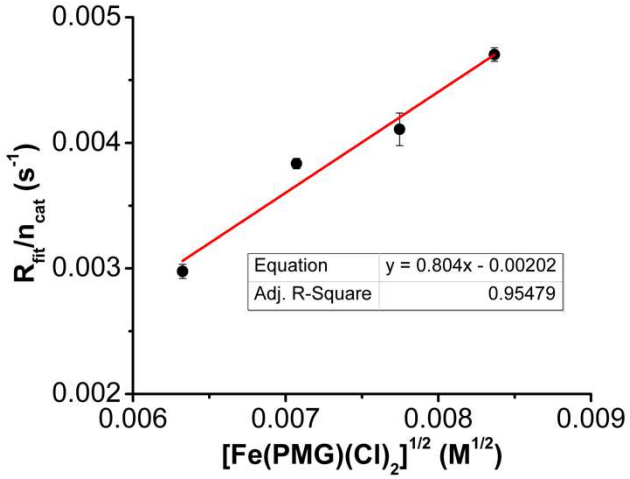

Figure S2.31. The calculated R_{fit}/n_{cat} values from stopped-flow spectrochemical experiments with AcOH, Cp^*_2Fe, O_2, and TBACl with varying $Fe(PMG)(Cl)_2$ concentration. Data were fit using Kinetic Studio 4.0 (2Exp+Mx+C). Concentrations: AcOH = 0.035 M, O_2 = 4.05 mM, Cp_2Fe = 1.5 mM, TBACl = 1 mM.

Variable-Temperature Methods Summary.

Keeping the concentrations of the various substrates constant while varying the temperature enables the determination of the thermodynamic parameters of the rate-determining transition state for the reaction of interest using the Eyring equation. The Eyring equation can be written as **Eq. S2.9**:

$$\ln\left(\frac{k_{cat}}{T}\right) = \frac{-\Delta H^{\ddagger}}{R}\left(\frac{1}{T}\right) + \ln\frac{k_B}{h} + \frac{\Delta S^{\ddagger}}{R} \qquad \textbf{(S2.9)}$$

Where R is the ideal gas constant, T is temperature, k_B is Boltzmann's constant, h is Planck's constant, $\Delta H^{\ddagger}$ is enthalpy, $\Delta S^{\ddagger}$ is the entropy of the transition state. Plotting R_{fit}/n_{cat} versus $1/T$ the entropy of the transition state of the reaction can be determined using the following equation (**Eq. S2.10**):

$$\Delta S^{\ddagger} = R[(y - intercept) - \ln\left(\frac{k_B}{h}\right)] \qquad \textbf{(S2.10)}$$

The enthalpy for the transition state of the reaction can be determined from the stop where (**Eq. S2.11**):

$$slope = \frac{-\Delta H^{\ddagger}}{R} \qquad \textbf{(S2.11)}$$

Using the Eyring equation above, along with obtaining R_{fit}/n_{cat} values at varying temperatures, the values for entropy and enthalpy for the transition state can be determined. Using these values for enthalpy and entropy, the free energy of the transition state can then be calculated at any temperature.

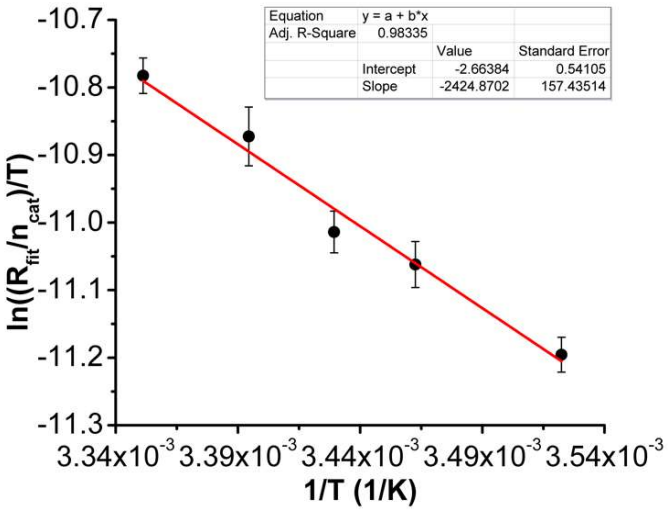

Figure S2.32. Eyring plot of the stopped-flow spectrochemical experiments with $Fe(PMG)(Cl)_2$ with AcOH. Data were fit using Kinetic Studio 4.0 (2Exp+Mx+C). Concentrations: $Fe(PMG)(Cl)_2$ = 50 μM, AcOH = 35 mM, Cp^*_2Fe = 1.5 mM, O_2 = 4.05 mM.

Electrochemistry with H_2O_2

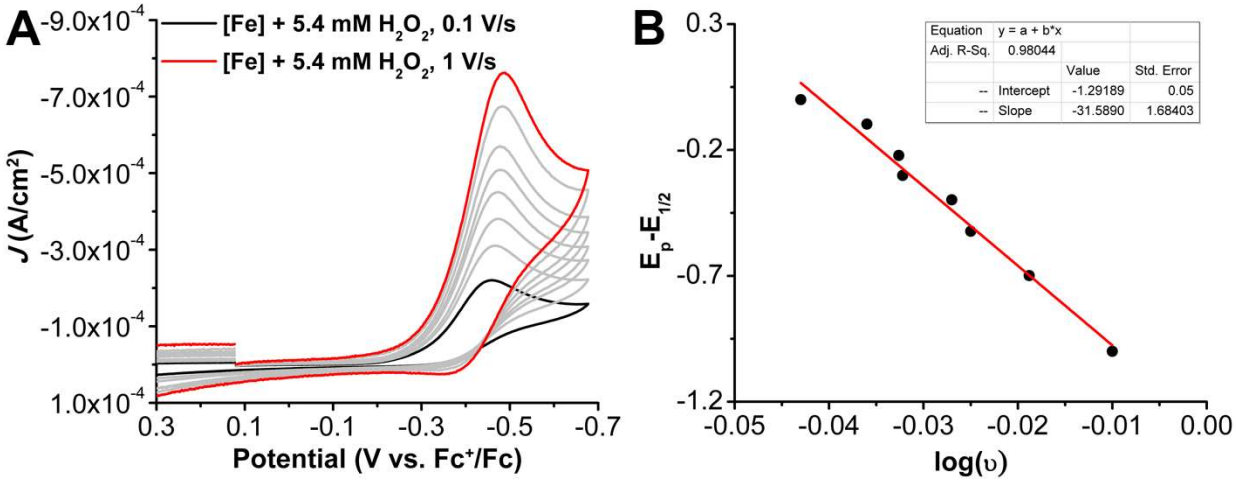

Figure S2.33. Determination of k_{H2O2} (**A**) CVs of $Fe(PMG)(Cl)_2$ under Ar saturation with 5.4 mM urea•H_2O_2 at 0.1 V/s (black) and 1 V/s (red) at varying scan rates (**B**) log(υ) vs. E_p-$E_{1/2}$ plot of variable scan rate data in A. Conditions: 1 mM $Fe(PMG)(Cl)_2$, 5.4 mM urea•H_2O_2, 0.1 M $TBAPF_6$ in MeCN; glassy carbon working electrode; Ag/AgCl pseudoreference electrode; referenced to internal ferrocene standard; scan rates: 0.1, 0.2, 0.3, 0.4, 0.5, 0.6, 0.8, 1 V/s.

Spectroscopic studies with Fe^{II}(PMG)Cl.

UV-vis Spectroscopic Analysis

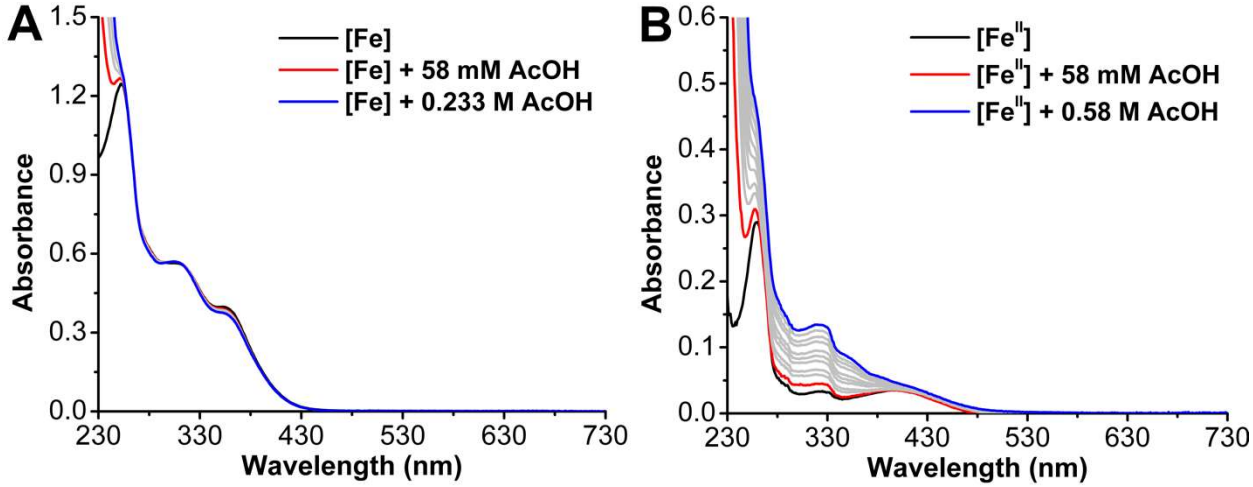

Figure S2.34. (A) Spectral changes of $Fe(PMG)(Cl)_2$ (78 μM) with increasing concentrations of AcOH added. (B) Spectral changes of Fe^{II}(PMG)Cl (50 μM) with increasing concentrations of AcOH. Conditions: 58 mM AcOH aliquots in MeCN under N_2.

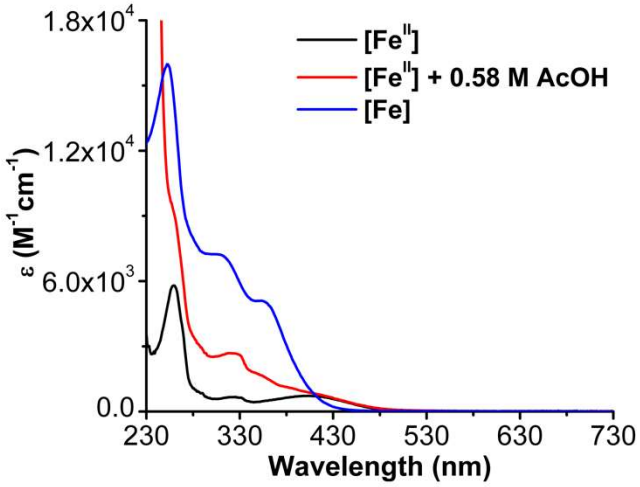

Figure S2.35. Molar extinction plot of Fe^{II}(PMG)Cl (black trace), Fe^{II}(PMG)Cl and 0.58 M AcOH (red trace), and $Fe(PMG)(Cl)_2$ (blue trace) from Figure S2.31.

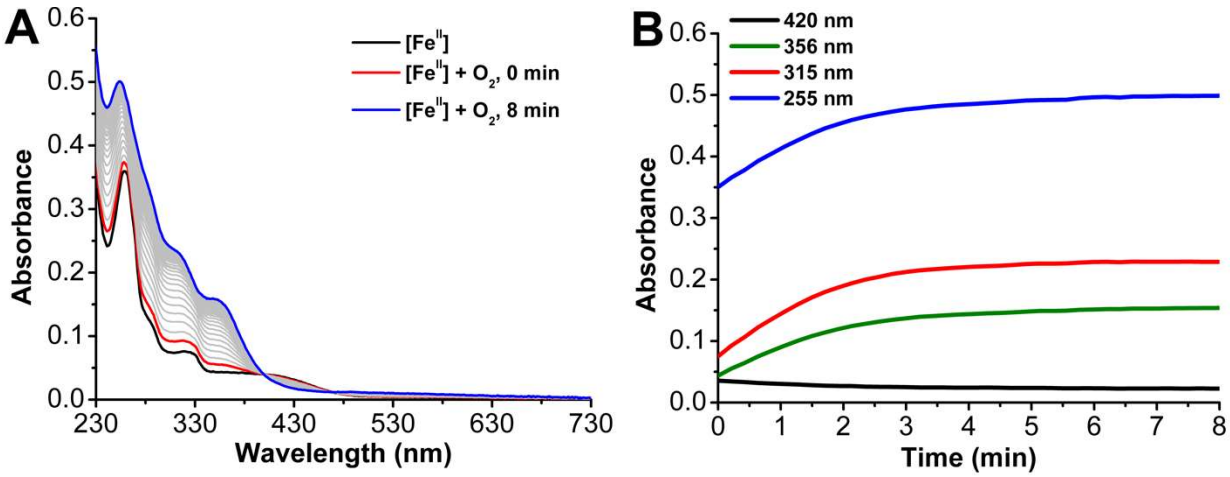

Figure S2.36. (A) Spectral changes of Fe^{II}(PMG)Cl upon air exposure over time. (B) Change in absorbance at 420, 356, 315, and 255 nm upon air exposure. Conditions: 50 μM [Fe^{II}(PMG)Cl], 1.62 mM O_2 in MeCN; all solutions were made under anaerobic conditions.

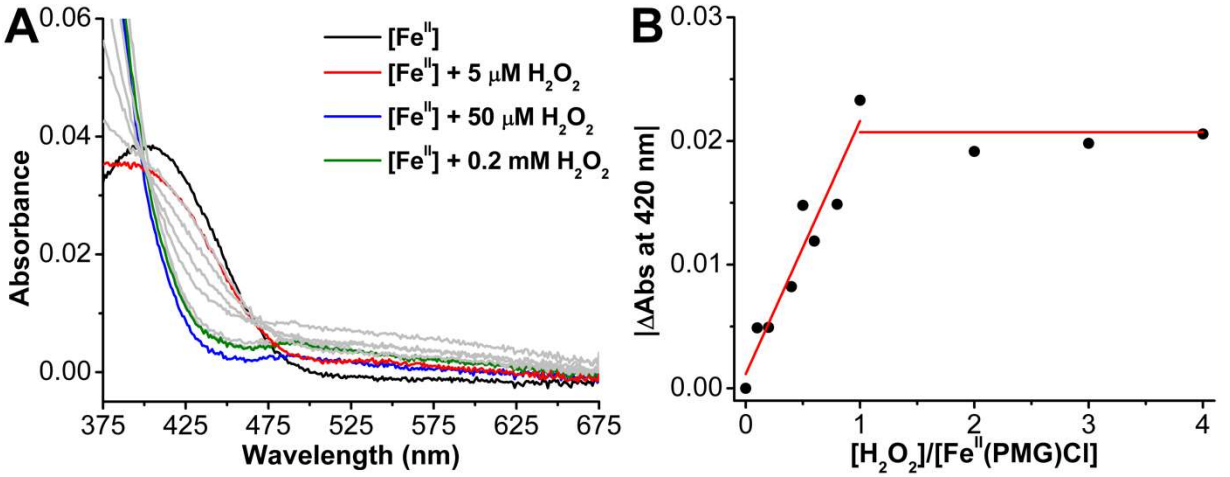

Figure S2.37. (A) Spectral changes upon addition of increasing amounts of urea•H2O2 to a 50 μM solution of Fe^{II}(PMG)Cl under N_2 in MeCN. (B) Plot of change in absorbance at 420 nm versus the ratio of [H2O2]:[Fe^{II}(PMG)Cl]. Conditions: 5, 10, 20, 25, 30, 40, 50, 100, 150, 200 μM urea•H_2O_2.

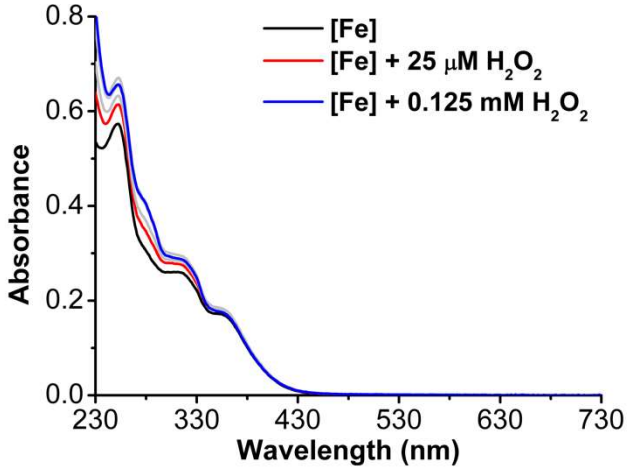

Figure S2.38. Spectral changes upon addition of increasing amounts of urea•H_2O_2 to 44 μM Fe(PMG)$(Cl)_2$ in MeCN. Conditions: 25, 50,75, 100, 125 μM urea•H_2O_2.

^{1}H-NMR Spectroscopic Analysis.

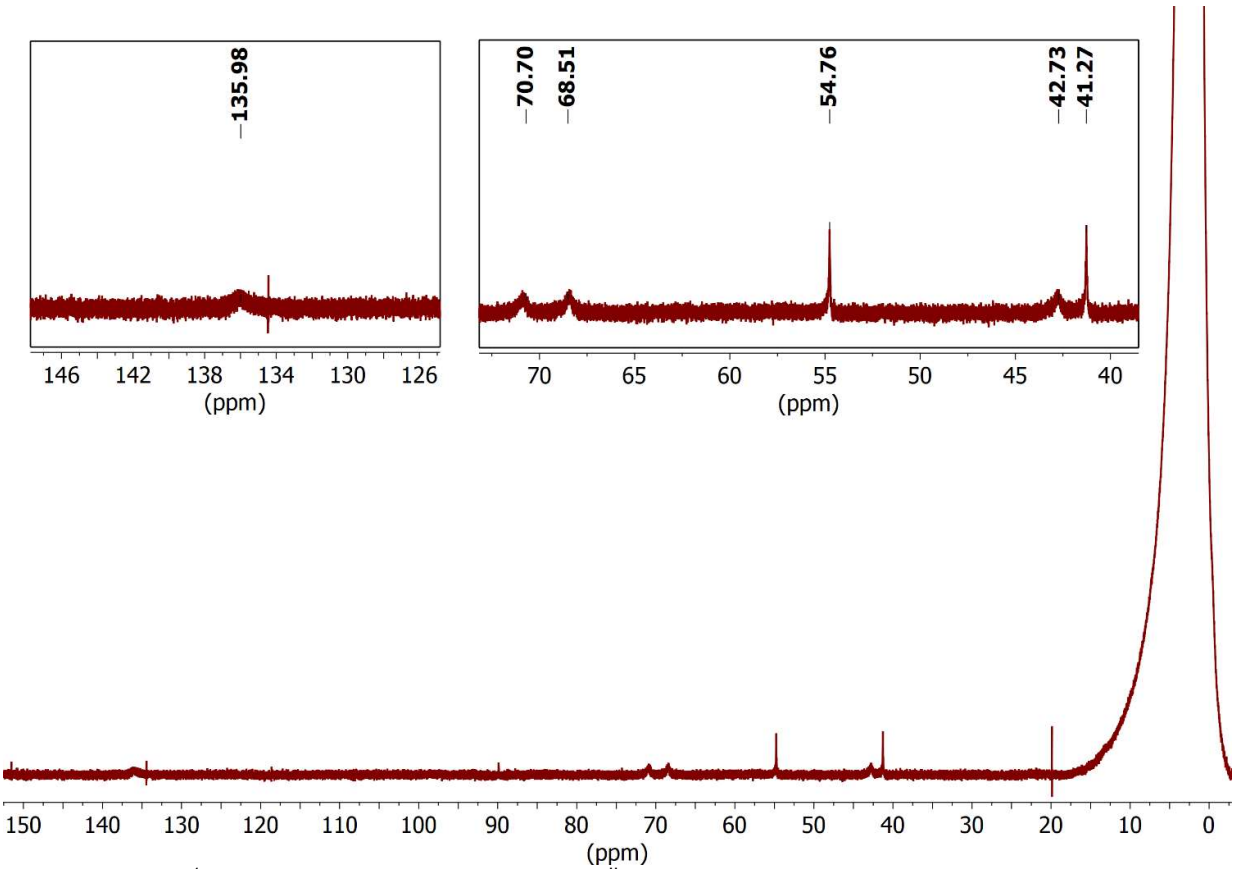

Figure S2.39. ^{1}H-NMR spectrum of 3.2 mM [Fe^{II}(PMG)Cl] under N_2 in MeCN-d_3; 600 MHz, Varian.

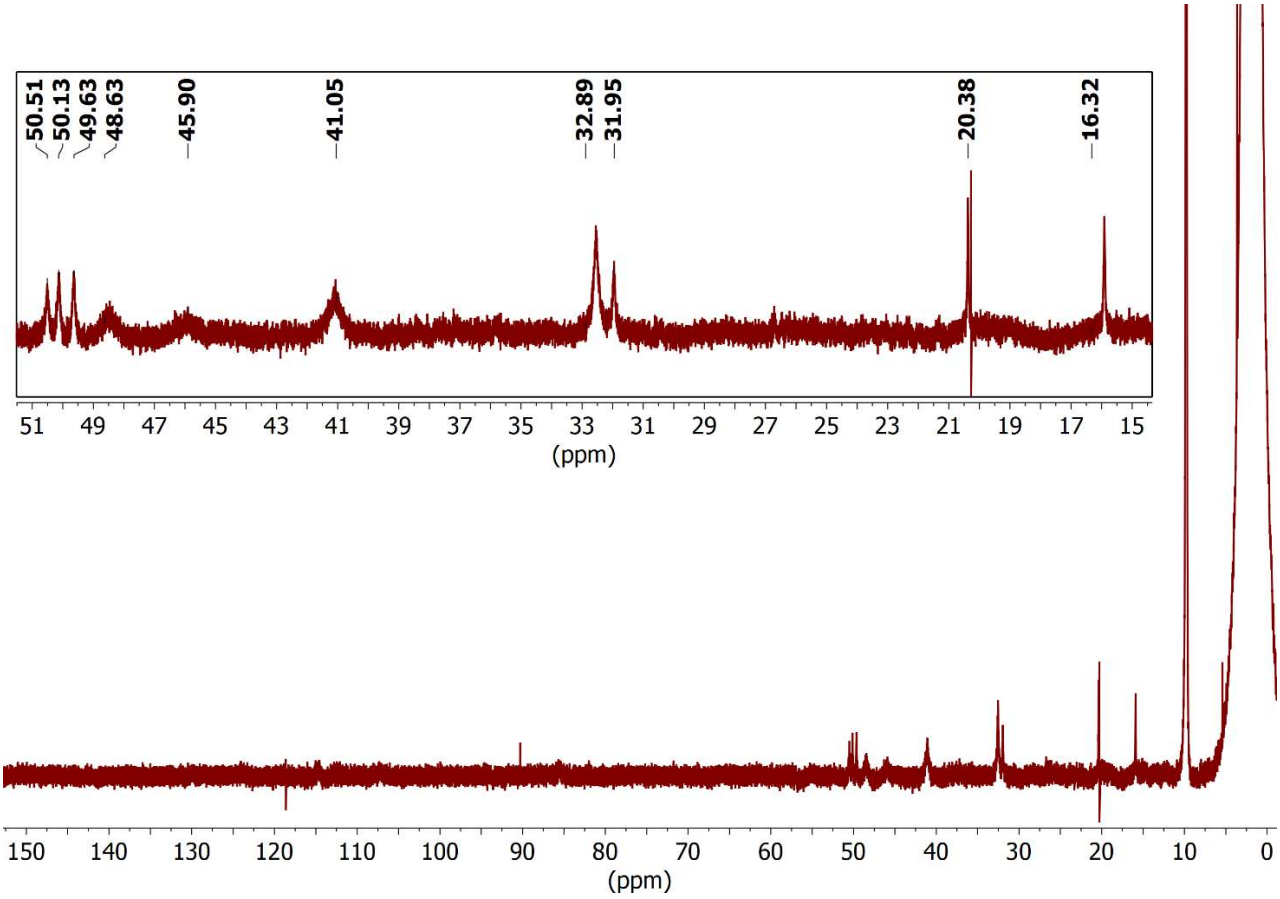

Figure S2.40. ^{1}H-NMR spectrum of 3.2 mM [Fe^{II}(PMG)Cl] + 0.3 M AcOH under N_2 in MeCN-d_3; 600 MHz, Varian. Broad and less well-resolved resonances appear at 114.6 ppm, 107.3 ppm, and 85.5 ppm.

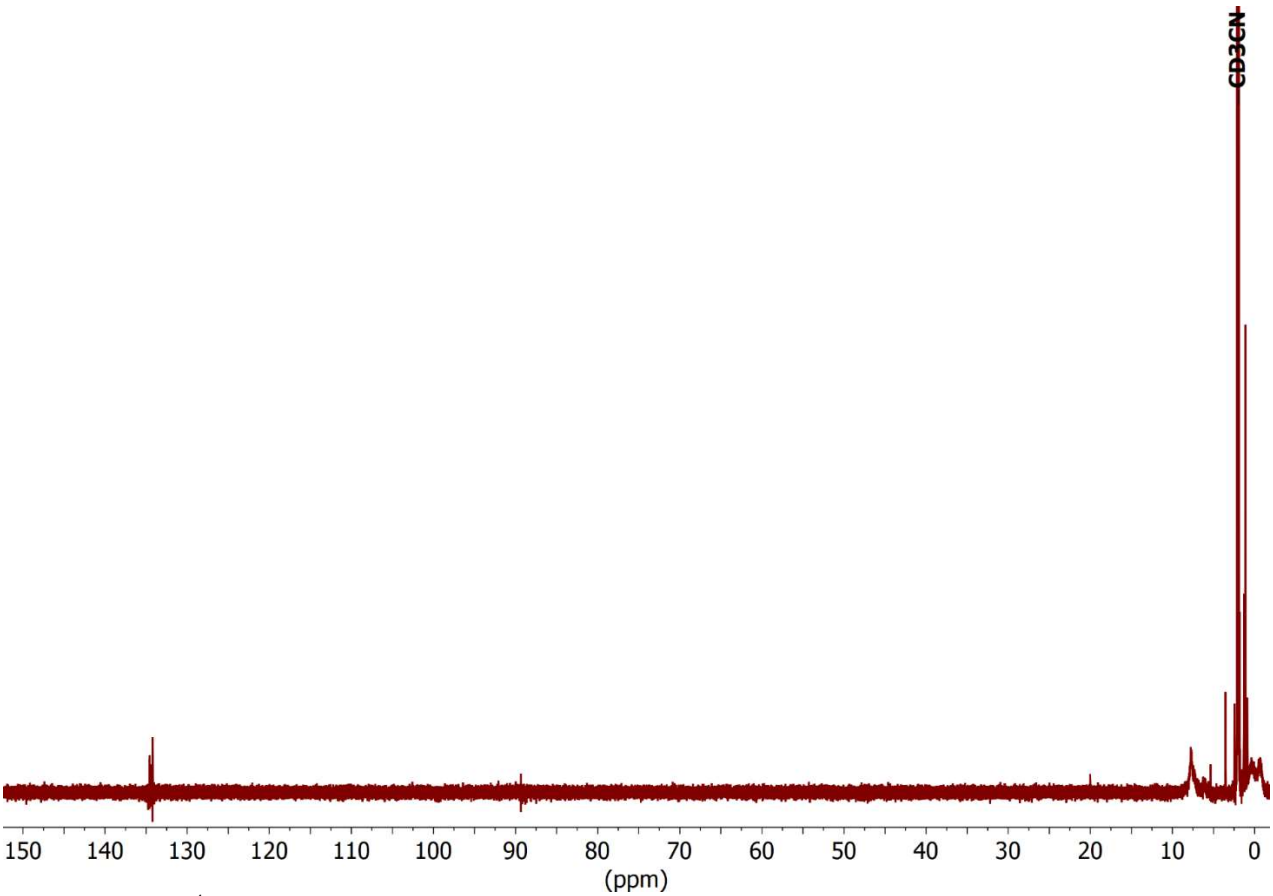

Figure S2.41. ^{1}H-NMR spectrum of 2.9 mM [Fe(PMG)$(Cl)_2$] in MeCN-d_3; 600 MHz, Varian.

X-ray Crystallography.

A single crystal of **PMGH**, **Fe(PMG)(Cl)$_2$** *or* **[Fe(TPA)Cl][Cl]** was coated with Paratone oil and mounted on a MiTeGen MicroLoop. The X-ray intensity data were measured on a Bruker Kappa APEXII Duo system equipped with a fine-focus sealed tube (Mo K_α, λ = 0.71073 Å) and a graphite monochromator (**PMGH**, **Fe(PMG)(Cl)$_2$***) or a* Bruker D8 Venture Kappa four-circle diffractometer system equipped with an Incoatec IμS 3.0 micro-focus sealed X-ray tube (Mo Kα, λ = 0.71073 Å) and a HELIOS double bounce multilayer mirror monochromator (**[Fe(TPA)Cl][Cl]**). The frames were integrated with the Bruker SAINT software package[76] using a narrow-frame algorithm. Data were corrected for absorption effects using the Multi-Scan method (SADABS).[76] Each structure was solved and refined using the Bruker SHELXTL Software Package[77] within APEX3[76] and OLEX2. [78] Non-hydrogen atoms were refined anisotropically. The O-H hydrogen atom in PMG was located in the electron density map and refined isotropically with U_{iso} = 1.5U_{equiv} of the parent atom. All other hydrogen atoms were placed in geometrically calculated positions with U_{iso} = 1.2U_{equiv} of the parent atom. The structure of *Fe(PMG)(Cl)$_2$* was refined as an inversion twin. The twin law was -1 0 0 0 -1 0 0 0 -1 and the BASF refined to 0.20012. There was extensive disorder in the structure. The relative occupancy of the positions was freely refined, and constraints/restraints were used as need on the anisotropic displacement parameters and bond lengths of the disordered atoms. In **[Fe(TPA)Cl][Cl]** one chloride anion was found to be disordered over two positions. The relative occupancy of the positions was freely refined and no constraints or restraints were need. CH_2Cl_2 solvent located in the crystal lattice was severely disordered and could not be adequately modeled with or without restraints. Thus, the structure factors were modified using the PLATON SQUEEZE[79] technique, in order to produce a "solvate-free" structure factor set. PLATON reported a total electron density of 99 e^- and total solvent accessible volume of 265 Å^3.

Table S2.1. X-ray crystallographic data for PMGH, **$Fe(PMG)(Cl)_2$** and **[Fe(TPA)Cl][Cl]**

	PMGH	**$Fe(PMG)(Cl)_2$**	**[Fe(TPA)Cl][Cl]**
CCDC number	2080838	2080839	2103084
Formula	$C_{14}H_{15}N_3O_2$	$C_{14}H_{14}Cl_2FeN_3O_2$	$C_{18}H_{18}Cl_3FeN_4$
FW (g/mol)	257.29	383.03	452.56
Temp (K)	100(2)	100(2)	100(2)
λ (Å)	0.71073	0.71073	0.71073
Size (mm)	0.198 x 0.278 x 0.297	0.054 x 0.125 x 0.402	0.123 x 0.215 x 0.236
Crystal habit	colorless block	yellow rod	yellow block
Crystal system	monoclinic	monoclinic	triclinic
Space group	P 2_1/c	P c	P -1
a (Å)	9.7965(7)	8.6463(9)	8.9879(6)
b(Å)	7.9342(6)	12.6402(11)	16.1348(12)
c (Å)	16.3382(12)	14.4498(13)	16.1747(12)
α (°)	90	90	108.575(2)
β (°)	94.2899(19)	92.768(3)	93.882(2)
γ (°)	90	90	90.569(2)
Volume ($Å^3$)	1266.37(16)	1577.4(3)	2217.1(3)
Z	4	4	4
Density (g/cm^3)	1.349	1.613	1.356
μ (mm^{-1})	0.093	1.303	1.050
F(000)	544	780	924
θ range (°)	2.08 to 31.54	1.61 to 25.73	2.27 to 29.60
Index ranges	-11 ≤ h ≤ 14 -9 ≤ k ≤ 11 -24 ≤ l ≤ 24	-10 ≤ h ≤ 10 -15 ≤ k ≤ 15 -17 ≤ l ≤ 17	-10 ≤ h ≤ 12 -22 ≤ k ≤ 22 -22 ≤ l ≤ 22
Reflns collected	16996	15180	69609
Independent reflns	4221 [R_{int} = 0.0322]	5681 [R_{int} = 0.0356]	12436 [R_{int} = 0.0362]
Data / restraints /parameters	4221 / 0 / 175	5681 / 28 / 466	12436 / 0 / 479
GOF on F^2	1.037	1.088	1.053
R_1 (I>2σ(I))	0.0366	0.0485	0.0430
wR_2 (all data)	0.0996	0.1025	0.1033

Determination of Overpotential:

The calculation of overpotential for this system is complicated by the inability to utilize buffered acids for kinetic experiments (**Figure S2.30**). As a lower limit approximation of overpotential, we have utilized reported pK_a (23.5) and log(K_{AHA}) (3.9) values for AcOH in MeCN and corrected the reported standard reduction potentials for ORR to include homoconjugation using the following equations:[1,51,52]

$$\mathrm{E}^0_{\mathrm{O2/H2O}} = 1.21 - 0.0592\mathrm{p}K_a + \frac{2.303RT}{4F}\log(4K_{\mathrm{AHA}})\ \mathrm{V\ vs\ Fc^+/Fc} \qquad (\mathbf{S2.12})$$

$$\mathrm{E}^0_{\mathrm{O2/H2O}}(\mathrm{MeCN, AcOH}) = -0.12\ \mathrm{V\ vs\ Fc^+/Fc}$$

$$\mathrm{E}^0_{\mathrm{H2O2/H2O}} = 1.74 - 0.0592\mathrm{p}K_a + \frac{2.303RT}{2F}\log(2K_{\mathrm{AHA}})\ \mathrm{V\ vs\ Fc^+/Fc} \qquad (\mathbf{S2.13})$$

$$\mathrm{E}^0_{\mathrm{H2O2/H2O}}(\mathrm{MeCN, AcOH}) = +0.22\ \mathrm{vs\ Fc^+/Fc}$$

where R is the ideal gas law (8.314 J·K^{-1}·mol^{-1}); T is the temperature (298 K); F is Faraday's constant (96485 C·mol^{-1}); K_{AHA} is the reported homoconjugation equilibrium constant for AcOH in MeCN ($10^{3.9}$).

For the $E_{1/2}$ of Fe(PMG)Cl$_2$, a value of −0.27 V of Fc$^+$/Fc was used, from electrochemical experiments (**Figure S2.5**; [Fe] = 1 mM; [AcOH] = 525 mM). Representative spectrochemical experiments were conducted at similar ratios ([Fe] = 0.050 mM; [AcOH] = 35 mM).

2.7. References

(1) Pegis, M. L.; Wise, C. F.; Martin, D. J.; Mayer, J. M. Oxygen Reduction by Homogeneous Molecular Catalysts and Electrocatalysts. *Chem. Rev.* **2018**, *118* (5), 2340-2391. DOI: 10.1021/acs.chemrev.7b00542.

(2) Machan, C. W. Advances in the Molecular Catalysis of Dioxygen Reduction. *ACS Catal.* **2020**, *10* (4), 2640-2655. DOI: 10.1021/acscatal.9b04477.

(3) Yoshikawa, S.; Shimada, A. Reaction mechanism of cytochrome c oxidase. *Chem. Rev.* **2015**, *115* (4), 1936-1989. DOI: 10.1021/cr500266a.

(4) Denisov, I. G.; Makris, T. M.; Sligar, S. G.; Schlichting, I. Structure and Chemistry of Cytochrome P450. *Chem. Rev.* **2005**, *105* (6), 2253-2278. DOI: 10.1021/cr0307143.

(5) Shao, M.; Chang, Q.; Dodelet, J.-P.; Chenitz, R. Recent Advances in Electrocatalysts for Oxygen Reduction Reaction. *Chem. Rev.* **2016**, *116* (6), 3594-3657. DOI: 10.1021/acs.chemrev.5b00462.

(6) Sahu, S.; Goldberg, D. P. Activation of Dioxygen by Iron and Manganese Complexes: A Heme and Nonheme Perspective. *J. Am. Chem. Soc.* **2016**, *138* (36), 11410-11428. DOI: 10.1021/jacs.6b05251.

(7) Campos-Martin, J. M.; Blanco-Brieva, G.; Fierro, J. L. G. Hydrogen peroxide synthesis: An outlook beyond the anthraquinone process. *Angew. Chem. Int. Ed.* **2006**, *45* (42), 6962-6984. DOI: 10.1002/anie.200503779.

(8) Pegis, M. L.; Martin, D. J.; Wise, C. F.; Brezny, A. C.; Johnson, S. I.; Johnson, L. E.; Kumar, N.; Raugei, S.; Mayer, J. M. Mechanism of Catalytic O2 Reduction by Iron Tetraphenylporphyrin. *J. Am. Chem. Soc.* **2019**, *141* (20), 8315-8326. DOI: 10.1021/jacs.9b02640.

(9) Lu, X.; Lee, Y. M.; Sankaralingam, M.; Fukuzumi, S.; Nam, W. Catalytic Four-Electron Reduction of Dioxygen by Ferrocene Derivatives with a Nonheme Iron(III) TAML Complex. *Inorg. Chem.* **2020**, *59* (24), 18010-18017. DOI: 10.1021/acs.inorgchem.0c02400.

(10) Wang, Y. H.; Pegis, M. L.; Mayer, J. M.; Stahl, S. S. Molecular Cobalt Catalysts for O2 Reduction: Low-Overpotential Production of H2O2 and Comparison with Iron-Based Catalysts. *J. Am. Chem. Soc.* **2017**, *139* (46), 16458-16461. DOI: 10.1021/jacs.7b09089.

(11) McGuire, R.; Dogutan, D. K.; Teets, T. S.; Suntivich, J.; Shao-Horn, Y.; Nocera, D. G. Oxygen reduction reactivity of cobalt(II) hangman porphyrins. *Chem. Sci.* **2010**, *1* (3), 411-414. DOI: 10.1039/c0sc00281j.

(12) Lieske, L. E.; Hooe, S. L.; Nichols, A. W.; Machan, C. W. Electrocatalytic reduction of dioxygen by Mn(iii) meso-tetra(N-methylpyridinium-4-yl)porphyrin in universal buffer. *Dalton Trans.* **2019**, *48*, 8633-8641, 10.1039/C9DT01436E. DOI: 10.1039/C9DT01436E.

(13) Passard, G.; Dogutan, D. K.; Qiu, M.; Costentin, C.; Nocera, D. G. Oxygen Reduction Reaction Promoted by Manganese Porphyrins. *ACS Catal.* **2018**, *8* (9), 8671-8679. DOI: 10.1021/acscatal.8b01944.

(14) Collman, J. P.; Boulatov, R.; Sunderland, C. J.; Fu, L. Functional Analogues of Cytochrome c Oxidase, Myoglobin, and Hemoglobin. *Chem. Rev.* **2004**, *104* (2), 561-588. DOI: 10.1021/cr0206059.

(15) Zhang, W.; Lai, W.; Cao, R. Energy-Related Small Molecule Activation Reactions: Oxygen Reduction and Hydrogen and Oxygen Evolution Reactions Catalyzed by Porphyrin- and Corrole-Based Systems. *Chem. Rev.* **2017**, *117* (4), 3717-3797. DOI: 10.1021/acs.chemrev.6b00299.

(16) Jones, R. D.; Summerville, D. A.; Basolo, F. Synthetic Oxygen Carriers Related to Biological Systems. *Chem. Rev.* **1979**, *79* (2), 139-179. DOI: 10.1021/cr60318a002.

(17) Kim, E.; Chufán, E. E.; Kamaraj, K.; Karlin, K. D. Synthetic Models for Heme-Copper Oxidases. *Chem. Rev.* **2004**, *104* (2), 1077-1133. DOI: 10.1021/cr0206162.

(18) Fukuzumi, S.; Lee, Y. M.; Nam, W. Mechanisms of Two-Electron versus Four-Electron Reduction of Dioxygen Catalyzed by Earth-Abundant Metal Complexes. *ChemCatChem* **2018**, *10* (1), 9-28. DOI: 10.1002/cctc.201701064.

(19) Nichols, A. W.; Kuehner, J. S.; Huffman, B. L.; Miedaner, P. R.; Dickie, D. A.; Machan, C. W. Reduction of dioxygen to water by a Co(N2O2) complex with a 2,2'-bipyridine backbone. *Chem. Commun.* **2021**, *57*, 516-519. DOI: 10.1039/d0cc06763f.

(20) Wada, T.; Maki, H.; Imamoto, T.; Yuki, H.; Miyazato, Y. Four-electron reduction of dioxygen catalysed by dinuclear cobalt complexes bridged by bis(terpyridyl)anthracene. *Chem. Commun.* **2013**, *49* (39), 4394-4396, 10.1039/C2CC36528F. DOI: 10.1039/C2CC36528F.

(21) Fukuzumi, S.; Kotani, H.; Lucas, H. R.; Doi, K.; Suenobu, T.; Peterson, R. L.; Karlin, K. D. Mononuclear copper complex-catalyzed four-electron reduction of oxygen. *J. Am. Chem. Soc.* **2010**, *132* (20), 6874-6875. DOI: 10.1021/ja100538x.

(22) Kakuda, S.; Peterson, R. L.; Ohkubo, K.; Karlin, K. D.; Fukuzumi, S. Enhanced Catalytic Four-Electron Dioxygen (O2) and Two-Electron Hydrogen Peroxide (H2O2) Reduction with a Copper(II) Complex Possessing a Pendant Ligand Pivalamido Group. *J. Am. Chem. Soc.* **2013**, *135* (17), 6513-6522. DOI: 10.1021/ja3125977.

(23) Hooe, S. L.; Machan, C. W. Dioxygen Reduction to Hydrogen Peroxide by a Molecular Mn Complex: Mechanistic Divergence between Homogeneous and Heterogeneous Reductants. *J. Am. Chem. Soc.* **2019**, *141* (10), 4379-4387. DOI: 10.1021/jacs.8b13373.

(24) Gennari, M.; Brazzolotto, D.; Pécaut, J.; Cherrier, M. V.; Pollock, C. J.; Debeer, S.; Retegan, M.; Pantazis, D. A.; Neese, F.; Rouzières, M.; et al. Dioxygen Activation and Catalytic Reduction to Hydrogen Peroxide by a Thiolate-Bridged Dimanganese(II) Complex with a Pendant Thiol. *J. Am. Chem. Soc.* **2015**, *137* (26), 8644-8653. DOI: 10.1021/jacs.5b04917.

(25) Hooe, S. L.; Cook, E. N.; Reid, A. G.; Machan, C. W. Non-covalent assembly of proton donors and p- benzoquinone anions for co-electrocatalytic reduction of dioxygen. *Chem. Sci.* **2021**, *12* (28), 9733-9741. DOI: 10.1039/d1sc01271a.

(26) Wang, L.; Gennari, M.; Cantú Reinhard, F. G.; Gutiérrez, J.; Morozan, A.; Philouze, C.; Demeshko, S.; Artero, V.; Meyer, F.; de Visser, S. P.; et al. A Non-Heme Diiron Complex for (Electro)catalytic Reduction of Dioxygen: Tuning the Selectivity through Electron Delivery. *J. Am. Chem. Soc.* **2019**, *141* (20), 8244-8253. DOI: 10.1021/jacs.9b02011.

(27) Ward, A. L.; Elbaz, L.; Kerr, J. B.; Arnold, J. Nonprecious metal catalysts for fuel cell applications: electrochemical dioxygen activation by a series of first row transition metal tris(2-pyridylmethyl)amine complexes. *Inorg. Chem.* **2012**, *51* (8), 4694-4706. DOI: 10.1021/ic2026957.

(28) Solomon, E. I.; Goudarzi, S.; Sutherlin, K. D. O2 Activation by Non-Heme Iron Enzymes. *Biochem.* **2016**, *55* (46), 6363-6374. DOI: 10.1021/acs.biochem.6b00635.

(29) Costas, M.; Mehn, M. P.; Jensen, M. P.; Que, L. Dioxygen Activation at Mononuclear Nonheme Iron Active Sites: Enzymes, Models, and Intermediates. *Chem. Rev.* **2004**, *104* (2), 939-986. DOI: 10.1021/cr020628n.

(30) Kovaleva, E. G.; Lipscomb, J. D. Versatility of biological non-heme Fe(II) centers in oxygen activation reactions. *Nat. Chem. Biol.* **2008**, *4* (3), 186-193. DOI: 10.1038/nchembio.71.

(31) Feig, A. L.; Lippard, S. J. Reactions of Non-Heme Iron(II) Centers with Dioxygen in Biology and Chemistry. *Chem. Rev.* **1994**, *94* (3), 759-805. DOI: 10.1021/cr00027a011.

(32) Que, L.; Ho, R. Y. N. Dioxygen activation by enzymes with mononuclear non-heme iron active sites. *Chem. Rev.* **1996**, *96* (7), 2607-2624. DOI: 10.1021/cr960039f.

(33) Viggiani, A.; Siani, L.; Notomista, E.; Birolo, L.; Pucci, P.; Di Donato, A. The role of the conserved residues His-246, His-199, and Tyr-255 in the catalysis of catechol 2,3-

dioxygenase from Pseudomonas stutzeri OX1. *J. Biol. Chem.* **2004**, *279* (47), 48630-48639. DOI: 10.1074/jbc.M406243200.

(34) Abu-Omar, M. M.; Loaiza, A.; Hontzeas, N. Reaction mechanisms of mononuclear non-heme iron oxygenases. *Chem. Rev.* **2005**, *105* (6), 2227-2252. DOI: 10.1021/cr040653o.

(35) Viswanathan, R.; Palaniandavar, M.; Balasubramanian, T.; Muthiah, T. P. Functional Models for Catechol 1,2-Dioxygenase. Synthesis, Structure, Spectra, and Catalytic Activity of Certain Tripodal Iron(III) Complexes. *Inorg. Chem.* **1998**, *37* (12), 2943-2951. DOI: 10.1021/ic970708n.

(36) Cox, D. D.; Que, L. Functional Models for Catechol 1,2-Dioxygenaes. The Role of the Iron(III) Center. *J. Am. Chem. Soc.* **1988**, *110* (24), 8085-8092. DOI: 10.1021/ja00232a021.

(37) Velusamy, M.; Mayilmurugan, R.; Palaniandavar, M. Iron(III) complexes of sterically hindered tetradentate monophenolate ligands as functional models for catechol 1,2-dioxygenases: The role of ligand stereoelectronic properties. *Inorg. Chem.* **2004**, *43* (20), 6284-6293. DOI: 10.1021/ic049802b.

(38) Li, F.; Wang, M.; Li, P.; Zhang, T.; Sun, L. Iron(III) complexes with a tripodal N3O ligand containing an internal base as a model for catechol intradiol-cleaving dioxygenases. *Inorg. Chem.* **2007**, *46* (22), 9364-9371. DOI: 10.1021/ic700664u.

(39) Visvaganesan, K.; Mayilmurugan, R.; Suresh, E.; Palaniandavar, M. Iron(III) complexes of tridentate 3N ligands as functional models for catechol dioxygenases: The role of ligand N-alkyl substitution and solvent on reaction rate and product selectivity. *Inorg. Chem.* **2007**, *46* (24), 10294-10306. DOI: 10.1021/ic700822y.

(40) Schmidt, S. B.; Husted, S. The biochemical properties of manganese in plants. *Plants* **2019**, *8* (10), 381-395. DOI: 10.3390/plants8100381.

(41) Banerjee, S. R.; Wei, L.; Levadala, M. K.; Lazarova, N.; Golub, V. O.; O'Connor, C. J.; Stephenson, K. A.; Valliant, J. F.; Babich, J. W.; Zubieta, J. {ReIIICl3} Core Complexes with Bifunctional Single Amino Acid Chelates. *Inorg. Chem.* **2002**, *41* (22), 5795-5802. DOI: 10.1021/ic020391d.

(42) Claude, P. Paramagnetic Susceptibility by NMR: The "Solvent Correction" Removed for Large Paramagnetic Molecules. *J. Chem. Educ.* **1997**, *74* (7), 815-816. DOI: 10.1021/ed074p815.

(43) Bain, G. A.; Berry, J. F. Diamagnetic corrections and Pascal's constants. *J. Chem. Educ.* **2008**, *85* (4), 532-536. DOI: 10.1021/ed085p532.

(44) Hooe, S. L.; Rheingold, A. L.; Machan, C. W. Electrocatalytic Reduction of Dioxygen to Hydrogen Peroxide by a Molecular Manganese Complex with a Bipyridine-Containing Schiff Base Ligand. *J. Am. Chem. Soc.* **2018**, *140* (9), 3232-3241. DOI: 10.1021/jacs.7b09027.

(45) Nichols, A. W.; Chatterjee, S.; Sabat, M.; Machan, C. W. Electrocatalytic Reduction of CO2 to Formate by an Iron Schiff Base Complex. *Inorg. Chem.* **2018**, *57* (4), 2111-2121. DOI: 10.1021/acs.inorgchem.7b02955.

(46) Mandon, D.; Machkour, A.; Goetz, S.; Welter, R. Trigonal Bipyramidal Geometry and Tridentate Coordination Mode of the Tripod in FeCl2 Complexes with Tris(2-pyridylmethyl)amine Derivatives Bis-α-Substituted with Bulky Groups. Structures and Spectroscopic Comparative Studies. *Inorg. Chem.* **2002**, *41* (21), 5364-5372. DOI: 10.1021/ic011104t.

(47) Savéant, J.-M. J. M.; Costentin, C. Chapter 2 Coupling of the Electrode Electron Transfers with Homogeneous Chemical Reactions. 2 ed.; John Wiley & Sons, Inc., 2019; pp 78-179.

(48) Zanello, P. Chapter 2 Voltammetric Techniques. The Royal Society of Chemistry, 2003; pp 49-135.

(49) Costentin, C.; Savéant, J.-M. Coupling of Electrode Electron Transfers with Homogeneous Chemical Reactions. In *Elements of Molecular and Biomolecular Electrochemistry*, 2019; pp 81-181.

(50) Elgrishi, N.; Kurtz, D. A.; Dempsey, J. L. Reaction parameters influencing cobalt hydride formation kinetics: Implications for benchmarking H2-evolution catalysts. *J. Am. Chem. Soc.* **2017**, *139* (1), 239-244. DOI: 10.1021/jacs.6b10148.

(51) McCarthy, B. D.; Martin, D. J.; Rountree, E. S.; Ullman, A. C.; Dempsey, J. L. Electrochemical reduction of brønsted acids by glassy carbon in acetonitrile-implications for electrocatalytic hydrogen evolution. *Inorg. Chem.* **2014**, *53* (16), 8350-8361. DOI: 10.1021/ic500770k.

(52) Matsubara, Y. Unified Benchmarking of Electrocatalysts in Noninnocent Second Coordination Spheres for CO2 Reduction. *ACS Energy Lett.* **2019**, *4* (8), 1999-2004. DOI: 10.1021/acsenergylett.9b01180.

(53) Anson, C. W.; Stahl, S. S. Cooperative Electrocatalytic O2 Reduction Involving Co(salophen) with p-Hydroquinone as an Electron–Proton Transfer Mediator. *J. Am. Chem. Soc.* **2017**, *139* (51), 18472-18475. DOI: 10.1021/jacs.7b11362.

(54) Burés, J. A simple graphical method to determine the order in catalyst. *Angew. Chem. Int. Ed.* **2016**, *55* (6), 2028-2031. DOI: 10.1002/anie.201508983.

(55) F. van Strijdonck, G. P.; Boele, M. D. K.; Kamer, P. C. J.; de Vries, J. G.; van Leeuwen, P. W. N. M. Fast Palladium Catalyzed Arylation of Alkenes Using Bulky Monodentate Phosphorus Ligands. *Eur. J. Inorg. Chem.* **1999**, *1999* (7), 1073-1076. DOI: 10.1002/(sici)1099-0682(199907)1999:7<1073::aid-ejic1073>3.3.co;2-k.

(56) Brunold, T. C.; Tamura, N.; Kitajima, N.; Moro-Oka, Y.; Solomon, E. I. Spectroscopic study of [Fe2(O2)(OBz)2{HB(pz')3}2]: Nature of the μ-1,2 peroxide-Fe(III) bond and its possible relevance to O2 activation by non-heme iron enzymes. *J. Am. Chem. Soc.* **1998**, *120* (23), 5674-5690. DOI: 10.1021/ja980129x.

(57) Feig, A. L.; Masschelein, A.; Bakac, A.; Lippard, S. J. Kinetic studies of reactions of dioxygen with carboxylate-bridged diiron(II) complexes leading to the formation of (μ-oxo)diiron(III) complexes. *J. Am. Chem. Soc.* **1997**, *119* (2), 334-342. DOI: 10.1021/ja962814e.

(58) Dong, Y.; Zang, Y.; Shu, L.; Wilkinson, E. C.; Que, L.; Kauffmann, K.; Münck, E. Models for Nonheme Diiron Enzymes. Assembly of a High-Valent Fe 2 (μ-O) 2 Diamond Core from Its Peroxo Precursor. *J. Am. Chem. Soc.* **1997**, *119* (51), 12683-12684. DOI: 10.1021/ja973115k.

(59) Li, Q.; Batchelor-McAuley, C.; Lawrence, N. S.; Hartshorne, R. S.; Compton, R. G. Anomalous solubility of oxygen in acetonitrile/water mixture containing tetra-n-butylammonium perchlorate supporting electrolyte; the solubility and diffusion coefficient of oxygen in anhydrous acetonitrile and aqueous mixtures. *J. Electroanal. Chem.* **2013**, *688*, 328-335. DOI: 10.1016/j.jelechem.2012.07.039.

(60) *Gaussian 16, Revision B.01*; Gaussian, Inc.: Wallingford CT, 2016. (accessed.

(61) Becke, A. D. Density-functional thermochemistry. III. The role of exact exchange. *J. Chem. Phys.* **1993**, *98* (7), 5648-5652. DOI: 10.1063/1.464913.

(62) Vosko, S. H.; Wilk, L.; Nusair, M. Accurate spin-dependent electron liquid correlation energies for local spin density calculations: a critical analysis. *Can. J. Phys.* **1980**, *58* (8), 1200-1211. DOI: 10.1139/p80-159.

(63) Lee, C.; Yang, W.; Parr, R. G. Development of the Colle-Salvetti correlation-energy formula into a functional of the electron density. *Phys. Rev. B* **1988**, *37* (2), 785-789.

(64) Stephen, P. J.; Devlin, F. J.; Chabalowski, C. F.; Frisch, M. J. Ab Initio Calculation of Vibrational Absorption and Circular Dichroism Spectra Using Density Functional Force Fields. *J. Phys. Chem.* **1994**, *98* (45), 11623-11627.

(65) Weigend, F. Accurate Coulomb-fitting basis sets for H to Rn. *Phys. Chem. Chem. Phys.* **2006**, *8* (9), 1057-1065. DOI: 10.1039/b515623h.

(66) Weigend, F.; Ahlrichs, R. Balanced basis sets of split valence, triple zeta valence and quadruple zeta valence quality for H to Rn: Design and assessment of accuracy. *Phys. Chem. Chem. Phys.* **2005**, *7* (18), 3297-3305. DOI: 10.1039/b508541a.

(67) Grimme, S.; Antony, J.; Ehrlich, S.; Krieg, H. A consistent and accurate ab initio parametrization of density functional dispersion correction (DFT-D) for the 94 elements H-Pu. *J. Chem. Phys.* **2010**, *132* (15), 154104-154104. DOI: 10.1063/1.3382344.

(68) Marenich, A. V.; Cramer, C. J.; Truhlar, D. G. Universal solvation model based on solute electron density and on a continuum model of the solvent defined by the bulk dielectric constant and atomic surface tensions. *J. Phys. Chem. B* **2009**, *113* (18), 6378-6396. DOI: 10.1021/jp810292n.

(69) Ribeiro, R. F.; Marenich, A. V.; Cramer, C. J.; Truhlar, D. G. Use of solution-phase vibrational frequencies in continuum models for the free energy of solvation. *J. Phys. Chem. B* **2011**, *115* (49), 14556-14562. DOI: 10.1021/jp205508z.

(70) *Goodvibes v.3.0.1*; 2019. (accessed.

(71) Grimme, S. Supramolecular binding thermodynamics by dispersion-corrected density functional theory. *Chem. Eur. J.* **2012**, *18* (32), 9955-9964. DOI: 10.1002/chem.201200497.

(72) Li, Y. P.; Gomes, J.; Sharada, S. M.; Bell, A. T.; Head-Gordon, M. Improved force-field parameters for QM/MM simulations of the energies of adsorption for molecules in zeolites and a free rotor correction to the rigid rotor harmonic oscillator model for adsorption enthalpies. *J. Phys. Chem. C* **2015**, *119* (4), 1840-1850. DOI: 10.1021/jp509921r.

(73) Au-Yeung, H. Y.; Chan, J.; Chantarojsiri, T.; Chang, C. J. Molecular imaging of labile iron(II) pools in living cells with a turn-on fluorescent probe. *J. Am. Chem. Soc.* **2013**, *135* (40), 15165-15173. DOI: 10.1021/ja4072964.

(74) Zhou, R.; Zheng, Y.; Jaroniec, M.; Qiao, S. Z. Determination of the Electron Transfer Number for the Oxygen Reduction Reaction: From Theory to Experiment. *ACS Catal.* **2016**, *6* (7), 4720-4728. DOI: 10.1021/acscatal.6b01581.

(75) Deadman, B. J.; Hellgardt, K.; Hii, K. K. A colorimetric method for rapid and selective quantification of peroxodisulfate, peroxomonosulfate and hydrogen peroxide. *React. Chem. Eng.* **2017**, *2* (4), 462-466. DOI: 10.1039/c7re00050b.

(76) *Saint; SADABS; APEX3*; Bruker AXS Inc.: Madison, Wisconsin, USA, 2012. (accessed.

(77) Sheldrick, G. M. SHELXT - Integrated space-group and crystal-structure determination. *Acta Cryst.* **2015**, *71* (1), 3-8. DOI: 10.1107/S2053273314026370.

(78) Dolomanov, O. V.; Bourhis, L. J.; Gildea, R. J.; Howard, J. A. K.; Puschmann, H. OLEX2: A Complete Structure Solution, Refinement and Analysis Program. *J. Appl. Cryst.* **2009**, *42*, 339-341. DOI: 10.1107/S0021889808042726.

(79) Spek, A. L. PLATON SQUEEZE: A tool for the calculation of the disordered solvent contribution to the calculated structure factors. *Acta Cryst. C* **2015**, *71*, 9-18. DOI: 10.1107/S2053229614024929.

Chapter 3:

Homogeneous Catalytic Reduction of O_2 to H_2O by a Terpyridine-Based FeN_3O Complex

Published as:

Cook, E. N.[#]; Hooe, S. L.[#]; Dickie, D. A.; Machan, C. W. *Inorganic Chemistry* **2022**, 61, 8387-8392. doi: 10.1021/acs.inorgchem.2c00524.

3.1. Abstract

We report a new terpyridine-based FeN_3O catalyst, $Fe(tpy^{tbu}pho)Cl_2$, which reduces O_2 to H_2O. Variable concentration and variable temperature spectrochemical studies with decamethylferrocene as a chemical reductant in acetonitrile solution enabled the elucidation of key reaction parameters for the catalytic reduction of O_2 to H_2O by $Fe(tpy^{tbu}pho)Cl_2$. These mechanistic studies suggest that a 2+2 mechanism is operative, where hydrogen peroxide is produced as a discrete intermediate, prior to further reduction to H_2O. Consistent with this proposal, the spectrochemically measured k_{cat} values for H_2O_2 reduction is larger than that for O_2 reduction. Further, significant H_2O_2 production is observed under hydrodynamic conditions in rotating ring-disk electrode measurements, where the product can be swept away from the cathode surface before further reduction occurs.

3.2. Introduction

In response to rising concerns over increasing energy demands and anthropogenic CO_2 emissions, the catalytic reduction of dioxygen to water remains a reaction of interest for the development of next-generation fuel cell technologies.[1-4] Of the earth abundant molecular catalysts for O_2 reduction,[2] Fe porphyrin- and phthalocyanine-based complexes remain among the most studied and robust catalysts.[5-12] It is conspicuous that non-heme systems are understudied relative to these examples, given the abundance of enzymes which contain a non-heme Fe center capable of reactivity with O_2 in order to carry out a variety of biologically relevant reactions.[13-18] In spite of this, molecular non-heme Fe catalysts capable of the O_2 reduction reaction (ORR) are exceedingly rare.[19-21]

Previous O_2 reduction studies from our lab identified non-heme molecular Mn[22-24] and Co[25, 26] catalyst systems based on a bpy-based dianionic N_2O_2 ligand framework (bpy = 2,2-bipyridine), as well as an Fe complex in a non-conjugated $[N_3O]^-$ donor framework inspired by mononuclear non-heme metallocofactors.[21] Motivated by the scarcity of non-heme Fe catalysts for ORR[20,21,27] and reasoning that conjugated polypyridine frameworks could be beneficial for similar reasons that they are useful in electrocatalytic carbon dioxide reduction,[28] we have identified a new Fe complex for the ORR using a conjugated tpy-based monoanionic $[N_3O]^-$ ligand framework. Herein, we present a new molecular Fe catalyst, Fe(tpy^{tbu}pho)Cl_2, where 2-([2,2':6',2''-terpyridin]-6-yl)-4,6-di-*tert*-butylphenolate = [tpy^{tbu}pho]$^-$, which is active for electrochemical O_2 reduction to H_2O. Mechanistic analysis using spectrochemical stopped-flow methods with decamethylferrocene (Cp^*_2Fe) as a homogeneous reductant in acetonitrile (MeCN) solution shows ORR is limited by O_2 binding to the singly reduced metal center and where H_2O_2 is implicated as a discrete intermediate prior to further reduction to H_2O.

3.3. Results

The synthesis of 2-([2,2':6',2''-terpyridin]-6-yl)-4,6-di-tert-butylphenol, tpy^{tbu}pho(H), was carried out via a modified literature procedure using Pd-catalyzed cross-coupling.[22,29] The Fe(tpy^{tbu}pho)Cl$_2$ complex was synthesized by sequentially combining the purified ligand with sodium acetate in ethanol solution followed by Fe(III) chloride hexahydrate, prior to isolation and recrystallization (See **Materials and Methods** Section of SI for detailed procedures).[30] Fe(tpy^{tbu}pho)Cl$_2$ was characterized via ESI-MS, EA, NMR, and UV-vis spectroscopies (SI **Materials and Methods** Section, **Table S3.1**, and **Figures S3.1-S3.2**). The proposed molecular connectivity was supported by structural data obtained from single-crystal X-ray diffraction studies (**Figure 1**).

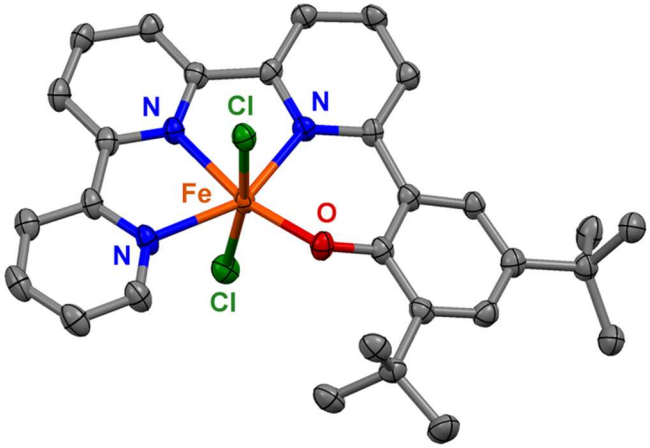

Figure 3.1. Molecular structure of Fe(tpy^{tbu}pho)Cl$_2$ obtained from single-crystal X-ray diffraction studies. Blue = N, red = O, gray = C, green = Cl, orange = Fe; thermal ellipsoids at 50%; hydrogen atoms and non-coordinating solvent omitted for clarity; CCDC 2097186.

Cyclic voltammetry (CV) experiments were performed on Fe(tpy^{tbu}pho)Cl$_2$ in a solution of 0.1 M tetrabutylammonium hexafluorophosphate (TBAPF$_6$) in MeCN. Under argon (Ar) saturation conditions, Fe(tpy^{tbu}pho)Cl$_2$ displays a single redox feature at $E_{1/2}$ = –0.51 V vs Fc$^+$/Fc (**Figure 3.2**, black). This reversible feature is attributed to a formal Fe$^{III/II}$ reduction, given its general agreement with related Fe(III) compounds.[30,31] Under O$_2$ saturation conditions, this redox feature becomes irreversible with E_p = –0.65 V vs Fc$^+$/Fc (**Figure 3.2**, red), suggesting O$_2$ binding to a

formally Fe(II) metal center. Variable scan rate studies at low scan rates under Ar saturation indicated that delayed chloride loss did not cause the observed loss of reversibility (**Figure S3.3**). Under Ar saturation conditions, there is an observed potential dependence on the presence of acetic acid (AcOH), where addition of 0.0875 M AcOH results in a positive shift of 0.15 V in the $Fe^{III/II}$ redox to an $E_{1/2}$ = –0.36 V vs Fc^+/Fc (**Figure 3.2**, green). This potential shift exhibited a concentration dependence suggestive of an equilibrium reaction: increasing the concentration of AcOH to 0.35 M resulted in a shift to $E_{1/2}$ = –0.25 V (**Figure S3.4**).

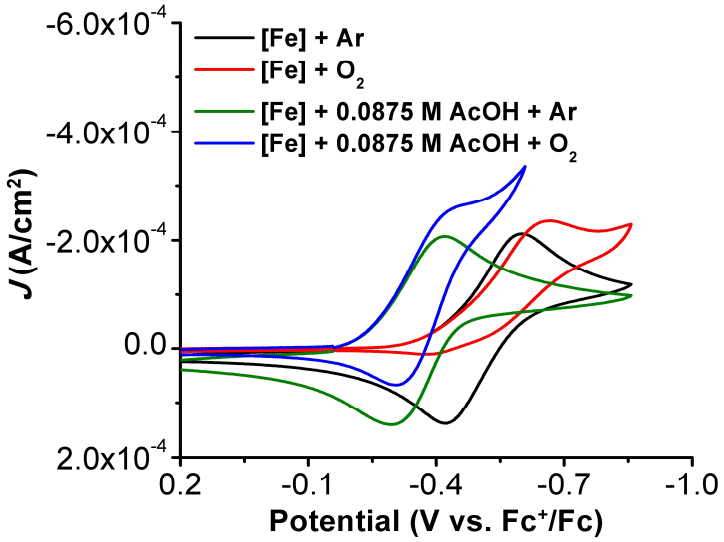

Figure 3.2. Comparison of CVs of $Fe(tpy^{tbu}pho)Cl_2$ under Ar and O_2 saturation conditions with and without 0.0875 M AcOH. Conditions: 1.0 mM $Fe(tpy^{tbu}pho)Cl_2$ in 0.1 M $TBAPF_6$/MeCN; glassy carbon working electrode, glassy carbon rod counter electrode, Ag/AgCl pseudoreference electrode; referenced to Fc^+/Fc internal standard; 100 mV/s scan rate.

To understand the nature of chloride ligand solvation under these conditions, we conducted an AcOH titration under an inert atmosphere (Ar) with $Fe(tpy^{tbu}pho)Cl_2$ in the presence of tetrabutylammonium chloride (TBACl) as a Cl^- donor (**Figure S3.5**). With excess Cl^- present, a negative potential shift of the $Fe^{III/II}$ feature to $E_{1/2}$ = –0.64 V vs Fc^+/Fc is observed for $Fe(tpy^{tbu}pho)Cl_2$, consistent with the inhibition of a pre-equilibrium displacement of an axial Cl^- ligands by MeCN. Titrating increasing amounts of AcOH up to 0.63 M in the presence of 0.1 M TBACl lead to a loss of reversibility at $E_{1/2}$ = –0.64 V vs Fc^+/Fc and the appearance of a new

reversible feature at $E_{1/2}$ = –0.40 V vs Fc^+/Fc. Based on these data, it is proposed that the observed shifts to positive potentials when AcOH is introduced into solution originates from the favorable solvation of the Cl^- counteranions, assisted by MeCN coordination to Fe. Therefore, the following assignments for the standard reduction potentials of the following chloro and solvento species can be made, where *L* = $[tpy^{tbu}pho]^-$. Note that **Eq (3.1)** and **Eq (3.2)** were assigned based on the data described above obtained with added TBACl and AcOH (**Figure S3.5**) while **Eq (3.3)** was determined from experiments with added AcOH only (**Figure S3.4**).

$$[Fe(L)Cl_2] + e^- \rightleftharpoons [Fe(L)Cl_2]^- \qquad E^0 = -0.64\ V\ vs\ Fc^+/Fc \qquad \textbf{Eq (3.1)}$$

$$[Fe(L)Cl(MeCN)]^+ + e^- \rightleftharpoons [Fe(L)Cl(MeCN)] \qquad E^0 = -0.40\ V\ vs\ Fc^+/Fc \qquad \textbf{Eq (3.2)}$$

$$[Fe(L)(MeCN)_2]^{2+} + e^- \rightleftharpoons [[Fe(L)(MeCN)_2]^+ \qquad E^0 = -0.25\ V\ vs\ Fc^+/Fc \qquad \textbf{Eq (3.3)}$$

Under O_2 saturation conditions with 0.0875 M AcOH there is an increase in current at the $Fe^{III/II}$ redox event, suggesting catalytic activity toward the ORR under electrochemical conditions (**Figure 3.2**, blue). Rotating ring-disk electrode methods were used to determine the selectivity of the ORR under electrochemical conditions, revealing a H_2O_2 selectivity of 70.0 ± 8.6%. At rotation rates greater than 1800 rpm, H_2O_2 is the exclusive product, suggesting that H_2O_2 is produced as a discrete intermediate, *vide infra* (See **SI**).

Because minimal catalytic current increase precluded us from further mechanistic analysis under electrochemical conditions, mechanistic studies were conducted using decamethylferrocene (Cp^*_2Fe) as a chemical reductant. In MeCN with 0.35 M AcOH present the $Fe^{III/II}$ reduction potential of $Fe(tpy^{tbu}pho)Cl_2$ ($E_{1/2}$ = –0.25 V vs Fc^+/Fc, **Figure S3.3**) is sufficiently positive of Cp^*_2Fe ($E_{1/2}$ = –0.51 V vs Fc^+/Fc[32]) for favorable electron transfer, with an equilibrium constant (K_{ET}) of 2.5 x 10^4 (See **SI**). We note that although there is a dependence of the $Fe^{III/II}$ redox potentials on AcOH concentration, $E_{1/2}$ values observed at lower AcOH concentrations are still sufficiently positive ($E_{1/2}$ = –0.36 V vs Fc^+/Fc with 0.0875 M AcOH) for favorable electron

transfer from Cp^*_2Fe, even as [AcOH] decreases over the course of the catalytic reaction. Rapid-mixing UV-vis stopped-flow experiments revealed that the ORR mediated by $Fe(tpy^{tbu}pho)Cl_2$ exhibits a first-order dependence on the $[O_2]$ and $[Cp^*_2Fe]$ (**Figure 3.3A** and **3.3B**, respectively). No dependence on [AcOH] was observed, suggesting saturation of the catalytic response at low acid concentrations (**Figure 3.3C**). Interestingly, when the concentration of $Fe(tpy^{tbu}pho)Cl_2$ was varied, two distinct regions were observed (**Figure 3.3D**). At low [Fe] (<12.6 μM), a first-order dependence is observed before the effect of increasing [Fe] on the apparent rate begins to saturate, and a plateau region is observed. Control studies showed negligible background reactivity without the presence of $Fe(tpy^{tbu}pho)Cl_2$ (**Figure S3.9**). Based on these mechanistic studies, we can propose the following rate expression for the ORR, **Eq (3.4)**:

$$rate = k_{cat}[Fe]^1[acid]^0[O_2]^1[Cp^*_2Fc]^1 \qquad \textbf{Eq (3.4)}$$

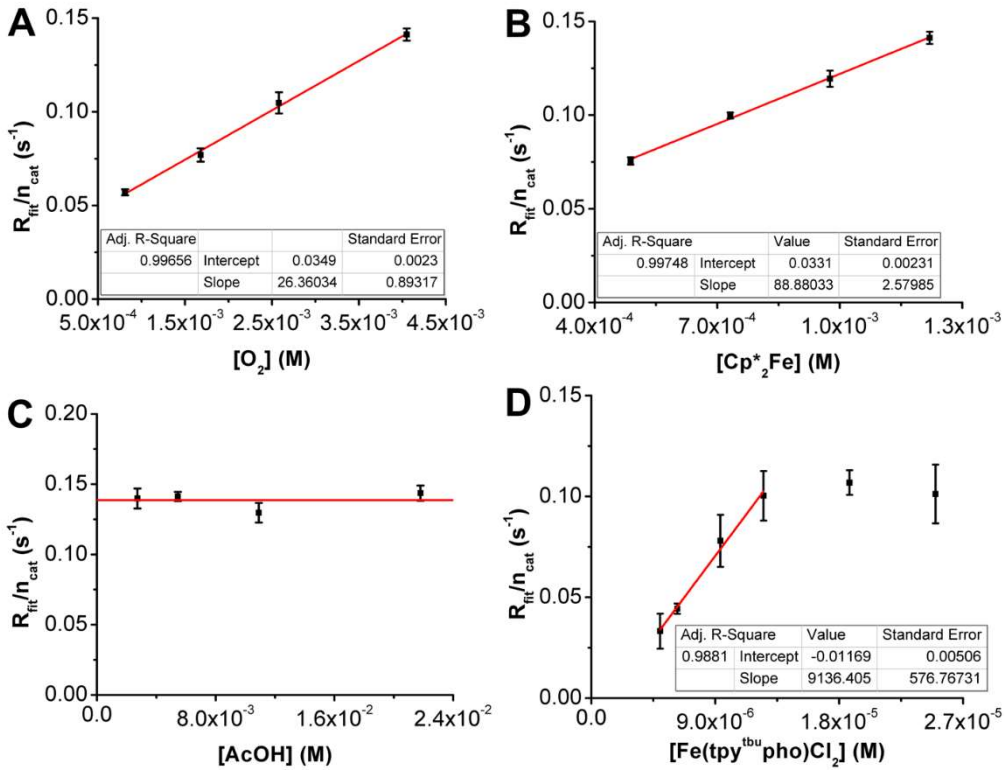

Figure 3.3. The calculated R_{fit}/n_{cat} from stopped-flow spectrochemical experiments where the concentration of O_2 (**A**), Cp^*_2Fe (**B**), AcOH (**C**), and $Fe(tpy^{tbu}pho)Cl_2$ (**D**), and were each independently varied at 25.5°C in MeCN. The horizontal line in (**C**) represents the global average rate observed across all experiments for variable [AcOH]. Data were fit using Kinetic Studio 4.0 (2 Exp + Mx + C). See Material and Methods section for syringe concentrations used.

With a fixed concentration ratio, analogous experiments were repeated at variable temperatures, enabling Eyring analysis to determine the reaction parameters of the rate-determining step (**Figure S3.10 and Table S3.2**). These lead to an estimated barrier $\Delta G^{\ddagger}_{298K}$ of +10.1 kcal/mol, **Eqs (3.5)** and **(3.6)**.

$$\Delta G^{\ddagger} = \Delta H^{\ddagger} - T\Delta S^{\ddagger} \qquad \textbf{Eq (3.5)}$$

$$\Delta G^{\ddagger} = 3.72\frac{kcal}{mol} - T\left(-21.4\frac{cal}{mol \cdot K}\right) \qquad \textbf{Eq (3.6)}$$

The product selectivity of ORR mediated by Fe(tpy^{tbu}pho)Cl_2 was determined by spectrophotometric methods to be quantitative for H_2O, with no detectable amount of H_2O_2 (**Figure S3.11**). UV-vis studies carried out with Fe(tpy^{tbu}pho)Cl_2 and urea•H_2O_2 eliminate disproportionation of H_2O_2 by Fe(tpy^{tbu}pho)Cl_2 as a possible mechanistic pathway (**Figure S3.12**). These data showed that H_2O_2 is stable in the presence of Fe(tpy^{tbu}pho)Cl_2 without added Cp*$_2$Fe (**Figures S3.12-S3.13**). However, with added chemical reductant in solution, the system catalytically reduces H_2O_2 to water via a $2H^+/2e^-$ pathway, implicating a 2+2 mechanism for the observed ORR. Control studies showed negligible reactivity for H_2O_2 reduction without the presence of Fe(tpy^{tbu}pho)Cl_2 (**Figure S3.14**). Further, reaction stoichiometry of hydrogen peroxide reduction (H_2O_2RR) by Fe(tpy^{tbu}pho)Cl_2 was found to be 2.09 ± 0.1 (**Figure S3.15**, see **SI**).

An average third-order rate constant ($k_{cat,ORR}$) for O_2 reduction to H_2O by Fe(tpy^{tbu}pho)Cl_2 was subsequently derived (n_{cat} = 4), based on the previously derived catalytic rate expression **Eq (3.7)** (see **SI**).

$$\frac{R_{fit}}{n_{cat}} = k_{cat}[catalyst]^1[O_2]^1[Cp^*_2Fc]^1 \qquad \textbf{Eq (3.7)}$$

$$k_{cat,ORR} = 1.13 \pm 0.62 \times 10^9\ M^{-2}\ s^{-1}$$

Based on the observed activity for H_2O_2RR (**Figure S3.14**), mechanistic studies were again conducted using UV-vis stopped-flow spectroscopy. Variable concentration studies under anaerobic conditions revealed a rate law of H_2O_2RR by Fe(tpy^{tbu}pho)Cl_2 that is first order with respect to [catalyst] and [H_2O_2], but zero order with respect to [Cp_2*Fe] and [AcOH] (**Eq (3.8)**,

Figures S3.16-S3.19) with an average second-order catalytic rate constant $k_{cat,H2O2RR}$ of 1.02 ± 0.10 x 10^7 M^{-1} s^{-1} using **Eq (3.8)** (see **SI**).

$$\frac{R_{fit}}{n_{cat}} = k_{cat}[catalyst]^1[H_2O_2]^1 \qquad \textbf{Eq (3.8)}$$

$$k_{cat,H2O2RR} = 1.02 \pm 0.20 \text{ x } 10^7 \text{ M}^{-1} \text{ s}^{-1}$$

Determination of effective overpotentials (η) for ORR and H_2O_2RR in this system is complicated due to the lack of catalytic activity under buffered conditions (**Figure S3.20**). However, we are able to generate approximate η values using corrected standard reduction potentials that account for pK_a (23.5) and log(K_{AHA}) of AcOH in MeCN (see SI), where η_{ORR} = 0.24 V and η_{H2O2RR} = 0.83 V.[33-35] We emphasize that these values should be considered a *lower-limit approximation* of the true thermodynamic potential since buffered conditions could not be directly assessed.

In order to better understand the mechanism of ORR mediated by Fe(tpy^{tbu}pho)Cl_2, we synthesized both [Fe(tpy^{tbu}pho)][OTf]$_2$ and a model of the Fe(II) intermediate [Fe^{II}(tpy^{tbu}pho)][OTf], where OTf is the non-coordinating anion trifluoromethanesulfonate. CVs of [Fe(tpy^{tbu}pho)][OTf]$_2$ obtained under Ar saturation show a small irreversible reduction wave at E_p = –0.26 V vs. Fc^+/Fc, followed by an irreversible reduction wave at E_p =–0.80 V vs. Fc^+/Fc, the latter of which is attributed to the Fe$^{III/II}$. Upon the addition of 0.35 M AcOH, the Fe$^{III/II}$ feature becomes reversible and shifts to $E_{1/2}$ = –0.32 V vs. Fc^+/Fc, consistent with the $E_{1/2}$ = –0.25 V observed for Fe(tpy^{tbu}pho)Cl_2 under comparable conditions (**Figure S3.22**). Additionally, UV-vis spectroscopic studies of both Fe(tpy^{tbu}pho)Cl_2 and [Fe(tpy^{tbu}pho)][OTf]$_2$ show similar spectral changes upon addition of increasing amounts of AcOH, supporting the proposal that both complexes form similar solvent species under protic conditions (**Figure S3.24**).

3.4. Discussion

From these data, we are able to propose a 2+2 catalytic cycle for the ORR by Fe(tpy^{tbu}pho)Cl_2 (**Scheme 3.1**). Based on electrochemical data (Figure S5), AcOH facilitates the loss of two Cl^-

anions with MeCN coordination to form $[Fe(tpy^{tbu}pho)(MeCN)_2]^{2+}$ (**2**) which undergoes a favorable one-electron reduction process (K_{ET} = 2.5 x 10^4, see SI) to form an Fe(II) species, **3**, that is the resting state of the catalyst. Rate-limiting O_2 binding is proposed to form an unobserved Fe(III) superoxide intermediate **4**. Consistent with this interpretation, mechanistic UV-vis and ^{1}H-NMR spectroscopic studies with a chemically prepared model of the active catalyst, $[Fe^{II}(tpy^{tbu}pho)][OTf]$, showed slow conversion following O_2 exposure, with Fe^{II} fully consumed after 18 h (**Figures S3.25-S3.28**).

Subsequently **4** undergoes net reduction and protonation to regenerate **2** and an equivalent of H_2O_2. As described above, control testing showed no interaction between H_2O_2 and the pre-catalytic Fe(III) state. The proposal of H_2O_2 as a discrete intermediate is directly supported by the observation of 70.0 ± 8.6% selectivity for H_2O_2 during RRDE experiments and quantitative selectivity for H_2O under spectrochemical conditions because of the difference in timescale of each experiment. During RRDE, H_2O_2 produced during the ORR, as well as any unreacted Fe(II) species, are rapidly swept away from the disk electrode for oxidation at the Pt ring electrode (~1 s). However, in the $Ti(O)SO_4$ titration experiment used for spectrochemical quantification, the catalytic solution that contains catalyst, reductant, O_2, and a proton source is not analyzed until the completion of the reaction (~5 min), such that any H_2O_2 produced during catalysis is further reduced to H_2O.

Since H_2O is observed to be the final product under spectrochemical conditions, we propose that **2** undergoes rapid reduction and H_2O_2 binding followed by additional reduction and protonation reactions to generate two equivalents of H_2O and reform **2**, based on the observed rate law of the ORR and H_2O_2RR by $Fe(tpy^{tbu}pho)Cl_2$. Comparable first-order rate constants k (s^{-1}) for ORR and H_2O_2RR are represented by the slopes of the variable O_2 (**Figure 3.3A**) and variable H_2O_2 (**Figure S3.15**) data: k for H_2O_2RR (178 s^{-1}) is more than 6-fold greater than for ORR (26.4 s^{-1}). The difference in first-order rate constants is consistent with the intermediate

reaction selectivity observed during RRDE experiments below 1800 rpm, as well as the shift to quantitative H_2O_2 production at higher rotation rates.

Scheme 3.1. Proposed Catalytic Cycle for ORR Mediated by Fe(tpy^{tbu}pho)Cl_2.

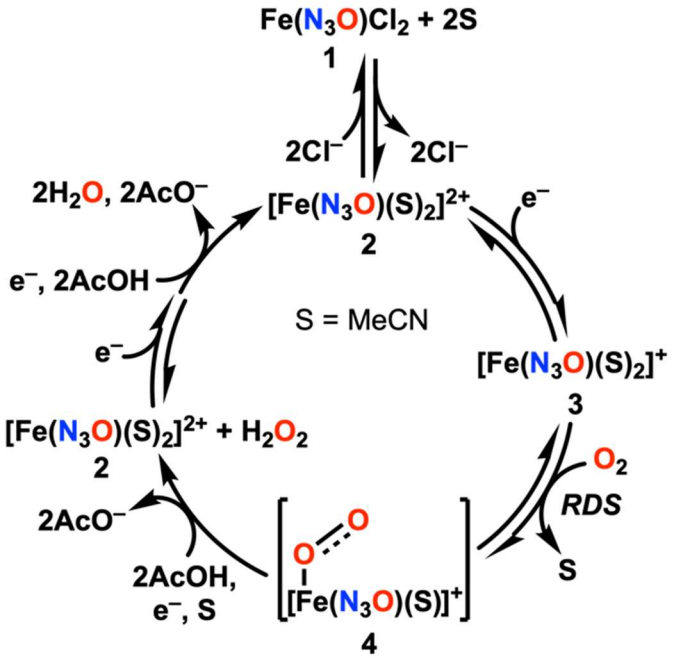

Recently, we reported 2+2 ORR activity by an Fe complex with a bioinspired $[N_3O]^-$ ligand framework, *N*,*N*′-bis(2-pyridylmethyl)glycinate or PMG.[21] Mechanistically, one of the defining features of the ORR mediated by Fe(PMG)Cl_2 is an off-cycle peroxo dimer, which was observed to be the resting state of the catalytic cycle. The 2+2 cycle itself also showed a greater disparity between the rates of the two reactions than is observed here for Fe(tpy^{tbu}pho)Cl_2: the observed TOF for ORR mediated by Fe(PMG)Cl_2 was 0.92 s^{-1} and that for H_2O_2RR was 2.9 x 10^3 s^{-1}, a ~3200-fold difference. Although in-depth mechanistic comparisons between the two complexes are beyond the scope of the present study, it is worth noting some of the key differences between the two in the context of their reactivity. Although when both complexes are reduced to the Fe(II) state a favorable reaction with O_2 occurs, the resulting superoxo species are likely to be quite different. For the Fe(tpy^{tbu}pho)Cl_2 system, an MeCN solvent molecule will be opposite the site of O_2 binding, whereas in Fe(PMG)Cl_2 a more basic trialkylamine fragment from the ligand

framework will occupy this position. Axial ligand effects on peroxo dimerization and O–O bond scission are well-known and previously reported trends are consistent with the increased H_2O_2RR TOF for Fe(PMG)Cl_2 and its greater axial ligand basicity in comparison to Fe(tpy^{tbu}pho)Cl_2.[2,36,37]

3.5. Conclusions

Non-heme iron electrocatalysts for the ORR have been relatively under-studied in comparison to porphyrin-based systems. Here, we have reported a novel non-heme Fe complex containing an N_3O terpyridine-based ligand framework (Fe(tpy^{tbu}pho)Cl_2) that is electrocatalytically active toward the reduction of O_2 to H_2O where H_2O_2 is produced as a discrete intermediate during catalysis. Mechanistic analysis revealed that the rate of ORR is limited by O_2 binding to the Fe(II) metal center. Additionally, it is implied that ORR by Fe(tpy^{tbu}pho)Cl_2 proceeds via 2+2 mechanism, where H_2O_2 produced during catalysis is further reduced by $2H^+/2e^-$ to two equivalents of H_2O. Ligand modification to tune ORR reactivity and selectivity is a focus of ongoing work.

3.6. Supplementary Information for Chapter 3

Materials and Methods

General

All chemicals and solvents (ACS or HPLC grade) were commercially available and used as received unless otherwise indicated. For all air-sensitive reactions and electrochemical experiments, HPLC-grade solvents were obtained as anhydrous and air-free from a PPT Glass Contour Solvent Purification System. Gas cylinders were obtained from Praxair (Ar as 5.0; O_2 as 4.0) and passed through activated molecular sieves prior to use. Gas mixing for variable concentration experiments was accomplished using a gas proportioning rotameter from Omega Engineering. UV-vis absorbance spectra were obtained on a Cary 60 from Agilent. An Anton-Parr Multiwave Pro SOLV, NXF-8 microwave reactor was used for microwave syntheses. The ligand tpy^{tbu}pho(H) was synthesized as previously reported.[38] The concentration of O_2 saturation in MeCN is reported to be 8.1 mM and the saturation concentration in MECN with added electrolyte to be 6.3 mM.[39]

Electrochemistry

All electroanalytical experiments were performed using a Metrohm Autolab PGSTAT302N potentiostat. Glassy carbon working (⌀ = 3 mm) and non-aqueous silver/silver chloride pseudoreference electrodes behind PTFE tips were obtained from CH Instruments. The pseudoreference electrodes were obtained by depositing chloride on bare silver wire in 10% HCl at oxidizing potentials and stored in a 0.1 M tetrabutylammonium hexafluorophosphate/acetonitrile solution in the dark prior to use. The counter electrode was a glassy carbon rod (⌀ = 3 mm). All CV experiments were performed in a modified scintillation vial (20 mL volume) as a single-chamber cell with a cap modified with ports for all electrodes and a sparging needle. Tetrabutylammonium hexafluorophosphate ($TBAPF_6$) was purified by recrystallization from ethanol and dried in a vacuum oven before being stored in a desiccator. All data were referenced to an internal ferrocene standard (ferricenium/ferrocene reduction potential under stated conditions) unless otherwise specified. All voltammograms were corrected for internal resistance. Ferrocene was purified by sublimation prior to use. In the event that the presence of electrochemical features precluded ferrocene addition, ferrocene was added to the electrochemical cell at the end of analysis for reference.

Stopped-Flow Spectrochemical Methods

Stopped-flow spectrochemical kinetics studies were performed with a CSF-61DX2 Stopped-Flow System from Hi-Tech Scientific. Kinetic Studio Software was used to monitor a single wavelength and Integrated CCD Software was used to monitor the entire visible spectrum. All data fits were performed within the Kinetic Studio 4.0 Software Suite. Prior to experiments, dried and degassed acetonitrile (MeCN) was passed through syringes and the cell block before reagents were loaded. In a typical experiment, syringes would be charged with known concentrations of reagent. All reagent solutions were prepared immediately before use. Concentrations reported as syringe

concentrations halve upon mixing in the cell block during an experiment. For all spectrochemical experiments, two of the four syringe mixing ports were utilized where one syringe contained only the reductant (decamethylferrorcene, Cp^*_2Fe) under N_2 saturation conditions and the second syringe contained known concentrations of O_2 or urea•H_2O_2, acid, and Fe(tpy^{tbu}pho)Cl_2. The appearance of the oxidized form of decamethylferrocene ($[Cp^*_2Fe]^+$) was observed by the increase in absorbance at 778 nm, where the rate of appearance can be used to determine kinetic information and allow mechanistic analysis.[40-42]

R_{fit} values (as R_1 in fitting function) were obtained by fitting the increase in absorbance at 778 nm versus time data in the Kinetic Studio 4.0 Software to a double exponential (2Exp+Mx+C) to achieve an R^2 value of 0.99 (See Figure **S3.20**). Where the fit equation contains two exponents (2Exp), a linear portion (Mx) and a non-zero intercept (C). The R_{fit} values were corrected for the number of electrons passed during catalysis (n_{cat} = 4 for ORR, n_{cat} = 2 for H_2O_2RR) and plotted against variable concentrations to obtain the experimental rate law (**Eq. 3.4**, main text). For ORR, the third-order rate constant, $k_{cat,ORR}$ ($M^{-2}\,s^{-1}$)), was determined according to **Eq. S3.1**, where the slopes of variable [Fe(tpy^{tbu}pho)Cl_2], [Cp_2*Fe], and [O_2] were corrected for the two reagents with fixed concentrations and averaged.

$$\frac{R_{fit}}{n_{cat}} = k_{cat}[Fe][Cp^*_2Fe][O_2] \qquad \textbf{(S3.1)}$$

$$k_{cat,ORR} = 1.13 \pm 0.62 \times 10^9\ M^{-2}\,s^{-1}$$

For H_2O_2RR, the second-order rate constant $k_{cat,H2O2RR}$ ($M^{-1}\,s^{-1}$) was determined according to **Eq. S3.2**, where the slopes of both variable [Fe(tpy^{tbu}pho)Cl_2] and [H_2O_2] were corrected for the reagent with a fixed concentration and averaged.

$$\frac{R_{fit}}{n_{cat}} = k_{cat}[Fe][H_2O_2] \ (\textbf{S3.2})$$

$$k_{cat,H2O2RR} = 1.02 \pm 0.2 \times 10^7\ M^{-1}\,s^{-1}$$

Syringe Concentrations for Experiments Displayed in Figure 2A-D:

Figure* 3.*2A: The calculated R_{fit}/n_{cat} from stopped-flow spectrochemical experiments with Cp^*_2Fe, AcOH, and Fe(tpy^{tbu}pho)Cl_2 with varying O_2 concentration at 25.5°C in MeCN. Data were fit using Kinetic Studio 4.0 (2 Exp + Mx + C). Syringe concentrations: Cp_2^*Fe = 2.44 x 10^{-3} M; Fe(tpy^{tbu}pho)Cl_2 = 5.60 x 10^{-5} M; AcOH = 1.09 x 10^{-2} M.

Figure* 3.*2B: The calculated R_{fit}/n_{cat} from stopped-flow spectrochemical experiments with O_2, AcOH, and Fe(tpy^{tbu}pho)Cl_2 with varying Cp^*_2Fe concentration at 25.5°C in MeCN. Data were fit using Kinetic Studio 4.0 (2 Exp + Mx + C). Syringe concentrations: O_2 = 8.1 x 10^{-3} M; Fe(tpy^{tbu}pho)Cl_2 = 5.60 x 10^{-5} M; AcOH = 1.09 x 10^{-2} M.

Figure* 3.*2C: The calculated R_{fit}/n_{cat} from stopped-flow spectrochemical experiments with O_2, Cp^*_2Fe, and Fe(tpy^{tbu}pho)Cl_2 with varying AcOH concentration at 25.5°C in MeCN. The horizontal line represents the global average rate across all experiments for variable [AcOH]. Data were fit using Kinetic Studio 4.0 (2 Exp + Mx + C). Syringe concentrations: O_2 = 8.1 x 10^{-3} M; Fe(tpy^{tbu}pho)Cl_2 = 5.60 x 10^{-5} M; Cp_2^*Fe = 2.44 x 10^{-3} M.

Figure* 3.*2D: The calculated R_{fit}/n_{cat} from stopped-flow spectrochemical experiments with decamethylferrocene (Cp^*_2Fe), AcOH, and O_2 with varying Fe(tpy^{tbu}pho)Cl_2 concentration at 25.5°C in MeCN. Data were fit using Kinetic Studio 4.0 (2 Exp + Mx + C). Syringe concentrations: Cp_2^*Fe = 2.44 x 10^{-3} M; O_2 = 8.1 x 10^{-3} M; AcOH = 1.0 x 10^{-2} M.

Synthesis of Fe(tpy^{tbu}pho)Cl_2

The protonated ligand tpy^{tbu}pho(H) (0.150 g, 0.343 mmol) was combined with 1 equivalent of sodium acetate (0.0281 g, 0.343 mmol) in absolute ethanol (50 mL). After refluxing for 30 min, one equivalent of iron(III) trichloride hexahydrate (0.0927 g, 0.343 mmol) was added to the reaction mixture and left to reflux for an additional five hours. The reaction mixture was brought to room temperature and filtered to obtain a green solid which was subsequently recrystallized from DCM/pentanes. The recrystallized solid was then dissolved in MeCN, filtered through a PTFE syringe filtered, and condensed down to obtain the product as a green solid. 75.1% isolated yield (145 mg). Elemental analysis for $C_{29}H_{30}Cl_2Fe_1N_3O_1 \bullet O_1H_2$ calc'd: C 59.92, H 5.55, N 7.23; found: C 59.81, H 5.31, N 7.20. MSMS (m/z): calc'd: 492.1738 found: 492.1733. Note: MS results align chloride ligand loss. Single crystals of two unique solvate species with identical connectivity at the Fe center suitable for X-ray diffraction were grown from a saturated mixture of CH_2Cl_2 and MeCN at room temperature.

Synthesis of [Fe^{II}(tpy^{tbu}pho)][OTf]

In a N_2 filled glovebox, NaH (20.4 mg, 0.850 mmol) was added to a solution of tpy^{tbu}pho(H) (93.0 mg, 0.213 mmol) in THF (15 mL) and allowed to stir at RT for 2 hours. The reaction solution was passed through a 0.45 µm PTFE syringe filter into a pressure flask. [Fe(II)][OTf]$_2$ (74.0 mg, 0.209 mmol) was added to the solution and allowed to stir at 66°C for 24 h. Upon addition of [Fe(II)][OTf]$_2$, the reaction solution turned from orange to dark purple. After 24 hours, the solution was allowed to cool to room temperature and transferred to a round bottom flask where the solvent was removed under vacuum. The solid was dissolved in acetonitrile and passed through a 0.45 µm PTFE syringe filter and the solvent was removed under vacuum. The solid was then dissolved in 30/70 THF/diethyl ether and passed through a 0.45 µm PTFE syringe filter and the solvent was removed under vacuum to yield pure product (47.0 mg, 36% yield). Elemental analysis for $C_{30}H_{30}F_3FeN_3O_4S$•2/3C_5H_{12} calc'd: C 58.06, H 5.55, N 6.09; found: C 58.25, H 5.63, N 5.93.

Synthesis of [Fe(tpy^{tbu}pho)][OTf]$_2$

Dry tpy^{tbu}pho[H] (70.0 mg, 0.160 mmol) and sodium acetate (13.0 mg, 0.160 mmol) were dissolved in absolute ethanol and brought to a reflux until all solids were dissolved. To the stirring solution, [Fe(III)][OTf]$_3$ (83.0 mg, 0.164 mmol) was added. Upon addition of [Fe(III)][OTf]$_3$, the reaction solution turned black and was allowed to reflux for 4 hours. After this time, the solution was cooled to RT and the solvent was removed via rotary evaporation. The resulting black solid was then dissolved in 50/50 THF/diethyl ether and passed through a 0.45 µm PTFE syringe filter and the solvent was removed via rotary evaporation. The resulting black solid was dissolved in minimal DCM and passed through a 0.45 µm PTFE syringe filter and the solvent was removed via rotary evaporation. Recrystallization from a mixture of DCM and hot hexanes yielded 29.0 mg of pure product (23 % yield). Elemental analysis for $C_{31}H_{30}F_6FeN_3O_7S_2$ calc'd: C 47.10, H 3.83, N 5.32; found: C 46.97, H 4.16, N 5.39.

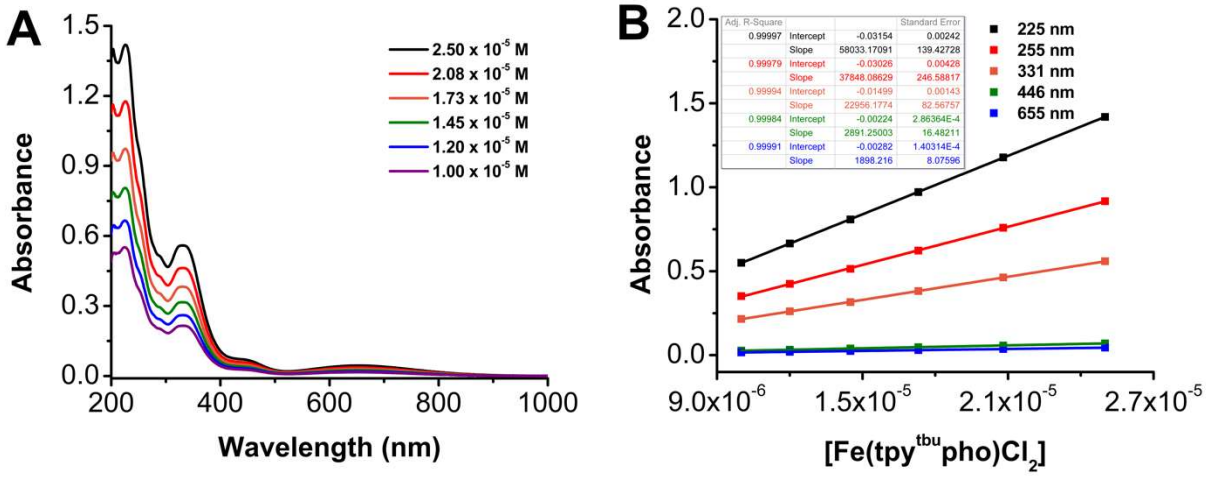

Figure S3.1. (A) UV-vis serial dilution absorbance data obtained from Fe(tpy^{tbu}pho)Cl_2 in a MeCN solution. Conditions: varying concentration; quartz cell with 1 cm pathlength. (**B**) Plot of absorbance versus concentration (M) for Fe(tpy^{tbu}pho)Cl_2 in MeCN. All: λ_{max} = 225 nm (58000 M^{-1} cm^{-1}), 255 nm (37800 M^{-1} cm^{-1}), 331 nm (23000 M^{-1} cm^{-1}), 446 nm (2890 M^{-1} cm^{-1}), and 655 nm (1900 M^{-1} cm^{-1}); R^2 = 0.999.

Table S3.1. Evans' method results for Fe(tpy^{tbu}pho)Cl_2 in MeCN supporting a high-spin d^5 complex.[43,44]

Trial	Chemical Shift (ppm)	Chemical Shift (Hz)	Total Magnetic Moment (emu mol^{-1})	Paramagnetic Moment (emu mol^{-1})	μeff (Bohr Magnetons)
1	0.1058	63.5	0.0133	1.33 x 10^{-2}	5.64
2	0.1045	62.7	0.0132	1.32 x 10^{-2}	5.61
3	0.1076	64.5	0.0136	1.36 x 10^{-2}	5.69

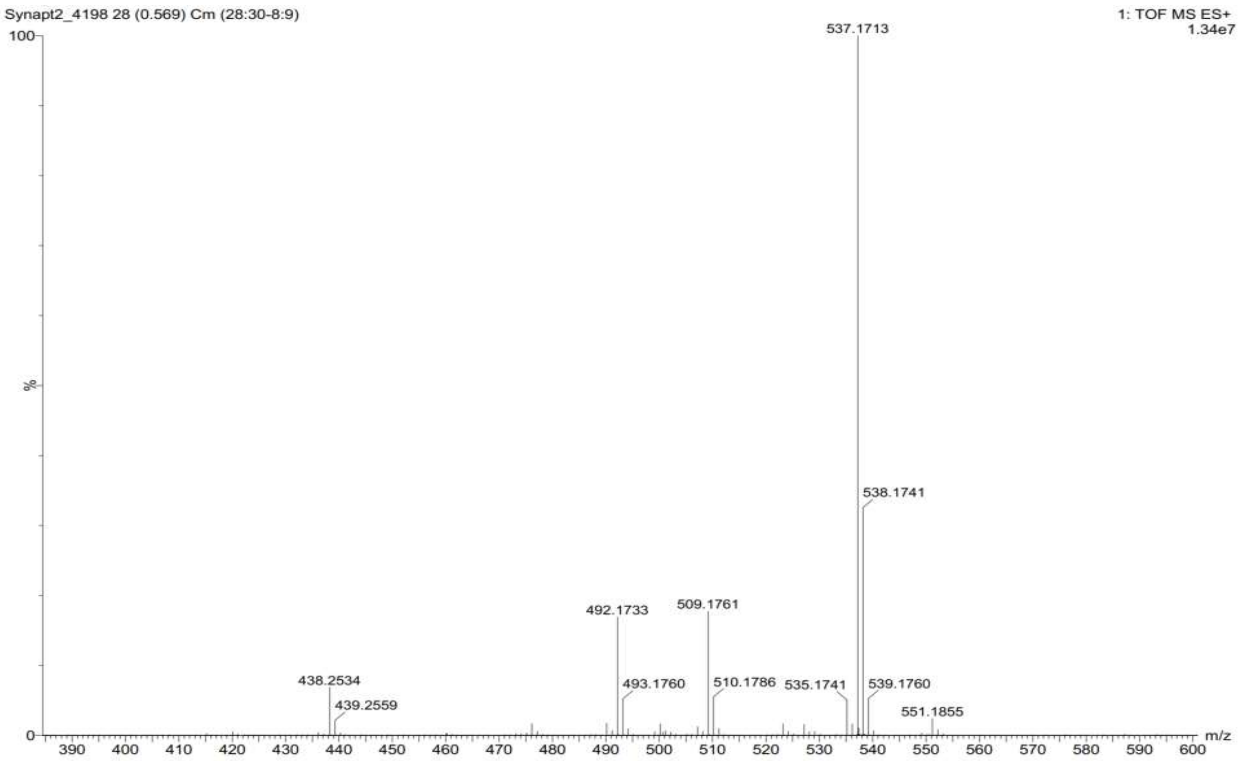

Elemental Composition Report

Single Mass Analysis

Tolerance = 5.0 PPM / DBE: min = -1.5, max = 200.0
Element prediction: Off
Number of isotope peaks used for i-FIT = 9

Monoisotopic Mass, Even Electron Ions
366 formula(e) evaluated with 4 results within limits (up to 50 best isotopic matches for each ma
Elements Used:
C: 0-110 H: 0-180 N: 0-3 O: 0-5 Cl: 0-2 Fe: 1-1

Mengnan Hu SLH-FETPY01 MSL, School of Chemical Sciences, UIUC
Synapt2_4198 28 (0.569) Cm (28:30-8:9)

Minimum:				-1.5				
Maximum:		5.0	5.0	200.0				
Mass	Calc. Mass	mDa	PPM	DBE	i-FIT	Norm	Conf(%)	Form
492.1733	492.1738	-0.5	-1.0	16.5	2161.6	0.000	100.00	C29
	492.1735	-0.2	-0.4	2.5	2177.5	15.961	0.00	C22
	492.1716	1.7	3.5	7.5	2177.7	16.131	0.00	C23
	492.1757	-2.4	-4.9	11.5	2178.2	16.642	0.00	C28

Figure S3.2. ESI-MS characterization of Fe(tpy^{tbu}pho)Cl_2.

Table S3.2. Evans' method results for [Fe(tpy^{tbu}pho)][OTf]$_2$ in MeCN supporting a high-spin d^5 complex.[43,44]

Trial	Chemical Shift (ppm)	Chemical Shift (Hz)	Total Magnetic Moment (emu mol^{-1})	Paramagnetic Moment (emu mol^{-1})	μeff (Bohr Magnetons)
1	0.0300	18	0.0129	1.32 x 10^{-2}	5.61
2	0.0378	22.68	0.0163	1.66 x 10^{-2}	6.28
3	0.0356	21.36	0.0153	1.56 x 10^{-2}	6.10

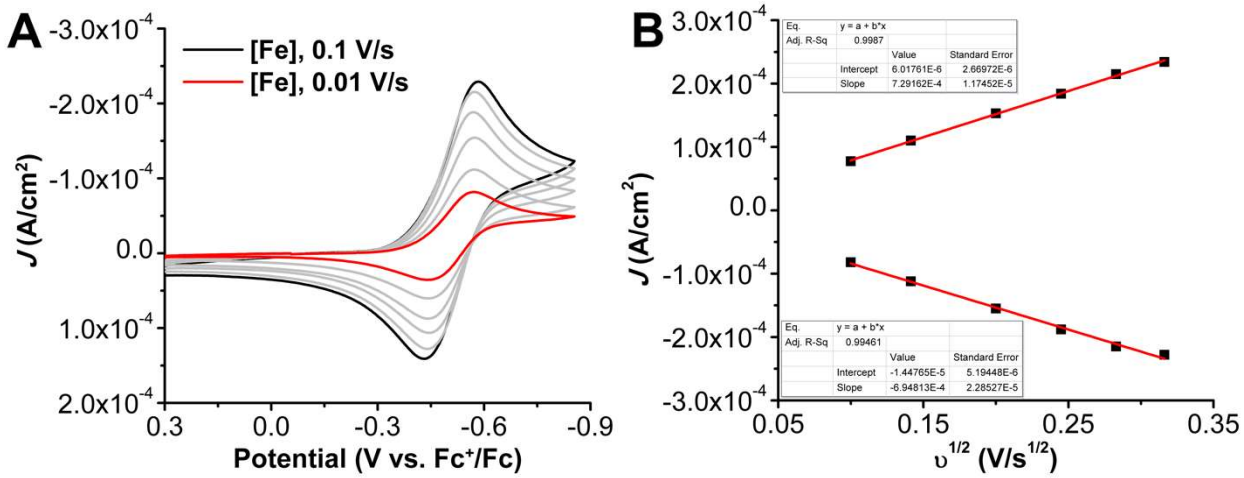

Figure S3.3. (A) Variable scan rate CVs of Fe(tpy^{tbu}pho)Cl$_2$ at low scan rates ranging from 0.01 (red) to 0.1 (black) V/s. (B) Linear fit of variable scan rate data from (A). Conditions: 1 mM Fe(tpy^{tbu}pho)Cl$_2$, 0.1 M TBAPF$_6$/MeCN; glassy carbon working electrode, glassy carbon counter electrode, Ag/AgCl pseudoreference electrode; scan rates: 0.01, 0.02, 0.04, 0.06, 0.08, 0.1 V/s; referenced to internal ferrocene standard.

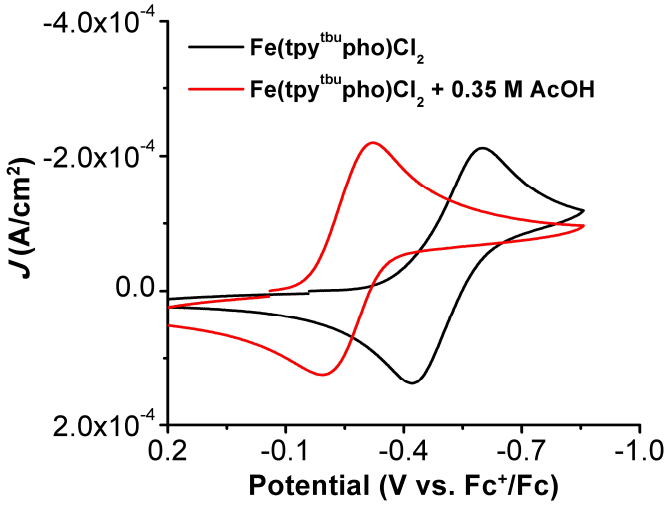

Figure S3.4. Comparison of CVs of Fe(tpy^{tbu}pho)Cl$_2$ under Ar and conditions with (red) and without (red) 0.35 M AcOH. Conditions: 1.0 mM Fe(tpy^{tbu}pho)Cl$_2$ in 0.1 M TBAPF$_6$/MeCN; glassy carbon working electrode, glassy carbon rod counter electrode, Ag/AgCl pseudoreference electrode; referenced to Fc$^+$/Fc internal standard; 100 mV/s scan rate.

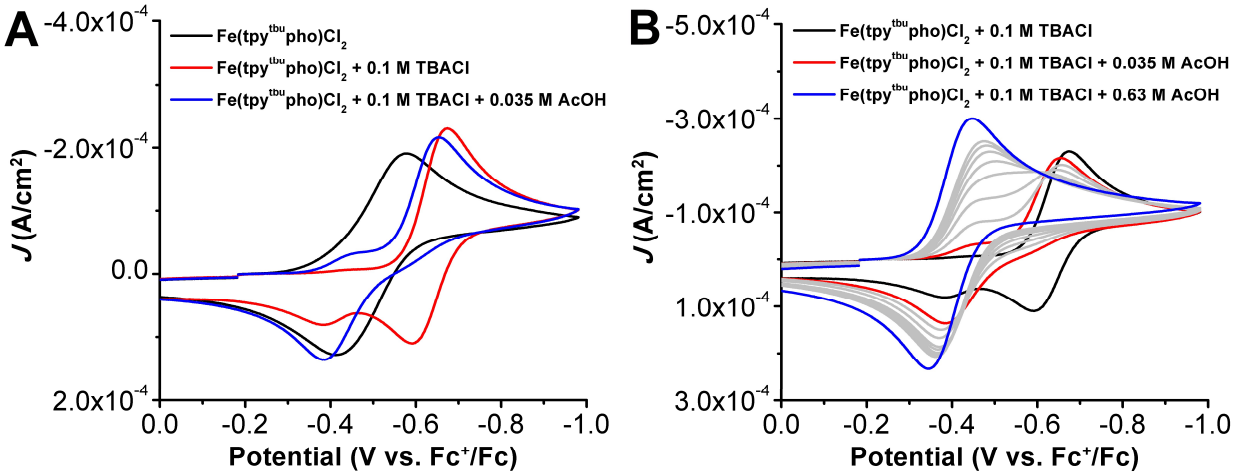

Figure S3.5. Cyclic voltammograms of Fe(tpy^{tbu}pho)Cl_2 with (red) and without (black) TBACl and AcOH (blue) under Ar saturation conditions (A) and Fe(tpy^{tbu}pho)Cl_2 with TBACl (black) and increasing amounts of AcOH (B). Conditions: 1 mM Fe(tpy^{tbu}pho)Cl_2, 0.1 M TBACl (if present), 0.1 M $TBAPF_6$/MeCN; glassy carbon working electrode, glassy carbon counter electrode, Ag/AgCl pseudoreference electrode; [AcOH]: 0.035, 0.07, 0.105, 0.140, 0.175, 0.21, 0.245, 0.28, and 0.63 M; referenced to internal ferrocene standard.

RRDE Experiments for Electrochemical Determination of ORR Selectivity of Fe(tpy^{tbu}pho)Cl_2

Description of RRDE Collection Efficiency. The collection efficiency was determined as previously reported.[45] Conditions: Ar saturation, 0.1 M $TBAPF_6$, 0.5 mM ferrocene in MeCN (50 mL), glassy carbon disk electrode (5 mm), Pt ring electrode, glassy carbon rod counter electrode, Ag/AgCl pseudoreference electrode; scan rate 0.01 V/s. To calculate the collection efficiency of the RRDE, the ratio of the limiting ring current (i_r) to the limiting disk current (i_d) at each rotation rate was used to determine $N_{empirical}$ (Eq. S3). The $N_{empirical}$ value at each rotation rate was multiplied by a factor of 100 to determine the collection efficiency % at each rotation rate (~27%).

$$N_{empirical} = \frac{i_{ring}}{i_{disk}} \qquad \textbf{(S3.3)}$$

RRDE Experiments. Conditions: Performed under Ar and O_2 saturation conditions, 0.1 M $TBAPF_6$, 0.5 mM Fe(tpy^{tbu}pho)Cl_2, 0.1 M AcOH, glassy carbon disk electrode (5 mm diameter), Pt ring electrode, glassy carbon rod counter electrode, Ag/AgCl pseudoreference electrode; scan rate 0.01 V/s.

The solution was sparged with Ar until saturation was achieved. Fe(tpy^{tbu}pho)Cl_2 (0.5 mM) was dissolved in solution and 0.1 M AcOH was added. A standard CV was taken of the solution to confirm the potential window to be used for the experiment (0.3 to –0.25 V). The Pt ring was set to +1.2 V. LSVs were obtained for various rotation rates between 200 and 1400 under the described conditions. In between each scan, the solution was sparged for 3 minutes. The reproducibility of scans was confirmed by repeating scans at the same rotation rate, producing exact overlays. The same procedure was repeated for O_2 saturation conditions, which were achieved by sparging the solution with O_2 for 3 minutes.

The arithmetic mean of the number of electrons received by O_2 (n_{cat}) during the ORR was calculated from the corrected disk current (i_d) and corrected ring current (i_r) according to Eq. S4:

$$n_{cat} = 4 \times \frac{i_d}{i_d + \frac{i_r}{N_{empirical}}} \qquad \textbf{(S3.4)}$$

Where the current was corrected by subtracting the current observed under Ar saturation from the current observed under O_2 saturation. The H_2O_2 ratio (p) is defined as the fraction of O_2 reduced to H_2O_2 and relates to n_{cat} by Eq. S5:

$$n_{cat} = 4 - 2p \qquad \textbf{(3.S5)}$$

Multiplying p by 100% provides the %H_2O_2 selectivity of the ORR. It was determined that under electrochemical conditions, this system shows a 70.0 ± 8.6% selectivity for H_2O_2. At higher scan rates, 1800 and 2200 rpm, we observed 100% selectivity for H_2O_2 and omitted these data points from analysis.

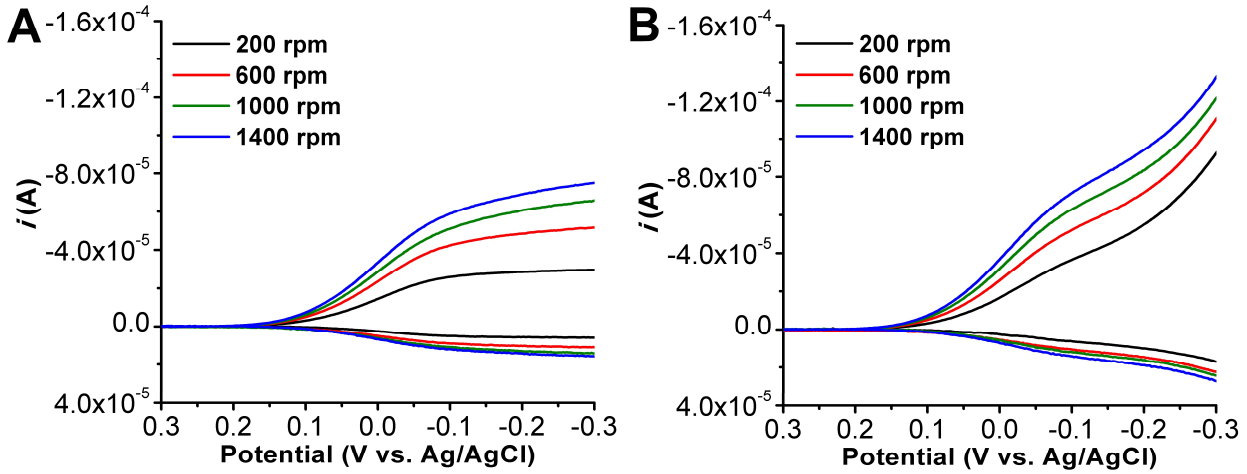

Figure S3.6. Linear sweep voltammograms of RRDE experiment with 0.5 mM Fe(tpy^{tbu}pho)Cl_2 and 0.1 M AcOH under Ar (A) and O_2 (B) saturation conditions*;* ring potential = 1.2 V vs Ag/AgCl. Conditions: 0.5 mM Fe(tpy^{tbu}pho)Cl_2, 0.1 M AcOH, 0.1 M $TBAPF_6$/MeCN; glassy carbon working electrode/Pt ring working electrode, glassy carbon counter electrode, Ag/AgCl pseudoreference electrode; scan rate 0.01 V/s.

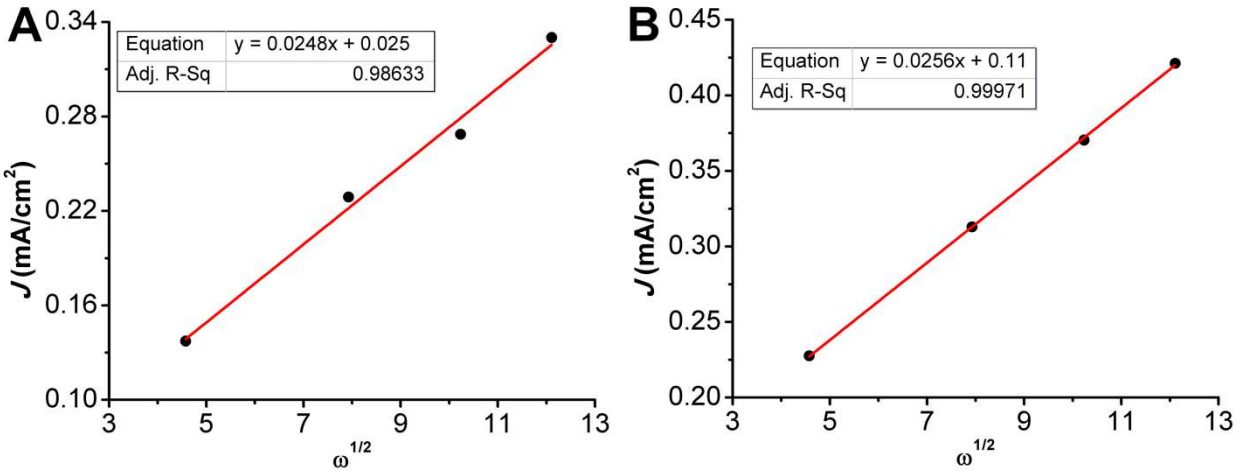

Figure S3.7. Levich plots from data obtained from Linear Sweep Voltammograms of Fe(tpy^{tbu}pho)Cl_2 (0.5 mM) by RRDE with 0.1 M AcOH under Ar (A) and O_2 (B) saturation conditions at various rotation rates*;* ring potential = 1.2 V vs. Ag/AgCl.

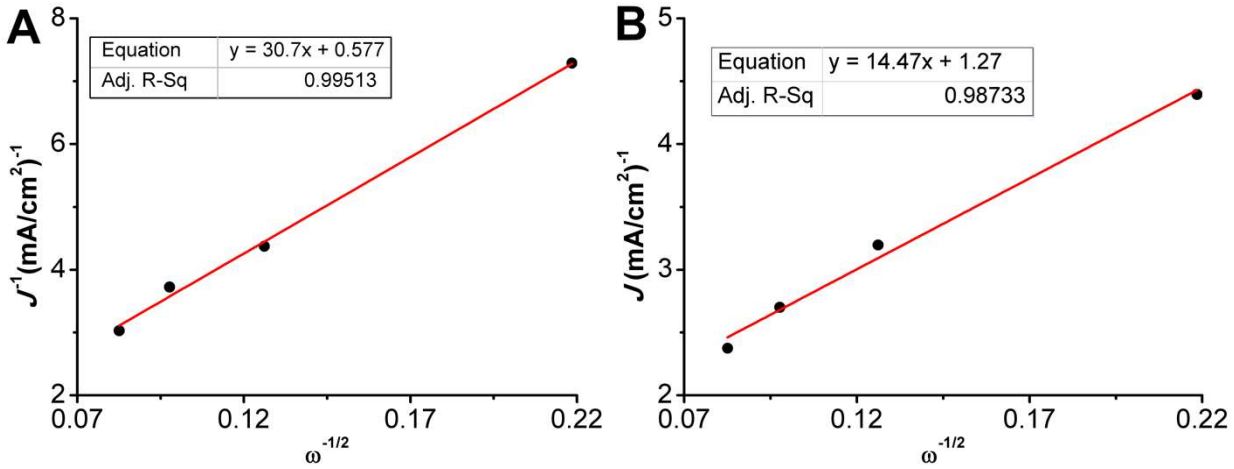

Figure S3.8. Koutecky-Levich plots from data obtained from linear sweep voltammograms of Fe(tpy^{tbu}pho)Cl_2 (0.5 mM) by RRDE with 0.1 M AcOH under Ar (A) and O_2 (B) saturation conditions at various rotation rates; ring potential = 1.2 V vs. Ag/AgCl.

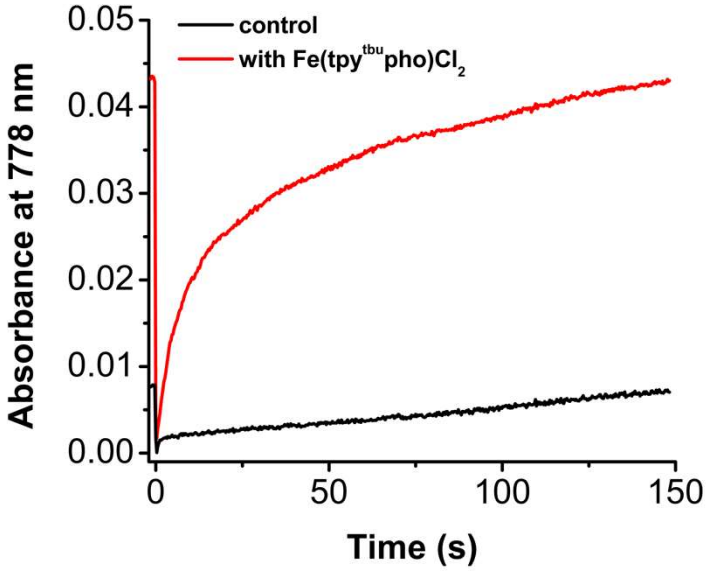

Figure S3.9. Representative spectral changes at 778 nm due to the formation of $[Cp^*_2Fe]^+$ comparing catalytic conditions with Fe(tpy^{tbu}pho)Cl_2 (red) versus identical conditions in the absence of Fe(tpy^{tbu}pho)Cl_2 as a control (black). Syringe Concentrations: Fe(tpy^{tbu}pho)Cl_2 (if present) = 1.73 x 10^{-5} M; AcOH = 1.09 x 10^{-2} M; O_2 = 1.62 x 10^{-3} M; and Cp^*_2Fe = 2.44 x 10^{-3} M.

Variable-Temperature Methods and Eyring Analyses (adapted[23])

Keeping the concentrations of the various substrates constant while varying the temperature enables the determination of thermodynamic and kinetic parameters for the reaction of interest. The Eyring equation can be used to calculate the thermodynamic values for the transition state of a reaction. The Eyring equation can be written as

$$ln\frac{k_{cat}}{T} = \frac{-\Delta H^{\ddagger}}{R}\left(\frac{1}{T}\right) + ln\frac{k_B}{h} + \frac{\Delta S^{\ddagger}}{R}$$

where R is the ideal gas constant, T is temperature, k_B is Boltzman's constant, h is Plank's constant, $\Delta H^{\ddagger}$ is the enthalpy, and $\Delta S^{\ddagger}$ is the entropy of the transition state. Plotting ln ((R_{fit}/n_{cat})/T) versus 1/T the entropy of the transition state of a reaction can be determined using the following equation

$$\Delta S^{\ddagger} = \left[(y - intercept) - \ln\left(\frac{k_B}{h}\right)\right]R$$

The enthalpy for the transition state of the reaction can be determined from the slope where

$$slope = \frac{-\Delta H^{\ddagger}}{R}$$

Using the Eyring equation above, along with obtaining k_{cat} values at varying temperatures, the values for entropy and enthalpy for the transition state can be determined. Using these values for enthalpy and entropy, the free energy can then be calculated at any temperature.

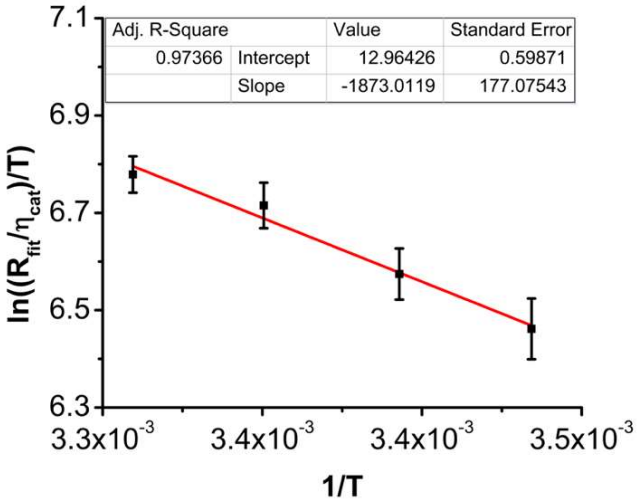

Figure S3.10. Eyring plot of the stopped-flow data spectrochemical experiments with Fe(tpy^{tbu}pho)Cl_2 in MeCN with AcOH. Data were fit using Kinetic Studio 4.0 (2 Exp + Mx + C). Syringe concentrations: Fe(tpy^{tbu}pho)Cl_2 = 5.14 x 10^{-5} M; O_2 = 1.62 x 10^{-3} M; Cp_2^*Fc = 2.44 x 10^{-3} M; AcOH = 1.31x 10^{-2} M.

Table S3.3. Eyring results obtained from spectrochemical experiments in **Figure S3.10**.

$\Delta H^{‡}$ (kcal mol^{-1})	+3.72
$\Delta S^{‡}$ (cal mol^{-1}K^{-1})	–21.4
$\Delta G^{‡}_{298K}$ (kcal mol^{-1})	+10.1

Spectroscopic Determination of Product Selectivity for ORR with Ti(O)SO_4 Colorimetric Assay.

Selectivity for H_2O_2 production via ORR has been carried out in the manner described in previous reports from our lab.[23] Briefly, 0.1 M Ti(O)SO_4 solution was prepared and utilized to identify and quantify H_2O_2 *in situ* via established spectrophotometric methods.

For the data in **Figure S3.11A** a 6 mL air-saturated MeCN solution was prepared containing Fe(tpy^{tbu}pho)Cl_2 **1** (4.44 x 10^{-5} M), AcOH (3.11 x 10^{-2} M), and Cp_2^*Fc (8.03 x 10^{-4} M) and left for 15 minutes. Then 3 mL of the solution was added to a UV-vis cuvette containing 0.1 mL of DI water and a spectrum was obtained (black, **A**). The remaining 3 mL were added to a second UV-vis cuvette contain 0.1 mL of the 0.1 M Ti(O)SO_4 solution (red, **A**). No change in the absorbance at 408 nm for the red spectrum in (**A**) containing 0.1 mL of the 0.1 M Ti(O)SO_4 solution suggests

that Fe(tpy^{tbu}pho)Cl_2 does not demonstrate appreciable selectivity for H_2O_2 under these conditions. These data support that Fe(tpy^{tbu}pho)Cl_2 is instead quantitatively selective for water. For the data in **Figure S3.11B**, this control experiment was carried out in the same manner and at identical concentrations as those described above for **Figure S3.11A**, but in the absence of Fe(tpy^{tbu}pho)Cl_2.

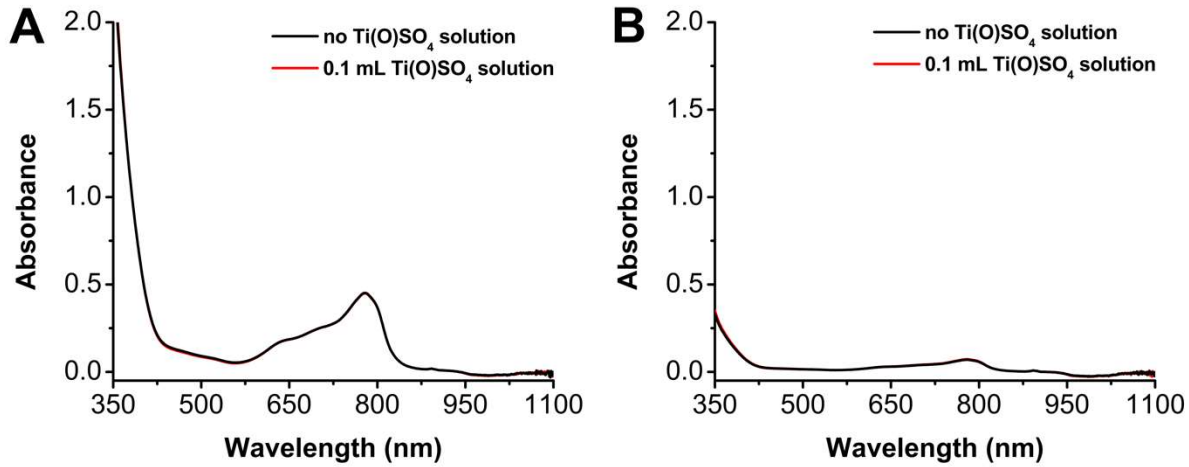

Figure S3.11. (A) H_2O_2 selectivity testing under catalytic conditions with Fe(tpy^{tbu}pho)Cl_2 and **(B)** identical conditions in the absence of Fe(tpy^{tbu}pho)Cl_2.

Stability of Fe(tpy^{tbu}pho)Cl_2 in the Presence of Urea•H_2O_2

To test if Fe(tpy^{tbu}pho)Cl_2 facilitates H_2O_2 disproportionation or interferes with the Ti(O)SO_4 colorimetric assay, a known amount of urea•H_2O_2 in MeCN (6.67 x 10^{-4} M final concentration) was added to a MeCN solution of Fe(tpy^{tbu}pho)Cl_2 (4.44 x 10^{-5} M final concentration) with AcOH (3.11 x 10^{-2} M final concentration) that was then saturated with air and left for 15 minutes. A 3 mL aliquot was then removed from the solution and added to a UV-vis cuvette containing 0.1 mL of DI water (**Figure S3.12A**, red). Then another 3 mL aliquot was removed and added to a second UV-vis cuvette containing 0.1 mL of the 0.1 M Ti(O)SO_4 solution (**Figure S3.12A**, blue).

Control spectra were obtained to detect any background contribution to the observed changes in the UV-vis spectra. For this, first a MeCN solution of Fe(tpy^{tbu}pho)Cl_2 (4.44 x 10^{-5} M final

concentration) with AcOH (3.11 x 10^{-2} M final concentration) was saturated with air and left for 15 minutes. A 3 mL aliquot was then removed from the solution and added to a UV-vis cuvette containing 0.1 mL of DI water (**Figure S3.12A**, black). Then another 3 mL aliquot was removed and added to a second UV-vis cuvette containing 0.1 mL of the 0.1 M $Ti(O)SO_4$ solution (**Figure S3.12A**, green). Lastly, a known amount of urea•H_2O_2 in MeCN (6.67 x 10^{-4} M final concentration) was added to a MeCN solution and left for 15 minutes under air saturation. A 3 mL aliquot was removed and added to another UV-vis cuvette containing 0.1 mL of the 0.1 M $Ti(O)SO_4$ solution (**Figure S3.12A**, purple). A control spectrum of 0.1 mL of the 0.1 M $Ti(O)SO_4$ solution with 3 mL of MeCN was also obtained as a control (**Figure S3.12A**, grey).

By subtracting the black spectrum from the blue spectrum in **Figure S3.12A**, the amount of H_2O_2 present in solution can be directly compared to the control solution in **Figure S3.12A**, grey. These spectra are overlayed for a clear comparison in **Figure S3.12B**. The absence of a change in absorbance at 408 nm reveals that H_2O_2 is stable in the presence of $Fe(tpy^{tbu}pho)Cl_2$.

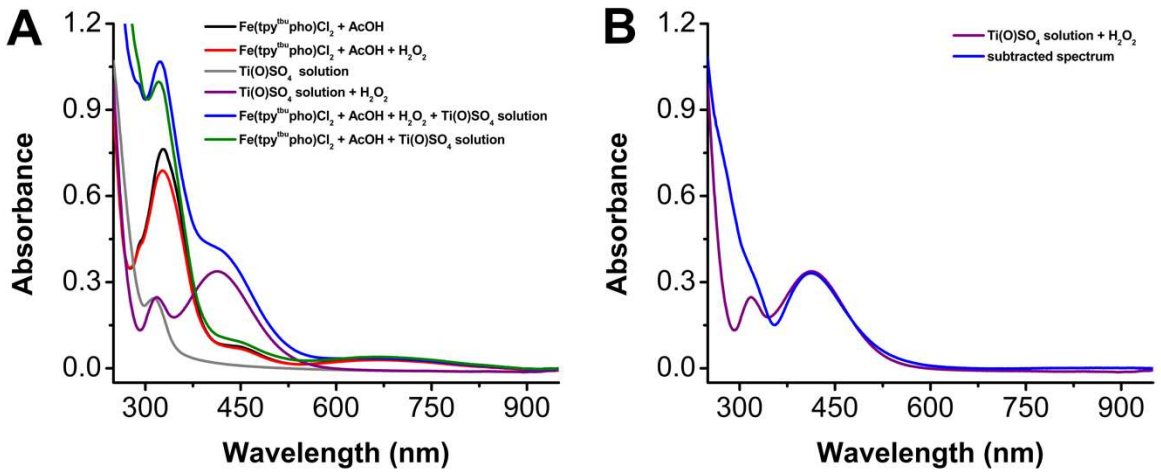

Figure S3.12. UV-vis data analyzing the stability of $Fe(tpy^{tbu}pho)Cl_2$ in the presence of urea•H_2O_2. Conditions: quartz cell with 1 cm pathlength.

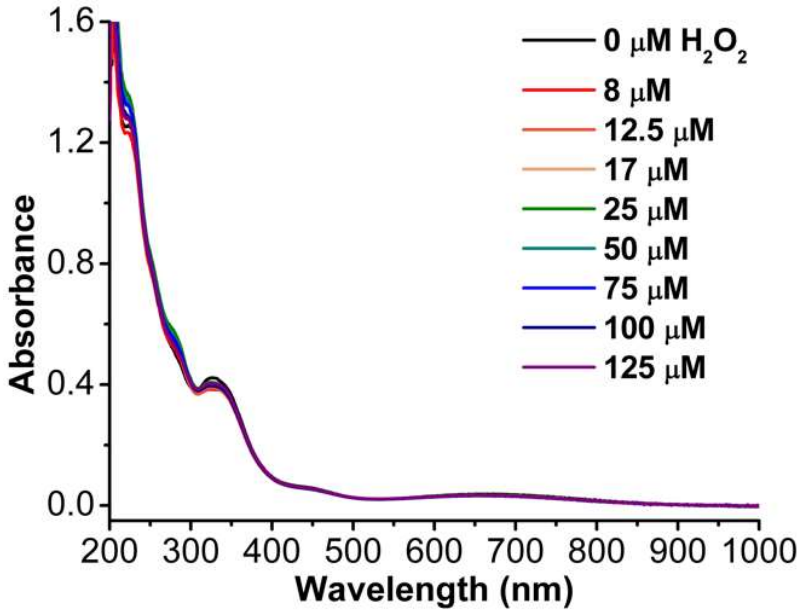

Figure S3.13. UV-vis spectral changes upon addition of increasing amounts of urea•H_2O_2 to 25 μM of Fe(tpy^{tbu}pho)Cl_2 in MeCN.

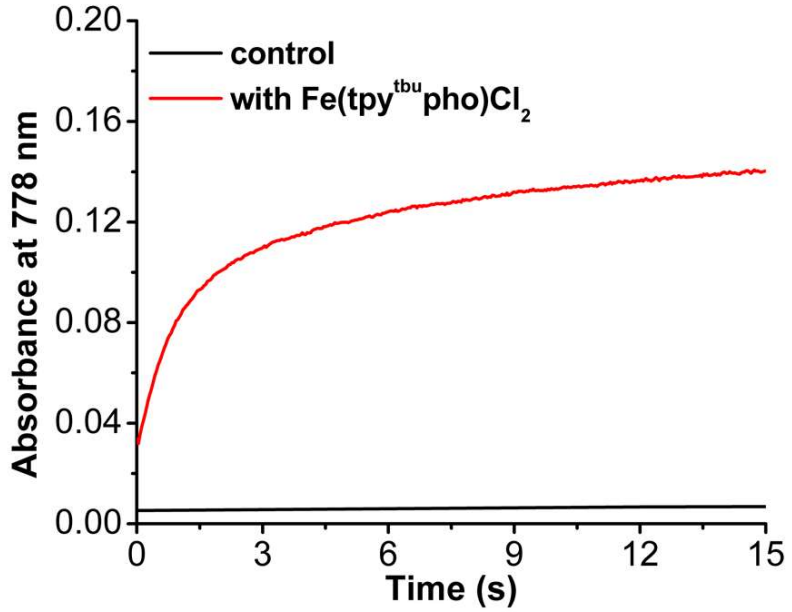

Figure S3.14. Representative spectral changes at 778 nm due to the formation of $[Cp^*_2Fe]^+$ comparing H_2O_2RR catalytic conditions with Fe(tpy***tbu***pho)Cl_2 (red) versus identical conditions in the absence of Fe(tpy***tbu***pho)Cl_2 as a control (black). Syringe Concentrations: Fe(tpy^{tbu}pho)Cl_2 (if present) = 4.0 x 10^{-5} M; AcOH = 2.65 x 10^{-2} M; urea•H_2O_2 = 4.0 x 10^{-3} M; and Cp^*_2Fe = 2.0 x 10^{-3} M.

Determination of Reaction Stoichiometry for Fe(tpy^{tbu}pho)Cl_2 with Respect to H2O2 Reduction

The stoichiometry of the H_2O_2 reduction reaction **Eq (S3.7)** was confirmed by quantifying the amount of oxidized decamethylferrocenium ($[Cp^*_2Fc]^+$) formed under anaerobic conditions where urea•H_2O_2 (2.8 x 10^{-4} M), Fe(tpy^{tbu}pho)Cl_2 (2.0 x 10^{-5} M), AcOH (3.11 x 10^{-2} M), and Cp^*_2Fc (1.0 x 10^{-3} M) were combined in an MeCN solution and allowed to react to completion. The amount of $[Cp^*_2Fe]^+$ was quantified using the molar extinction coefficient at 778 nm (ε = 466 M^{-1} cm^{-1} as determind by serial dilution of a chemically prepared sample of $[Cp^*_2Fc][BF_4]$). The number of equiv. of Cp^*_2Fc consumed per equiv. H_2O_2 was determined by **Eq (S3.8)**:

$$H_2O_2 + 2Cp^*_2Fe + 2AcOH \xrightarrow{cat.Fe} 2H_2O + 2[Cp^*_2Fe]^+ + 2AcO^- \qquad \textbf{(S3.7)}$$

$$\frac{[(Cp^*_2Fc)^+]_{exp}}{[H_2O_2]} = Eq.\, Cp^*_2Fe\ consumed\ per\ H_2O_2 \qquad \textbf{(S3.8)}$$

It was determined that 2.09 ± 0.1 equiv of Cp^*_2Fe was consumed per equiv of H_2O_2, consistent with stoichiometric reduction of H_2O_2.

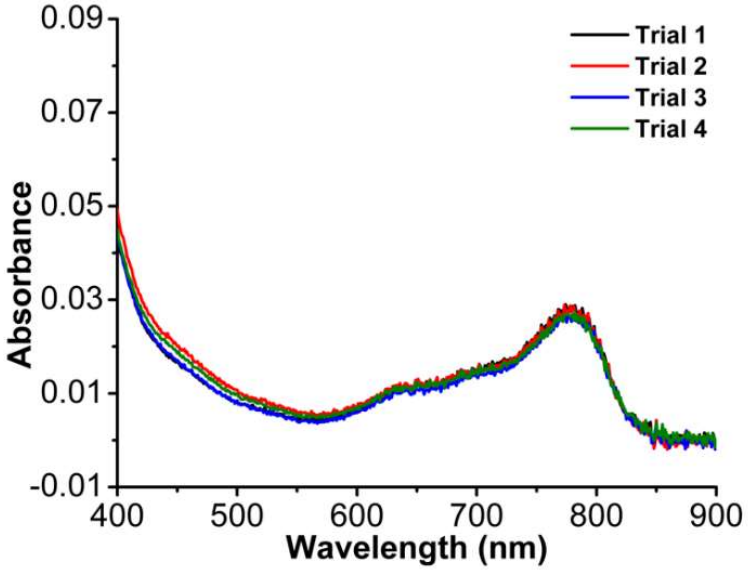

Figure S3.15. UV-vis data to determine the H_2O_2RR reaction stoichiometry described above.

Rate Law Determination of H_2O_2 Reduction by Fe(tpy^{tbu}pho)Cl_2

Variable concentration studies using UV-vis stopped-flow spectroscopy were also used to for kinetic analysis of H_2O_2RR by Fe(tpy^{tbu}pho)Cl_2.

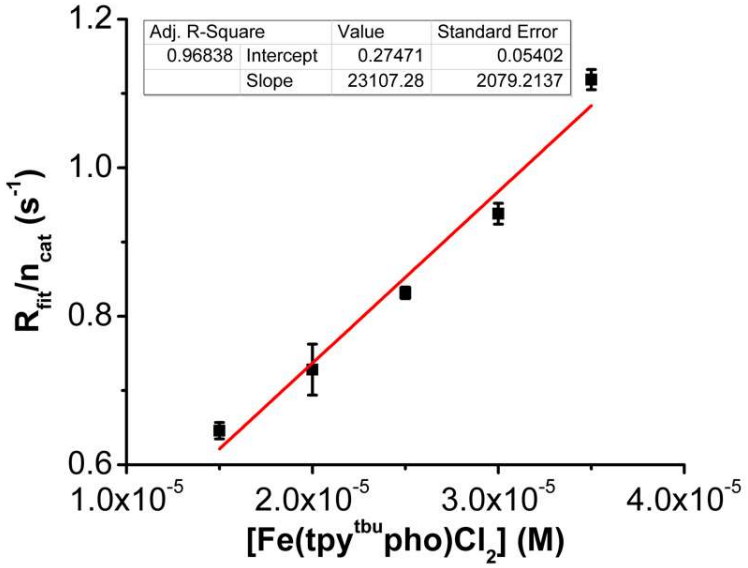

Figure S3.16. The calculated R_{fit}/n_{cat} from stopped-flow spectrochemical experiments with Cp*$_2$Fe, AcOH, urea•H_2O_2 with varying Fe(tpy^{tbu}pho)Cl_2 concentration at 25.5°C in MeCN. Data were fit using Kinetic Studio 4.0 (2Exp + Mx + C). Syringe concentrations: Cp*$_2$Fe = 2.0 x 10^{-3} M, AcOH = 2.65 x 10^{-2} M, urea•H_2O_2 = 4 x 10^{-3} M.

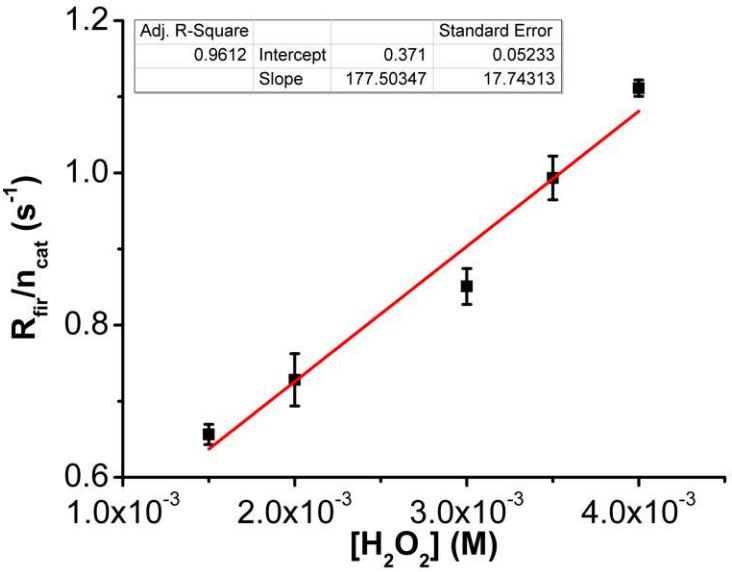

Figure S3.17. The calculated R_{fit}/n_{cat} from stopped-flow spectrochemical experiments with Cp*$_2$Fe, AcOH, Fe(tpy^{tbu}pho)Cl_2, with varying urea•H_2O_2 concentration at 25.5°C in MeCN. Data were fit using Kinetic Studio 4.0 (2Exp + Mx + C). Syringe concentrations: Cp*$_2$Fe = 2.0 x 10^{-3} M, AcOH = 2.65 x 10^{-2} M, Fe(tpy^{tbu}pho)Cl_2 = 4 x 10^{-5} M.

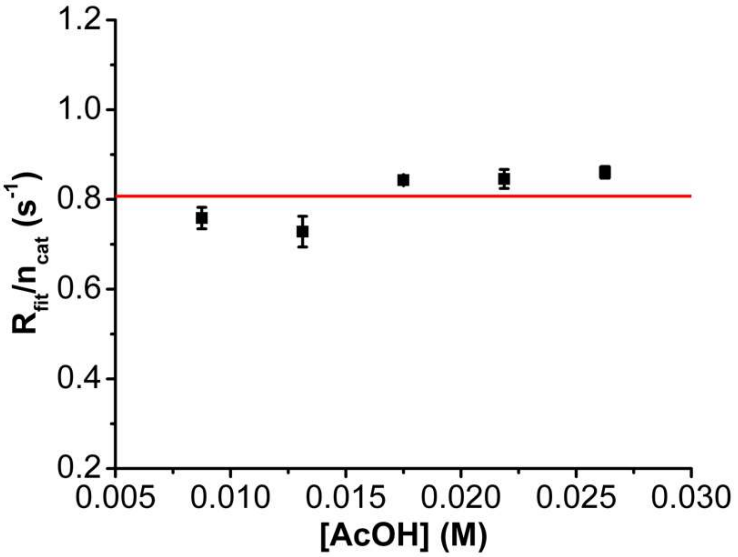

Figure S3.18. The calculated R_{fit}/n_{cat} from stopped-flow experiments with Cp^*_2Fe, $Fe(tpy^{tbu}pho)Cl_2$, urea•H_2O_2 with varying AcOH concentration at 25.5°C in MeCN. The horizontal line represents the global average rate observed across all experiments for variable [AcOH]. Data were fit using Kinetic Studio 4.0 (2Exp + Mx + C). Syringe concentrations: Cp^*_2Fe = 2.0 x 10^{-3} M, urea•H_2O_2 = 4 x 10^{-3} M., $Fe(tpy^{tbu}pho)Cl_2$ = 4 x 10^{-5} M.

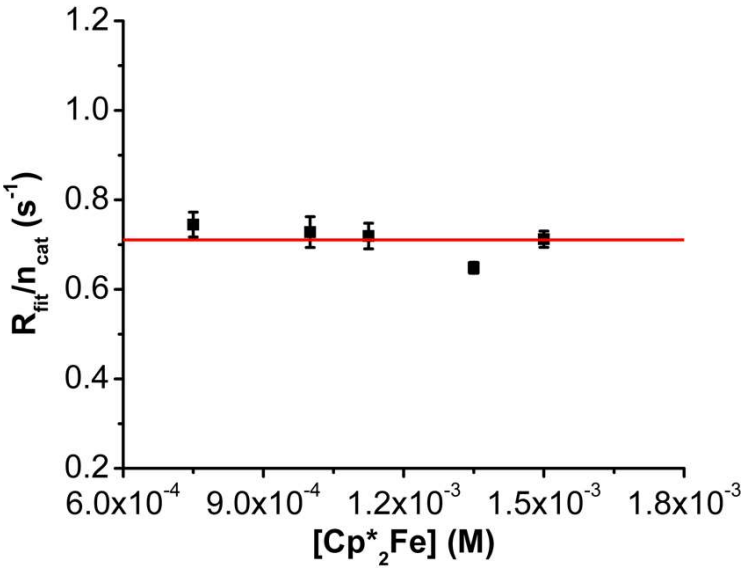

Figure S3.19. The calculated R_{fit}/n_{cat} from stopped-flow experiments with AcOH, $Fe(tpy^{tbu}pho)Cl_2$, urea•H_2O_2 with varying Cp^*_2Fe concentration at 25.5°C in MeCN. The horizontal line represents the global average rate observed across all experiments for variable [Cp^*_2Fe]. Data were fit using Kinetic Studio 4.0 (2Exp + Mx + C). Syringe concentrations: AcOH = 2.65 x 10^{-2} M, urea•H_2O_2 = 4 x 10^{-3} M., $Fe(tpy^{tbu}pho)Cl_2$ = 4 x 10^{-5} M.

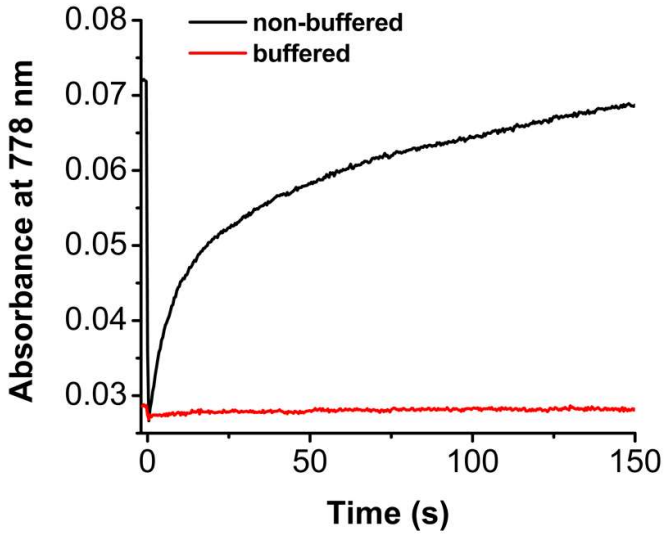

Figure S3.20. Representative spectral changes at 778 nm due to the formation of $[Cp^*_2Fe]^+$ comparing $Fe(tpy^{tbu}pho)Cl_2$ under non-buffered (black) and buffered (red) conditions. Syringe Concentrations: $Fe(tpy^{tbu}pho)Cl_2$ = 1.73 x 10^{-5} M; TBAAcO/AcOH = 1.09 x 10^{-2} M; O_2 = 1.62 x 10^{-3} M; and Cp_2^*Fc = 2.44 x 10^{-3} M.

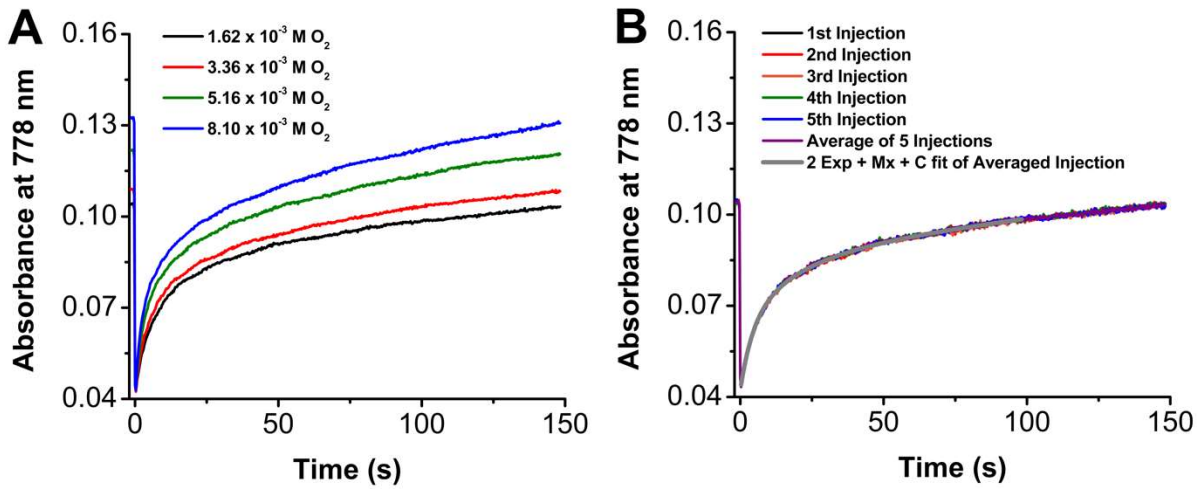

Figure S3.21. Sample variable O_2 concentration data under catalytic conditions. (**A**) Plots of the average of 5 injections across a series of variable O_2 concentration data under catalytic conditions. (**B**) Plot of data of all five injections at a single O_2 concentration (1.62 x 10^{-3} M), the average of those five injections (purple) and the second exponential linear fit of the average (grey).

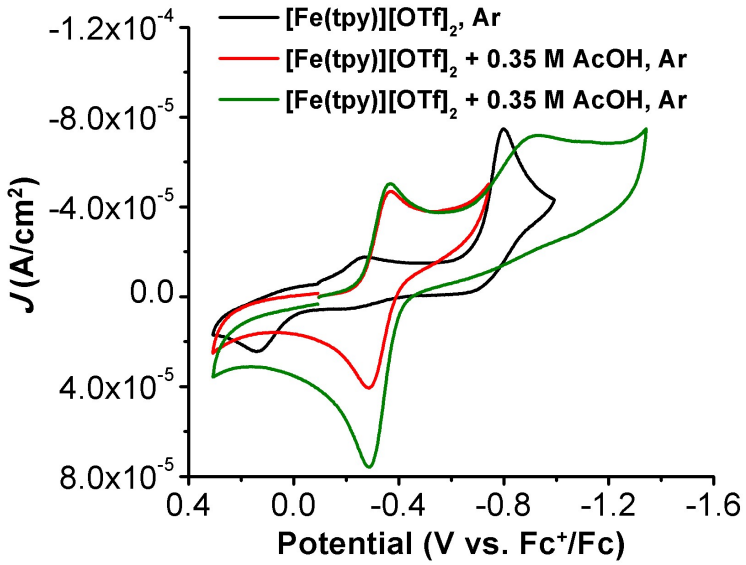

Figure S3.22. CVs of 0.5 mM [Fe(tpy^{tbu}pho)][OTf]$_2$ under Ar saturation with (red and green traces) and without (black trace) the addition of 0.35 M AcOH. Conditions: 0.5 mM [Fe(tpy^{tbu}pho)][OTf]$_2$ in 0.1 M TBAPF$_6$/MeCN; glassy carbon working electrode, glassy carbon rod counter electrode, Ag/AgCl pseudoreference electrode; referenced to Fc$^+$/Fc internal standard; 100 mV/s scan rate.

Spectroscopic Studies with [Fe^{II}(tpy^{tbu}pho)][OTf] and [Fe(tpy^{tbu}pho)][OTf]$_2$.

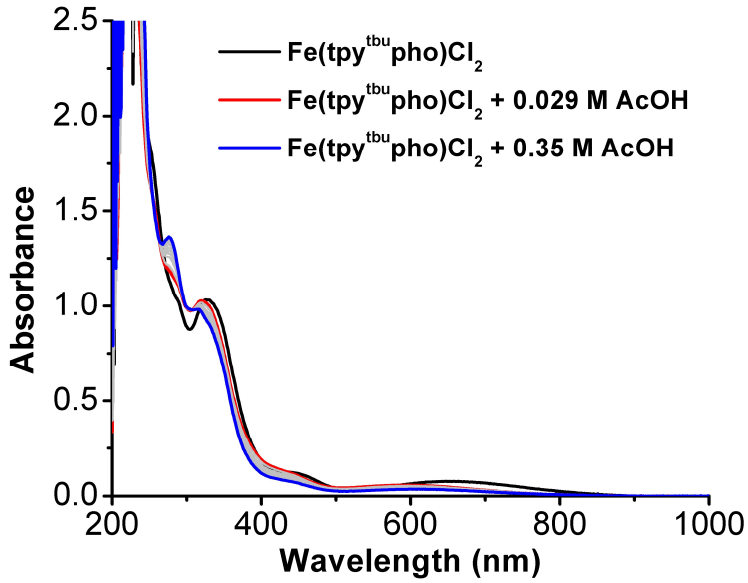

Figure S3.23. UV-vis spectral changes of 50 μM Fe(tpy^{tbu}pho)Cl$_2$ upon addition of increasing amounts of AcOH in MeCN. Conditions: 0.029 M increments of AcOH added.

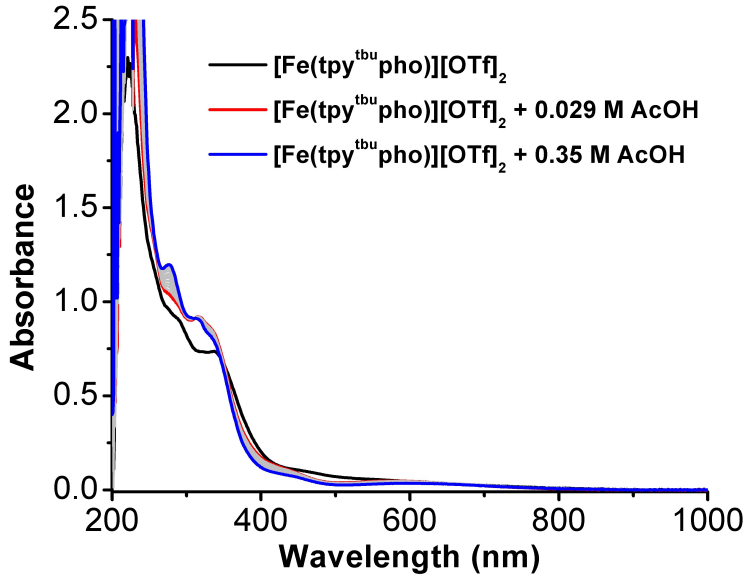

Figure S3.24. UV-vis spectral changes of 36 μM [Fe(tpy^{tbu}pho)][OTf]$_2$ upon addition of increasing amounts of AcOH in MeCN. Conditions: 0.029 M increments of AcOH added.

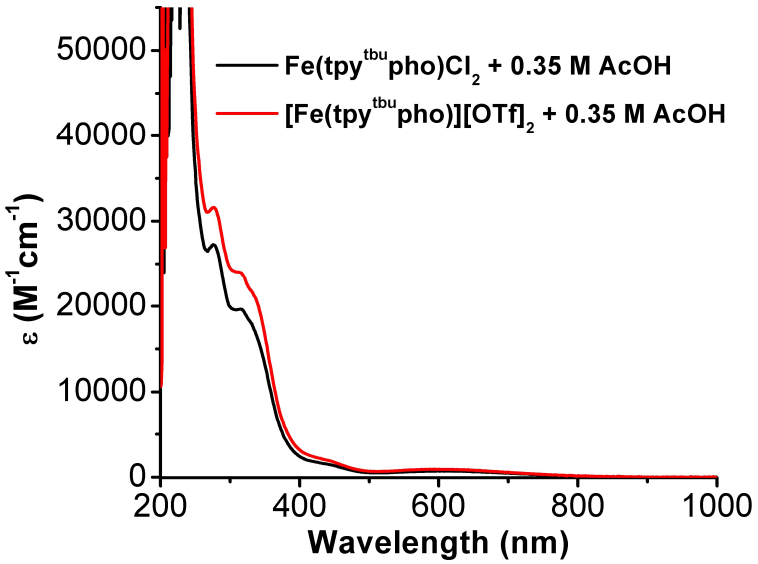

Figure S3.25. Molar extinction plot of Fe(tpy^{tbu}pho)Cl$_2$ and [Fe(tpy^{tbu}pho)][OTf]$_2$ upon exposure to 0.35 M AcOH in MeCN from **Figures S3.23** and **S3.24**.

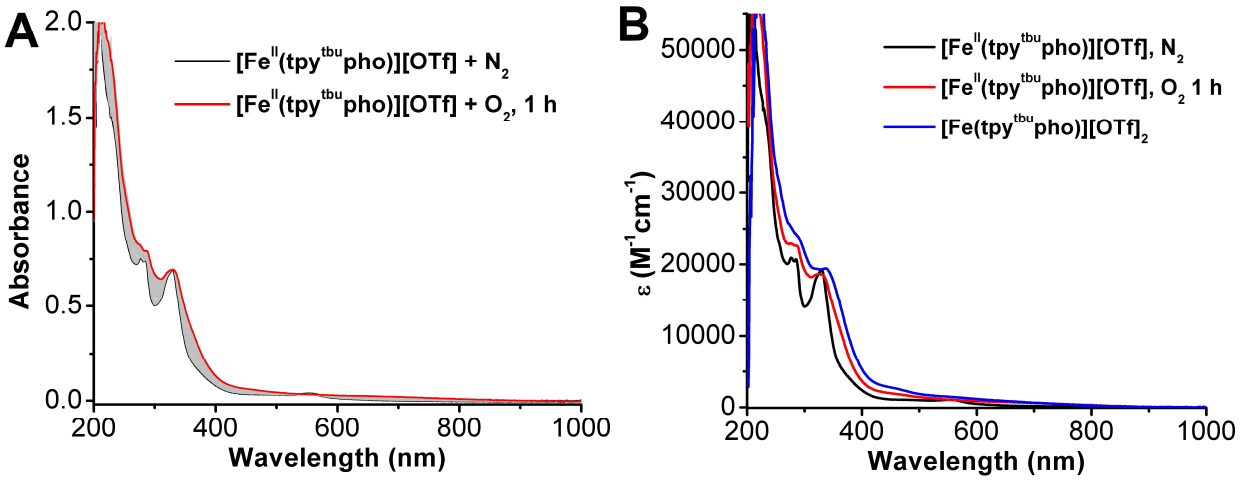

Figure S3.26. (A) UV-vis spectral changes upon exposure of 36 μM [Fe^{II}(tpy^{tbu}pho)][OTf] to O_2 over the course of 1 h in MeCN (B) molar extinction plot of [Fe^{II}(tpy^{tbu}pho)][OTf] under N_2 and 1 h after O_2 exposure and [Fe(tpy^{tbu}pho)][OTf]$_2$.

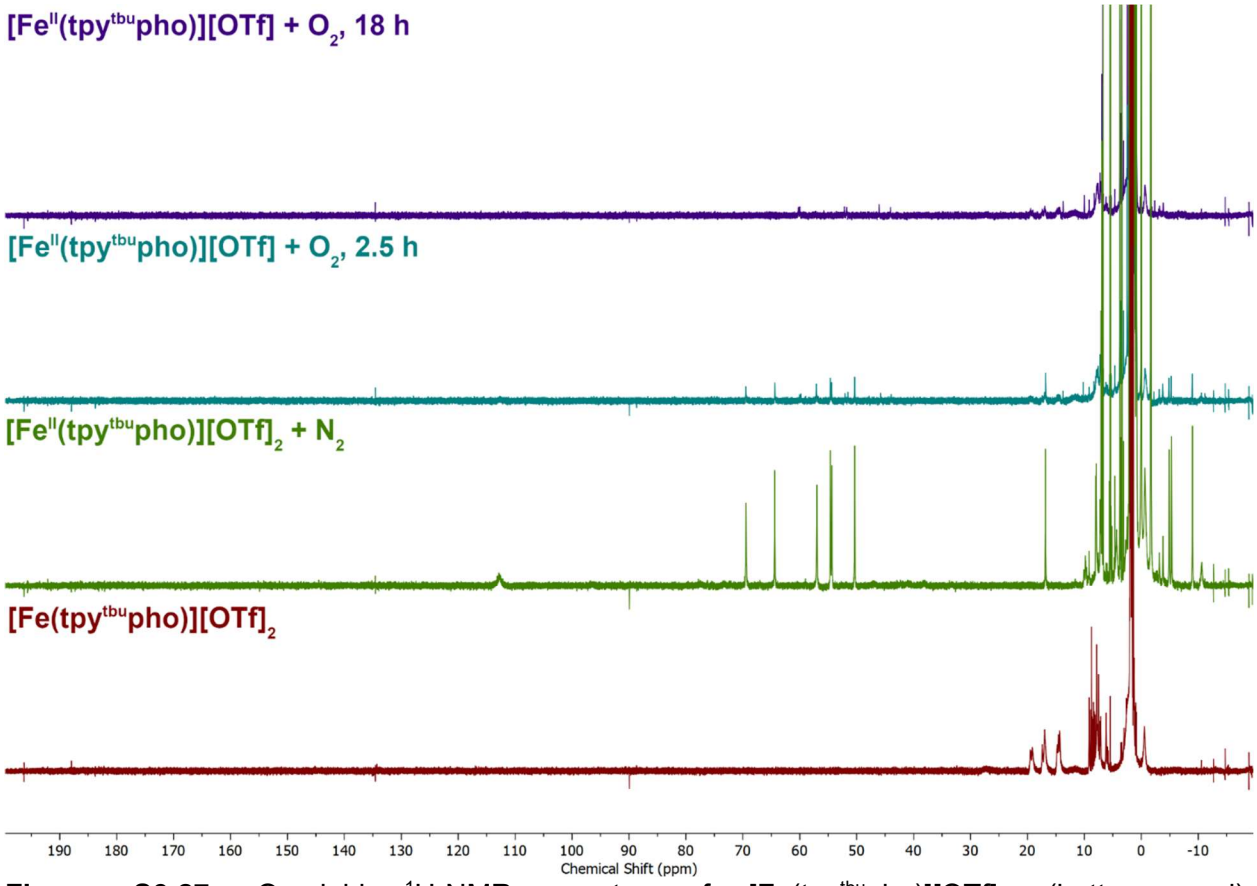

Figure S3.27. Overlaid ^{1}H-NMR spectra of [Fe(tpy^{tbu}pho)][OTf]$_2$ (bottom, red), [Fe^{II}(tpy^{tbu}pho)][OTf] under N_2 (second from bottom, green) and exposed to O_2 after 2.5 h (third from bottom, cyan) and 18 h (top, purple). Varian, 600 MHz, MeCN-d_3.

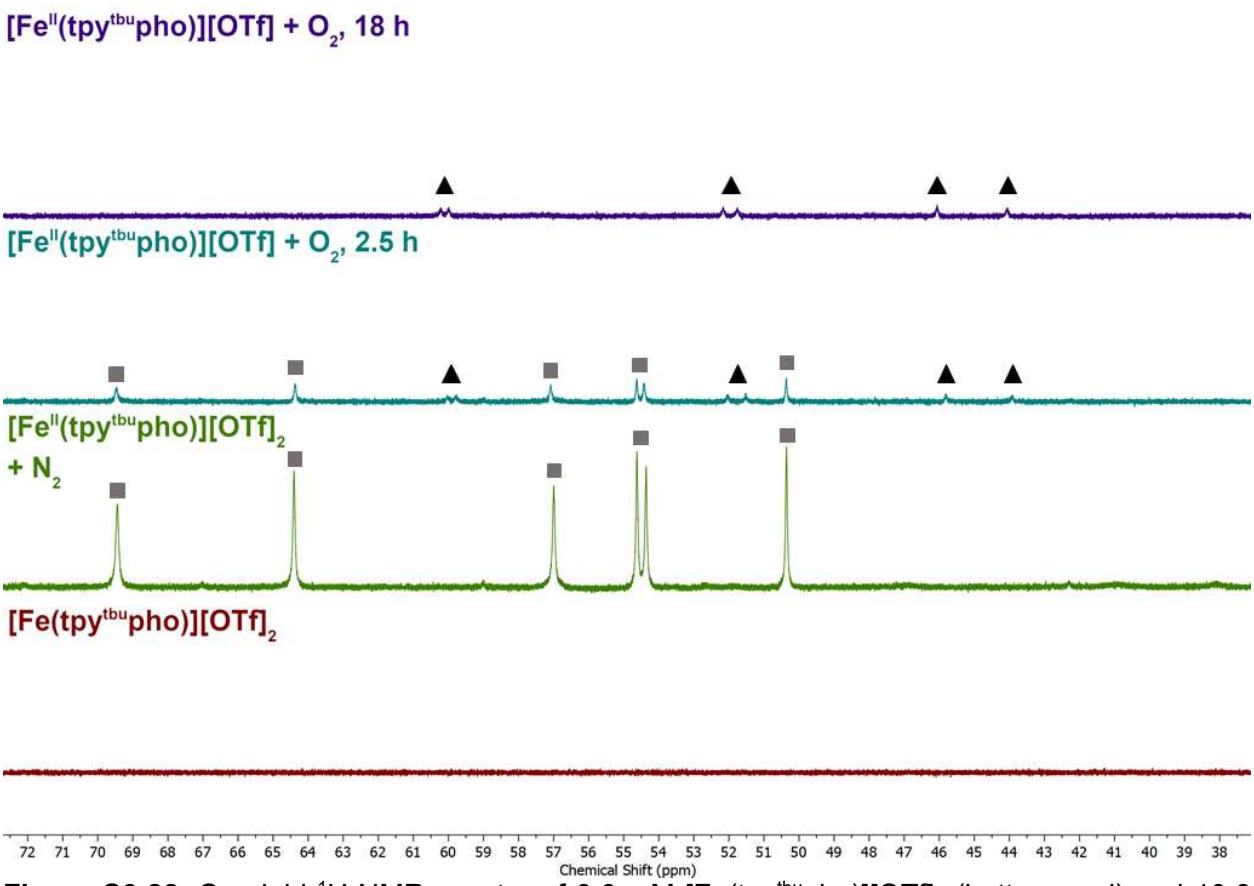

Figure S3.28. Overlaid ^{1}H-NMR spectra of 8.6 mM [Fe(tpy^{tbu}pho)][OTf]$_2$ (bottom, red) and 10.6 mM [Fe^{II}(tpy^{tbu}pho)][OTf] under N_2 (second from bottom, green) and exposed to O_2 after 2.5 h (third from bottom, cyan) and 18 h (top, purple) from 37 to 72 ppm. Varian, 600 MHz, MeCN-d_3. Where ● = features due to [Fe(tpy^{tbu}pho)][OTf]$_2$, ■ = features due to [Fe^{II}(tpy^{tbu}pho)][OTf], and ▲= features due to an identified intermediate.

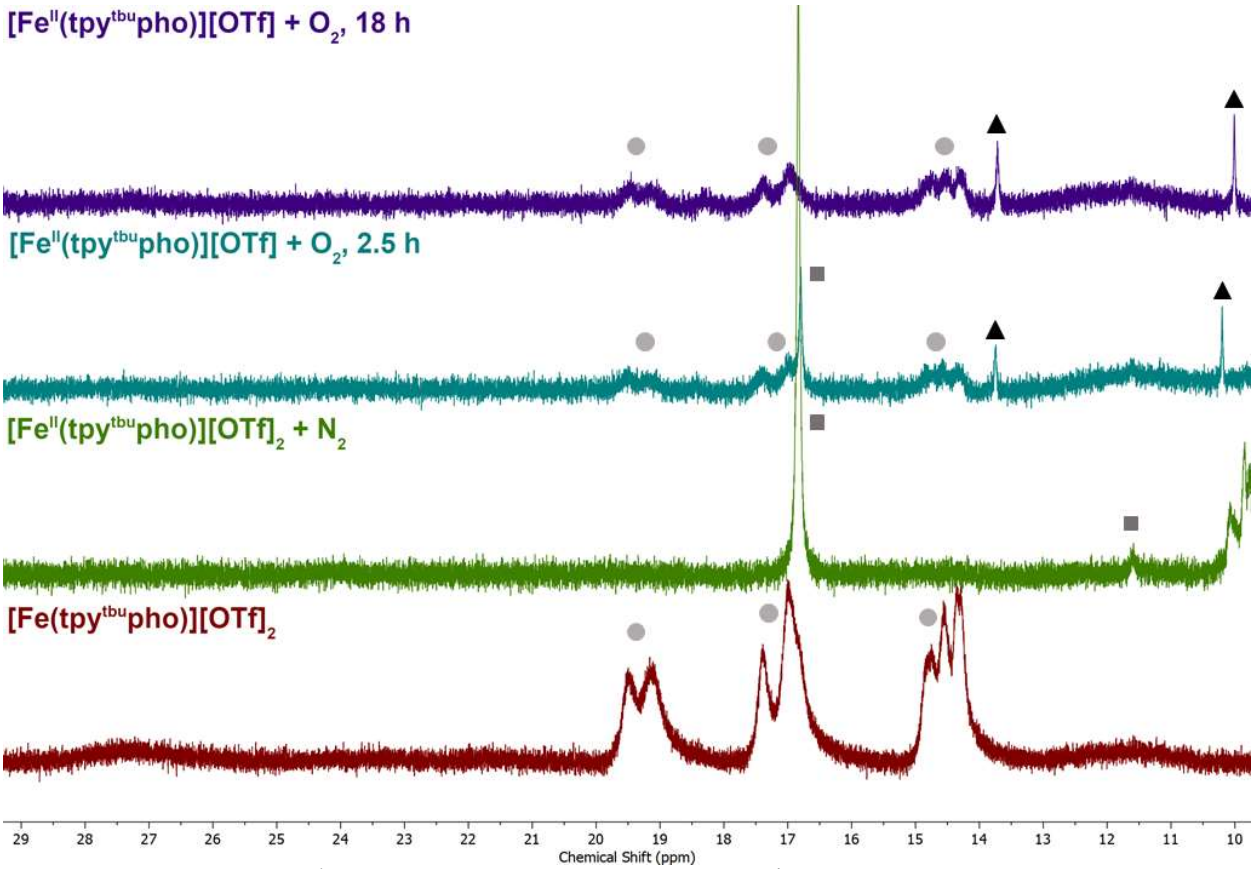

Figure S3.29. Overlaid ^{1}H-NMR spectra of 8.6 mM [Fe(tpy^{tbu}pho)][OTf]$_2$ (bottom, red), 10.6 mM [Fe^{II}(tpy^{tbu}pho)][OTf] under N_2 (second from bottom, green) and exposed to O_2 after 2.5 h (third from bottom, cyan) and 18 h (top, purple) from 10 to 30 ppm. Varian, 600 MHz, MeCN-d_3. Where ● = features due to [Fe(tpy^{tbu}pho)][OTf]$_2$, ■ = features due to [Fe^{II}(tpy^{tbu}pho)][OTf], and ▲ = features due to an identified intermediate.

Determination of K_{ET} for Cp^*_2Fe and $Fe(tpy^{tbu}pho)Cl_2$

The equilibrium constant of electron transfer (K_{ET}) between Cp^*_2Fe and $Fe(tpy^{tbu}pho)Cl_2$ was determined experimentally from the $E_{1/2}$ (V vs. Fc^+/Fc) of 1 mM $Fe(tpy^{tbu}pho)Cl_2$ for Fe(III/II) reduction and the $E_{1/2}$ (V vs. Fc^+/Fc) of 1 mM Cp^*_2Fe for $Cp^*_2Fe/[Cp^*_2Fe]^+$ reduction in the presence of 0.35 M AcOH. See **Figure S3** for CVs of $Fe(tpy^{tbu}pho)Cl_2$ with 0.35 M AcOH.

$$Cp^*_2Fe \rightarrow [Cp^*_2Fe]^+ + e^- \qquad E_{1/2} = -0.51 \text{ (V vs. } Fc^+/Fc)$$

$$Fe^{III} + e^- \rightarrow Fe^{II} \qquad E_{1/2,0.35\text{ M AcOH}} = -0.25 \text{ (V vs. } Fc^+/Fc)$$

$$\text{Overall: } Fe^{III} + Cp^*_2Fe \rightarrow [Cp^*_2Fe]^+ + Fe^{II}$$

$$E_{cell} = E_{1/2(Fe^{III}/Fe^{II})} - E_{1/2(Cp^*_2Fe/[Cp^*_2Fe]^+)} = 0.26 \text{ V} \qquad (\mathbf{S9})$$

$$E_{cell} = \frac{0.059}{n} \log K_{ET}, \text{ where n = 1} \qquad (\mathbf{S10})$$

$$K_{ET} = 10^{(\frac{0.26\text{ V}}{0.0592})} = 2.5 \times 10^4$$

3.6.13. Determination of Effective Overpotential (adapted[46])

The calculation of effective overpotential for this system is complicated by the inability to utilize buffered acids for kinetic experiments (**Figure 3.2**). Utilizing reported pK_a (23.5) and $\log(K_{AHA})$ (3.9) values for AcOH in MeCN, we have corrected the reported standard reduction potentials for ORR using the following equations:[2,33-35]

$$\mathrm{E}^0_{\mathrm{O2/H2O}} = 1.21 - 0.0592\mathrm{p}K_a + \frac{2.303RT}{4F}\log(4K_{\mathrm{AHA}})\ \mathrm{V\ vs\ Fc^+/Fc} \qquad (\mathbf{S3.11})$$

$$\mathrm{E}^0_{\mathrm{O2/H2O}}(\mathrm{MeCN, AcOH}) = -0.12\ \mathrm{V\ vs\ Fc^+/Fc}$$

$$\mathrm{E}^0_{\mathrm{H2O2/H2O}} = 1.74 - 0.0592\mathrm{p}K_a + \frac{2.303RT}{2F}\log(2K_{\mathrm{AHA}})\ \mathrm{V\ vs\ Fc^+/Fc} \qquad (\mathbf{S3.12})$$

$$\mathrm{E}^0_{\mathrm{H2O2/H2O}}(\mathrm{MeCN, AcOH}) = +0.47\ \mathrm{vs\ Fc^+/Fc}$$

where R is the ideal gas law (8.314 $J{\cdot}K^{-1}{\cdot}mol^{-1}$); T is the temperature (298 K); F is Faraday's constant (96485 $C{\cdot}mol^{-1}$); K_{AHA} is the reported homoconjugation equilibrium constant for AcOH in MeCN (3.9).

For the $E_{1/2}$ of Fe(tpy^{tbu}pho)Cl_2, a value of −0.36 V of Fc^+/Fc was used, from electrochemical experiments (**Figure 3.2**, green; [Fe(tpy^{tbu}pho)Cl_2] = 1 mM; [AcOH] = 87.5 mM).

Single Crystal X-ray Diffraction

A single crystal of **Fe(tpy^{tbu}pho)Cl_2·2MeCN** or **Fe(tpy^{tbu}pho)Cl_2·H_2O** was coated with Paratone oil and mounted on a MiTeGen MicroLoop. The X-ray intensity data were measured on a Bruker D8 Venture Photon III Kappa four-circle diffractometer system equipped with an Incoatec IμS 3.0 micro-focus sealed X-ray tube (Cu Kα, λ = 1.54178 Å) and a HELIOS double bounce multilayer mirror monochromator. The frames were integrated with the Bruker SAINT software package[47] using a narrow-frame algorithm. Data were corrected for absorption effects using the Multi-Scan method (SADABS).[47] Each structure was solved and refined using the Bruker SHELXTL Software Package[48] within APEX3[47] and OLEX2.[49] Non-hydrogen atoms were refined anisotropically. The O-H hydrogen atoms in **Fe(tpy^{tbu}pho)Cl_2·H_2O** were located in the electron density map and refined isotropically with restraints on their bond lengths. All other hydrogen atoms in both structures were placed in geometrically calculated positions with U_{iso} = 1.2U_{equiv} of the parent atom (U_{iso} = 1.5U_{equiv} for methyl). For **Fe(tpy^{tbu}pho)Cl_2·H_2O**, a two-domain twin was identified using the TWINROTMAT feature of Platon.[50] The twin law for the two-fold rotation around the (1 0 0) axis was 1.000 0.000 0.352 / 0.000 -1.000 0.000/ 0.000 0.000 -1.000, and the BASF refined to 0.03937.

***Table S3.4**. Crystallographic Details*

	Fe(tpy^{tbu}pho)Cl$_2$·2MeCN	**Fe(tpy^{tbu}pho)Cl$_2$·H$_2$O**
CCDC number	2097186	2097187
Formula	$C_{33}H_{36}Cl_2FeN_5O$	$C_{29}H_{32}Cl_2FeN_3O_2$
FW (g/mol)	645.42	581.32
Temp (K)	100(2)	100(2)
λ (Å)	1.54178	1.54178
Size (mm)	0.045 x 0.087 x 0.106	0.017 x 0.043 x 0.182
Crystal habit	green-yellow plate	yellow rod
Crystal system	monoclinic	monoclinic
Space group	P 2_1/c	P 2_1/c
a (Å)	13.6379(9)	19.8776(14)
b(Å)	14.5045(10)	15.7122(13)
c (Å)	17.2579(10)	8.8813(7)
α (°)	90	90
β (°)	111.761(4)	94.505(5)
γ (°)	90	90
Volume (Å^3)	3170.5(4)	2765.2(4)
Z	4	4
Density (g/cm^3)	1.352	1.396
μ (mm^{-1})	5.632	6.399
F(000)	1348	1212
θ range (°)	3.49 to 68.51	2.81 to 59.12
Index ranges	-16 ≤ h ≤ 16 -17 ≤ k ≤ 13 -20 ≤ l ≤ 20	-22 ≤ h ≤ 22 -16 ≤ k ≤ 14 -9 ≤ l ≤ 9
Reflns collected	32468	17956
Independent reflns	5823 [R_{int} = 0.0863]	3851 [R_{int} = 0.1853]
Data / restraints /parameters	5823 / 0 / 387	3851 / 2 / 347
GOF on F^2	1.017	1.060
R_1 (I>2σ(I))	0.0499	0.1023
wR_2 (all data)	0.1373	0.3441

3.7. References

(1) Sahu, S.; Goldberg, D. P. Activation of Dioxygen by Iron and Manganese Complexes: A Heme and Nonheme Perspective. *J. Am. Chem. Soc.* **2016**, *138* (36), 11410-11428. DOI: 10.1021/jacs.6b05251.

(2) Pegis, M. L.; Wise, C. F.; Martin, D. J.; Mayer, J. M. Oxygen Reduction by Homogeneous Molecular Catalysts and Electrocatalysts. *Chem. Rev.* **2018**, *118* (5), 2340-2391. DOI: 10.1021/acs.chemrev.7b00542.

(3) IPCC. *Global Warming of 1.5°C. An IPCC Special Report*; World Meterological Organization, Geneva, Switzerland, 2018.

(4) Machan, C. W. Advances in the Molecular Catalysis of Dioxygen Reduction. *ACS Catal.* **2020**, *10* (4), 2640-2655. DOI: 10.1021/acscatal.9b04477.

(5) Martin, D. J.; Wise, C. F.; Pegis, M. L.; Mayer, J. M. Developing Scaling Relationships for Molecular Electrocatalysis through Studies of Fe-Porphyrin-Catalyzed O2 Reduction. *Acc. Chem. Res.* **2020**, *53* (5), 1056-1065. DOI: 10.1021/acs.accounts.0c00044.

(6) Pegis, M. L.; Martin, D. J.; Wise, C. F.; Brezny, A. C.; Johnson, S. I.; Johnson, L. E.; Kumar, N.; Raugei, S.; Mayer, J. M. Mechanism of Catalytic O2 Reduction by Iron Tetraphenylporphyrin. *J. Am. Chem. Soc.* **2019**, *141* (20), 8315-8326. DOI: 10.1021/jacs.9b02640.

(7) Pegis, M. L.; McKeown, B. A.; Kumar, N.; Lang, K.; Wasylenko, D. J.; Zhang, X. P.; Raugei, S.; Mayer, J. M. Homogenous Electrocatalytic Oxygen Reduction Rates Correlate with Reaction Overpotential in Acidic Organic Solutions. *ACS Cent. Sci.* **2016**, *2* (11), 850-856. DOI: 10.1021/acscentsci.6b00261.

(8) Pegis, M. L.; Wise, C. F.; Koronkiewicz, B.; Mayer, J. M. Identifying and Breaking Scaling Relations in Molecular Catalysis of Electrochemical Reactions. *J. Am. Chem. Soc.* **2017**, *139* (32), 11000-11003. DOI: 10.1021/jacs.7b05642.

(9) Wasylenko, D. J.; Rodríguez, C.; Pegis, M. L.; Mayer, J. M. Direct Comparison of Electrochemical and Spectrochemical Kinetics for Catalytic Oxygen Reduction. *J. Am. Chem. Soc.* **2014**, *136* (36), 12544-12547. DOI: 10.1021/ja505667t.

(10) Wang, Y.-H.; Pegis, M. L.; Mayer, J. M.; Stahl, S. S. Molecular Cobalt Catalysts for O2 Reduction: Low-Overpotential Production of H2O2 and Comparison with Iron-Based Catalysts. *J. Am. Chem. Soc.* **2017**, *139* (46), 16458-16461. DOI: 10.1021/jacs.7b09089.

(11) Brezny, A. C.; Johnson, S. I.; Raugei, S.; Mayer, J. M. Selectivity-Determining Steps in O2 Reduction Catalyzed by Iron(tetramesitylporphyrin). *J. Am. Chem. Soc.* **2020**, *142* (9), 4108-4113. DOI: 10.1021/jacs.9b13654.

(12) Kobayashi, N.; Nevin, W. A. Electrocatalytic Reduction of Oxygen Using Water-Soluble Iron and Cobalt Phthalocyanines and Porphyrins. *Appl. Organomet. Chem.* **1996**, *10* (8), 579-590, DOI: 10.1002/(SICI)1099-0739(199610)10:8<579::AID-AOC523>3.0.CO;2-Q

(13) Yang, Y.-S.; Baldwin, J.; Ley, B. A.; Bollinger, J. M.; Solomon, E. I. Spectroscopic and Electronic Structure Description of the Reduced Binuclear Non-Heme Iron Active Site in Ribonucleotide Reductase from E. coli: Comparison to Reduced Δ9 Desaturase and Electronic Structure Contributions to Differences in O2 Reactivity. *J. Am. Chem. Soc.* **2000**, *122* (35), 8495-8510. DOI: 10.1021/ja994406r.

(14) Wang, Y.; Li, J.; Liu, A. Oxygen activation by mononuclear nonheme iron dioxygenases involved in the degradation of aromatics. *JBIC J. Biol. Inorg. Chem.* **2017**, *22* (2), 395-405. DOI: 10.1007/s00775-017-1436-5.

(15) Bassan, A.; Blomberg, M. R. A.; Borowski, T.; Siegbahn, P. E. M. Oxygen Activation by Rieske Non-Heme Iron Oxygenases, a Theoretical Insight. *J. Phys. Chem. B* **2004**, *108* (34), 13031-13041. DOI: 10.1021/jp048515q.

(16) Brown, K. A.; Guo, Z.; Tokmina-Lukaszewska, M.; Scott, L. W.; Lubner, C. E.; Smolinski, S.; Mulder, D. W.; Bothner, B.; King, P. W. The oxygen reduction reaction catalyzed by Synechocystis sp. PCC 6803 flavodiiron proteins. *Sustain. Energy & Fuels* **2019**, *3* (11), 3191-3200. DOI: 10.1039/C9SE00523D.

(17) Solomon, E. I.; Decker, A.; Lehnert, N. Non-heme iron enzymes: Contrasts to heme catalysis. *Proc. Natl. Acad. Sci. USA* **2003**, *100* (7), 3589-3594. DOI: 10.1073/pnas.0336792100.

(18) Abu-Omar, M. M.; Loaiza, A.; Hontzeas, N. Reaction Mechanisms of Mononuclear Non-Heme Iron Oxygenases. *Chem. Rev.* **2005**, *105* (6), 2227-2252. DOI: 10.1021/cr040653o.

(19) Lu, X.; Lee, Y.-M.; Sankaralingam, M.; Fukuzumi, S.; Nam, W. Catalytic Four-Electron Reduction of Dioxygen by Ferrocene Derivatives with a Nonheme Iron(III) TAML Complex. *Inorg. Chem.* **2020**, *59* (24), 18010-18017. DOI: 10.1021/acs.inorgchem.0c02400.

(20) Wang, L.; Gennari, M.; Cantú Reinhard, F. G.; Gutiérrez, J.; Morozan, A.; Philouze, C.; Demeshko, S.; Artero, V.; Meyer, F.; de Visser, S. P.; et al. A Non-Heme Diiron Complex for (Electro)catalytic Reduction of Dioxygen: Tuning the Selectivity through Electron Delivery. *J. Am. Chem. Soc.* **2019**, *141* (20), 8244-8253. DOI: 10.1021/jacs.9b02011.

(21) Cook, E. N.; Dickie, D. A.; Machan, C. W. Catalytic Reduction of Dioxygen to Water by a Bioinspired Non-Heme Iron Complex via a 2+2 Mechanism. *J. Am. Chem. Soc.* **2021**, *143* (40), 16411-16418. DOI: 10.1021/jacs.1c04572.

(22) Hooe, S. L.; Rheingold, A. L.; Machan, C. W. Electrocatalytic Reduction of Dioxygen to Hydrogen Peroxide by a Molecular Manganese Complex with a Bipyridine-Containing Schiff Base Ligand. *J. Am. Chem. Soc.* **2018**, *140* (9), 3232-3241. DOI: 10.1021/jacs.7b09027.

(23) Hooe, S. L.; Machan, C. W. Dioxygen Reduction to Hydrogen Peroxide by a Molecular Mn Complex: Mechanistic Divergence between Homogeneous and Heterogeneous Reductants. *J. Am. Chem. Soc.* **2019**, *141* (10), 4379-4387. DOI: 10.1021/jacs.8b13373.

(24) Hooe, S. L.; Cook, E. N.; Reid, A. G.; Machan, C. W. Non-covalent assembly of proton donors and p-benzoquinone anions for co-electrocatalytic reduction of dioxygen. *Chem. Sci.* **2021**, *12* (28), 9733-9741, 10.1039/D1SC01271A. DOI: 10.1039/D1SC01271A.

(25) Nichols, A. W.; Kuehner, J. S.; Huffman, B. L.; Miedaner, P. R.; Dickie, D. A.; Machan, C. W. Reduction of dioxygen to water by a Co(N2O2) complex with a 2,2′-bipyridine backbone. *Chem. Commun.* **2021**, *57* (4), 516-519, 10.1039/D0CC06763F. DOI: 10.1039/D0CC06763F.

(26) Nichols, A. W.; Cook, E. N.; Gan, Y. J.; Miedaner, P. R.; Dressel, J. M.; Dickie, D. A.; Shafaat, H. S.; Machan, C. W. Pendent Relay Enhances H2O2 Selectivity during Dioxygen Reduction Mediated by Bipyridine-Based Co–N2O2 Complexes. *J. Am. Chem. Soc.* **2021**, *143* (33), 13065-13073. DOI: 10.1021/jacs.1c03381.

(27) Gordon, J. B.; Vilbert, A. C.; Dimucci, I. M.; MacMillan, S. N.; Lancaster, K. M.; Moënne-Loccoz, P.; Goldberg, D. P. Activation of Dioxygen by a Mononuclear Nonheme Iron Complex: Sequential Peroxo, Oxo, and Hydroxo Intermediates. *J. Am. Chem. Soc.* **2019**, *141* (44), 17533-17547. DOI: 10.1021/jacs.9b05274.

(28) Elgrishi, N.; Chambers, M. B.; Wang, X.; Fontecave, M. Molecular polypyridine-based metal complexes as catalysts for the reduction of CO2. *Chem. Soc. Rev.* **2017**, *46* (3), 761-796, 10.1039/C5CS00391A. DOI: 10.1039/C5CS00391A.

(29) Hooe, S. L.; Moreno, J. J.; Reid, A. G.; Dickie, D. A.; Machan, C. W. Homogeneous Electrocatalytic Reduction of CO2 by a CrN3O Complex: Electronic Coupling with Redox-Active Terpyridine Fragment Favors Selectivity for CO. *ChemRxiv* **2021**, 10.33774/chemrxiv-32021-lplvt.

(30) Nichols, A. W.; Chatterjee, S.; Sabat, M.; Machan, C. W. Electrocatalytic Reduction of CO2 to Formate by an Iron Schiff Base Complex. *Inorg. Chem.* **2018**, *57* (4), 2111-2121. DOI: 10.1021/acs.inorgchem.7b02955.

(31) Nichols, A. W.; Hooe, S. L.; Kuehner, J. S.; Dickie, D. A.; Machan, C. W. Electrocatalytic CO2 Reduction to Formate with Molecular Fe(III) Complexes Containing Pendent Proton Relays. *Inorg. Chem.* **2020**, *59* (9), 5854-5864. DOI: 10.1021/acs.inorgchem.9b03341.

(32) Noviandri, I.; Brown, K. N.; Fleming, D. S.; Gulyas, P. T.; Lay, P. A.; Masters, A. F.; Phillips, L. The Decamethylferrocenium/Decamethylferrocene Redox Couple: A Superior Redox Standard to the Ferrocenium/Ferrocene Redox Couple for Studying Solvent Effects on the Thermodynamics of Electron Transfer. *J. Phys. Chem. B* **1999**, *103* (32), 6713-6722. DOI: 10.1021/jp991381+.

(33) McCarthy, B. D.; Martin, D. J.; Rountree, E. S.; Ullman, A. C.; Dempsey, J. L. Electrochemical Reduction of Brønsted Acids by Glassy Carbon in Acetonitrile—Implications for Electrocatalytic Hydrogen Evolution. *Inorg. Chem.* **2014**, *53* (16), 8350-8361. DOI: 10.1021/ic500770k.

(34) Matsubara, Y. Unified Benchmarking of Electrocatalysts in Noninnocent Second Coordination Spheres for CO2 Reduction. *ACS Energy Lett.* **2019**, *4* (8), 1999-2004. DOI: 10.1021/acsenergylett.9b01180.

(35) Costentin, C. Molecular Catalysis of Electrochemical Reactions. Overpotential and Turnover Frequency: Unidirectional and Bidirectional Systems. *ACS Catalysis* **2021**, *11* (9), 5678-5687. DOI: 10.1021/acscatal.1c00744.

(36) Tsuda, M.; Kasai, H. Imidazole ligand effect on O2 interaction with metalloporphyrins. *Surf. Sci.* **2007**, *601*, 5200–5206. DOI: 10.1016/j.susc.2007.04.229.

(37) Ohta, T.; Nagaraju, P.; Liu, J.-G.; Ogura, T.; Naruta, Y. The secondary coordination sphere and axial ligand effects on oxygen reduction reaction by iron porphyrins: a DFT computational study. *J. Biol. Inorg. Chem.* **2016**, *21* (5), 745-755. DOI: 10.1007/s00775-016-1380-9.

(38) Hooe, S. L.; Moreno, J. J.; Reid, A. G.; Dickie, D. A.; Machan, C. W. Homogeneous Electrocatalytic Reduction of CO2 by a CrN3O Complex: Electronic Coupling with Redox-Active Terpyridine Fragment Favors Selectivity for CO. *ChemRxiv* **2021**. DOI: 10.33774/chemrxiv-2021-lplvt.

(39) Li, Q.; Batchelor-McAuley, C.; Lawrence, N. S.; Hartshorne, R. S.; Compton, R. G. Anomalous solubility of oxygen in acetonitrile/water mixture containing tetra-n-butylammonium perchlorate supporting electrolyte; the solubility and diffusion coefficient of oxygen in anhydrous acetonitrile and aqueous mixtures. *Journal of Electroanalytical Chemistry* **2013**, *688*, 328-335. DOI: https://doi.org/10.1016/j.jelechem.2012.07.039.

(40) Fukuzumi, S.; Mochizuki, S.; Tanaka, T. Metalloporphyrin-Catalyzed Reduction of Dioxygen by Ferrocene Derivatives. *Chemistry Letters* **1989**, *18* (1), 27-30. DOI: 10.1246/cl.1989.27 (acccessed 2022/04/21).

(41) Fukuzumi, S.; Mochizuki, S.; Tanaka, T. Efficient reduction of dioxygen with ferrocene derivatives, catalyzed by metalloporphyrins in the presence of perchloric acid. *Inorganic Chemistry* **1989**, *28* (12), 2459-2465. DOI: 10.1021/ic00311a042.

(42) Wasylenko, D. J.; Rodríguez, C.; Pegis, M. L.; Mayer, J. M. Direct Comparison of Electrochemical and Spectrochemical Kinetics for Catalytic Oxygen Reduction. *Journal of the American Chemical Society* **2014**, *136* (36), 12544-12547. DOI: 10.1021/ja505667t.

(43) Grant, D. H. Paramagnetic Susceptibility by NMR: The "Solvent Correction" Reexamined. *J. Chem. Educ.* **1995**, *72* (1), 39. DOI: 10.1021/ed072p39.

(44) Bain, G. A.; Berry, J. F. Diamagnetic corrections and Pascal's constants. *J. Chem. Educ.* **2008**, *85* (4), 532-536, 10.1021/ed085p532. DOI: 10.1021/ed085p532.

(45) Hooe, S. L.; Rheingold, A. L.; Machan, C. W. Electrocatalytic Reduction of Dioxygen to Hydrogen Peroxide by a Molecular Manganese Complex with a Bipyridine-Containing Schiff Base Ligand. *Journal of the American Chemical Society* **2018**, *140* (9), 3232-3241. DOI: 10.1021/jacs.7b09027.

(46) Cook, E. N.; Dickie, D. A.; Machan, C. W. Catalytic Reduction of Dioxygen to Water by a Bioinspired Non-Heme Iron Complex via a 2+2 Mechanism. *J. Am. Chem. Soc.* **2021**, DOI: 10.1021/jacs.1021c04572.

(47) Saint, S. APEX3, Bruker AXS Inc. *Madison, WI, USA* **2012**.

(48) Sheldrick, G. SHELXT - Integrated space-group and crystal-structure determination. *Acta Crys. A* **2015**, *71* (1), 3-8. DOI: doi:10.1107/S2053273314026370.

(49) Dolomanov, O. V.; Bourhis, L. J.; Gildea, R. J.; Howard, J. A. K.; Puschmann, H. OLEX2: a complete structure solution, refinement and analysis program. *J. Appl. Cryst.* **2009**, *42* (2), 339-341. DOI: doi:10.1107/S0021889808042726.

(50) Spek, A. Structure validation in chemical crystallography. *Acta Cryst. D* **2009**, *65* (2), 148-155. DOI: doi:10.1107/S090744490804362X.

Chapter 4:

Controlling Product Selectivity During Dioxygen Reduction with Mn Complexes Using Pendent Proton Donor Relays and Added Base

Published as:

Cook, E.N; Courter, I. M.; Dickie, D. A.; and Machan, C.W.*, *Chemical Science* **2024**, 15, 4478-4488. doi: 10.1039/D3SC02611F.

4.1 Abstract

The catalytic reduction of dioxygen (O_2) is important in biological energy conversion and alternative energy applications. In comparison to Fe- and Co-based systems, examples of catalytic O_2 reduction by homogeneous Mn-based systems is relatively sparse. Motivated by this lack of knowledge, two Mn-based catalysts for the oxygen reduction reaction (ORR) containing a bipyridine-based non-porphyrinic ligand framework have been developed to evaluate how pendent proton donor relays alter activity and selectivity for the ORR, where Mn($^{p\text{-}tbu}$dhbpy)Cl (**1**) was used as a control complex and Mn(^{nPr}dhbpy)Cl (**2**) contains a pendent –OMe group in the secondary coordination sphere. Using an ammonium-based proton source, *N,N*′-diisopropylethylammonium hexafluorophosphate, we analyzed catalytic activity for the ORR: **1** was found to be 64% selective for H_2O_2 and **2** is quantitative for H_2O_2, with O_2 binding to the reduced Mn(II) center being the rate-determining step. Upon addition of the conjugate base, *N,N*′-diisopropylethylamine, the observed catalytic selectivity of both **1** and **2** shifted to H_2O as the primary product. Interestingly, while the shift in selectivity suggests a change in mechanism for both **1** and **2**, the catalytic activity of **2** is substantially enhanced in the presence of base and the rate-determining step becomes the bimetallic cleavage of the O–O bond in a Mn-hydroperoxo species. These data suggest that the introduction of pendent relay moieties can improve selectivity for H_2O_2 at the expense of diminished reaction rates from strong hydrogen bonding interactions. Further, although catalytic rate enhancements are observed with a change in product selectivity when base is added to buffer proton activity, the pendent relays stabilize dimer intermediates, limiting the maximum rate.

4.2 Introduction

Increasing atmospheric CO_2 concentrations has led to global warming and climate change, creating an undeniable need for renewable energy processes. Activation and reduction of dioxygen (O_2) is an attractive route for the development of alternative energy and industrial-scale oxidation reactions due to its abundance and oxidizing power. [1-9] The oxygen reduction reaction (ORR) to the $4H^+/4e^-$ product, H_2O, is an ideal cathodic half reaction in hydrogen fuel cells and selectivity for the $2H^+/2e^-$ product, H_2O_2, is also attractive because of the large-scale use of H_2O_2 as an oxidant in a number of industrial processes.[2,3,7,9-11] Molecular complexes offer a compelling way to study and optimize these electrocatalytic reactions because of the fidelity with which the active sites can be characterized relative to heterogeneous systems that may contain a distribution of active sites, as well as the possibility of using iterative synthetic modifications to test mechanistic hypotheses.

Interest in bioinspired and biomimetic systems has spurred the development of a significant number of Fe- and Co-based porphyrinic systems.[3,9,12,13] By comparison, Mn has been less widely studied, despite its reactivity toward O_2 and prevalence in dioxygen-dependent biological systems.[1,2,9] Because of the relatively high spin-pairing energy of Mn ions, open-shell configurations with side-on coordination modes of O_2 are often observed to be relatively stable on the potential energy surface of catalytic reactions, limiting activity.[2,14-16] This issue arises, in part, as a result of the low basicity of O atoms in side-on $Mn–O_2$ species, preventing effective protonation and cleavage of the O–O bond.[2,14] This remains a challenge in the development of Mn-based catalysts for ORR, where destabilization of side-on $Mn–O_2$ intermediates (and other stable reactive oxygen species, ROSs) is crucial to achieve enhanced rates of catalytic turnover (**Figure 4.1**).[2,14]

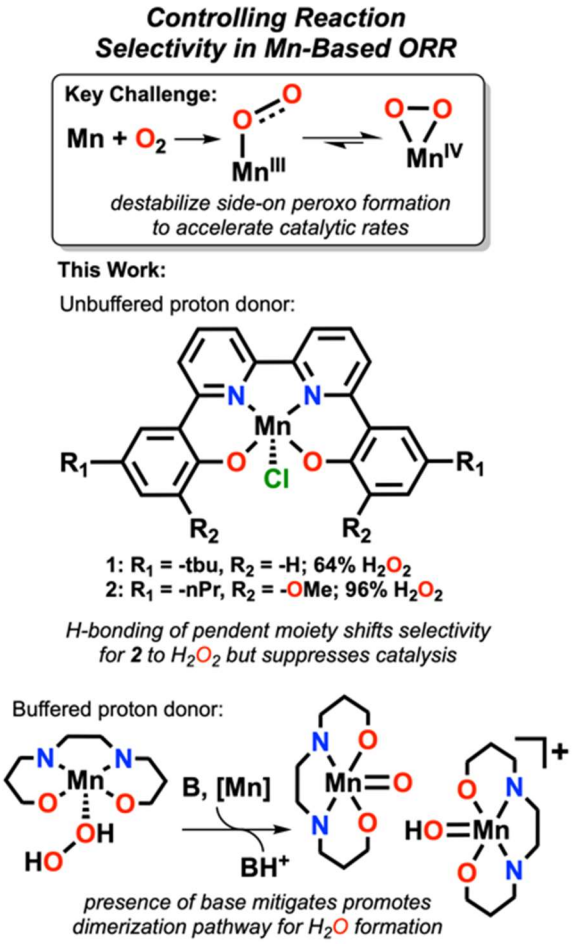

Figure 4.1. Summary of the work described here.

There are a number of strategies that can be employed to avoid stable Mn ROS intermediates, including synthetically modifying the supporting ligand framework to tune the electronic structure at the metal center, the introduction of hydrogen-bonding interactions that alter the potential energy surface for Mn–O_2 intermediates, or the use of steric hindrance at the active site.[2] For instance, to explore how secondary-sphere ligand modification influenced ORR activity and selectivity, Nocera and coworkers introduced a xanthene-based pendent hangman moiety in a Mn tetraphenylporphyrin complex for ORR.[17] They found that the hangman group promoted intramolecular proton transfer during catalysis and that hydrogen-bonding interactions between Mn-bound O_2 and proton donors helped to favor end-on coordination modes.[17] A firm fundamental understanding of how synthetic control over ORR at Mn-based active sites can avoid these

potential thermodynamic limitations during catalysis remains an important question. Among the reports on Mn-based ORR catalysts, there are only a handful of non-porphyrinic based systems, despite the possibilities for alternative synthetic approaches for reaction control.[2,18-23]

Previous studies on the electrochemical ORR mediated by Co(N_2O_2) molecular complexes with 2,2′-bipyridine based ligand backbone[24] found that the introduction of a –OMe pendent relay in the secondary coordination sphere resulted in a shift in selectivity from H_2O to H_2O_2, as well as a shift in the observed RDS based on acid strength.[25] It was hypothesized that directed protonation of the proximal oxygen of a Co–OOH intermediate was mediated by the pendent –OMe group.[25] Reasoning that pendent relays could favor end-on O_2 coordination and accelerate proton transfer in analogous Mn-based systems,[22,23,26] two new Mn-based non-porphyrinic electrocatalysts for ORR have been prepared. Using an alkyl ammonium-based proton source, it was found that a secondary sphere –OMe pendent relay shifts selectivity to quantitative H_2O_2 formation under unbuffered conditions (proton donor is present without its conjugate base), although the rate of catalysis is suppressed. However, under buffered conditions (the proton donor and its conjugate base are present in significant quantities), hydrogen bonding between the ligand framework and the added acid is mitigated, resulting in a dramatic increase in rate and a shift in selectivity to H_2O production. Interestingly, the shift in selectivity occurs in complexes with and without the pendent relay, with systematic variation of added base concentration implying that the change in mechanism is related to the deprotonation of a Mn(III)–OOH intermediate. Further, the complex with the pendent relay experiences a shift in rate-determining step (RDS) for catalysis under buffered conditions, which is proposed to originate from the pendent relay stabilizing Mn–O_2–Mn dimer formation relative to O_2 binding and activation.

Overall, the proposed mechanism suggests that the $4H^+/4e^-$ product H_2O is accessed by deprotonating an intermediate Mn(III) hydroperoxo species, implying that proton activity buffering at the pK_a of an intermediate metal hydroperoxo is a potential point of reaction control over the selectivity of product formation, as well as a mode of control over hydrogen-bonding interactions.

These observations are representative of the complexity of ORR with Mn active sites: proton transfer is required to facilitate the reduction of superoxide to hydroperoxide (which we attribute to the competition between end-on and side-on coordination modes), but O–O bond scission occurs most efficiently from a deprotonated peroxo intermediate.

4.3 Results and Discussion

4.3.1 Synthesis and Characterization

The $^{p\text{-}tbu}$dhbpy[H]$_2$ and ^{nPr}dhbpy[H]$_2$ ligands were synthesized according to previously reported procedures. [25] Metalation of $^{p\text{-}tbu}$dhbpy[H]$_2$ to generate Mn($^{p\text{-}tbu}$dhbpy)Cl **1** was achieved via a modified literature procedure,[22] where a stoichiometric amount of manganese(II) acetate tetrahydrate was sparged with compressed air, allowed to reflux with $^{p\text{-}tbu}$dhbpy[H]$_2$ for 3 hours in MeOH solution, and induced to precipitate by the addition of a saturated NaCl solution. Metalation of ^{nPr}dhbpy[H]$_2$ was achieved by an analogous synthetic procedure.

UV-vis, ESI-MS, and microanalyses are consistent with the proposed formulation of the Mn complexes shown in **Figure 4.1**. Evans' method measurements exhibited μ_{eff} = 4.78 ± 0.11 and μ_{eff} = 4.59 ± 0.10 for **1** and **2**, respectively; both values are consistent with high-spin d^4 Mn(III) complexes (**Tables S4.1** and **S4.2**).[27,28] Single crystals suitable for X-ray diffraction studies of complex **2** were grown by slow cooling of a saturated, boiling acetonitrile (MeCN) solution layered with diethyl ether. The solid-state structure of **2** is a dimeric species where a single O atom from each atom is coordinated in the axial position of a second equivalent of complex **2** to create a six-coordinate environment for each Mn center, analogous to our previous studies on a comparable Fe complex (**Figures 4.2C-2D**).[29]

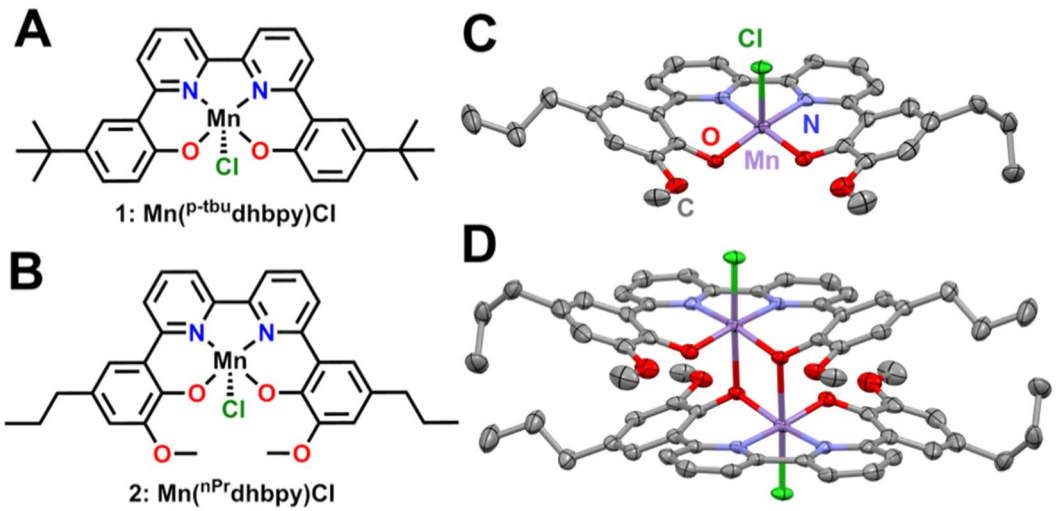

Figure 4.2. (A) Structure of **1** Mn($^{p\text{-}tbu}$dhbpy)Cl, (B) structure of **2** Mn(^{nPr}dhbpy)Cl, (C) Molecular structure of Mn(^{nPr}dhbpy)Cl **2** from single crystal X-ray diffraction studies showing the (D) dimeric solid-state species. Purple = Mn, red = O, green = Cl, gray = C; thermal ellipsoids 50%, H atoms and disordered atoms omitted for clarity. CCDC 2255849.

Diisopropylethylammonium hexafluorophosphate (DIPEAHPF$_6$) was synthesized according to a previously reported procedure.[30] Toluene was brought to reflux in the presence of ammonium hexafluorophosphate (PF$_6$) and diisopropylethylamine (DIPEA), resulting in the precipitation of a solid product after 48 hours. The suspension was cooled to 0°C on an ice bath before being filtered and washed with DCM. Rotary evaporation of the DCM solvent yielded a spectroscopically pure product: NMR spectroscopic characterization and microanalysis were consistent with a disopropylethylammonium salt with a PF_6^- counteranion. Single crystals suitable for X-ray diffraction studies were grown via slow evaporation from a concentrated DCM solution (**Figure S4.3**). ^{1}H NMR spectroscopy was used to estimate a pK_a of 18.7 for DIPEAHPF$_6$ in MeCN via titration and competition experiments (See SI).[31]

4.3.2. Electrochemical Analysis of 1 and 2

Cyclic voltammetry studies were performed on **1** and **2** in MeCN solution with 0.1 M tetrabutylammonium hexafluorophosphate (TBAPF$_6$) supporting electrolyte (**Figure 3**). Under an inert Ar atmosphere, **1** (**Figure S4.9**) and **2** (**Figure S4.16**) show reversible features attributed to

a Mn(III/II) redox event at –0.58 and –0.55 V vs. Fc^+/Fc, respectively. Variable scan-rate studies of both **1** and **2** under Ar gas saturation showed a diffusion-limited response, consistent with homogenous species (**Figures S4.8** and **S4.15**, respectively). Upon dioxygen (O_2) saturation, there is an observed slight increase in current density at the Mn(III/II) redox event as well as the partial loss of the return oxidation feature for both **1** (**Figure S4.9**) and **2** (**Figure S4.16**), indicative of a reaction involving O_2 and the reduced Mn(II) metal center. Conversely, there is a quasi-reversible redox feature observed at more negative potentials for **2** under O_2 saturation, suggestive of a Mn superoxide/peroxide reduction following O_2 binding and activation.

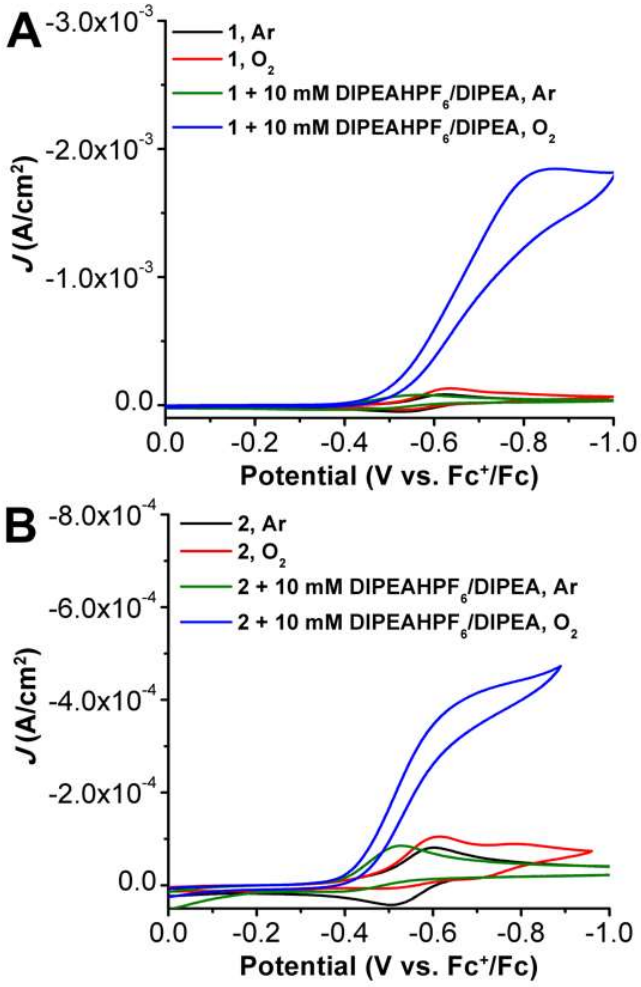

Figure 4.3. (A) CVs of Mn($^{p\text{-}tbu}$dhbpy)Cl **1** under Ar and O_2 with and without 10 mM $DIPEAHPF_6$/DIPEA present. (B) CVs of Mn(^{nPr}dhbpy)Cl **2** under Ar and O_2 with and without 10 mM $DIPEAHPF_6$/DIPEA present. Conditions: 0.5 mM Mn, 0.1 M $TBAPF_6$/MeCN; glassy carbon working electrode, glassy carbon rod counter electrode, Ag/AgCl pseudoreference electrode; referenced to Fc^+/Fc internal standard; 100 mV/s scan rate.

Initial addition of 10 mM of the $DIPEAHPF_6$ proton donor to both **1** and **2** under inert conditions resulted in the loss of reversibility of the Mn(III/II) redox couple as well as a shift to more positive potentials, $E_{p,a}$ = –0.56 V vs Fc^+/Fc for **1** (**Figure S4.9**) and –0.53 V vs Fc^+/Fc for **2** (**Figure S4.16**). This is consistent with a contribution from an *EC* mechanism (reversible electron transfer followed by an irreversible chemical reaction), which is proposed to be the protonation of an O atom in the inner-coordination sphere following formal reduction to Mn(II), consistent with our previous studies on acids with similar pK_a values.[22,32] Although titration of increasing amounts of $DIPEAHPF_6$ beyond 10 mM did not cause a further potential shift for **1**, the maximum positive potential shift for **2** was reached after the addition of 20 mM. Similarly, titration of increasing amounts of the $DIPEAHPF_6$ proton donor in the presence of 10 mM DIPEA revealed that the Mn(III) reduction potential observed for **1** and **2** shifted to more positive potentials, however this shift was not dependent on the concentration of $DIPEAHPF_6$ (**Figures S4.11** and **S4.17**).

The observation of these shifts in the presence of the proton donor and its conjugate base, as well as the absence of a Nernstian relationship suggested that the axial chloride ligand was participating in related chemical steps during the *EC* mechanism. To better understand the role of DIPEA and $DIPEAHPF_6$ in axial Cl^- ligand solvation, CVs of **1** (**Figure S4.13** and **S4.14**, respectively) were taken in the presence of 0.1 M TBACl. The addition of increasing amounts of both DIPEA by itself and $DIPEAHPF_6$ with a fixed concentration of DIPEA (buffered) in the presence of excess Cl^- under Ar saturation conditions suppressed positive potential shifts of the Mn(III/II) redox feature in **1**. The suppression of the potential shift in the presence of excess Cl^- suggests that the shift observed originally is due to axial ligand solvation. Since it was observed that increasing concentrations of $DIPEAHPF_6$ led to a loss of reversibility for the Mn(III/II) feature, these data taken in aggregate imply that axial Cl^- ligand loss enables protonation of the O atom in the inner coordination sphere upon reduction.

Similar studies were conducted on **2**, where the addition of 0.1 M TBACl to a solution of **2** resulted in a negative potential shift of a quasireversible Mn(III/II) feature to –0.76 V vs. Fc^+/Fc

(**Figure S4.22)**. Addition of 10 mM DIPEA caused a positive potential shift of this Mn(III/II) redox feature back to –0.56 V vs. Fc^+/Fc (**Figure S4.22**) and the titration of increasing amounts of $DIPEAHPF_6$ under buffered conditions suppressed the observed positive potential shift (**Figure S4.23**). As was the case with complex **1**, it is hypothesized that the presence of both DIPEA and $DIPEAHPF_6$ contribute to axial Cl^- ligand loss for **2**, with irreversibility again suggesting protonation of a ligand O atom bound to Mn. Consistent with this, UV-vis spectroscopic analysis of **1** and **2** in the presence of DIPEA and $DIPEAHPF_6$ showed no evidence of interaction with Mn(III) (**Figures S4.58-S4.61**).

Under O_2 saturation in the presence of 10 mM $DIPEAHPF_6$, there is an increase in current at the Mn(III/II) reduction feature for both **1** (**Figure S4.9**) and **2** (**Figure S4.16**), indicative of electrocatalytic activity for the ORR. Likewise, under O_2 saturation in the presence of buffered $DIPEAHPF_6$ (1:1 ratio of ammonium to its conjugate base), there is an increase in current density at the Mn(III/II) redox couple for both **1** and **2**, consistent with catalytic O_2 reduction (**Figure 4.3**). Effective overpotentials (η) for the ORR by **1** and **2** calculated under buffered conditions were determined to be 0.58 and 0.56 V, respectively. Notably, the catalytic current density observed under buffered conditions with complex **2** is much higher than unbuffered conditions (**Figure S4.19**), suggesting that the presence of conjugate base enhances electrocatalytic ORR by **2**, *vide infra*. Oxidative current due to amine oxidation precludes the use of rotating ring-disk methods for H_2O_2 detection under these conditions for both **1** and **2** (**Figure S4.24**).

4.3.3. Spectrochemical Studies with 1 and 2

Catalytic ORR experiments with **1** and **2** were then run under spectrochemical conditions using decamethylferrocene (Cp^*_2Fe) as a chemical reductant in solution with the DIPEAH proton donor under unbuffered and buffered (1:1 ratio of $DIPEAHPF_6$ to DIPEA) conditions. UV-vis stopped-flow spectroscopy was used to determine the kinetic parameters of the ORR by monitoring the accumulation of oxidized $[Cp^*_2Fe]^+$ at 780 nm (Figure 4). Consistent with the electrochemical data, ORR by 1 showed minimal differences in activity under catalytic conditions

with buffered and unbuffered proton donor (Figure 4A). Likewise, the catalytic response mediated by 2 showed a significant enhancement under buffered conditions compared to unbuffered (Figure 4B), similar to what was observed under electrochemical conditions, *vide supra*.

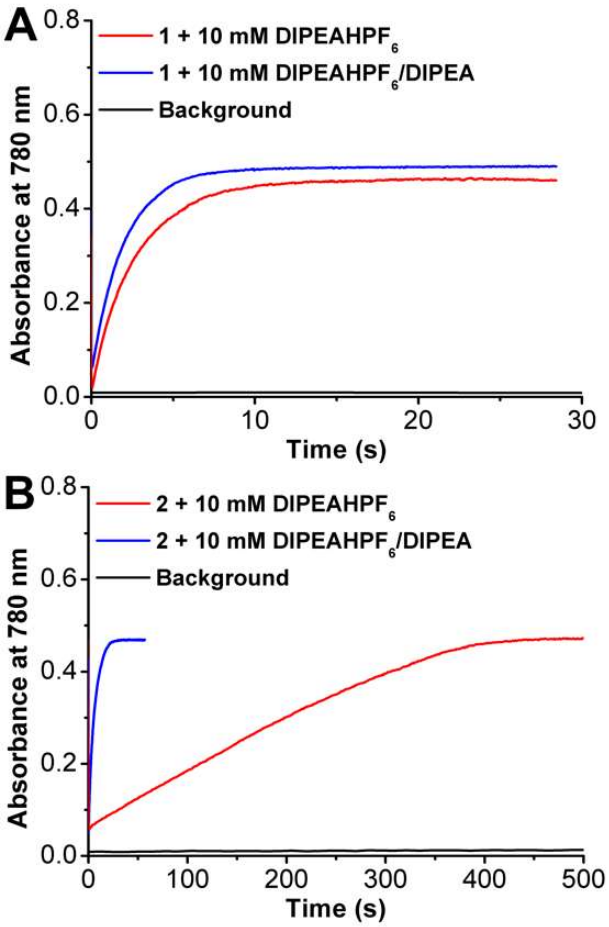

Figure 4.4. Change in absorbance at 780 nm over time as a result of the formation of $[Cp^*_2Fe]^+$ by ORR catalyzed by Mn($^{p\text{-}tbu}$dhbpy)Cl **1** (**A**) with $DIPEAHPF_6$ (red) and $DIPEAHPF_6$/DIPEA (blue) and Mn(^{nPr}dhbpy)Cl **2** (**B**) with $DIPEAHPF_6$ (red) and $DIPEAHPF_6$/DIPEA (blue). Black: buffered control. Conditions: 40 μM [Mn], 4.05 mM [O_2], 1 mM [Cp^*_2Fe], 10 mM [$DIPEAHPF_6$/DIPEA]; control: 4.05 mM O_2, 1 mM Cp^*_2Fe, 12.5 mM $DIPEAHPF_6$/DIPEA.

Variable concentration studies with **1** and $DIPEAHPF_6$ under unbuffered conditions revealed a rate law for the ORR with first-order dependencies on [**1**] and [O_2] and zero-order dependencies on [$DIPEAHPF_6$] and [Cp^*_2Fe] (**Figures S4.36-S4.39**), corresponding to the rate law shown in **Eq (4.1)**.

$$rate_{unbuffered} = k_{cat}[Mn^{p-tbu}]^1[O_2]^1 \quad \textbf{Eq (4.1)}$$

A $Ti(O)SO_4$ colorimetric assay was used to determine the selectivity of the ORR as previously described.[23,33] Aliquots were taken after the reaction was allowed to reach completion and the amount of H_2O_2 produced was quantified. Selectivity testing under unbuffered conditions revealed that **1** is 64.2 ± 6.9% selective for H_2O_2 corresponding to an n_{cat} of 2.72 (**Figure S4.26** and **Table 4.1**). Under these unbuffered conditions (only proton donor present), control studies showed no degradation of H_2O_2 via disproportionation, with quantitative recovery of H_2O_2 (**Figure S4.28** and **Table S4.6**).

Similarly, variable concentration studies of ORR by **2** with unbuffered $DIPEAHPF_6$ showed first-order dependencies on [**2**] and [O_2] (**Figures S4.45-S4.49**). Selectivity studies showed 96.2 ± 4.1% H_2O_2 selectivity corresponding to an n_{cat} = 2.08 (**Figure S4.27** and **Table S4.5**), with control studies showing that 93.6 ± 4.6% H_2O_2 was recovered after 20 minutes (**Figure S4.29** and **Table S4.7**), consistent with very slight activity for H_2O_2 disproportionation. Notably, the observation of an increased amount of the H_2O_2 product for complex **2** – which contains pendent proton donor relays – mirrors similar observations made with Co-based analogues of these compounds previously.[25] Thus, **Eq (4.2)** is proposed as the rate law for ORR mediated by **2** under unbuffered conditions.

$$rate_{unbuffered} = k_{cat}[Mn^{nPr}]^1[O_2]^1 \quad \textbf{Eq (4.2)}$$

Subsequent re-examination of **1** under buffered conditions (equal amounts of ammonium proton donor and its conjugate base) showed first-order dependencies on [**1**] and [O_2] and zero-order dependencies on [1:1 $DIPEAHPF_6$:DIPEA] and [Cp^*_2Fe] (**Figures S4.40-S4.44**). Systematically varying the concentration of either [$DIPEAHPF_6$] or [DIPEA] against a fixed concentration of the other also exhibited no concentration dependence on the catalytic reaction (**Figure S4.42**). Selectivity studies revealed that after 15 s, **1** showed 81.9 ± 4.1% selectivity for H_2O as the product (**Figure S4.30** and **Table 4.1**). H_2O_2 disproportionation was observed under

catalytic conditions: only 10.8 ± 6.6% H_2O_2 was recovered after 105 s with 1:1 DIPEAHPF$_6$:DIPEA present (**Figure S4.32** and **Table S4.10**). Interestingly, control studies under buffered catalytic conditions without the presence of O_2 revealed minimal degradation of H_2O_2 by the Mn(II) form of the complex (**Figure S4.34** and **Table S4.12**), suggesting that the observed reaction selectivity difference is not due to disproportionation alone. These results are summarized in the following rate law, **Eq (4.3)**, for ORR mediated by **1** under buffered conditions:

$$rate_{buffered} = k_{cat}[Mn^{p-tbu}]^1[O_2]^1 \qquad \textbf{Eq (4.3)}$$

Conversely, variable concentration studies of ORR catalyzed by **2** under buffered conditions revealed mechanistic differences in comparison to the data obtained for **1** and **2** under unbuffered conditions, as well as a change in selectivity. The ORR mediated by **2** showed a second-order dependence on [**2**], a first-order dependence on [1:1 DIPEAHPF$_6$:DIPEA], an inverse first-order dependence on [Cp*$_2$Fe] and a zero-order dependence on [O_2] (**Figures S4.49-S4.53**). Unlike **1**, when [DIPEA] was varied against a fixed concentration of [DIPEAHPF$_6$] with **2**, a first-order dependence on rate was observed; experiments where [DIPEAHPF$_6$] was varied against a fixed [DIPEA] showed a zero-order dependence. These results lead to the proposed rate law shown in **Eq (4.4)**. The observed first-order dependence on [DIPEA] implies that the dependence observed on [1:1 DIPEAHPF$_6$:DIPEA] is a result of varying DIPEA concentration. This interpretation is validated by the zero-order dependence on [DIPEAHPF$_6$] with fixed [DIPEA], ruling out proton activity or proton donor concentration as influencing the observed reaction rate.

$$rate = k_{cat}[Mn^{nPr}]^2[DIPEA]^1[Cp^*{}_2Fe]^{-1} \qquad \textbf{Eq (4.4)}$$

Selectivity studies of ORR under buffered conditions showed that after 15 s, **2** is 62.1 ± 6.7% selective for H_2O (**Figure S4.33** and **Table 4.1**). Control studies showed H_2O_2 degradation consistent with disproportionation: after 150 s only 3.81 ± 0.83% of H_2O_2 was recovered under buffered conditions with complex **2**. Again, H_2O_2 reduction was not observed under the buffered

catalytic conditions when placed under an inert N_2 atmosphere, suggesting that the change in selectivity is not exclusively due to disproportionation (**Figure S4.35** and **Table S4.13**).

Table 4.1. Summary of ORR selectivity under spectrochemical conditions of **1** and **2** under unbuffered and buffered conditions.

	Unbuffered		Buffered (15 s)	
	% H_2O_2	%H_2O	%H_2O_2	%H_2O
1	64.2 ± 6.9	35.8 ± 6.9	18.1 ± 4.1	81.9 ± 4.1
2	96.2 ± 4.1	3.8 ± 4.1	37.9 ± 6.7	62.1 ± 6.7

4.3.4. Computational Studies on Complex 2

To evaluate the initial steps of the reaction, computational studies on the thermodynamic positioning of likely intermediates for complex **2** during O_2 reduction to H_2O_2 were subsequently undertaken (see SI for details). Geometry optimization was done with the Gaussian 16 package[34] at B3LYP-D3(BJ)/def2-SVP level[35-42] with a complete structural model and single point calculations for refining energy differences were completed with Orca 5.0[43] at the ωB97M-D4/def2-TZVPP level.[39,40,44-48] At this level of theory, the calculated reduction potential of –0.53 V vs $Fc^{+/0}$ showed satisfactory agreement with the experimental potential of –0.55 V. Further, the anticipated ground states of S=2 for Mn(III) and S=5/2 for Mn(II) in this coordination environment were accurately reproduced, lending confidence to the chosen method.[22] Electron transfer-proton transfer (ET-PT), proton transfer-electron transfer (PT-ET), and concerted electron-proton transfer (CEPT) pathways for reaction steps where a net hydrogen atom transfer occurred were considered; in all cases CEPT was found to be the most favorable and produced results consistent with experimental observation.

The most probable thermodynamic step from the starting complex $[Mn(^{nPr}dhbpy)(Cl)]^0$ under protic conditions is reduction followed by a hydrogen-bonding interaction between the ligand framework and an equivalent of $[DIPEAH]^+$ to generate $[Mn(^{nPr}dhbpy[AH])(Cl)]^0$. (**Figure 4.5**). Note that the [AH] notation indicates the hydrogen-bonding interaction involving a Mn-bound O atom from the ligand framework. Although formal proton transfer to the ligand framework with loss

of DIPEA is exergonic by –7.2 kcal/mol, the binding of O_2 with accompanying Cl^- release to generate the cationic species [Mn(^{nPr}dhbpy[H])(η^2-O_2)]$^+$ is uphill by 34.2 kcal/mol, precluding its involvement in the catalytic cycle. Instead, O_2 binding with loss of [DIPEAH][Cl] is endergonic by 20.2 kcal/mol, which is consistent with experimental observations, generating [Mn(^{nPr}dhbpy)(η^2-O_2)]^0. In this structure, the bound O_2 is in a side-on coordination mode with a bond length of 1.309 Å, consistent with reduction to superoxide, $O_2^{\bullet-}$. Reduction and protonation of this species had a favorable CEPT pathway (–0.01 V vs $Fc^{+/0}$), where proton transfer has occurred from [DIPEAH]$^+$ to generate [Mn(^{nPr}dhbpy)(η^1-O_2H)]^0. The shift in coordination mode of the O_2 fragment from side-on to end-on reflects additional reduction: the bond lengthens to 1.451 Å, consistent with a peroxide. Protonation of the distal O atom to generate [Mn(^{nPr}dhbpy)(η^1-O_2H_2)]$^+$ by an equivalent of [DIPEAH]$^+$ is endergonic by 9.9 kcal/mol and displacement by Cl^- to facilitate H_2O_2 release is favorable by –23.6 kcal/mol. These reaction steps align with experimental observations on the catalytic cycle which produces H_2O_2 under unbuffered conditions.

Next the favorability of dimerization from the hydroperoxide was assessed to explore the implied dimeric pathway to H_2O production (**Figure S4.77**). The experimental studies described above established the viability of H_2O_2 as an intermediate species, therefore the [Mn(^{nPr}dhbpy)(η^1-O_2H_2)]$^+$ adduct was considered as the starting point. Deprotonation of Mn-bound H_2O_2 by DIPEA to generate [Mn(^{nPr}dhbpy)(η^1-O_2H)]^0 is favorable by 9.9 kcal/mol. Subsequent dimerization of [Mn(^{nPr}dhbpy)(η^2-O_2H)]^0 with an equivalent of [Mn(^{nPr}dhbpy)(Cl)]^0 is endergonic by 19.7 kcal/mol, with [Mn(^{nPr}dhbpy)(O)]^0 (S=3/2), [Mn(^{nPr}dhbpy)(OH)]$^+$ (S=3/2), and Cl^- as the products. Attempts to examine a stabilized bridging hydroperoxo dimer were unsuccessful, homolytic O–O bond scission occurred spontaneously in all cases. From the terminal manganese oxo [Mn(^{nPr}dhbpy)(O)]^0, a calculated CEPT potential of +1.00 V vs Fc^+/Fc was obtained for the production of a Mn(III) hydroxide [Mn(^{nPr}dhbpy)(OH)]^0, while the convergent pathway via the reduction of [Mn(^{nPr}dhbpy)(OH)]$^+$ was estimated to be +0.62 V; both processes are expected to be facile at the considered operating potential of –0.55 V vs Fc^+/Fc. Protonation of the neutral

Mn–OH species to make the corresponding aquo species is uphill by 1.2 kcal/mol and subsequent H_2O loss with Cl^- coordination to Mn to regenerate the starting species and close the H_2O_2 reduction cycle is downhill by –20.2 kcal/mol.

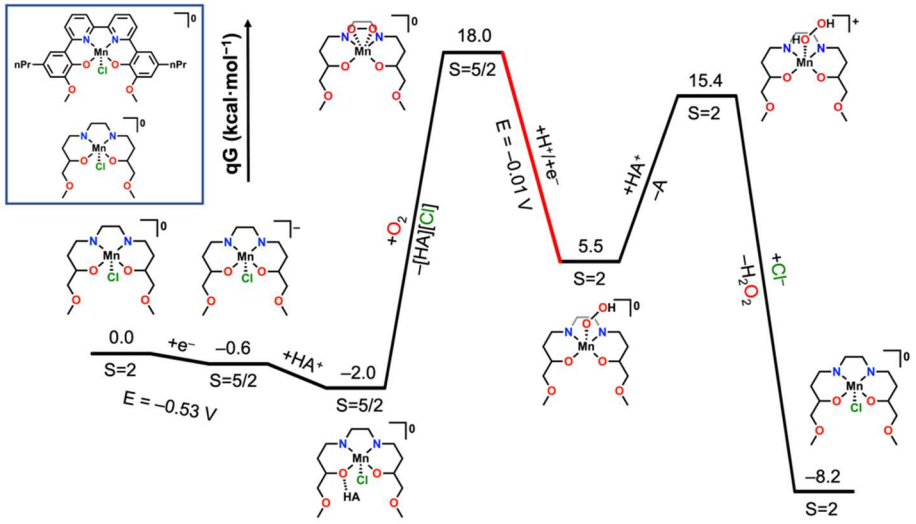

Figure 4.5. Free energy diagram from DFT methods showing key thermodynamic intermediates in the production of H_2O_2 by complex **2**. Diagram considers the operating potential of catalysis to be –0.55 V vs $Fc^{+/0}$ and red indicates CEPT steps. DIPEA = A and $DIPEAH^+$ = HA^+.

4.3.5. Discussion

From the data summarized above, we are able to propose the following mechanisms for the ORR catalyzed by **1** and **2** under unbuffered and buffered conditions, described in **Scheme 4.1**. Starting at *i*, the reduction of Mn(III) to Mn(II) induces a hydrogen-bonding interaction between $[DIPEAH]^+$ and the O atom in the inner coordination sphere to form *ii*, the resting state of the catalyst in solution. It is likely that this species exists in equilibrium with formal proton transfer, based on DFT results, UV-vis studies on chemically reduced species (**Figures S4.64** and **S4.71**), and the observed irreversibility of the Mn(III)/(II) reduction. Control studies showed that neither $DIPEAHPF_6$ or DIPEA interacted substantially with complexes in the Mn(III) oxidation state

(**Figures S4.58-S4.61**). However, formal proton transfer renders O_2 binding to Mn less favorable by 14 kcal/mol according to DFT methods, indicating that this pathway isn't viable catalytically.

Scheme 4.1. Proposed catalytic cycle for ORR, with the key equilibrium for switching between the two reaction pathways indicated in gray.

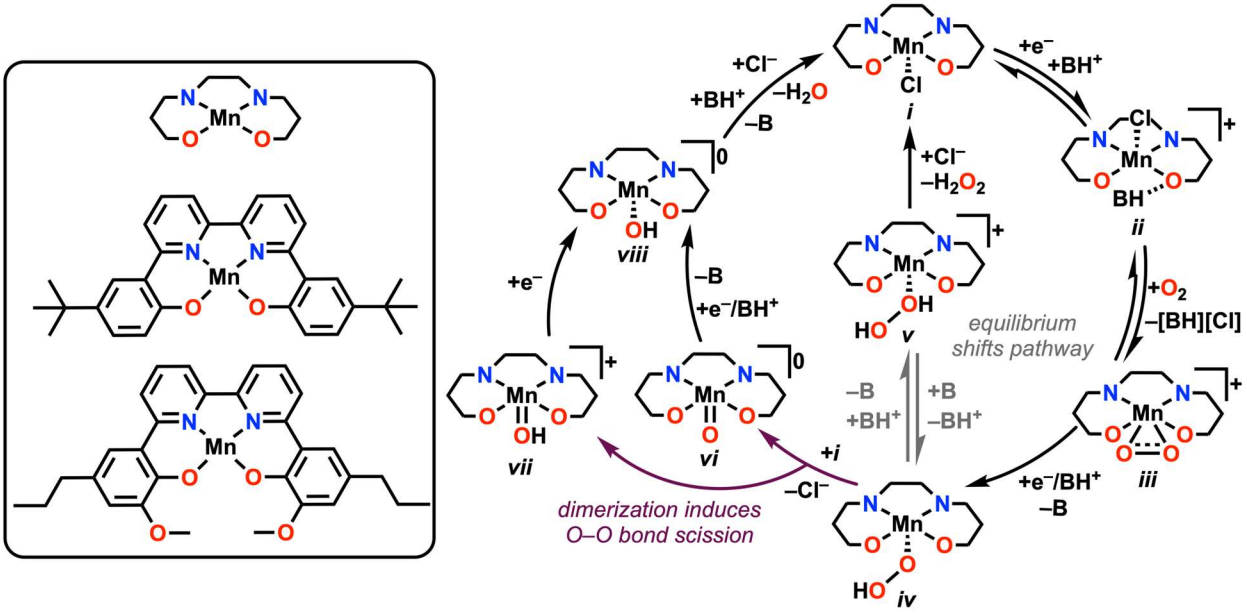

Following this activation of the catalyst, rate-limiting O_2 binding to Mn(II) to form a Mn(III)-superoxide species, *iii*, occurs with loss of [DIPEAH][Cl]. Based on this assignment, species *ii* is considered to be the resting state of the catalytic cycle under these conditions. Reduction and protonation by a CEPT pathway results in the formation of a Mn-hydroperoxo species, *iv*, whose protonation leads to the formation of a Mn–H_2O_2 intermediate, *v*. This is the primary reaction pathway for **1** (64.2 ± 6.9% selectivity) and **2** (96.2 ± 4.1% selectivity) under unbuffered conditions, as suggested by selectivity studies and the relative absence of activity for H_2O_2 disproportionation in separate testing. The observed selectivity enhancement for H_2O_2 during ORR mediated by **2** is consistent with the participation of the pendent methoxy group in hydrogen bonding interactions with added acid, as we have observed previously.[25] This mechanistic proposal is consistent with the general thermodynamic landscape obtained by DFT methods (**Figure 4.5**). It is worth noting that H_2O_2 disproportionation is observed by the parent Mn(III) species of both complexes in the

presence of DIPEA. Further, control studies with Mn(II) revealed minimal interaction with H_2O_2 (**Figure S4.34**), suggesting that disproportionation is reliant on the availability of formally Mn(III) complexes.

Under buffered conditions, complex **2** demonstrated a substantial increase in the observed catalytic rate in comparison to unbuffered conditions with an accompanying mechanistic divergence involving dimerization. While we do not observe a change in the rate-determining step or infer a change in the resting state for **1**, it is proposed that the shift in selectivity from H_2O_2 under unbuffered conditions to H_2O under buffered conditions is similarly due to the accessibility of a dimerization pathway in the presence of added base. Based on the experimental and computational data presented, it is likely that the observed mechanistic divergence arises from differences in equilibrium control over the speciation of complexes *iv* and *v*, as depicted in **Eq (4.5)**.

$$Mn(O_2H) + BH^+ \rightleftharpoons [Mn(H_2O_2)]^+ + B \qquad \textbf{Eq (4.5)}$$

Therefore, under buffered conditions, an alternative reaction pathway dominates the observed selectivity. With suitable concentrations of base present, **Eq (4.5)** shifts to the left, favoring the hydroperoxo species, *iv*, which becomes the resting state for **2** under buffered conditions. Species *iv* dimerizes with an equiv of the Mn(III) complex *i* leading to the formation of species *vi* and *vii* from O–O bond cleavage, with accompanying chloride loss. Following one-electron reduction or a one-electron CPET process, these products converge at a Mn(III) hydroxide species *viii*. Following this, formal protonation and displacement of H_2O by Cl^- complete the catalytic cycle. For complex **2**, O–O bond cleavage from dimerization becomes the RDS of the reaction, which is attributed to the pendent relay groups stabilizing the dimer intermediate through coordination and hydrogen bonding. This proposal is consistent with the second-order rate dependence on [Mn] and first-order rate dependence on [DIPEA] under buffered conditions. Further, the inverse first-order dependence observed for [Cp^*_2Fe] implies that Mn(III) is required

for dimer formation, rather than Mn(II). This reaction pathway is in good agreement with that computed using DFT methods (**Figure S4.77**).

The differences in ORR catalyzed by **2** under unbuffered and buffered conditions in comparison to **1** suggest an important role for the pendent –OMe moiety in the secondary coordination sphere, as well as for the added base. Under unbuffered conditions, catalytic activity of **2** is suppressed in comparison to **1**, which is observed under both electrochemical and spectrochemical conditions. This is attributed to strong hydrogen-bonding interactions between the –OMe groups and $DIPEAHPF_6$ kinetically inhibiting O_2 binding, the rate-determining step of the catalytic cycle. In addition to catalytic suppression, we observe a shift in selectivity from approximately 64% for H_2O_2 by **1** to 96% for H_2O_2 by **2** under unbuffered catalytic conditions. As introduced above, we propose that the observed shift in product selectivity is due to the hydrogen-bonding interaction of the –OMe group assisting in proton transfer to the proximal Mn–OOH oxygen in species *iv*, as we have previously suggested in similar Co systems.[25]

Interestingly, upon the addition of the DIPEA conjugate base to catalytic conditions with **2**, catalysis is significantly enhanced under electro- and spectrochemical conditions. There is an accompanying change in mechanism, where the equilibrium responsible for H_2O_2 formation becomes unfavorable, allowing dimerization with accompanying O–O bond scission to become rate-determining. It is also likely that DIPEA mitigates the effects of the strong H-bonding interaction between $DIPEAHPF_6$ and the –OMe moiety, allowing an increased rate of hydroperoxo intermediate generation. Indeed, in control studies with **2** chemically reduced to Mn(II) by $CoCp_2$ *in situ,* the addition of $DIPEAHPF_6$ inhibited reactivity with O_2: under unbuffered conditions the reaction between **2** and O_2 took approximately 100 min to go to completion (**Figure S4.72**), compared with approximately 25 m for complex **1** (**Figure S4.65**). It is also worth noting the difference in selectivity under buffered conditions between **1** and **2**, where **1** is 81.9% selective for H_2O (**Table 4.1**) and **2** is only 62.7% selective for H_2O. We attribute this difference to the H-bonding ability of the –OMe groups of **2** promoting the formation of species *v* during catalysis by

directing the proton donor. However, the dimer pathway to water formation is the primary pathway under buffered conditions, as evidenced by the shift in observed rate law and the shift in product selectivity to H_2O.

The observed rate constants (R_{fit}/n_{cat} values) under identical buffered conditions for **1** and **2** were k_{obs} = 1.23 ± 0.17 x 10^{-1} s^{-1} and k_{obs} = 0.706 ± 0.25 x 10^{-1} s^{-1}, respectively. While addition of one equivalent of conjugate base for every equivalent of proton donor mitigates some of the hydrogen-bonding induced suppression observed for **2** under unbuffered conditions, the accompanying stabilization of the intermediate dimer results in a slight decrease in the rate of catalysis relative to **1**. Therefore, it has been demonstrated that the introduction of a pendent relay into homogeneous molecular Mn-based electrocatalysts plays an essential role in ORR through the hydrogen bond-assisted stabilization of key intermediates and by favoring the direct protonation of the proximal oxygen of the Mn-OOH intermediate. The relative hydrogen-bond donor ability of $DIPEAHPF_6$ is such that inhibition of catalysis can also occur, which is mitigated through the introduction of the conjugate base. However, the mitigation of this effect results in a change in mechanism, where O–O bond scission occurs after dimerization. Thus, the conjugate base plays an important role during catalysis, allowing for an on-cycle dimer pathway that shifts the reaction pathway towards the formation of water.

It is worth briefly discussing the comparison between the data reported here for **1** and those reported previously with phenolic proton donors for a related complex with additional *tert*-butyl substituents.[22,23] With buffered phenolic proton donors, the observed rate law for the ORR mediated by this more sterically hindered complex showed first-order dependencies on the on [catalyst] and [O_2], but no dependence on proton donor activity. Similarly, the results obtained in the presence of a buffered ammonium proton donor with higher activity (pK_a(MeCN) = 18.7) described here again demonstrate that proton activity is not relevant to the observed rate laws. The observed relevance of an off-cycle *EC* reaction involving the protonation of the ligand framework also aligns with the results of a potential-pK_a diagram obtained during the previous

study where acids with pK_a < 20.11 were found to protonate the ligand framework of the tetra *tert*-butylated complex. The systems reported here show greater stability with respect to any H_2O_2 generated, which we had previously observed not to be the case in the presence of phenol and phenolate derivatives, consistent with the ease with which they can be oxidized as well as their competency as ligands relative to the sterically hindered ammonium/amine pairs used here.[49,50] Indeed, control testing shows that the DIPEA does not react under experimental conditions (**Figures S4.58-S4.59**) and is too sterically hindered to coordinate to Mn.

4.4. Conclusions

Here we report the synthesis and characterization of two new Mn(N_2O_2) homogeneous catalysts for ORR with an ammonium-based proton source in MeCN solution. Introduction of a pendent –OMe group in the secondary coordination sphere proved to play an important role during catalysis. Under unbuffered conditions, the pendent relay enabled quantitative selectivity for H_2O_2 due to directed protonation of the proximal O atom in a key Mn(III)–OOH intermediate. However, strong hydrogen-bonding interactions between the proton source and the pendent –OMe moiety suppressed catalytic activity. The addition of the proton donor's conjugate base enhanced the catalytic response and shifted the rate-determining step to O–O bond cleavage in an on-cycle Mn-peroxo dimer species. These results describe the importance of secondary sphere ligand modifications in the tunability of catalytic ORR mediated by Mn complexes, including the role of hydrogen-bond donor ability in directing product selectivity and the benefits of buffered conditions. Destabilization of certain Mn–O_2 intermediates can be achieved through secondary sphere modifications, however, later steps in the catalytic cycle must also be considered, since they can impact in negative ways. The continued challenge for improved Mn-based ORR catalysts is to drive the initial O=O reduction with a proton donor while retaining activity for subsequent O–O bond scission. Based on these conclusions, we are exploring the use of proton relays with variable basicity in ligand frameworks which disfavor dimerization, in order to improve the activity of monomeric catalyst pathways mediated by Mn complexes.

4.5. Supporting Information for Chapter 4

Materials and Methods

General Considerations

All chemicals and solvents (ACS or HPLC grade) were commercially available and used as received unless otherwise indicated. For all air-sensitive reactions and electrochemical experiments, HPLC-grade solvents were obtained as anhydrous and air-free from a PPT Glass Contour Solvent Purification System. Gas cylinders were obtained from Praxair (Ar as 5.0; O2 as 4.0) and passed through activated molecular sieves prior to use. Gas mixing for variable concentration experiments was accomplished using a gas proportioning rotameter from Omega Engineering. UV-vis absorbance spectra were obtained on a Cary 60 from Agilent. An Anton-Parr Multiwave Pro SOLV, NXF-8 microwave reactor was used for microwave syntheses. The concentration of O2 saturation in MeCN is reported to be 8.1 mM and the saturation concentration in MeCN with added electrolyte to be 6.3 mM.[51]

Synthesis and Characterization

Synthesis of Mn($^{p\text{-}tbu}$dhbpy)Cl

$^{p\text{-}tbu}$dhbpy[H]$_2$ was synthesized according to our previously reported procedure. [25] Mn($^{p\text{-}tbu}$dhbpy)Cl was synthesized according to previously reported procedures. [22] To a 2-neck, 100 mL round bottom flask, $^{p\text{-}tbu}$dhbpy[H]$_2$ (0.200 g, 0.442 mmol) was added with 50 mL of methanol and allowed to reflux for 1 h. Then, manganese(II) acetate tetrahydrate (0.108 g, 0.442 mmol) was added with dichloromethane (10 mL) and sparged with compressed air for 2 minutes. The dark green solution was allowed to reflux for 3 hours. After this time, saturated NaCl solution (50 mL) was added to the flask resulting in a dark reddish-brown suspension. The suspension was filtered, dissolved in DCM, and extracted with saturated NaCl solution (3 x 100 mL). The organic layer was separated, dried over $MgSO_4$ and the solvent was removed under reduced pressure to yield a reddish-brown solid. The solid was then dissolved in 1:1 DCM:MeCN, passed through a syringe filter and the solvent was removed under pressure to yield a reddish-brown solid. Finally, the solid was

recrystallized in DCM and hexanes to yield a spectroscopically pure product in 46% yield (0.203 mmol, 0.11 g). Elemental analysis for $C_{30}H_{30}ClMnN_2O_2$ calc'd: C 66.61; H 5.59; N 5.18, found: C 66.31, H 5.98, N 5.15. ESI-MS (*m/z*) $[M - Cl]^+$: calc'd: 505.1688; found 505.1675.

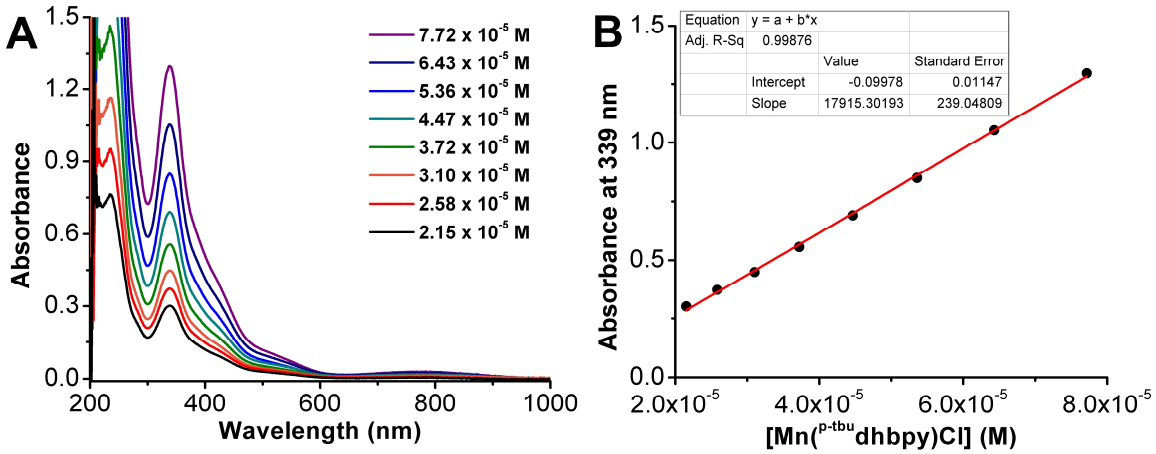

Figure S4.1. (A) UV-vis serial dilution absorbance data from Mn($^{p\text{-tbu}}$dhbpy)Cl **1** in MeCN solution. Conditions: varying concentration; quartz cell with 1 cm pathlength. (B) Plot of absorbance concentration (M) for Mn($^{p\text{-tbu}}$dhbpy)Cl 1 in MeCN solution at 339 nm (17915 $M^{-1}cm^{-1}$); R^2=0.999. All: λ_{max} = 236 nm (44786 $M^{-1}cm^{-1}$), 422 nm (5320 $M^{-1}cm^{-1}$), 525 nm (1269 $M^{-1}cm^{-1}$), 777 nm (410 $M^{-1}cm^{-1}$).

Table S4.1. Summary of Evans' Method Data from Mn($^{p\text{-tbu}}$dhbpy)Cl **1** in *N,N'*-DMF (chosen for solubility reasons) supporting a high-spin d^4 complex.

Trial	Chemical Shift (ppm)	Chemical Shift (Hz)	Total Magnetic Moment (emu mol^{-1})	Paramagnetic Moment (emu mol^{-1})	μ_{eff} (Bohr Magnetons)
1	0.12	72	8.94 x 10^{-3}	9.33 x 10^{-3}	4.72
2	0.12	72	8.94 x 10^{-3}	9.33 x 10^{-3}	4.72
3	0.13	78	9.69 x 10^{-3}	1.01 x 10^{-2}	4.90

Synthesis of Mn(^{nPr}dhbpy)Cl

^{nPr}dhbpy$[H]_2$ was synthesized according to our previously reported procedure. Mn(^{nPr}dhbpy)Cl was synthesized according to previously reported procedures. To a 2-neck, 100 mL round bottom flask, ^{nPr}dhbpy$[H]_2$ (0.195 g, 0.4 mmol) was brought to reflux in 75 mL methanol for 1 h. After this time, manganese(II) acetate tetrahydrate (0.104 g, 0.4 mmol) and DCM (10 mL) were added to the reaction mixture and the solution was sparged with compressed air for 2 minutes, which then turned dark green. After refluxing for 5 hours, saturated NaCl was added (75 mL). The suspension was filtered, dissolved in DCM, and extracted with saturated NaCl (3 x 100 mL). The organic layer

was separated and dried over $MgSO_4$, passed through a syringe filter and the solvent was reduced under pressure to yield a dark brown solid. The solid was recrystallized in minimal THF and excess hexanes to yield pure product in 24% yield (55 mg). Elemental analysis for $C_{30}H_{30}ClMnN_2O_2$•1/3CH_2Cl_2 calc'd: C 60.59; H 5.14; N 4.66, found: C 60.45, H 5.02, N 5.07. ESI-MS (*m/z*) $[M - Cl]^+$: calc'd: 537.1586; found 537.1564.

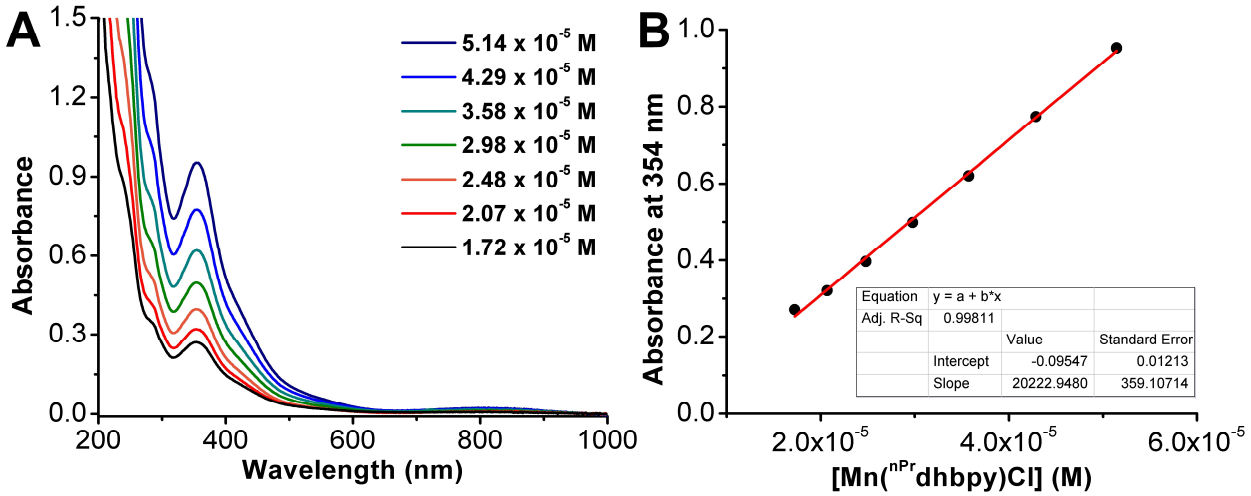

Figure S4.2. UV-vis serial dilution of Mn(^{nPr}dhbpy)Cl **2** in MeCN solution. Conditions: varying concentration; 1 cm pathlength (B) plot of concentration of Mn(^{nPr}dhbpy)Cl (M) versus absorbance at 356 nm (20223 M^{-1} cm^{-1}), R^2 = 0.998. All: 288 nm (25576 $M^{-1}cm^{-1}$), 440 nm (7626 $M^{-1}cm^{-1}$), 540 nm (1447 $M^{-1}cm^{-1}$), 802 nm (496 $M^{-1}cm^{-1}$).

Table S4.2. Table of Evans' Method data from Mn(^{nPr}dhbpy)Cl **2** in *N,N'*-DMF (chosen for solubility reasons) supporting a high spin d^4 complex.

Trial	Chemical Shift (ppm)	Chemical Shift (Hz)	Total Magnetic Moment (emu mol^{-1})	Paramagnetic Moment (emu mol^{-1})	μ_{eff} (Bohr Magnetons)
1	0.12	72	8.21 x 10^{-3}	8.61 x 10^{-3}	4.53
2	0.13	78	8.89 x 10^{-3}	9.29 x 10^{-3}	4.71
3	0.12	72	8.21 x 10^{-3}	8.61 x 10^{-3}	4.53

Synthesis of DIPEAHPF$_6$

N,N-diisopropylethylammonium hexafluorophosphate (DIPEAHPF$_6$) was synthesized according to previously reported procedures. [30] A solution of ammonium hexafluorophosphate (2.81 g, 17.2 mmol) and N,N-diisopropylethylamine (3.30 mL, 19.0 mmol) was allowed to reflux in toluene (20 mL) for 48 hours to obtain a white solid. The solution was filtered and the solid was rinsed toluene

(with 2 x 10 mL). The solid was dissolved in DCM, filtered, and the solvent was removed under reduced pressure to yield a white crystalline solid in 25.5% yield (1.2 g). White x-ray suitable single crystals were grown by slow evaporation from DCM. Elemental analysis for $C_8H_{20}F_6NP$: calc'd: C 34.91, H 7.33, N 5.09; found: C 35.00, H 7.46, N 5.09. ^{1}H NMR (MeCN-d_3, 600 MHz) δ (ppm): 6.18 (t, 1H), 3.67 (sept, 2H), 3.16 (q, 2H), 1.32 (m, 15H). $^{13}C\{^1H\}$ (MeCN-d_3, 150 MHz) δ (ppm): 56.19, 44.13, 18.79, 17.42, 13.00.

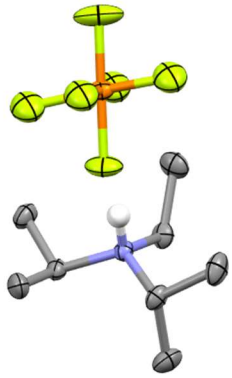

Figure S4.3. Molecular structure of $DIPEAHPF_6$ from single crystal X-ray diffraction studies. Blue = N, gray = C, white = H, green = F, orange; thermal ellipsoids at 50%, H atoms (except N–H) and disordered F atoms omitted for clarity. CCDC 2255850.

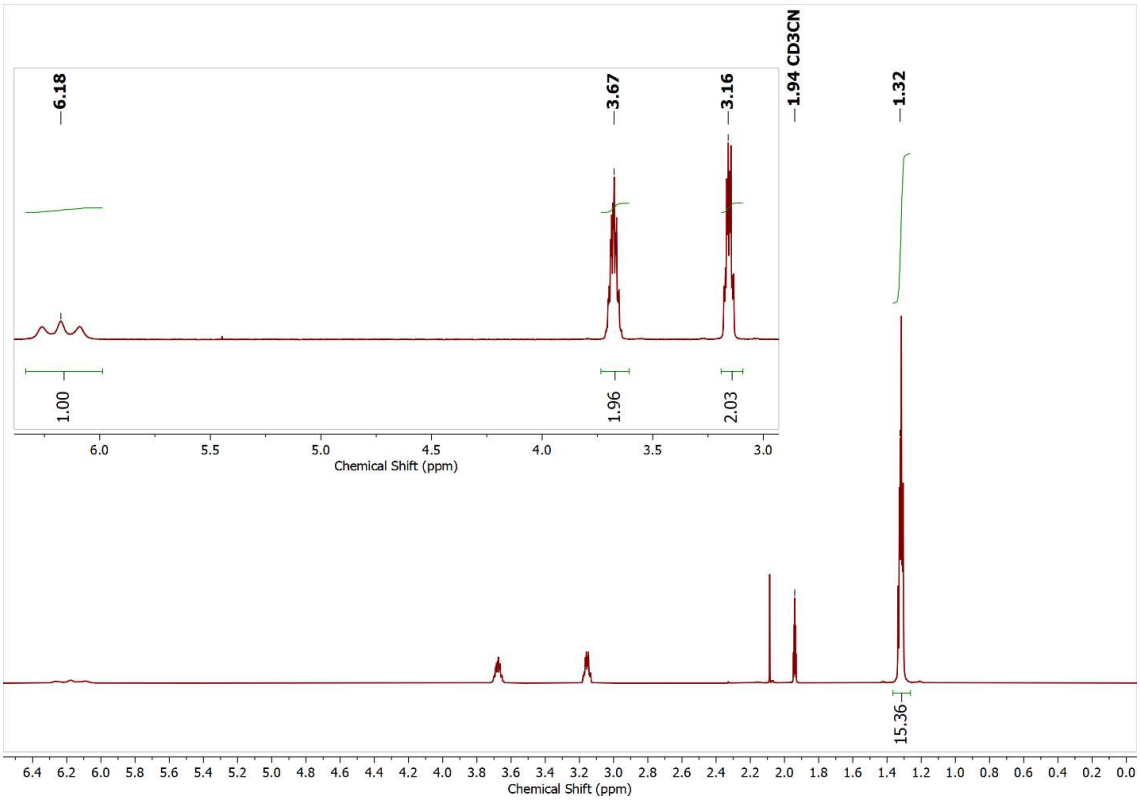

Figure S4.4. ^{1}H-NMR spectrum of DIPEAHPF$_6$ in MeCN-d$_3$; Varian 600 MHz.

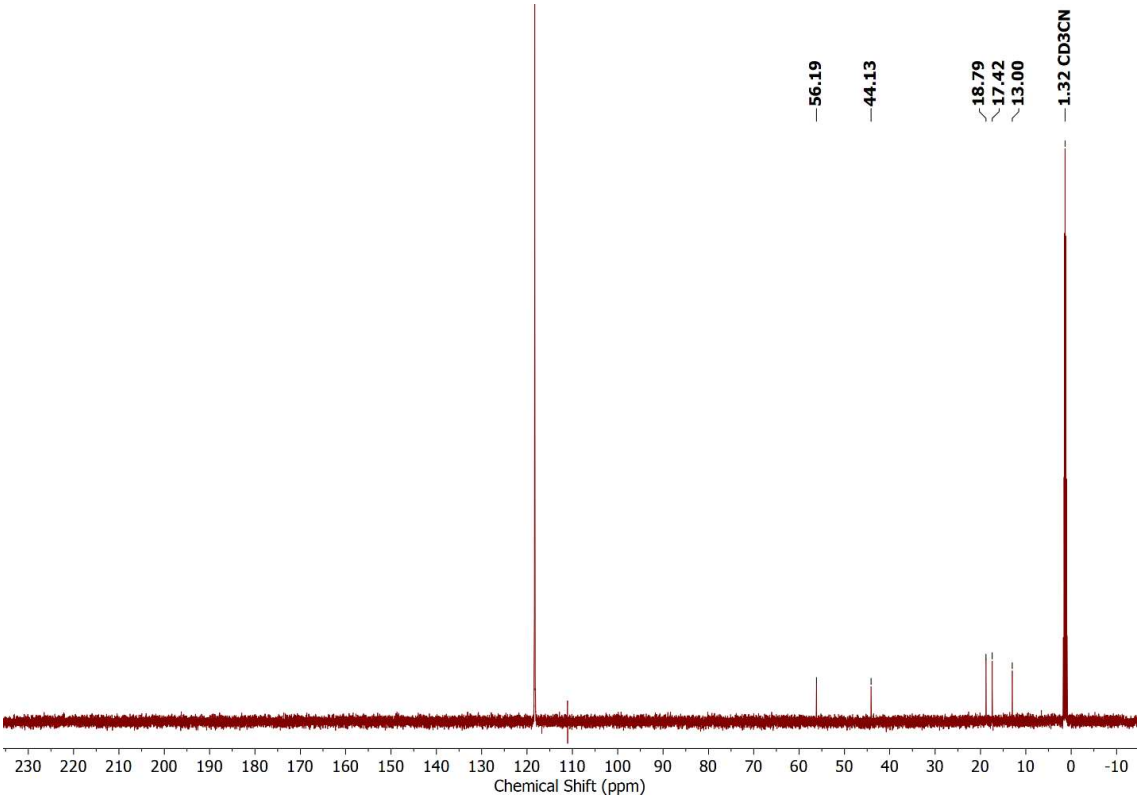

Figure S4.5. ^{13}C{^{1}H}-NMR spectrum of DIPEAHPF$_6$ in MeCN-d$_3$; Varian 150 MHz.

Estimation of $DIPEAHPF_6$ pK_a in MeCN

^{1}H-NMR spectroscopy was used to estimate the pK_a of $DIPEAHPF_6$ in acetonitrile relative to triethylamine (pK_a(MeCN) = 18.81), as previously reported. [31] Triethylamine (TEA) was titrated into a solution of 0.02 M $DIPEAHPF_6$ in MeCN-d_3 and a ^{1}H-NMR spectrum was taken (**Figure S4.7**). The difference in chemical shift was used to determine the relative change in pK_a units according to **Eqs S4.1-S4.3**. Triethylammonium hexfluorophosphate ($TEAHPF_6$) was synthesized according to a literature procedure.[30]

$$DIPEAH^+\left(B-H_j^+\right)+TEA\ (B_i) \rightleftharpoons TEAH^+(B-H_i^+)+DIPEA\ (B_j) \qquad \textbf{Eq S4.1}$$

$$\frac{K_{a_i}}{K_{a_j}}=\frac{(\delta_j^{obs}-\delta_j^B)(\delta_i^{B-H^+}-\delta_i^{obs})}{(\delta_i^{obs}-\delta_i^B)(\delta_j^{B-H^+}-\delta_j^{obs})} \qquad \textbf{Eq S4.2}$$

$$\Delta pK_{a_{ij}}=\log\left|\frac{K_{a_i}}{K_{a_j}}\right|=0.142\ \pm 0.083 \qquad \textbf{Eq S4.3}$$

Table S4.3. Summary of the chemical shifts for the estimation of $DIPEAHPF_6$ pK_a.

TEA:$DIPEAHPF_6$	$\delta^B{}_j$ (ppm)	$\delta^{obs}{}_j$ (ppm)	$\delta^{B\text{-}H+}{}_j$ (ppm)	$\delta^B{}_i$ (ppm)	$\delta^{obs}{}_i$ (ppm)	$\delta^{B\text{-}H+}{}_i$ (ppm)	K_{ai}/K_{aj}	$\log\lvert K_{ai}/K_{aj}\rvert$
0.10	3.01	3.63	3.68	2.46	3.07	3.14	–1.42	0.153
0.20		3.58			3.03		–1.10	0.0414
0.35		3.53			2.96		–1.25	0.0962
0.49		3.48			2.91		–1.20	0.0800
0.64		3.45			2.87		–1.26	0.100
0.79		3.42			2.84		–1.24	0.0951
0.94		3.39			2.81		–1.24	0.0918
1.1		3.31			2.71		–1.39	0.144
5.7		3.12			2.55		–1.29	0.110
11		3.06			2.5		–1.29	0.111
18		3.05			2.49		–1.38	0.139
20		3.05			2.48		–2.10	0.321
23		3.04			2.48		–1.55	0.190
25		3.03			2.47		–2.06	0.314
							Average	0.142
							Standard Deviation	0.083

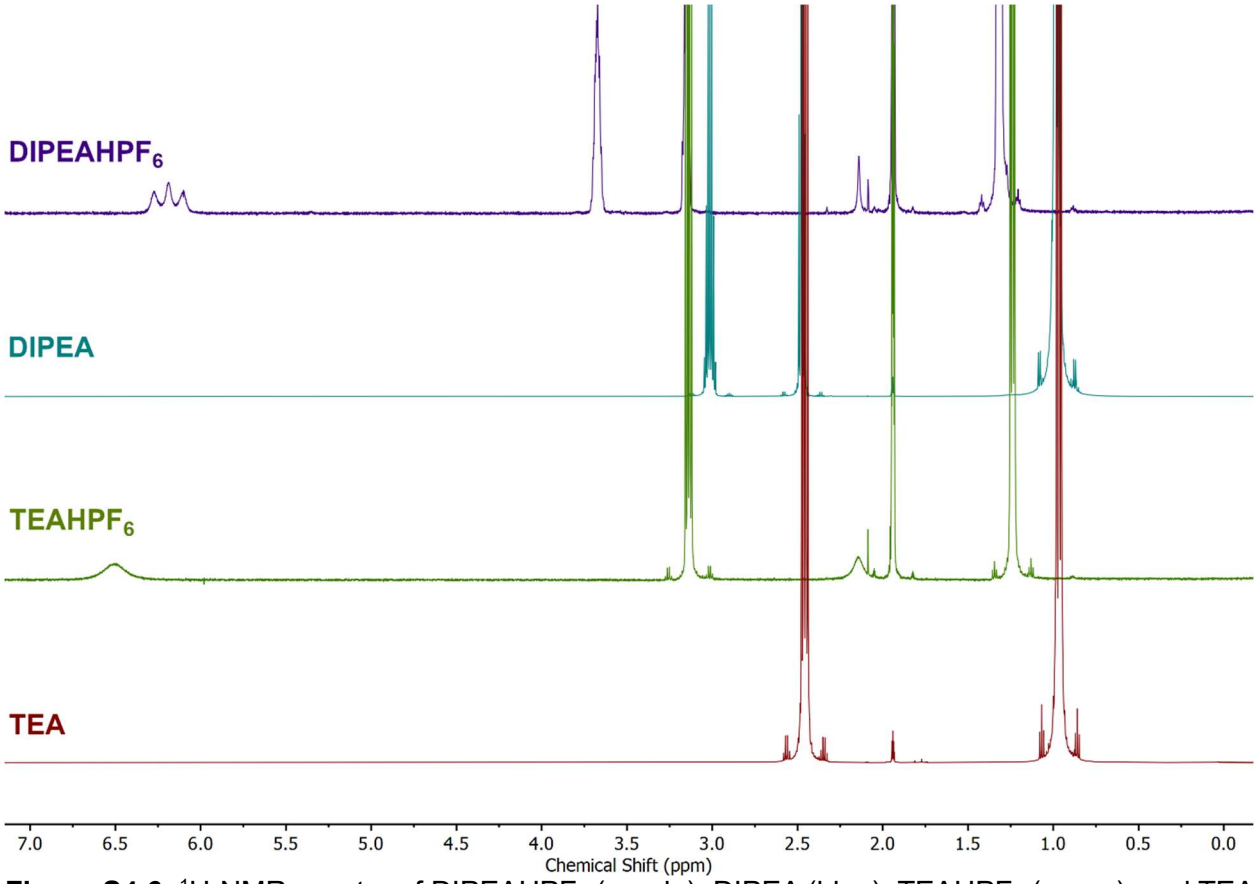

Figure S4.6. ^{1}H-NMR spectra of $DIPEAHPF_6$ (purple), DIPEA (blue), $TEAHPF_6$ (green), and TEA (red) used to estimate the pK_a of $DIPEAHPF_6$ in MeCN. MeCN-d_3; Varian 600 MHz.

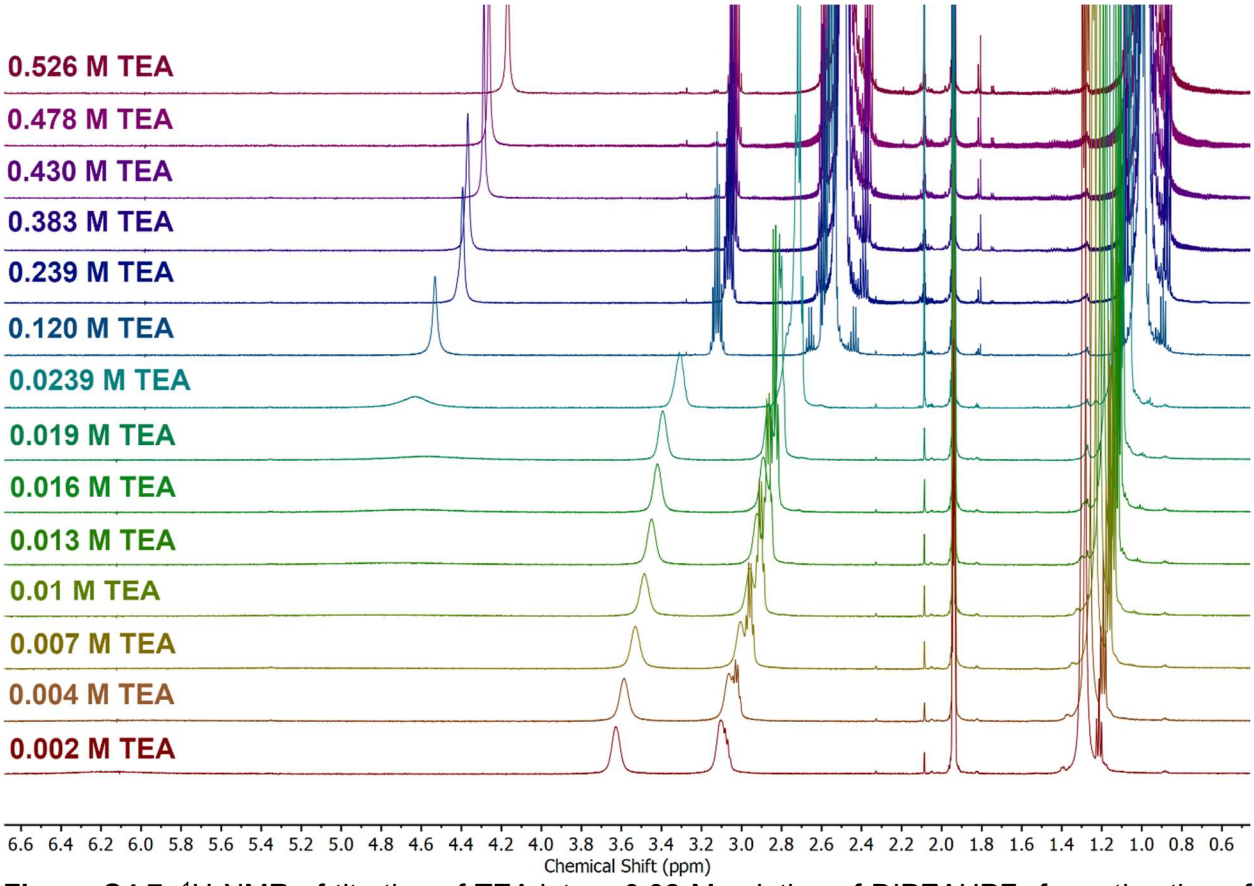

Figure S4.7. ^{1}H NMR of titration of TEA into a 0.02 M solution of DIPEAHPF$_6$ for estimation of pK_a of DIPEAHPF$_6$ in MeCN. MeCN-d_3; Varian 600 MHz.

Electrochemical Analysis

All electroanalytical experiments were performed using a Metrohm Autolab PGSTAT302N potentiostat. Glassy carbon working (⌀ = 3 mm) and non-aqueous silver/silver chloride pseudoreference electrodes behind PTFE tips were obtained from CH Instruments. The pseudoreference electrodes were obtained by depositing chloride on bare silver wire in 10% HCl at oxidizing potentials and stored in a 0.1 M tetrabutylammonium hexafluorophosphate solution in acetonitrile in the dark prior to use. The counter electrode was a glassy carbon rod (⌀ = 3 mm). All CV experiments were performed in a modified scintillation vial (20 mL volume) as a single-chamber cell with a cap modified with ports for all electrodes and a sparging needle. Tetrabutylammonium hexafluorophosphate ($TBAPF_6$) was purified by recrystallization from ethanol and dried in a vacuum oven before being stored in a desiccator. All data were referenced to an internal ferrocene standard (ferrocenium/ferrocene reduction potential under stated conditions) unless otherwise specified. All voltammograms were corrected for internal resistance. Ferrocene was purified by sublimation prior to use. In the event that the presence of electrochemical features precluded ferrocene addition, ferrocene was added to the electrochemical cell at the end of analysis for reference.

Electrochemistry with 1

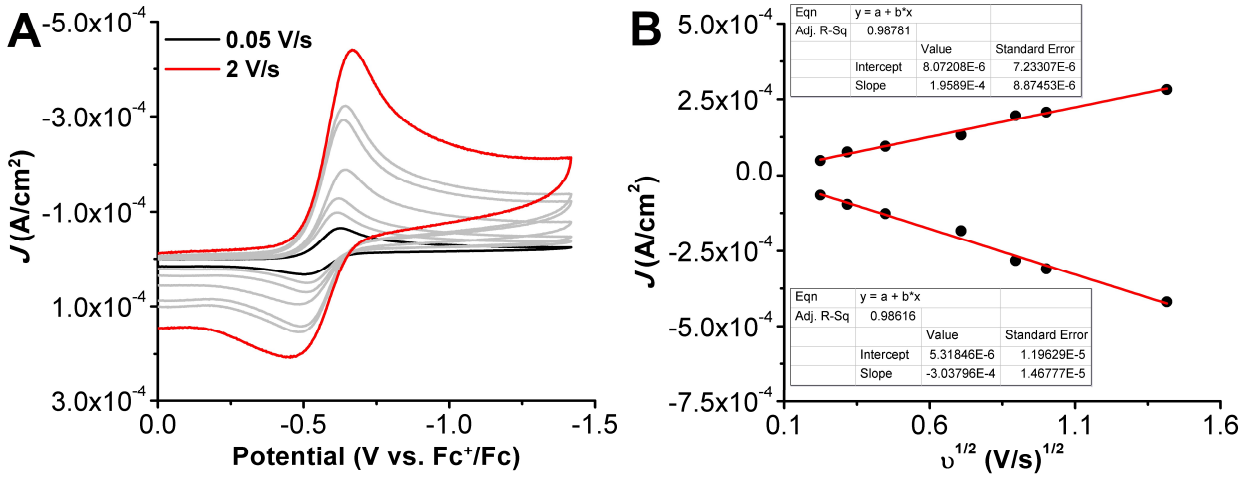

Figure S4.8. (A) CVs of Mn($^{p\text{-tbu}}$dhbpy)Cl **1** at variable scan rates ranging from 0.05 V/s (black) to 2 V/s (red) under Ar saturation conditions. (B) Linear fit data from A showing that Mn($^{p\text{-tbu}}$dhbpy)Cl

is a diffusion-limited current response. Conditions: 0.5 mM Mn, 0.1 M $TBAPF_6$/MeCN; glassy carbon working electrode, glassy carbon rod counter electrode, Ag/AgCl pseudoreference electrode; referenced to Fc^+/Fc internal standard; 100 mV/s scan rate.

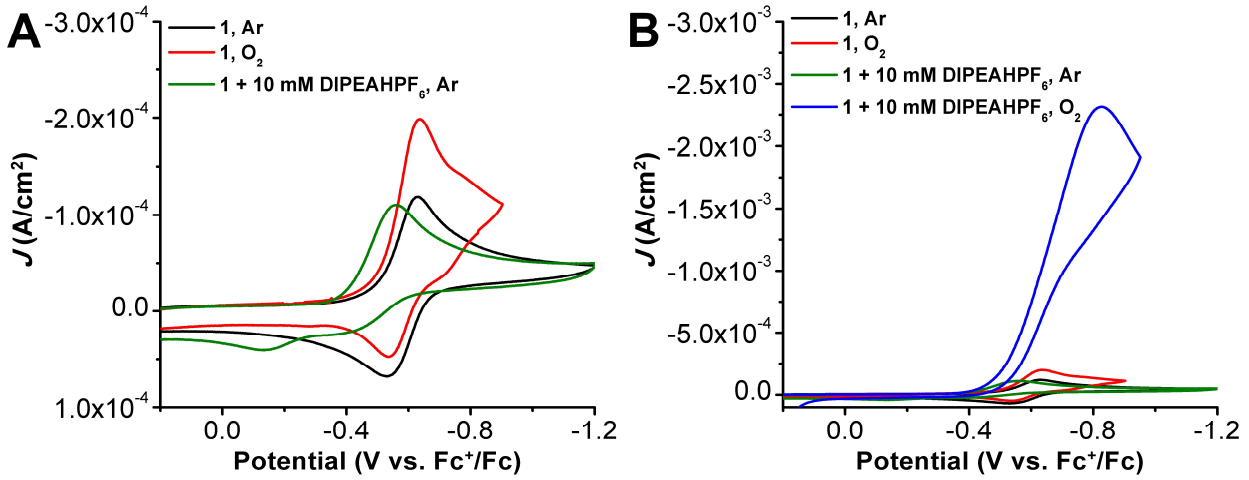

Figure S4.9. (A) CVs of Mn($^{p\text{-tbu}}$dhbpy)Cl **1** under Ar (black), O_2 (red) and with 10 mM $DIPEAHPF_6$ under Ar saturation (green). (B) CVs from A and catalytic trace shown (blue) with Mn($^{p\text{-tbu}}$dhbpy)Cl 1 and 10 mM $DIPEAHPF_6$ under O_2 saturation. Conditions: 0.5 mM Mn, 0.1 M $TBAPF_6$/MeCN; glassy carbon working electrode, glassy carbon rod counter electrode, Ag/AgCl pseudoreference electrode; referenced to Fc^+/Fc internal standard; 100 mV/s scan rate.

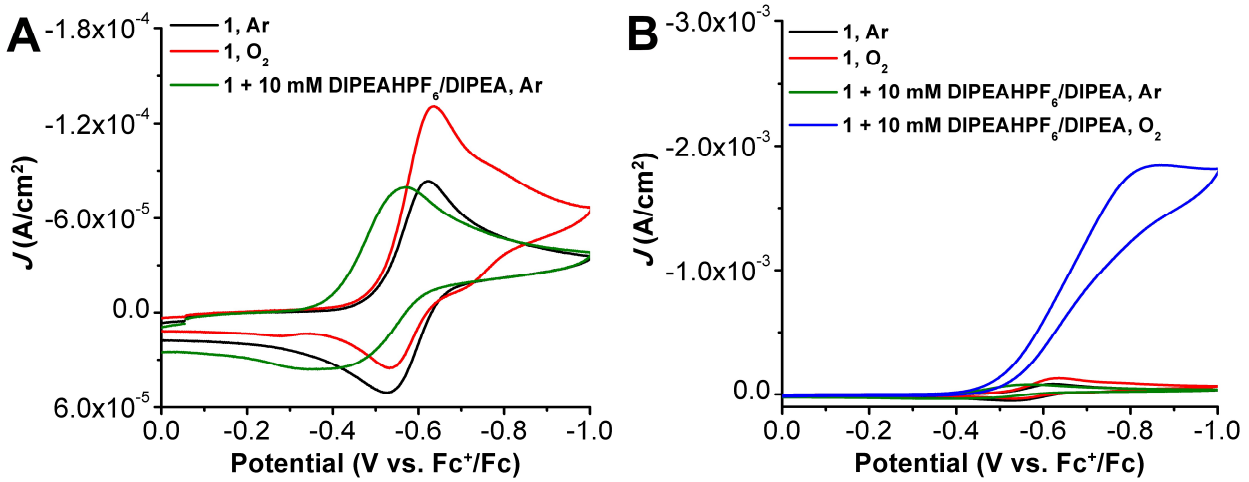

Figure S4.10. (A) CVs of Mn($^{p\text{-tbu}}$dhbpy)Cl **1** under Ar (black), O_2 (red) and with 10 mM buffer ($DIPEAHPF_6$/DIPEA) under Ar saturation (green). (B) CVs from A with catalytic trace shown (blue) with Mn($^{p\text{-tbu}}$dhbpy)Cl and 10 mM $DIPEAHPF_6$/DIPEA under O_2 saturation. Conditions: 0.5 mM Mn, 0.1 M $TBAPF_6$/MeCN; glassy carbon working electrode, glassy carbon rod counter electrode, Ag/AgCl pseudoreference electrode; referenced to Fc^+/Fc internal standard; 100 mV/s scan rate.

Determination of Effective Overpotential of 1

Utilizing the estimated pK_a of $DIPEAHPF_6$ (18.7) in MeCN, we can determine the effective overpotential according to **Eqs S4.4-S4.5**. Where E_{app} is the $E_{1/2}$ of Mn($^{p\text{-}tbu}$dhbpy)Cl with 10 mM $DIPEAHPF_6$ buffer determined by taking the first derivative of the irreversible feature in **Figure S4.10**.[52]

$$E^0_{O2/H2O} = 1.21 - 0.0592pK_a$$

$$E^0_{O2/H2O}(MeCN, DIPEAHPF_6) = 0.10\,V\ vs.\,Fc^+/Fc \qquad \textbf{Eq S4.4}$$

$$\eta = \left|E_{app} - E^0_{O2/H2O}\right| = |-0.48 - 0.10| = 0.58\,V \qquad \textbf{Eq S4.5}$$

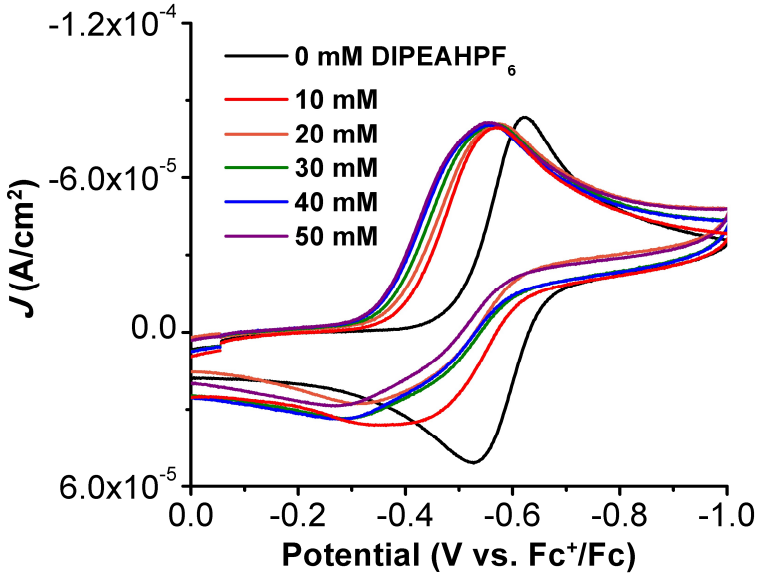

Figure S4.11. CVs of Mn($^{p\text{-}tbu}$dhbpy)Cl **1** with increasing $DIPEAHPF_6$ concentrations under Ar saturation conditions with 10 mM DIPEA. Conditions: 0.5 mM Mn, 10 mM DIPEA, 0.1 M $TBAPF_6$/MeCN; glassy carbon working electrode, glassy carbon rod counter electrode, Ag/AgCl pseudoreference electrode; referenced to Fc^+/Fc internal standard; 100 mV/s scan rate.

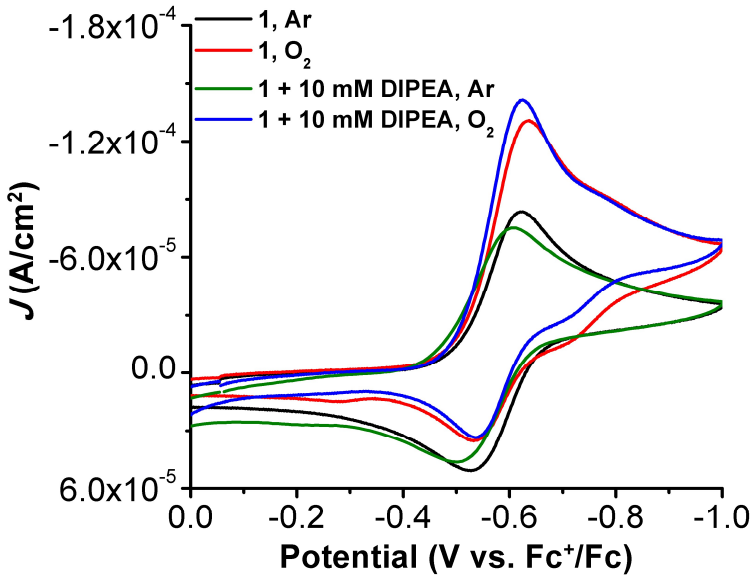

Figure S4.12. Control CVs of Mn($^{p\text{-}tbu}$dhbpy)Cl **1** with and without the presence of 10 mM DIPEA. Conditions: 0.5 mM Mn, 10 mM DIPEA, 0.1 M $TBAPF_6$/MeCN; glassy carbon working electrode, glassy carbon rod counter electrode, Ag/AgCl pseudoreference electrode; referenced to Fc^+/Fc internal standard; 100 mV/s scan rate.

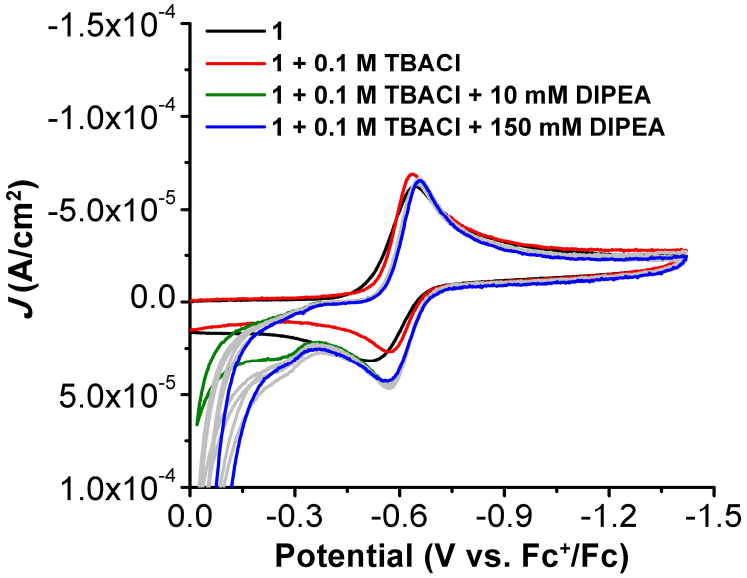

Figure S4.13. CVs of Mn($^{p\text{-}tbu}$dhbpy)Cl **1** (black trace) in the presence of 0.1 M TBACl (red trace) with increasing concentrations of DIPEA added. Conditions: 0.3 mM Mn, 0.1 M TBACl (if present), [DIPEA]: 10 mM (green trace), 20 mM, 30 mM, 50 mM, 100 mM, 150 mM (blue trace), 0.1 M $TBAPF_6$/MeCN; glassy carbon working electrode, glassy carbon rod counter electrode, Ag/AgCl pseudoreference electrode; referenced to Fc^+/Fc internal standard; 100 mV/s scan rate.

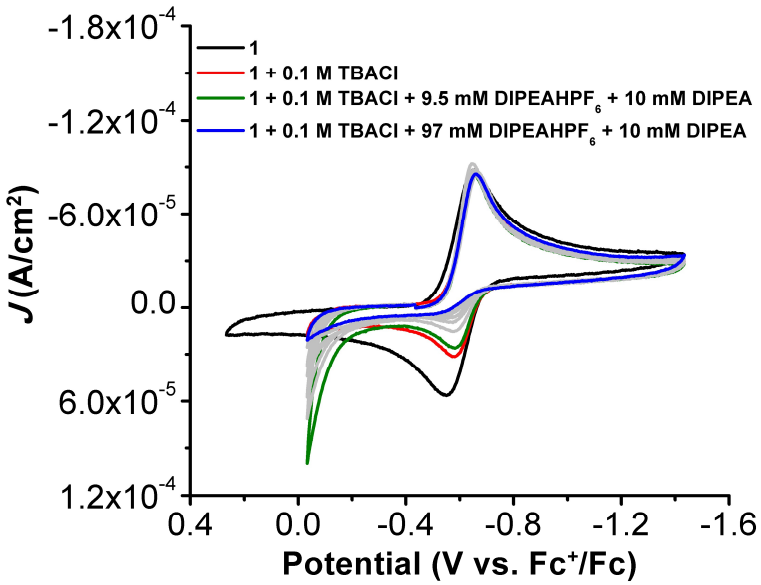

Figure S4.14. CVs of Mn($^{p\text{-}tbu}$dhbpy)Cl **1** (black trace) in the presence of 0.1 M TBACl (red trace) and 10 mM DIPEA with increasing concentrations of $DIPEAHPF_6$ under Ar saturation. Conditions: 0.3 mM Mn, 0.1 M TBACl (if present), 10 mM DIPEA (if present), 0.1 M $TBAPF_6$/MeCN; glassy carbon working electrode, glassy carbon rod counter electrode, Ag/AgCl pseudoreference electrode; referenced to Fc^+/Fc internal standard; 100 mV/s scan rate. Concentration of $DIPEAHPF_6$: 9.5 (green trace), 18.9, 29.2, 38.5, 47.8, 57.8, 97 mM (blue trace).

Electrochemistry with 2

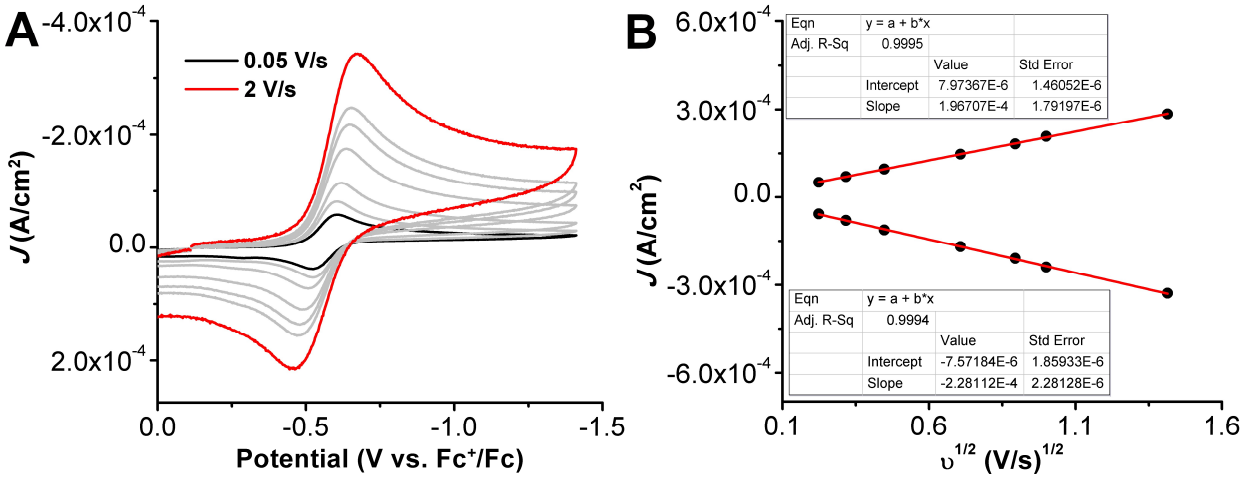

Figure S4.15. A) CVs of Mn($^{n\text{Pr}}$dhbpy)Cl **2** at variable scan rates ranging from 0.05 V/s (black) to 2 V/s (red) under Ar saturation conditions. (B) Linear fit data from A showing that Mn($^{n\text{Pr}}$dhbpy)Cl is a diffusion-limited current response. Conditions: 0.5 mM Mn, 0.1 M $TBAPF_6$/MeCN; glassy carbon working electrode, glassy carbon rod counter electrode, Ag/AgCl pseudoreference electrode; referenced to Fc^+/Fc internal standard; 100 mV/s scan rate.

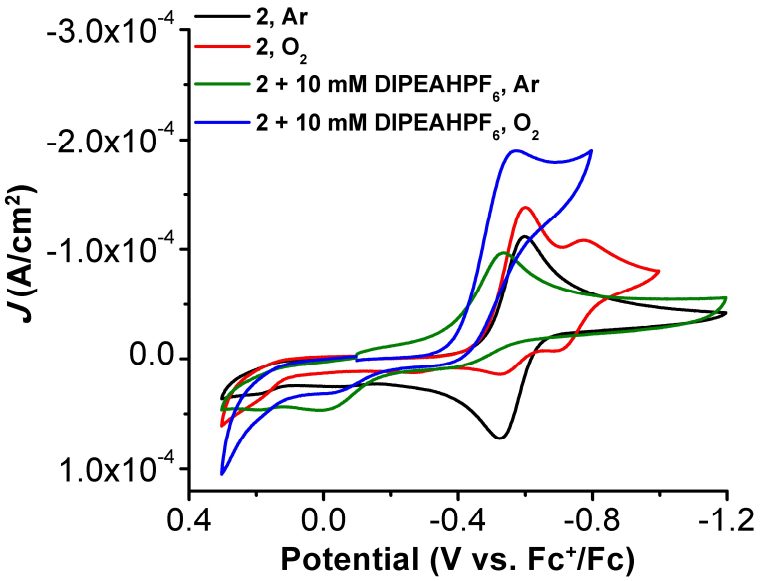

Figure S4.16. CVs of Mn(^{nPr}dhbpy)Cl **2** under Ar (black), O_2 (red) and with 10 mM DIPEAHPF$_6$ under Ar saturation (green). Conditions: 0.5 mM Mn, 0.1 M TBAPF$_6$/MeCN; glassy carbon working electrode, glassy carbon rod counter electrode, Ag/AgCl pseudoreference electrode; referenced to Fc^+/Fc internal standard; 100 mV/s scan rate.

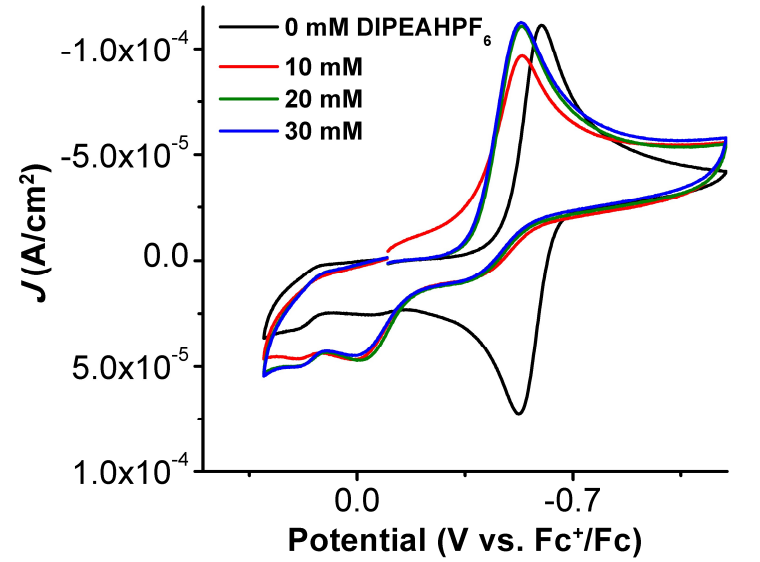

Figure S4.17. (A) CVs of Mn(^{nPr}dhbpy)Cl **2** under Ar with increasing amounts of DIPEAHPF$_6$ added. Conditions: 0.5 mM Mn, 0.1 M TBAPF$_6$/MeCN; glassy carbon working electrode, glassy carbon rod counter electrode, Ag/AgCl pseudoreference electrode; referenced to Fc^+/Fc internal standard; 100 mV/s scan rate.

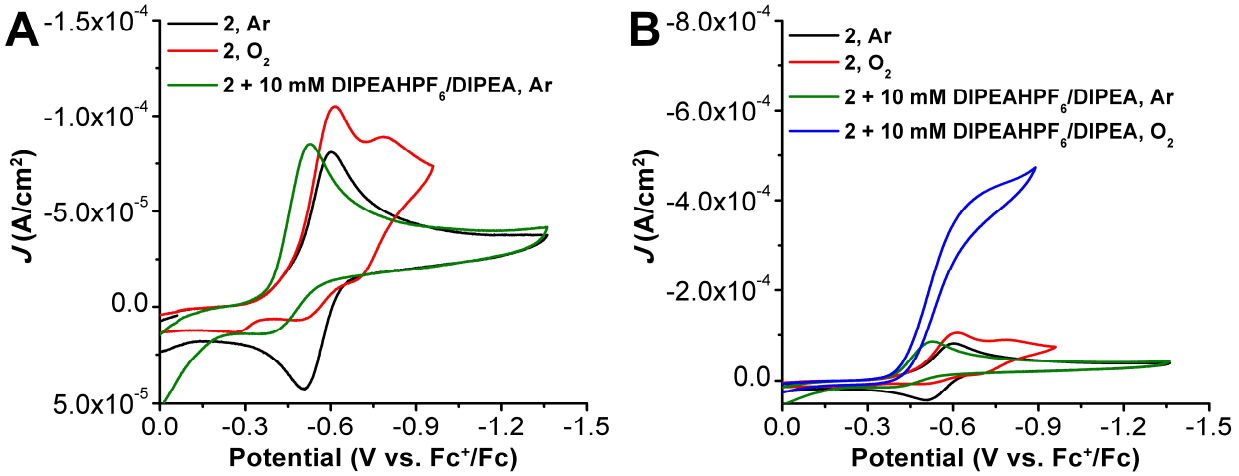

Figure S4.18. (A) CVs of Mn(^{nPr}dhbpy)Cl **2** under Ar (black), O_2 (red) and with 10 mM DIPEAHPF$_6$/DIPEA under Ar saturation (green). (B) CVs from A with catalytic trace shown (blue) with Mn(^{nPr}dhbpy)Cl and 10 mM DIPEAHPF$_6$/DIPEA under O_2 saturation. Conditions: 0.5 mM Mn, 0.1 M TBAPF$_6$/MeCN; glassy carbon working electrode, glassy carbon rod counter electrode, Ag/AgCl pseudoreference electrode; referenced to Fc^+/Fc internal standard; 100 mV/s scan rate.

Determination of Effective Overpotential of 2

Utilizing the estimated pK_a of DIPEAHPF$_6$ (18.7) in MeCN, we can determine the effective overpotential according to **Eqs S4.6-S4.7**. Where E_{app} is the $E_{1/2}$ of Mn(^{nPr}dhbpy)Cl **2** with 10 mM DIPEAHPF$_6$ buffer determined by taking the first derivative of the irreversible feature in **Figure S4.18**.[52]

$$E^0_{O2/H2O} = 1.21 - 0.0592pK_a$$

$$E^0_{O2/H2O}(MeCN, DIPEAHPF_6) = 0.10\ V\ vs.Fc^+/Fc \qquad \textbf{Eq S4.6}$$

$$\eta = \left|E_{app} - E^0_{O2/H2O}\right| = |-0.46 - 0.10| = 0.56\ V \qquad \textbf{Eq S4.7}$$

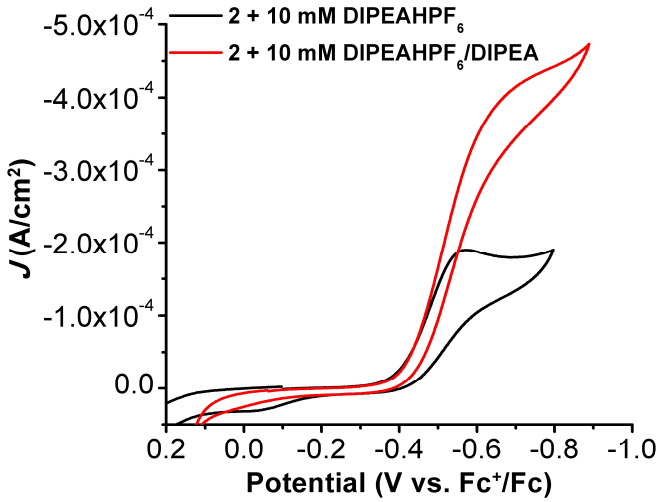

Figure S4.19. Comparison of electrocatalytic ORR by Mn(^{nPr}dhbpy)Cl **2** with 10 mM DIPEAHPF$_6$ with (red) and without (black) the presence of 10 mM DIPEA (traces from **Figure S16** and **S18** for black and red traces, respectively). Conditions: 0.5 mM Mn, 0.1 M TBAPF$_6$/MeCN; glassy carbon working electrode, glassy carbon rod counter electrode, Ag/AgCl pseudoreference electrode; referenced to Fc$^+$/Fc internal standard; 100 mV/s scan rate.

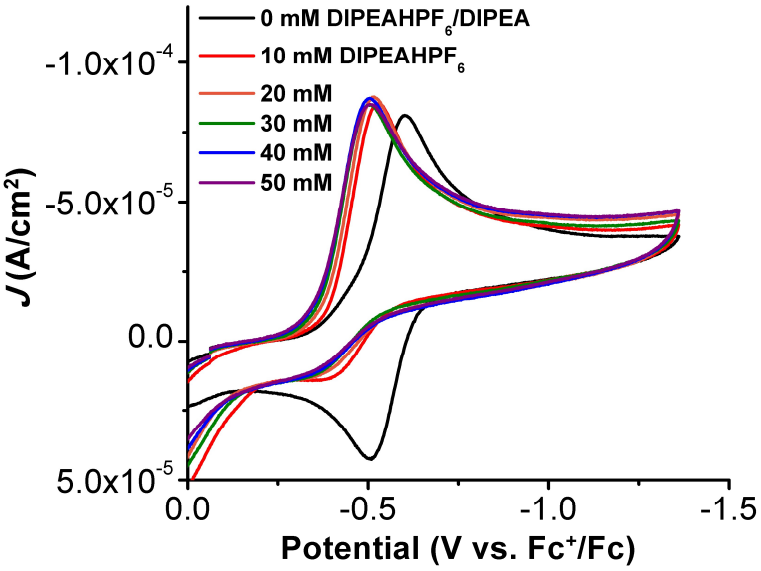

Figure S4.20. CVs of Mn(^{nPr}dhbpy)Cl **2** with increasing DIPEAHPF$_6$ concentrations under Ar saturation conditions with 10 mM DIPEA. Conditions: 0.5 mM Mn, 10 mM DIPEA, 0.1 M TBAPF$_6$/MeCN; glassy carbon working electrode, glassy carbon rod counter electrode, Ag/AgCl pseudoreference electrode; referenced to Fc$^+$/Fc internal standard; 100 mV/s scan rate.

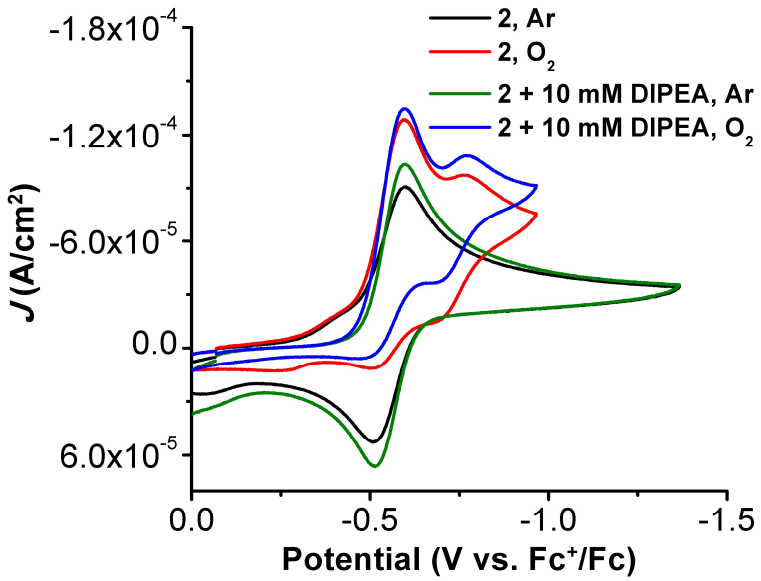

Figure S4.21. Control CVs of Mn(^{nPr}dhbpy)Cl **2** with and without the presence of 10 mM DIPEA. Conditions: 0.5 mM Mn, 10 mM DIPEA, 0.1 M $TBAPF_6$/MeCN; glassy carbon working electrode, glassy carbon rod counter electrode, Ag/AgCl pseudoreference electrode; referenced to Fc^+/Fc internal standard; 100 mV/s scan rate.

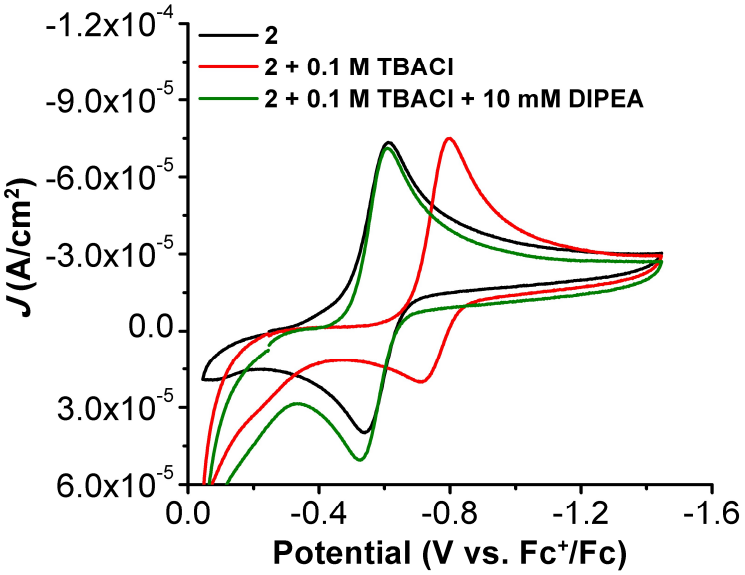

Figure S4.22. CVs of Mn(^{nPr}dhbpy)Cl **2** (black trace) in the presence of 0.1 M TBACl (red trace) and DIPEA (green trace). Conditions: 0.3 mM Mn, 0.1 M $TBAPF_6$/MeCN; glassy carbon working electrode, glassy carbon rod counter electrode, Ag/AgCl pseudoreference electrode; referenced to Fc^+/Fc internal standard; 100 mV/s scan rate.

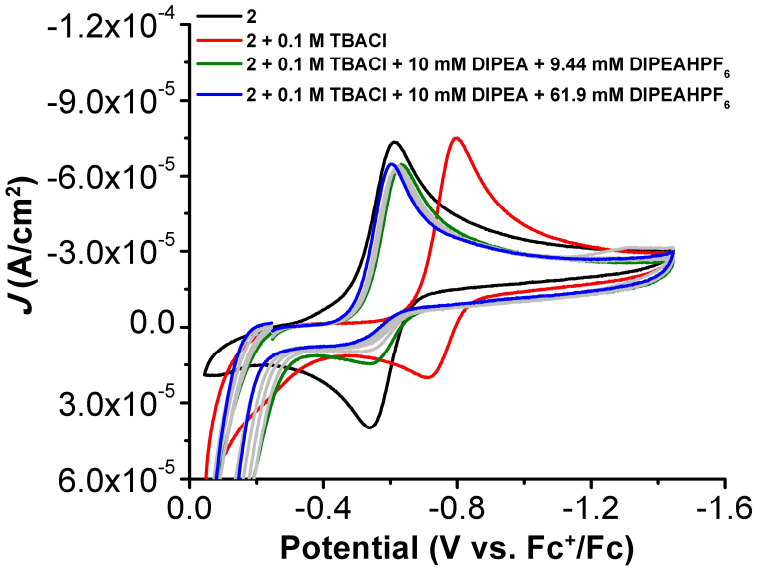

Figure S4.23. CVs of Mn(^{nPr}dhbpy)Cl **2** (black trace) in the presence of 0.1 M TBACl (red trace) and increasing amounts of $DIPEAHPF_6$. Conditions: 0.3 mM Mn, 10 mM DIPEA (if present), 0.1 M $TBAPF_6$/MeCN; glassy carbon working electrode, glassy carbon rod counter electrode, Ag/AgCl pseudoreference electrode; referenced to Fc^+/Fc internal standard; 100 mV/s scan rate. Concentrations of $DIPEAHPF_6$: 9.44 (green trace), 19.1, 29.3, 39.2, 51.7, 61.9 mM (blue trace).

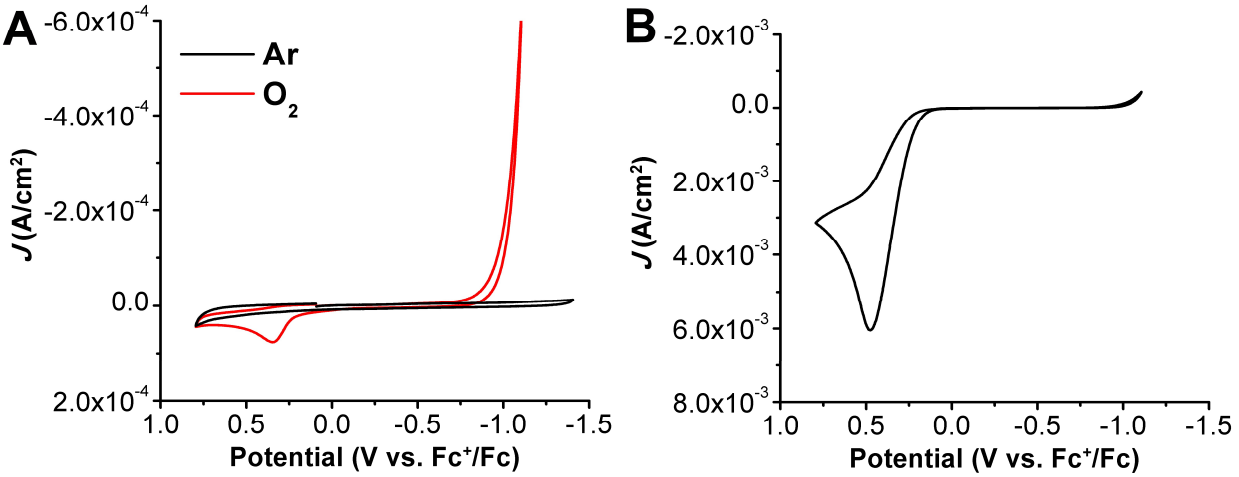

Figure S4.24. (A) Control CVs of 24 mM $DIPEAHPF_6$ under Ar (black) and O_2 (red trace). (B) Control CVs of 24 mM $DIPEAHPF_6$ and 25 mM DIPEA under O_2. Conditions: 24 mM $DIPEAHPF_6$, 0.1 M $TBAPF_6$/MeCN; glassy carbon working electrode, glassy carbon rod counter electrode, Ag/AgCl pseudoreference electrode; referenced to Fc^+/Fc internal standard; 100 mV/s scan rate.

Description of Spectrochemical ORR Product Quantification

The concentration of catalytically produced H_2O_2 was determined by $Ti(O)SO_4$ as previously reported.[23,53] A calibration curve (**Figure S4.25**) was obtained through a serial dilution of a stock solution of urea•H_2O_2 in MeCN. H_2O_2 was extracted by adding 2 mL of a standard solution to 10 mL DCM and 5 mL of DI H_2O, inverted and allowed to separate. Then, 3 mL of the aqueous layer was removed and put into the cuvette where a UV-vis spectrum was taken before and after the addition of 0.1 mL of $Ti(O)SO_4$ solution. The difference in absorbance at 408 nm was used to construct the calibration curve (**Figure S4.25**).

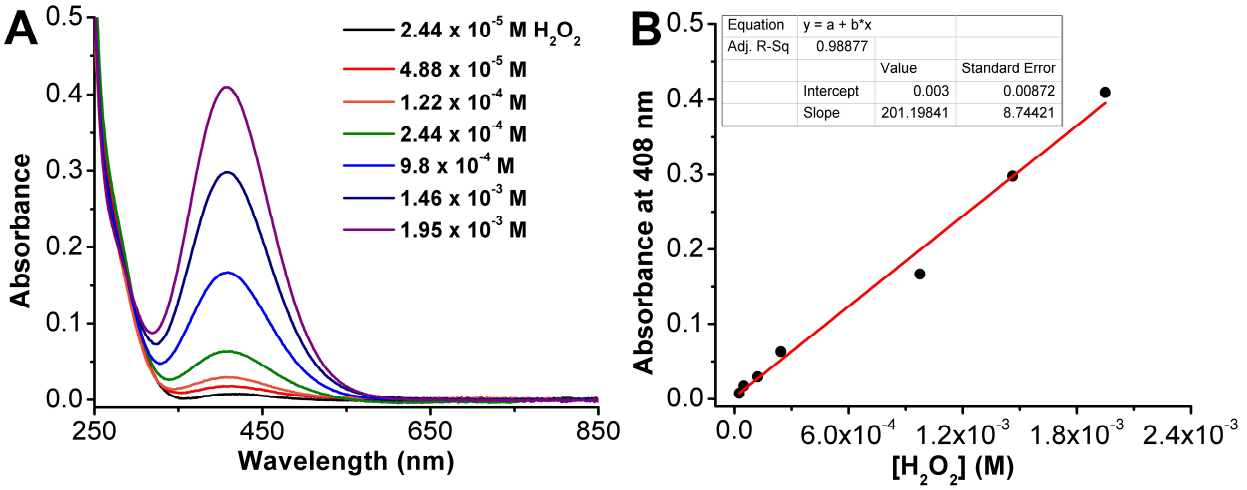

Figure S4.25. Calibration curve of H_2O_2 quantification using a $Ti(O)SO_4$ colorimetric assay. (A) Serial dilution of urea•H_2O_2 using the method described above. (B) Calibration curve made from data in A.

Generally, to determine the ORR selectivity of Mn(^{nPr}dhbpy)Cl **1** and Mn($^{p\text{-}tbu}$dhbpy)Cl **2**, solutions containing 80 μM [Mn] and 20 mM DIPEAHPF$_6$ and DIPEA (if present) were sparged with O_2 gas and rapidly mixed in a 1:1 ratio with a N_2 saturated 2 mM Cp^*_2Fe solution with a final volume of 8 mL (final concentrations: 40 μM Mn, 1 mM Cp^*_2Fe, 10 mM DIPEAHPF$_6$ and 10 mM DIPEA). Over the course of the reaction, 2 mL aliquots of the catalytic solution were removed and extracted with 10 mL of DCM and 5 mL of DI H_2O. The aqueous layer (3 mL) was removed and put into the cuvette and a UV-vis spectrum was taken before and after the addition of 0.1 mL of $Ti(O)SO_4$.

Aliquots were taken at the indicated time points and experiments were done in triplicate. **Eqs S4.8-S4.9** were used to calculate the % selectivity of H_2O_2.

$$O_2 + 2Cp^*_2Fe(1\ mM) + 2DIPEAHPF_6 \xrightarrow{cat.[Mn]} H_2O_2(0.5\ mM) + 2[Cp^*_2Fe]^+ + 2DIPEA \quad \textbf{Eq S4.8}$$

Abs@408 nm (red trace) – Abs@408 nm (black trace) = $201.2[H_2O_2]_{exp} + 0.003$

$$\frac{[H_2O_2]_{exp}}{0.5\ mM\ H_2O_2} \times 100 = \%\ H_2O_2\ selectivity \qquad \textbf{Eq S4.9}$$

Unbuffered Conditions

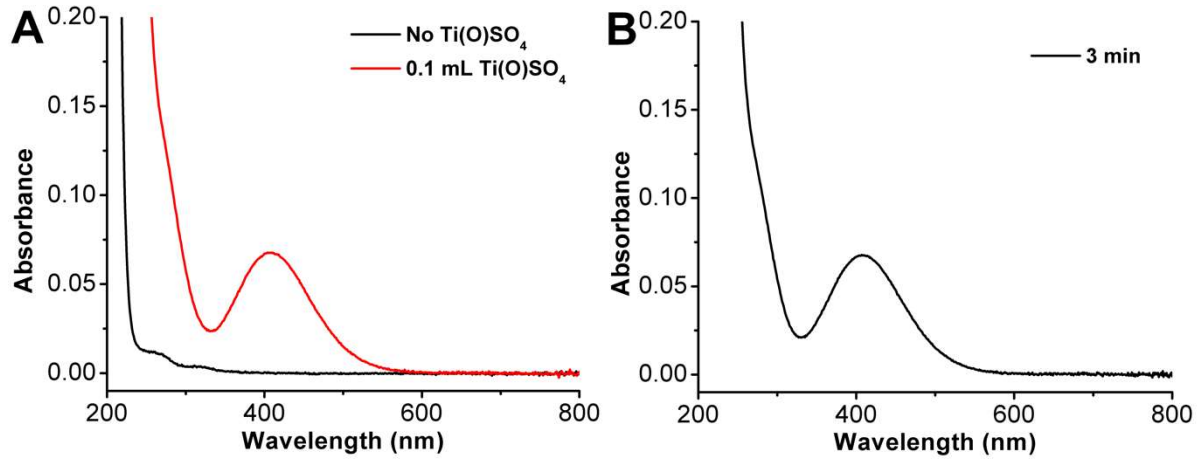

Figure S4.26. H_2O_2 product quantification of ORR by Mn($^{p\text{-}tbu}$dhbpy)Cl **1** with DIPEAHPF$_6$. (A) UV-vis spectrum of extracted solution after 3 min of reaction time before (black) and after (red) 0.1 mL of 0.1 M Ti(O)SO$_4$ solution was added. (B) Corrected spectra (red – black trace from A). Conditions: 40 μM Mn($^{p\text{-}tbu}$dhbpy)Cl, 10 mM DIPEAHPF$_6$, 1 mM Cp*$_2$Fe, 4.05 mM O_2 in MeCN.

Table S4.4. Summary of H_2O_2 selectivity of ORR by Mn($^{p\text{-}tbu}$dhbpy)Cl **1** with 10 mM DIPEAHPF$_6$ (**Figure S4.26**).

Time (min)	% H_2O_2	% H_2O
3	64.2 ± 6.9	35.8 ± 6.9

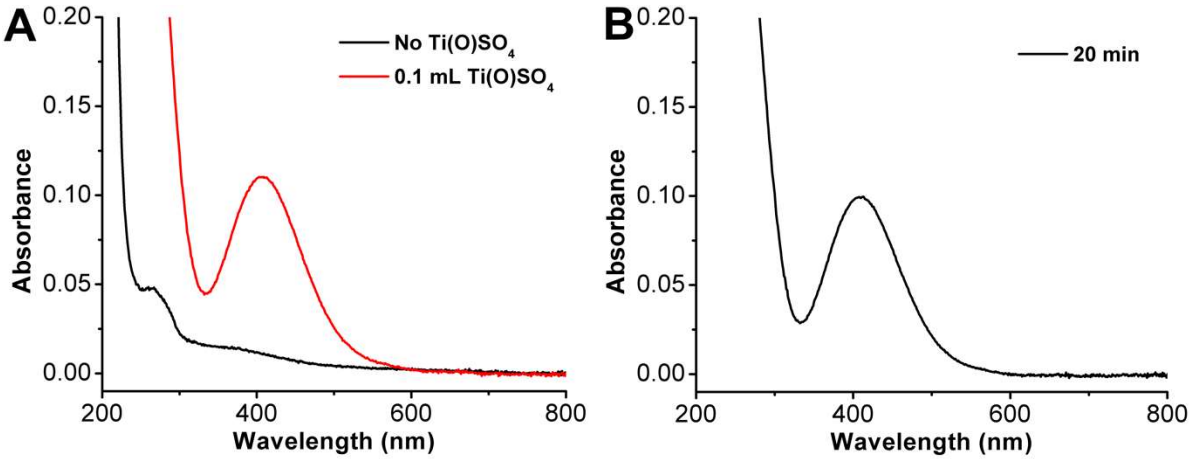

Figure S4.27. H_2O_2 product quantification of ORR by Mn(^{nPr}dhbpy)Cl **2** with DIPEAHPF$_6$. (A) UV-vis spectrum of extracted solution before (black) and after (red) 0.1 mL of 0.1 M Ti(O)SO$_4$ solution was added, 20 min. (B) Corrected spectra (red – black trace from A). Conditions: 40 μM Mn(^{nPr}dhbpy)Cl, 10 mM DIPEAHPF$_6$/DIPEA, 1 mM Cp*$_2$Fe, 4.05 mM O_2 in MeCN.

Table S4.5. Summary of H_2O_2 selectivity of ORR by Mn(^{nPr}dhbpy)Cl **2** with 10 mM DIPEAHPF$_6$ (**Figure S4.27**).

Time (min)	% H_2O_2	% H_2O
20	96.2 ± 4.1	3.8 ± 4.1

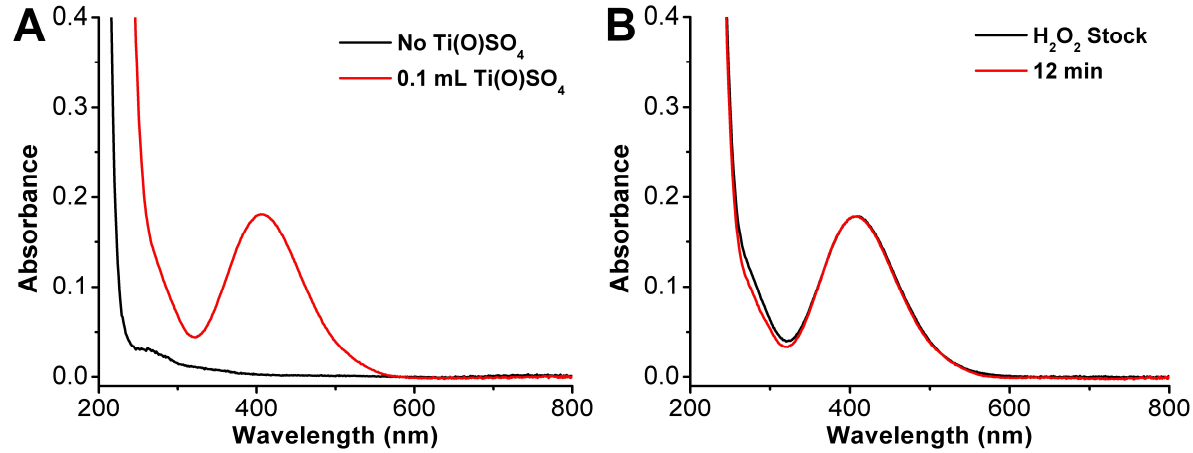

Figure S4.28. Stability test of urea•H_2O_2 in the presence of Mn($^{p\text{-}tbu}$dhbpy)Cl **1**, DIPEAHPF$_6$, and O_2. (A) UV-vis spectra of an extracted sample after 12 minutes of reaction time before (black) and after (red) the addition of 0.1 mL of 0.1 M Ti(O)SO$_4$. (B) Corrected UV-vis spectra (red – black trace from A) of H_2O_2 only (black) and after 12 min (red). Conditions: 40 μM Mn($^{p\text{-}tbu}$dhbpy)Cl, 10 mM DIPEAHPF$_6$, 0.87 mM urea•H_2O_2, 4.05 mM O_2 in MeCN.

Table S4.6. Summary of H_2O_2 disproportionation by Mn($^{p\text{-}tbu}$dhbpy)Cl **1** with 10 mM DIPEAHPF$_6$ (**Figure S4.28**) relative to 0.87 mM H_2O_2 stock solution.

Time (min)	% H_2O_2 Recovered
12	104 ± 8.8

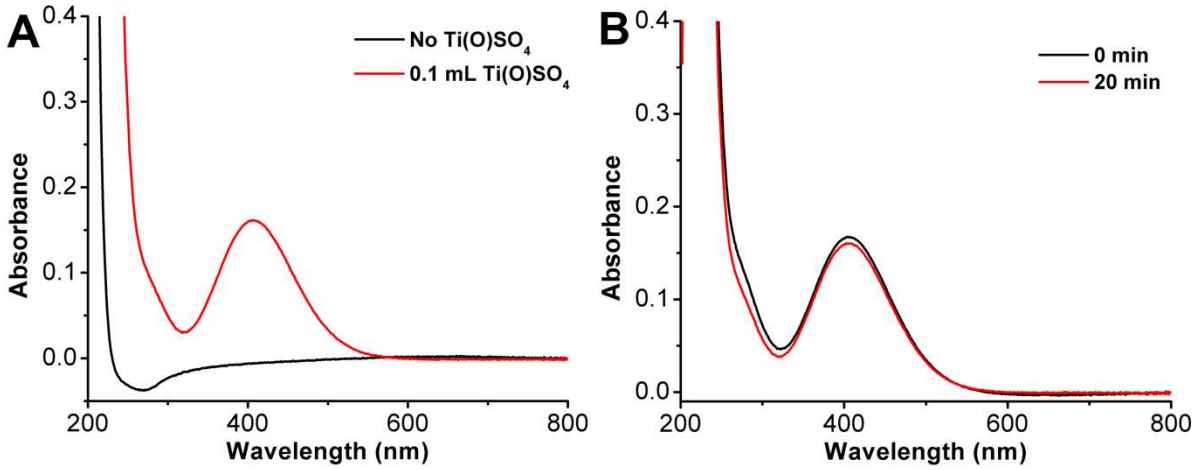

Figure S4.29. Stability test of urea•H_2O_2 in the presence of Mn(^{nPr}dhbpy)Cl **1**, DIPEAHPF$_6$, and O_2. (A) UV-vis spectra of an extracted sample after 20 minutes of reaction time before (black) and after (red) the addition of 0.1 mL of 0.1 M Ti(O)SO$_4$. (B) Corrected UV-vis spectra (red – black traces from A) at 0 min (black trace) and after 20 min (red). Conditions: 40 μM Mn(^{nPr}dhbpy)Cl, 10 mM DIPEAHPF$_6$, 0.80 mM urea•H_2O_2, 4.05 mM O_2 in MeCN.

Table S4.7. Summary of H_2O_2 disproportionation by Mn(^{nPr}dhbpy)Cl **2** with 10 mM DIPEAHPF$_6$ (**Figure S4.29**) relative to 0 min with 0.80 mM H_2O_2.

Time (min)	% H_2O_2 Recovered
20	93.6 ± 4.6

Buffered Conditions

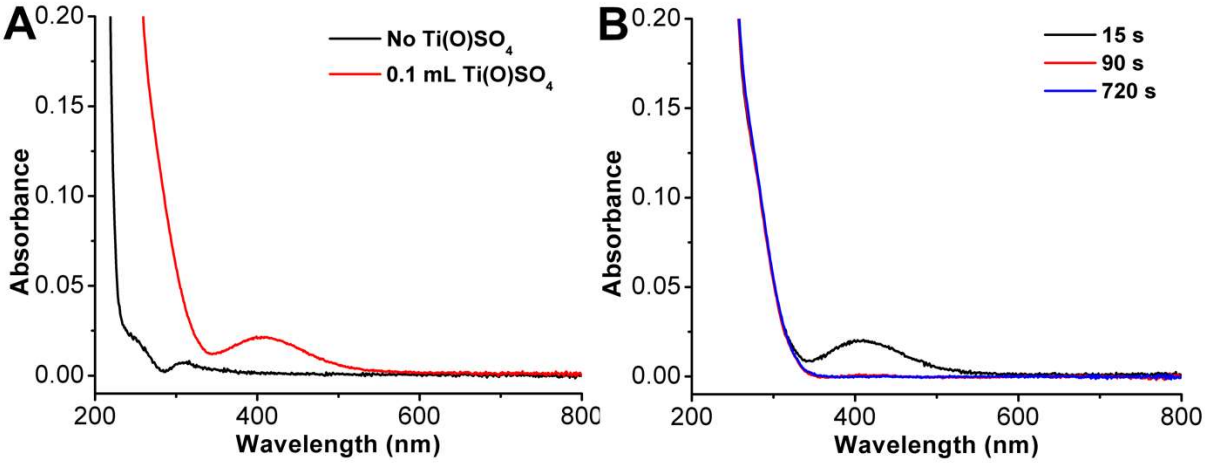

Figure S4.30. H_2O_2 product quantification of ORR by Mn($^{p\text{-}tbu}$dhbpy)Cl **1** with DIPEAHPF$_6$ and DIPEA. (A) UV-vis spectrum of extracted solution before (black) and after (red) 0.1 mL of 0.1 M Ti(O)SO$_4$ solution was added, 15 s. (B) Corrected spectra (red – black trace from A) for 15, 90, and 720 s aliquots. Conditions: 40 μM Mn($^{p\text{-}tbu}$dhpby)Cl, 10 mM DIPEAHPF$_6$/DIPEA, 1 mM Cp*$_2$Fe, 4.05 mM O_2 in MeCN.

Table S4.8. Summary of H_2O_2 selectivity over the course of catalytic ORR by Mn($^{p\text{-}tbu}$dhbpy)Cl **1** with 10 mM DIPEAHPF$_6$/DIPEA (**Figure S4.30**).

Time (s)	% H_2O_2	% H_2O
15	18.1 ± 4.1	81.9 ± 4.1
90	–1.32 ± 2.4	101 ± 2.4
720	–2.08 ± 1.1	102 ± 1.1

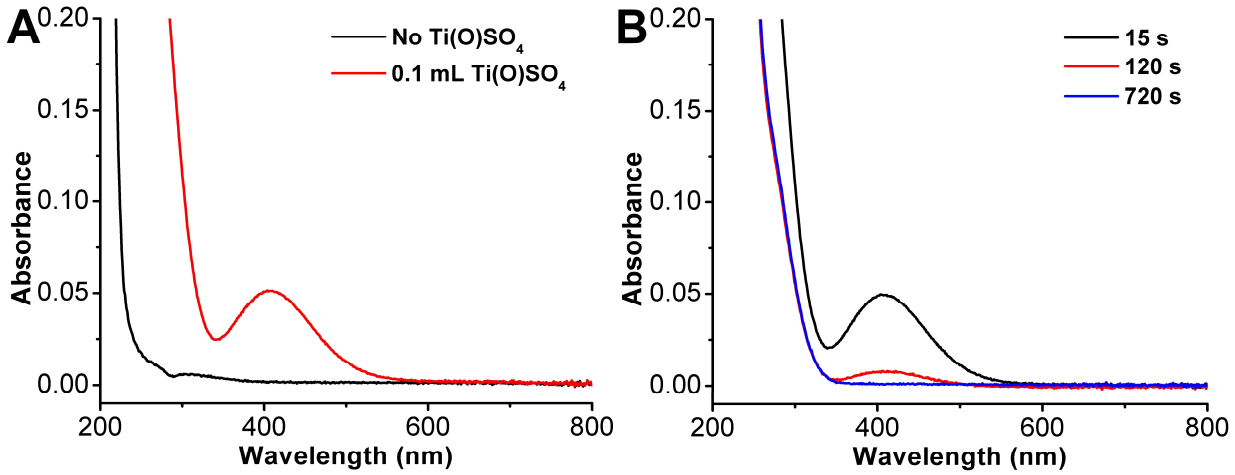

Figure S4.31. H_2O_2 product quantification of ORR by Mn(^{nPr}dhbpy)Cl **2** with DIPEAHPF$_6$ and DIPEA. (A) UV-vis spectra of extracted solution before (black) and after (red) 0.1 mL of 0.1 M Ti(O)SO$_4$ solution was added, 15 s. (B) Corrected spectra (red – black trace from A) for 15, 120, and 720 s aliquots. Conditions: 40 µM Mn(^{nPr}dhbpy)Cl, 10 mM DIPEAHPF$_6$/DIPEA, 1 mM Cp*$_2$Fe, 4.05 mM O_2 in MeCN.

Table S4.9. Summary of H_2O_2 selectivity over the course of catalytic ORR by Mn(^{nPr}dhbpy)Cl **2** with 10 mM DIPEAHPF$_6$/DIPEA (**Figure S4.31**).

Time (s)	% H_2O_2	% H_2O
15	37.9 ± 6.7	62.1 ± 6.7
120	6.42 ± 1.8	93.6 ± 1.8
720	-3.79 ± 1.2	103 ± 1.2

H_2O_2 Stability Testing under Buffered Conditions

To determine the stability of H_2O_2 under catalytic conditions, control studies were conducted in the presence of Mn catalyst, DIPEAHPF$_6$, DIPEA, and O_2. Generally, solutions containing 80 µM Mn catalyst and 20 mM DIPEAHPF$_6$ and DIPEA (if present) were sparged with O_2 gas and rapidly mixed in a 1:1 ratio with a N_2 saturated urea•H_2O_2 solution (final concentrations: 40 µM Mn, 10 mM DIPEAHPF$_6$ and 10 mM DIPEA). As the solution was allowed to react 2 mL aliquots were removed, extracted with 10 mL DCM and 5 mL DI H_2O. Then, 3 mL of the aqueous layer was

removed and added to the cuvette. A UV-vis spectrum was taken before and after the addition of 0.1 mL of 0.1 M $Ti(O)SO_4$ solution and the difference at 408 nm was used to determine the amount of H_2O_2 present ($[H_2O_2]_{detected}$). The % recovery was determined according to **Eq S4.10** from measured $[H_2O_2]_{expected}$ of the H_2O_2 stock solution or time point 0 min using the described extraction method.

$$\frac{[H_2O_2]_{detected}}{[H_2O_2]_{expected}} \times 100 = \%\ H_2O_2\ recovery \qquad \textbf{Eq S4.10}$$

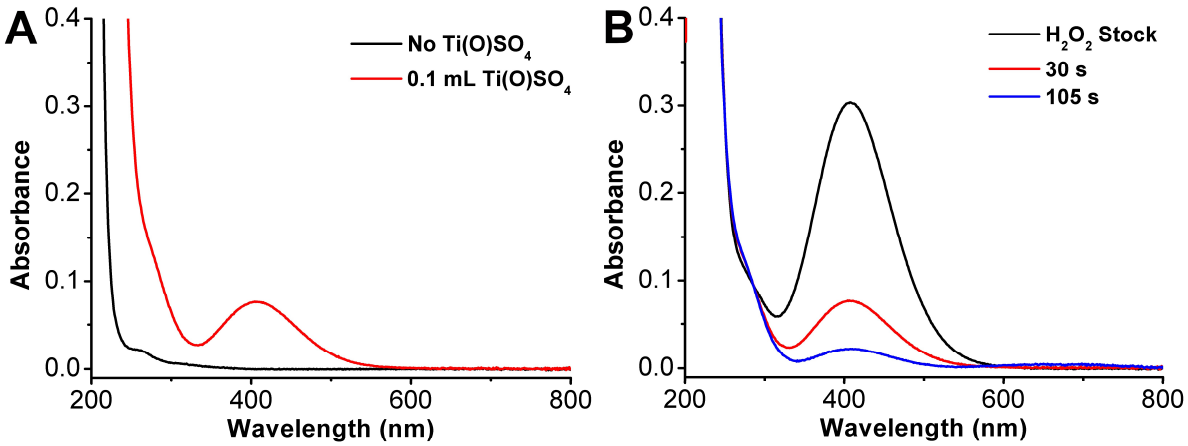

Figure S4.32. Stability test of urea•H_2O_2 in the presence of Mn($^{p\text{-}tbu}$dhbpy)Cl **1**, DIPEAHPF$_6$, DIPEA, and O_2. (A) UV-vis spectra before (black) and after (red) the addition of 0.1 mL of 0.1 M $Ti(O)SO_4$ to an extracted aliquot after 30 s. (B) Corrected UV-vis spectra (red – black traces) of H_2O_2 only (black) and after 30 (red) and 105 s (blue). Conditions: 40 μM Mn($^{p\text{-}tbu}$dhbpy)Cl, 10 mM DIPEAHPF$_6$/DIPEA, 1.49 mM urea•H_2O_2, 4.05 mM O_2 in MeCN.

Table S4.10. Summary of H_2O_2 disproportionation by Mn($^{p\text{-}tbu}$dhbpy)Cl **1** with 10 mM DIPEAHPF$_6$/DIPEA (**Figure S4.32**) relative to 1.49 mM H_2O_2 stock solution.

Time (s)	% H_2O_2 Recovered
30	31.3 ± 5.2
105	10.8 ± 6.6

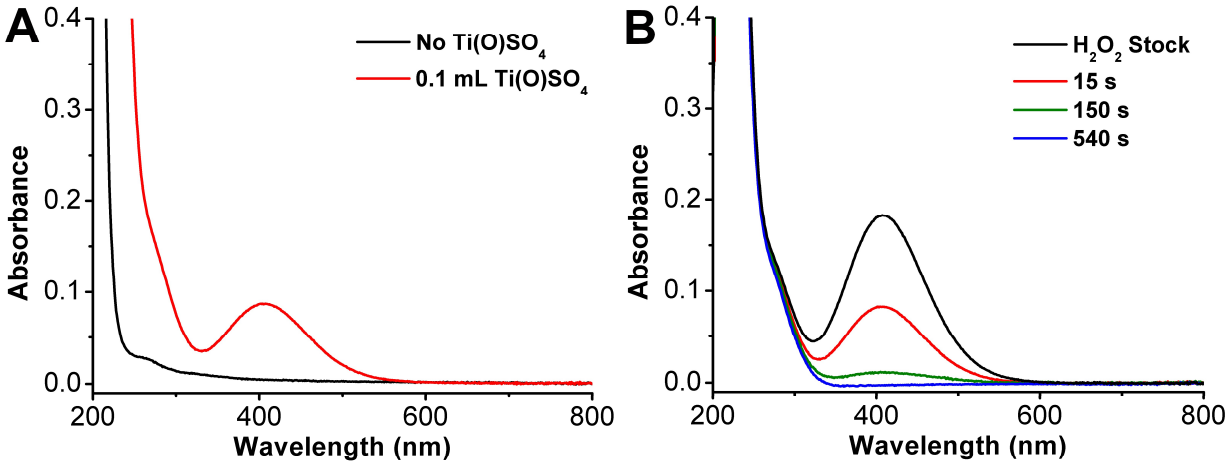

Figure S4.33. Stability test of urea•H_2O_2 in the presence of Mn(^{nPr}dhbpy)Cl **2**, DIPEAHPF$_6$, DIPEA, and O_2. (A) UV-vis spectra before (black) and after (red) the addition of 0.1 mL of 0.1 M Ti(O)SO$_4$ to an extracted aliquot after 15 s. (B) Corrected UV-vis spectra (red – black trace from A) of H_2O_2 only (black) and after 15 (red), 150 (green), and 540 s (blue). Conditions: 40 μM Mn(^{nPr}dhbpy)Cl, 10 mM DIPEAHPF$_6$/DIPEA, 0.89 mM urea•H_2O_2, 4.05 mM O_2 in MeCN.

Table S4.11. Summary of H_2O_2 disproportionation by Mn(^{nPr}dhbpy)Cl **2** with 10 mM DIPEAHPF$_6$/DIPEA (**Figure S4.33**) relative to 0.89 mM H_2O_2 stock solution.

Time (s)	% H_2O_2 Recovered
15	43.9 ± 4.9
150	3.81 ± 0.83
540	-3.14 ± 1.0

To determine the stability of H_2O_2 in the presence of Mn(II), control studies were conducted in the presence of Mn, DIPEAHPF$_6$, DIPEA, Cp*$_2$Fe, under an N_2 atmosphere. In a N_2 filled glovebox, urea•H_2O_2 was added to a solution containing Mn, DIPEAHPF$_6$/DIPEA, and Cp*$_2$Fe (final concentrations: 40 μM Mn, 10 mM DIPEAHPF$_6$/DIPEA, 1 mM Cp*$_2$Fe, 2.3 mM urea•H_2O_2). After 30 s, 2 min and 9 min, 2 mL aliquots were removed from the 'catalytic' solution and extracted with 10 mL of dry, degassed DCM and 5 mL of degassed water. Then, 3 mL of the aqueous layer was removed and a UV-vis spectrum was taken before and after the addition of 0.1 mL of Ti(O)SO$_4$ solution. The difference in absorbance at 408 nm was used to quantify the amount of H_2O_2 present according to **Eq S4.9** and **Eq S4.10** was used to determine the amount of H_2O_2 recovered.

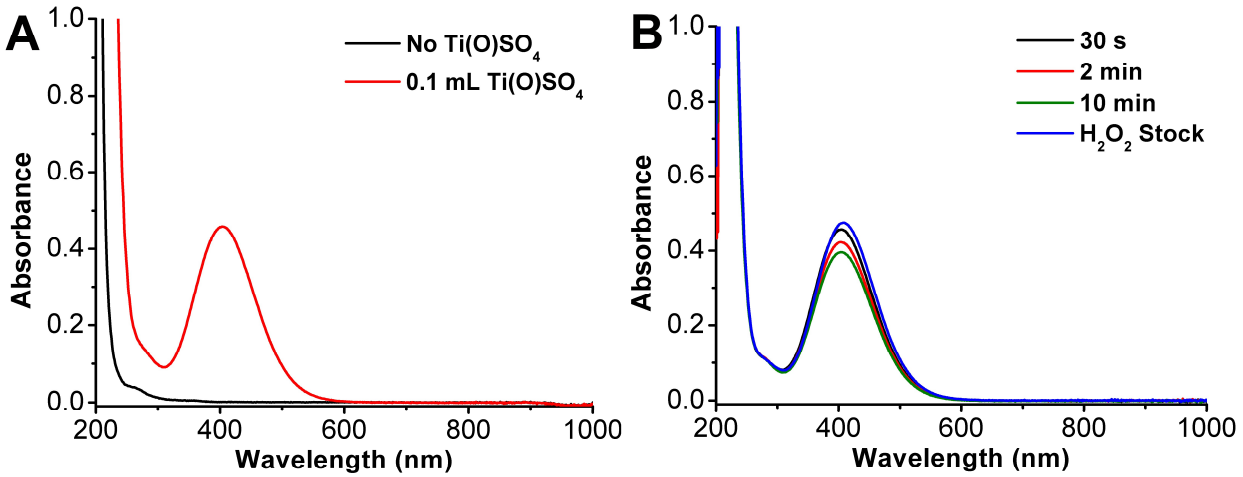

Figure S4.34. Stability test of urea•H_2O_2 in the presence of Mn($^{p\text{-}tbu}$dhbpy)Cl **1**, DIPEAHPF$_6$, DIPEA, and FeCp*$_2$ (A) before (black trace) and after (red trace) the addition of 0.1 mL of 0.1 M Ti(O)SO$_4$ to an extracted aliquot after 30 s. (B) Corrected UV-vis spectra (red – black from A) after 30 s (black), 120 s (red), 600 s (green), and H_2O_2 only (blue). Conditions: 40 μM Mn($^{p\text{-}tbu}$dhbpy)Cl, 10 mM DIPEAHPF$_6$/DIPEA, 2.3 mM urea•H_2O_2, 1 mM FeCp*$_2$ in MeCN.

Table S4.12. Summary of H_2O_2RR by Mn($^{p\text{-}tbu}$dhbpy)Cl **1** with 10 mM DIPEAHPF$_6$/DIPEA and 1 mM FeCp*$_2$ (**Figure S4.34**) relative to 2.3 mM H_2O_2 stock solution.

Time (s)	% H_2O_2 Recovered
30	94.1 ± 2.3
120	88.3 ± 1.9
540	82.9 ± 2.2

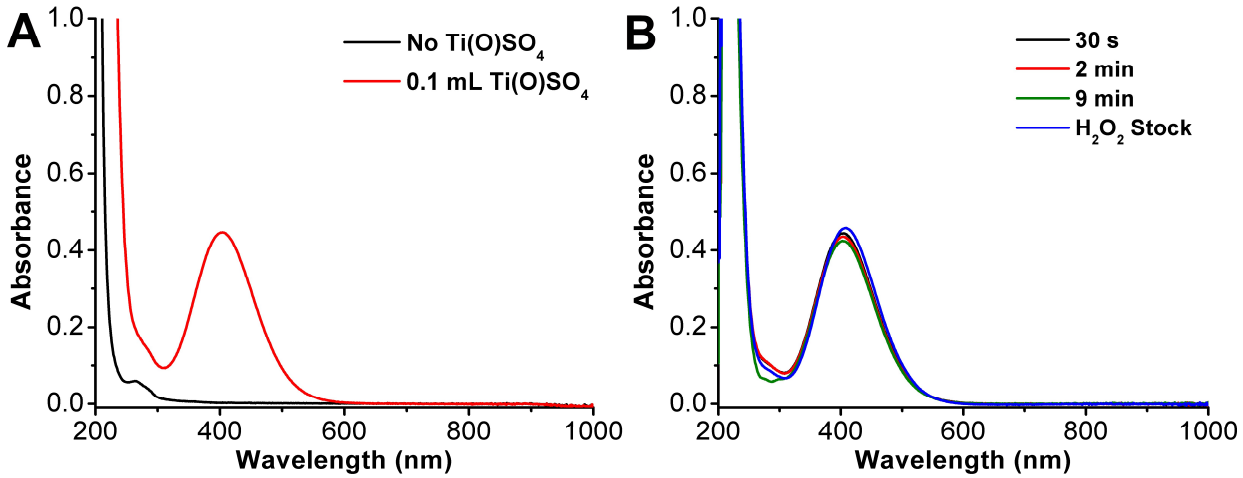

Figure S4.35. Stability test of urea•H_2O_2 in the presence of Mn(^{nPr}dhbpy)Cl **2**, DIPEAHPF$_6$, DIPEA, and FeCp*$_2$ (A) before (black trace) and after (red trace) the addition of 0.1 mL of 0.1 M Ti(O)SO$_4$ to an extracted aliquot after 30 s. (B) Corrected UV-vis spectra (red – black from A) after 30 s (black), 120 s (red), 600 s (green), and H_2O_2 only (blue). Conditions: 40 μM Mn(^{nPr}dhbpy)Cl, 10 mM DIPEAHPF$_6$/DIPEA, 2.3 mM urea•H_2O_2, 1 mM FeCp*$_2$ in MeCN.

Table S4.13. Summary of H_2O_2RR by Mn(^{nPr}dhbpy)Cl **2** with 10 mM DIPEAHPF$_6$/DIPEA and 1 mM FeCp*$_2$ (**Figure S4.35**) relative to 2.3 mM H_2O_2 stock solution.

Time (s)	% H_2O_2 Recovered
30	88.5 ± 1.2
120	91.1 ± 3.6
540	86.5 ± 4.5

Stopped-Flow Spectrochemical Methods

Stopped-flow spectrochemical kinetics studies were performed with a CSF-61DX2 Stopped-Flow System from Hi-Tech Scientific. Kinetic Studio Software was used to monitor a single wavelength and Integrated CCD Software was used to monitor the entire visible spectrum. All data fits were performed within the Kinetic Studio 4.0 Software Suite. Prior to experiments, dried and degassed MeCN was passed through syringes and the cell block before reagents were loaded. In a typical experiment, syringes would be charged with known concentrations of reagent. All reagent solutions were prepared immediately before use.

In general, a vial containing Mn catalyst and proton source (and conjugate base, if present) was sparged with O_2, drawn into a syringe and loaded into the stopped-flow. A second syringe containing N_2-saturated Cp*$_2$Fe solution loaded into the stopped-flow. All reported concentrations are the mixed concentrations in the spectroscopic cell.

Determination of the Rate Law for ORR by 1 under Unbuffered Conditions

$$\text{rate} = k_{cat}[Mn^{p-tbu}]^1[O_2]^1 \qquad \textbf{Eq S4.11}$$

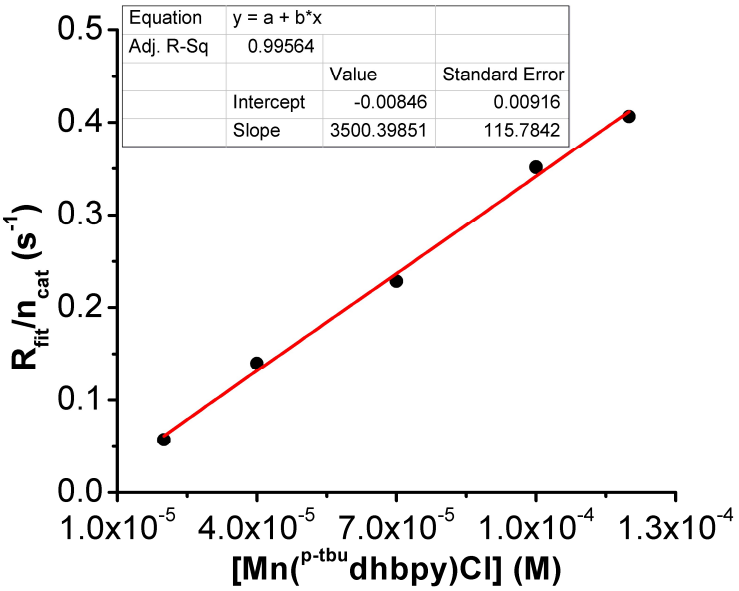

Figure S4.36. The calculated R_{fit}/n_{cat} values from stopped-flow spectrochemical experiments with DIPEAHPF$_6$, O_2, and Cp*$_2$Fe with varying Mn($^{p\text{-tbu}}$dhbpy)Cl **1** concentration. Data were fit using Kinetic Studio 4.0 (1Exp+Mx+C), n_{cat} = 2.72. Concentrations: DIPEAHPF$_6$ = 10 mM, O_2 = 4.05 mM, Cp*$_2$Fe = 1 mM.

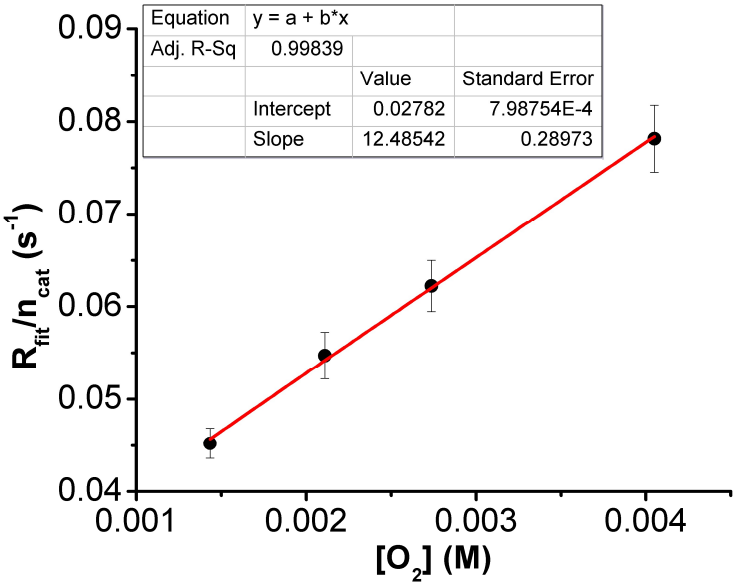

Figure S4.37. The calculated R_{fit}/n_{cat} values from stopped-flow spectrochemical experiments with Mn($^{p\text{-tbu}}$dhbpy)Cl **1**, DIPEAHPF$_6$, and Cp*$_2$Fe with varying O_2 concentration. Data were fit using Kinetic Studio 4.0 (1Exp+Mx+C), n_{cat} = 2.72. Concentrations: Mn($^{p\text{-tbu}}$dhbpy)Cl = 40 μM, DIPEAHPF$_6$ = 10 mM, Cp*$_2$Fe = 1 mM.

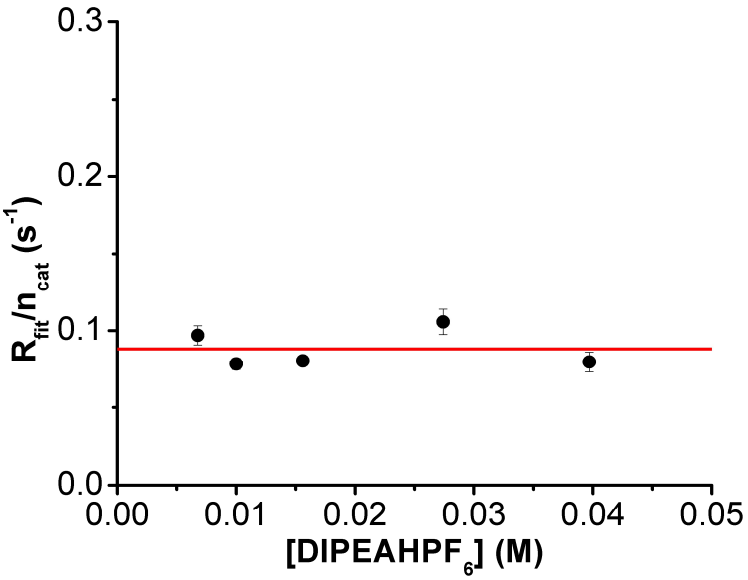

Figure S4.38. The calculated R_{fit}/n_{cat} values from stopped-flow spectrochemical experiments with Mn($^{p\text{-}tbu}$dhbpy)Cl **1**, O_2, and Cp*$_2$Fe with varying DIPEAHPF6 concentration. Data were fit using Kinetic Studio 4.0 (1Exp+Mx+C), n_{cat} = 2.72. The red line represents the global average over all points. Concentrations: Mn($^{p\text{-}tbu}$dhbpy)Cl = 40 μM, O_2 = 4.05 mM, Cp*$_2$Fe = 1 mM.

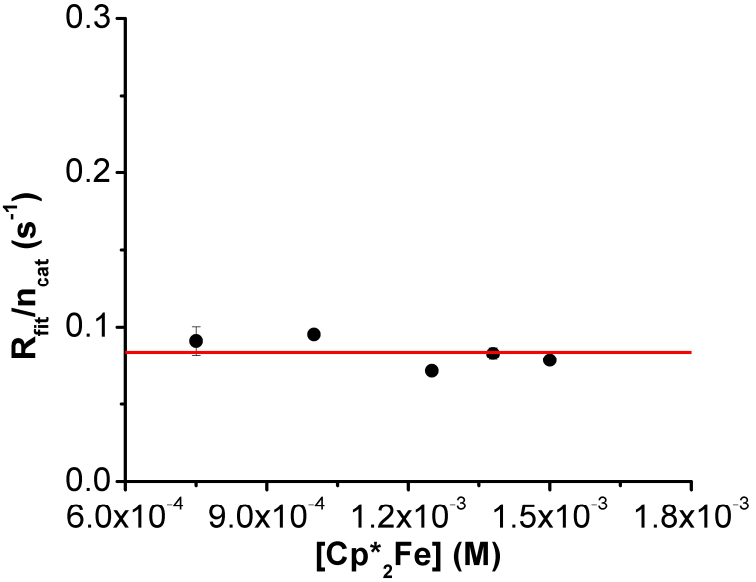

Figure S4.39. The calculated R_{fit}/n_{cat} values from stopped-flow spectrochemical experiments with Mn($^{p\text{-}tbu}$dhbpy)Cl **1**, O_2, and DIPEAHPF$_6$ with varying Cp*$_2$Fe concentration. Data were fit using Kinetic Studio 4.0 (1Exp+Mx+C), n_{cat} = 2.72. The red line represents the global average over all points. Concentrations: Mn($^{p\text{-}tbu}$dhbpy)Cl = 40 μM, O_2 = 4.05 mM, DIPEAHPF$_6$ = 10 mM.

Determination of the Rate Law of ORR by 1 under Buffered Conditions

$$rate = k_{cat}[Mn^{p-tbu}]^1[O_2]^1 \qquad \textbf{Eq S4.12}$$

Comparable k_{obs} values can be obtained from the average of R_{fit}/n_{cat} values across independent experimental data points at identical conditions: 40 μM [Mn], 10 mM [DIPEAHPF$_6$/DIPEA], 4.05 mM [O_2], and 1 mM [Cp*$_2$Fe] (**Figures S4.40–S4.44**).

k_{obs} = 1.23 ± 0.17 x 10^{-1} s^{-1}

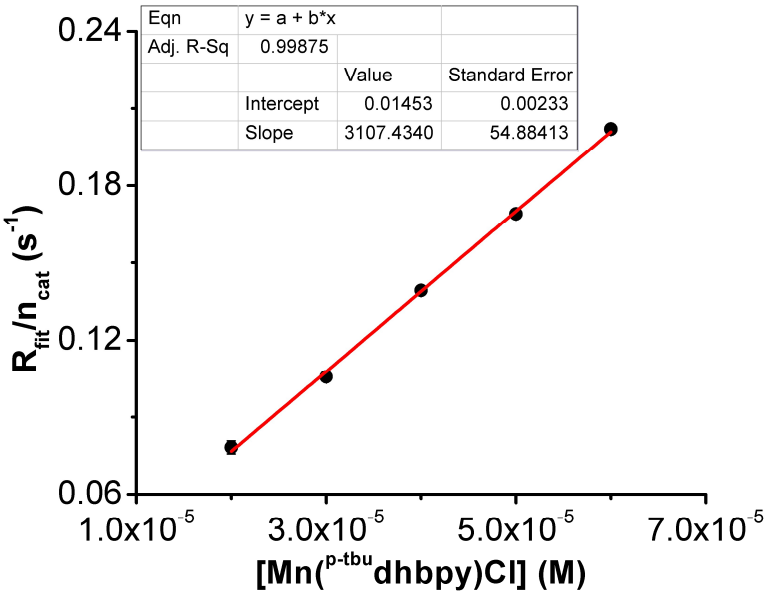

Figure S4.40. The calculated R_{fit}/n_{cat} values from stopped-flow spectrochemical experiments with DIPEAHPF$_6$, DIPEA, O_2, and Cp*$_2$Fe with varying Mn($^{p\text{-}tbu}$dhbpy)Cl **1** concentration. Data were fit using Kinetic Studio 4.0 (1Exp+Mx+C), n_{cat} = 3.64. Concentrations: DIPEAHPF$_6$/DIPEA = 10 mM, O_2 = 4.05 mM, Cp*$_2$Fe = 1 mM.

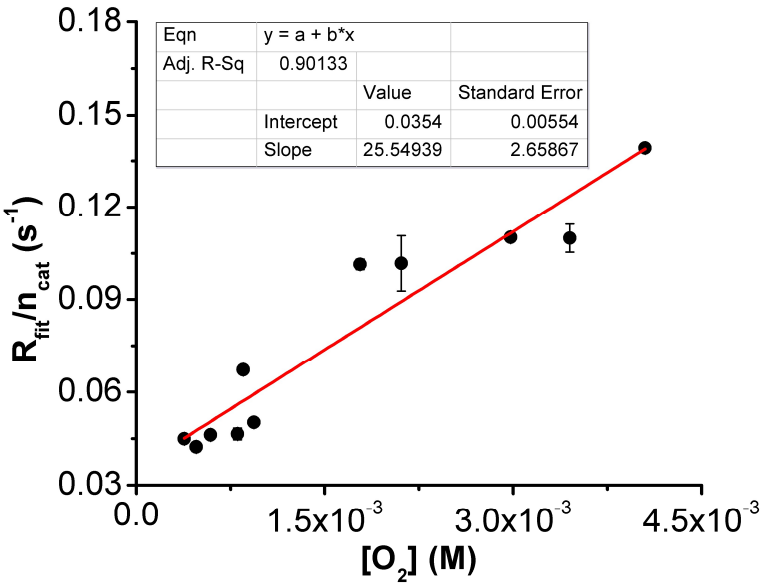

Figure S4.41. The calculated R_{fit}/n_{cat} values from stopped-flow spectrochemical experiments with Mn($^{p\text{-tbu}}$dhbpy)Cl **1**, DIPEAHPF$_6$, DIPEA, and Cp*$_2$Fe with varying O_2 concentration. Data were fit using Kinetic Studio 4.0 (1Exp+Mx+C), n_{cat} = 3.64. Concentrations: Mn($^{p\text{-tbu}}$dhbpy)Cl = 40 μM, DIPEAHPF$_6$/DIPEA = 10 mM, Cp*$_2$Fe = 1 mM.

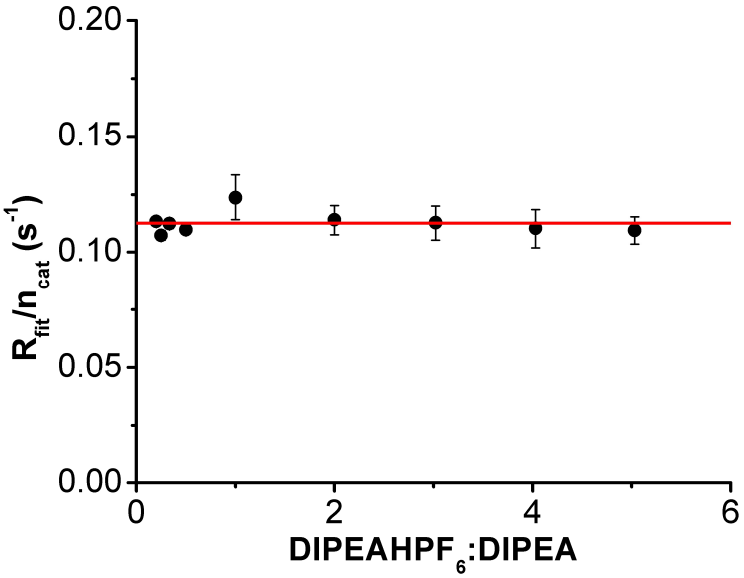

Figure S4.42. The calculated R_{fit}/n_{cat} values from stopped-flow spectrochemical experiments with Mn($^{p\text{-tbu}}$dhbpy)Cl **1**, O_2, DIPEA, and Cp*$_2$Fe with varying DIPEAHPF$_6$:DIPEA ratio. Data were fit using Kinetic Studio 4.0 (1Exp+Mx+C). The red line represents the global average over all points, n_{cat} = 3.64. Concentrations: Mn($^{p\text{-tbu}}$dhbpy)Cl = 40 μM, DIPEA = 10 mM, O_2 = 4.05 mM, Cp*$_2$Fe = 1 mM; 1:1 DIPEAHPF$_6$:DIPEA = 10 mM of each and all concentrations are relative to this point.

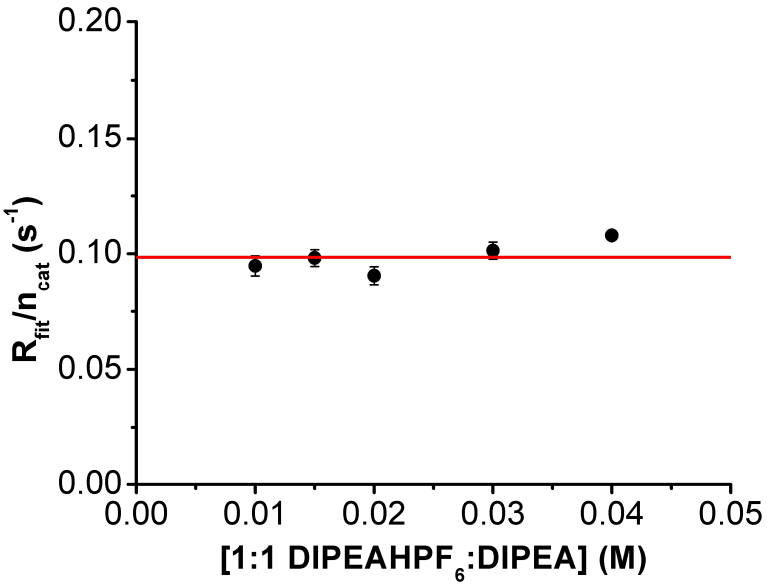

Figure S4.43. The calculated R_{fit}/n_{cat} values from stopped-flow spectrochemical experiments with Mn($^{p\text{-}tbu}$dhbpy)Cl **1**, O_2, and Cp*$_2$Fe with varying buffer (DIPEAHPF$_6$ and DIPEA, 1:1 ratio) concentration. Data were fit using Kinetic Studio 4.0 (1Exp+Mx+C). The red line represents the global average over all points, n_{cat} = 3.64. Concentrations: Mn($^{p\text{-}tbu}$dhbpy)Cl = 40 μM, O_2 = 4.05 mM, Cp*$_2$Fe = 1 mM.

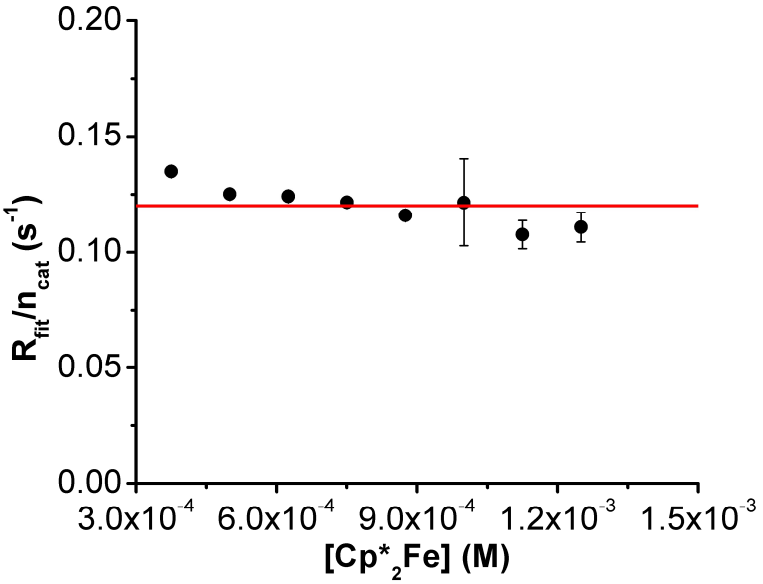

Figure S4.44. The calculated R_{fit}/n_{cat} values from stopped-flow spectrochemical experiments with Mn($^{p\text{-}tbu}$dhbpy)Cl **1**, DIPEAHPF$_6$, DIPEA, and O_2 with varying Cp*$_2$Fe concentration. Data were fit using Kinetic Studio 4.0 (1Exp+Mx+C). The red line represents the global average over all points, n_{cat} = 3.64. Concentrations: Mn($^{p\text{-}tbu}$dhbpy)Cl = 40 μM, O_2 = 4.05 mM, DIPEAHPF$_6$/DIPEA = 10 mM.

Determination of Rate Law of ORR by 2 under Unbuffered Conditions

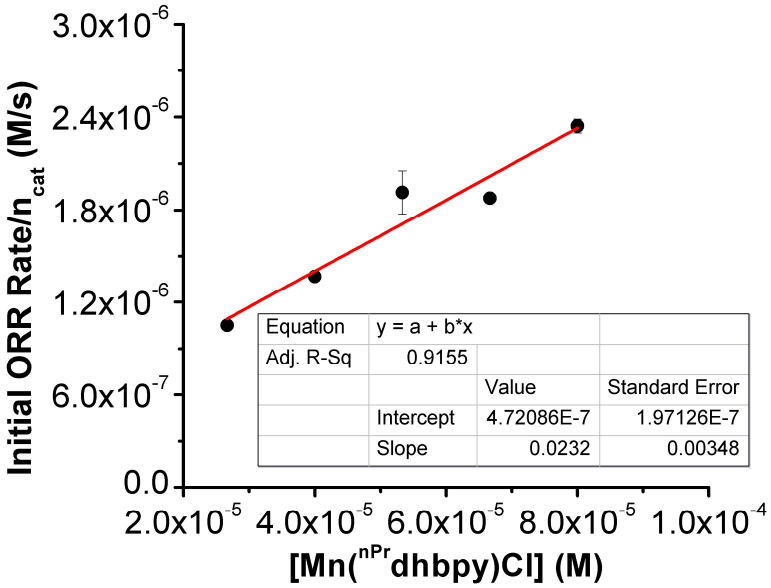

Figure S4.45. The calculated initial ORR rate from stopped-flow spectrochemical experiments with $DIPEAHPF_6$, O_2, Cp^*_2Fe with varying Mn(^{nPr}dhbpy)Cl **2** concentration. Data were fit using Kinetic Studio 4.0 (Linear) correcting for the concentration of Cp^*_2Fe and n_{cat} = 2.08 Concentrations: $DIPEAHPF_6$ = 10 mM, O_2 = 4.05 mM, and Cp^*_2Fe = 1 mM.

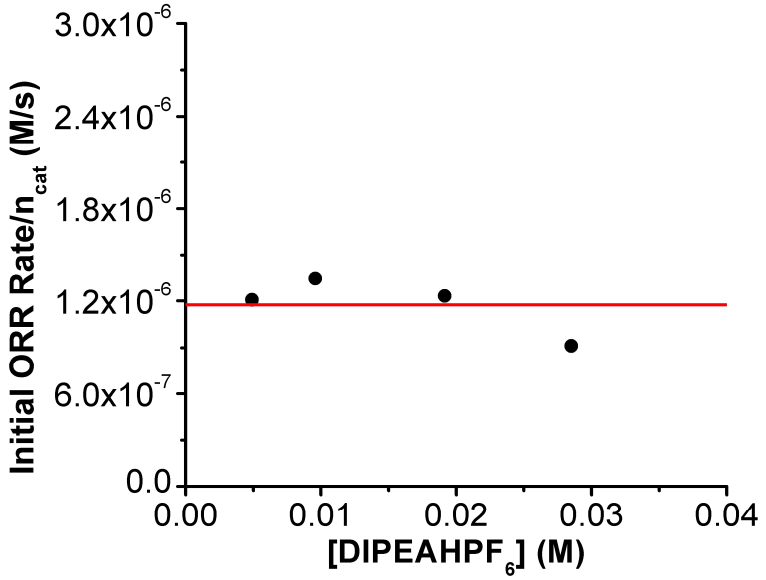

Figure S4.46. The calculated initial ORR rate from stopped-flow spectrochemical experiments with, Mn(^{nPr}dhbpy)Cl **2**, O_2, Cp^*_2Fe with varying $DIPEAHPF_6$ concentration. Data were fit using Kinetic Studio 4.0 (Linear) correcting for the concentration of Cp^*_2Fe and n_{cat} = 2.08. Concentrations: Mn(^{nPr}dhbpy)Cl = 40 μM, O_2 = 4.05 mM, and Cp^*_2Fe = 1 mM.

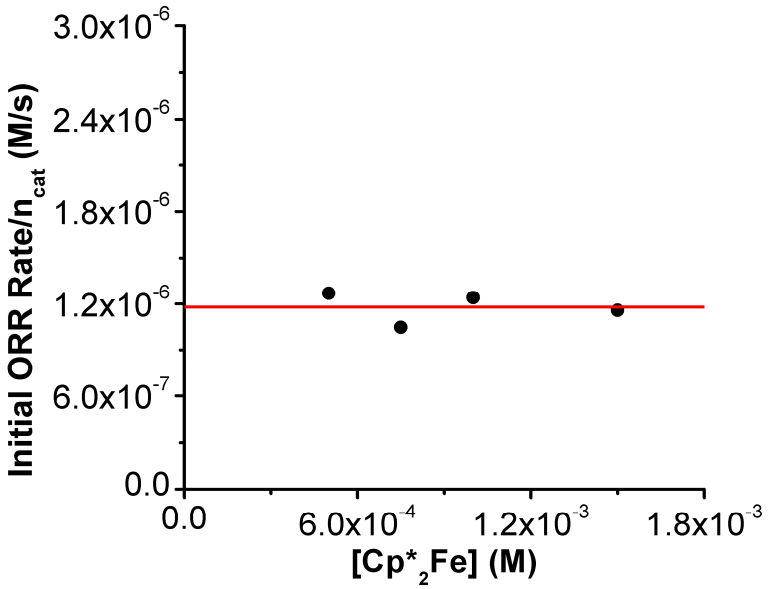

Figure S4.47. The calculated initial ORR rate from stopped-flow spectrochemical experiments with, Mn(^{nPr}dhbpy)Cl **2**, DIPEAHPF$_6$, O_2, with varying Cp*$_2$Fe concentration. Data were fit using Kinetic Studio 4.0 (Linear) and correcting for the concentration of Cp*$_2$Fe and n_{cat} = 2.08. Concentrations: Mn(^{nPr}dhbpy)Cl = 40 μM, O_2 = 4.05 mM, and DIPEAHPF$_6$ = 10 mM.

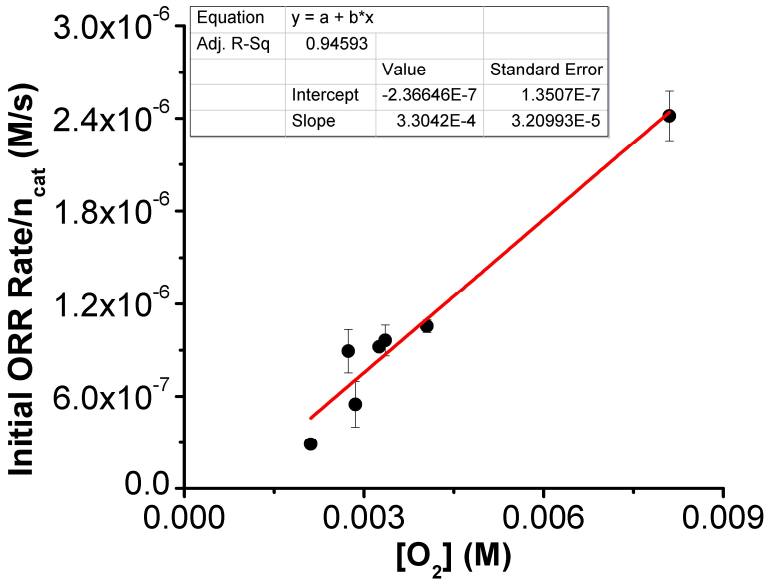

Figure S4.48. The calculated initial ORR rate from stopped-flow spectrochemical experiments with, Mn(^{nPr}dhbpy)Cl **2**, DIPEAHPF$_6$, Cp*$_2$Fe with varying O_2, concentration. Data were fit using Kinetic Studio 4.0 (Linear) and correcting for the concentration of Cp*$_2$Fe and n_{cat} = 2.08. Concentrations: Mn(^{nPr}dhbpy)Cl = 40 μM, O_2 = 4.05 mM, and DIPEAHPF$_6$ = 10 mM.

Determination of Rate Law for ORR by 2 under Buffered Conditions

$$rate = k_{cat}[Mn^{nPr}]^2[DIPEA]^1[Cp^*{}_2Fe]^{-1} \quad \textbf{Eq S4.13}$$

Comparable k_{obs} values can be obtained from the average of R_{fit}/n_{cat} values across independent experimental data points at identical conditions: 40 μM [Mn], 10 mM [DIPEAHPF$_6$/DIPEA], 4.05 mM [O_2], and 1 mM [Cp*$_2$Fe] (**Figures S4.49-S4.53**).

$$k_{obs} = 0.706 \pm 0.25 \times 10^{-1}\ s^{-1}$$

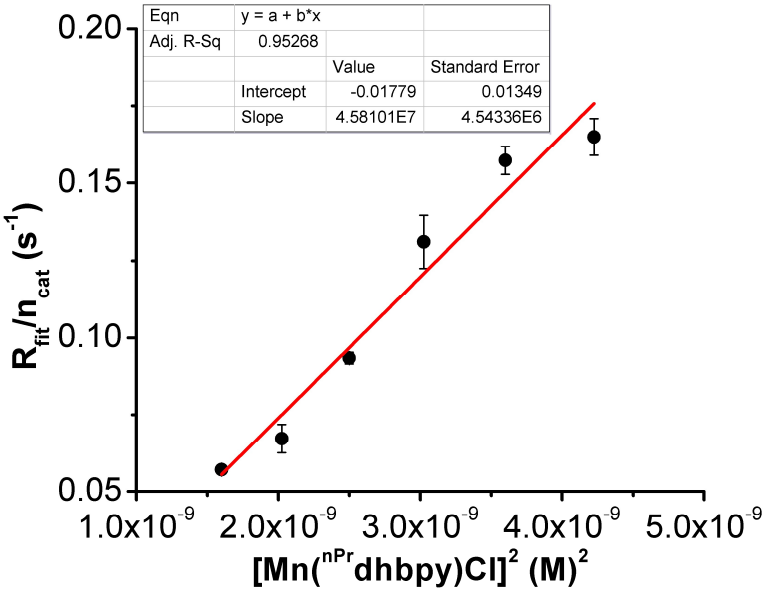

Figure S4.49. The calculated R_{fit}/n_{cat} values from stopped-flow spectrochemical experiments with DIPEAHPF$_6$, DIPEA, O_2, and Cp*$_2$Fe with varying Mn(^{nPr}dhbpy)Cl **2** concentration. Data were fit using Kinetic Studio 4.0 (1Exp+Mx+C), n_{cat} = 3.24. Concentrations: DIPEAHPF$_6$/DIPEA = 10 mM, O_2 = 4.05 mM, Cp*$_2$Fe = 1 mM.

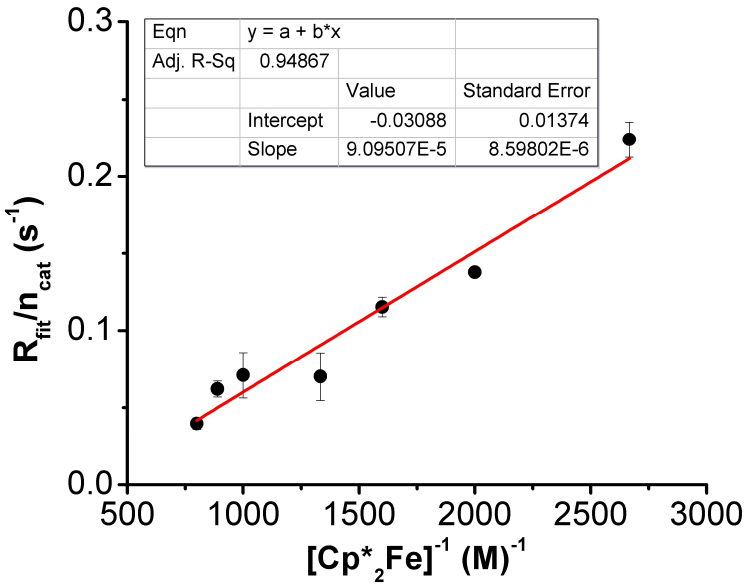

Figure S4.50. The calculated R_{fit}/n_{cat} values from stopped-flow spectrochemical experiments with Mn(^{nPr}dhbpy)Cl **2**, DIPEAHPF$_6$, DIPEA, and O_2 with varying Cp^*_2Fe concentration. Data were fit using Kinetic Studio 4.0 (1Exp+Mx+C); n_{cat} = 3.24. Concentrations: Mn(^{nPr}dhbpy)Cl = 40 μM, O_2 = 4.05 mM, DIPEAHPF$_6$/DIPEA = 10 mM.

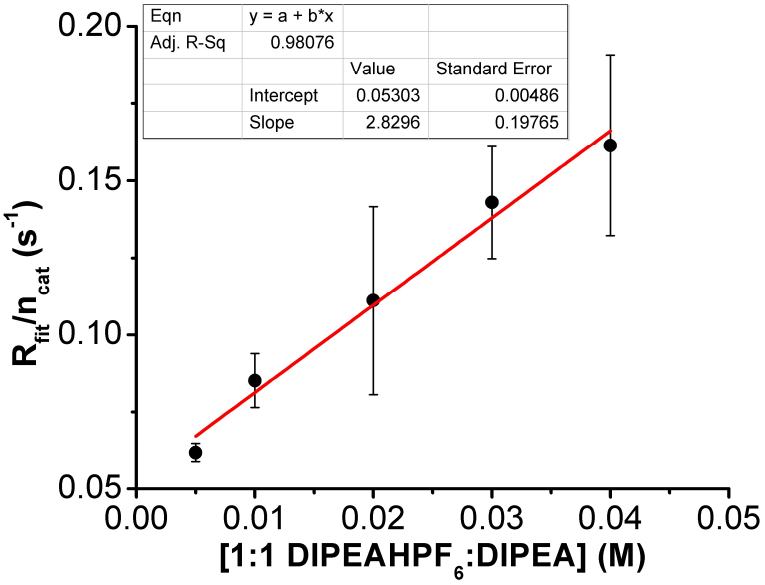

Figure S4.51. The calculated R_{fit}/n_{cat} values from stopped-flow spectrochemical experiments with Mn(^{nPr}dhbpy)Cl **2**, O_2, and Cp^*_2Fe with varying buffer (DIPEAHPF$_6$ and DIPEA, 1:1 ratio) concentration. Data were fit using Kinetic Studio 4.0 (1Exp+Mx+C); n_{cat} = 3.24. Concentrations: Mn(^{nPr}dhbpy)Cl = 40 μM, O_2 = 4.05 mM, Cp^*_2Fe = 1 mM.

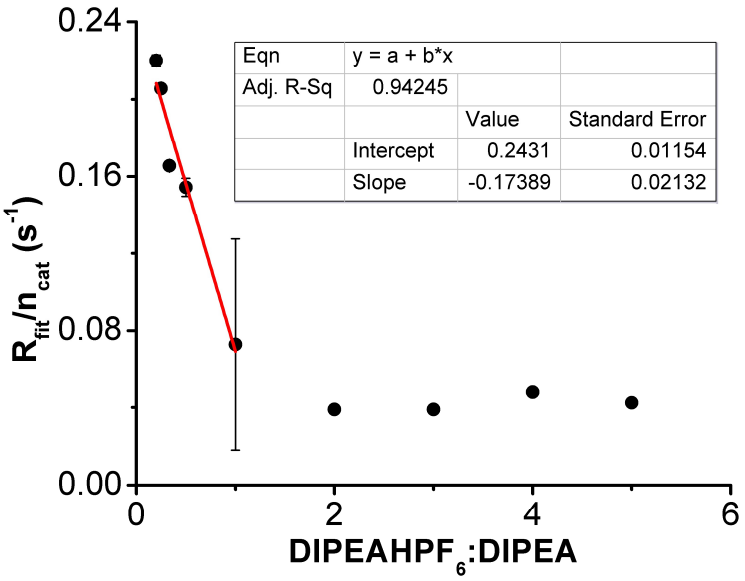

Figure S4.52. The calculated R_{fit}/n_{cat} values from stopped-flow spectrochemical experiments with Mn(^{nPr}dhbpy)Cl **2**, O_2, and Cp*$_2$Fe with varying DIPEAHPF$_6$:DIPEA ratio. Data were fit using Kinetic Studio 4.0 (1Exp+Mx+C); n_{cat} = 3.24. Concentrations: Mn($^{p\text{-}tbu}$dhbpy)Cl = 40 μM, O_2 = 4.05 mM, 1:1 DIPEAHPF$_6$:DIPEA = 10 mM, Cp*$_2$Fe = 1 mM; 1:1 DIPEAHPF$_6$:DIPEA = 10 mM and all concentrations are relative to this point.

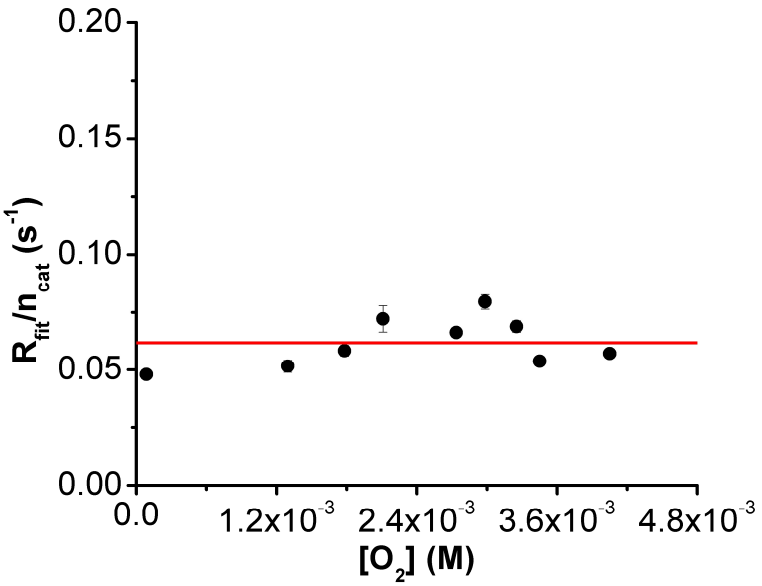

Figure S4.53. The calculated R_{fit}/n_{cat} values from stopped-flow spectrochemical experiments with Mn(^{nPr}dhbpy)Cl **2**, DIPEAHPF$_6$, DIPEA, and Cp*$_2$Fe with varying O_2 concentration. Data were fit using Kinetic Studio 4.0 (1Exp+Mx+C); n_{cat} = 3.24. Concentrations: Mn(^{nPr}dhbpy)Cl = 40 μM, DIPEAHPF$_6$ = 10 mM, DIPEA = 10 mM, Cp*$_2$Fe = 1 mM.

Description of Stopped-Flow Data Fitting

1Exp+Mx+C Fits

For the rate law determination of ORR by Mn($^{p\text{-}tbu}$dhbpy)Cl **1** with and without the presence of DIEPA and by Mn(^{nPr}dhbpy)Cl **2** with the presence of DIPEA, Kinetic Studio 4.0 was used to fit data sets with 1Exp+Mx+C. R_{fit} values were obtained by fitting the increase in absorbance at 780 nm versus time to a single exponential (1Exp+Mx+C) to achieve an R^2 value of 0.99 (See Figures S54-S56). Where the fit equation contains an exponent (1Exp), a linear portion (Mx) and a non-zero intercept (C). The R_{fit} values were corrected for the number of electrons passed during catalysis and plotted against variable concentrations to obtain the experimental rate law.

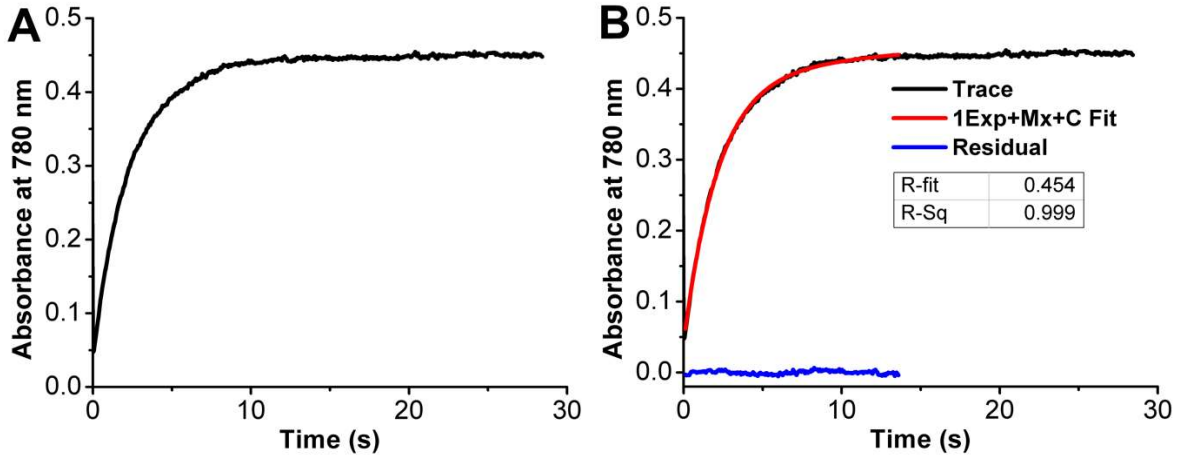

Figure S4.54. (A) Representative trace of time versus absorbance at 780 nm for ORR catalyzed by Mn($^{p\text{-}tbu}$dhbpy)Cl **1** with DIPEAHPF$_6$/DIPEA and (B) the 1Exp+Mx+C fit (red) and residual (blue) used for data analysis using the Kinetic Studio 4.0 software. Conditions: Mn($^{p\text{-}tbu}$dhbpy)Cl = 40 μM, Cp*$_2$Fe = 1 mM, O_2 = 4.05 mM, and DIPEAHPF$_6$/DIEPA = 10 mM.

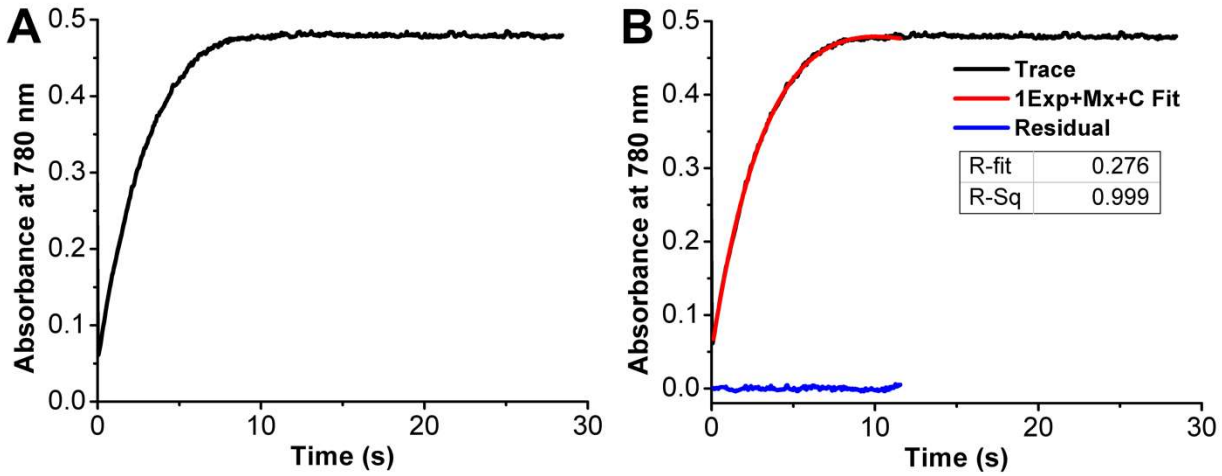

Figure S4.55. (A) Representative trace of time versus absorbance at 780 nm for ORR catalyzed by Mn(^{nPr}dhbpy)Cl **2** with DIPEAHPF$_6$/DIPEA and (B) the 1Exp+Mx+C fit (red) and residual (blue) used for data analysis using the Kinetic Studio 4.0 software. Conditions: Mn(^{nPr}dhbpy)Cl = 40 μM, Cp*$_2$Fe = 1 mM, O_2 = 4.05 mM, and DIPEAHPF$_6$/DIEPA = 10 mM.

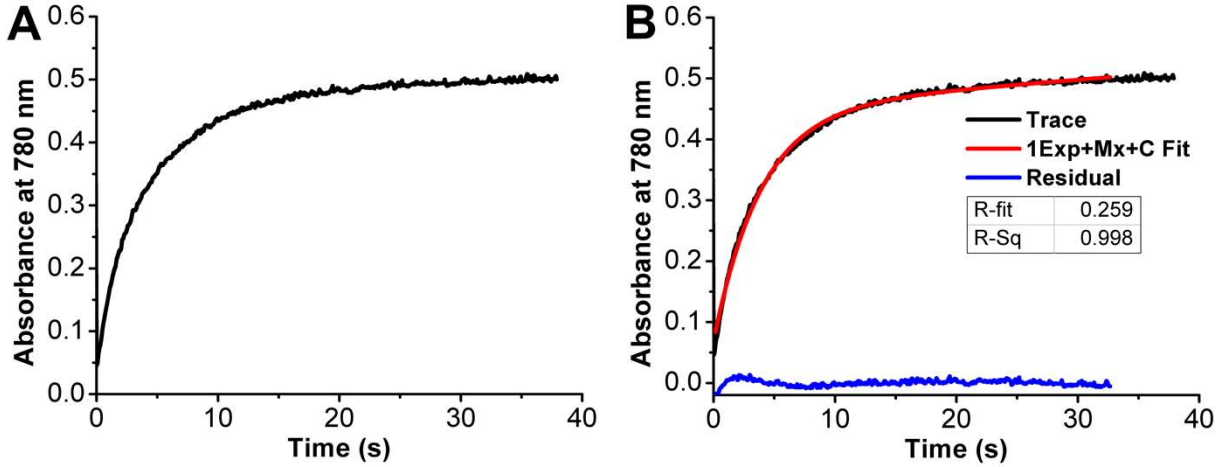

Figure S4.56. (A) Representative trace of time versus absorbance at 780 nm for ORR catalyzed by Mn($^{p\text{-}tbu}$dhbpy)Cl **1** with DIPEAHPF$_6$ and (B) the 1Exp+Mx+C fit (red) and residual (blue) used for data analysis using the Kinetic Studio 4.0 software. Conditions: Mn($^{p\text{-}tbu}$dhbpy)Cl = 40 μM, Cp*$_2$Fe = 1 mM, O_2 = 4.05 mM, and DIPEAHPF$_6$ = 10 mM.

Initial Rates Method

For the rate law determination of ORR by Mn(^{nPr}dhbpy)Cl **2** without the presence of DIPEA, the initial rates method was used due to the linearity of the observed curve. In this case, Initial ORR Rate values were obtained by taking slope of the linear fit of the initial region (~1.5 to ~50 s) in the Kinetic Studio 4.0 software of [Cp*$_2$Fe]$^+$ growth at 780 nm (units = relative absorbance/second). The results of the linear fit were processed to reflect the rate of ORR by

converting the relative absorbance units to concentration using the molar extinction coefficient of $[Cp^*_2Fe]^+$ (ε = 461 $M^{-1}cm^{-1}$ as determined by serial dilution of a chemical prepared sample of $[Cp^*_2Fe][BF_4]$) and correcting for the number of electrons passed during catalysis (n_{cat} = 2.08). See **Figure S4.57** for description of the linear fits.

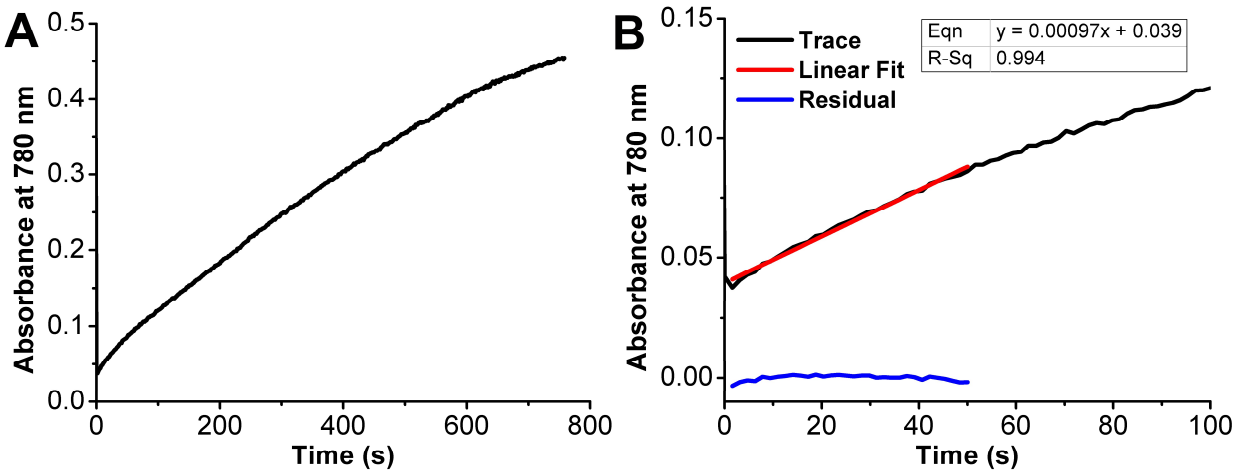

Figure S4.57. (A) Representative trace of time versus absorbance at 780 nm for ORR catalyzed by Mn(^{nPr}dhbpy)Cl **2** with $DIPEAHPF_6$ and (B) the initial Linear fit (red) and residual (blue) used for data analysis using the Kinetic Studio 4.0 software. Conditions: Mn(^{nPr}dhbpy)Cl = 40 μM, Cp^*_2Fe = 1 mM, O_2 = 4.05 mM, and $DIPEAHPF_6$ = 10 mM.

UV-vis Spectroscopic Analysis

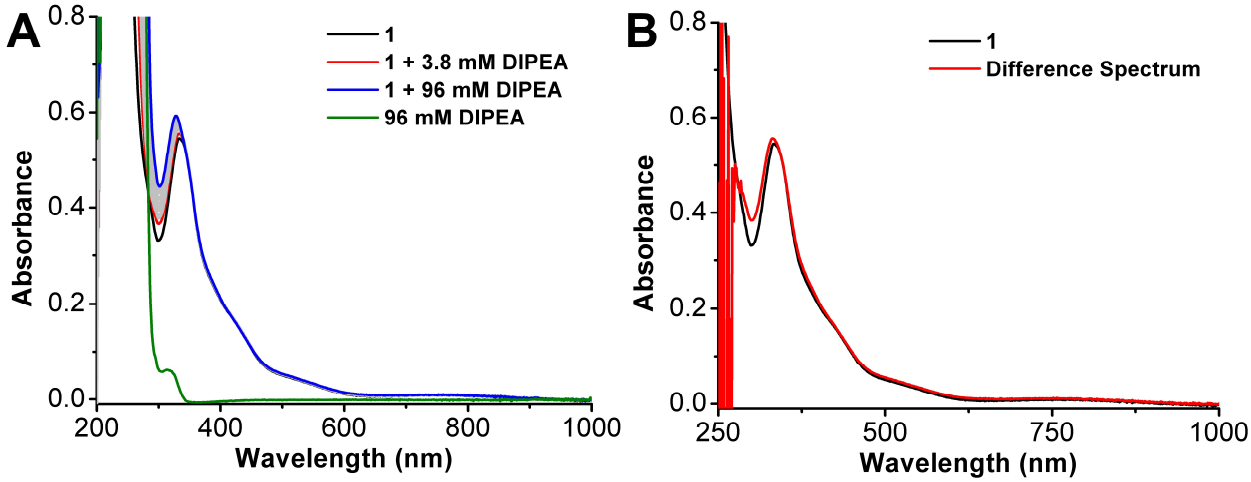

Figure S4.58. (A) UV-vis of spectra of 23 μM Mn($^{p\text{-}tbu}$dhbpy)Cl **1** with increasing amounts of DIPEA in MeCN (B) difference spectrum of the final titration point (blue – green traces). Conditions: quartz cuvette with 1 cm pathlength; [DIPEA] = 3.8, 7.7, 12, 15.3, 19, 29, 38, 48, 57, 67, 77, 86, 96 mM.

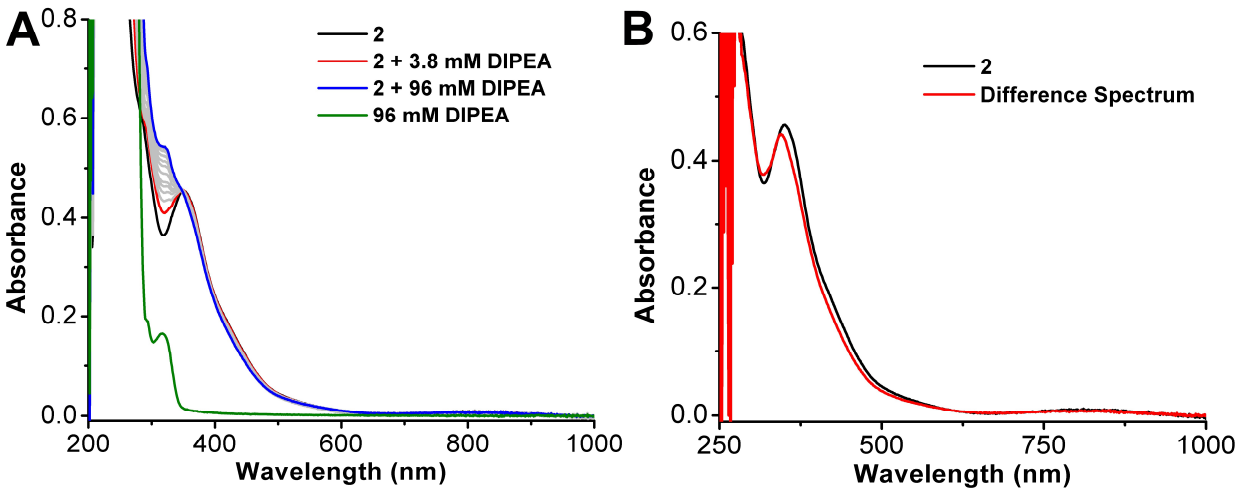

Figure S4.59. (A) UV-vis of spectra of 26.8 μM Mn(^{nPr}dhbpy)Cl **2** with increasing amounts of DIPEA in MeCN (B) difference spectrum of the final titration point (blue – green traces). Conditions: quartz cuvette with 1 cm pathlength; [DIPEA] = 3.8, 7.7, 12, 15.3, 19, 29, 38, 48, 57, 67, 77, 86, 96 mM.

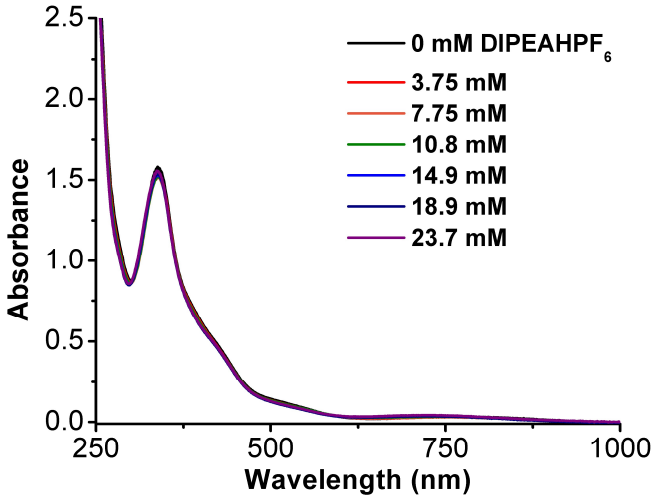

Figure S4.60. UV-vis of spectra of 80 μM Mn($^{p\text{-}tbu}$dhbpy)Cl **1** with increasing amounts of DIPEAHPF$_6$. Conditions: quartz cuvette with 1 cm pathlength.

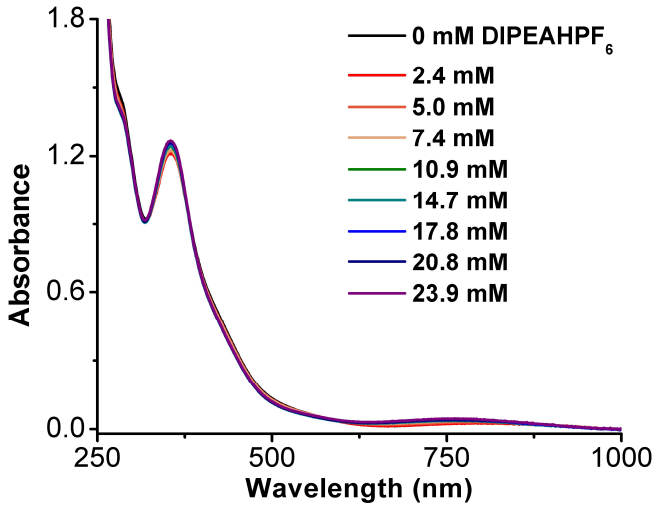

Figure S4.61. (A) UV-vis spectra of 80 μM Mn(^{nPr}dhbpy)Cl **2** with increasing amounts of $DIPEAHPF_6$ in MeCN. Conditions: quartz cuvette with 1 cm pathlength.

UV-vis Spectroscopic Studies of Mn($^{p\text{-}tbu}$dhbpy)Cl 1 and Cobaltocene

In order to better understand the reactivity of reduced Mn($^{p\text{-}tbu}$dhbpy)Cl **1** and Mn(^{nPr}dhbpy)Cl **2**, we used cobaltocene ($CoCp_2$) as a chemical reductant in solution. Solutions were prepared in a N_2 filled glovebox. To expose solutions to O_2, the cuvette was opened and inverted.

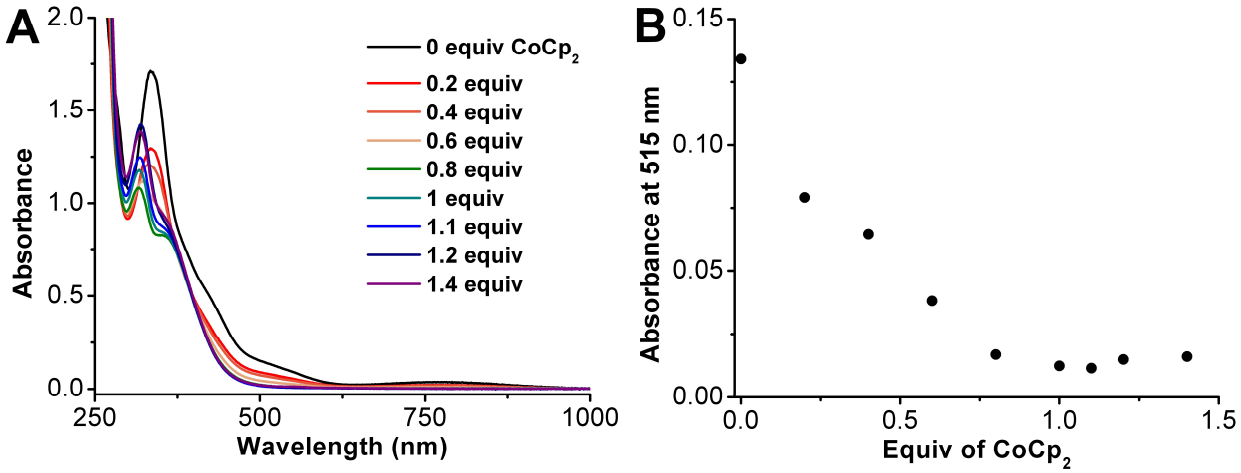

Figure S4.62. (A) UV-vis spectra of an 80 μM solution of Mn($^{p\text{-}tbu}$dhbpy)Cl **1** with increasing amounts of $CoCp_2$ in MeCN under N_2. (B) Absorbance at 515 nm versus equivalents of $CoCp_2$ relative to [**1**]. Conditions: quartz cuvette with 1 cm pathlength.

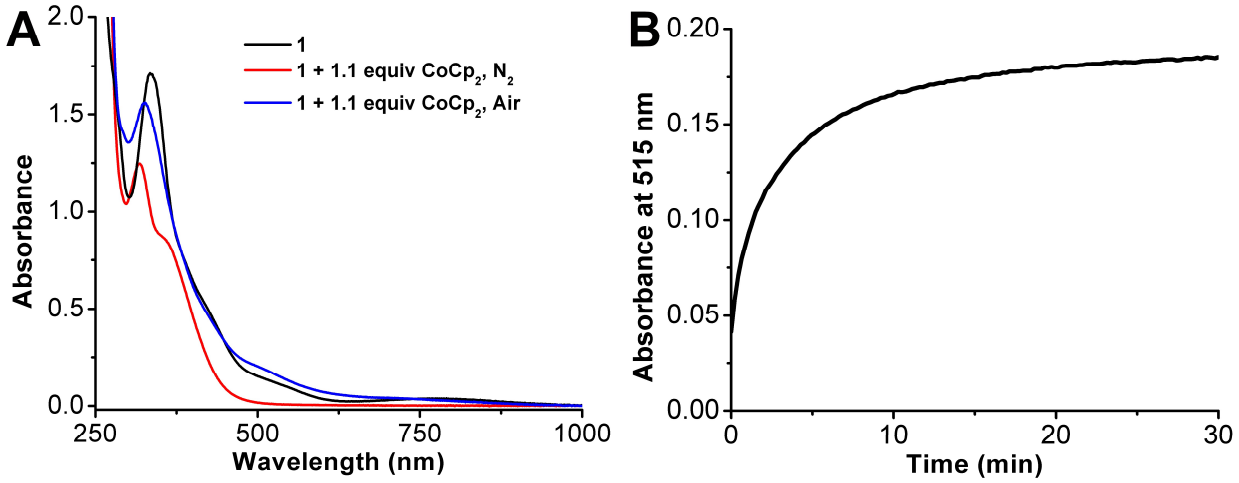

Figure S4.63. (A) UV-vis spectra of 80 μM solution of Mn($^{p\text{-tbu}}$dhbpy)Cl **1** in MeCN (black) under N_2 with 1.1 equiv of $CoCp_2$ (red) and after being exposed to air for 30 min (blue). (B) Time versus absorbance at 515 nm upon exposure of a 80 μM solution of Mn($^{p\text{-tbu}}$dhbpy)Cl with 1.1 equiv $CoCp_2$ to air. Conditions: quartz cuvette with 1 cm pathlength.

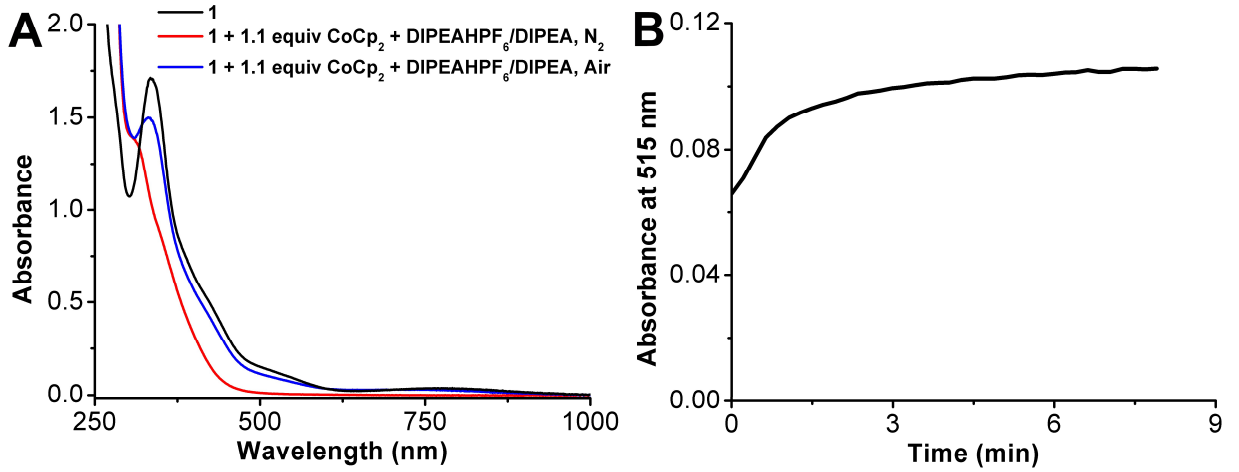

Figure S4.64. (A) UV-vis spectra of 80 μM solution of Mn($^{p\text{-tbu}}$dhbpy)Cl **1** in MeCN (black) under N_2 with 1.1 equiv of $CoCp_2$ and 19.7 mM DIPEAHPF6/DIPEA (red) and after being exposed to air for 8 min (blue). (B) Time versus absorbance at 515 nm upon exposure of a 80 μM solution of Mn($^{p\text{-tbu}}$dhbpy)Cl with 1.1 equiv $CoCp_2$ and 19 mM $DIPEAHPF_6$/DIPEA to air. Conditions: quartz cuvette with 1 cm pathlength.

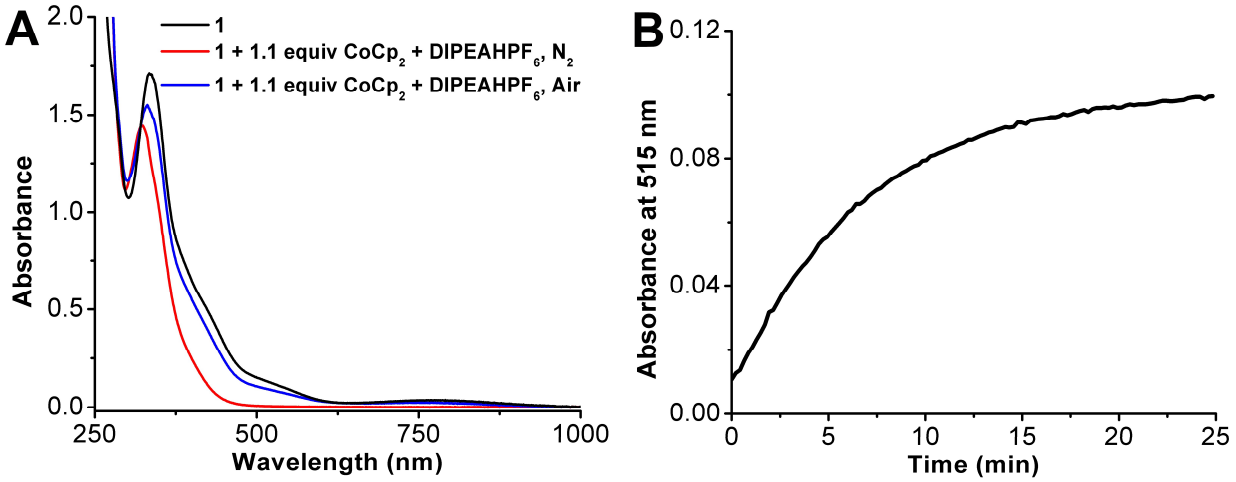

Figure S4.65. (A) UV-vis spectra of 80 μM solution of Mn($^{p\text{-}tbu}$dhbpy)Cl **1** in MeCN (black) under N_2 with 1.1 equiv of $CoCp_2$ and 19.7 mM $DIPEAHPF_6$ (red) and after being exposed to air for 25 min (blue). (B) Time versus absorbance at 515 nm upon exposure of a 80 μM solution of Mn($^{p\text{-}tbu}$dhbpy)Cl with 1.1 equiv $CoCp_2$ and 19.7 mM $DIPEAHPF_6$ to air. Conditions: quartz cuvette with 1 cm pathlength.

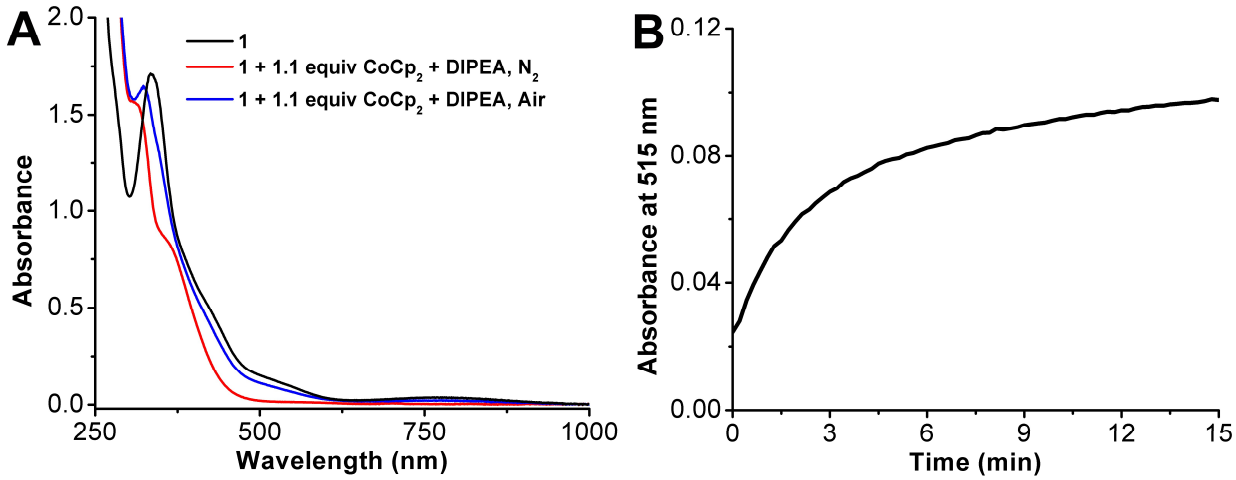

Figure S4.66. (A) UV-vis spectra of 80 μM solution of Mn($^{p\text{-}tbu}$dhbpy)Cl **1** in MeCN (black) under N_2 with 1.1 equiv of $CoCp_2$ and 19 mM DIPEA (red) and after being exposed to air for 15 min (blue). (B) Time versus absorbance at 515 nm upon exposure of a 80 μM solution of Mn($^{p\text{-}tbu}$dhbpy)Cl with 1.1 equiv $CoCp_2$ and 19 mM DIPEA to air. Conditions: quartz cuvette with 1 cm pathlength.

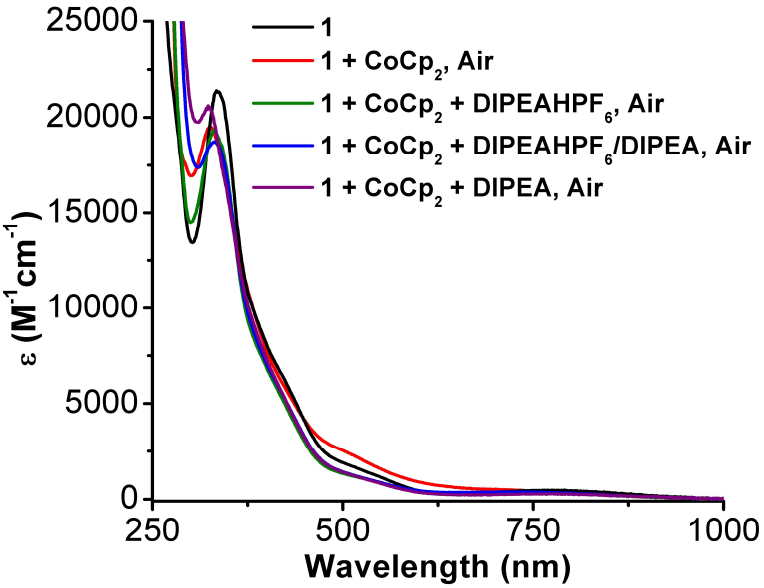

Figure S4.67. Overlay of data involving Mn($^{p\text{-tbu}}$dhbpy)Cl **1** from **Figs S63-S66** after samples were allowed to react with air completely.

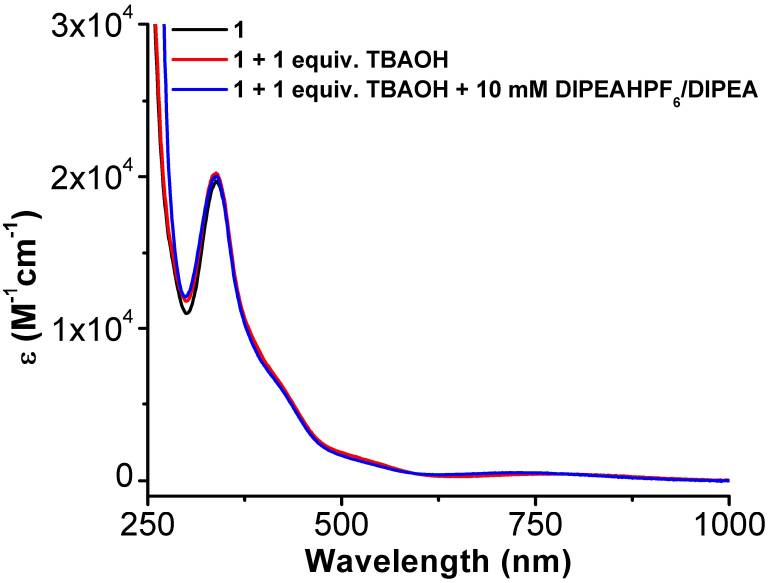

Figure S4.68. UV-vis spectra of 80 μM Mn($^{p\text{-tbu}}$dhbpy)Cl **1** with (red) and without (black) 1 equiv TBAOH•30H_2O and with of 10 mM buffer (1:1 DIPEAHPF_6:DIPEA) in the presence of 1 equiv TBAOH•30H_2O (blue). Conditions: quartz cuvette with 1 cm pathlength.

UV-vis Spectroscopic Studies of Mn(^{nPr}dhbpy)Cl 2 and Cobaltocene

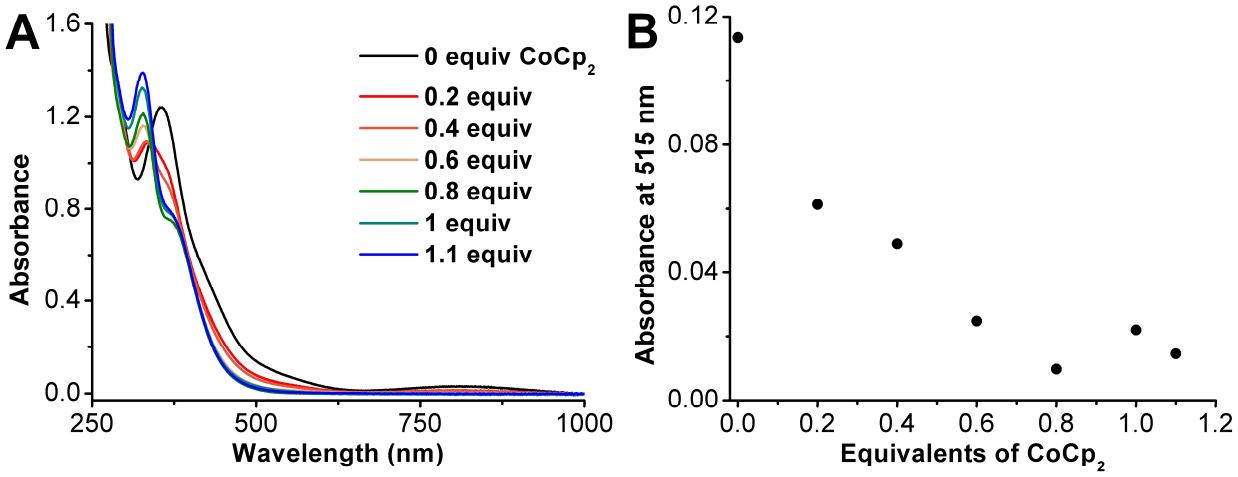

Figure S4.69. (A) UV-vis spectra of an 80 μM solution of Mn(^{nPr}dhbpy) **2** with increasing amounts of $CoCp_2$ in MeCN under N_2. (B) Absorbance at 515 nm versus equivalents of $CoCp_2$ relative to [**2**]. Conditions: quartz cuvette with 1 cm pathlength.

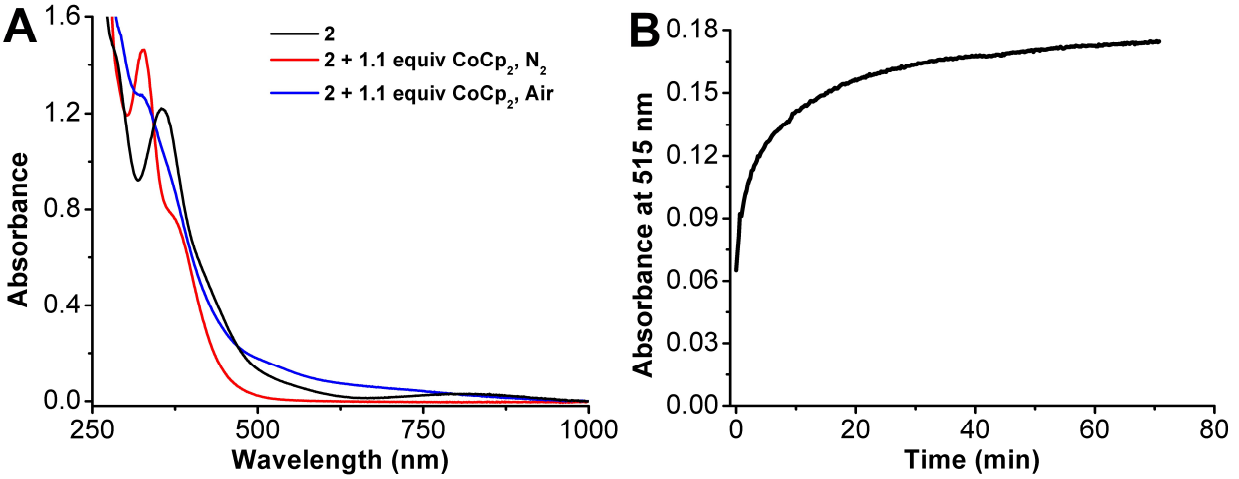

Figure S4.70. (A) UV-vis spectra of 80 μM solution of Mn(^{nPr}dhbpy)Cl **2** in MeCN (black) under N_2 with 1.1 equiv of $CoCp_2$ (red) and after being exposed to air for 70 min (blue). (B) Time versus absorbance at 515 nm upon exposure of an 80 μM solution of Mn(^{nPr}dhbpy)Cl with 1.1 equiv $CoCp_2$ to air. Conditions: quartz cuvette with 1 cm pathlength.

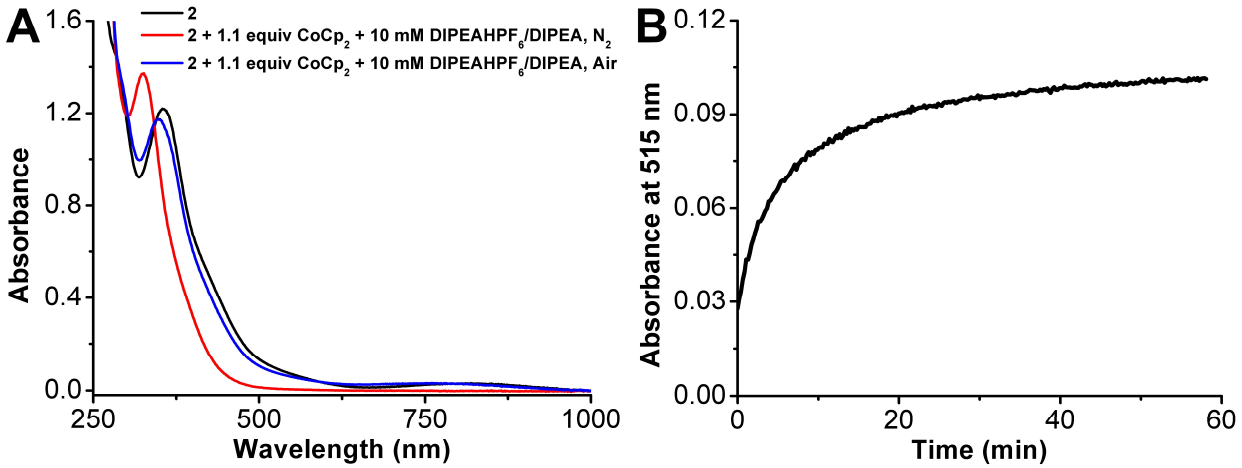

Figure S4.71. (A) UV-vis spectra of 80 μM solution of Mn(^{nPr}dhbpy)Cl **2** in MeCN (black) under N_2 with 1.1 equiv of $CoCp_2$ and 10 mM $DIPEAHPF_6$/DIPEA (red) and after being exposed to air for 60 min (blue). (B) Time versus absorbance at 515 nm upon exposure of an 80 μM solution of Mn(^{nPr}dhbpy)Cl with 1.1 equiv $CoCp_2$ and 10 mM $DIPEAHPF_6$/DIPEA to air. Conditions: quartz cuvette with 1 cm pathlength.

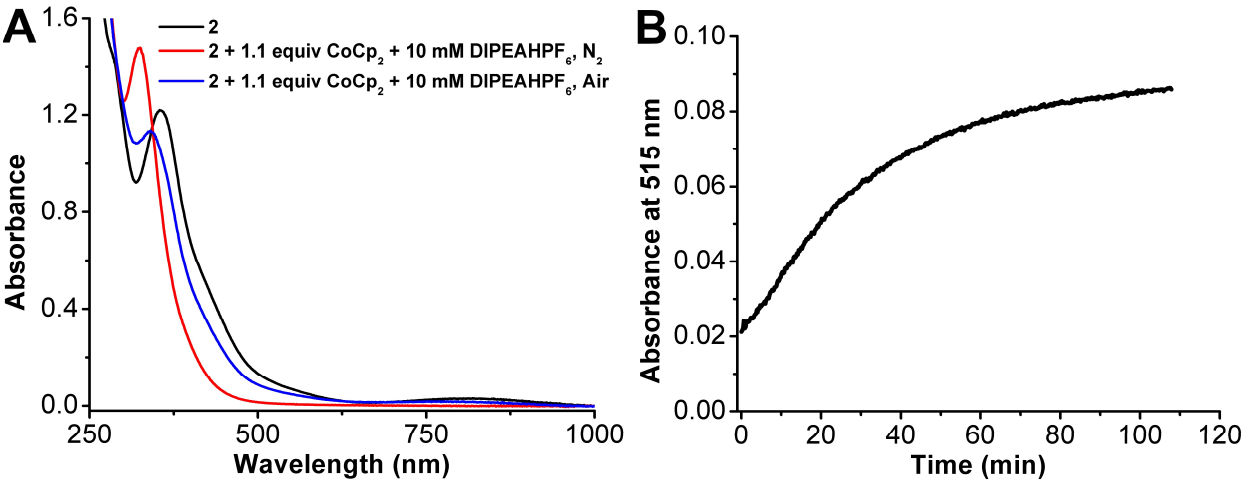

Figure S4.72. (A) UV-vis spectra of 80 μM solution of Mn(^{nPr}dhbpy)Cl **2** in MeCN (black) under N_2 with 1.1 equiv of $CoCp_2$ and 10 mM $DIPEAHPF_6$ (red) and after being exposed to air for 110 min (blue). (B) Time versus absorbance at 515 nm upon exposure of an 80 μM solution of Mn(^{nPr}dhbpy)Cl with 1.1 equiv $CoCp_2$ and 10 mM $DIPEAHPF_6$ to air. Conditions: quartz cuvette with 1 cm pathlength.

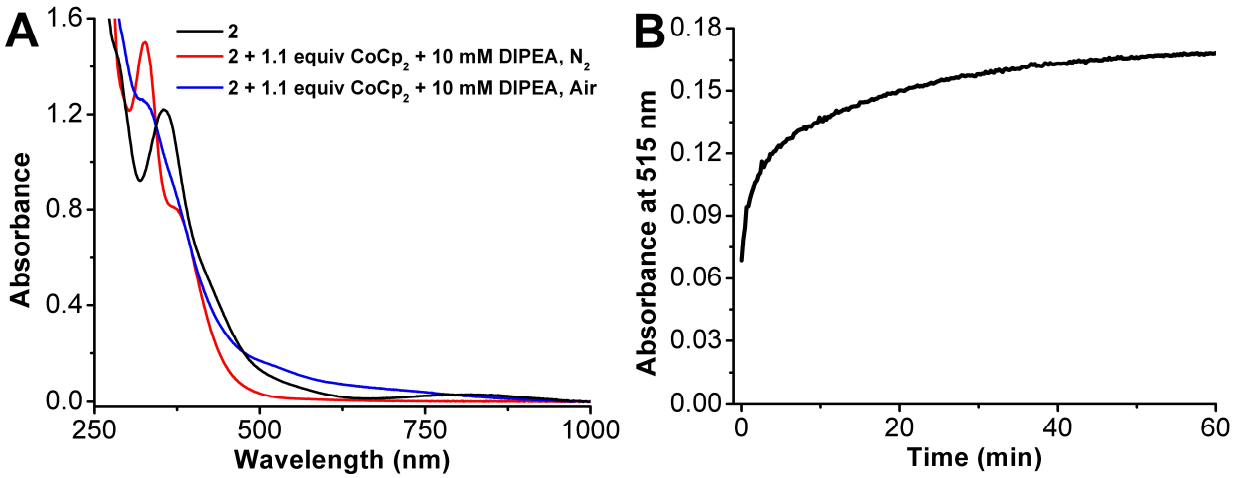

Figure S4.73. (A) UV-vis spectra of 80 μM solution of Mn(^{nPr}dhbpy)Cl **2** in MeCN (black) under N_2 with 1.1 equiv of $CoCp_2$ and 10 mM DIPEA (red) and after being exposed to air for 60 min (blue). (B) Time versus absorbance at 515 nm upon exposure of an 80 μM solution of Mn(^{nPr}dhbpy)Cl with 1.1 equiv $CoCp_2$ and 10 mM DIPEA to air. Conditions: quartz cuvette with 1 cm pathlength.

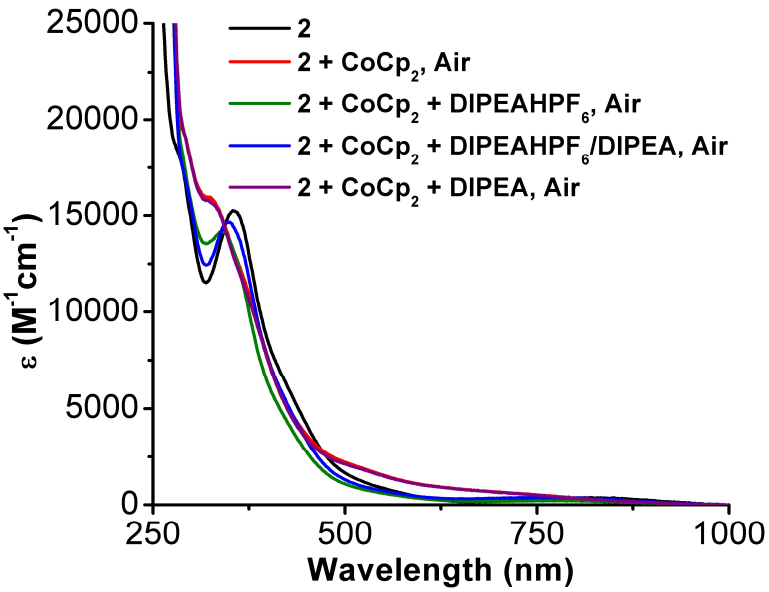

Figure S4.74. Overlay of data involving Mn(^{nPr}dhbpy)Cl **2** from **Figs S70-S73** after samples were allowed to react with air completely.

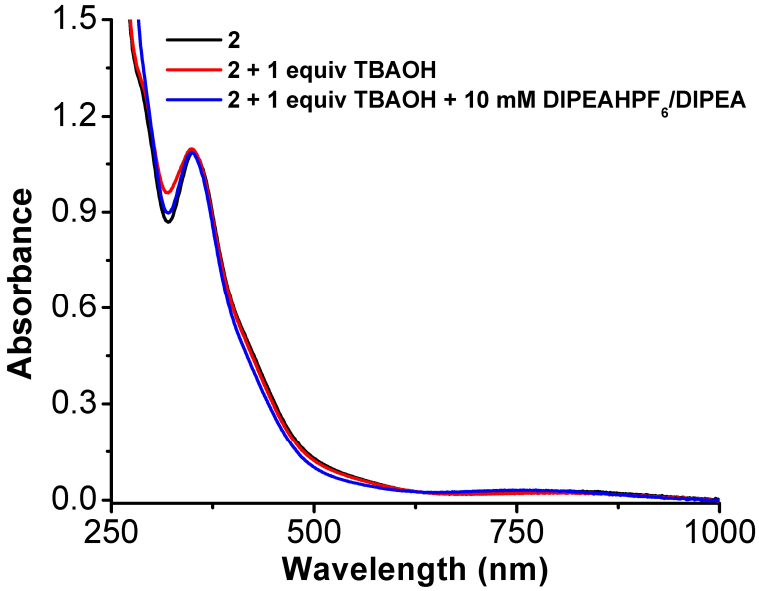

Figure S4.75. UV-vis spectra of 80 μM Mn(^{nPr}dhbpy)Cl **2** with (red) and without (black) 1 equiv TBAOH•30H_2O and with of 10 mM buffer (1:1 DIPEAHPF_6:DIPEA) in the presence of 1 equiv TBAOH•30H_2O (blue). Conditions: quartz cuvette with 1 cm pathlength.

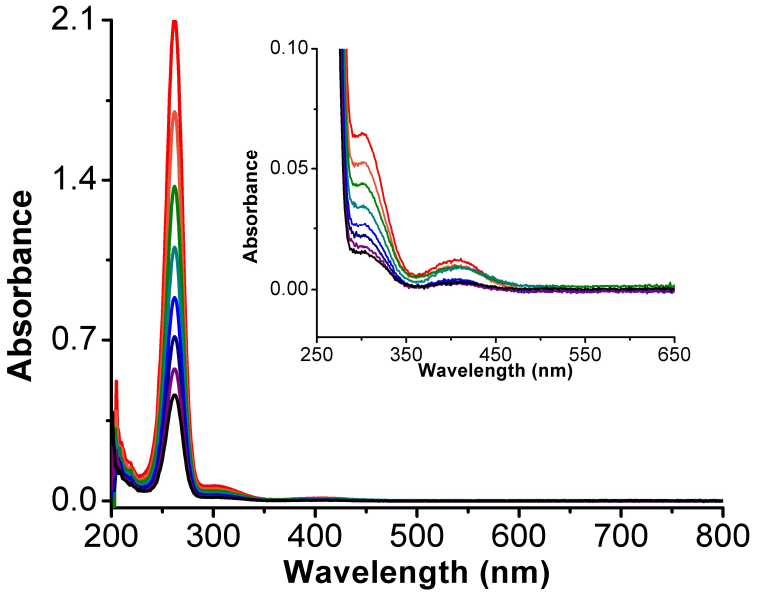

Figure S4.76. (A) UV-vis titration of [$CoCp_2$][PF_6] in MeCN. Conditions: [$CoCp_2$][PF_6] = 1.97 x 10^{-4}, 1.64 x 10^{-4}, 1.37 x 10^{-4}, 1.14 x 10^{-4}, 9.50 x 10^{-5}, 7.91 x 10^{-5}, 6.59 x 10^{-5}, 5.50 x 10^{-5} M; 1 cm pathlength cuvette.

Computational Methods

Geometry optimizations were performed without geometry constraints at the DFT level with the Gaussian 16 program, Rev B.01,[54] employing the hybrid functional B3LYP[35-37,55] and the def2-SVP basis set was used for all atoms.[39,40] Dispersion and bulk solvent effects (acetonitrile = MeCN) were accounted for at the optimization stage, by using Grimme's D3 parameter set with Becke-Johnson (BJ) damping[41,42] and the SMD continuum model,[56] respectively. The stationary points and their nature as minima (no imaginary frequencies) were characterized by vibrational analysis using the IGRRHO approach as implemented by default in the software package, which also produced enthalpy (H), entropy (S) and Gibbs energy (G) data at 298.15 K. The minima connected by a given transition state were determined by perturbing the transition states along the TS coordinate and optimizing to the nearest minimum. Free energies were corrected (ΔG_{qh}) to account for concentration effects and for errors associated with the harmonic oscillator approximation. Thus, according to Truhlars's quasi-harmonic approximation for vibrational entropy and enthalpy, all vibrational frequencies below 100 cm^{-1} were set to this value. [57] These anharmonic and concentration corrections were calculated with the Goodvibes code.[58] Concentrations were set at 0.001 M for metal complexes, 0.05 M for DIPEAH and DIPEA, 0.004 M for O_2 and 18.9 M for MeCN. Energies were refined by means of single point calculations with the ORCA 5.0 program,[43] employing the range-separated hybrid functional ωB97M-V[44] and the def2-TZVPP basis set.[39,40,45] Dispersion effects were treated with Grimme's D4 parameter set[46, 47] according to the method of Najibi and Goerigk[48] and solvation again by the SMD model. The stability of the wavefunction and spin contamination were studied at the double- and triple-zeta levels of theory. The labelling scheme for minima is $^{\text{multiplicity}}_{\text{charge}}\mathbf{Mn}(\boldsymbol{axial\ ligands})$ for metal complexes; the dianionic tetradentate ligand framework is a common feature of all Mn species and does not change its coordination mode during the reaction, so it is omitted in the notation where possible for clarity.

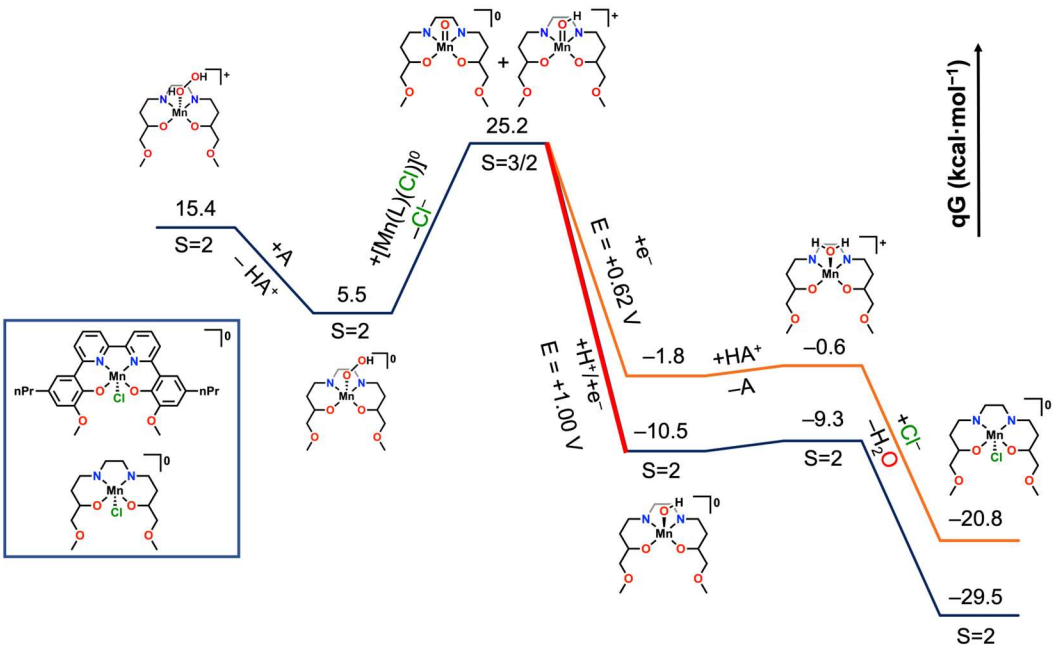

Figure S4.77. Free energy diagram of ORR by Mn(^{nPr}dhbpy)Cl **2** to H_2O.

Single Crystal Diffraction Studies

A single crystal of **2** Mn(^{nPr}dhbpy)Cl or DIPEAPF$_6$ was coated with Paratone oil and mounted on a MiTeGen MicroLoop. The X-ray intensity data were measured on a Bruker D8 Venture Photon III Kappa four-circle diffractometer system equipped with Incoatec IμS 3.0 micro-focus sealed X-ray tubes (Cu Kα, λ = 1.54178 Å; Mo Kα, λ = 0.71073 Å) and HELIOS double bounce multilayer mirror monochromators. The frames were integrated with the Bruker SAINT software package package[59] a narrow-frame algorithm. Data were corrected for absorption effects using the Multi-Scan method (SADABS). [60] Each structure was solved and refined using the Bruker SHELXTL Software Package[61] within APEX4[59] and OLEX2. [62] Non-hydrogen atoms were refined anisotropically. The N-H hydrogen atom in DIPEAHPF$_6$ was located in the electron density map and refined isotropically. All other hydrogen atoms in both structures were placed in geometrically calculated positions with U_{iso} = 1.2U_{equiv} of the parent atom (1.5U_{equiv} for methyl). The relative occupancy of the disordered atoms in each structure was freely refined, with constraints and restraints used on the anisotropic displacement parameters and bond lengths of the disordered F atoms only.

Table S4.14. Crystallographic details for Mn(^{nPr}dhbpy)Cl **2** and DIPEAHPF$_6$

	2 Mn(^{nPr}dhbpy)Cl	DIPEAHPF$_6$
CCDC number	2255849	2255850
Formula	$C_{64}H_{66}Cl_2Mn_2N_6O_8$	$C_8H_{20}F_6NP$
FW (g/mol)	1228.00	275.22
Temp (K)	100(2)	100(2)
λ (Å)	1.54178	0.71073
Size (mm)	0.030 x 0.047 x 0.505	0.085 x 0.088 x 0.122
Crystal habit	brown-yellow rod	colourless needle
Crystal system	monoclinic	monoclinic
Space group	P 2_1/c	P 2_1/n
a (Å)	15.3780(4)	8.2349(2)
b(Å)	9.8097(2)	17.2894(6)
c (Å)	20.2954(5)	8.9716(3)
α (°)	90	90
β (°)	109.0756(18)	97.3780(10)
γ (°)	90	90
Volume (Å^3)	2893.51(12)	1266.77(7)
Z	2	4
Density (g/cm^3)	1.409	1.443
μ (mm^{-1})	4.904	0.266
F(000)	1280	576
θ range (°)	3.04 to 68.36	2.36 to 28.29
Index ranges	-18 ≤ h ≤ 18 -11 ≤ k ≤ 10 -24 ≤ l ≤ 24	-10 ≤ h ≤ 10 -23 ≤ k ≤ 22 -10 ≤ l ≤ 11
Reflns collected	34823	30006
Independent reflns	5293 [R_{int} = 0.0881]	3123 [R_{int} = 0.0428]
Data / restraints /parameters	5293 / 0 / 404	3123 / 28 / 173
GOF on F^2	1.027	1.059
R_1 (I>2σ(I))	0.0505	0.0401
wR_2 (all data)	0.1376	0.1041

4.6. References

(1) Cook, E. N.; Machan, C. W. Bioinspired mononuclear Mn complexes for O2 activation and biologically relevant reactions. *Dalton Trans.* **2021**, *50* (46), 16871-16886, 10.1039/D1DT03178C. DOI: 10.1039/D1DT03178C.

(2) Cook, E. N.; Machan, C. W. Homogeneous catalysis of dioxygen reduction by molecular Mn complexes. *Chem. Commun.* **2022**, *58* (84), 11746-11761, 10.1039/D2CC04628H. DOI: 10.1039/D2CC04628H.

(3) Pegis, M. L.; Wise, C. F.; Martin, D. J.; Mayer, J. M. Oxygen Reduction by Homogeneous Molecular Catalysts and Electrocatalysts. *Chem. Rev.* **2018**, *118* (5), 2340-2391. DOI: 10.1021/acs.chemrev.7b00542.

(4) Machan, C. W. Advances in the Molecular Catalysis of Dioxygen Reduction. *ACS Catal.* **2020**, *10* (4), 2640-2655. DOI: 10.1021/acscatal.9b04477.

(5) Solomon, E. I.; Goudarzi, S.; Sutherlin, K. D. O2 Activation by Non-Heme Iron Enzymes. *Biochem.* **2016**, *55* (46), 6363-6374. DOI: 10.1021/acs.biochem.6b00635.

(6) Solomon, E. I.; Stahl, S. S. Introduction: Oxygen Reduction and Activation in Catalysis. *Chem. Rev.* **2018**, *118* (5), 2299-2301. DOI: 10.1021/acs.chemrev.8b00046.

(7) Huang, X.; Groves, J. T. Oxygen Activation and Radical Transformations in Heme Proteins and Metalloporphyrins. *Chem. Rev.* **2018**, *118* (5), 2491-2553. DOI: 10.1021/acs.chemrev.7b00373.

(8) Hong, S.; Lee, Y.-M.; Ray, K.; Nam, W. Dioxygen activation chemistry by synthetic mononuclear nonheme iron, copper and chromium complexes. *Coord. Chem. Rev.* **2017**, *334*, 25-42. DOI: 10.1016/j.ccr.2016.07.006.

(9) Bhunia, S.; Ghatak, A.; Dey, A. Second Sphere Effects on Oxygen Reduction and Peroxide Activation by Mononuclear Iron Porphyrins and Related Systems. *Chem. Rev.* **2022**, *122* (14), 12370-12426. DOI: 10.1021/acs.chemrev.1c01021.

(10) Campos-Martin, J. M.; Blanco-Brieva, G.; Fierro, J. L. G. Hydrogen peroxide synthesis: An outlook beyond the anthraquinone process. *Angew. Chem. Int. Ed.* **2006**, *45* (42), 6962-6984. DOI: 10.1002/anie.200503779.

(11) Kiani, M.; Tian, X. Q.; Zhang, W. Non-precious metal electrocatalysts design for oxygen reduction reaction in polymer electrolyte membrane fuel cells: Recent advances, challenges and future perspectives. *Coord. Chem. Rev.* **2021**, *441*, 213954. DOI: 10.1016/j.ccr.2021.213954.

(12) Pegis, M. L.; Martin, D. J.; Wise, C. F.; Brezny, A. C.; Johnson, S. I.; Johnson, L. E.; Kumar, N.; Raugei, S.; Mayer, J. M. Mechanism of Catalytic O2 Reduction by Iron Tetraphenylporphyrin. *J. Am. Chem. Soc.* **2019**, *141* (20), 8315-8326. DOI: 10.1021/jacs.9b02640.

(13) Zhang, R.; Warren, J. J. Recent Developments in Metalloporphyrin Electrocatalysts for Reduction of Small Molecules: Strategies for Managing Electron and Proton Transfer Reactions. *ChemSusChem* **2021**, *14* (1), 293-302. DOI: 10.1002/cssc.202001914 (acccessed 2023/04/18).

(14) Phung, Q. M.; Pierloot, K. The dioxygen adducts of iron and manganese porphyrins: electronic structure and binding energy. *Phys. Chem. Chem. Phys.* **2018**, *20* (25), 17009-17019, 10.1039/C8CP03078B. DOI: 10.1039/C8CP03078B.

(15) Zaragoza, J. P. T.; Goldberg, D. P. CHAPTER 1 Dioxygen Binding and Activation Mediated by Transition Metal Porphyrinoid Complexes. In *Dioxygen-dependent Heme Enzymes*, The Royal Society of Chemistry, 2019; pp 1-36.

(16) VanAtta, R. B.; Strouse, C. E.; Hanson, L. K.; Valentine, J. S. Peroxo(tetraphenylporphinato)manganese(III) and chloro(tetraphenylporphinato)manganese(II) anions. Synthesis, crystal structures, and electronic structures. *J. Am. Chem. Soc.* **1987**, *109* (5), 1425-1434. DOI: 10.1021/ja00239a024.

(17) Passard, G.; Dogutan, D. K.; Qiu, M.; Costentin, C.; Nocera, D. G. Oxygen Reduction Reaction Promoted by Manganese Porphyrins. *ACS Catal.* **2018**, *8* (9), 8671-8679. DOI: 10.1021/acscatal.8b01944.

(18) Gennari, M.; Brazzolotto, D.; Pécaut, J.; Cherrier, M. V.; Pollock, C. J.; Debeer, S.; Retegan, M.; Pantazis, D. A.; Neese, F.; Rouzières, M.; et al. Dioxygen Activation and Catalytic

Reduction to Hydrogen Peroxide by a Thiolate-Bridged Dimanganese(II) Complex with a Pendant Thiol. *J. Am. Chem. Soc.* **2015**, *137* (26), 8644-8653. DOI: 10.1021/jacs.5b04917.

(19) Hamilton, G. A.; Revesz, A. Oxidation by Molecular Oxygen. IV. A Possible Model Reaction for Some Amine Oxidases1-3. *J. Am. Chem. Soc.* **1966**, *88* (9), 2069-2070. DOI: 10.1021/ja00961a054.

(20) Evans, D. F.; Sheriff, T. S. The production of hydrogen peroxide from dioxygen and hydroxylamine catalysed by manganese complexes. *J. Chem. Soc., Chem. Commun.* **1985**, (20), 1407-1408, 10.1039/C39850001407. DOI: 10.1039/C39850001407.

(21) Shook, R. L.; Peterson, S. M.; Greaves, J.; Moore, C.; Rheingold, A. L.; Borovik, A. S. Catalytic Reduction of Dioxygen to Water with a Monomeric Manganese Complex at Room Temperature. *J. Am. Chem. Soc.* **2011**, *133* (15), 5810-5817. DOI: 10.1021/ja106564a.

(22) Hooe, S. L.; Rheingold, A. L.; Machan, C. W. Electrocatalytic Reduction of Dioxygen to Hydrogen Peroxide by a Molecular Manganese Complex with a Bipyridine-Containing Schiff Base Ligand. *J. Am. Chem. Soc.* **2018**, *140* (9), 3232-3241. DOI: 10.1021/jacs.7b09027.

(23) Hooe, S. L.; Machan, C. W. Dioxygen Reduction to Hydrogen Peroxide by a Molecular Mn Complex: Mechanistic Divergence between Homogeneous and Heterogeneous Reductants. *J. Am. Chem. Soc.* **2019**, *141* (10), 4379-4387. DOI: 10.1021/jacs.8b13373.

(24) Nichols, A. W.; Kuehner, J. S.; Huffman, B. L.; Miedaner, P. R.; Dickie, D. A.; Machan, C. W. Reduction of dioxygen to water by a Co(N2O2) complex with a 2,2'-bipyridine backbone. *Chem. Commun.* **2021**, *57*, 516-519. DOI: 10.1039/d0cc06763f.

(25) Nichols, A. W.; Cook, E. N.; Gan, Y. J.; Miedaner, P. R.; Dressel, J. M.; Dickie, D. A.; Shafaat, H. S.; Machan, C. W. Pendent Relay Enhances H_2O_2 Selectivity during Dioxygen Reduction Mediated by Bipyridine-Based Co–N_2O_2 Complexes. *J. Am. Chem. Soc.* **2021**, *143* (33), 13065-13073. DOI: 10.1021/jacs.1c03381.

(26) Hooe, S. L.; Cook, E. N.; Reid, A. G.; Machan, C. W. Non-covalent assembly of proton donors and p- benzoquinone anions for co-electrocatalytic reduction of dioxygen. *Chem. Sci.* **2021**, *12* (28), 9733-9741. DOI: 10.1039/d1sc01271a.

(27) Claude, P. Paramagnetic Susceptibility by NMR: The "Solvent Correction" Removed for Large Paramagnetic Molecules. *J. Chem. Educ.* **1997**, *74* (7), 815-816. DOI: 10.1021/ed074p815.

(28) Bain, G. A.; Berry, J. F. Diamagnetic corrections and Pascal's constants. *J. Chem. Educ.* **2008**, *85* (4), 532-536. DOI: 10.1021/ed085p532.

(29) Nichols, A. W.; Hooe, S. L.; Kuehner, J. S.; Dickie, D. A.; Machan, C. W. Electrocatalytic CO2 Reduction to Formate with Molecular Fe(III) Complexes Containing Pendent Proton Relays. *Inorg. Chem.* **2020**, *59* (9), 5854-5864. DOI: 10.1021/acs.inorgchem.9b03341.

(30) Saba, S.; Hernandez, R.; Choy, C. C.; Carta, K.; Bennett, Y.; Bondi, S.; Kolaj, S.; Bennett, C. A simple and efficient one-step protocol for the preparation of alkyl-substituted ammonium tetrafluoroborate and hexafluorophosphate salts. *J. Fluor. Chem.* **2013**, *153*, 168-171. DOI: 10.1016/j.jfluchem.2013.05.007.

(31) Shivapurkar, R.; Jeannerat, D. Determination of the relative pKa's of mixtures of organic acids using NMR titration experiments based on aliased 1H–13C HSQC spectra. *Analytical Methods* **2011**, *3* (6), 1316-1322, 10.1039/C0AY00771D. DOI: 10.1039/C0AY00771D.

(32) Zanello, P. Chapter 2 Voltammetric Techniques. The Royal Society of Chemistry, 2003; pp 49-135.

(33) Anson, C. W.; Stahl, S. S. Cooperative Electrocatalytic O2 Reduction Involving Co(salophen) with p-Hydroquinone as an Electron–Proton Transfer Mediator. *J. Am. Chem. Soc.* **2017**, *139* (51), 18472-18475. DOI: 10.1021/jacs.7b11362.

(34) *Gaussian 16, Revision B.01*; Gaussian, Inc.: Wallingford CT, 2016. (accessed.

(35) Becke, A. D. Density-functional thermochemistry. III. The role of exact exchange. *J. Chem. Phys.* **1993**, *98* (7), 5648-5652. DOI: 10.1063/1.464913.

(36) Lee, C.; Yang, W.; Parr, R. G. Development of the Colle-Salvetti correlation-energy formula into a functional of the electron density. *Phys. Rev. B* **1988**, *37* (2), 785-789.

(37) Vosko, S. H.; Wilk, L.; Nusair, M. Accurate spin-dependent electron liquid correlation energies for local spin density calculations: a critical analysis. *Can. J. Phys.* **1980**, *58* (8), 1200-1211. DOI: 10.1139/p80-159.

(38) Stephen, P. J.; Devlin, F. J.; Chabalowski, C. F.; Frisch, M. J. Ab Initio Calculation of Vibrational Absorption and Circular Dichroism Spectra Using Density Functional Force Fields. *J. Phys. Chem.* **1994**, *98* (45), 11623-11627.

(39) Weigend, F.; Ahlrichs, R. Balanced basis sets of split valence, triple zeta valence and quadruple zeta valence quality for H to Rn: Design and assessment of accuracy. *Phys. Chem. Chem. Phys.* **2005**, *7* (18), 3297-3305. DOI: 10.1039/b508541a.

(40) Weigend, F. Accurate Coulomb-fitting basis sets for H to Rn. *Phys. Chem. Chem. Phys.* **2006**, *8* (9), 1057-1065. DOI: 10.1039/b515623h.

(41) Grimme, S.; Antony, J.; Ehrlich, S.; Krieg, H. A consistent and accurate ab initio parametrization of density functional dispersion correction (DFT-D) for the 94 elements H-Pu. *J. Chem. Phys.* **2010**, *132* (15), 154104-154104. DOI: 10.1063/1.3382344.

(42) Grimme, S.; Ehrlich, S.; Goerigk, L. Effect of the damping function in dispersion corrected density functional theory. *J. Comput. Chem.* **2011**, *32* (7), 1456-1465. DOI: 10.1002/jcc.21759.

(43) Neese, F. Software update: The ORCA program system—Version 5.0. *WIREs Computational Molecular Science* **2022**, *12* (5), e1606. DOI: 10.1002/wcms.1606.

(44) Mardirossian, N.; Head-Gordon, M. ωB97M-V: A combinatorially optimized, range-separated hybrid, meta-GGA density functional with VV10 nonlocal correlation. *J. Chem. Phys.* **2016**, *144* (21), 214110. DOI: 10.1063/1.4952647.

(45) Hellweg, A.; Hättig, C.; Höfener, S.; Klopper, W. Optimized accurate auxiliary basis sets for RI-MP2 and RI-CC2 calculations for the atoms Rb to Rn. *Theor. Chem. Acc.* **2007**, *117* (4), 587-597. DOI: 10.1007/s00214-007-0250-5.

(46) Caldeweyher, E.; Bannwarth, C.; Grimme, S. Extension of the D3 dispersion coefficient model. *J. Chem. Phys.* **2017**, *147* (3), 034112. DOI: 10.1063/1.4993215.

(47) Caldeweyher, E.; Ehlert, S.; Hansen, A.; Neugebauer, H.; Spicher, S.; Bannwarth, C.; Grimme, S. A generally applicable atomic-charge dependent London dispersion correction. *J. Chem. Phys.* **2019**, *150* (15), 154122. DOI: 10.1063/1.5090222 (acccessed 5/15/2023).

(48) Najibi, A.; Goerigk, L. DFT-D4 counterparts of leading meta-generalized-gradient approximation and hybrid density functionals for energetics and geometries. *J. Comput. Chem.* **2020**, *41* (30), 2562-2572. DOI: 10.1002/jcc.26411.

(49) Li, J.-Z.; Hu, W.; Wang, Y.; Zhong, J.-B.; Li, S.-X. A Kinetic Study of Phenol Oxidation with H2O2 Catalysed by Crowned Schiff Base Mn(Iii) Complexes in Micellar Media. *Progress in*

Reaction Kinetics and Mechanism **2012**, *37* (1), 30-41. DOI: 10.3184/146867812X13242290723318 (acccessed 2023/03/29).

(50) Broughton, D. B.; Wentworth, R. L. Mechanism of Decomposition of Hydrogen Peroxide Solutions with Manganese Dioxide. I. *J. Am. Chem. Soc.* **1947**, *69* (4), 741-744. DOI: 10.1021/ja01196a003.

(51) Li, Q.; Batchelor-McAuley, C.; Lawrence, N. S.; Hartshorne, R. S.; Compton, R. G. Anomalous solubility of oxygen in acetonitrile/water mixture containing tetra-n-butylammonium perchlorate supporting electrolyte; the solubility and diffusion coefficient of oxygen in anhydrous acetonitrile and aqueous mixtures. *J. Electroanal. Chem.* **2013**, *688*, 328-335. DOI: 10.1016/j.jelechem.2012.07.039.

(52) Espinoza, E. M.; Clark, J. A.; Soliman, J.; Derr, J. B.; Morales, M.; Vullev, V. I. Practical Aspects of Cyclic Voltammetry: How to Estimate Reduction Potentials When Irreversibility Prevails. *Journal of The Electrochemical Society* **2019**, *166* (5), H3175. DOI: 10.1149/2.0241905jes.

(53) Anson, C. W.; Stahl, S. S. Cooperative Electrocatalytic O2 Reduction Involving Co(salophen) with p-Hydroquinone as an Electron-Proton Transfer Mediator. *J. Am. Chem. Soc.* **2017**, *139* (51), 18472-18475. DOI: 10.1021/jacs.7b11362.

(54) *Gaussian 16 Rev. B.01*; Wallingford, CT, 2016. (accessed.

(55) Stephens, P. J.; Devlin, F. J.; Chabalowski, C. F.; Frisch, M. J. Ab Initio Calculation of Vibrational Absorption and Circular Dichroism Spectra Using Density Functional Force Fields. *J. Phys. Chem.* **1994**, *98* (45), 11623-11627. DOI: 10.1021/j100096a001.

(56) Marenich, A. V.; Cramer, C. J.; Truhlar, D. G. Universal solvation model based on solute electron density and on a continuum model of the solvent defined by the bulk dielectric constant and atomic surface tensions. *J. Phys. Chem. B* **2009**, *113* (18), 6378-6396. DOI: 10.1021/jp810292n.

(57) Ribeiro, R. F.; Marenich, A. V.; Cramer, C. J.; Truhlar, D. G. Use of solution-phase vibrational frequencies in continuum models for the free energy of solvation. *J. Phys. Chem. B* **2011**, *115* (49), 14556-14562. DOI: 10.1021/jp205508z.

(58) *Goodvibes v.3.0.1*; 2019. (accessed.

(59) *Saint; APEX4*; Bruker AXS Inc.: Madison, Wisconsin, USA, 2019. (accessed.

(60) Krause, L.; Herbst-Irmer, R.; Sheldrick, G. M.; Stalke, D. Comparison of silver and molybdenum microfocus X-ray sources for single-crystal structure determination. *J. Appl. Cryst.* **2015**, *48* (1), 3-10. DOI: 10.1107/S1600576714022985.

(61) Sheldrick, G. M. SHELXT - Integrated space-group and crystal-structure determination. *Acta Cryst.* **2015**, *71* (1), 3-8. DOI: 10.1107/S2053273314026370.

(62) Dolomanov, O. V.; Bourhis, L. J.; Gildea, R. J.; Howard, J. A. K.; Puschmann, H. OLEX2: A Complete Structure Solution, Refinement and Analysis Program. *J. Appl. Cryst.* **2009**, *42*, 339-341. DOI: 10.1107/S0021889808042726.

Chapter 5:

Metal-Free Homogeneous O_2 Reduction by an Iminium-based Electrocatalyst

Published as:

Cook, E. N.; Davis, A. E.; Hilinski, M. K.; Machan, C. W. *Journal of the American Chemical Society* **2024**, 146, 12, 7931-7935 doi: 10.1021/jacs.3c14549

5.1 Abstract

The oxygen reduction reaction (ORR) is important to alternative energy and industrial oxidation processes. Herein, an iminium-based organoelectrocatalyst (**im**$^+$) for the ORR with trifluoroacetic acid as a proton source in acetonitrile solution under both electrochemical and spectrochemical conditions using decamethylferrocene as a chemical reductant is reported. Under spectrochemical conditions H_2O_2 is the primary reaction product, while under electrochemical conditions H_2O is produced. This difference in selectivity is attributed to the interception of the free superoxide intermediate under electrochemical conditions by the reduced catalyst, accessing an alternate inner-sphere pathway.

5.2 Introduction

Increasing atmospheric carbon dioxide (CO_2) concentrations has had detrimental impacts on our environment and creates a drastic need for alternative energy processes. The oxygen reduction reaction (ORR) is important in fuel cells and alternative energy devices such as zinc-air batteries, in addition to a green alternative for H_2O_2 production.[1,2] Researchers have focused on open-shell transition metal complexes as catalysts for this reaction due to their often facile reactivity with the triplet ground state of dioxygen (O_2). There has also been some advancement in the development of carbon-based catalysts for the ORR.[2-8] Comparatively, the use of homogeneous organic molecules for catalytic ORR has been less widely studied, since reduced oxygen species (ROSs) formed as intermediates (e.g., superoxide $O_2^{\bullet-}$) can degrade organic molecules.

In 2020, Karimi *et. al* reported the ORR activity of carbenium dications using decamethylferrocene (Cp^*_2Fe) as a chemical reductant with methanesulfonic acid as a proton source.[9] The reduced carbene radicals were found to rapidly react via an inner-sphere mechanism to form an intermediate peroxide which is protonated to release H_2O_2. Recently, Kiatisevi and co-workers reported imidazole-benzimidazole electrocatalysts for ORR under aqueous conditions.[10] They proposed that O_2 binds to the reduced catalyst to form a superoxide species, which is further reduced and protonated to produce H_2O_2. Homogeneous organic species have also been shown to be active for the outer-sphere reduction of O_2, with free $O_2^{\bullet-}$ as an intermediate. Electrocatalytic ORR by an outer-sphere mechanism was first reported in 1985 by Andrieux *et. al.* using methylviologen to generate H_2O_2 in acidic DMSO.[11] Outer-sphere electron transfer to generate $O_2^{\bullet-}$ was followed by protonation to $HO_2^{\bullet}$, which was subsequently reduced by the regenerated methylviologen monocation to HO_2^-, then protonated to form H_2O_2. Following this, a 1993 study by Audebert and Hapiot found that substituted 9-(4-X-phenyl)-*N*-methylacridinium salts in acidic DMSO also effectively reduces O_2 to H_2O_2 via an analogous mechanism.[12]

Previously, 3,4-dihydro-2,4,4-trimethyl-1-(trifluoromethylisoquinolinium) (**im$^+$**, **Figure 5.1**) was reported to be a hydroxylation catalyst with H_2O_2 as an oxidant.[13,14] It was hypothesized that this iminium could mediate outer-sphere O_2 reduction similar to related organic cations and that its intrinsic stability to H_2O_2 would be beneficial to catalyst stability.[15] Catalytic and mechanistic experiments reveal that the iminium salt is an efficient catalyst for ORR to H_2O and H_2O_2 in acetonitrile (MeCN) with trifluoroacetic acid (TFAH) as a proton source. Under spectrochemical conditions with Cp^*_2Fe as a chemical reductant in solution, O_2 is quantitatively reduced via an outer-sphere mechanism to H_2O_2. Under electrochemical conditions, $O_2^{\bullet-}$ is intercepted by the reduced iminium in solution, accessing an inner-sphere mechanism to quantitatively produce H_2O. The difference in selectivity is proposed to be regulated by the simultaneous availability of $O_2^{\bullet-}$ and the reduced iminium in higher concentrations in the reaction-diffusion layer.

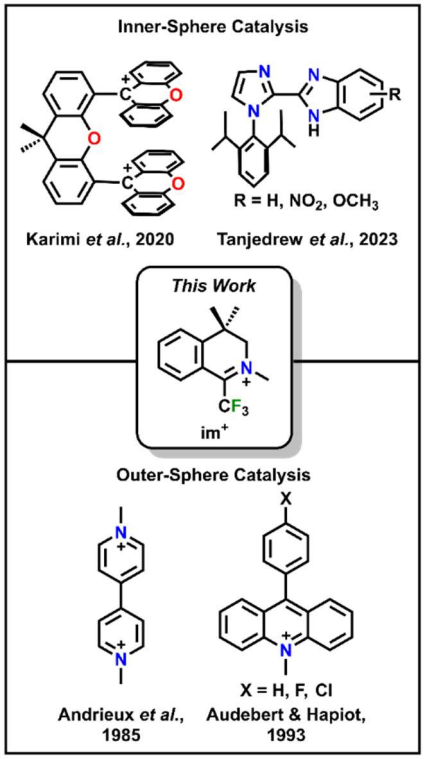

Figure 5.1. Summary of previously reported organic-based catalysts for the ORR and the catalyst (**im$^+$**) described here.

5.3 Results and Discussion

Im$^+$ was analyzed by cyclic voltammetry (CV) with tetrabutylammonium hexafluorophosphate ($TBAPF_6$) as the supporting electrolyte in MeCN (**Figure 5.2**). Under Ar saturation conditions, there is a diffusion-limited irreversible reduction feature, which is attributed to the reduction of the iminium to a carbon-based radical species (**im^0**, see below) at E_p = –0.82 V vs. Fc^+/Fc. Due to irreversibility at scan rates below 2 V/s, the $E_{1/2}$ was estimated to be –0.77 V vs. Fc^+/Fc by taking the first derivative of the current density (**Figures S5.1 & S5.6**).[16] This irreversible feature is consistent with a radical-radical dimerization (RRD) mechanism occurring between two equivalents of **im^0**, as evidenced by an evaluation of peak potential dependence on both scan rate and concentration (**Figures S5.1 & S5.2**).[17] Upon saturation of the solution with O_2, there is an observed 150 mV positive potential shift of the irreversible reduction feature to E_p = –0.67 V vs. Fc^+/Fc, suggestive of a strong binding interaction. Interestingly, variable concentration and scan rate studies suggested a shift to a radical-substrate dimerization (RSD) mechanism, based on the observed dependence of E_p on scan rate and concentration under these conditions (**Figures S5.3 & S5.4**). This observation is proposed to correlate to a favorable interaction between **im^0** and $O_2^{\bullet-}$ at reducing potentials.[17] Addition of TFAH (pK_a(MeCN) = 12.65)[18] as a proton source under Ar saturation conditions resulted in an increase in current (**Figure 5.2 & S5.5**); the dependence of E_p on scan rate and concentration suggests an RSD mechanism, implying that a reaction with TFAH proceeds the dimerization of the **im^0** radical (**Figures S5.6-S5.7**). However, under O_2 saturation in the presence of TFAH, a large increase in current density is again observed 150 mV positive of the Faradaic response, consistent with catalytic O_2 reduction, implying that dimerization is not relevant under these conditions. A CV rinse test and control experiments demonstrated that the observed catalytic response is homogeneous and from **im$^+$** (**Figure S5.8**).

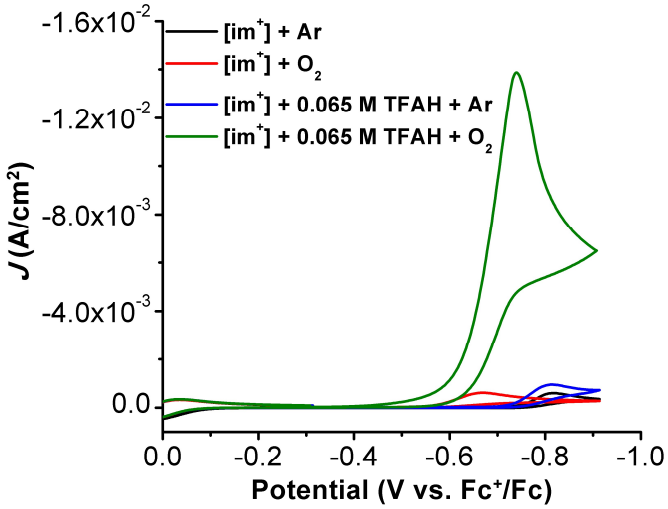

Figure 5.2. CVs of **im⁺** under Ar and O_2 saturation conditions with and without acid. Conditions: 1.3 mM **im⁺**, 0.1 M $TBAPF_6$/MeCN; glassy carbon working electrode, glassy carbon counter electrode, Ag/AgCl pseudoreference electrode; 100 mV/s scan rate.

Independently varying the concentrations of **im⁺**, O_2 and TFAH revealed a first-order concentration dependence on **im⁺**, O_2, and TFAH in the current response (**Eq 5.1**, **Figures S5.9-S5.11**). As the concentration of **im⁺** decreases, there is an observed negative potential shift (**Figure S5.9**), which conforms to the behavior expected for an outer-sphere electron transfer followed by rapid catalytic reaction steps.[11] As the concentration of O_2 decreases, a decrease in the catalytic wave at E_p = –0.67 V vs. Fc^+/Fc is observed, as well as the recovery of the **im⁺/im⁰** redox feature at E_p = –0.82 V vs. Fc^+/Fc. The reappearance of the intrinsic redox feature suggests the system is operating under total catalysis conditions, where O_2 is rapidly consumed within the reaction-diffusion layer and excess **im⁺** is available for reduction at more negative potentials. The recovery of the Faradaic redox response has also been observed for ORR mediated by methyl viologen and phenylacridinium salts, which are proposed to have an outer-sphere mechanism.[11,12]

$$electrochemical\ k_{obs} = k_{cat}[im^+][O_2][TFAH] \qquad \textbf{Eq 5.1}$$

Rotating ring-disk electrode (RRDE) methods with a glassy carbon disk and roughened gold ring[19] were used to determine the selectivity of ORR by **im⁺** under electrochemical conditions. Under air saturation, this system was found to be 92.6 ± 1.3 % selective for H_2O (see SI, **Figures**

S6.14-S5.16). Control CV studies with added urea•H_2O_2 showed a slight decrease in current density (**Figures S5.12-S5.13**) under Ar saturation conditions without a shift to positive potentials, which suggests a relatively slower reaction between **im^0** and H_2O_2. Consistent with this, under O_2 saturation the catalytic current density is recovered, as is the shift to more positive potentials, confirming that **im^0** preferably reacts with O_2 over H_2O_2.

Catalytic ORR activity of **im$^+$** was then studied by stopped-flow UV-vis methods using Cp^*_2Fe as a chemical reductant and TFAH as the proton source. The growth of the spectral handle of $[Cp^*_2Fe]^+$ at 780 nm was monitored to extract kinetic parameters for the reaction (**Figure 5.3**). The rate law under these conditions (**Eq 5.2**) was determined by independently varying the concentration of **im$^+$**, TFAH, O_2, and Cp^*_2Fe (**Figures S5.18-S5.21**). These studies revealed that ORR shows a first-order concentration dependence on [**im$^+$**] and is independent of TFAH, O_2 and Cp^*_2Fe concentration, indicative of saturation kinetics at low catalyst concentration (4 μM). A $Ti(O)SO_4$ colorimetric assay was used to determine the selectivity of ORR by **im$^+$** under spectrochemical conditions, finding that this system is 102 ± 8.4% selective for H_2O_2 (n_{cat} = 2; **Figure S5.22**), in contrast to the electrochemical studies. Additional control testing showed no degradation of H_2O_2 by disproportionation or catalytic H_2O_2 reduction with Cp^*_2Fe as the reductant (**Figures S5.23-S5.24**). Therefore, based on the apparent rate law, the slope of variable [**im$^+$**] studies (**Figure S5.18**) could be used to estimate an apparent TOF of 6.66 x 10^3 s^{-1}.

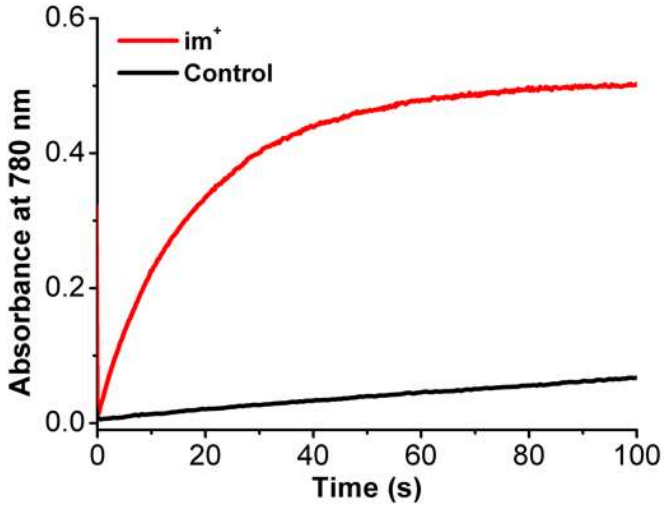

Figure 5.3. Formation of $[Cp^*_2Fe]^+$ at 780 nm from ORR catalyzed by **im⁺** (red trace) and control (black trace). Concentrations: **im⁺** = 4 μM, TFAH = 25 mM, O_2 = 4.05 mM, Cp^*_2Fe = 1 mM; control: no **im⁺**.

$$spectrochemical\ k_{obs} = \frac{d[Cp^*_2Fe]^+}{dt} \bullet \frac{1}{n_{cat}} = k_{cat}[im^+] \qquad \textbf{Eq 5.2}$$

To evaluate the thermodynamics of the reaction, computational studies of likely intermediates during O_2 reduction were undertaken (see SI). Evaluation of spin density showed that the radical character of **im⁰** is localized on the imine C atom with some electron density shared by the N atom (**Figure S5.25**). Positioning the neutral radical and O_2 within a sufficient radius for a covalent interaction did not result in bond formation, however, electron transfer between the two occurred resulting in the formation of superoxide $O_2^{\bullet-}$ and **im⁺**, although free energy of the reaction was endergonic overall (+8.8 kcal/mol). In the presence of TFAH (and considering the exergonicity of homoconjugation between TFAH and trifluoroacetate), the formation of protonated superoxide $HO_2^\bullet$ is favorable by –33.2 kcal/mol. Subsequent disproportionation of two equivalents of $HO_2^\bullet$ to form O_2 and H_2O_2 is comparably favorable at –33.1 kcal/mol. The reduction potential of $HO_2^\bullet$ is estimated to be 0.58 V negative of the **im⁺/⁰** couple, excluding outer-sphere reduction.

Since the minimal electrocatalytic current is observed with H_2O_2 in comparison to O_2 and **im⁺** was not observed to reduce H_2O_2 under spectrochemical conditions (**Figure S5.24**), subsequent calculations focused on alternative pathways to produce water. The reaction between an equivalent of **im⁰** and $O_2^{\bullet-}$ to produce a monoanionic C-bound end-on peroxide species is

exergonic by –21.7 kcal/mol. Protonation by TFAH to generate a neutral hydroperoxide is further downhill by –42.0 kcal/mol, considering homoconjugation. The alternative generation of this intermediate by the reaction of $\mathbf{im^0}$ and $HO_2^{\bullet}$ is favorable by –30.6 kcal/mol.

Protonation of the hydroperoxide to generate an oxaziridinium with water co-product is downhill by an additional –18.2 kcal/mol. The reduction potential of the oxaziridinium is calculated to be approximately 0.21 V more negative than $\mathbf{im^{+/0}}$, however, protonation to produce a cationic C–OH is favorable by –49.0 kcal/mol. Given the rate of catalysis observed electrochemically, it is probable that these steps occur as a single proton-coupled electron transfer step, which would be favored overall by –44.2 kcal/mol (+1.92 V vs Fc^+/Fc). Reduction of this cationic species is expected to be facile, with a calculated reduction potential of +1.34 V vs $Fc^{+/0}$ (**Figure S5.26**). The protonation of the resultant neutral C–OH group to generate water and reform $\mathbf{im^+}$ is then favorable, with an estimated free energy change of –10.4 kcal/mol.

Based on electrochemical, spectrochemical and computation analyses, separate cycles for the reduction of dioxygen by $\mathbf{im^+}$ under electrochemical and spectrochemical conditions can be proposed (**Scheme 5.1**). Starting at *i*, an electron transfer to form carbon-centered radical species, *ii*, which reacts with O_2 to reform *i* and an equivalent of $O_2^{\bullet-}$. The product $O_2^{\bullet-}$ is then protonated by TFAH to form two equivalents of $HO_2^{\bullet}$, which favorably disproportionate to one equiv each of O_2 and H_2O_2.[20] Under spectroscopic conditions, the catalytic cycle closes here, as supported by the observed quantitative selectivity for H_2O_2 (**Figure S5.27**). Under electrochemical conditions, control experiments show that reactivity with H_2O_2 is slow relative to O_2, suggesting that these conditions have a divergent mechanistic pathway. Instead, it is proposed that under electrochemical conditions, the neutral radical *ii* is available in sufficient concentrations in the reaction-diffusion layer to bind available $O_2^{\bullet-}$, and is supported by the RSD pathway observed in electrochemical studies (**Figures S5.3 & S5.4**). Based on these data and the empirically determined rate law, it is likely that species *iv* represents the resting state of the catalytic cycle, with the protonation reaction to generate *v* representing the rate-determining step (**Figure S5.28**).

Scheme 5.1. Proposed Catalytic Cycle for ORR by **im**$^{+}$

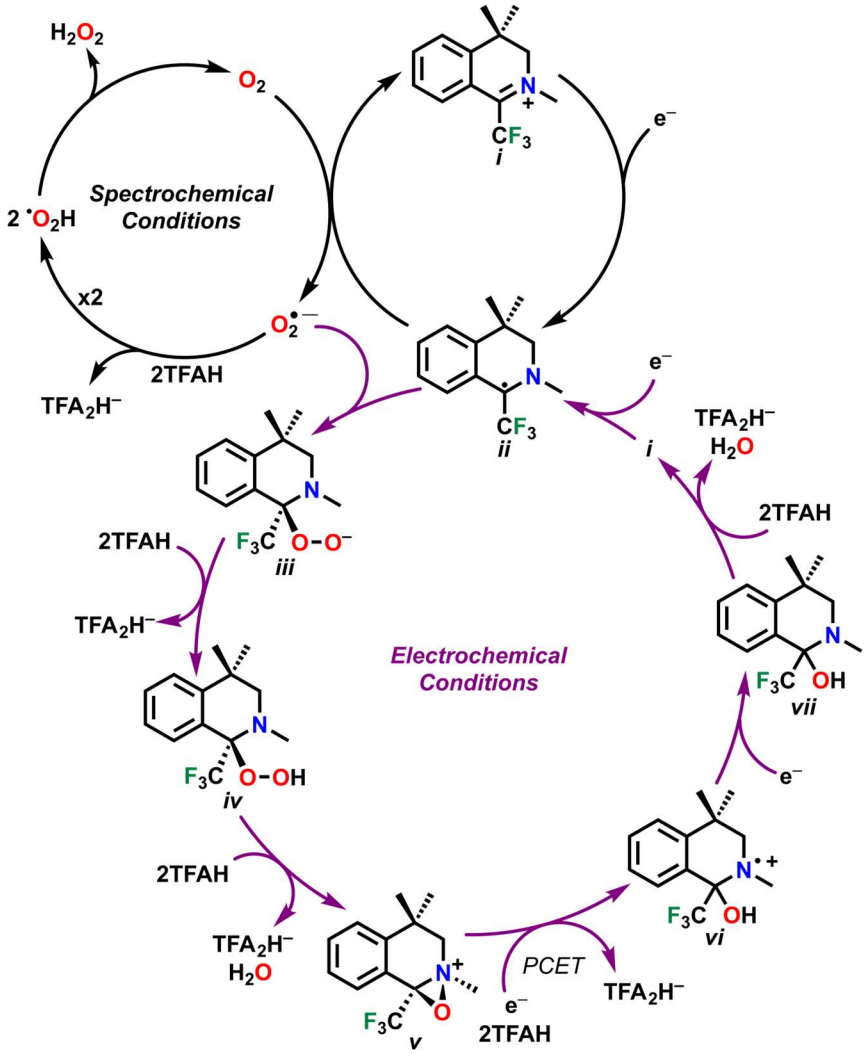

The change in accessible pathways can then be ascribed to the concentration differences under each reaction condition. The reaction-diffusion layer during electrochemical experiments is likely to both contain an excess of **im**^{0} because of rapid consumption of O_2, as well as suitable concentrations of superoxide from rapid outer-sphere reduction. Comparatively, under spectrochemical conditions, the relative concentrations of **im**^{0} and $O_2^{\bullet-}$ are significantly more dilute, allowing thermodynamically viable disproportionation pathways to generate H_2O_2. Outer-sphere reduction of $HO_2^{\bullet}$ by of **im**^{0} is excluded based on the difference in calculated reduction potentials.

Here, catalytic ORR conditions for H_2O or H_2O_2 production with an iminium-based catalyst have been reported. The difference in accessible reaction pathways under electrochemical and spectrochemical conditions, where the primary product shifts from H_2O to H_2O_2, respectively, is the result of the relative available concentrations of the key **im^0** and $O_2^{\bullet-}$ intermediates available under the respective reaction conditions. Since catalysis is initiated by an outer-sphere electron transfer, the $O_2/O_2^{\bullet-}$ reduction potential of –1.29 vs Fc^+/Fc in MeCN defines the overall ORR reaction mediated by **im$^+$**.[21] However, the favorable pre-equilibrium reaction between **im^0** and $O_2^{\bullet-}$ causes a positive potential shift from this redox couple, indicating that further optimization of the operating potential could be possible. [22] The work described here reports a novel mechanism whereby the electrocatalytic reduction of O_2 occurs via both an inner-sphere and outer-sphere mechanism, resulting in product selectivity being controlled by the nature of electron delivery. Given that there are few known organoelectrocatalysts for the ORR, mechanistic understanding will enable the development of additional examples, as well as inform the development of new classes of doped carbons as heterogeneous catalysts.

5.4. Supplementary Information for Chapter 5

General Considerations

All chemicals and solvents (ACS or HPLC grade) were commercially available and used as received unless otherwise indicated. For all air-sensitive reactions and electrochemical experiments, HPLC-grade solvents were obtained as anhydrous and air-free from a PPT Glass Contour Solvent Purification System. Gas cylinders were obtained from Praxair (Ar as 5.0; O_2 as 4.0) and passed through activated molecular sieves prior to use. Gas mixing for variable concentration experiments was accomplished using a gas proportioning rotameter from Omega Engineering. UV-vis absorbance spectra were obtained on a Cary 60 from Agilent using a quartz cuvette with 1 cm pathlength. The concentration of O_2 saturation in MeCN is reported to be 8.1 mM and the saturation concentration in MeCN with added electrolyte to be 6.3 mM. [23] Flash column chromatography was performed using silica gel or alumina gel (230 - 400 mesh)

purchased from Fisher Scientific. Elution of compounds was monitored by UV. 1H and 13C NMR spectra were measured on a Varian Inova 600 (600 MHz) or Bruker Avance III 800 (800 MHz) spectrometer and acquired at 300 K. Chemical shifts are reported in parts per million (ppm δ) referenced to the residual 1H or 13C resonance of the solvent. The following abbreviations are used to indicate the multiplicity of signals: s - singlet, d - doublet, t - triplet, q - quartet, m - multiplet and br - broad.

Synthesis of im$^+$ Catalyst

Procedures taken and adapted from "Improved Parent Iminium Synthesis Procedure."[24]

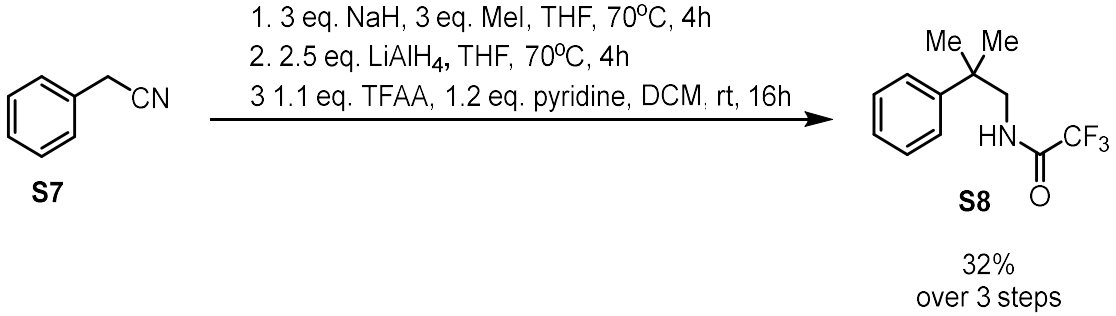

S7 **S8**

32%
over 3 steps

Under N_2 atmosphere, benzyl cyanide (**S7**, 1 equiv) was added into a flame-dried round-bottom flask equipped with a stir bar. Tetrahydrofuran (0.4 M) was added and the suspension was cooled to 0 °C with stirring. 60% sodium hydride (dispersion in paraffin liquid) (3 equiv) was added to the mixture and stirred for 1 hour. Iodomethane (3 equiv) was then added dropwise to the solution at 0°C and the solution was heated to 70 °C for 4 hours. Upon completion, the crude reaction mixture was cooled to room temperature then quenched with ice. The organic layer was extracted 3 times with ethyl acetate, and the combined organics were washed with brine, dried over anhydrous $MgSO_4$, and concentrated *in vacuo*. The crude product was carried on to the next step.

Under N_2 atmosphere, crude methylated benzyl cyanide (1 equiv) was dissolved in tetrahydrofuran (0.4 M) in a round bottom equipped with a stir bar and cooled to 0 °C with stirring. The solution was cooled to 0 °C and 2.4 M solution of lithium aluminum hydride in tetrahydrofuran

(2.5 equiv) was added dropwise by addition funnel. The solution was heated to 70 °C and stirred for 4 hours. Upon completion, the crude reaction mixture was worked up following the Fieser Method: The white suspension was cooled to 0ºC and diluted to roughly twice its volume with diethyl ether. “x” mL water was slowly added to the reaction mixture, where “x” is the amount of lithium aluminum hydride used for the reduction in grams. “x” mL 15% aqueous sodium hydroxide was then added, followed by “3x” mL water. The mixture was then warmed to rt and stirred 15 minutes, followed by addition of anhydrous $MgSO_4$. Upon stirring for an additional 15 minutes, the mixture was filtered over a pad of celite and concentrated *in vacuo*. The crude product was carried onto the next step.

Under N_2 atmosphere, the crude amine (1 equiv) was dissolved in anhydrous dichloromethane (0.1 M) in a round-bottom flask equipped with a stir bar. Pyridine (1.2 equiv) was added with stirring, followed by dropwise addition of trifluoroacetic anhydride (1.1 equiv) via syringe. The reaction mixture was stirred at room temperature overnight (ca. 16 h). Upon completion, the orange-brown solution was quenched with a brine wash, dried over $MgSO_4$, and concentrated *in vacuo*. The residue was purified by flash chromatography with isocratic 20% ethyl acetate in hexanes to give acetamide **S8** a white crystalline solid (32% yield over 3 steps).

2,2,2-trifluoro-N-(2-methyl-2-phenylpropyl)acetamide (S8)

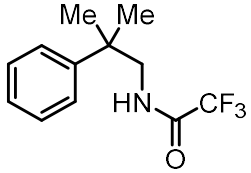

1H NMR (600 MHz, $CDCl_3$): δ 7.33 – 7.38 (m, 3H), 7.25 – 7.27 (m, 1H), 5.89 (br. s, 1H), 3.53 (d, J = 4.8 Hz, 2H), 1.37 (s, 6H).
13C NMR (151 MHz, $CDCl_3$): δ 157.1, 145.0, 128.9, 126.8, 125.7, 50.9, 38.7, 26.3.
NMR spectra are consistent with literature reports. [13]

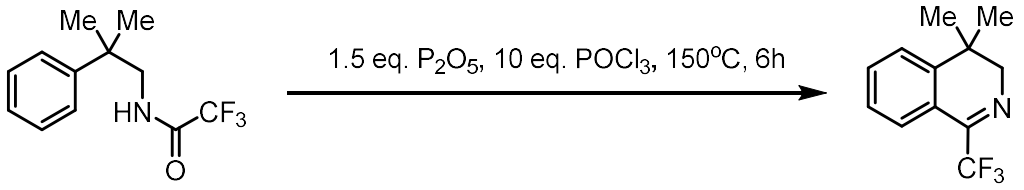

S8 **S9** 63%

Under N_2 atmosphere, phosphorus pentoxide (1.5 equiv) was added to a 2-neck round-bottom flask equipped with a stir bar. Half the volume of phosphorus oxychloride (5 equiv) was added to the solution and heated to 70 °C, then immediately heated to 120 °C. The acetamide (**S8**, 1 equiv) was dissolved in the remaining half volume (5 equiv) of phosphorus oxychloride and added to the solution slowly. The solution turned brown and then black, and was further heated to 150 °C and allowed to stir for 5 hours. Upon completion, the mixture was cooled to room temperature, carefully diluted to twice the original volume with dichloromethane, and transferred to a large Erlenmeyer flask. In the flask, the brown-black solution was quenched slowly with excess water, then saturated aqueous sodium bicarbonate with stirring. The mixture was treated with base until it was light tan in color and the pH measured at 8 or greater. The resultant solution was extracted 3 times with dichloromethane and the combined organic layers were washed with brine, dried over $MgSO_4$, and concentrated *in vacuo*. The crude residue was purified by flash chromatography with 0 – 5% ethyl acetate/hexanes to give the cyclized imine as a yellow oil (**S9**, 63% yield).

4,4-dimethyl-1-(trifluoromethyl)-3,4-dihydroisoquinoline (S9)

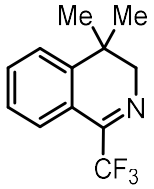

1H NMR (600 MHz, $CDCl_3$): δ 7.60 – 7.63 (m, 1H), 7.49 – 7.51 (m, 1H), 7.40 – 7.42 (m, 1H), 7.31 – 7.34 (m, 1H), 3.74 (d, J = 4.8 Hz, 2H), 1.24 (s, 6H).
13C NMR (151 MHz, $CDCl_3$): δ 155.6, 146.7, 132.7, 126.7, 125.7, 124.0, 121.1, 59.9, 31.7, 26.0.
NMR spectra are consistent with literature reports. [13]

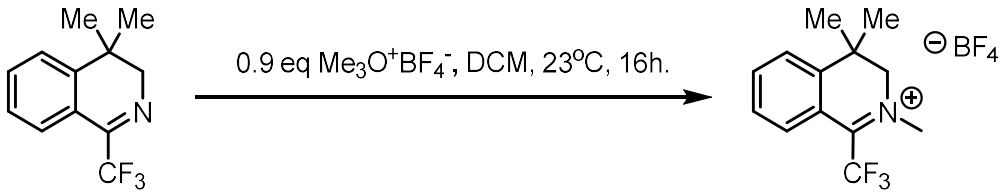

S9 **im$^+$**

In an N_2 glovebox, imine (**S9**, 1 equiv) was dissolved in anhydrous dichloromethane (0.5 M) in a vial equipped with a stir bar. Trimethyloxonium tetrafluoroborate (0.9 equiv) was added to the solution and stirred at room temperature overnight (ca.16 h) and removed from the glovebox. Solvent was removed *in vacuo* and the resulting solid was washed with anhydrous diethyl ether, then recrystallized from dichloromethane and diethyl ether to yield the iminium catalyst as a white crystalline solid (**im$^+$**, 90% yield).

3,4-Dihydro-2,4,4-trimethyl-1-(trifluoromethyl)isoquinolinium tetrafluoroborate (im$^+$)

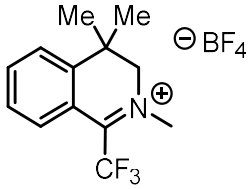

1H NMR (600 MHz, $CDCl_3$): δ 8.03 – 8.11 (m, 2H), 8.03 – 8.04 (m, 1H), 7.69 – 7.85 (m, 1H), 4.45 (s, 2H), 4.30 (s, 3H), 1.49 (s, 6H).
13C NMR (151 MHz, $CDCl_3$): δ 148.0, 139.7, 131.2, 128.3, 125.2, 121.4, 119.3, 65.8, 48.9, 33.0, 24.1.

NMR spectra are consistent with literature reports. [13]

Electrochemical Analysis

All cyclic voltammetry experiments were performed using a Metrohm Autolab PGSTAT302N potentiostat. Glassy carbon working (⌀ = 3 mm) and non-aqueous silver/silver chloride pseudoreference electrodes behind PTFE tips were obtained from CH Instruments. The pseudoreference electrodes were obtained by depositing chloride on bare silver wire in 10% HCl at oxidizing potentials and stored in a 0.1 M tetrabutylammonium hexafluorophosphate solution in acetonitrile in the dark prior to use. The counter electrode was a glassy carbon rod (⌀ = 3 mm).

All CV experiments were performed in a modified scintillation vial (20 mL volume) as a single-chamber cell with a cap modified with ports for all electrodes and a sparging needle. Tetrabutylammonium hexafluorophosphate ($TBAPF_6$) was purified by recrystallization from ethanol and dried in a vacuum oven before being stored in a desiccator. All data were referenced to an internal ferrocene standard (ferrocenium/ferrocene reduction potential under stated conditions) unless otherwise specified. All voltammograms were corrected for internal resistance. Ferrocene was purified by sublimation prior to use. In the event that the presence of electrochemical features precluded ferrocene addition, ferrocene was added to the electrochemical cell at the end of analysis for reference. All CVs were scanned to negative potentials before sweeping to positive potentials. Rotating ring-disk electrode electroanalytical experiments were performed using a BioLogic VSP Bipotentiostat and a Pine Research MSR Rotator. Glassy carbon working electrode (⌀ = 5 mm) with a gold ring were obtained from Pine Research.

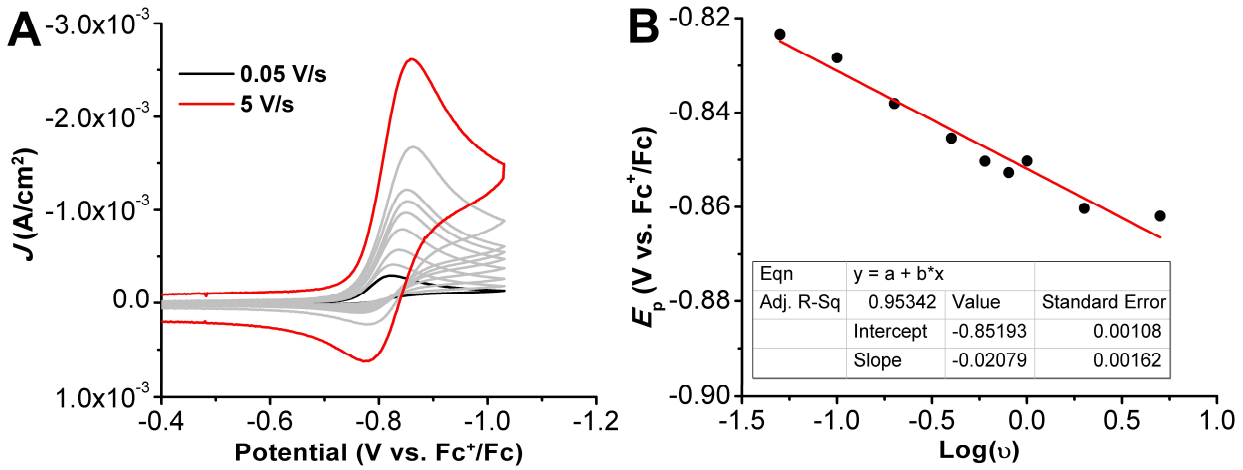

Figure S5.1. (A) CVs of **im⁺** under Ar saturation at variable scan rates. (B) Logarithm of scan rate versus reduction peak potential from CVs in (A). Conditions: 1.3 mM **im⁺**, 0.1 M $TBAPF_6$/MeCN; glassy carbon working electrode, glassy carbon counter electrode, Ag/AgCl pseudoreference electrode; referenced to an internal ferrocene standard. Scan rates: 0.05, 0.1, 0.2, 0.4, 0.6, 0.8 1, 2, 5 V/s.

Mechanism	λ	$\frac{\delta E_p}{\delta \log \nu}$ (*)	$\frac{\delta E_p}{\delta \log C^0}$ (*)	$E_p - E^0$
EC	$\frac{RT}{F}\frac{k_+}{\upsilon}$	–29.6	0.0	$-0.780\frac{RT}{F}+\frac{RT}{2F}ln\left(\frac{RT}{F}\frac{k_+}{\upsilon}\right)$
RRD	$\frac{RT}{F}\frac{k_d C^0}{\upsilon}$	–19.7	19.7	$-0.903\frac{RT}{F}+\frac{RT}{3F}ln\left(\frac{4RT}{3F}\frac{k_d C^0}{\upsilon}\right)$

(*) – at 25 ºC.[17] For **Figures S5.1 and S5.2**.

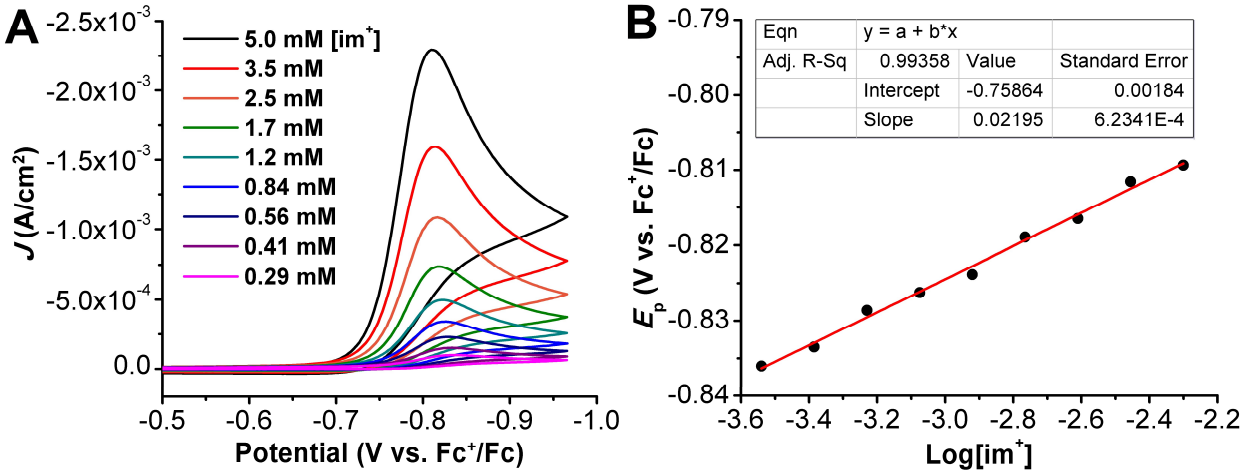

Figure S5.2. (A) CVs of **im⁺** under Ar saturation at varying concentrations. (B) Logarithm of **im⁺** concentration versus the reduction peak potential in (A). Conditions: varying [im⁺], 0.1 M $TBAPF_6$/MeCN; glassy carbon working electrode, glassy carbon counter electrode, Ag/AgCl pseudoreference electrode; referenced to an internal ferrocene standard.

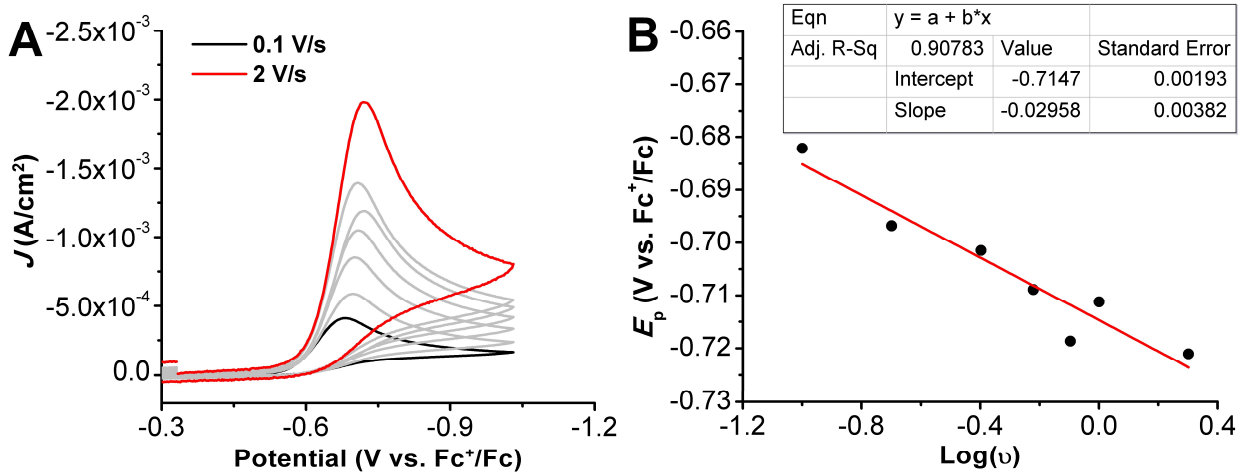

Figure S5.3. (A) CVs of **im⁺** under O_2 saturation at variable scan rates. (B) Logarithm of scan rate versus reduction peak potential from CVs in (A). Conditions: 1.3 mM **im⁺**, 0.1 M $TBAPF_6$/MeCN; glassy carbon working electrode, glassy carbon counter electrode, Ag/AgCl pseudoreference electrode; referenced to an internal ferrocene standard. Scan rates: 0.1, 0.2, 0.4, 0.6, 0.8 1, 2 V/s.

Mechanism	λ	$\frac{\delta E_p}{\delta \log \nu}$ (*)	$\frac{\delta E_p}{\delta \log C^0}$ (*)	$E_p - E^0$
RSD-ECE	$\frac{RT}{F}\frac{k_d C^0}{\upsilon}$	–29.6	29.6	$-1.15\frac{RT}{F}+\frac{RT}{2F}ln\left(\frac{4RT}{F}\frac{k_d C^0}{\upsilon}\right)$
RSD-DISP1	$\frac{RT}{F}\frac{k_d C^0}{\upsilon}$	–29.6	29.6	$-1.15\frac{RT}{F}+\frac{RT}{2F}ln\left(\frac{2RT}{F}\frac{k_d C^0}{\upsilon}\right)$

(*) – at 25 ºC.[17] For **Figures S5.3-S5.7**.

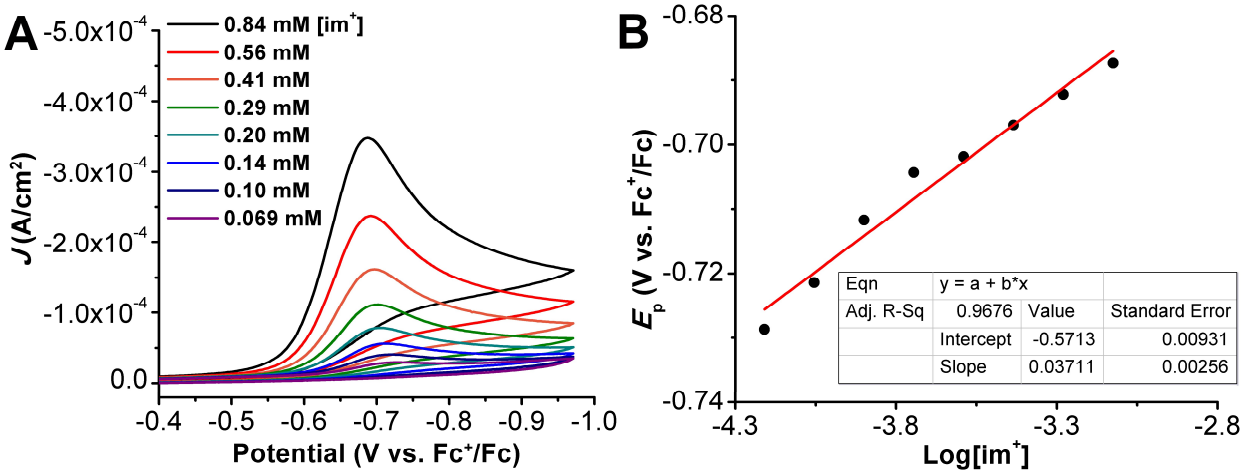

Figure S5.4. (A) CVs of **im⁺** under O_2 saturation at varying concentrations. (B) Logarithm of im+ concentration versus the reduction peak potential in (A). Conditions: varying [im+], 0.1 M TBAPF6/MeCN; glassy carbon working electrode, glassy carbon counter electrode, Ag/AgCl pseudoreference electrode; referenced to an internal ferrocene standard.

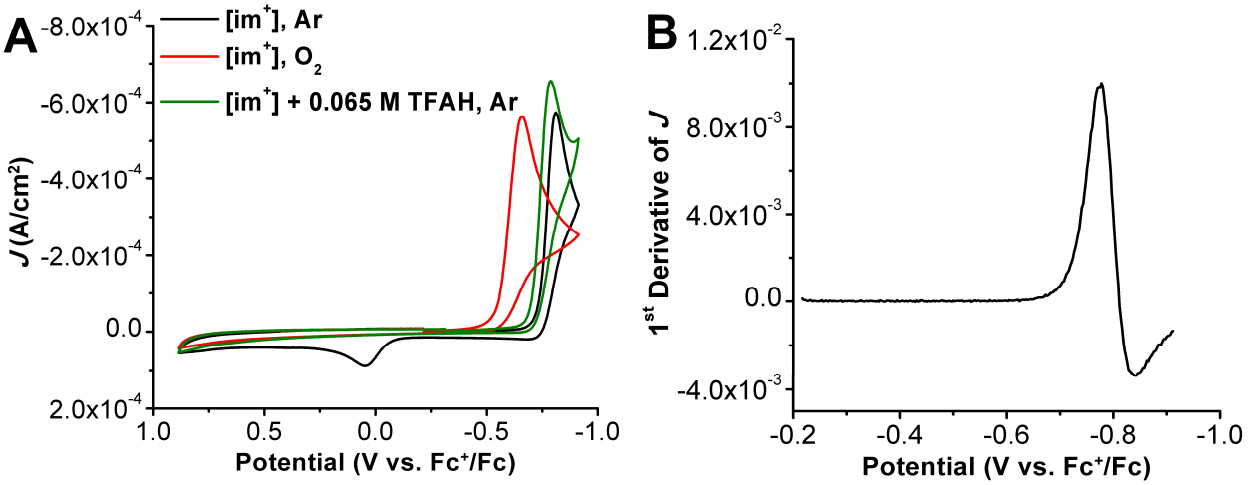

Figure S5.5. (A) CVs of **im**$^+$ under Ar (black) and O_2 (red) saturation with 0.065 M TFAH added (green). (B) First derivative of current density of **im**$^+$ under Ar saturation (from black trace in A) Conditions: Conditions: 1.3 mM **im**$^+$, 0.1 M $TBAPF_6$/MeCN; 100 mV/s; glassy carbon working electrode, glassy carbon counter electrode, Ag/AgCl pseudoreference electrode; referenced to an internal ferrocene standard.

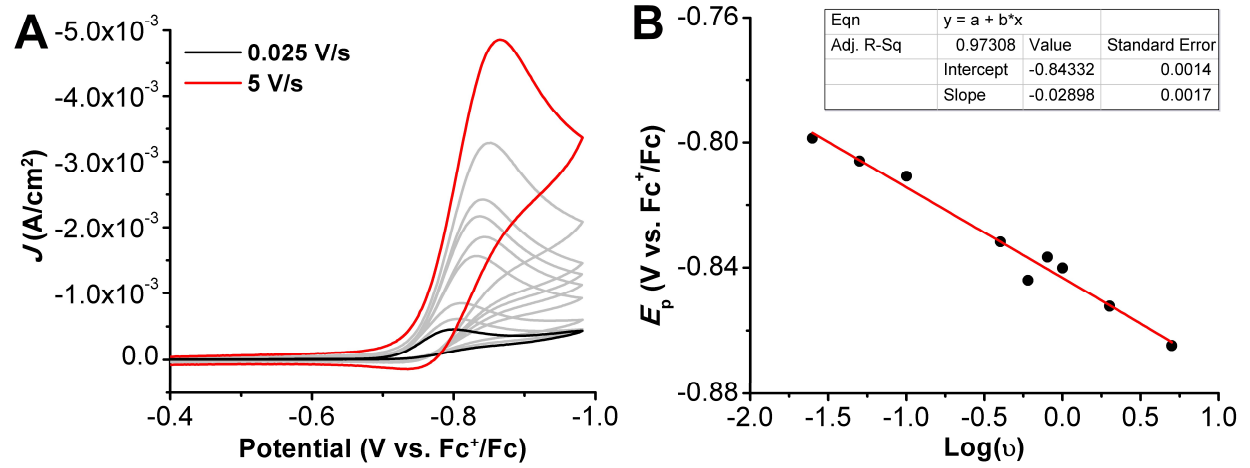

Figure S5.6. (A) CVs of **im**$^+$ under Ar saturation in the presence of 0.261 M TFAH at variable scan rates. (B) Logarithm of scan rate versus reduction peak potential from CVs in (A). Conditions: 1.3 mM **im**$^+$, 0.261 M TFAH, 0.1 M $TBAPF_6$/MeCN; glassy carbon working electrode, glassy carbon counter electrode, Ag/AgCl pseudoreference electrode; referenced to an internal ferrocene standard. Scan rates: 0.025, 0.05, 0.1, 0.4, 0.6, 0.8 1, 2, 5 V/s.

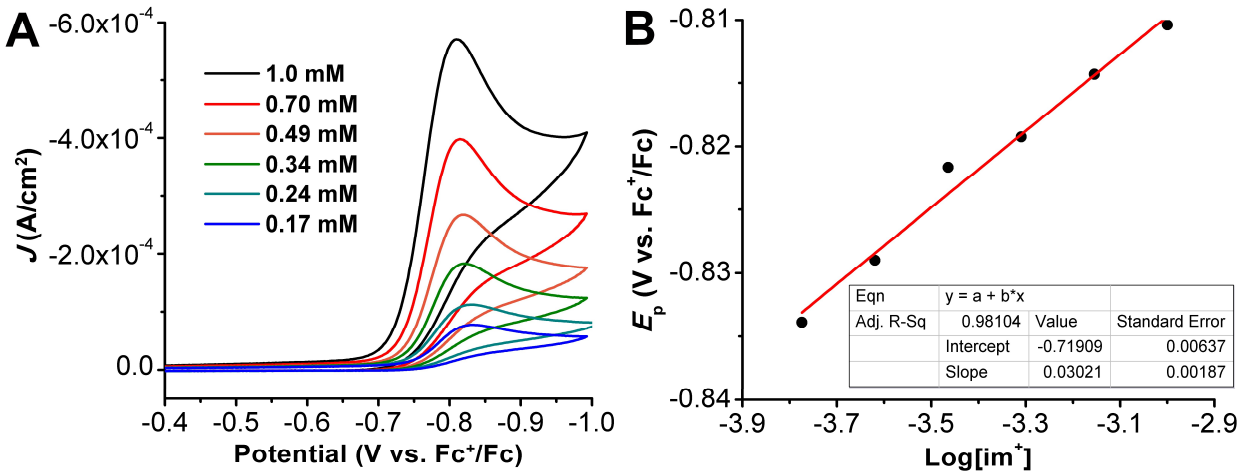

Figure S5.7. (A) CVs of **im⁺** under Ar saturation in the presence of 0.261 M TFAH at varying concentrations. (B) Logarithm of **im⁺** concentration versus the reduction peak potential in (A). Conditions: varying [**im⁺**], 0.261 M TFAH, 0.1 M $TBAPF_6$/MeCN; glassy carbon working electrode, glassy carbon counter electrode, Ag/AgCl pseudoreference electrode; referenced to an internal ferrocene standard.

To ensure that species adsorbed to the electrode, a rinse test was performed with **im⁺** and TFAH (**Figure S5.8**). A CV was taken under catalytic conditions after which the electrode was removed and the sides were wiped and placed in a blank solution containing TFAH and a CV was taken.

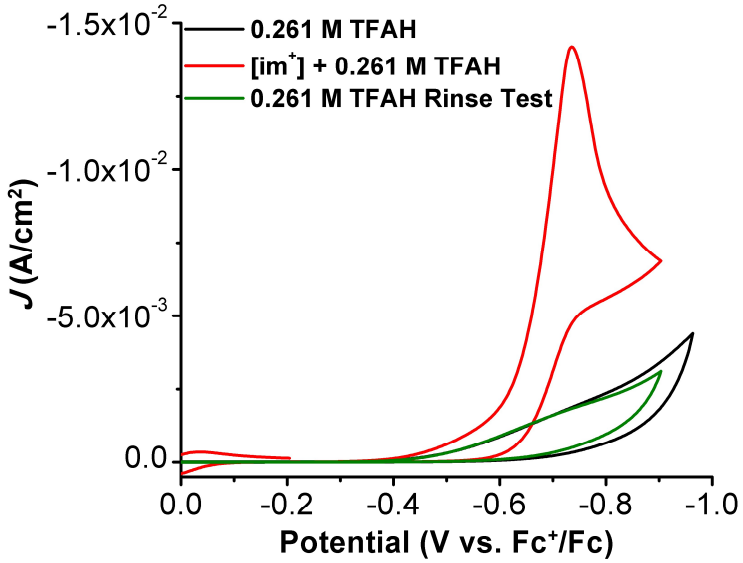

Figure S5.8. Rinse test of **im⁺** and TFAH. CV of TFAH under O_2 saturation (black trace), **im⁺** under catalytic conditions (red trace), and rinse test (green trace). Conditions: 1.3 mM **im⁺** 0.261 M TFAH, 0.1 M $TBAPF_6$/MeCN, O_2 saturation; 100 mV/s; glassy carbon working electrode, glassy carbon counter electrode, Ag/AgCl pseudoreference electrode; referenced to an internal ferrocene standard.

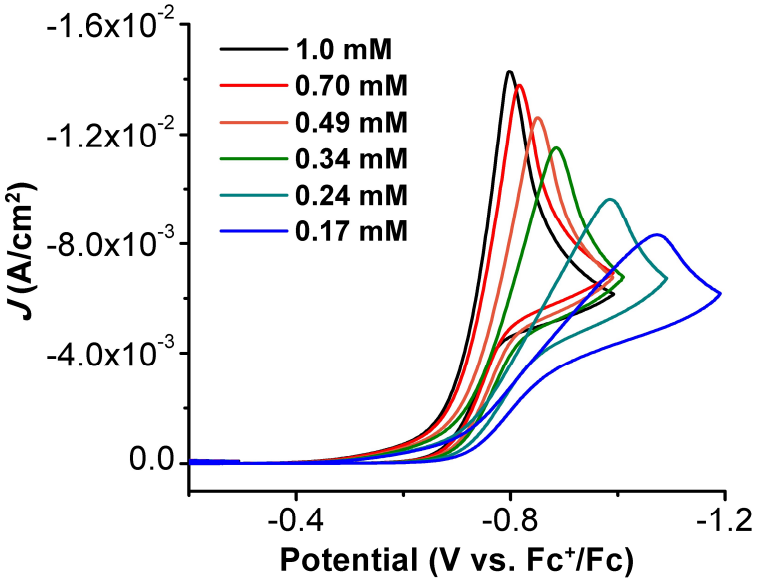

Figure S5.9. CVs of **im**$^+$ under catalytic conditions with variable **im**$^+$ concentrations. Conditions: 0.261 M TFAH, 0.1 M $TBAPF_6$/MeCN; 100 mV/s; glassy carbon working electrode, glassy carbon counter electrode, Ag/AgCl pseudoreference electrode; referenced to an internal ferrocene standard.

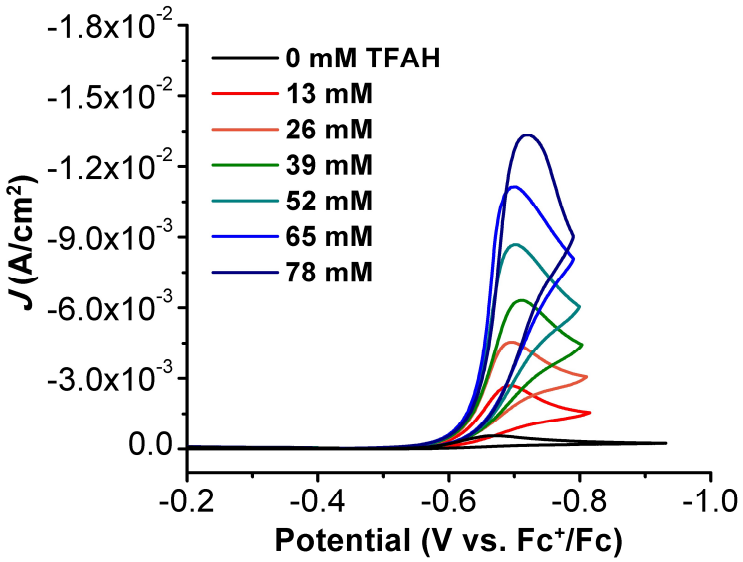

Figure S5.10. CVs of **im**$^+$ under catalytic conditions with variable TFAH concentrations. Conditions: 1.3 mM **im**$^+$, 0.1 M $TBAPF_6$/MeCN; 100 mV/s; glassy carbon working electrode, glassy carbon counter electrode, Ag/AgCl pseudoreference electrode; referenced to an internal ferrocene standard.

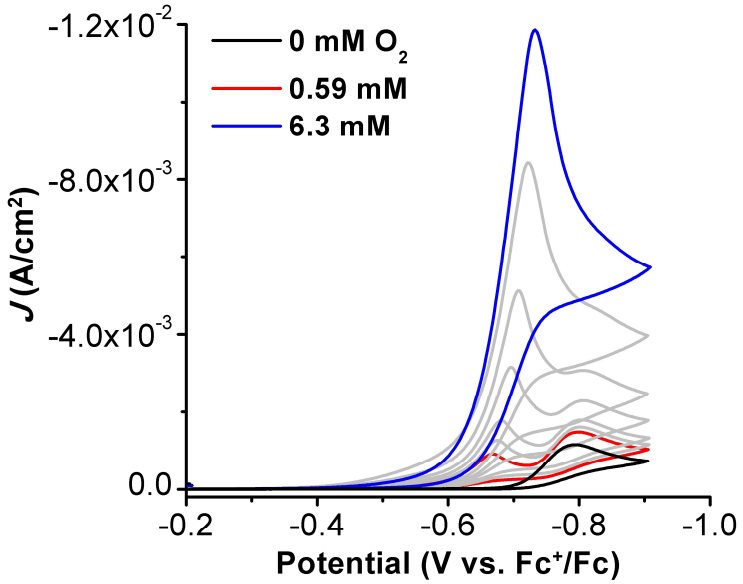

Figure S5.11. CVs of **im**$^+$ under catalytic conditions with variable O_2 concentrations. Conditions: 1.3 mM **im**$^+$, 0.261 M TFAH, 0.1 M $TBAPF_6$/MeCN; 100 mV/s; glassy carbon working electrode, glassy carbon counter electrode, Ag/AgCl pseudoreference electrode; referenced to an internal ferrocene standard. O_2 concentrations: 6.3, 5.06, 3.3, 1.45, 0.92, 0.74, 0.59 mM.

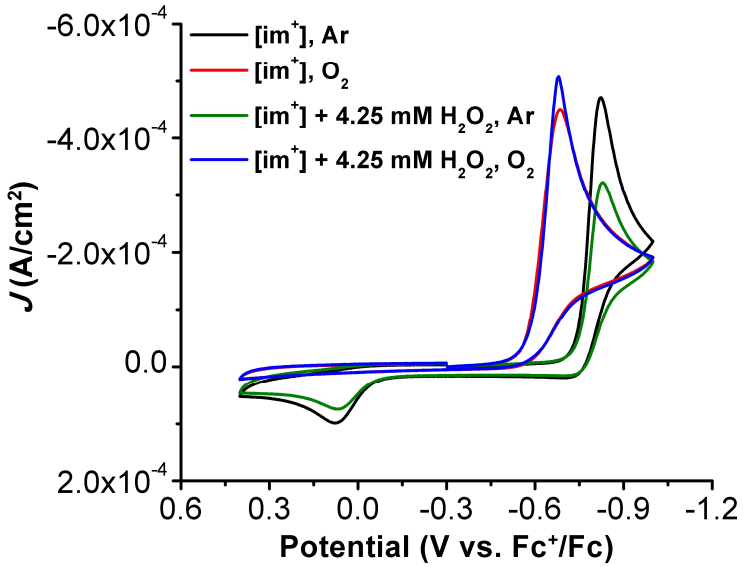

Figure S5.12. CVs of **im**$^+$ with and without added 4.25 mM urea•H_2O_2 under Ar and O_2 saturation. Conditions: 1.3 mM **im**$^+$, 0.261 M TFAH, 0.1 M $TBAPF_6$/MeCN; 100 mV/s; glassy carbon working electrode, glassy carbon counter electrode, Ag/AgCl pseudoreference electrode; referenced to an internal ferrocene standard.

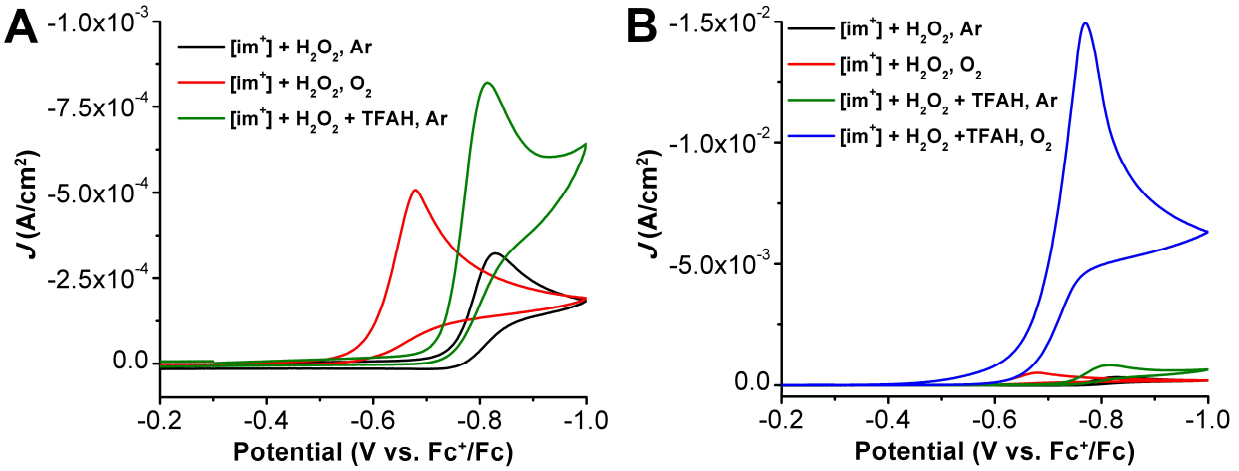

Figure S5.13. (A) CVs of **im⁺** in the presence of 4.25 mM urea•H_2O_2 under Ar and O_2 saturation with added 0.261 M TFAH. (B) CVs of **im⁺** in the presence of 4.25 mM urea•H_2O_2 with added 0.261 M TFAH under O_2 saturation. Conditions: 1.3 mM **im⁺**, 0.261 M TFAH, 0.1 M $TBAPF_6$/MeCN; 100 mV/s; glassy carbon working electrode, glassy carbon counter electrode, Ag/AgCl pseudoreference electrode; referenced to an internal ferrocene standard.

Rotating Ring-Disk Electrode Methods

Description of Au Ring Roughening Procedure. The Au ring electrode was roughened according to a previously reported method.[19] The electrodes were polished first on a felt polishing pad with 0.3 micron alumina, then with 0.05 micron alumina and rinsed with water and ethanol. Cyclic voltammograms were obtained in 0.5 M H_2SO_4 by scanning from 0 to 1.6 V vs. Ag/AgCl at 100 mV/s, then at 20 mV/s for an additional 2 cycles to obtain the pre-roughening, surface oxide reduction charge. The electrode was then pulsed between 2.4 and 0.2 V vs Ag/AgCl for 2.4 ms each and repeated for 250,000 cycles. Bubbles formed during electrolysis pulses were dislodged by contacting with a large bubble from a glass pipette. After electrolysis, the electrode was held at 0.3 V vs. Ag/AgCl for 2 minutes and the roughening was evaluated by CV.

Description of RRDE Collection Efficiency. The collection efficiency was determined as previously reported.[25-27] Conditions: Ar saturation, 0.1 M $TBAPF_6$, 0.5 mM ferrocene in MeCN, glassy carbon disk electrode (5 mm), roughened Au ring electrode, glassy carbon rod counter electrode, Ag/AgCl pseudoreference electrode; scan rate 0.1 V/s. To calculate the collection efficiency of the RRDE,

the ratio of the ring current (i_r) to the disk current (i_d) at each rotation rate was used to determine $N_{empirical}$ (**Eq S5.1**). The $N_{empirical}$ value at each rotation rate was multiplied by a factor of 100 to determine the collection efficiency % at each rotation rate (~15%).

$$N_{empirical} = \frac{i_{ring\ corrected}}{i_{disk\ corrected}} \qquad \textbf{(Eq S5.1)}$$

RRDE Experiments. Conditions: Performed under Ar and air saturation conditions, 0.1 M $TBAPF_6$, 0.5 mM **im⁺**, 0.1 M TFAH, glassy carbon disk electrode (5 mm diameter), roughened Au ring electrode, glassy carbon rod counter electrode, Ag/AgCl pseudoreference electrode; scan rate 0.1 V/s.

The solution was sparged until saturation was achieved. **Im⁺** (0.5 mM) was dissolved in solution and 0.1 M TFAH was added. A standard CV was taken of the solution to confirm the potential window to be used for the experiment. The roughened Au ring was set to +1.2 V. LSVs were obtained for various rotation rates between 400 and 2400 under the described conditions. In between each scan, the solution was sparged for 3 minutes. The reproducibility of scans was confirmed by repeating scans at the same rotation rate, producing exact overlays. The same procedure was repeated for air saturation conditions, which were achieved by sparging the solution with air for 3 minutes. Disk (i_d) and ring (i_r) currents were corrected by subtracting the current observed under Ar to ensure that the current observed was a result of H_2O_2 formation.

The arithmetic mean of the number of electrons received by O_2 (n_{cat}) during the ORR was calculated from the disk current (i_d) and ring current (i_r) according to **Eq S5.2:**

$$n_{cat} = 4 \times \frac{i_d}{i_d + \frac{i_r}{N_{empirical}}} \qquad \textbf{(Eq S5.2)}$$

The H_2O_2 ratio (p) is defined as the fraction of O_2 reduced to H_2O_2 and relates to n_{cat} by **Eq S5.3**:

$$n_{cat} = 4 - 2p \qquad \textbf{(Eq S5.3)}$$

Multiplying p by 100% provides the $\%H_2O_2$ selectivity of the ORR. It was determined that under electrochemical conditions, this system shows a 7.50 ± 1.3% selectivity for H_2O_2.

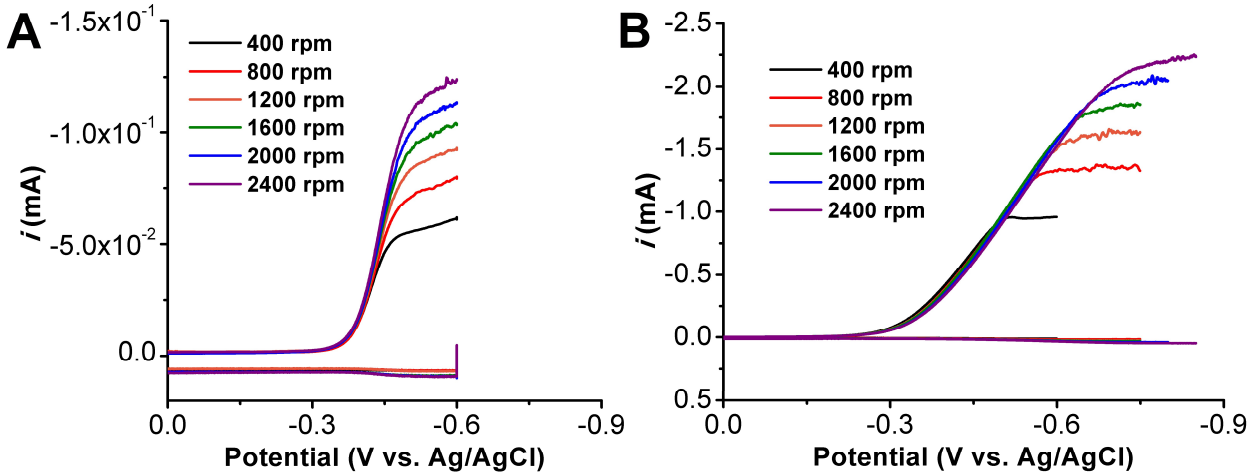

Figure S5.14. Linear sweep voltammograms of RRDE experiment with 0.5 mM im+ and 0.1 M TFAH under Ar (A) and air (B) saturation conditions; ring potential = 1.2 V vs Ag/AgCl. Conditions: 0.5 mM **im**$^{+}$, 0.1 M TFAH, 0.1 M $TBAPF_6$/MeCN; glassy carbon working electrode/roughened Au ring working electrode, glassy carbon counter electrode, Ag/AgCl pseudoreference electrode; scan rate 0.1 V/s.

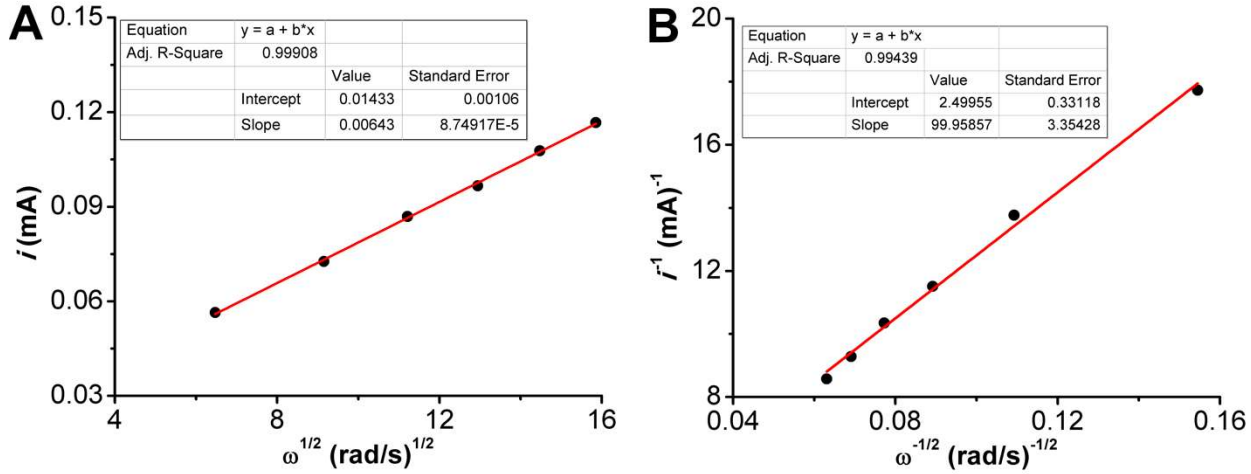

Figure S5.15. (A) Levich and Koutecky-Levich (B) plots from data obtained from linear sweep voltammograms of **im**$^{+}$ (0.5 mM) by RRDE with 0.1 M TFAH under Ar saturation conditions at various rotation rates; ring potential = 1.2 V vs. Ag/AgCl.

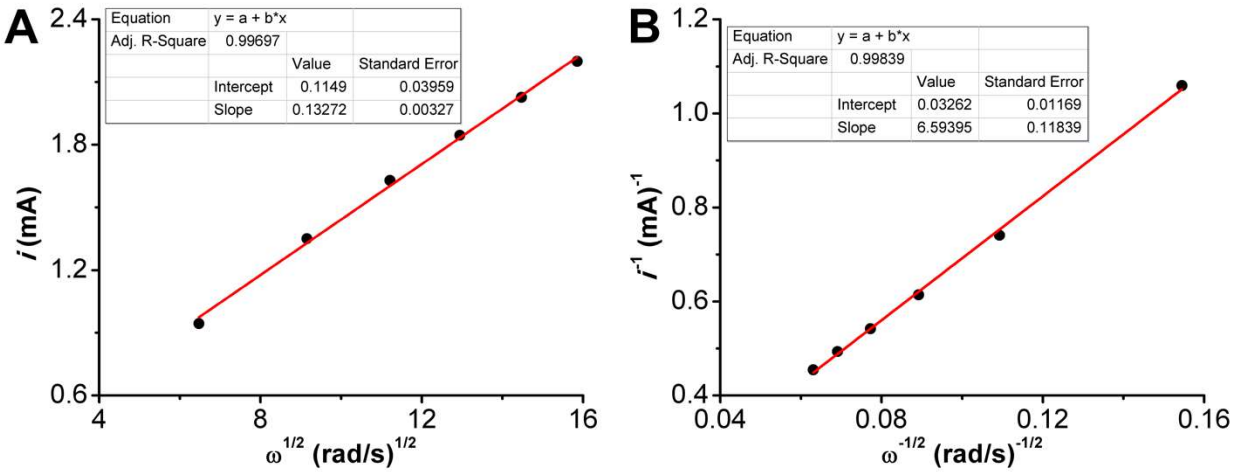

Figure S5.16. (A) Levich and Koutecky-Levich (B) plots from data obtained from linear sweep voltammograms of **im**$^+$ (0.5 mM) by RRDE with 0.1 M TFAH under air saturation conditions at various rotation rates; ring potential = 1.2 V vs. Ag/AgCl.

Stopped-Flow Spectroscopic Analysis

Stopped-flow spectrochemical kinetics studies were performed with a CSF-61DX2 Stopped-Flow System from Hi-Tech Scientific. Kinetic Studio Software was used to monitor a single wavelength and Integrated CCD Software was used to monitor the entire visible spectrum. All data fits were performed within the Kinetic Studio 4.0 Software Suite. Prior to experiments, dried and degassed MeCN was passed through syringes and the cell block before reagents were loaded. In a typical experiment, syringes would be charged with known concentrations of reagent. All reagent solutions were prepared immediately before use. In general, a vial containing **im**$^+$ catalyst and TFAH was sparged with O_2, drawn into a syringe and loaded into the stopped-flow. A second syringe containing N_2-saturated Cp^*_2Fe solution was loaded into the stopped-flow. All reported concentrations are the mixed concentrations in the spectroscopic cell.

$$rate = k_{cat}[im^+]^1[TFAH]^0[O_2]^0[Cp^*_2Fe]^0$$

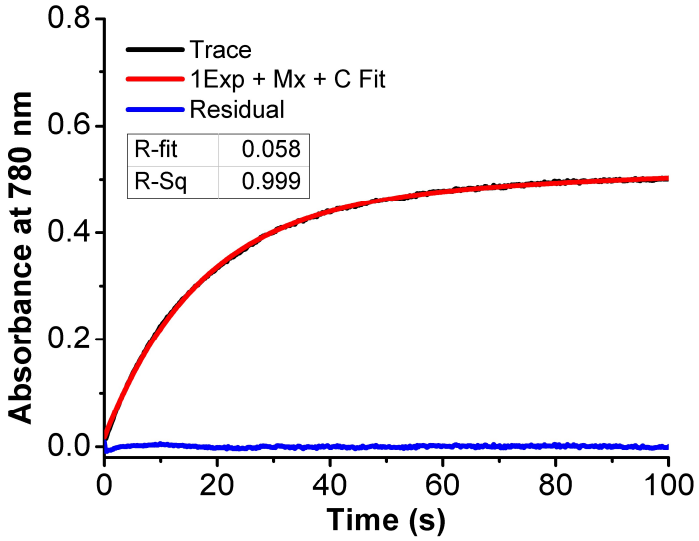

Figure S5.17. Change in absorbance at 780 nm over time as a result of the formation of $[Cp^*_2Fe]^+$ by ORR catalyzed by **im**$^+$ with TFAH (black trace), example of 1Exp + Mx + C fit in Kinetic Studio 4.0 (red trace), and residual fit (blue trace). Concentrations: **im**$^+$ = 4 μM, TFAH = 25 mM, O_2 = 4.05 mM, Cp^*_2Fe = 1 mM.

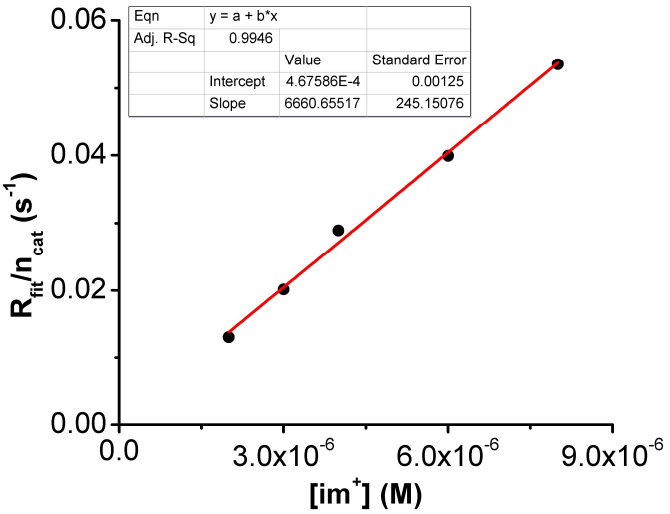

Figure S5.18. Calculated R_{fit}/n_{cat} values from stopped-flow spectrochemical experiments with TFAH, O_2, and Cp^*_2Fe with varying **im**$^+$ concentration. Data were fit using Kinetic Studio 4.0 (1Exp+Mx+C); n_{cat} = 2. Concentrations: TFAH = 25 mM, O_2 = 4.05 mM, Cp^*_2Fe = 1 mM.

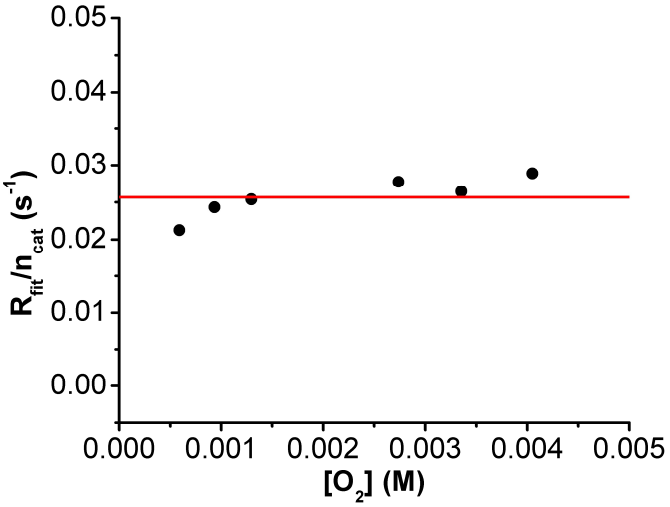

Figure S5.19. Calculated R_{fit}/n_{cat} values from stopped-flow spectrochemical experiments with **im$^+$**, TFAH, Cp*$_2$Fe with varying O_2 concentration. Data were fit using Kinetic Studio 4.0 (1Exp+Mx+C); n_{cat} = 2. The horizontal line represents the global average rate observed across all experiments for variable [O_2]. Concentrations: **im$^+$** = 4 μM, TFAH = 25 mM, Cp*$_2$Fe = 1 mM.

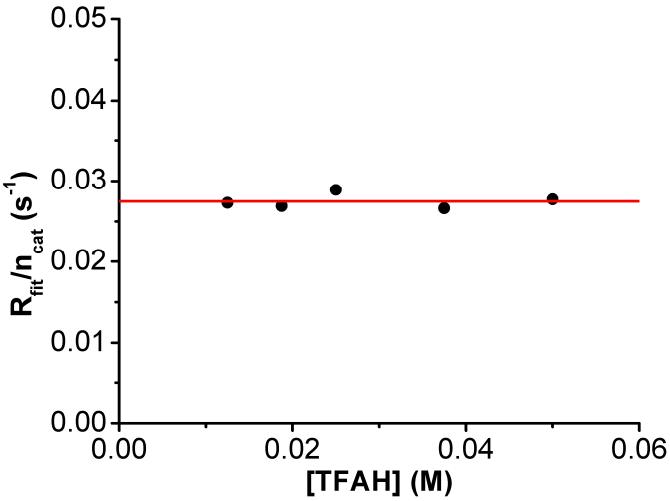

Figure S5.20. Calculated R_{fit}/n_{cat} values from stopped-flow spectrochemical experiments with **im$^+$**, O_2, Cp*$_2$Fe with varying TFAH concentration. Data were fit using Kinetic Studio 4.0 (1Exp+Mx+C); n_{cat} = 2. The horizontal line represents the global average rate observed across all experiments for variable [TFAH]. Concentrations: **im$^+$** = 4 μM, O_2 = 4.05 mM, Cp*$_2$Fe = 1 mM.

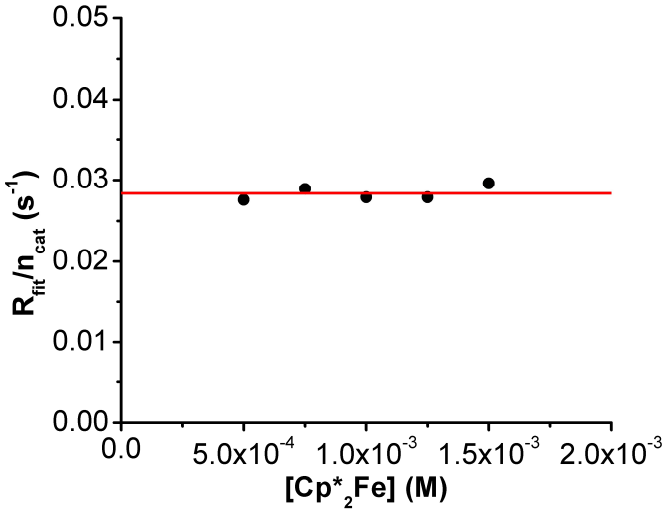

Figure S5.21. Calculated R_{fit}/n_{cat} values from stopped-flow spectrochemical experiments with **im$^+$**, TFAH, O_2 with varying Cp*$_2$Fe concentration. Data were fit using Kinetic Studio 4.0 (1Exp+Mx+C); n_{cat} = 2. The horizontal line represents the global average rate observed across all experiments for variable [Cp*$_2$Fe]. Concentrations: **im$^+$** = 4 μM, TFAH = 25 mM, O_2 = 4.05 mM.

Spectrochemical Selectivity Determination

Generally, to determine the ORR selectivity of **im$^+$**, solutions containing 8 μM [**im$^+$**] and 50 mM TFAH were sparged with O_2 gas and rapidly mixed in a 1:1 ratio with a N_2 saturated 2 mM Cp*$_2$Fe solution to a final volume of 12 mL (final concentrations: 4 μM **im$^+$**, 1 mM Cp*$_2$Fe, 25 mM TFAH, 4.05 mM O_2). Over the course of the reaction, 2 mL aliquots of the catalytic solution were removed and extracted with 10 mL of DCM and 5 mL of DI H_2O. The aqueous layer (3 mL) was removed and put into the cuvette and a UV-vis spectrum was taken before and after the addition of 0.1 mL of $Ti(O)SO_4$, as previously reported.[26-30] Aliquots were taken at ~15 s, ~30 s, ~1 min, and ~2 mins. Experiments were done in triplicate. A calibration curve was used to establish **Eqs S5.4-S5.5** and were used to calculate the % selectivity of H_2O_2, which was determined to be 102 ± 8.4% after 2 min.

$$O_2 + 2Cp^*{}_2Fe(1\ mM) + 2TFAH \xrightarrow{cat.[\boldsymbol{im}^+]} H_2O_2(0.5\ mM) + 2[Cp^*{}_2Fe]^+ + 2TFA^- \quad \textbf{(Eq S5.4)}$$

Abs@408 nm (red trace) – Abs@408 nm (black trace) = 201.2$[H_2O_2]_{exp}$ + 0.003

$$\frac{[H_2O_2]_{exp}}{0.5\ mM\ H_2O_2} \times 100 = \%\ H_2O_2\ \text{selectivity} \qquad \textbf{(Eq S5.5)}$$

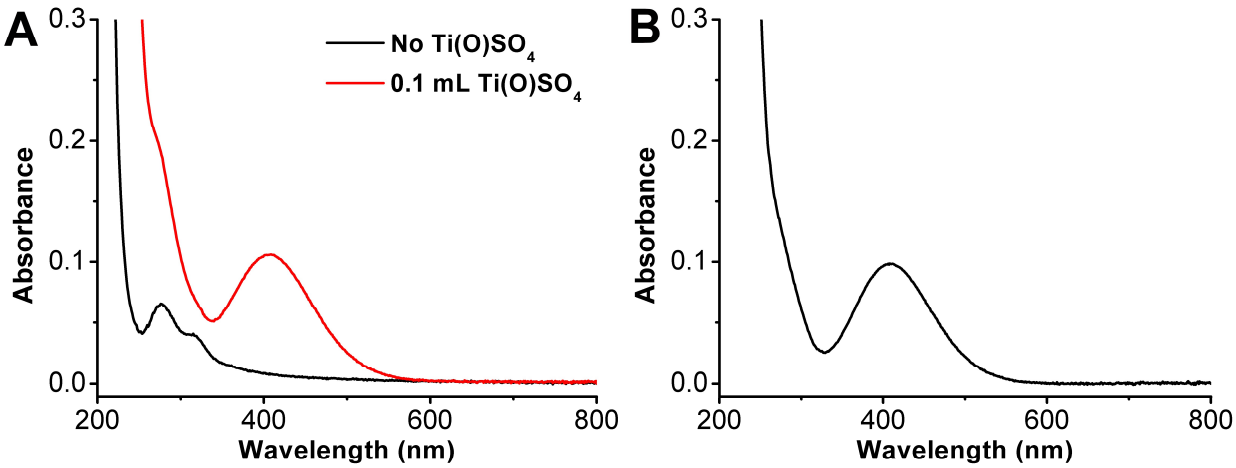

Figure S5.22. H_2O_2 product quantification of ORR by **im**$^+$ with TFAH after 2 min. (A) UV-vis spectra of extracted solution before (black) and after (red) 0.1 mL of 0.1 M $Ti(O)SO_4$ solution was added. (B) Corrected spectra (red – black trace from A). Conditions: 4 μM **im**$^+$, 25 mM TFAH, 1 mM Cp^*_2Fe, 4.05 mM O_2 in MeCN.

Disproportionation Control

To determine the stability of H_2O_2 under catalytic conditions, control studies were conducted in the presence of **im**$^+$, TFAH, and O_2. Generally**,** solutions containing 8 μM [**im**$^+$] and 50 mM TFAH were sparged with O_2 gas and rapidly mixed in a rapidly mixed in a 1:1 ratio with a N_2 saturated urea•H_2O_2 solution (final concentrations: 4 μM **im**$^+$, 0.93 mM urea•H_2O_2, 25 mM TFAH, 4.05 mM O_2). As the solution was allowed to react, 2 mL aliquots were removed at 0 s and after 2 min, extracted with 10 mL DCM and 5 mL DI H_2O. Then, 3 mL of the aqueous layer was removed and added to the cuvette. A UV-vis spectrum was taken before and after the addition of 0.1 mL of 0.1 M $Ti(O)SO_4$ solution and the difference at 408 nm was used to determine the amount of H_2O_2 present ($[H_2O_2]_{detected}$). The % recovery was determined according to **Eq S5.6** from measured $[H_2O_2]_{expected}$ of the H_2O_2 stock solution. After 2 min, 104 ± 3.6 % H_2O_2 was recovered.

$$\frac{[H_2O_2]_{detected}}{[H_2O_2]_{expected}} \times 100 = \%\ H_2O_2\ recovery \qquad \textbf{(Eq S5.6)}$$

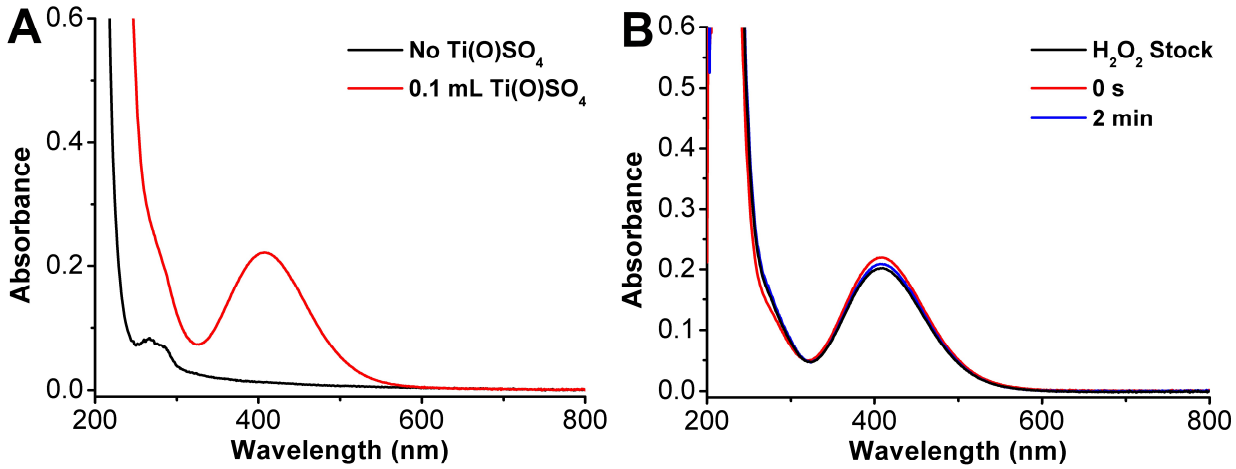

Figure S5.23. Stability test of urea•H_2O_2 in the presence of **im**$^+$, TFAH, and O_2 (A) before (black trace) and after (red trace) the addition of 0.1 mL of 0.1 M Ti(O)SO4 to an extracted aliquot. (B) Corrected UV-vis spectra (red – black from A) after 0 s (red) and 2 min (blue) with the H_2O_2 stock (black). Conditions: 4 μM **im**$^+$, 25 mM TFAH, 4.05 mM O_2, 0.93 mM urea•H_2O_2 in MeCN.

H_2O_2RR Control

To determine the stability of H_2O_2 in the presence of **im**^{0} and TFAH, control studies were conducted in the presence of **im**$^+$, TFAH, and Cp*$_2$Fe, under an N_2 atmosphere. In a N_2-filled glovebox, urea•H_2O_2 was added to a solution containing **im**$^+$, TFAH, and Cp*$_2$Fe (final concentrations: 4 μM **im**$^+$, 25 mM TFAH, 1 mM Cp*$_2$Fe, and 1.5 mM urea•H_2O_2). After 2 min, a 2 mL aliquot was removed from the 'catalytic' solution and extracted with 10 mL of dry, degassed DCM and 5 mL of degassed water. Then, 3 mL of the aqueous layer was removed, and a UV-vis spectrum was taken before and after the addition of 0.1 mL of Ti(O)SO_4 solution. The difference in the absorbance at 408 nm was used to quantify the amount of H_2O_2 present according to **Eq S5.5**, **Eq S5.6** was used to calculate % H_2O_2 recovered relative to the stock H_2O_2 solution.

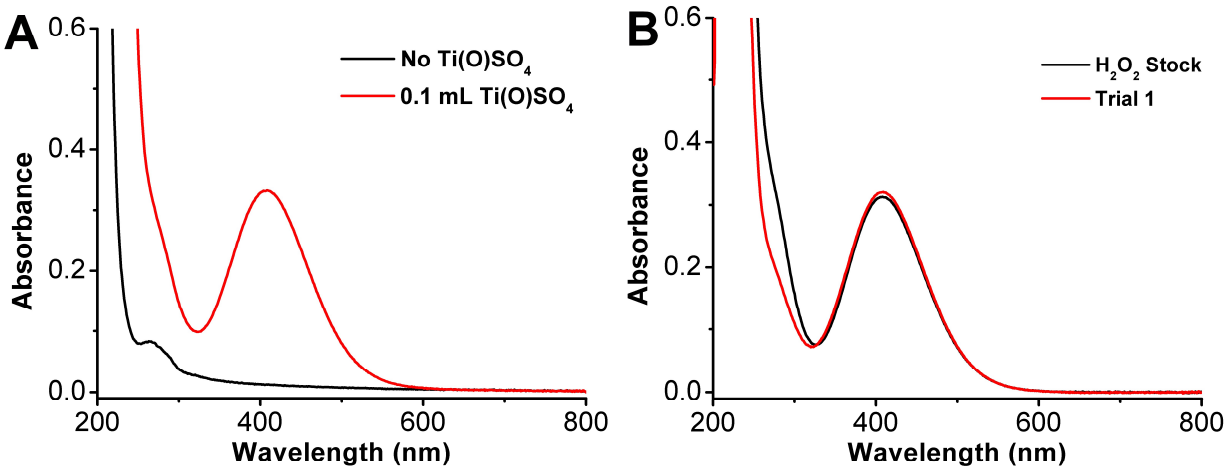

Figure S5.24. Stability test of urea•H_2O_2 in the presence of **im**$^+$, TFAH, and Cp*$_2$Fe (A) before (black trace) and after (red trace) the addition of 0.1 mL of 0.1 M $Ti(O)SO_4$ to an extracted aliquot after 2 min. (B) Corrected UV-vis spectra (red – black from A) after 2 min (red) and H_2O_2 only (black). Conditions: Conditions: 4 μM **im**$^+$, 25 mM TFAH, 4.05 mM O_2, 1.5 mM urea•H_2O_2 in MeCN.

Computational Methods

Geometry optimization was done with the Gaussian 16 package[31] at the B3LYP-D3(BJ)/def2-TZVP level[32-39] with a complete structural model. Dispersion and bulk solvent effects (acetonitrile = MeCN; ε = 35.688) were accounted for at the optimization stage, by using Grimme's D3 parameter set with Becke-Johnson (BJ) damping[38,39] and the SMD continuum model, [40] respectively. The stationary points and their nature as minima (no imaginary frequencies) were characterized by vibrational analysis using the IGRRHO approach as implemented by default in the software package, which also produced enthalpy (H), entropy (S) and Gibbs energy (G) data at 298.15 K. The minima connected by a given transition state were determined by perturbing the transition states along the TS coordinate and optimizing to the nearest minimum. Free energies were corrected (ΔG_{qh}) to account for concentration effects and for errors associated with the harmonic oscillator approximation. Thus, according to Truhlars's quasi-harmonic approximation for vibrational entropy and enthalpy, all vibrational frequencies below 100 cm^{-1} were set to this value. [41] These anharmonic and concentration corrections were calculated with the Goodvibes code. [42] Concentrations were set at 0.001 M for all species unless otherwise indicated, 0.004 M for O_2, 0.500 M for TFAH, and 18.9 M for MeCN. Single point calculations for refining energy

differences were completed with Orca 5.0[43] at the DLPNO-CCSD(T1)/cc-pVTZ level.[37,44,45] Evaluation of spin density was done at the ωB97M-D4/def2-TZVPPD level. [36, 37, 46-50] The stability of the wavefunction and spin contamination were studied at the double- and triple-zeta levels of theory. Reduction potentials from computational data were obtained according to our previous methodology by using the calculated free energy of reduction of the species of interest by [phenazine]$^{-}$, corrected to the experimental potential of phenazine reduction vs Fc^{+}/Fc.[51]

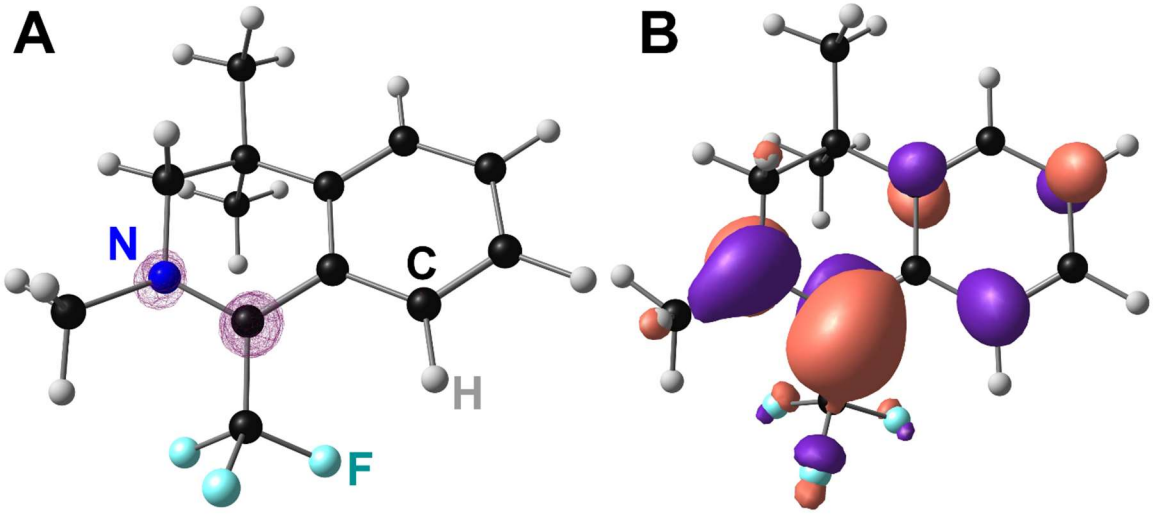

Figure S5.25. (A) spin density plots (0.025 iso) and (B) Kohn-Sham Orbitals (0.05 iso) of the neutral radical **im^{0}** (S = ½) showing localization at C with contributions from N. Generated from the EPR calculation at the ωB97M-D4/def2-TZVPPD level of theory.

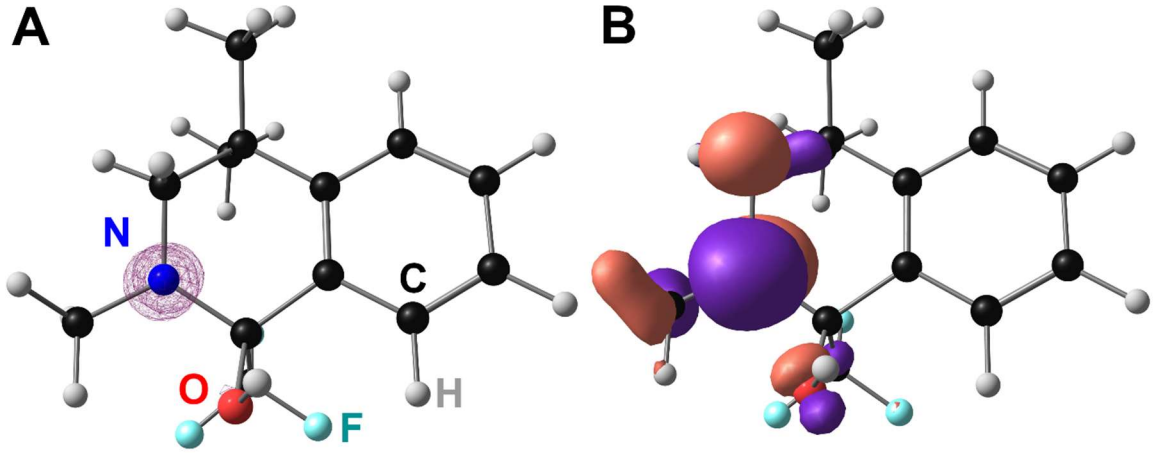

Figure S5.26. (A) spin density plots (0.025 iso) and (B) Kohn-Sham Orbitals (0.05 iso) of the neutral radical $C(CF_3)$–OH species (S = ½) showing localization at N. Generated from the EPR calculation at the ωB97M-D4/def2-TZVPPD level of theory.

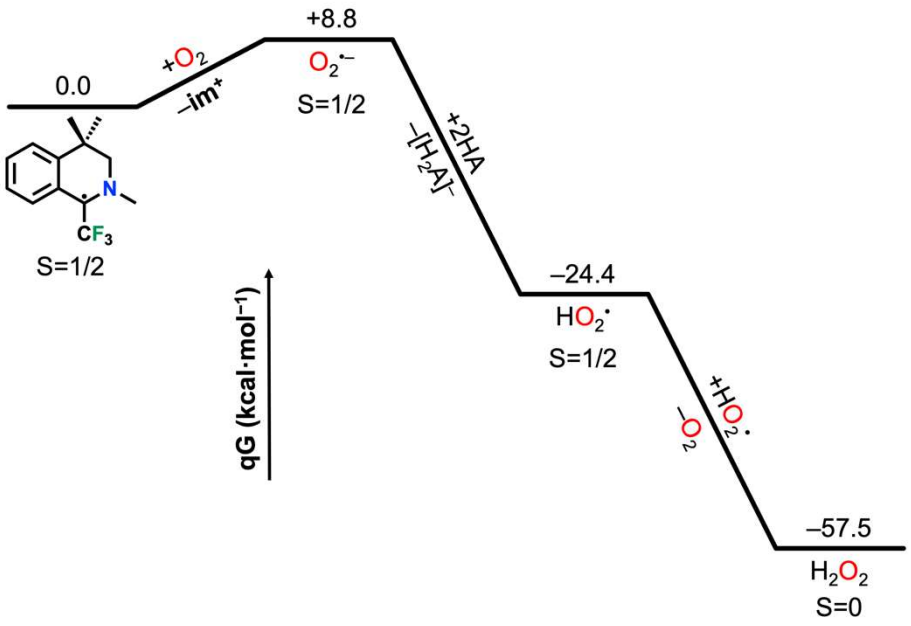

Figure S5.27. Thermodynamics of the catalytic cycle which produces H_2O_2 at an applied potential of –0.87 V vs Fc^+/Fc (the standard reduction potential calculated for **im$^+$**). B3LYP-D3(BJ)/def2-TZVP// DLPNO-CCSD(T1)/cc-pVTZ.

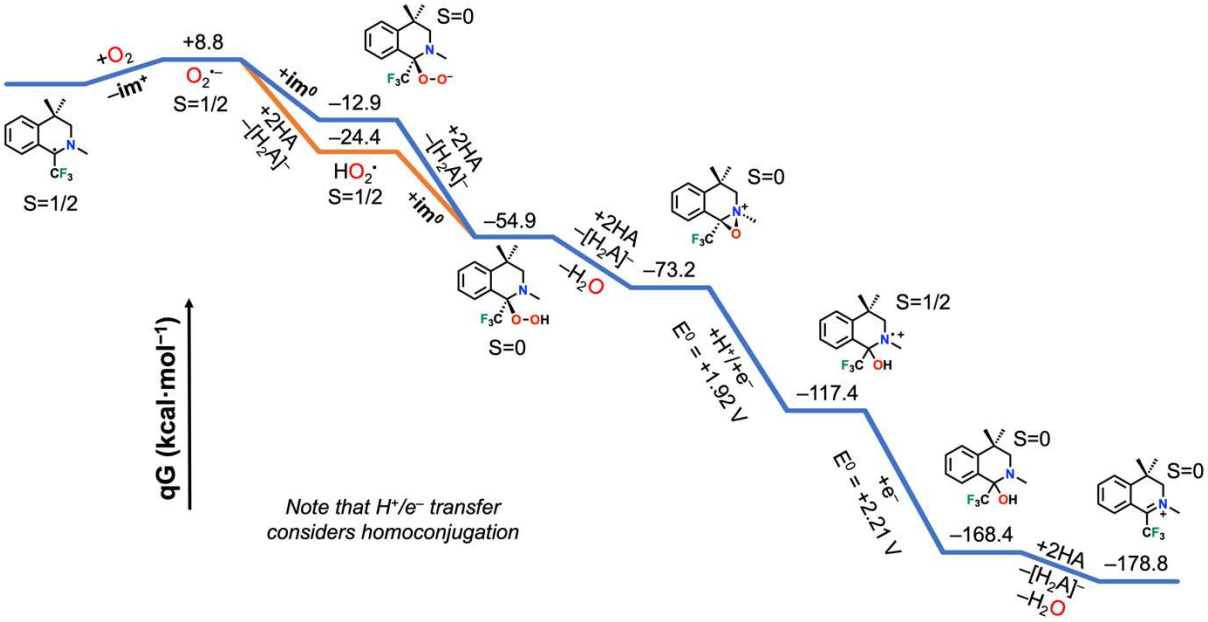

Figure S5.28. Thermodynamics of the catalytic cycle which produces H_2O at an applied potential of –0.87 V vs Fc^+/Fc (the standard reduction potential calculated for **im$^+$**). B3LYP-D3(BJ)/def2-TZVP// DLPNO-CCSD(T1)/cc-pVTZ.

5.5. References

(1) Campos-Martin, J. M.; Blanco-Brieva, G.; Fierro, J. L. G. Hydrogen peroxide synthesis: An outlook beyond the anthraquinone process. *Angew. Chem. Int. Ed.* **2006**, *45* (42), 6962-6984. DOI: 10.1002/anie.200503779.

(2) Pegis, M. L.; Wise, C. F.; Martin, D. J.; Mayer, J. M. Oxygen Reduction by Homogeneous Molecular Catalysts and Electrocatalysts. *Chem. Rev.* **2018**, *118* (5), 2340-2391. DOI: 10.1021/acs.chemrev.7b00542.

(3) Dai, L.; Xue, Y.; Qu, L.; Choi, H.-J.; Baek, J.-B. Metal-Free Catalysts for Oxygen Reduction Reaction. *Chem. Rev.* **2015**, *115* (11), 4823-4892. DOI: 10.1021/cr5003563.

(4) Zhai, Q.; Pan, Y.; Dai, L. Carbon-Based Metal-Free Electrocatalysts: Past, Present, and Future. *Acc. Mater. Res.* **2021**, *2* (12), 1239-1250. DOI: 10.1021/accountsmr.1c00190.

(5) Trojánek, A.; Langmaier, J.; Šebera, J.; Záliš, S.; Barbe, J.-M.; Girault, H. H.; Samec, Z. Fine tuning of the catalytic effect of a metal-free porphyrin on the homogeneous oxygenreduction. *Chem. Commun.* **2011**, *47* (19), 5446-5448, 10.1039/C1CC11075F. DOI: 10.1039/C1CC11075F.

(6) Payattikul, L.; Chen, C.-Y.; Chen, Y.-S.; Raja Pugalenthi, M.; Punyawudho, K. Recent Advances and Synergistic Effects of Non-Precious Carbon-Based Nanomaterials as ORR Electrocatalysts: A Review. In *Molecules*, 2023; Vol. 28.

(7) Huang, X.; Shen, T.; Sun, S.; Hou, Y. Synergistic Modulation of Carbon-Based, Precious-Metal-Free Electrocatalysts for Oxygen Reduction Reaction. *ACS Appl. Mater. Interfaces* **2021**, *13* (6), 6989-7003. DOI: 10.1021/acsami.0c19922.

(8) Ma, R.; Lin, G.; Zhou, Y.; Liu, Q.; Zhang, T.; Shan, G.; Yang, M.; Wang, J. A review of oxygen reduction mechanisms for metal-free carbon-based electrocatalysts. *Npj Comput. Mater.* **2019**, *5* (1), 78. DOI: 10.1038/s41524-019-0210-3.

(9) Karimi, M.; Borthakur, R.; Dorsey, C. L.; Chen, C.-H.; Lajeune, S.; Gabbaï, F. P. Bifunctional Carbenium Dications as Metal-Free Catalysts for the Reduction of Oxygen. *J. Am. Chem. Soc.* **2020**, *142* (32), 13651-13656. DOI: 10.1021/jacs.0c04841.

(10) Tanjedrew, N.; Thammanatpong, K.; Surawatanawong, P.; Chakthranont, P.; Chantarojsiri, T.; Unjarern, T.; Kiatisevi, S. Tunable Metal-free Imidazole-Benzimidazole Electrocatalysts for Oxygen Reduction in Aqueous Solutions. *Chem. Eur. J.* **2023**, *30* (5), e202302854. DOI: 10.1002/chem.202302854.

(11) Andrieux, C. P.; Hapiot, P.; Sa Véant, J. M. Electron transfer coupling of diffusional pathways. Homogeneous redox catalysis of dioxygen reduction by the methylviologen cation radical in acidic dimethylsulfoxide. *J. Electroanal. Chem. Interf. Electrochem.* **1985**, *189* (1), 121-133. DOI: 10.1016/0368-1874(85)85630-6.

(12) Audebert, P.; Hapiot, P. Preparation and electrochemistry of several substituted 9-(4-R-phenyl)-N-methylacridinium salts.: Kinetic analysis of the O2 catalytic reduction in acidic dimethylsulfoxide and in hydrophobic Nafion® gels. *J. Electroanal. Chem.* **1993**, *361* (1), 177-183. DOI: 10.1016/0022-0728(93)87052-W.

(13) Wang, D.; Shuler, W. G.; Pierce, C. J.; Hilinski, M. K. An Iminium Salt Organocatalyst for Selective Aliphatic C–H Hydroxylation. *Organic Letters* **2016**, *18* (15), 3826-3829. DOI: 10.1021/acs.orglett.6b01832.

(14) Dyer, R. M. B.; Hahn, P. L.; Hilinski, M. K. Selective Heteroaryl N-Oxidation of Amine-Containing Molecules. *Organic Letters* **2018**, *20* (7), 2011-2014. DOI: 10.1021/acs.orglett.8b00558.

(15) Wang, R.; Okajima, T.; Kitamura, F.; Kawauchi, S.; Matsumoto, N.; Thiemann, T.; Mataka, S.; Ohsaka, T. Catalytic Reduction of O2 by Pyrazine Derivatives. *J. Phys. Chem. A* **2004**, *108* (11), 1891-1899. DOI: 10.1021/jp036024k.

(16) Espinoza, E. M.; Clark, J. A.; Soliman, J.; Derr, J. B.; Morales, M.; Vullev, V. I. Practical Aspects of Cyclic Voltammetry: How to Estimate Reduction Potentials When Irreversibility Prevails. *Journal of The Electrochemical Society* **2019**, *166* (5), H3175. DOI: 10.1149/2.0241905jes.

(17) Costentin, C.; Savéant, J.-M. Coupling of Electrode Electron Transfers with Homogeneous Chemical Reactions. In *Elements of Molecular and Biomolecular Electrochemistry*, 2019; pp 81-181.

(18) McCarthy, B. D.; Martin, D. J.; Rountree, E. S.; Ullman, A. C.; Dempsey, J. L. Electrochemical reduction of brønsted acids by glassy carbon in acetonitrile-implications for electrocatalytic hydrogen evolution. *Inorg. Chem.* **2014**, *53* (16), 8350-8361. DOI: 10.1021/ic500770k.

(19) Harraz, D. M.; Weng, S.; Surendranath, Y. Electrochemically Quantifying Oxygen Reduction Selectivity in Nonaqueous Electrolytes. *ACS Catal.* **2023**, *13* (2), 1462-1469. DOI: 10.1021/acscatal.2c04564.

(20) Savéant, J.-M. Molecular Catalysis of Electrochemical Reactions. Mechanistic Aspects. *Chem. Rev.* **2008**, *108* (7), 2348-2378. DOI: 10.1021/cr068079z.

(21) Singh, P. S.; Evans, D. H. Study of the Electrochemical Reduction of Dioxygen in Acetonitrile in the Presence of Weak Acids. *The J. Phys. Chem. B* **2006**, *110* (1), 637-644. DOI: 10.1021/jp055296f.

(22) Pattanayak, S.; Berben, L. A. Pre-Equilibrium Reaction Mechanism as a Strategy to Enhance Rate and Lower Overpotential in Electrocatalysis. *J. Am. Chem. Soc.* **2023**, *145* (6), 3419-3426. DOI: 10.1021/jacs.2c10942.

(23) Li, Q.; Batchelor-McAuley, C.; Lawrence, N. S.; Hartshorne, R. S.; Compton, R. G. Anomalous solubility of oxygen in acetonitrile/water mixture containing tetra-n-butylammonium perchlorate supporting electrolyte; the solubility and diffusion coefficient of oxygen in anhydrous acetonitrile and aqueous mixtures. *J. Electroanal. Chem.* **2013**, *688*, 328-335. DOI: 10.1016/j.jelechem.2012.07.039.

(24) Dyer, R. M. B. Advances in Organocatalytic Site Selective Oxidations. University of Virginia, Charlottesville, VA, 2023.

(25) Hooe, S. L.; Rheingold, A. L.; Machan, C. W. Electrocatalytic Reduction of Dioxygen to Hydrogen Peroxide by a Molecular Manganese Complex with a Bipyridine-Containing Schiff Base Ligand. *J. Am. Chem. Soc.* **2018**, *140* (9), 3232-3241. DOI: 10.1021/jacs.7b09027.

(26) Cook, E. N.; Dickie, D. A.; Machan, C. W. Catalytic Reduction of Dioxygen to Water by a Bioinspired Non-Heme Iron Complex via a 2+2 Mechanism. *J. Am. Chem. Soc.* **2021**, *143* (40), 16411-16418. DOI: 10.1021/jacs.1c04572.

(27) Cook, E. N.; Hooe, S. L.; Dickie, D. A.; Machan, C. W. Homogeneous Catalytic Reduction of O2 to H2O by a Terpyridine-Based FeN3O Complex. *Inorg. Chem.* **2022**, *61* (22), 8387-8392. DOI: 10.1021/acs.inorgchem.2c00524.

(28) Hooe, S. L.; Machan, C. W. Dioxygen Reduction to Hydrogen Peroxide by a Molecular Mn Complex: Mechanistic Divergence between Homogeneous and Heterogeneous Reductants. *J. Am. Chem. Soc.* **2019**, *141* (10), 4379-4387. DOI: 10.1021/jacs.8b13373.

(29) Nichols, A. W.; Cook, E. N.; Gan, Y. J.; Miedaner, P. R.; Dressel, J. M.; Dickie, D. A.; Shafaat, H. S.; Machan, C. W. Pendent Relay Enhances H_2O_2 Selectivity during Dioxygen Reduction Mediated by Bipyridine-Based Co–N_2O_2 Complexes. *J. Am. Chem. Soc.* **2021**, *143* (33), 13065-13073. DOI: 10.1021/jacs.1c03381.

(30) Anson, C. W.; Stahl, S. S. Cooperative Electrocatalytic O2 Reduction Involving Co(salophen) with p-Hydroquinone as an Electron-Proton Transfer Mediator. *J. Am. Chem. Soc.* **2017**, *139* (51), 18472-18475. DOI: 10.1021/jacs.7b11362.

(31) *Gaussian 16, Revision B.01*; Gaussian, Inc.: Wallingford CT, 2016. (accessed.

(32) Becke, A. D. Density-functional thermochemistry. III. The role of exact exchange. *J. Chem. Phys.* **1993**, *98* (7), 5648-5652. DOI: 10.1063/1.464913.

(33) Lee, C.; Yang, W.; Parr, R. G. Development of the Colle-Salvetti correlation-energy formula into a functional of the electron density. *Phys. Rev. B* **1988**, *37* (2), 785-789.

(34) Vosko, S. H.; Wilk, L.; Nusair, M. Accurate spin-dependent electron liquid correlation energies for local spin density calculations: a critical analysis. *Can. J. Phys.* **1980**, *58* (8), 1200-1211. DOI: 10.1139/p80-159.

(35) Stephen, P. J.; Devlin, F. J.; Chabalowski, C. F.; Frisch, M. J. Ab Initio Calculation of Vibrational Absorption and Circular Dichroism Spectra Using Density Functional Force Fields. *J. Phys. Chem.* **1994**, *98* (45), 11623-11627.

(36) Weigend, F.; Ahlrichs, R. Balanced basis sets of split valence, triple zeta valence and quadruple zeta valence quality for H to Rn: Design and assessment of accuracy. *Phys. Chem. Chem. Phys.* **2005**, *7* (18), 3297-3305. DOI: 10.1039/b508541a.

(37) Weigend, F. Accurate Coulomb-fitting basis sets for H to Rn. *Phys. Chem. Chem. Phys.* **2006**, *8* (9), 1057-1065. DOI: 10.1039/b515623h.

(38) Grimme, S.; Antony, J.; Ehrlich, S.; Krieg, H. A consistent and accurate ab initio parametrization of density functional dispersion correction (DFT-D) for the 94 elements H-Pu. *J. Chem. Phys.* **2010**, *132* (15), 154104-154104. DOI: 10.1063/1.3382344.

(39) Grimme, S.; Ehrlich, S.; Goerigk, L. Effect of the damping function in dispersion corrected density functional theory. *J. Comput. Chem.* **2011**, *32* (7), 1456-1465. DOI: 10.1002/jcc.21759.

(40) Marenich, A. V.; Cramer, C. J.; Truhlar, D. G. Universal solvation model based on solute electron density and on a continuum model of the solvent defined by the bulk dielectric constant and atomic surface tensions. *J. Phys. Chem. B* **2009**, *113* (18), 6378-6396. DOI: 10.1021/jp810292n.

(41) Ribeiro, R. F.; Marenich, A. V.; Cramer, C. J.; Truhlar, D. G. Use of solution-phase vibrational frequencies in continuum models for the free energy of solvation. *J. Phys. Chem. B* **2011**, *115* (49), 14556-14562. DOI: 10.1021/jp205508z.

(42) *Goodvibes v.3.0.1*; 2019. (accessed.

(43) Neese, F. Software update: The ORCA program system—Version 5.0. *WIREs Computational Molecular Science* **2022**, *12* (5), e1606. DOI: 10.1002/wcms.1606.

(44) Dunning, T. H., Jr. Gaussian basis sets for use in correlated molecular calculations. I. The atoms boron through neon and hydrogen. *J. Chem. Phys.* **1989**, *90* (2), 1007-1023. DOI: 10.1063/1.456153.

(45) Weigend, F.; Köhn, A.; Hättig, C. Efficient use of the correlation consistent basis sets in resolution of the identity MP2 calculations. *J. Chem. Phys.* **2002**, *116* (8), 3175-3183. DOI: 10.1063/1.1445115.

(46) Mardirossian, N.; Head-Gordon, M. ωB97M-V: A combinatorially optimized, range-separated hybrid, meta-GGA density functional with VV10 nonlocal correlation. *J. Chem. Phys.* **2016**, *144* (21), 214110. DOI: 10.1063/1.4952647.

(47) Hellweg, A.; Hättig, C.; Höfener, S.; Klopper, W. Optimized accurate auxiliary basis sets for RI-MP2 and RI-CC2 calculations for the atoms Rb to Rn. *Theor. Chem. Acc.* **2007**, *117* (4), 587-597. DOI: 10.1007/s00214-007-0250-5.

(48) Caldeweyher, E.; Bannwarth, C.; Grimme, S. Extension of the D3 dispersion coefficient model. *J. Chem. Phys.* **2017**, *147* (3), 034112. DOI: 10.1063/1.4993215.

(49) Caldeweyher, E.; Ehlert, S.; Hansen, A.; Neugebauer, H.; Spicher, S.; Bannwarth, C.; Grimme, S. A generally applicable atomic-charge dependent London dispersion correction. *J. Chem. Phys.* **2019**, *150* (15), 154122. DOI: 10.1063/1.5090222 (acccessed 5/15/2023).

(50) Najibi, A.; Goerigk, L. DFT-D4 counterparts of leading meta-generalized-gradient approximation and hybrid density functionals for energetics and geometries. *J. Comput. Chem.* **2020**, *41* (30), 2562-2572. DOI: 10.1002/jcc.26411.

(51) Moreno, J. J.; Hooe, S. L.; Machan, C. W. DFT Study on the Electrocatalytic Reduction of CO2 to CO by a Molecular Chromium Complex. *Inorg. Chem.* **2021**, *60* (6), 3635-3650. DOI: 10.1021/acs.inorgchem.0c03136.

Chapter 6:

Acid Strength Effects on Off-Cycle Dimerization
During Metal-Free Catalytic Dioxygen Reduction

This chapter contains material for upcoming publication and has been incorporated with consent of all current contributing authors. These authors include Luke A. Flaxman, Amelia G. Reid, Diane A. Dickie, and Charles W. Machan. The work in this chapter was published in preprint form and is available at DOI: 10.26434/chemrxiv-2024-zk3xs.

6.1. Abstract

Development of earth-abundant catalysts for the reduction of dioxygen (ORR) is essential for the development of alternative industrial processes and energy sources. Here, we report a transition metal-free diium organocatalyst (**Ph_2Phen^{2+}**) for the ORR via an outer-sphere mechanism. The ORR performance of this compound was studied in acetonitrile solution under both electrochemical conditions and spectrochemical conditions, using halogenated acetic acid derivatives spanning a pK_a range of 12.65 to 20.3. Interestingly, it was found that under electrochemical conditions, an off-cycle dimer species forms via an inner-sphere reaction due to the relatively high concentration of **$Ph_2Phen^{\bullet+}$** in the reaction-diffusion layer. However, under spectrochemical conditions, strong acids were able to rapidly protonate $O_2^{\bullet-}$ en route to disproportionation, avoiding the off-cycle dimeric species, whereas weaker acids were found to be rate-limited by the dimer equilibrium. Together, these results provide insight into the mechanisms of ORR by organic-based, metal-free catalysts, suggesting that balancing redox activity and unsaturated character of these molecules with respect to the pK_a of intermediates can enable tuning analogous to transition metal-based systems.

6.2. Introduction

The oxygen reduction reaction (ORR) is central to the development of new alternative energy devices as well as a possible route to more environmentally friendly chemical oxidant production.[1-5] Currently, the best catalysts for the ORR are platinum-based materials, however, the high cost and low earth abundance of Pt preclude it from being a sustainable option.[6] Inspiration from nature, in combination with the perceived desirability of intrinsic redox flexibility and favorable open-shell ground state configurations, has led to significant focus on first-row transition metals as the basis for developing new electrocatalysts for the ORR.[1-3,7-9] Substantial work has been done to better understand reactivity of dioxygen (O_2) at molecular transition metal centers, including assessing the structure-function parameters which control selectivity and activity.[1-3,10-14]

The instability of many organic molecules toward the reactive oxygen species (ROSs) that are intermediates of the ORR has slowed their development as catalysts relative to transition metal complexes. However, there have been a few reports on homogeneous ORR mediated by organic molecules, including methyl viologen[15] and substituted methylacridinium salts.[16] Mechanistic studies showed that both of these catalysts operate via an outer-sphere mechanism to selectively produce H_2O_2. More recently, ORR catalysis reliant on inner-sphere mechanisms has been reported for organic molecules. Gabbaï and co-workers reported a dicarbenium system where a bridging peroxide species was a crucial intermediate during catalysis.[17] Protonation of this catalyst-bound intermediate resulted in the release of H_2O_2. Subsequently, Kiatisevi and co-workers studied an imidazole/benzimidazole-based system for the reduction of O_2 to either H_2O_2 or H_2O based on the electron-donating or -withdrawing ability of the substituents.[18] It is worth noting that there has also been significant work on heterogeneous carbon-based catalysts for the ORR.[1,19-22]

Recently, we reported an iminium-based organoelectrocatalyst (im^+) whose accessible mechanistic pathway (and therefore reaction selectivity) was controlled by the electron source.[23] Under electrochemical conditions, the concentration of reduced im^0 was high enough relative to

$O_2^{\bullet-}$ in the reaction-diffusion layer to proceed via an inner-sphere mechanism to generate H_2O. However, under spectrochemical conditions with decamethylferrocene (Cp^*_2Fe) as a chemical reductant, catalysis operated via an outer-sphere mechanism to form quantitative amounts of H_2O_2.

These previous studies suggested that cationic and unsaturated organic compounds could be viable precatalysts for the ORR. Here, we report the synthesis and catalytic activity of a phenanthroline-based dication (**Ph_2Phen^{2+}**) which can serve as an ORR catalyst with halogenated acetic acid derivates as proton sources (**Figure 6.1**). Under both electrochemical and spectrochemical conditions (decamethylferrocene, Cp^*_2Fe as a chemical reductant) we find that **Ph_2Phen^{2+}** catalytically reduces O_2 via an outer-sphere mechanism. Based on mechanistic studies, however, it is proposed that a dimer species with a bridging peroxo unit between two equivalents of **Ph_2Phen^{2+}** forms under equilibrium control in all reaction conditions. Further, the observed relationship of proton activity to catalytic behavior suggests that the ability to re-enter the catalytic cycle from this off-cycle dimeric equilibrium is dependent on acid choice. Overall, these studies suggest that when factors of redox activity and unsaturated character are adjusted relative to the pK_a of ROS intermediates, organoelectrocatalytic activity can be tuned in a manner analogous to transition metal-based catalysts.

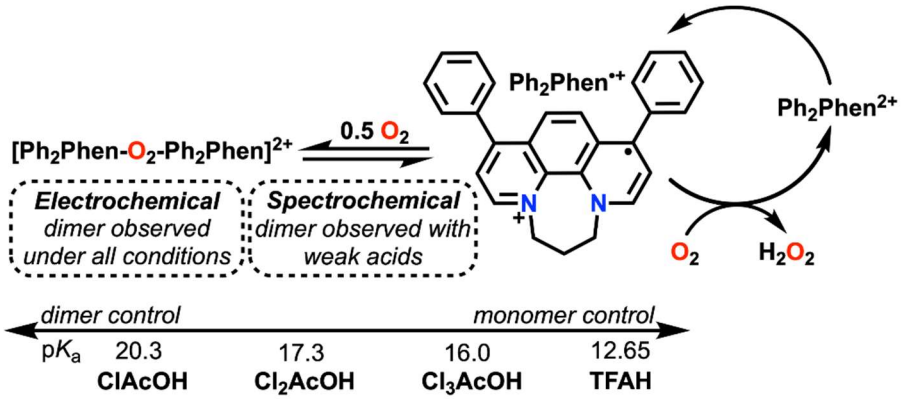

Figure 6.1. Summary of the work described here, note that a simplified representation of the equilibrium dimerization reaction is depicted.

6.3. Results

6.3.1. Synthesis and Characterization

The synthesis of 1,11-diphenyl-6,7-dihydro-5H-[1,4]diazepino[1,2,3,4-lmn][1,10]phenanthroline-4,8-diium bromide (**Ph_2Phen^{2+}**) was achieved via a previously reported procedure.[24] A solution of 4,7-diphenyl-1,10-phenanthroline was allowed to reflux in toluene with a stoichiometric amount of 1,3-dibromopropane until a precipitate formed. Recrystallization of the crude material from dichloromethane (DCM) resulted in a spectroscopically pure bright orange solid of the dibromide salt of the diium compound. The diium **Ph_2Phen^{2+}** was characterized with elemental analysis (EA), NMR and UV-vis spectroscopies (See SI). Single crystals suitable for X-ray diffraction studies were obtained by slow evaporation from MeCN-d_3 (**Figure 6.2**).

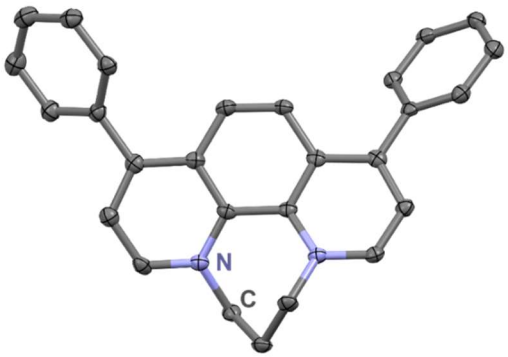

Figure 6.2. Molecular structure of **Ph_2Phen^{2+}** obtained from single-crystal X-ray diffraction studies. H-atoms and occluded Br counteranions have been removed for clarity. Gray = C, blue = N; thermal ellipsoids at 50%. CCDC 2346924

6.3.2. Electrochemical Analysis

Ph_2Phen^{2+} was analyzed by cyclic voltammetry (CV) in MeCN with tetrabutylammonium hexafluorophosphate ($TBAPF_6$) as supporting electrolyte. Under Ar saturation conditions there are two, one-electron reversible redox features at –0.73 V vs. Fc^+/Fc and –1.16 V vs. Fc^+/Fc (**Figure S6.4**). All further analysis focused on the more positive feature, due to its relevance to O_2 reactivity. Variable scan rate studies under Ar saturation showed that the peak current density at the reversible reduction feature at –0.73 V vs. Fc^+/Fc had a linear dependence with the square

root of the scan rate between 0.025 and 3 V/s, indicative of a diffusion-limited redox response (**Figure S6.5**); a diffusion coefficient of 1.14 x 10^{-5} $cm^2 \cdot s^{-1}$ was calculated from the slope.

Upon saturation with O_2, the first reduction feature becomes irreversible and shifts to more positive potentials (E_p = –0.71 V vs. Fc^+/Fc), indicating an irreversible chemical reaction occurs following reduction. Evaluating peak potential with respect to scan rate and concentration for irreversible reactions can provide insight into the nature of the electrochemical mechanism.[23,25] Evolution of peak potential with respect to scan rate revealed a slope of –24.3 mV/decade (**Figure S6.6**) while a slope of –12.3 mV/decade (**Figure S6.7**) was observed for variable $\mathbf{Ph_2Phen^{2+}}$ concentration studies under comparable conditions. These values are intermediate to those expected for *EC* (reversible electron transfer followed by irreversible chemical reaction) and *RSD*-type reactions (radical substrate dimerization reactions), either of which could result from the binding of superoxide $O_2^{\bullet-}$ to $\mathbf{Ph_2Phen^{2+}}$ **or** $\mathbf{Ph_2Phen^{\bullet+}}$. Based on these data and experiments discussed in detail below, it is hypothesized that an outer-sphere electron transfer occurs from $\mathbf{Ph_2Phen^{\bullet+}}$ to produce $O_2^{\bullet-}$ and that a dimeric equilibrium involving $[\mathbf{Ph_2Phen^{2+}}\bullet O_2^{\bullet-}]^+$ and $\mathbf{Ph_2Phen^{\bullet+}}$ exists which generates $[\mathbf{Ph_2Phen}–O_2–\mathbf{Ph_2Phen}]^{2+}$.[23]

Upon addition of TFAH (pK_a(MeCN) = 12.65)[26] under Ar saturation conditions, there is minimal change to the initial one-electron redox feature (**Figure S6.9**), suggesting that TFAH does not interact with $\mathbf{Ph_2Phen^{2+}}$ or its reduced form $\mathbf{Ph_2Phen^{\bullet+}}$. However, upon saturation with O_2 there is an increase in current suggestive of catalytic activity for the ORR (**Figure 6.3**, blue). Control rinse tests confirmed that the catalytic current response was due to homogeneous activity of $\mathbf{Ph_2Phen^{2+}}$ (**Figure S6.11**). It should be noted that cross-tracing can be observed on the return sweep of the catalytic trace at a higher concentration of acid, however, this is overcome at higher scan rates (≥0.8 V/s). Therefore, it is proposed that the cross-tracing can be attributed to the accumulation of an intermediate of the catalytic reaction which is reduced at more positive potentials than the catalytic potential (**Figure S6.10**). Rotating-ring disk electrode (RRDE) methods with a glassy carbon disk and roughened gold ring[27] were used to determine the

electrochemical selectivity of ORR by **Ph_2Phen^{2+}**. Under air saturation, this system was found to be 97.3 ± 2.6% selective for H_2O_2 with TFAH as the proton source (**Figure S6.16**). The estimated overpotential (η_{H2O2}) for H_2O_2 production is 0.67 V under these conditions (See SI).[26,28]

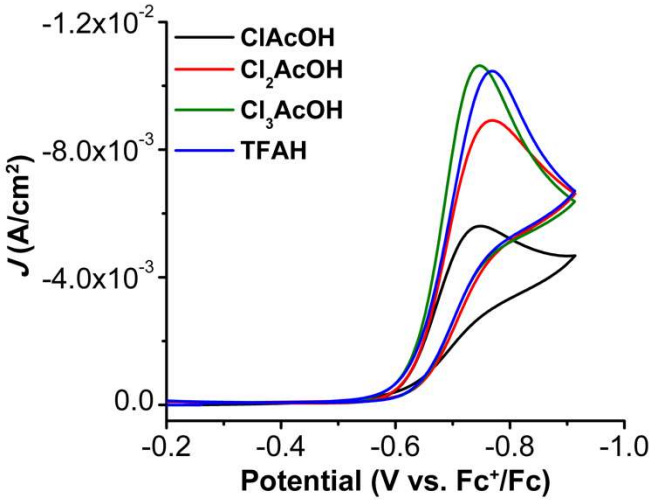

Figure 6.3. CVs of **Ph_2Phen^{2+}** under catalytic conditions with ClAcOH (black), Cl_2AcOH (red), Cl_3AcOH (green), and TFAH (blue) as proton sources. Conditions: 1 mM **Ph_2Phen^{2+}**, 0.1 M AH, 0.1 M $TBAPF_6$/MeCN; O_2 saturation; glassy carbon working electrode, glassy carbon rod counter electrode, Ag/AgCl pseudoreference electrode; referenced to Fc^+/Fc internal standard; 100 mV/s scan rate.

To better understand the mechanism of the ORR and its dependence on proton activity, we undertook analogous studies with a variety of acetic acid derivatives: Cl_3AcOH, Cl_2AcOH, ClAcOH, which have estimated pK_a values in MeCN of 16.0, 17.3, and 20.3, respectively (**Table S6.1**, See SI).[29] In the presence of added proton donor and O_2, there is a catalytic increase in current for all three (**Figure 6.3**). Again, cross-tracing is observed on the return sweep of the catalytic trace that can be overcome at high scan rates (**Figures S6.19**, **S6.28**, and **S6.37**). RRDE methods were again used to determine the electrochemical selectivity of the ORR by **Ph_2Phen^{2+}** with each acid. Under air saturation, Ph_2Phen^{2+} was found to be 96.9 ± 0.85 and 98.2 ± 7.8% selective for H_2O_2 with Cl_3AcOH and Cl_2AcOH, respectively. However, under catalytic conditions with ClAcOH as a proton source, reducing current was observed at the Au ring (**Figure S6.43**), suggestive of the reduction of an intermediate produced at the disk, precluding selectivity

assessment. Control studies with added H_2O_2 under aprotic electrochemical conditions revealed that H_2O_2 does not interact substantially with reduced **$Ph_2Phen^{\bullet+}$** on the electrochemical timescale. However, in the presence of acid (**Figures S6.15**, **S6.24**, **S6.33**, and **S6.42**) there is a modest increase in current at the **$Ph_2Phen^{2+/\bullet+}$** reduction event and the feature becomes irreversible, suggesting that there is minor activity for H_2O_2 reduction. However, upon saturating the protic solution with O_2 ORR catalytic current is recovered in all cases, which is proposed to be consistent with a catalytic reaction where H_2O_2 is not a discrete intermediate *en route* to further reduction under these conditions.

Variable concentration studies were performed in order to develop a better mechanistic picture of the ORR.[30] Interestingly, for each added acid there is an observed half-order dependence on catalyst concentration (**Figures S6.12, S6.21, S6.30,** & **S6.39**). A first-order dependence on acid concentration was observed for TFAH (**Figure S6.13**), Cl_2AcOH (**Figure S6.31**), and ClAcOH (**Figure S6.48),** while Cl_3AcOH deviated from expected behavior (**Figure S6.22**). Finally, mixed-order dependence on O_2 concentration was observed for all proton sources (**Figures S6.14**, **S6.32**, & **S6.41**), with the exception of Cl_3AcOH (**Figure S6.23**), precluding definitive rate law expressions. Based on the half-order rate dependence on **Ph_2Phen^{2+}** concentration and the general observance of mixed-order dependence on O_2 concentration, it is proposed that a bridging off-cycle dimer species forms in the presence of excess **$Ph_2Phen^{\bullet+}$** in the reaction-diffusion layer.

6.3.3. Spectrochemical Analysis

Catalytic ORR activity of **Ph_2Phen^{2+}** with each acid was also studied by stopped-flow UV-vis methods using Cp^*_2Fe as a chemical reductant (**Figure 6.4**). The spectral handle of $[Cp^*_2Fe]^+$ at 780 nm was used to monitor the progress of the reaction to extract kinetic parameters. The observed rate law for each system was determined by independently varying the concentration of **Ph_2Phen^{2+}**, acid, O_2, and reductant (See SI). With TFAH, there is an observed first-order dependence on **Ph_2Phen^{2+}**, TFAH, and O_2 concentration (**Eq 6.1**). With Cl_3AcOH, the rate law

becomes independent of O_2 concentration, and there is an observed first-order dependence on **Ph_2Phen^{2+}** and acid concentration (**Eq 6.2**). Interestingly, with weaker acids, Cl_2AcOH and ClAcOH, there is a shift in rate law to a half-order dependence on **Ph_2Phen^{2+}** and first-order dependence on ClAcOH (**Eq 6.3**).

$$Rate_{TFAH} = k_{cat}[Ph_2Phen^{2+}]^1[AH]^1[O_2]^1 \quad \textbf{Eq (6.1)}$$

$$Rate_{Cl3Ac} = k_{cat}[Ph_2Phen^{2+}]^1[AH]^1 \quad \textbf{Eq (6.2)}$$

$$Rate_{Cl2AcOH,ClAcOH} = k_{cat}[Ph_2Phen^{2+}]^{1/2}[AH]^1 \quad \textbf{Eq (6.3)}$$

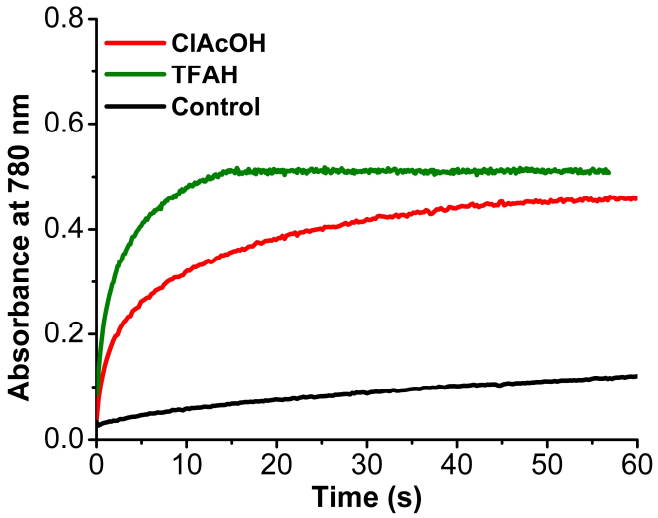

Figure 6.4. Change in absorbance at 780 nm over time as a result of the formation of $[Cp^*_2Fe]^+$ by ORR catalyzed by **Ph_2Phen^{2+}** with ClAcOH (red), TFAH (green), and TFAH control (black). Conditions: **Ph_2Phen^{2+}** = 40 μM, AH = 50 mM, O_2 = 4.05 mM, Cp^*_2Fe = 1 mM; control: TFAH = 50 mM, O_2 = 4.05 mM, Cp^*_2Fe = 1 mM.

A $Ti(O)SO_4$ colorimetric assay was used to determine the selectivity for the ORR by **Ph_2Phen^{2+}** with each acid, as previously reported.[10,11,31-34] It was found that the selectivity of **Ph_2Phen^{2+}** for H_2O_2 shows an apparent inverse dependence on acid activity, going from 93.2 ± 1.4 % selectivity with TFAH to 24.0 ± 6.2 % selectivity for H_2O_2 with ClAcOH (**Table 6.1**, **Figures S6.68-S6.72**) after all Cp^*_2Fe is consumed. H_2O_2 selectivity was evaluated over the course of the ORR with ClAcOH to determine if hydrogen peroxide reduction H_2O_2RR was a competing process (**Figures S6.67** and **S6.72**, **Table S6.6.4**). After 30 s there was an observed 67.4 ± 5.9 %

selectivity for H_2O_2, however, after 5 minutes H_2O_2 selectivity diminished to 22.0 ± 5.2 %. This suggests that H_2O_2 is being produced during catalysis before being further reduced to H_2O.

Analysis of H_2O_2RR with all acids under spectrochemical conditions showed slight activity (**Figures S6.49**, **S6.55**, **S6.61**, & **S6.67**), however, the difference in apparent activity between the apparent rates of the ORR and the H_2O_2RR was the smallest in the case of ClAcOH. It is also important to emphasize that all spectrochemical conditions are limited by the amount of reductant by experimental design, so that they can be run to completion without being limited in other substrate. Therefore, it is proposed that the apparent lower selectivity for H_2O_2 with the ClAcOH proton donor is the result of competitive H_2O_2 reduction while reductant is available; for stronger acids the chemical reductant is almost completely consumed by the relatively faster ORR process, given the greater difference in rate with H_2O_2RR. Consistent with this interpretation, stability tests showed that H_2O_2 was stable in the presence of **Ph_2Phen^{2+}** with each of the acids (**Figures S6.73-S6.76**), with quantitative recovery of added H_2O_2, verifying that reductant must be present for this reaction to occur.

Table 6.1. Summary of spectrochemical activity and selectivity of ORR by **Ph_2Phen^{2+}** with each proton donor.

Acid (pK_a(MeCN))	**k_{obs} (x 10^2 s^{-1})**	**% H_2O_2 Selectivity (n_{cat})**
TFAH (12.65)	173	93.2 ± 1.4 (2.14)
Cl_3AcOH (16.0)	115	84.8 ± 5.8 (2.30)
Cl_2AcOH (17.3)	1.06	82.3 ± 3.2 (2.35)
ClAcOH (20.3)	0.431	24.0 ± 6.2 (3.52)

6.4. Discussion

Scheme 6.1. Proposed Mechanism for the ORR catalyzed by **Ph_2Phen^{2+}**.

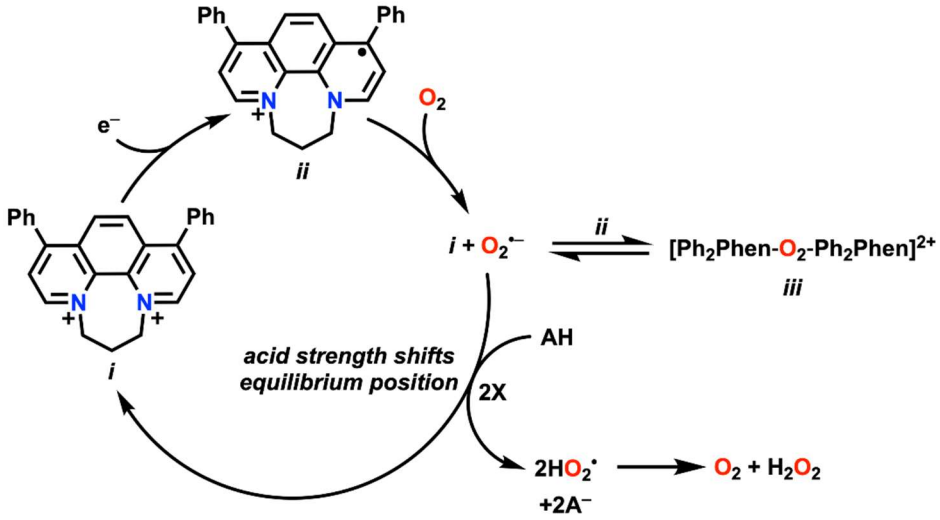

Based on both electrochemical and spectrochemical results, we are able to propose a catalytic cycle for the ORR by **Ph_2Phen^{2+}** with TFAH, Cl_3AcOH, Cl_2AcOH, and ClAcOH (**Scheme 6.1**). Starting from *i*, a single-electron reduction results in the formation of *ii*, which transfers an electron to O_2 via an outer-sphere mechanism to form superoxide ($O_2^{\bullet-}$) and reforms *i*. Based on previous reports on similar systems,[15,16,23] we propose that this system operates via an outer-sphere mechanism. The resulting $O_2^{\bullet-}$ can be protonated by acid to form two equiv of $HO_2^{\bullet}$, which is proposed to be the rate-determining step under spectrochemical conditions when Cl_3AcOH is used as a proton source. Then, two equiv of $HO_2^{\bullet}$ favorably disproportionate into O_2 and H_2O_2,[23] which is the rate-determining step under spectrochemical conditions when TFAH is used as the proton source. It has previously been established that TFAH is sufficiently acidic to protonate $O_2^{\bullet-}$,[23] which in this system renders $HO_2^{\bullet}$ as the resting state during catalysis and the subsequent disproportionation reaction rate-determining. However, with weaker acids formation of $O_2^{\bullet-}$ by *ii* becomes relatively more facile than its protonation, making superoxide protonation rate-limiting.

Based on the overall kinetic analysis, it is also proposed that an off-cycle bridging peroxo dimer species forms. Under electrochemical conditions, there is an excess of reduced **$Ph_2Phen^{\bullet+}$**

(*ii*) in the diffusion layer, which pushes the equilibrium towards dimer formation. This is supported by the observed half-order dependence on catalyst concentration under electrochemical conditions for all acids as well as the mixed-order dependence on O_2 concentration.[35,36] However, under spectrochemical conditions only the two weakest acids, Cl_2AcOH and ClAcOH, show a half-order dependence of activity on catalyst concentration. Unlike the reaction-diffusion layer of the electrode under electrochemical conditions, it would normally be expected that the relative concentration of the catalytically active **$Ph_2Phen^{\bullet+}$** would be diminished when using a chemical reductant, disfavoring dimer formation. However, these data show that the complete elimination of the off-cycle dimer species from kinetic relevance becomes dependent on acid strength under spectrochemical conditions, where sufficiently strong acids will drive the reaction pathway toward formation of $HO_2^{\bullet}$ more rapidly than dimerization can occur. Importantly, the observed first-order dependence on catalyst concentration for the stronger acids TFAH and Cl_3AcOH suggests that the dimeric species is not on the catalytic cycle, although there are potential parallels to the bridging mechanism of the dicarbenium catalyst reported by Gabbaï and co-workers.[17] Based on this, under conditions where there is a half-order dependence on catalyst concentration, the rate-determining step is assigned to protonation $O_2^{\bullet-}$ to form $HO_2^{\bullet}$, which is under the control of the dimer pre-equilibrium.

^{1}H-NMR studies of **Ph_2Phen^{2+}** in the presence of Cp^*_2Fe and O_2 demonstrated the appearance of a new species with a small amount of the precursor **Ph_2Phen^{2+}**, consistent with the proposal of an inner-sphere interaction during dimerization (**Figure S6.77**). When **$Ph_2Phen^{\bullet+}$** is exposed to O_2 and a slight excess TFAH, full conversion back to **Ph_2Phen^{2+}** is observed (**Figure S6.78**). However, with a slight excess ClAcOH as a proton source some **Ph_2Phen^{2+}** is recovered but there remains a mixture of products, suggesting that the weaker acid is not sufficiently strong enough to completely shift the proposed dimeric equilibrium involving a [**Ph_2Phen**-O_2-**Ph_2Phen**]$^{2+}$ species back into the catalytic cycle at low acid concentrations (**Figure S6.79**). These observations are consistent with the observed half-order concentration dependence on catalyst

when weaker acids are used as the proton donor under spectrochemical conditions. Under electrochemical conditions, a half-order concentration dependence on the diium is observed for all acids because of the greater concentration of the cationic radical species **$Ph_2Phen^{\bullet+}$** in the reaction-diffusion layer. However, proton donors with greater activity than ClAcOH are required to quantify H_2O_2 production by RRDE methods, since have sufficient driving force to the dimer equilibrium back towards the monomeric catalytic pathway.

In order to understand the relative thermodynamics of dimerization, computational studies were undertaken using the approach previously used for the iminium-based catalyst (See SI).[23] Using concentration-corrected thermochemistry, a reduction potential of –0.85 V vs Fc^+/Fc was estimated for **$Ph_2Phen^{2+/\bullet+}$**, in good agreement with the experimental value of –0.73 V. Outer-sphere electron transfer from **$Ph_2Phen^{\bullet+}$** to generate $O_2^{\bullet-}$ was uphill by 24.9 kcal/mol. Capture of $O_2^{\bullet-}$ at the 4-position of one of the pyridine subunits of a second equiv of **$Ph_2Phen^{\bullet+}$** to generate a bound peroxo was downhill by –10.1 kcal/mol. Subsequent binding of **Ph_2Phen^{2+}** to the peroxo group at the 4-position of a pyridine subunit to create a bridging dimer was further downhill by –28.6 kcal/mol (**Figure 6.5**). Having validated the thermodynamic viability of the dimer, an assessment of the disproportionation pathway was next evaluated. Previously, the protonation of $O_2^{\bullet-}$ by TFAH to generate $HO_2^{\bullet}$ had been assessed to be favorable by –33.2 kcal/mol by analogous computational methods, when homoconjugation was considered as a part of the thermochemistry.[23] The mechanistic data presented above suggested that this step should be less favorable with weaker acids. Indeed, comparable calculations using ClAcOH as the proton source found that the protonation of $O_2^{\bullet-}$ was favored by –25.7 kcal/mol, which was approximately 8 kcal/mol less favorable than with TFAH. The disproportionation reaction of two equiv of $HO_2^{\bullet}$ to generate one each of O_2 and H_2O_2 that closes the outer-sphere catalytic cycle was previously found to be downhill by –33.1 kcal/mol.[23]

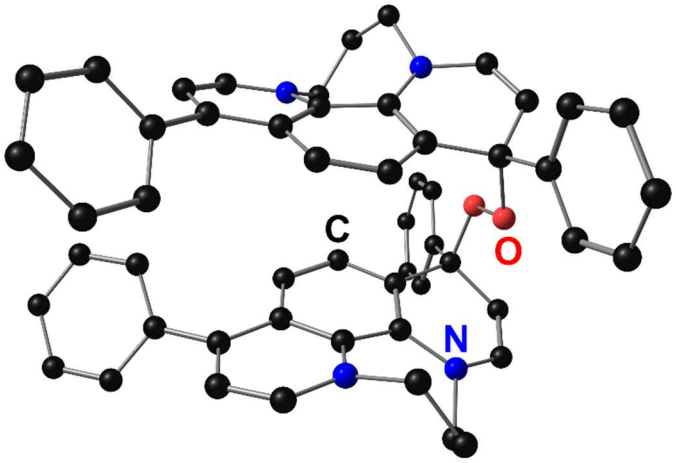

Figure 6.5. Proposed off-cycle dimer species implied by mechanistic data. A peroxo subunit bridges two equiv of **Ph_2Phen^{2+}** at the 4-position of a pyridine subunit. Gray = C, blue = N, red = O.

As described above, the low observed selectivity for H_2O_2 when ClAcOH is used as a proton donor can be explained by the relatively enhanced role of H_2O_2RR during the progress of ORR, which can consume some of the H_2O_2 produced by ORR. By comparison, for stronger acids, ORR is significantly more rapid than H_2O_2RR, minimizing its impact on the observed % H_2O_2 selectivity. ^{1}H-NMR studies of **$Ph_2Phen^{\bullet+}$** with added urea•H_2O_2 suggest an inner-sphere interaction with H_2O_2 in the presence of a chemical reductant. Again, **Ph_2Phen^{2+}** is reformed with a sufficiently strong acid, as was observed under analogous conditions with O_2 (**Figure S6.80**). Importantly, the loss of molecular symmetry in the NMR data imply that it is again the 4-position of a pyridyl subunit which forms an inner-sphere reaction. This suggests that there is a possibility of accessing selectivity for H_2O in future studies, with proper synthetic modification of the phenyl group appended here.

6.5. Conclusions

Here, a new organic-based catalyst for the ORR under both electrochemical and spectrochemical conditions is described. We found that the activity and mechanism of the ORR by **Ph_2Phen^{2+}** can be tuned by acid strength. Using acetic acid derivates with pK_a values ranging from 12.65 to 20.3, it was found that on off-cycle bridging peroxo dimer species formed in the

presence of O_2 and excess reduced catalyst, **$Ph_2Phen^{\bullet+}$**. Further, acid strength can tune the reaction mechanism: for the strongest acid, TFAH, the rate-limiting step becomes the disproportionation of 2 equiv of $HO_2^{\bullet}$ into one each of O_2 and H_2O_2. However, with the weakest acid Cl_3AcOH, the rate-determining step of the reaction is instead the protonation of $O_2^{\bullet-}$, which is inhibited by a favorable off-cycle dimerization pre-equilibrium. Excitingly, these data imply a comparable tunability of the ORR activity of metal-free electrocatalysts to that employed for transition metal-based systems. The implications of these mechanistic observations are currently being explored under additional reaction conditions and through the modification of the diium framework.

6.6. Supplementary Information for Chapter 6

General Considerations

All chemicals and solvents (ACS or HPLC grade) were commercially available and used as received unless otherwise indicated. For all air-sensitive reactions and electrochemical experiments, HPLC-grade solvents were obtained as anhydrous and air-free from a PPT Glass Contour Solvent Purification System. Gas cylinders were obtained from Praxair (Ar as 5.0; O2 as 4.0) and passed through activated molecular sieves prior to use. Gas mixing for variable concentration experiments was accomplished using a gas proportioning rotameter from Omega Engineering. UV-vis absorbance spectra were obtained on a Cary 60 from Agilent. An Anton-Parr Multiwave Pro SOLV, NXF-8 microwave reactor was used for microwave syntheses. The concentration of O_2 saturation in MeCN is reported to be 8.1 mM and the saturation concentration in MeCN with added electrolyte to be 6.3 mM. [37]

Synthesis and Characterization

Synthesis of 1,11-diphenyl-6,7-dihydro-5H-[1,4]diazepino[1,2,3,4-lmn][1,10]phenanthroline-4,8-diium bromide (**Ph_2Phen^{2+}**). In a round bottom flask, 4,7-diphenyl-1,10-phenanthroline (2.0 g, 6.0 mmol) was added to 20 mL of toluene. The solution was stirred and brought to 70°C. Once the

temperature was reached, 1,3-dibromopropane (2.8 mL, 28 mmol) was added. The solution was brought to reflux and allowed to stir overnight. The resulting bright orange solid was filtered, washed with hexanes, and recrystallized from hot dichloromethane to obtain 0.80 g (25% yield) of pure yellow-orange solid. ^{1}H-NMR (MeOD-d_4, 600 MHz Varian): δ 9.75 (d, 2H), 8.55 (d, 2H), 8.43 (s, 2H), 7.79 (m, 10H), 5.01 (t, 4H), 3.44 (quint, 2H). ^{13}C{^{1}H}-NMR (MeOD-d_4, 150 MHz Varian): δ 158.66, 149.77, 134.79, 134.27, 132.22, 131.09, 130.31, 129.23, 127.97, 126.90, 60.01, 30.81. Elemental analysis calculated for $C_{27}H_{22}Br_2N_2$•1/3CH_2Cl_2: C 58.35, H 4.06, N 4.98; Found: C 58.10, H 3.91, N 4.95.

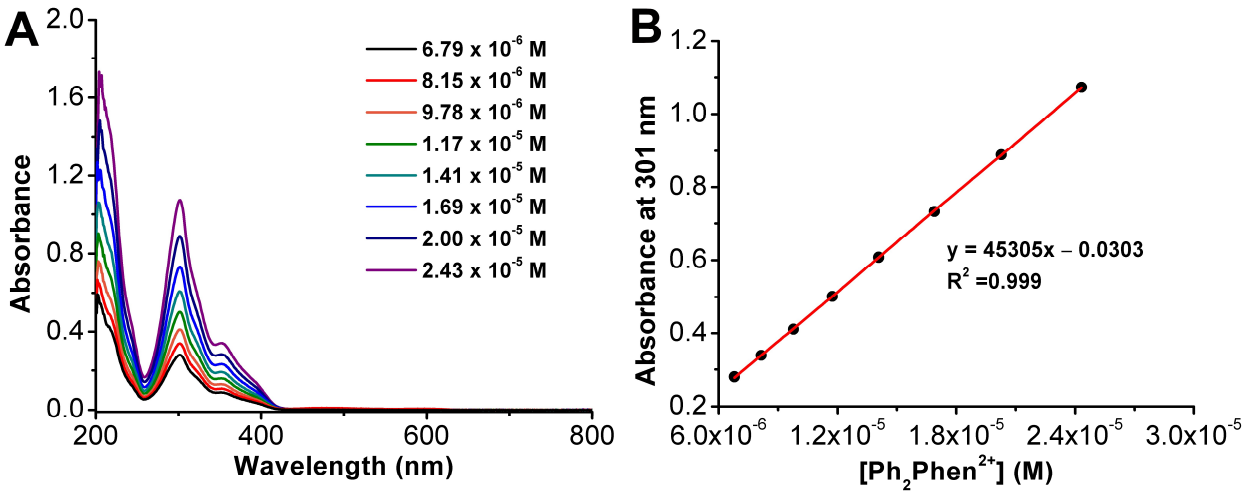

Figure S6.1. (A) UV-vis serial dilution absorbance data from **Ph_2Phen^{2+}** in MeCN solution. Conditions: varying concentration; quartz cell with 1 cm pathlength. (B) Plot of absorbance concentration (M) for **Ph_2Phen^{2+}** in MeCN solution at 301 nm (45305 M^{-1} cm^{-1}); R^2=0.999. All: λ_{max} = 351 nm (14411 $M^{-1}cm^{-1}$), 394 nm (5760 $M^{-1}cm^{-1}$).

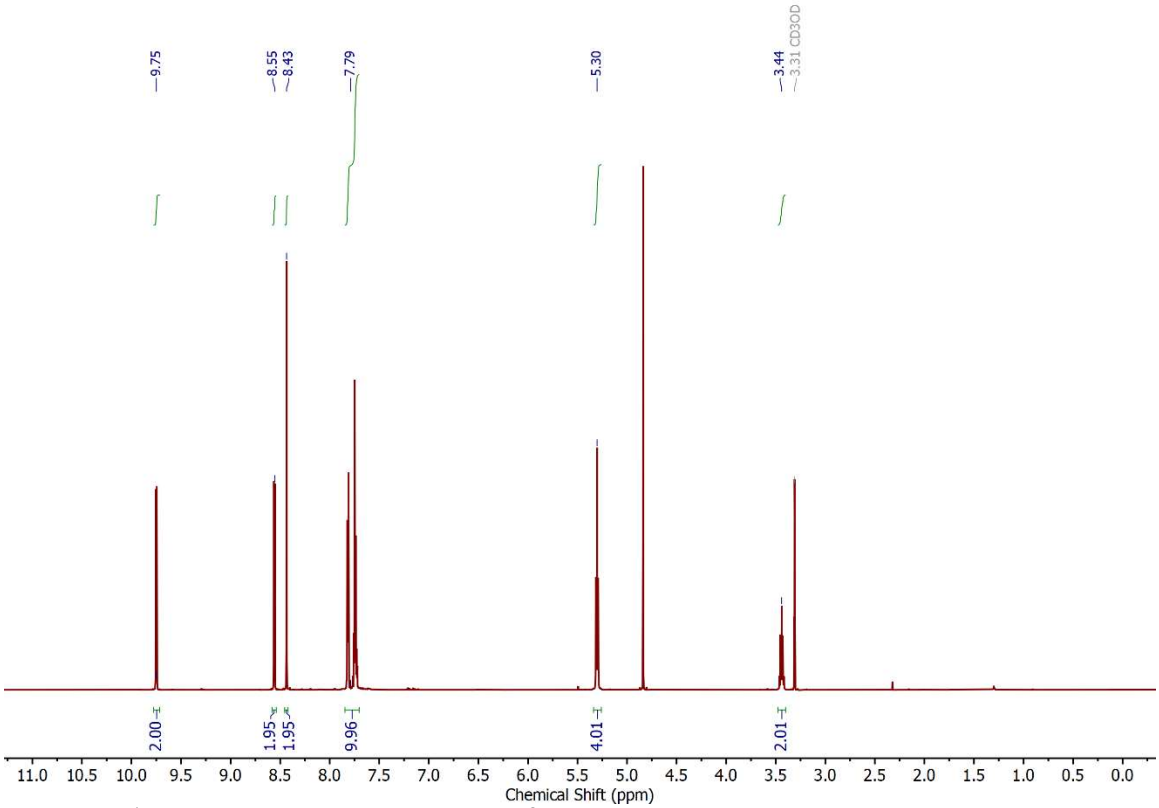

Figure S6.2. ^{1}H-NMR spectrum of **Ph_2Phen^{2+}** in MeOD-d_4; Varian 600 MHz.

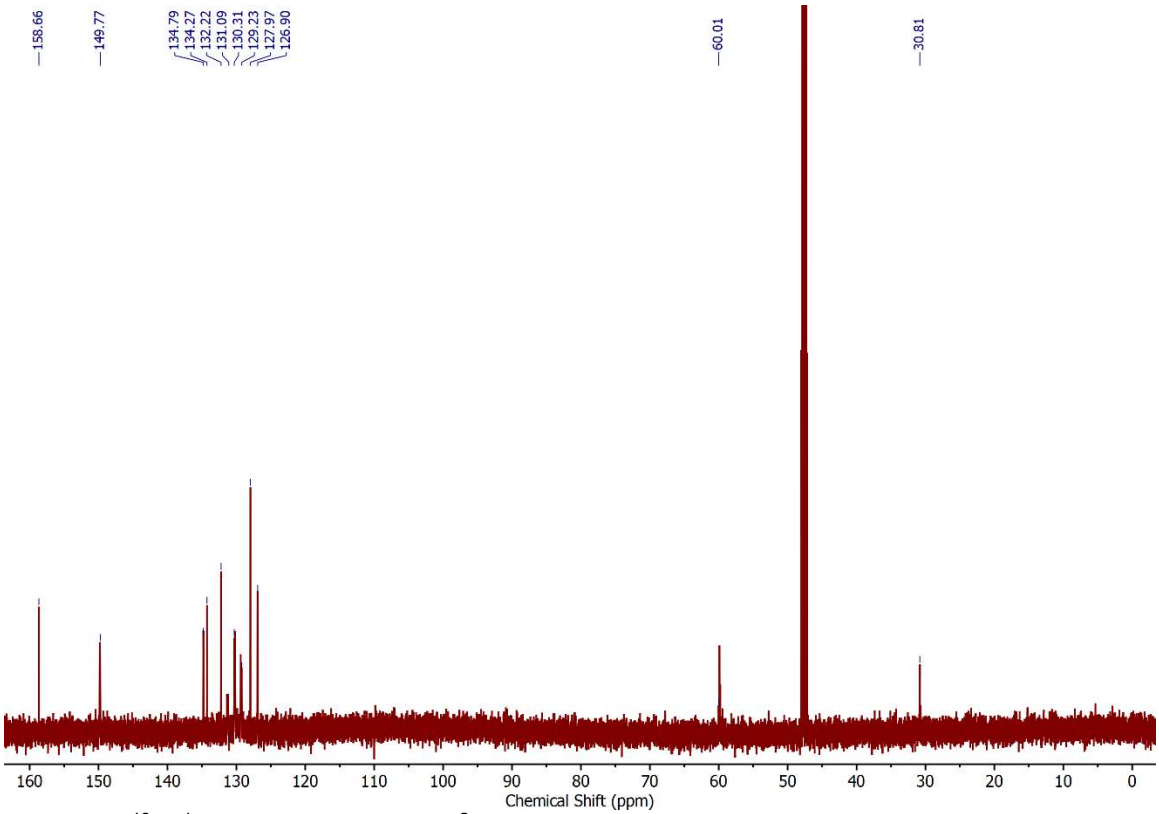

Figure S6.3. ^{13}C{^{1}H} NMR of **Ph_2Phen^{2+}** in MeOD-d_4; Varian 150 MHz.

Synthesis of 1,11-diphenyl-6,7-dihydro-5H-[1,4]diazepino[1,2,3,4-lmn][1,10]phenanthroline-4,8-diium hexafluorophosphate (**$Ph_2Phen(PF_6)_2$**). In a vial, 0.25 g (0.37 mmol) of the dibromide salt of **Ph_2Phen^{2+}** (0.25 g, 0.37 mmol) was dissolved in a minimal amount of methanol. A saturated solution of NH_4PF_6 (0.3 g, 1.86 mmol in minimal methanol) was passed through a syringe filter and added to the **Ph_2Phen^{2+}** solution. **$Ph_2Phen(PF_6)_2$** immediately precipitated out of solution. The light orange solid was filtered and rinsed with excess methanol to obtain pure product (0.15 g, 61% yield). Elemental analysis calculated for $C_{27}H_{22}N_2P_2F_{12}$: C 48.81, H 3.34, N 4.22; Found: C 48.05, H 3.23, N 4.13.

Estimation of pK_a Values for Cl_3AcOH, Cl_2AcOH, and ClAcOH in MeCN

The pK_as of Cl_3AcOH, Cl_2AcOH, and ClAcOH in MeCN were estimated from pK_a(H_2O) using a linear scaling relationship reported by Leito and coworkers, described in **Eq (S6.1)**.[29] Where (X–CO) is the number of carbonyl groups attached directly to the acidity center, nC is the number of C atoms in the molecule, and MW is the molecular weight.

$$pK_a(H_2O) = pK_a(MeCN) \times 0.55 - (X - CO) \times 2.2 + nC \times 0.13 + MW \times 0.0017 - 6.5 \qquad \textbf{(Eq S6.1)}$$

Table S6.1. Summary of calculated pK_a values in MeCN.

Acid	pK_a(H_2O)	X–CO	nC	MW (g/mol)	pK_a(MeCN)
Cl_3AcOH	0.65	1	2	163.38	16.0
Cl_2AcOH	1.29	1	2	128.94	17.3
ClAcOH	2.86	1	2	94.5	20.3

Electrochemical Analysis of Ph_2Phen^{2+}

Electrochemistry

Electroanalytical experiments were performed using Metrohm Autolab PGSTAT302N and BioLogic SP-50 potentiostats. RRDE experiments were performed using BioLogic VSP Bipotentiostat with a Pine Research MSR Rotator. Glassy carbon working (⌀ = 3 mm) and non-aqueous silver/silver chloride pseudoreference electrodes behind PTFE tips were obtained from CH Instruments. The pseudoreference electrodes were obtained by depositing chloride on bare silver wire in 10% HCl at oxidizing potentials and stored in a 0.1 M tetrabutylammonium

hexafluorophosphate solution in acetonitrile in the dark prior to use. The counter electrode was a glassy carbon rod (⌀ = 3 mm). All CV experiments were performed in a modified scintillation vial (20 mL volume) as a single-chamber cell with a cap modified with ports for all electrodes and a sparging needle. Tetrabutylammonium hexafluorophosphate ($TBAPF_6$) was purified by recrystallization from ethanol and dried in a vacuum oven before being stored in a desiccator. All data were referenced to an internal ferrocene standard (ferrocenium/ferrocene reduction potential under stated conditions) unless otherwise specified. All voltammograms were corrected for internal resistance. Ferrocene was purified by sublimation prior to use. In the event that the presence of electrochemical features precluded ferrocene addition, ferrocene was added to the electrochemical cell at the end of analysis for reference.

Rotating Ring-Disk Electrode Methods

Description of Au Ring Roughening Procedure. The Au ring electrode was roughened according to a previously reported method.[27] The electrodes were polished first on a felt polishing pad with 0.3 micron alumina, then with 0.05 micron alumina and rinsed with water and ethanol. Cyclic voltammograms were obtained in 0.5 M H_2SO_4 by scanning from 0 to 1.6 V vs. Ag/AgCl at 100 mV/s, then at 20 mV/s for an additional 2 cycles to obtain the pre-roughening, surface oxide reduction charge. The electrode was then pulsed between 2.4 and 0.2 V vs Ag/AgCl for 2.4 ms each and repeated for 250,000 cycles. Bubbles formed during electrolysis pulses were dislodged by contacting with a large bubble from a glass pipette. After electrolysis, the electrode was held at 0.3 V vs. Ag/AgCl for 2 minutes and the roughening was evaluated by CV.

Description of RRDE Collection Efficiency. The collection efficiency was determined as previously reported.[32,33,38] Conditions: Air saturation, 0.1 M $TBAPF_6$, 0.5 mM ferrocene in MeCN, glassy carbon disk electrode (5 mm), roughened Au ring electrode, glassy carbon rod counter electrode, Ag/AgCl pseudoreference electrode; scan rate 0.01 V/s. To calculate the collection efficiency of the RRDE, the ratio of the ring current (i_r) to the disk current (i_d) at each rotation rate was used to

determine $N_{empirical}$ (**Eq S2**). The $N_{empirical}$ value at each rotation rate was multiplied by a factor of 100 to determine the collection efficiency % at each rotation rate (~23%).

$$N_{empirical} = \frac{i_{ring\ corrected}}{i_{disk\ corrected}} \qquad \textbf{(Eq S2)}$$

RRDE Experiments. Conditions: Performed under Ar and air saturation conditions, 0.1 M $TBAPF_6$, 0.5 mM **Ph_2Phen^{2+}**, 0.1 M acid, glassy carbon disk electrode (5 mm diameter), roughened Au ring electrode, glassy carbon rod counter electrode, Ag/AgCl pseudoreference electrode; scan rate 0.01 V/s.

The solution was sparged with air until saturation was achieved. **Ph_2Phen^{2+}** (0.5 mM) was dissolved in MeCN and 0.1 M acid was added. A standard CV was taken of the solution to confirm the potential window to be used for the experiment. The roughened Au ring was set to +1.0 V. LSVs were obtained for various rotation rates between 600 and 2200 under the described conditions. In between each scan, the solution was sparged for 2 minutes. The reproducibility of scans was confirmed by repeating scans at the same rotation rate, producing exact overlays. The same procedure was repeated and the roughened Au ring was set to +1.2 V. The ring current (i_r) was corrected for by subtracting limiting current observed at the ring when it was set at +1.0 V.

The arithmetic mean of the number of electrons received by O_2 (n_{cat}) during the ORR was calculated from the disk current (i_d) and ring current (i_r) according to **Eq S3:** [39]

$$n_{cat} = 4 \times \frac{i_d}{i_d + \frac{i_r}{N_{empirical}}} \qquad \textbf{(Eq S3)}$$

The H_2O_2 ratio (p) is defined as the fraction of O_2 reduced to H_2O_2 and relates to n_{cat} by **Eq S4**:

$$n_{cat} = 4 - 2p \qquad \textbf{(Eq S4)}$$

Multiplying p by 100% provides the $\%H_2O_2$ selectivity of the ORR.

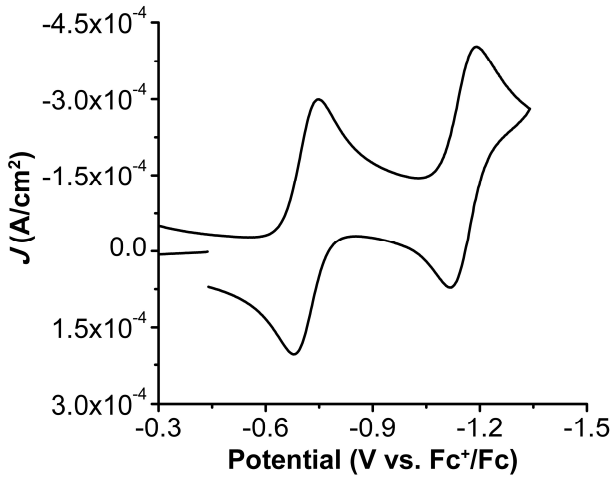

Figure S6.4. CV of **Ph_2Phen^{2+}** under Ar. Conditions: 1 mM **Ph_2Phen^{2+}**, 0.1 M $TBAPF_6$/MeCN; glassy carbon working electrode, glassy carbon rod counter electrode, Ag/AgCl pseudoreference electrode; referenced to Fc^+/Fc internal standard; 100 mV/s scan rate.

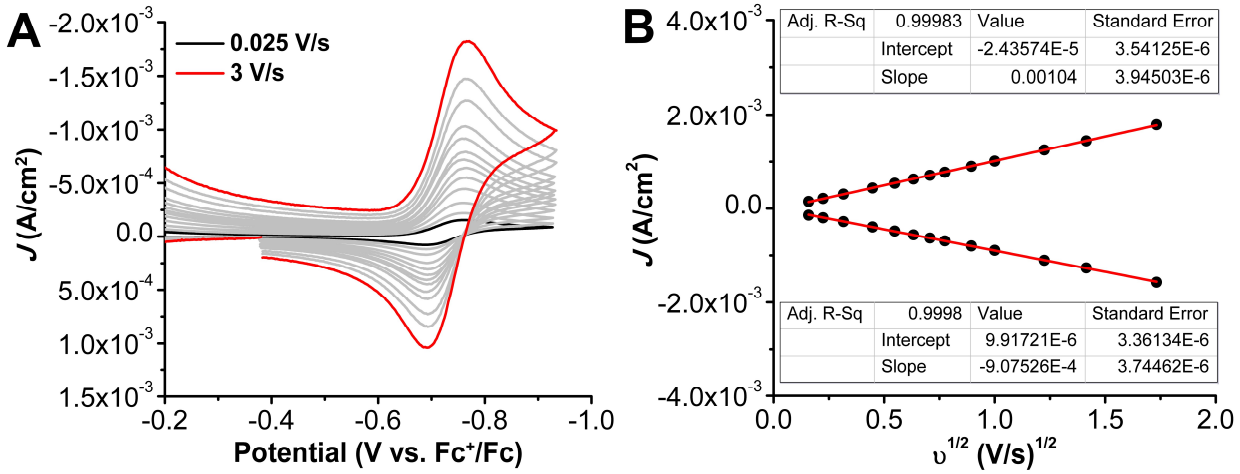

Figure S6.5. (A) CVs of **Ph_2Phen^{2+}** under Ar saturation at various scan rates. (B) Square root of scan rate versus current density in (A). Conditions: 1 mM **Ph_2Phen^{2+}**, 0.1 M $TBAPF_6$/MeCN; glassy carbon working electrode, glassy carbon rod counter electrode, Ag/AgCl pseudoreference electrode; referenced to an internal ferrocene standard; scan rates: 0.025, 0.05, 0.1, 0.2, 0.3, 0.4, 0.5, 0.6, 0.8, 1, 1.5, 2, 3 V/s.

The diffusion coefficient of **Ph_2Phen^{2+}** was calculated using the slope from **Figure S6.5B** and **Eq S5**, where i_p is the current (A), n is the number of electrons, A is the area of the electrode (cm^2), C is the concentration (mol/cm^2), v is the scan rate (V/s), and D is the diffusion coefficient (cm^2/s).

$$i_p = (2.69 \times 10^5) n^{\frac{3}{2}} A C D^{\frac{1}{2}} v^{\frac{1}{2}} \qquad \textbf{Eq S6.5}$$

$$D = \frac{(slope)^2}{n^3 C^2 (2.69 \times 10^5)^2}$$

$$D = 1.14 \times 10^{-5}\ cm^2 \cdot s^{-1}$$

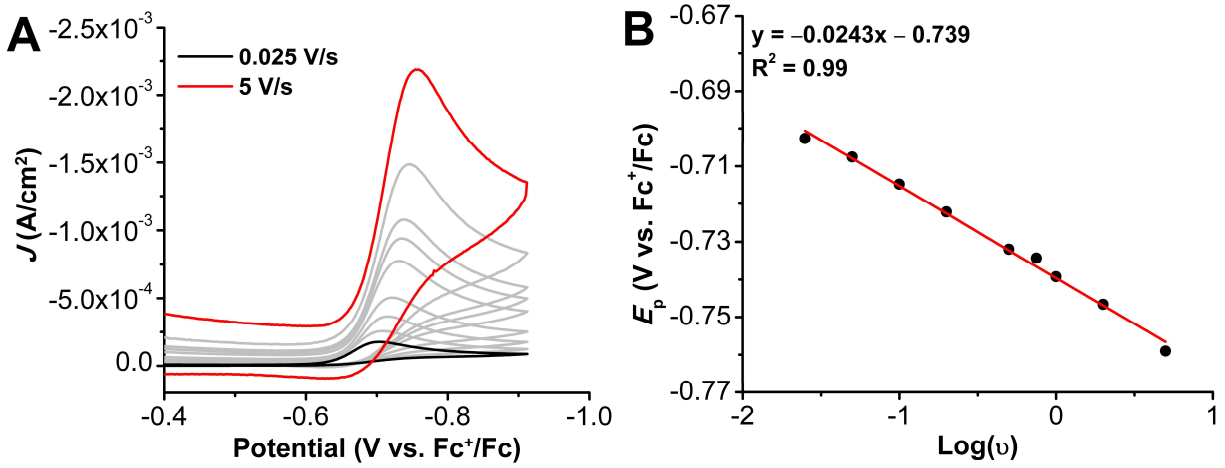

Figure S6.6. (A) CVs of **Ph_2Phen^{2+}** under O_2 saturation at various scan rates. (B) Logarithm of the scan rate versus the reduction peak potential in (A). Conditions: 1 mM **Ph_2Phen^{2+}**, 0.1 M $TBAPF_6$/MeCN; glassy carbon working electrode, glassy carbon rod counter electrode, Ag/AgCl pseudoreference electrode; referenced to an internal ferrocene standard; scan rates: 0.025, 0.05, 0.1, 0.2, 0.3, 0.4, 0.5, 0.6, 0.8, 1, 1.5, 2, 3, 4, 5 V/s.

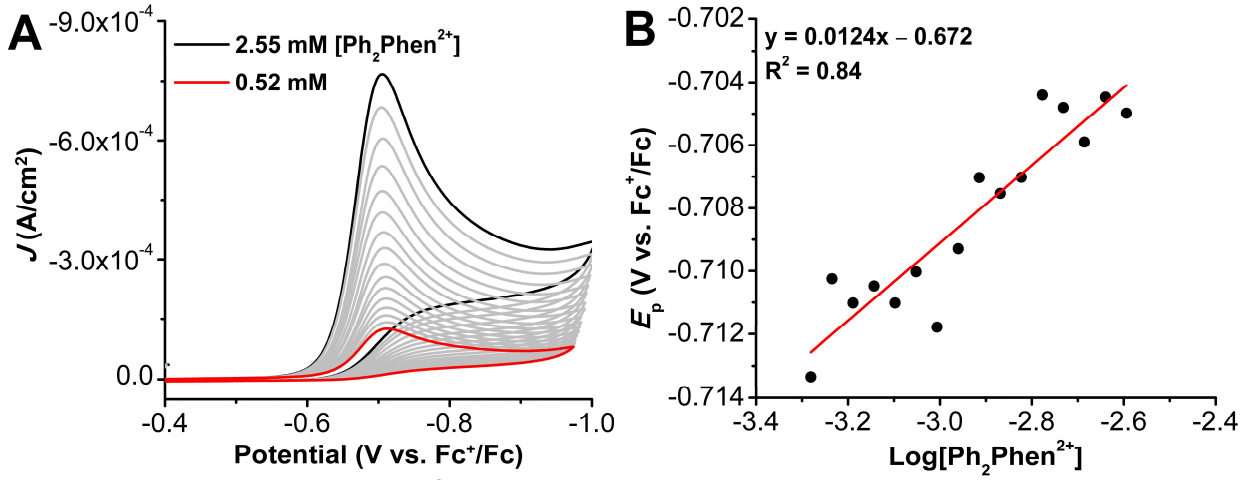

Figure S6.7. (A) CVs of **Ph_2Phen^{2+}** under O_2 saturation at varying concentrations. (B) Logarithm of **Ph_2Phen^{2+}** concentration versus the reduction peak potential in (A). Conditions: varying **Ph_2Phen^{2+}** concentration, 0.1 M $TBAPF_6$/MeCN; glassy carbon working electrode, glassy carbon rod counter electrode, Ag/AgCl pseudoreference electrode; referenced to an internal ferrocene standard; 100 mV/s scan rate. [**Ph_2Phen^{2+}**]: 2.55, 2.23, 2.06, 1.86, 1.67, 1.50, 1.35, 1.22, 1.10, 0.986, 0.888, 0.799, 0.719, 0.647, 0.582, 0.524 mM

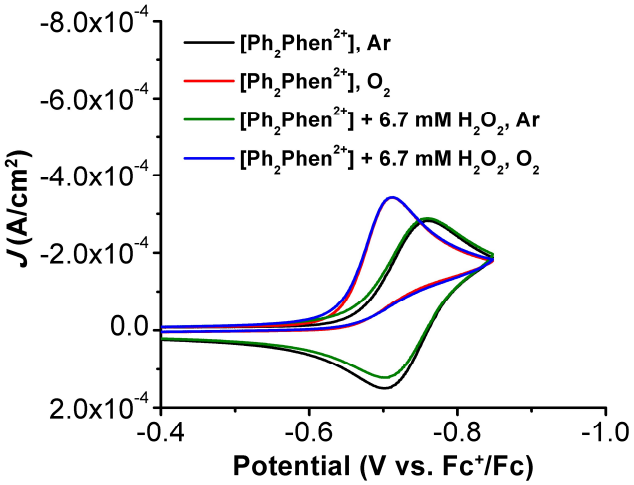

Figure S6.8. CVs of Ph_2Phen^{2+} with and without added 6.7 mM urea•H_2O_2 under Ar and O_2 saturation. Conditions: 1 mM **Ph_2Phen^{2+}**, 0.1 M $TBAPF_6$/MeCN; 100 mV/s; glassy carbon working electrode, glassy carbon counter electrode, Ag/AgCl pseudoreference electrode; referenced to an internal ferrocene standard.

Electrochemical Analysis with TFAH

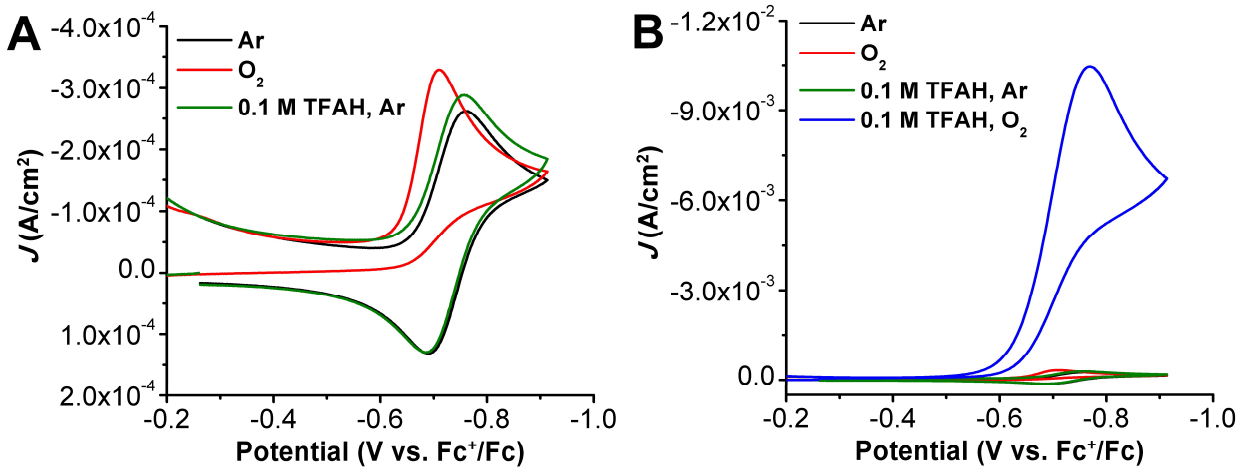

Figure S6.9. (A) CVs of **Ph_2Phen^{2+}** under Ar (black), O_2 (red) and with 0.1 M TFAH under Ar saturation (green). (B) CVs from A and catalytic trace shown (blue) with Ph_2Phen^{2+} and 0.1 M TFAH under O_2 saturation. Conditions: 1 mM **Ph_2Phen^{2+}**, 0.1 M $TBAPF_6$/MeCN; glassy carbon working electrode, glassy carbon rod counter electrode, Ag/AgCl pseudoreference electrode; referenced to an internal ferrocene standard; 100 mV/s scan rate.

*Determination of Effective Overpotential of **Ph_2Phen^{2+}** with TFAH*

Utilizing the pK_a (12.65) and log(K_{AHA}) (3.9) values for TFAH in MeCN, we have corrected the reported standard reduction potentials for ORR using **Eqs S6 & S7**.

$$E^0_{O2/H2O} = 1.21 - 0.0592pK_a + \frac{2.30RT}{4F}\log(4K_{AHA})\ V\ vs.\ Fc^+/Fc \qquad \textbf{Eq (S6)}$$

$$E^0_{O2/H2O}(MeCN, TFAH) = \ 0.42\ V\ vs.\ Fc^+/Fc$$

$$E^0_{O2/H2O2} = 0.68 - 0.0592pK_a + \frac{2.30RT}{2F}\log(2K_{AHA})\ V\ vs.\ Fc^+/Fc \qquad \textbf{Eq (S7)}$$

$$E^0_{O2/H2O2}(MeCN, TFAH) = \ +0.06\ V\ vs.\ Fc^+/Fc$$

where R is the ideal gas law (8.314 J·K^{-1}·mol^{-1}); T is the temperature (298 K); F is Faraday's constant (96485 C·mol^{-1}); K_{AHA} is the reported homoconjugation equilibrium constant for TFAH in MeCN (log K_{AHA} = 3.9). The effective overpotential was calculated according to **Eqs S6.8 & S6.9**. Where E_{app} is the $E_{1/2}$ of Ph_2Phen^{2+} with 0.1 M TFAH (**Figure S6.9**).

$$\eta = \ \left|E_{app} - E^0_{O2/H2O}\right| = |-0.72 - 0.42| = 1.14\ V \qquad \textbf{Eq (S6.8)}$$

$$\eta = \ \left|E_{app} - E^0_{O2/H2O2}\right| = |-0.72 - 0.06| = 0.78\ V \qquad \textbf{Eq (S6.9)}$$

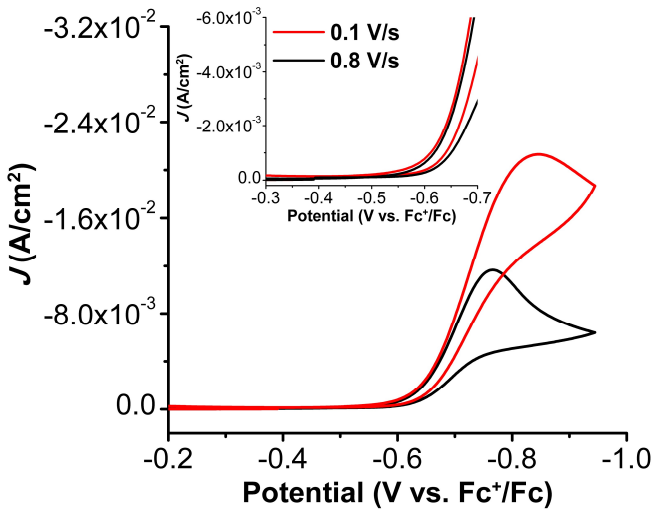

Figure S6.10. CVs of **Ph_2Phen^{2+}** under catalytic conditions with 0.13 M TFAH at 0.1 V/s (black) and 0.8 V/s (red). Conditions: 1 mM **Ph_2Phen^{2+}**, 0.13 M TFAH, 0.1 M $TBAPF_6$/MeCN; glassy carbon working electrode, glassy carbon rod counter electrode, Ag/AgCl pseudoreference electrode; referenced to an internal ferrocene standard.

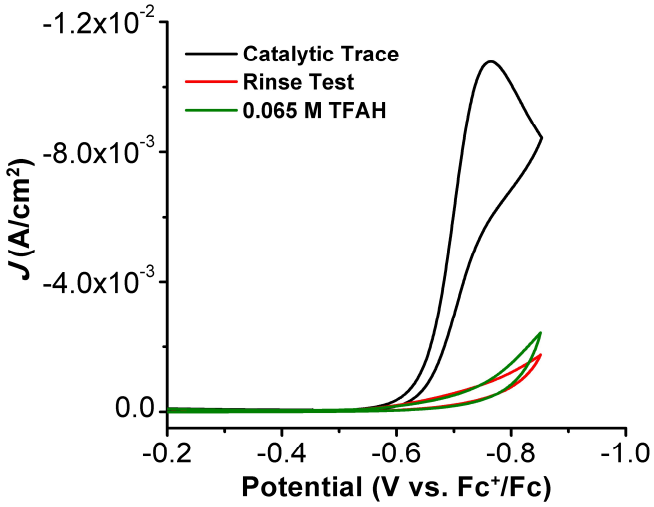

Figure S6.11. Rinse test of **Ph_2Phen^{2+}** and TFAH. Ph2Phen2+ under catalytic conditions (black trace), rinse test (red trace), and CV of TFAH under O_2 saturation (green trace). Conditions: 1 mM **Ph_2Phen^{2+}**, 0.12 M Cl_3AcOH, 0.1 M $TBAPF_6$/MeCN, O_2 saturation; 100 mV/s; glassy carbon working electrode, glassy carbon counter electrode, Ag/AgCl pseudoreference electrode; referenced to an internal ferrocene standard.

To establish mechanistic information under electrochemical conditions, variable concentration studies were performed, analysis was adapted from Sathrum and Kubiak *J. Phys. Chem. Lett.* **2011**, *2*, 2372.[30] Where, *F* is Faraday's constant, *A* is the electrode area, [Q] is the substrate concentration, k_{cat} is the catalytic rate, *D* is the diffusion constant of the catalyst, [cat] is the concentration of the catalyst and n_{cat} is the number of electrons in the catalytic process.

$$i_{cat} = n_{cat}FA[cat](Dk_{cat}[Q]^{y})^{1/2}$$

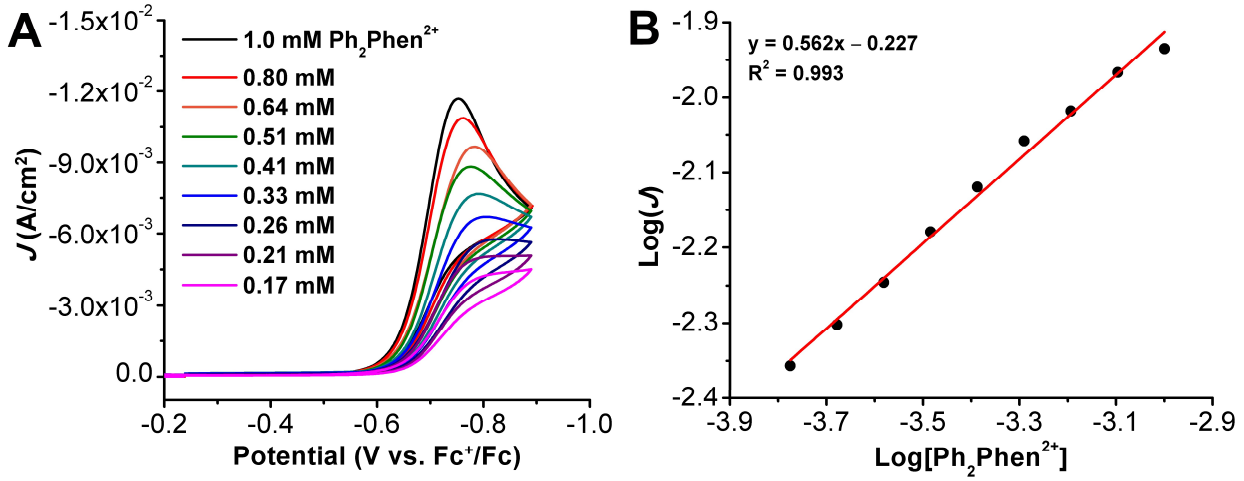

Figure S6.12. (A) CVs of **Ph_2Phen^{2+}** under catalytic conditions with variable **Ph_2Phen^{2+}** concentrations. (B) Logarithm of **Ph_2Phen^{2+}** concentration versus the logarithm of current density from (A). Conditions: 0.1 M TFAH, 0.1 M $TBAPF_6$/MeCN; 100 mV/s; glassy carbon working electrode, glassy carbon counter electrode, Ag/AgCl pseudoreference electrode; referenced to an internal ferrocene standard.

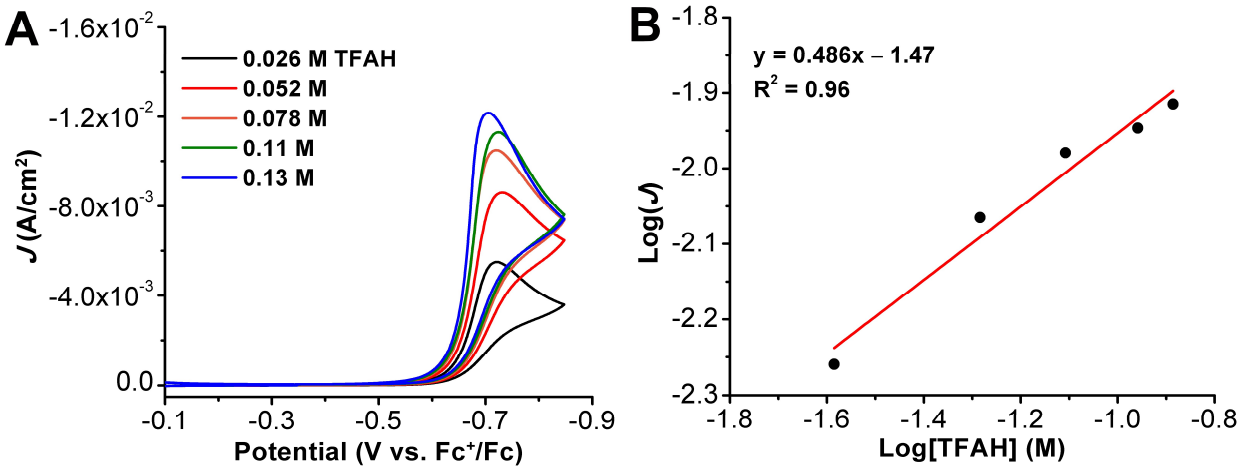

Figure S6.13. (A) CVs of **Ph_2Phen^{2+}** under catalytic conditions with variable TFAH concentrations. (B) Logarithm of TFAH concentration versus the logarithm of current density from (A). Conditions: 1 mM **Ph_2Phen^{2+}**, 0.1 M $TBAPF_6$/MeCN, O_2 saturation; 100 mV/s; glassy carbon working electrode, glassy carbon counter electrode, Ag/AgCl pseudoreference electrode; referenced to an internal ferrocene standard.

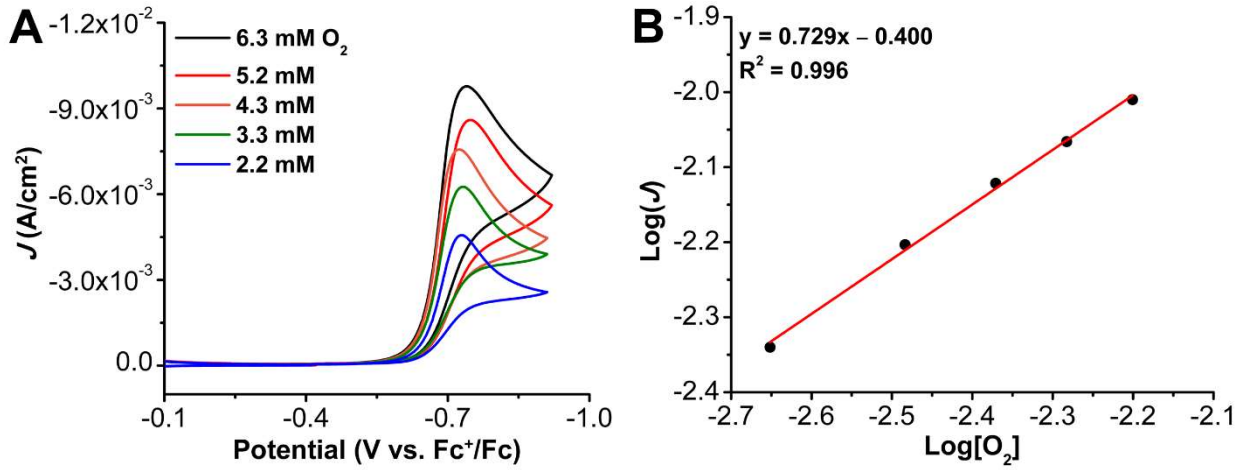

Figure S6.14. (A) CVs of **Ph_2Phen^{2+}** under catalytic conditions with variable O_2 concentrations. (B) Logarithm of O_2 concentration versus the logarithm of current density from (A). Conditions: 1 mM **Ph_2Phen^{2+}**, 0.1 M TFAH, 0.1 M $TBAPF_6$/MeCN; 100 mV/s; glassy carbon working electrode, glassy carbon counter electrode, Ag/AgCl pseudoreference electrode; referenced to an internal ferrocene standard.

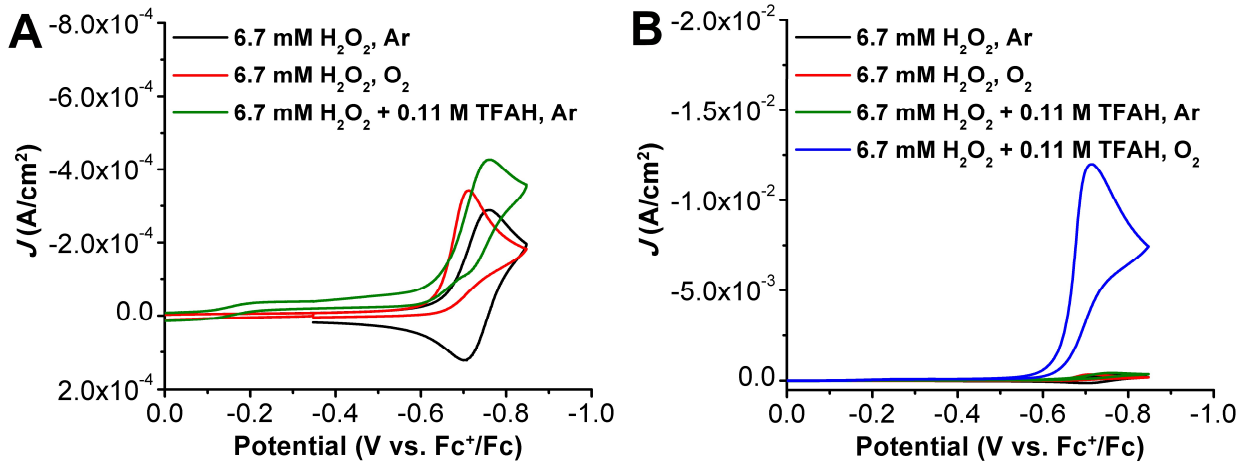

Figure S6.15. (A) CVs of **Ph_2Phen^{2+}** in the presence of 6.7 mM urea•H_2O_2 under Ar and O_2 saturation with added 0.11 M TFAH. (B) CVs of **Ph_2Phen^{2+}** in the presence of 6.7 mM urea•H_2O_2 with added 0.11 M TFAH under O_2 saturation. Conditions: 1 mM **Ph_2Phen^{2+}**, 0.11 M TFAH, 0.1 M TBAPF6/MeCN; 100 mV/s; glassy carbon working electrode, glassy carbon counter electrode, Ag/AgCl pseudoreference electrode; referenced to an internal ferrocene standard.

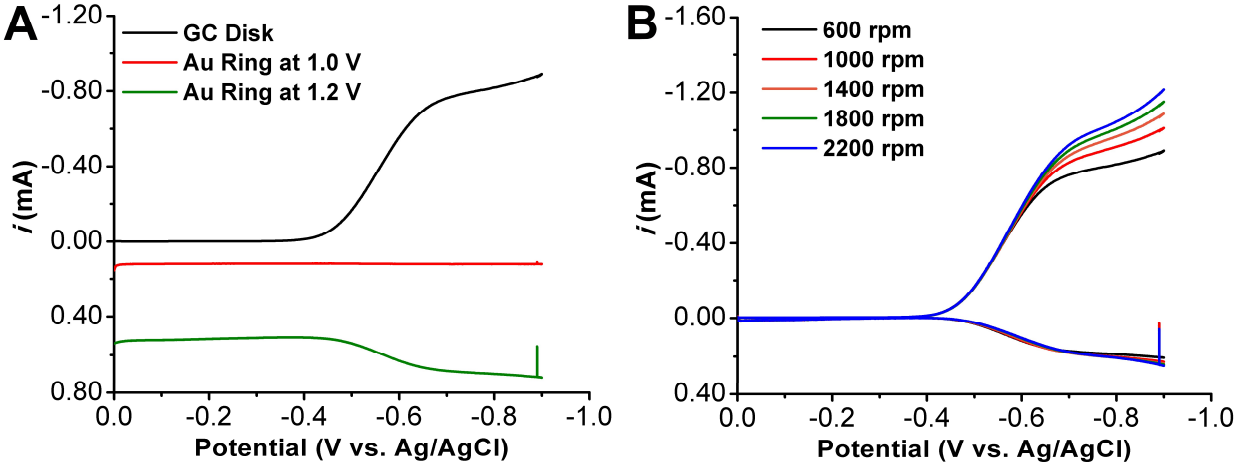

Figure S6.16. Linear sweep voltammograms of RRDE experiment with 0.5 mM **Ph_2Phen^{2+}** and 0.1 M TFAH under air saturation conditions. (A) Uncorrected LSVs at 600 rpm. (B) Corrected LSVs at various rotation rates used for quantification of %H_2O_2. Ring potential = 1.0 or 1.2 V vs Ag/AgCl. Conditions: 0.5 mM **Ph_2Phen^{2+}**, 0.1 M TFAH, 0.1 M TBAPF$_6$/MeCN; glassy carbon working electrode/roughened Au ring working electrode, glassy carbon counter electrode, Ag/AgCl pseudoreference electrode; scan rate 0.01 V/s.

Calculated ORR selectivity under electrochemical conditions using RRDE is 97.3 ± 2.6% H_2O_2.

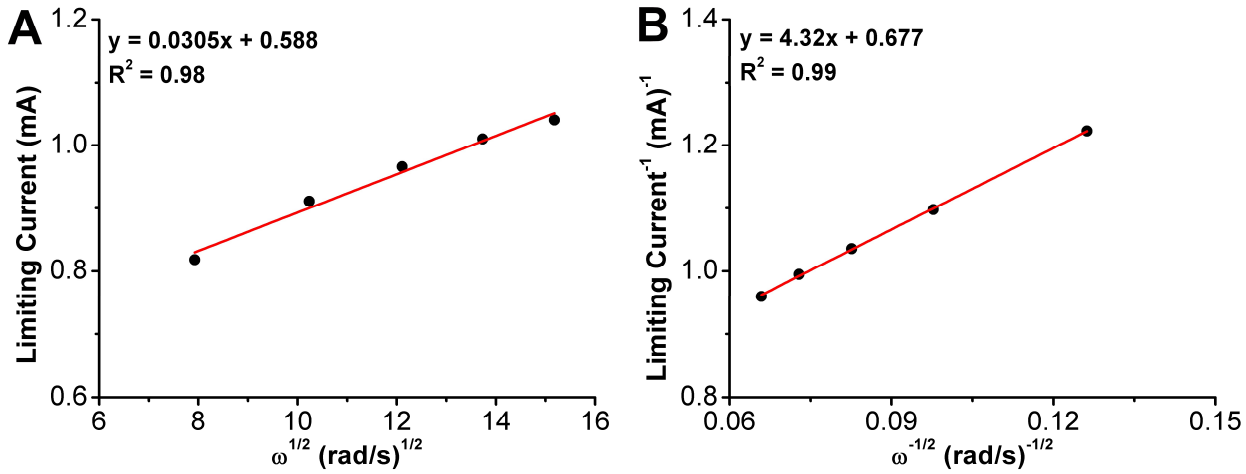

Figure S6.17. (A) Levich and (B) Koutecky-Levich plots from data obtained from linear sweep voltammograms of **Ph_2Phen^{2+}** (0.5 mM) by RRDE with 0.1 M TFAH under air saturation conditions at various rotation rates (600, 1000, 1400, 1800, & 2200 rpm).

Electrochemical Analysis with Cl_3AcOH

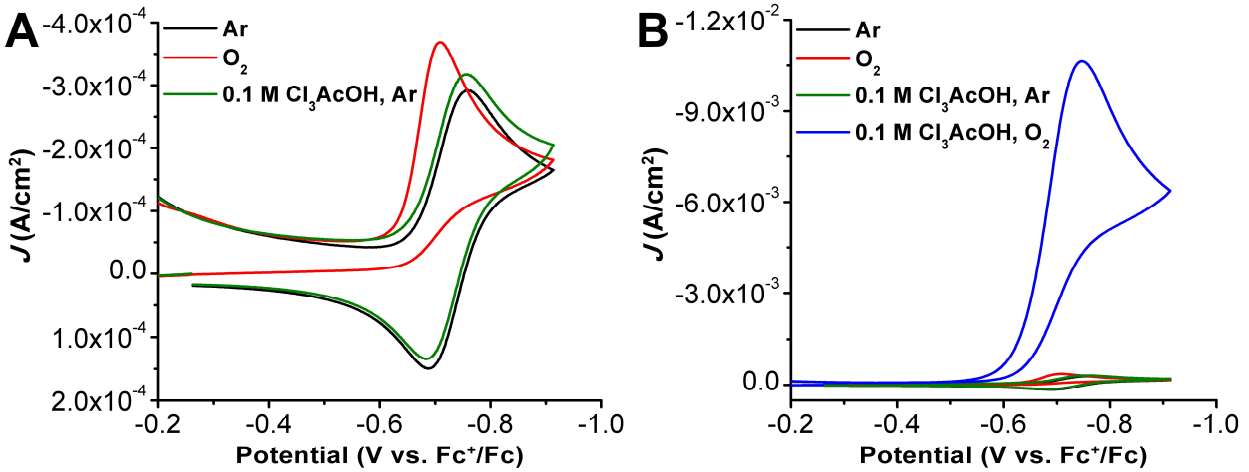

Figure S6.18. (A) CVs of **Ph_2Phen^{2+}** under Ar (black), O_2 (red) and with 0.1 M Cl_3AcOH under Ar saturation (green). (B) CVs from A and catalytic trace shown (blue) with **Ph_2Phen^{2+}** and 0.1 M Cl_3AcOH under O_2 saturation. Conditions: 1 mM **Ph_2Phen^{2+}**, 0.1 M $TBAPF_6$/MeCN; 100 mV/s; glassy carbon working electrode, glassy carbon rod counter electrode, Ag/AgCl pseudoreference electrode; referenced to an internal ferrocene standard.

Determination of Effective Overpotential of ***Ph₂Phen²⁺*** *with Cl_3AcOH*

Utilizing the estimated pK_a of Cl_3AcOH (16.0) in MeCN, we can determine the effective overpotential according to **Eqs S6.10-S6.13**. Where E_{app} is the $E_{1/2}$ of **Ph₂Phen²⁺** with 0.1 M Cl_3AcOH (**Figure S6.18**). We are unaware of a homoconjugation constant for further correction.

$$E^0_{O2/H2O} = 1.21 - 0.0592pK_a \qquad \textbf{Eq (S6.10)}$$

$$E^0_{O2/H2O}(MeCN, Cl_3AcOH) = \ 0.26\ V\ vs.\ Fc^+/Fc$$

$$\eta = \ \left|E_{app} - E^0_{O2/H2O}\right| = |-0.72 - 0.26| = 0.98\ V \qquad \textbf{Eq (S6.11)}$$

$$E^0_{O2/H2O2} = 0.695 - 0.0592pK_a \qquad \textbf{Eq (S6.12)}$$

$$E^0_{O2/H2O2}(MeCN, Cl_3AcOH) = \ -0.25\ V\ vs.\ Fc^+/Fc$$

$$\eta = \ \left|E_{app} - E^0_{O2/H2O2}\right| = |-0.72 - 0.25| = 0.47\ V \qquad \textbf{Eq (S6.13)}$$

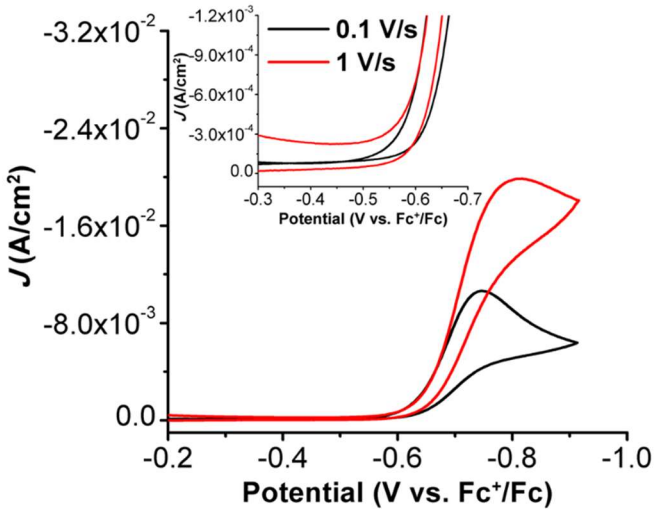

Figure S6.19. CVs of **Ph₂Phen²⁺** under catalytic conditions with 0.1 M Cl_3AcOH at 0.1 V/s (black) and 1 V/s (red). Conditions: 1 mM **Ph₂Phen²⁺**, 0.1 M Cl_3AcOH, 0.1 M $TBAPF_6$/MeCN; 100 mV/s; glassy carbon working electrode, glassy carbon rod counter electrode, Ag/AgCl pseudoreference electrode; referenced to an internal ferrocene standard.

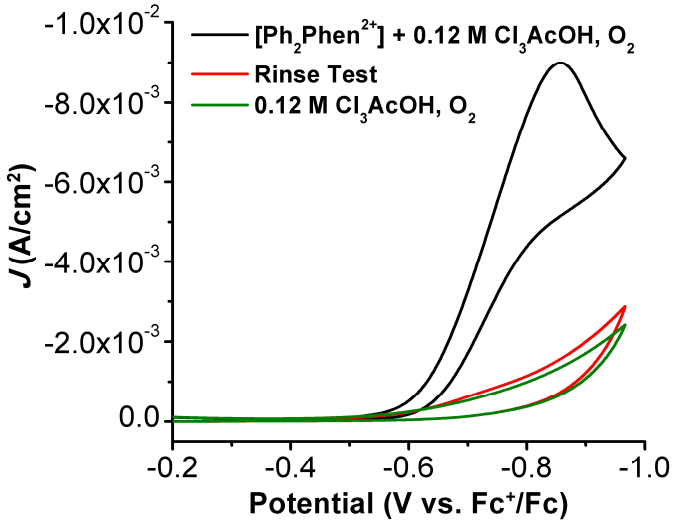

Figure S6.20. Rinse test of **Ph_2Phen^{2+}** and Cl_3AcOH. **Ph_2Phen^{2+}** under catalytic conditions (black trace), rinse test (red trace), and CV of Cl_3AcOH under O_2 saturation (green trace). Conditions: 1 mM **Ph_2Phen^{2+}**, 0.12 M Cl_3AcOH, 0.1 M $TBAPF_6$/MeCN, O_2 saturation; 100 mV/s; glassy carbon working electrode, glassy carbon counter electrode, Ag/AgCl pseudoreference electrode; referenced to an internal ferrocene standard.

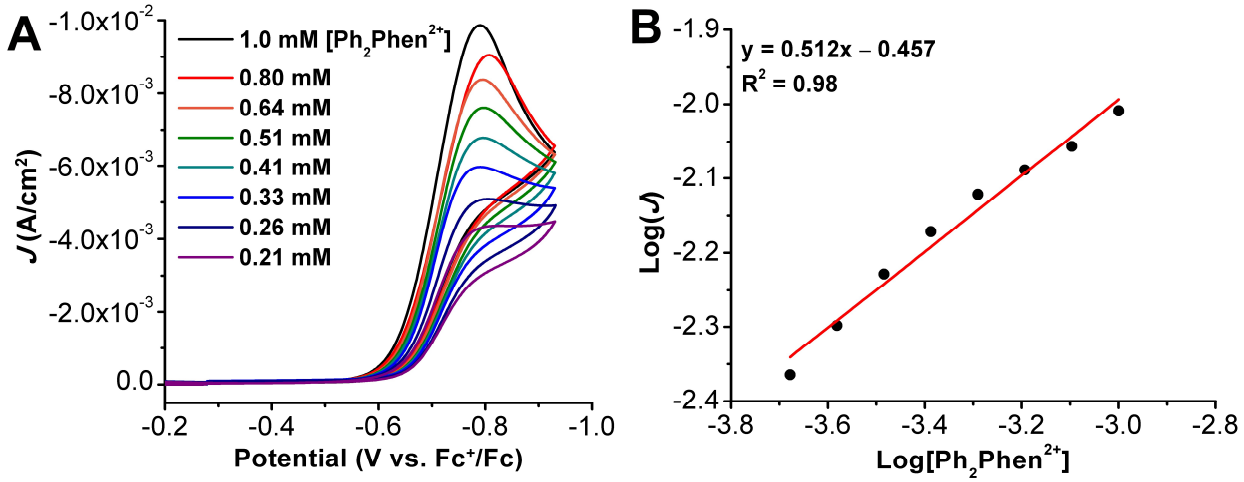

Figure S6.21. (A) CVs of **Ph_2Phen^{2+}** under catalytic conditions with variable **Ph_2Phen^{2+}** concentrations. (B) Logarithm of **Ph_2Phen^{2+}** concentration versus the logarithm of current density from (A). Conditions: 0.1 M Cl_3AcOH 0.1 M Cl_3AcOH, 0.1 M $TBAPF_6$/MeCN; 100 mV/s; glassy carbon working electrode, glassy carbon rod counter electrode, Ag/AgCl pseudoreference electrode; referenced to an internal ferrocene standard.

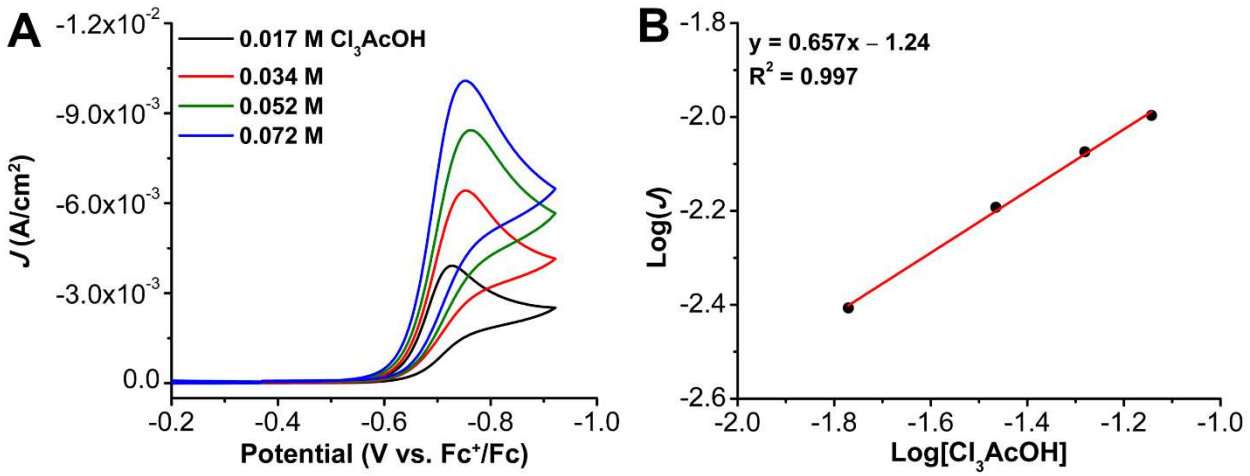

Figure S6.22. CVs of **Ph_2Phen^{2+}** under catalytic conditions with variable Cl_3AcOH concentrations. Conditions: 1 mM **Ph_2Phen^{2+}**, 0.1 M $TBAPF_6$/MeCN, O_2 saturation; 100 mV/s; glassy carbon working electrode, glassy carbon counter electrode, Ag/AgCl pseudoreference electrode; referenced to an internal ferrocene standard.

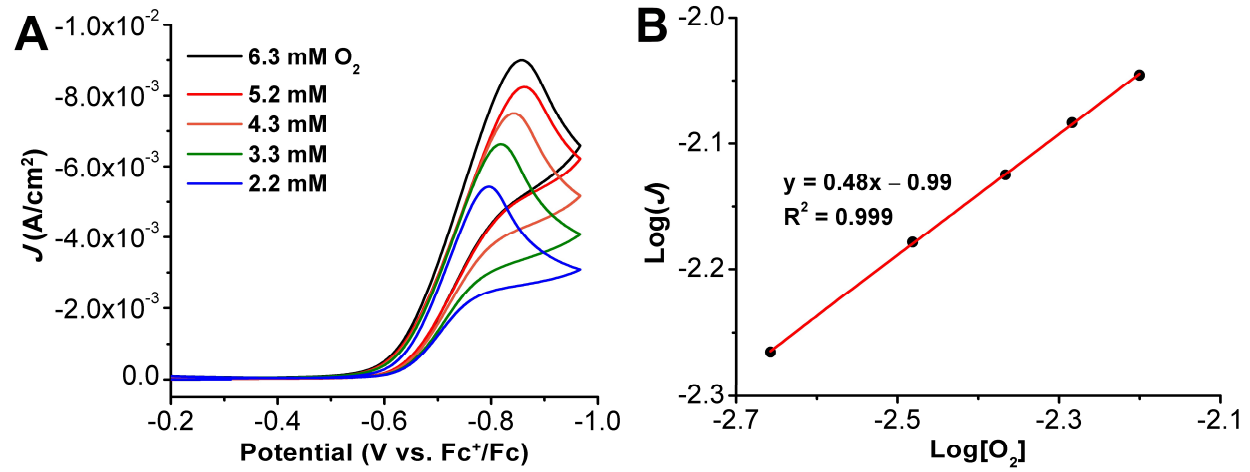

Figure S6.23. (A) CVs of **Ph_2Phen^{2+}** under catalytic conditions with variable O_2 concentrations. (B) Logarithm of O_2 concentration versus the logarithm of current density from (A). Conditions: 1 mM **Ph_2Phen^{2+}**, 0.12 M Cl_3AcOH, 0.1 M $TBAPF_6$/MeCN; 100 mV/s; glassy carbon working electrode, glassy carbon counter electrode, Ag/AgCl pseudoreference electrode; referenced to an internal ferrocene standard.

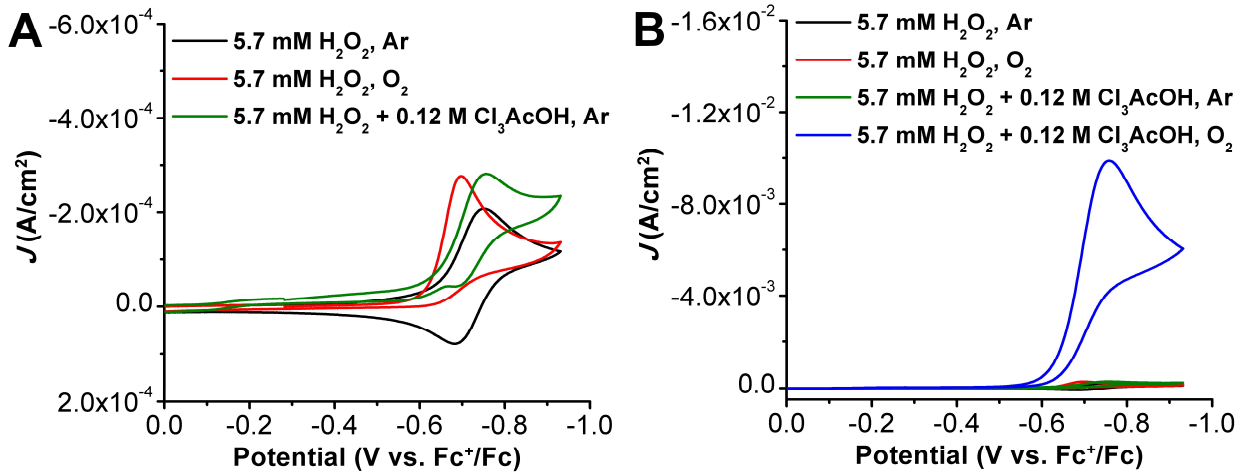

Figure S6.24. (A) CVs of **Ph_2Phen^{2+}** in the presence of 5.7 mM urea•H_2O_2 under Ar and O_2 saturation with added 0.12 M Cl_3AcOH. (B) CVs of **Ph_2Phen^{2+}** in the presence of 5.7 mM urea•H_2O_2 with added 0.12 M Cl_3AcOH under O_2 saturation. Conditions: 1 mM **Ph_2Phen^{2+}**, 0.12 M Cl_3AcOH, 0.1 M $TBAPF_6$/MeCN; 100 mV/s; glassy carbon working electrode, glassy carbon counter electrode, Ag/AgCl pseudoreference electrode; referenced to an external ferrocene standard.

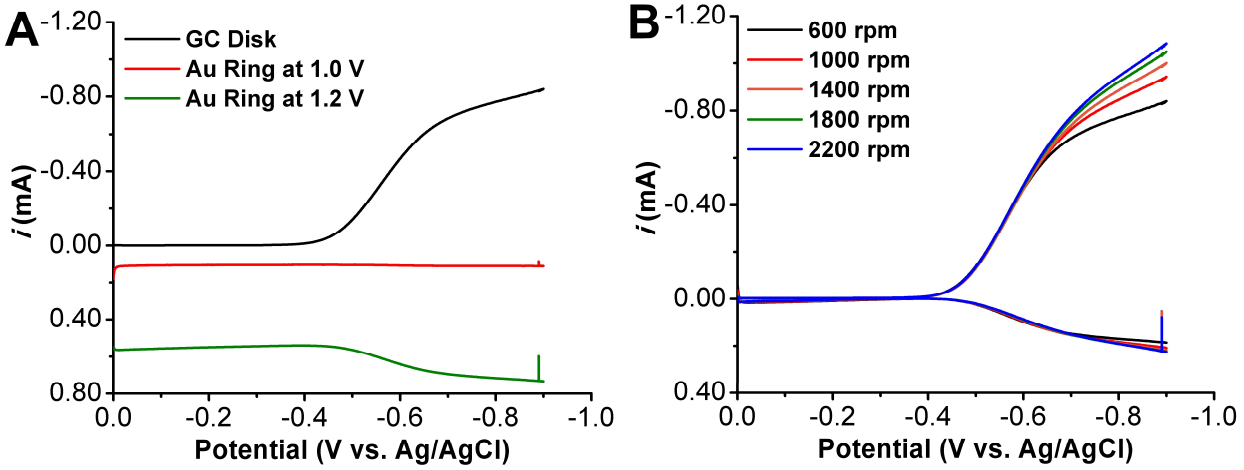

Figure S6.25. Linear sweep voltammograms of RRDE experiment with 0.5 mM **Ph_2Phen^{2+}** and 0.1 M Cl_3AcOH under air saturation conditions. (A) Uncorrected LSVs at 600 rpm. (B) Corrected LSVs at various rotation rates used for quantification of %H_2O_2. Ring potential = 1.0 or 1.2 V vs Ag/AgCl. Conditions: 0.5 mM Ph_2Phen^{2+}, 0.1 M Cl_3AcOH, 0.1 M $TBAPF_6$/MeCN; glassy carbon working electrode/roughened Au ring working electrode, glassy carbon counter electrode, Ag/AgCl pseudoreference electrode; scan rate 0.01 V/s.

Calculated ORR selectivity under electrochemical conditions using RRDE is 96.9 ± 0.85% H_2O_2.

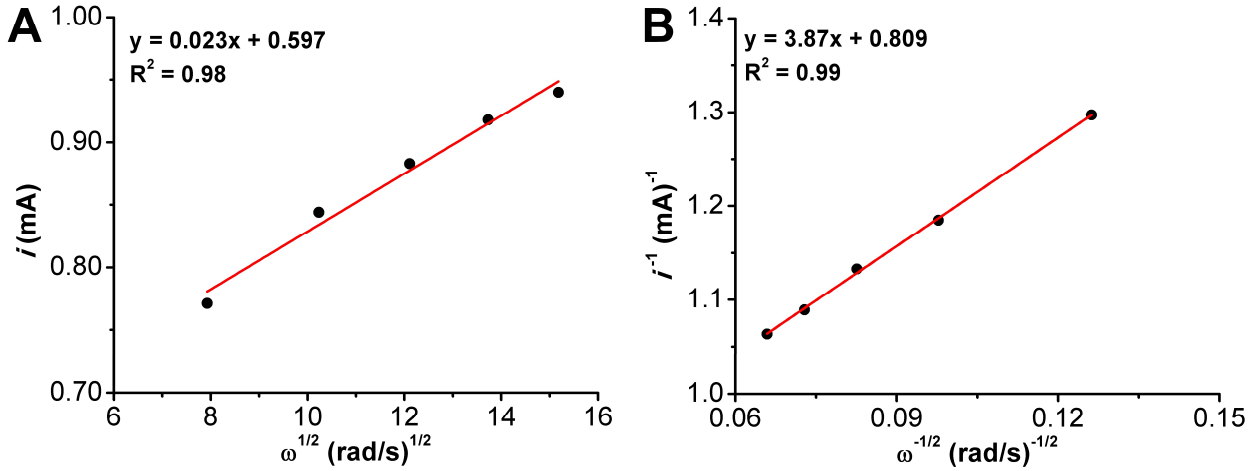

Figure S6.26. (A) Levich and (B) Koutecky-Levich plots from data obtained from linear sweep voltammograms of **Ph_2Phen^{2+}** (0.5 mM) by RRDE with 0.1 M Cl_3AcOH under air saturation conditions at various rotation rates (600, 1000, 1400, 1800, & 2200 rpm).

Electrochemical Analysis with Cl_2AcOH

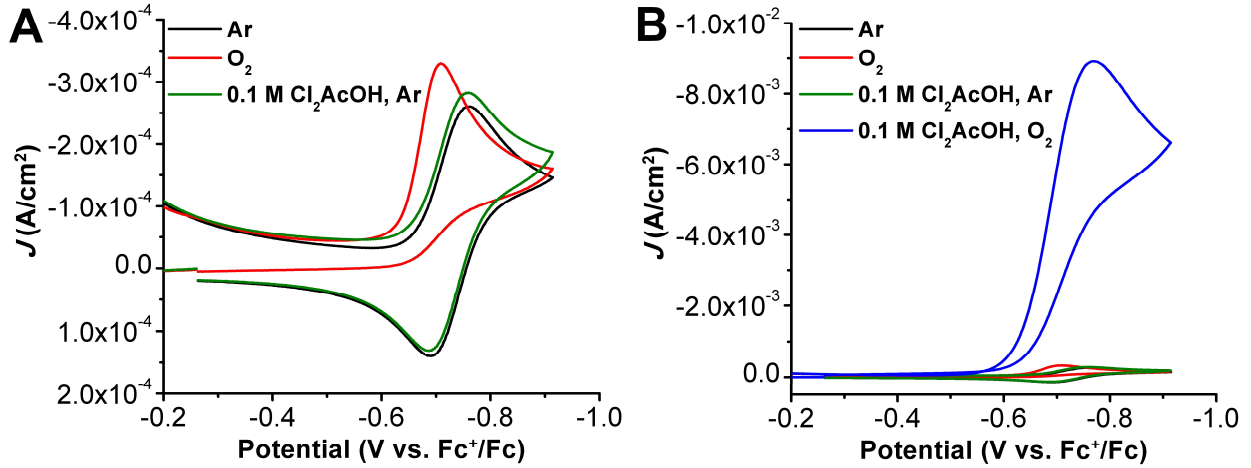

Figure S6.27. (A) CVs of **Ph_2Phen^{2+}** under Ar (black), O_2 (red) and with 0.1 M Cl_2AcOH under Ar saturation (green). (B) CVs from A and catalytic trace shown (blue) with Ph_2Phen^{2+} and 0.1 M Cl_2AcOH under O_2 saturation. Conditions: 1 mM **Ph_2Phen^{2+}**, 0.1 M $TBAPF_6$/MeCN; 100 mV/s; glassy carbon working electrode, glassy carbon rod counter electrode, Ag/AgCl pseudoreference electrode; referenced to an internal ferrocene standard.

Determination of Effective Overpotential of Ph_2Phen^{2+} with Cl_2AcOH

Utilizing the estimated pK_a of Cl_2AcOH (17.3) in MeCN, we can determine the effective overpotential according to **Eqs S6.13-S6.16**. Where E_{app} is the $E_{1/2}$ of Ph_2Phen^{2+} with 0.1 M Cl_2AcOH (**Figure S6.27**). We are unaware of a homoconjugation constant for further correction.

$$E^0_{O2/H2O} = 1.21 - 0.0592pK_a \qquad \textbf{Eq (S6.13)}$$

$$E^0_{O2/H2O}(MeCN, Cl_2AcOH) = \ 0.19\ V\ vs.\ Fc^+/Fc$$

$$\eta = \left|E_{app} - E^0_{O2/H2O}\right| = |-0.72 - 0.19| = 0.91\ V \qquad \textbf{Eq (S6.14)}$$

$$E^0_{O2/H2O2} = 0.695 - 0.0592pK_a \qquad \textbf{Eq (S6.15)}$$

$$E^0_{O2/H2O2}(MeCN, Cl_2AcOH) = \ -0.33\ V\ vs.\ Fc^+/Fc$$

$$\eta = \left|E_{app} - E^0_{O2/H2O2}\right| = |-0.72 - 0.33| = 0.39\ V \qquad \textbf{Eq (S6.16)}$$

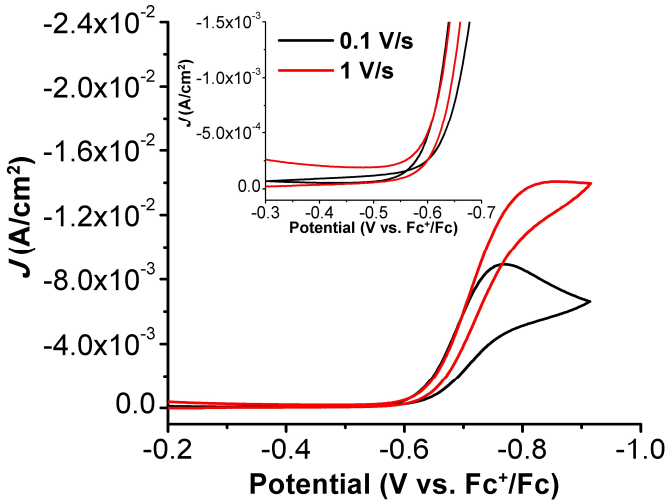

Figure S6.28. CVs of **Ph_2Phen^{2+}** under catalytic conditions with 0.1 M Cl_2AcOH at 0.1 V/s (black) and 1 V/s (red). Conditions: 1 mM **Ph_2Phen^{2+}**, 0.1 M Cl_2AcOH, 0.1 M $TBAPF_6$/MeCN; glassy carbon working electrode, glassy carbon rod counter electrode, Ag/AgCl pseudoreference electrode; referenced to an internal ferrocene standard.

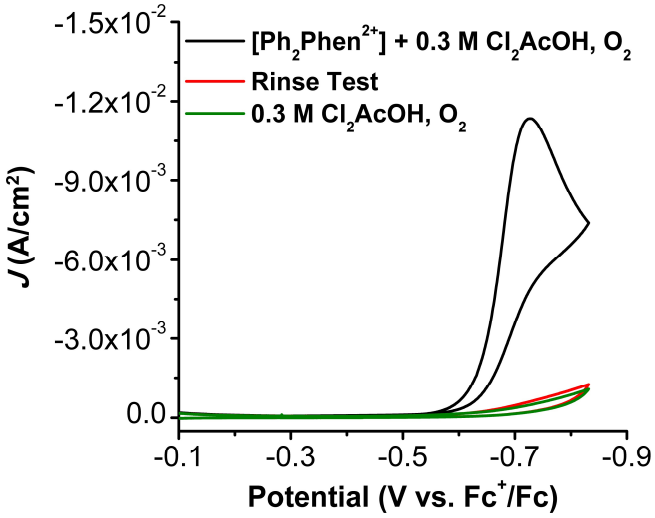

Figure S6.29. Rinse test of **Ph_2Phen^{2+}** and Cl_2AcOH. **Ph_2Phen^{2+}** under catalytic conditions (black trace), rinse test (red trace), and CV of Cl_2AcOH under O_2 saturation (green trace). Conditions: 1 mM **Ph_2Phen^{2+}**, 0.3 M Cl_2AcOH, 0.1 M $TBAPF_6$/MeCN, O_2 saturation; 100 mV/s; glassy carbon working electrode, glassy carbon counter electrode, Ag/AgCl pseudoreference electrode; referenced to an internal ferrocene standard.

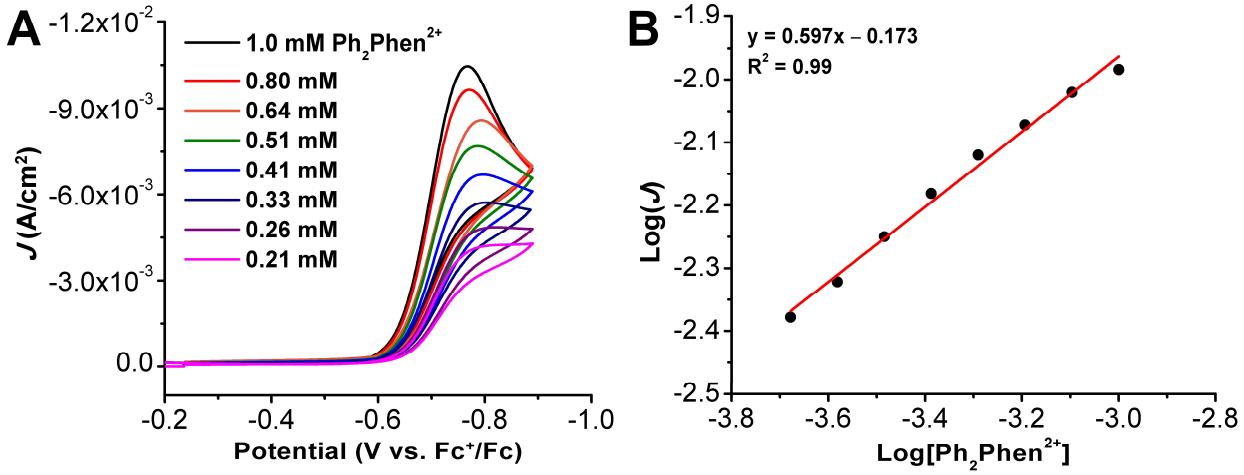

Figure S6.30. CVs of **Ph_2Phen^{2+}** under catalytic conditions with variable **Ph_2Phen^{2+}** concentrations. (B) Logarithm of **Ph_2Phen^{2+}** concentration versus the logarithm of current density from (A). Conditions: 0.3 M Cl_2AcOH, 0.1 M $TBAPF_6$/MeCN; 100 mV/s; glassy carbon working electrode, glassy carbon counter electrode, Ag/AgCl pseudoreference electrode; referenced to an internal ferrocene standard.

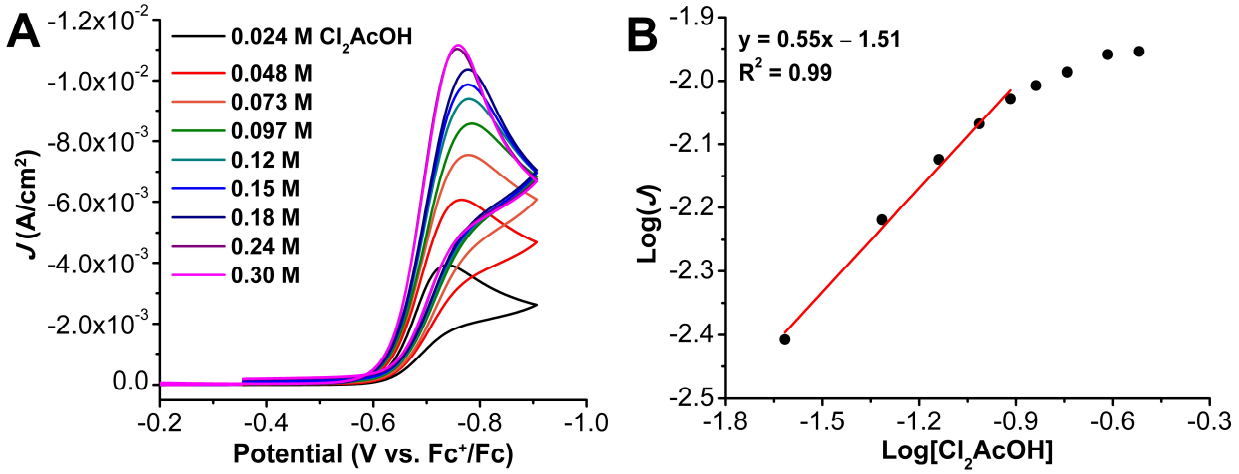

Figure S6.31. (A) CVs of $\mathbf{Ph_2Phen^{2+}}$ under catalytic conditions with variable Cl_2AcOH concentrations. (B) Logarithm of Cl_2AcOH concentration versus the logarithm of current density from (A). Conditions: 1 mM $\mathbf{Ph_2Phen^{2+}}$, 0.1 M $TBAPF_6$/MeCN, O_2 saturation; 100 mV/s; glassy carbon working electrode, glassy carbon counter electrode, Ag/AgCl pseudoreference electrode; referenced to an internal ferrocene standard.

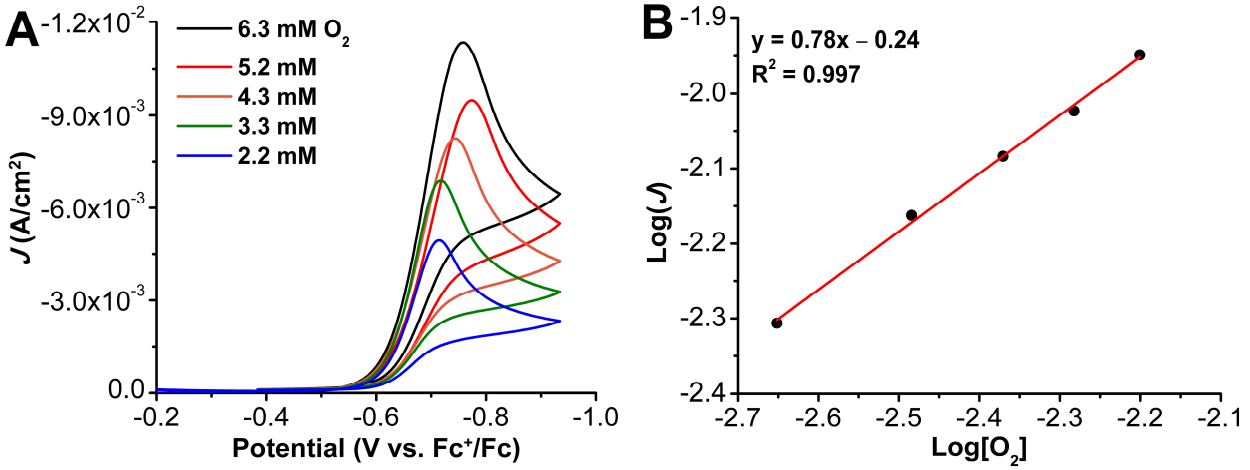

Figure S6.32. (A) CVs of $\mathbf{Ph_2Phen^{2+}}$ under catalytic conditions with variable O_2 concentrations. (B) Logarithm of O_2 concentration versus the logarithm of current density from (A). Conditions: 1 mM $\mathbf{Ph_2Phen^{2+}}$, 0.3 M Cl_2AcOH, 0.1 M $TBAPF_6$/MeCN; 100 mV/s; glassy carbon working electrode, glassy carbon counter electrode, Ag/AgCl pseudoreference electrode; referenced to an internal ferrocene standard.

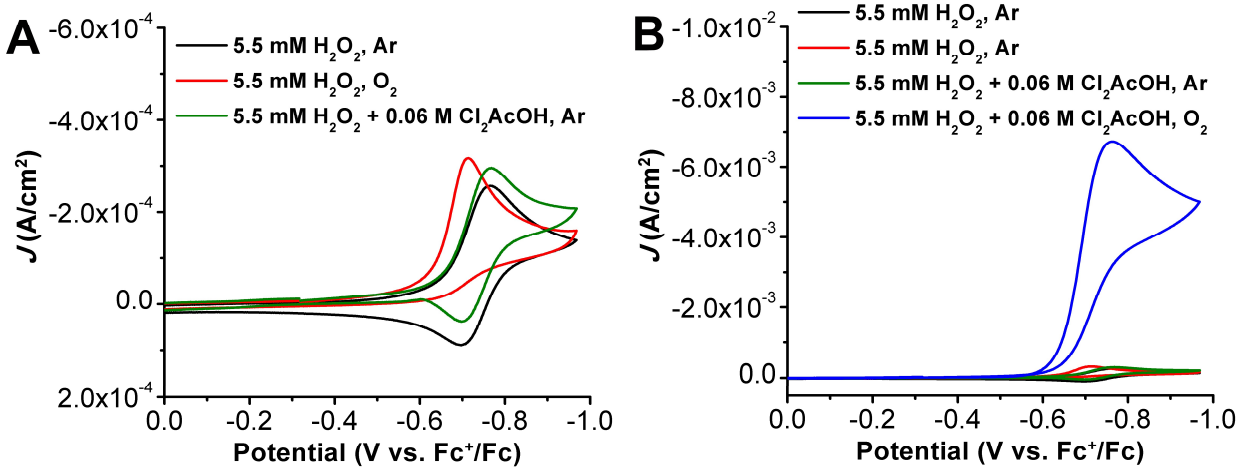

Figure S6.33. (A) CVs of **Ph_2Phen^{2+}** in the presence of 5.5 mM urea•H_2O_2 under Ar and O_2 saturation with added 0.06 M Cl_2AcOH. (B) CVs of **Ph_2Phen^{2+}** in the presence of 5.7 mM urea•H_2O_2 with added 0.06 M Cl_2AcOH under O_2 saturation. Conditions: 1 mM **Ph_2Phen^{2+}**, 0.06 M Cl_2AcOH, 0.1 M $TBAPF_6$/MeCN; 100 mV/s; glassy carbon working electrode, glassy carbon counter electrode, Ag/AgCl pseudoreference electrode; referenced to an external ferrocene standard.

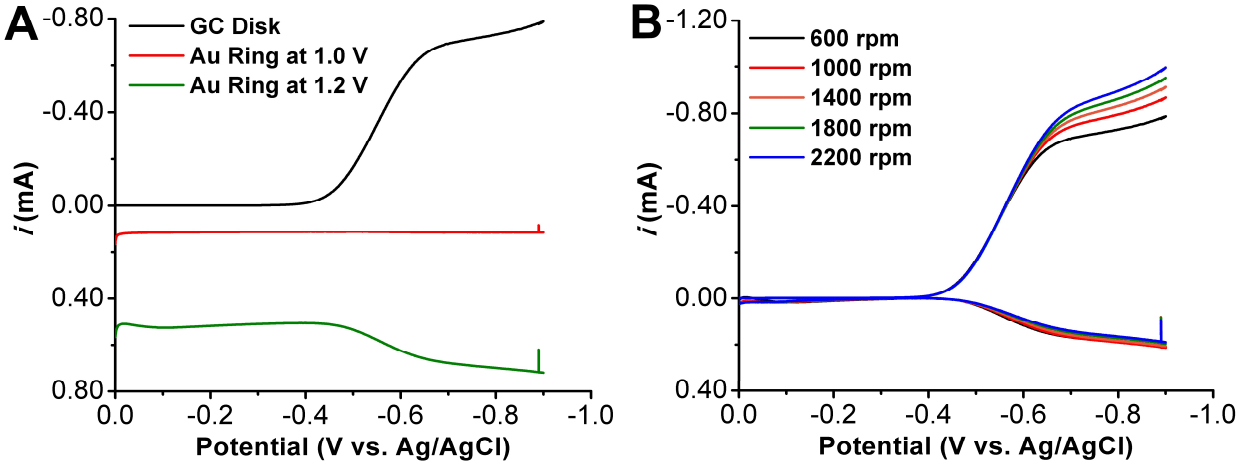

Figure S6.34. Linear sweep voltammograms of RRDE experiment with 0.5 mM **Ph_2Phen^{2+}** and 0.1 M Cl_2AcOH under air saturation conditions. (A) Uncorrected LSVs at 600 rpm. (B) Corrected LSVs at various rotation rates used for quantification of %H_2O_2. Ring potential = 1.0 or 1.2 V vs Ag/AgCl. Conditions: 0.5 mM **Ph_2Phen^{2+}**, 0.1 M Cl_2AcOH, 0.1 M $TBAPF_6$/MeCN; glassy carbon working electrode/roughened Au ring working electrode, glassy carbon counter electrode, Ag/AgCl pseudoreference electrode; scan rate 0.01 V/s.

Calculated ORR selectivity under electrochemical conditions using RRDE is 98.2 ± 7.8% H_2O_2.

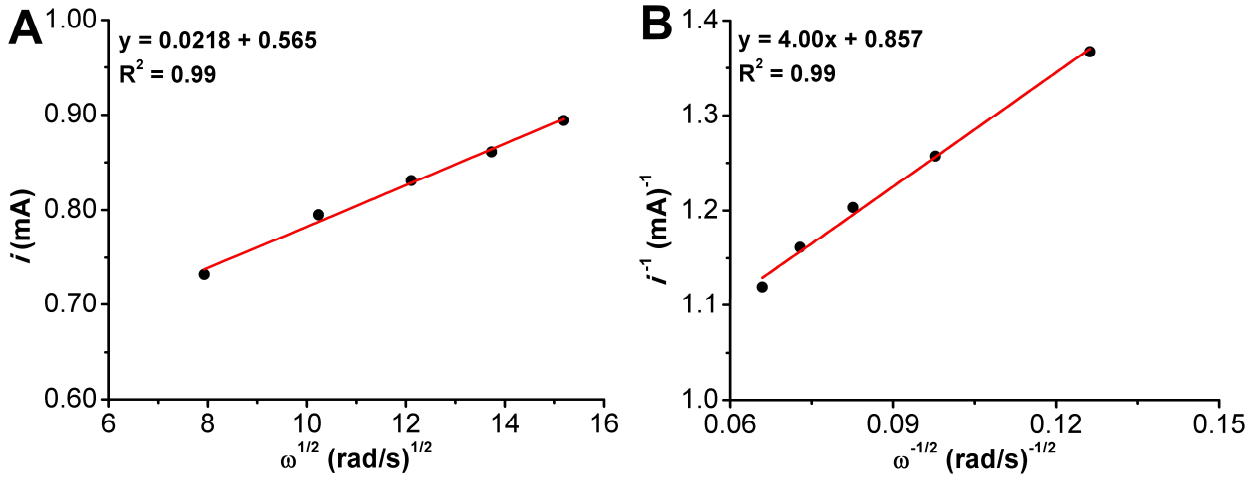

Figure S6.35. (A) Levich and (B) Koutecky-Levich plots from data obtained from linear sweep voltammograms of **Ph_2Phen^{2+}** (0.5 mM) by RRDE with 0.1 M Cl_2AcOH under air saturation conditions at various rotation rates (600, 1000, 1400, 1800, & 2200 rpm).

Electrochemical Analysis with ClAcOH

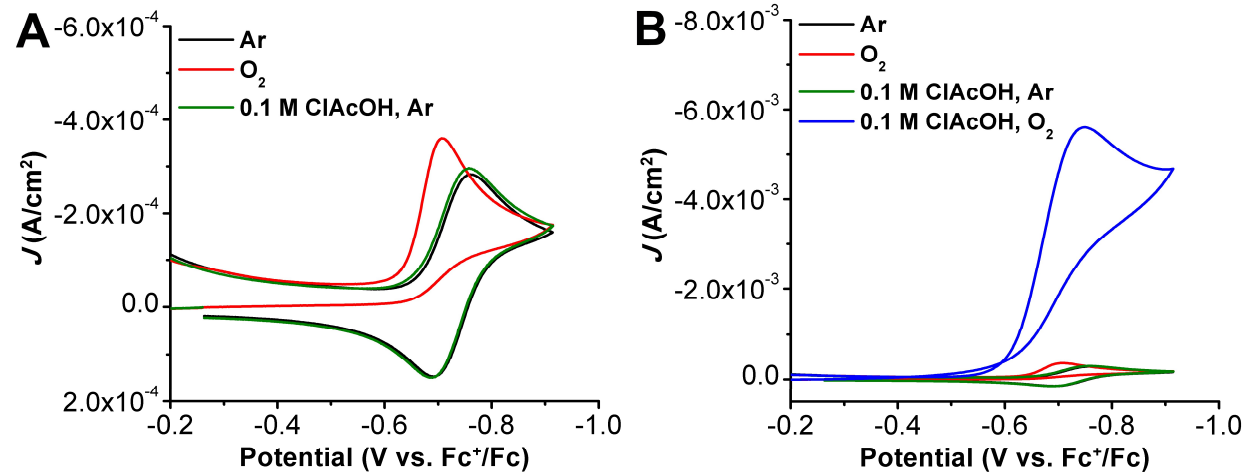

Figure S6.36. (A) CVs of **Ph_2Phen^{2+}** under Ar (black), O_2 (red) and with 0.1 M ClAcOH under Ar saturation (green). (B) CVs from A and catalytic trace shown (blue) with **Ph_2Phen^{2+}** and 0.1 M ClAcOH under O_2 saturation. Conditions: 1 mM **Ph_2Phen^{2+}**, 0.1 M $TBAPF_6$/MeCN; 100 mV/s; glassy carbon working electrode, glassy carbon rod counter electrode, Ag/AgCl pseudoreference electrode; referenced to an internal ferrocene standard.

Determination of Effective Overpotential of ***Ph₂Phen²⁺*** *with ClAcOH*

Utilizing the estimated pK_a of ClAcOH (20.25) in MeCN, we can determine the effective overpotential according to **Eqs S6.17-S6.20**. Where E_{app} is the $E_{1/2}$ of Ph_2Phen^{2+} with 0.1 M ClAcOH (**Figure S6.36)**. We are unaware of a homoconjugation constant for further correction.

$$E^0_{O2/H2O} = 1.21 - 0.0592pK_a \qquad \textbf{Eq (S6.17)}$$

$$E^0_{O2/H2O}(MeCN, ClAcOH) = \ 0.01\ V\ vs.\ Fc^+/Fc$$

$$\eta = \left|E_{app} - E^0_{O2/H2O}\right| = |-0.72 - 0.01| = 0.73\ V \qquad \textbf{Eq (S6.18)}$$

$$E^0_{O2/H2O2} = 0.695 - 0.0592pK_a \qquad \textbf{Eq (S6.19)}$$

$$E^0_{O2/H2O2}(MeCN, ClAcOH) = \ -0.50\ V\ vs.\ Fc^+/Fc$$

$$\eta = \left|E_{app} - E^0_{O2/H2O2}\right| = |-0.72 - 0.50| = 0.22\ V \qquad \textbf{Eq (S6.20)}$$

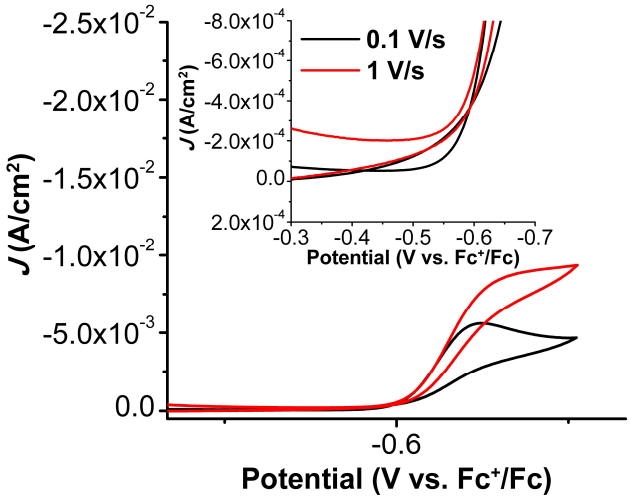

Figure S6.37. CVs of **Ph_2Phen^{2+}** under catalytic conditions with 0.1 M ClAcOH at 0.1 V/s (black) and 1 V/s (red). Conditions: 1 mM **Ph_2Phen^{2+}**, 0.1 M ClAcOH, 0.1 M $TBAPF_6$/MeCN; glassy carbon working electrode, glassy carbon rod counter electrode, Ag/AgCl pseudoreference electrode; referenced to an internal ferrocene standard.

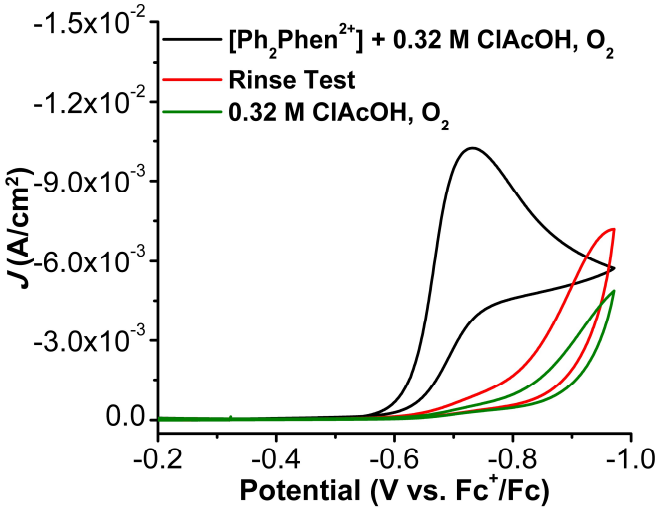

Figure S6.38. Rinse test of **Ph_2Phen^{2+}** and ClAcOH. **Ph_2Phen^{2+}** under catalytic conditions (black trace), rinse test (red trace), and CV of Cl_2AcOH under O_2 saturation (green trace). Conditions: 1 mM **Ph_2Phen^{2+}**, 0.32 M ClAcOH, 0.1 M $TBAPF_6$/MeCN, O_2 saturation; 100 mV/s; glassy carbon working electrode, glassy carbon counter electrode, Ag/AgCl pseudoreference electrode; referenced to an internal ferrocene standard.

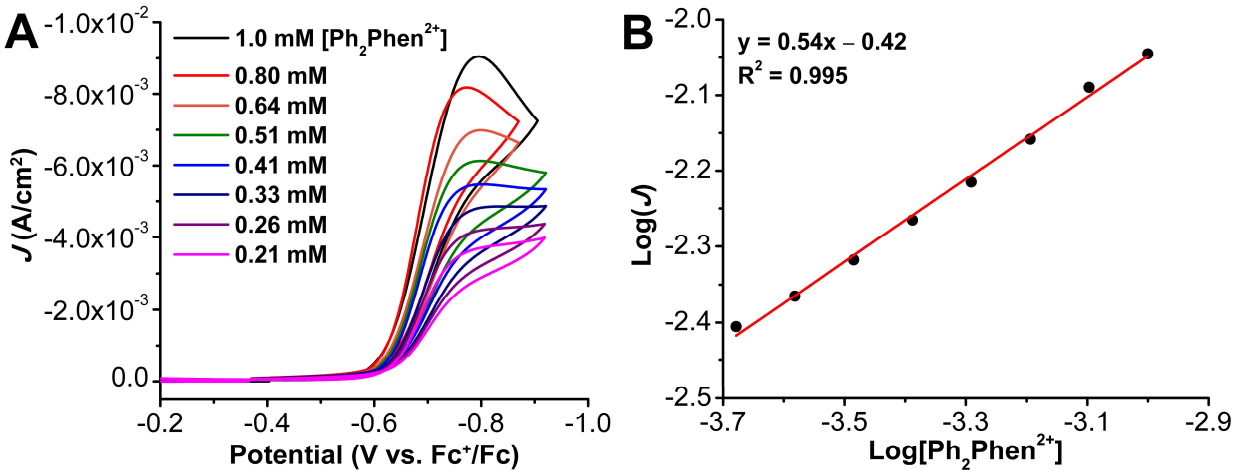

Figure S6.39. CVs of **Ph_2Phen^{2+}** under catalytic conditions with variable **Ph_2Phen^{2+}** concentrations. (B) Logarithm of **Ph_2Phen^{2+}** concentration versus the logarithm of current density from (A). Conditions: 0.3 M ClAcOH, 0.1 M $TBAPF_6$/MeCN; 100 mV/s; glassy carbon working electrode, glassy carbon counter electrode, Ag/AgCl pseudoreference electrode; referenced to an internal ferrocene standard.

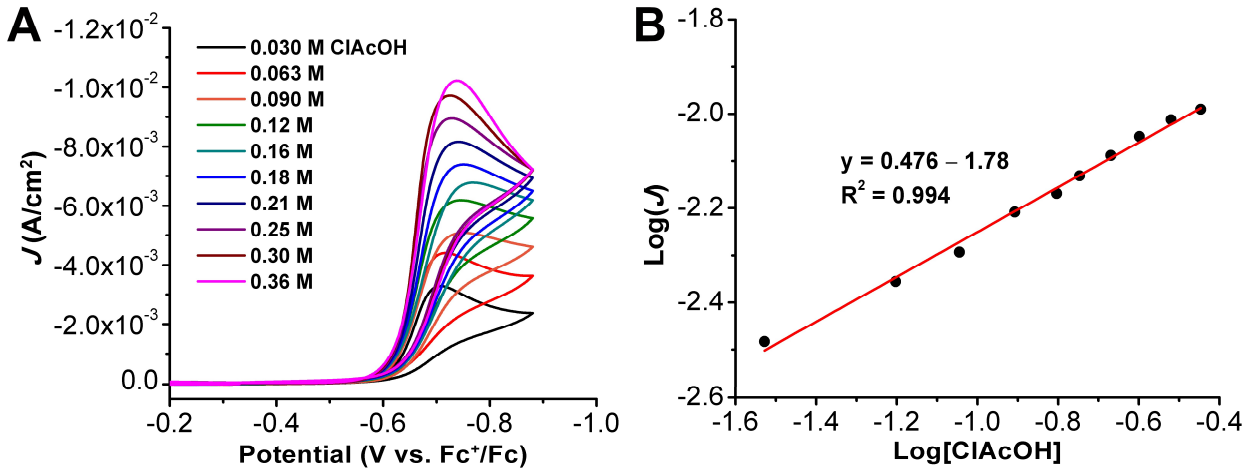

Figure S6.40. (A) CVs of **Ph_2Phen^{2+}** under catalytic conditions with variable ClAcOH concentrations. (B) Logarithm of ClAcOH concentration versus the logarithm of current density from (A). Conditions: 1 mM Ph_2Phen^{2+}, 0.1 M $TBAPF_6$/MeCN; 100 mV/s; glassy carbon working electrode, glassy carbon counter electrode, Ag/AgCl pseudoreference electrode; referenced to an internal ferrocene standard.

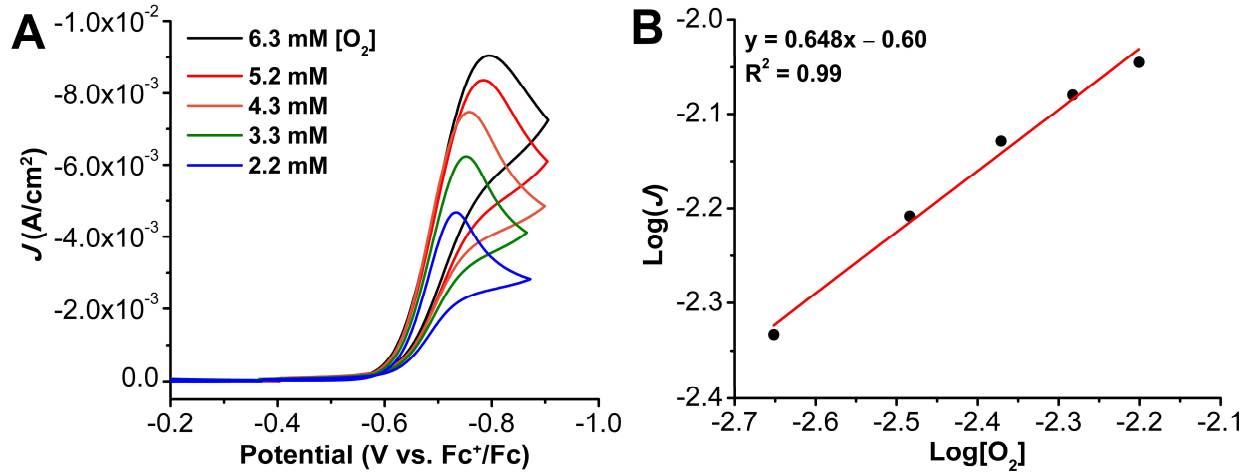

Figure S6.41. (A) CVs of **Ph_2Phen^{2+}** under catalytic conditions with variable O_2 concentrations. (B) Logarithm of O_2 concentration versus the logarithm of current density from (A). Conditions: 1 mM **Ph_2Phen^{2+}**, 0.3 M ClAcOH, 0.1 M $TBAPF_6$/MeCN; 100 mV/s; glassy carbon working electrode, glassy carbon counter electrode, Ag/AgCl pseudoreference electrode; referenced to an internal ferrocene standard.

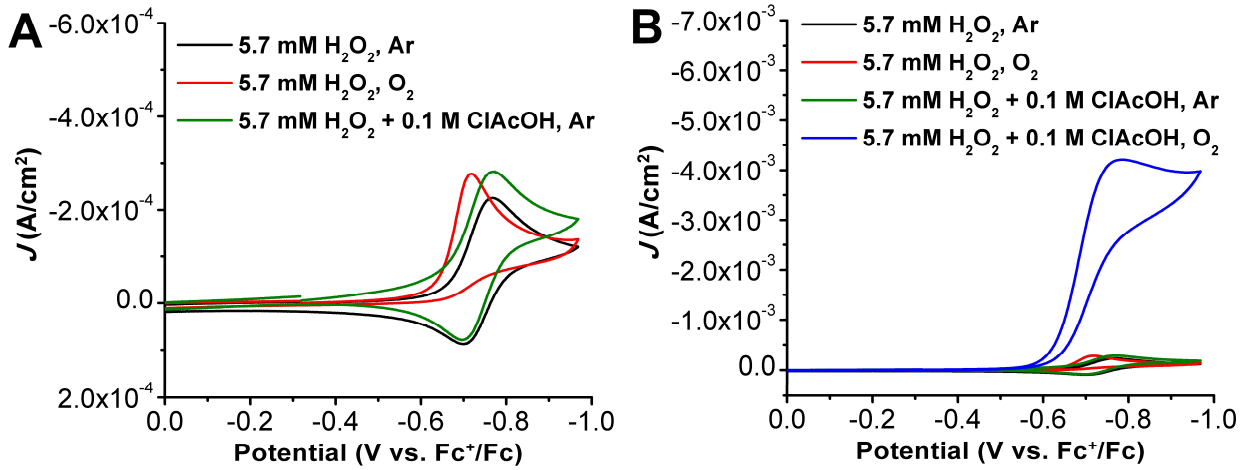

Figure S6.42. (A) CVs of **Ph_2Phen^{2+}** in the presence of 5.7 mM urea•H_2O_2 under Ar and O_2 saturation with added 0.1 M ClAcOH. (B) CVs of **Ph_2Phen^{2+}** in the presence of 5.7 mM urea•H_2O_2 with added 0.1 M ClAcOH under O_2 saturation. Conditions: 1 mM **Ph_2Phen^{2+}**, 0.1 M ClAcOH, 0.1 M TBAPF6/MeCN; 100 mV/s; glassy carbon working electrode, glassy carbon counter electrode, Ag/AgCl pseudoreference electrode; referenced to an external ferrocene standard.

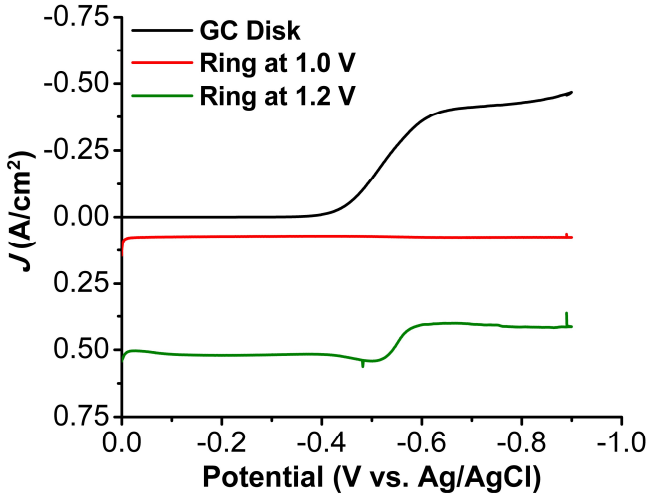

Figure S6.43. Linear sweep voltammogram of RRDE experiment with 0.5 mM **Ph_2Phen^{2+}** and 0.1 M ClAcOH under air saturation conditions at 200 rpm. Ring potential = 1.0 or 1.2 V vs Ag/AgCl. Conditions: 0.5 mM **Ph_2Phen^{2+}**, 0.1 M Cl_2AcOH, 0.1 M $TBAPF_6$/MeCN; glassy carbon working electrode/roughened Au ring working electrode, glassy carbon counter electrode, Ag/AgCl pseudoreference electrode; scan rate 0.01 V/s.

Stopped-Flow Kinetic Analysis of Ph_2Phen^{2+}

Stopped-flow spectrochemical kinetics studies were performed with a CSF-61DX2 Stopped-Flow System from Hi-Tech Scientific. Kinetic Studio Software was used to monitor a single wavelength and Integrated CCD Software was used to monitor the entire visible spectrum. All data fits were performed within the Kinetic Studio 4.0 Software Suite. Prior to experiments, dried and degassed MeCN was passed through syringes and the cell block before reagents were loaded. In a typical experiment, syringes would be charged with known concentrations of reagent. All reagent solutions were prepared immediately before use. In general, a vial containing **Ph_2Phen^{2+}** catalyst and acid was sparged with O_2, drawn into a syringe and loaded into the stopped-flow. A second syringe containing N_2-saturated Cp^*_2Fe solution was loaded into the stopped-flow. All reported concentrations are the mixed concentrations in the spectroscopic cell.

Stopped-Flow with TFAH

$$\frac{R_{fit}}{n_{cat}} = k_{cat}[Ph_2Phen^{2+}]^1[TFAH]^1[O_2]^1[Cp^*{}_2Fe]^0$$

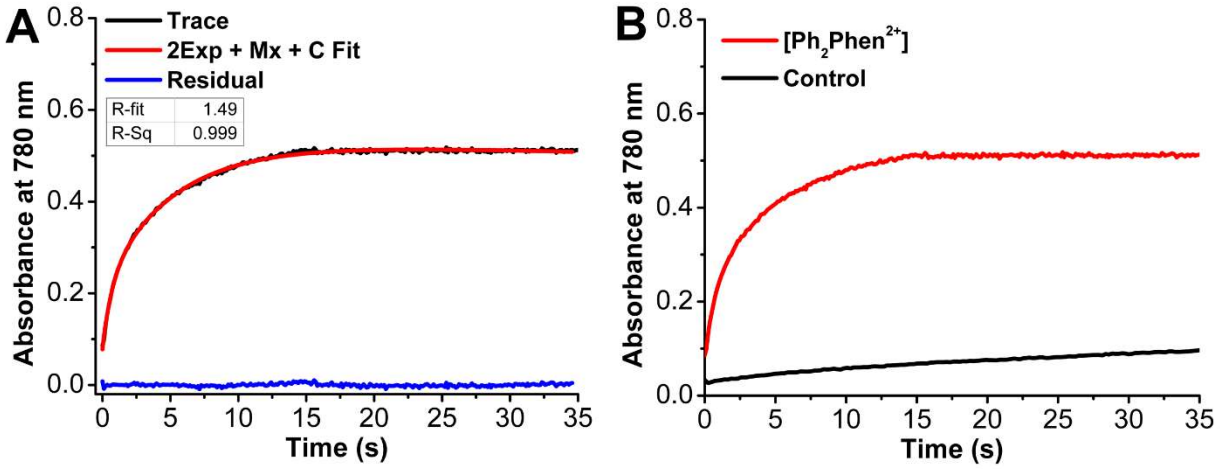

Figure S6.44. (A) Change in absorbance at 780 nm over time as a result of the formation of [Cp*2Fe]+ by ORR catalyzed by **Ph_2Phen^{2+}** with TFAH (black trace), example of 2Exp + Mx + C fit in Kinetic Studio 4.0 (red trace), and residual fit (blue trace). (B) Black trace from (A) with TFAH only control (no **Ph_2Phen^{2+}** present). Concentrations: **Ph_2Phen^{2+}** (if present) = 40 μM, TFAH = 50 mM, O_2 = 4.05 mM, Cp^*_2Fe = 1 mM.

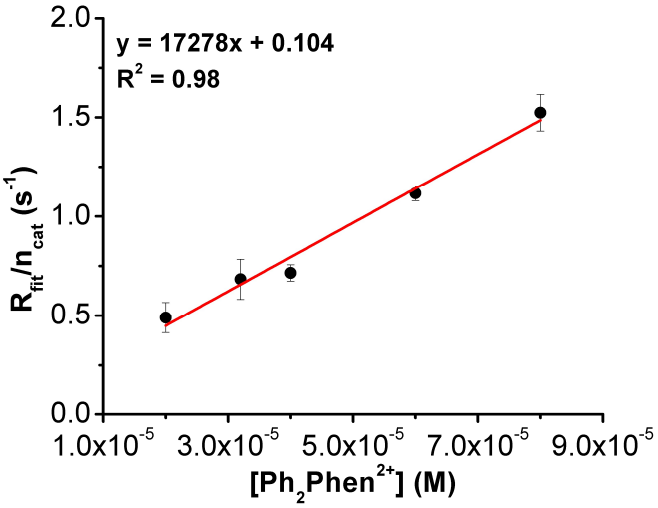

Figure S6.45. Calculated R_{fit}/n_{cat} values from stopped-flow spectrochemical experiments with TFAH, O_2, and Cp^*_2Fe with varying **Ph_2Phen^{2+}** concentration. Data were fit using Kinetic Studio 4.0 (2Exp+Mx+C); n_{cat} = 2.14. Concentrations: TFAH = 50 mM, O_2 = 4.05 mM, Cp^*_2Fe = 1 mM.

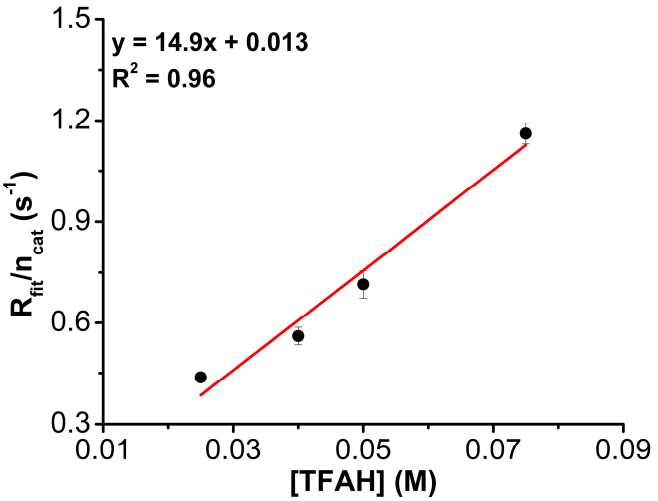

Figure S6.46. Calculated R_{fit}/n_{cat} values from stopped-flow spectrochemical experiments with **Ph2Phen^{2+},** O_2, and Cp^*_2Fe with varying TFAH concentration. Data were fit using Kinetic Studio 4.0 (2Exp+Mx+C); n_{cat} = 2.14. Concentrations: **Ph_2Phen^{2+}** = 40 μM, O_2 = 4.05 mM, Cp^*_2Fe = 1 mM.

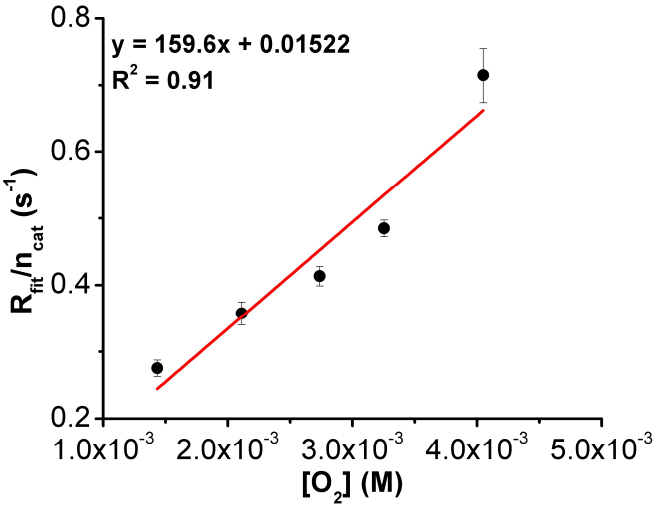

Figure S6.47. Calculated R_{fit}/n_{cat} values from stopped-flow spectrochemical experiments with **Ph_2Phen^{2+}**, TFAH, and Cp^*_2Fe with varying O_2 concentration. Data were fit using Kinetic Studio 4.0 (2Exp+Mx+C); n_{cat} = 2.14. Concentrations: **Ph_2Phen^{2+}** = 40 μM, TFAH = 50 mM, Cp^*_2Fe = 1 mM.

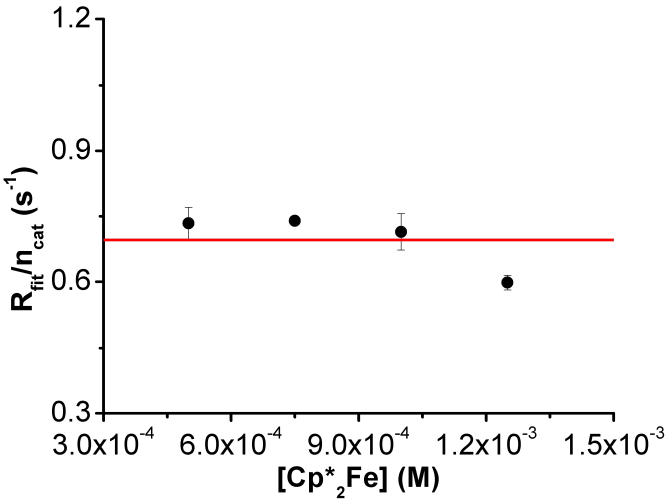

Figure S6.48. Calculated R_{fit}/n_{cat} values from stopped-flow spectrochemical experiments with **Ph_2Phen^{2+}**, TFAH, and O_2 with varying Cp^*_2Fe concentration. Data were fit using Kinetic Studio 4.0 (2Exp+Mx+C); n_{cat} = 2.14. The horizontal line represents the global average rate observed across all experiments for variable [Cp^*_2Fe]. Concentrations: **Ph_2Phen^{2+}** = 40 μM, TFAH = 50 mM, O_2 = 4.05 mM.

Comparison of ORR and H_2O_2RR with TFAH

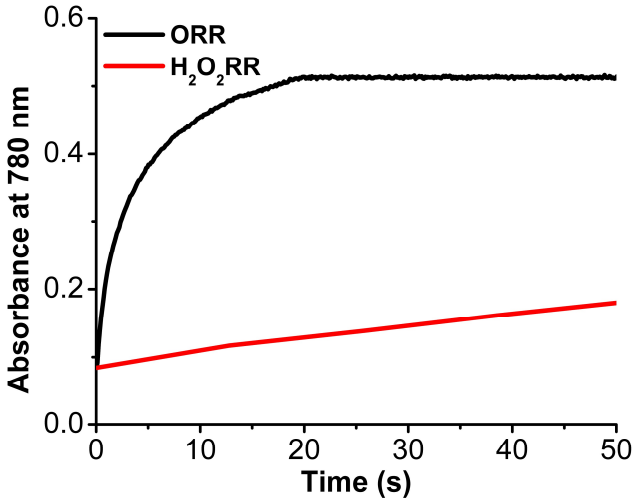

Figure S6.49. Change in absorbance at 780 nm over time as a result of the formation of $[Cp^*_2Fe]^+$ from the ORR (black trace) or H_2O_2RR (red trace) by **Ph^{2}Phen^{2+}** with TFAH. Conditions: **Ph-$_2$Phen^{2+}** = 40 μM, TFAH = 25 mM, Cp*Fe = 1 mM, O_2 = 4.05 mM, urea•H_2O_2 = 0.96 mM.

Stopped-Flow with Cl_3AcOH

$$\frac{\mathrm{R}_{fit}}{n_{cat}} = k_{\mathrm{cat}}[\mathrm{Ph_2Phen^{2+}}]^1[\mathrm{Cl_3AcOH}]^1[\mathrm{O_2}]^0[Cp^*{}_2Fe]^0$$

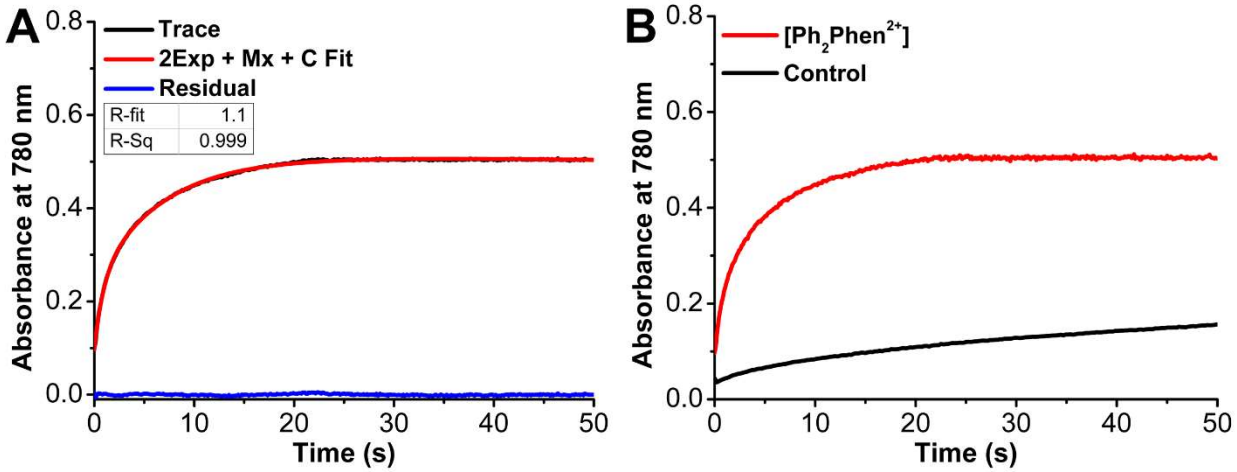

Figure S6.50. Change in absorbance at 780 nm over time as a result of the formation of $[Cp^*_2Fe]^+$ by ORR catalyzed by **Ph$_2$Phen^{2+}** with Cl_3AcOH (black trace), example of 2Exp + Mx + C fit in Kinetic Studio 4.0 (red trace), and residual fit (blue trace). (B) Black trace from (A) with Cl_3AcOH only control (no **Ph$_2$Phen^{2+}** present). Concentrations: **Ph$_2$Phen^{2+}** = 40 μM, Cl_3AcOH = 50 mM, O_2 = 4.05 mM, Cp^*_2Fe = 1 mM.

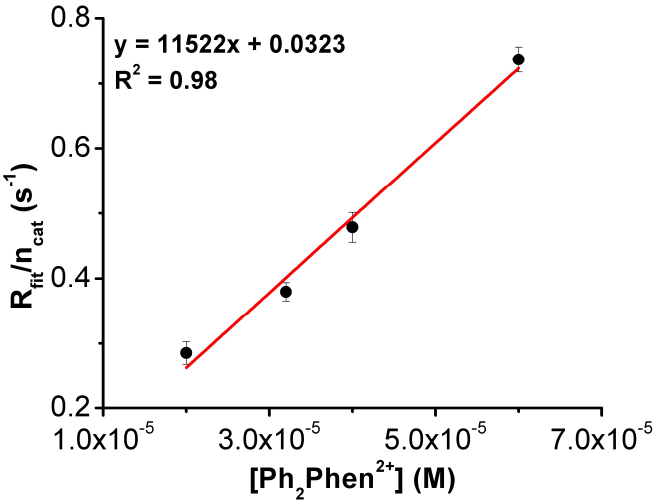

Figure S6.51. Calculated R_{fit}/n_{cat} values from stopped-flow spectrochemical experiments with Cl_3AcOH, O_2, and Cp^*_2Fe with varying **Ph_2Phen^{2+}** concentration. Data were fit using Kinetic Studio 4.0 (2Exp+Mx+C); n_{cat} = 2.3. Concentrations: Cl_3AcOH = 50 mM, O_2 = 4.05 mM, Cp^*_2Fe = 1 mM.

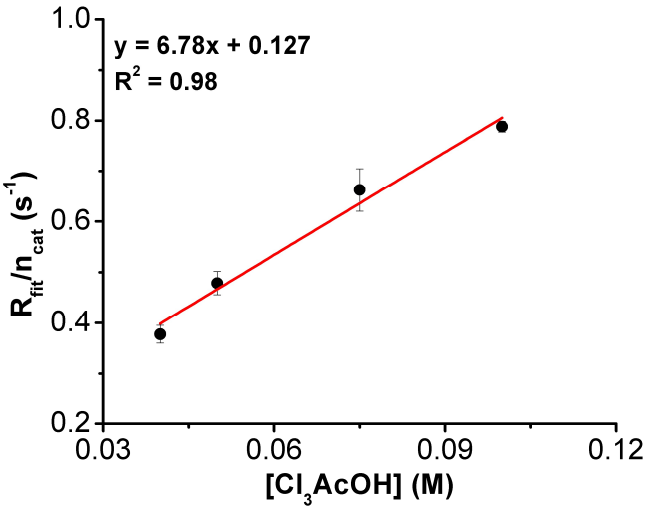

Figure S6.52. Calculated R_{fit}/n_{cat} values from stopped-flow spectrochemical experiments with **Ph_2Phen^{2+}**, O_2, and Cp^*_2Fe with varying Cl_3AcOH concentration. Data were fit using Kinetic Studio 4.0 (2Exp+Mx+C); n_{cat} = 2.3. Concentrations: **Ph_2Phen^{2+}** = 40 μM, O_2 = 4.05 mM, Cp^*_2Fe = 1 mM.

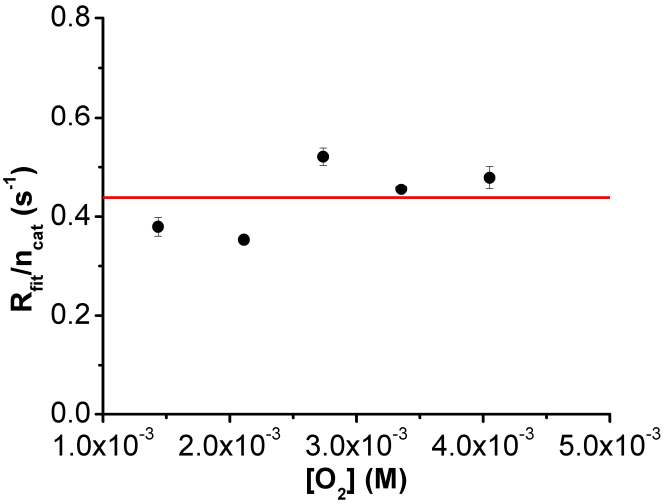

Figure S6.53. Calculated R_{fit}/n_{cat} values from stopped-flow spectrochemical experiments with **Ph_2Phen^{2+}**, Cl_3AcOH, and Cp^*_2Fe with varying O_2 concentration. Data were fit using Kinetic Studio 4.0 (2Exp+Mx+C); n_{cat} = *2.3.* The horizontal line represents the global average rate observed across all experiments for variable [O_2]. Concentrations: **Ph_2Phen^{2+}** = 40 μM, Cl_3AcOH = 50 mM, Cp^*_2Fe = 1 mM.

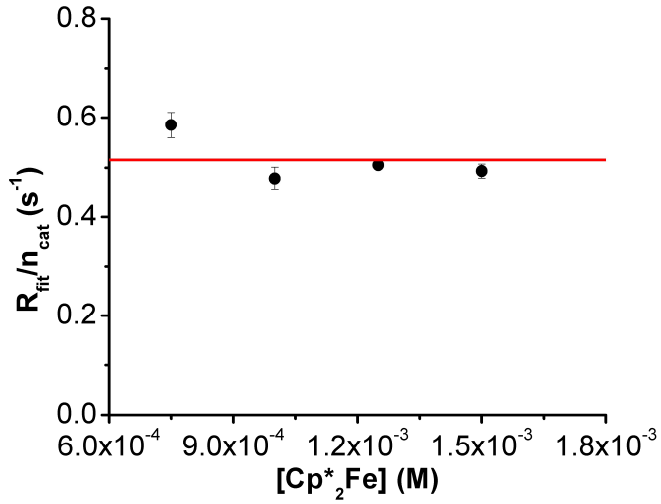

Figure S6.54. Calculated R_{fit}/n_{cat} values from stopped-flow spectrochemical experiments with **Ph_2Phen^{2+}**, Cl_3AcOH, and O_2 with varying Cp^*_2Fe concentration. Data were fit using Kinetic Studio 4.0 (2Exp+Mx+C); n_{cat} = 2.3. The horizontal line represents the global average rate observed across all experiments for variable [Cp^*_2Fe]. Concentrations: **Ph_2Phen^{2+}** = 40 μM, Cl_3AcOH = 50 mM, O_2 = 4.05 mM.

Comparison of ORR and H_2O_2RR with Cl_3AcOH

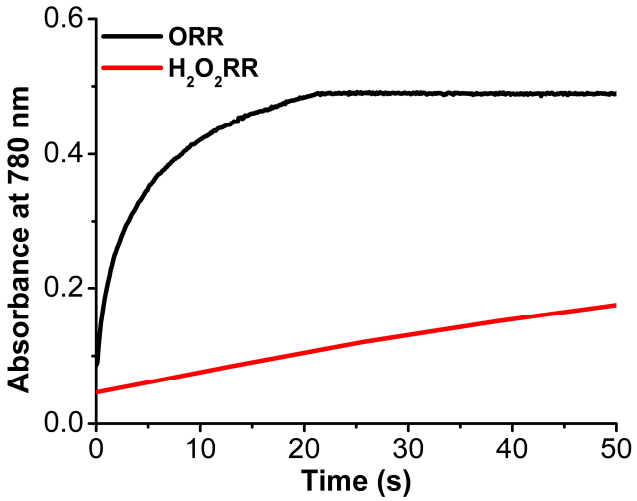

Figure S6.55. Change in absorbance at 780 nm over time as a result of the formation of $[Cp^*_2Fe]^+$ from the ORR (black trace) or H_2O_2RR (red trace) by **Ph_2Phen^{2+}** with Cl_3AcOH. Conditions: **Ph_2Phen^{2+}** = 40 μM, Cl_3AcOH = 25 mM, Cp*Fe = 1 mM, O_2 = 4.05 mM, urea•H_2O_2 = 0.96 mM.

Stopped-Flow with Cl_2AcOH

$$\frac{\mathrm{R}_{fit}}{n_{cat}} = k_{\mathrm{cat}}[\mathrm{Ph_2Phen^{2+}}]^{0.5}[\mathrm{Cl_2AcOH}]^1[\mathrm{O_2}]^0[Cp^*{}_2Fe]^0$$

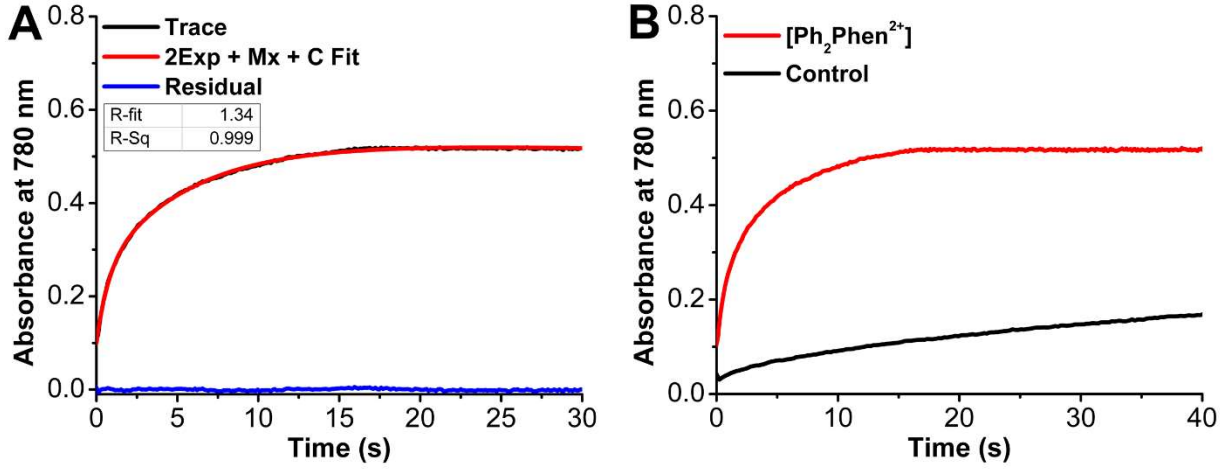

Figure S6.56. (A) Change in absorbance at 780 nm over time as a result of the formation of $[Cp^*_2Fe]^+$ by ORR catalyzed by **Ph_2Phen^{2+}** with Cl_2AcOH (black trace), example of 2Exp + Mx + C fit in Kinetic Studio 4.0 (red trace), and residual fit (blue trace). (B) Black trace from (A) with Cl_2AcOH only control (no **Ph_2Phen^{2+}** present). Concentrations: **Ph_2Phen^{2+}** = 40 μM, Cl_2AcOH = 50 mM, O_2 = 4.05 mM, Cp^*_2Fe = 1 mM.

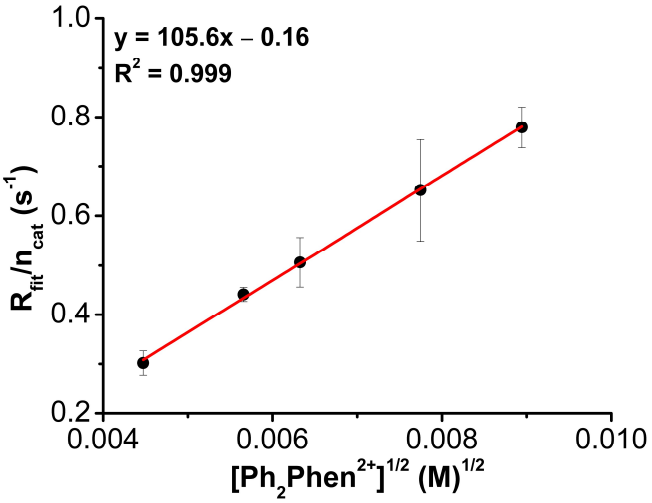

Figure S6.57. Calculated R_{fit}/n_{cat} values from stopped-flow spectrochemical experiments with Cl_2AcOH, O_2, and Cp^*_2Fe with varying **Ph_2Phen^{2+}** concentration. Data were fit using Kinetic Studio 4.0 (2Exp+Mx+C); n_{cat} = 2.35. Concentrations: Cl_2AcOH = 50 mM, O_2 = 4.05 mM, Cp^*_2Fe = 1 mM.

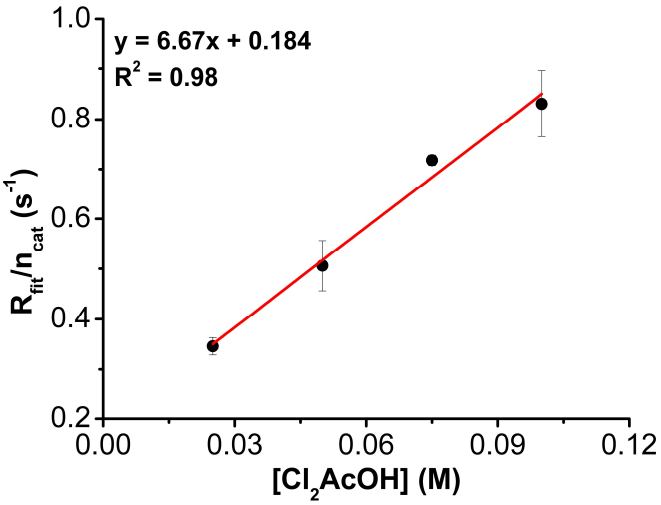

Figure S6.58. Calculated R_{fit}/n_{cat} values from stopped-flow spectrochemical experiments with **Ph_2Phen^{2+}**, O_2, and Cp^*_2Fe with varying Cl_2AcOH concentration. Data were fit using Kinetic Studio 4.0 (2Exp+Mx+C); n_{cat} = 2.35. Concentrations: **Ph_2Phen^{2+}** = 40 μM, O_2 = 4.05 mM, Cp^*_2Fe = 1 mM.

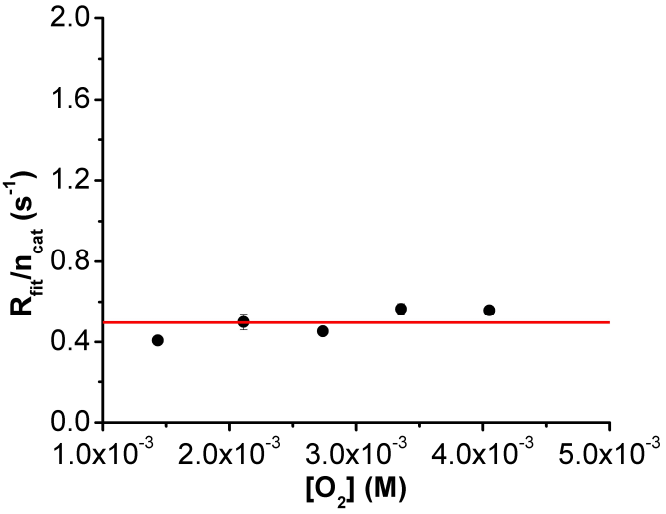

Figure S6.59. Calculated R_{fit}/n_{cat} values from stopped-flow spectrochemical experiments with **Ph_2Phen^{2+}**, Cl_2AcOH, and Cp^*_2Fe with varying O_2 concentration. Data were fit using Kinetic Studio 4.0 (2Exp+Mx+C); n_{cat} = 2.35. The horizontal line represents the global average rate observed across all experiments for variable [O_2]. Concentrations: **Ph_2Phen^{2+}** = 40 μM, Cl_2AcOH = 50 mM, Cp^*_2Fe = 1 mM.

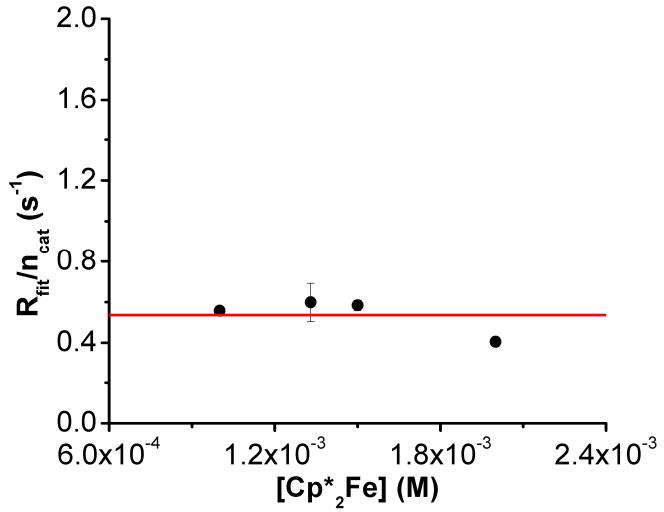

Figure S6.60. Calculated R_{fit}/n_{cat} values from stopped-flow spectrochemical experiments with **Ph_2Phen^{2+}**, Cl_2AcOH, and O_2 with varying Cp^*_2Fe concentration. Data were fit using Kinetic Studio 4.0 (2Exp+Mx+C); n_{cat} = 2.35. The horizontal line represents the global average rate observed across all experiments for variable [Cp^*_2Fe]. Concentrations: **Ph_2Phen^{2+}** = 40 μM, Cl_2AcOH = 50 mM, O_2 = 4.05 mM.

Comparison of ORR and H_2O_2RR with Cl_2AcOH

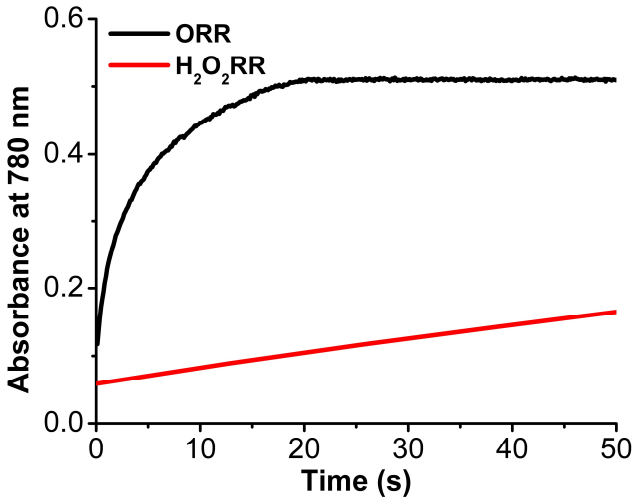

Figure S6.61. Change in absorbance at 780 nm over time as a result of the formation of $[Cp^*_2Fe]^+$ from the ORR (black trace) or H_2O_2RR (red trace) by **Ph_2Phen^{2+}** with Cl_2AcOH. Conditions: **Ph_2Phen^{2+}** = 40 μM, Cl_2AcOH = 25 mM, Cp*Fe = 1 mM, O_2 = 4.05 mM, urea•H_2O_2 = 0.96 mM.

Stopped-Flow with ClAcOH

$$\mathbf{Rate} = k_{\mathbf{cat}}[\mathbf{Ph_2Phen^{2+}}]^{0.5}[\mathbf{ClAcOH}]^{1}[\mathbf{O_2}]^{0}[\boldsymbol{Cp^*_2Fe}]^{0}$$

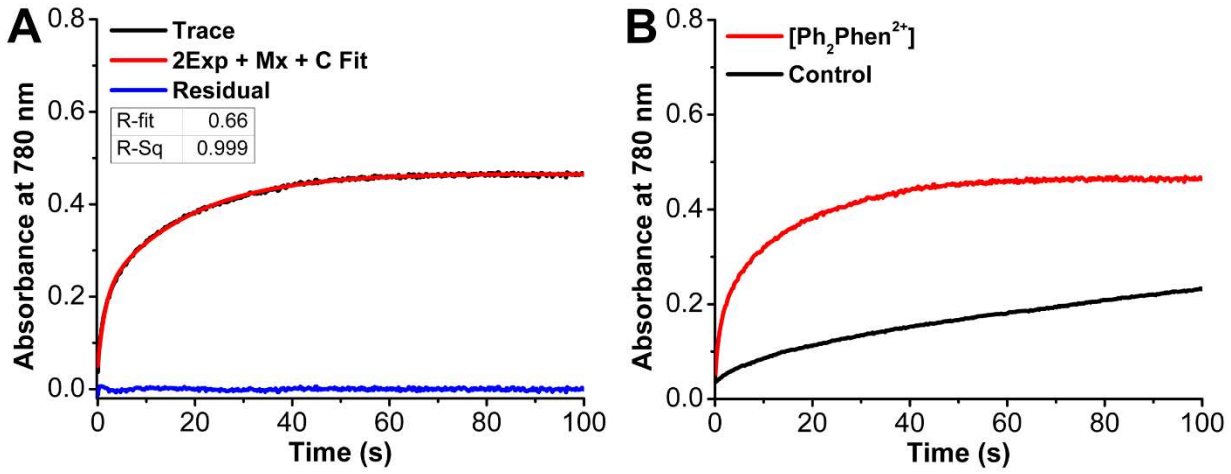

Figure S6.62. Change in absorbance at 780 nm over time as a result of the formation of $[Cp^*_2Fe]^+$ by ORR catalyzed by **Ph_2Phen^{2+}** with ClAcOH (black trace), example of 2Exp + Mx + C fit in Kinetic Studio 4.0 (red trace), and residual fit (blue trace). (B) Black trace from (A) with ClAcOH only control (no **Ph_2Phen^{2+}** present). Concentrations: **Ph_2Phen^{2+}** = 40 μM, ClAcOH = 50 mM, O_2 = 4.05 mM, Cp^*_2Fe = 1 mM.

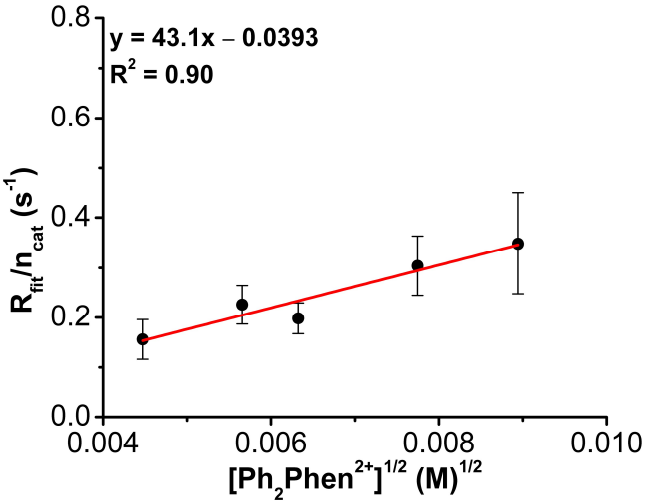

Figure S6.63. Calculated R_{fit}/n_{cat} values from stopped-flow spectrochemical experiments with ClAcOH, O_2, and Cp^*_2Fe with varying **Ph_2Phen^{2+}** concentration. Data were fit using Kinetic Studio 4.0 (2Exp+Mx+C); n_{cat} = 3.52. Concentrations: ClAcOH = 50 mM, O_2 = 4.05 mM, Cp^*_2Fe = 1 mM.

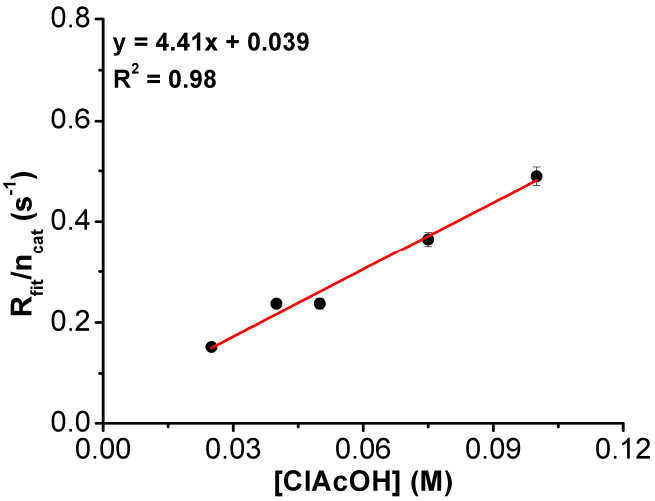

Figure S6.64. Calculated R_{fit}/n_{cat} values from stopped-flow spectrochemical experiments with **Ph_2Phen^{2+}**, O_2, and Cp^*_2Fe with varying ClAcOH concentration. Data were fit using Kinetic Studio 4.0 (2Exp+Mx+C); n_{cat} = 3.52. Concentrations: **Ph_2Phen^{2+}** = 40 μM, O_2 = 4.05 mM, Cp^*_2Fe = 1 mM.

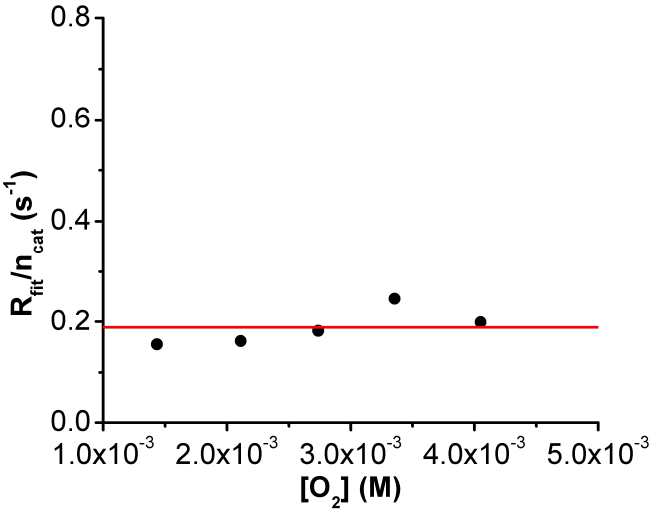

Figure S6.65. Calculated R_{fit}/n_{cat} values from stopped-flow spectrochemical experiments with **Ph_2Phen^{2+}**, ClAcOH, and Cp^*_2Fe with varying O_2 concentration. Data were fit using Kinetic Studio 4.0 (2Exp+Mx+C); n_{cat} = 3.52. The horizontal line represents the global average rate observed across all experiments for variable [O_2]. Concentrations: **Ph_2Phen^{2+}** = 40 μM, ClAcOH = 50 mM, Cp^*_2Fe = 1 mM.

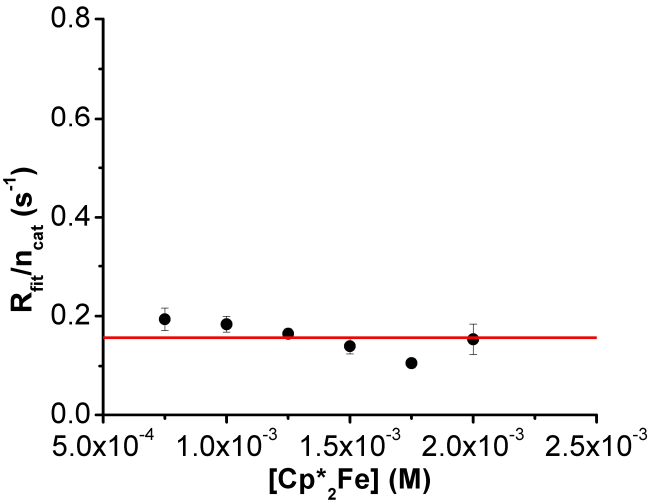

Figure S6.66. Calculated R_{fit}/n_{cat} values from stopped-flow spectrochemical experiments with **Ph_2Phen^{2+}**, ClAcOH, and O_2 with varying Cp^*_2Fe concentration. Data were fit using Kinetic Studio 4.0 (2Exp+Mx+C); n_{cat} = 3.52. The horizontal line represents the global average rate observed across all experiments for variable [Cp^*_2Fe]. Concentrations: **Ph_2Phen^{2+}** = 40 μM, ClAcOH = 50 mM, O_2 = 4.05 mM.

Comparison of ORR and H_2O_2RR with ClAcOH

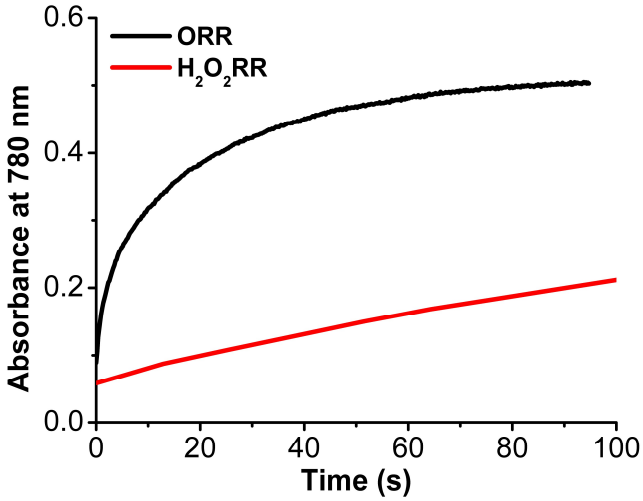

Figure S6.67. Change in absorbance at 780 nm over time as a result of the formation of $[Cp^*_2Fe]^+$ from the ORR (black trace) or H_2O_2RR (red trace) by **Ph_2Phen^{2+}** with ClAcOH. Conditions: **Ph_2Phen^{2+}** = 40 μM, ClAcOH = 25 mM, Cp*Fe = 1 mM, O_2 = 4.05 mM, urea•H_2O_2 = 0.96 mM.

Spectrochemical Analysis

ORR Selectivity

The ORR selectivity of **Ph_2Phen^{2+}** was determined using a previously reported procedure. [32] Generally, solutions containing 80 μM [**Ph_2Phen^{2+}**] and 50 mM acid (TFAH, Cl_3AcOH, Cl_2AcOH, or ClAcOH) were sparged with O_2 gas and rapidly mixed in a 1:1 ratio with a N_2 saturated 2 mM Cp^*_2Fe solution to a final volume of 4 mL (final concentrations: 40 μM **Ph_2Phen^{2+},** 1 mM Cp^*_2Fe, 25 mM acid, 4.05 mM O_2). The reactions were allowed to reach completion and 2 mL of the reaction solution was added to 2 mL of water. Then, 3 mL of this solution was added to the cuvette and a UV-vis spectrum was taken before and after the addition of 0.1 mL of $Ti(O)SO_4$ solution, as previously reported. [11, 31-33, 40] A calibration curve was used to establish **Eqs S6.21-S6.22**[32] and were used to calculate the % selectivity of H_2O_2.

$$O_2 + 2Cp^*_2Fe(1\ mM) + 2AH \xrightarrow{cat.[Ph_2Phen^{2+}]} H_2O_2(0.5\ mM) + 2[Cp^*_2Fe]^+ + 2A^- \quad \textbf{(Eq S6.21)}$$

Abs@408 nm (red trace) – Abs@408 nm (black trace) = $405.6[H_2O_2]_{exp} - 0.01122$

$$\frac{[H_2O_2]_{exp}}{0.5\ mM\ H_2O_2} \times 100 = \%\ H_2O_2\ \text{selectivity} \qquad \textbf{(Eq S6.22)}$$

Table S6.2. Summary of ORR selectivity by **Ph_2Phen^{2+}** with each acid.[a]

	Time (s)[b]	% H_2O_2	% H_2O	n_{cat}
TFAH	90	93.2 ± 1.4	6.8 ± 1.4	2.14
Cl_3AcOH	90	84.8 ± 5.8	15.2 ± 5.8	2.30
Cl_2AcOH	120	82.3 ± 3.2	17.7 ± 3.2	2.35
ClAcOH	180	24.0 ± 6.2	76.0 ± 6.2	3.52

[a] 40 μM [**Ph_2Phen^{2+}**], 25 mM [AH], 4.05 mM [O_2], 1 mM [Cp^*_2Fe]; [b]time when all Cp^*Fe_2 is consumed

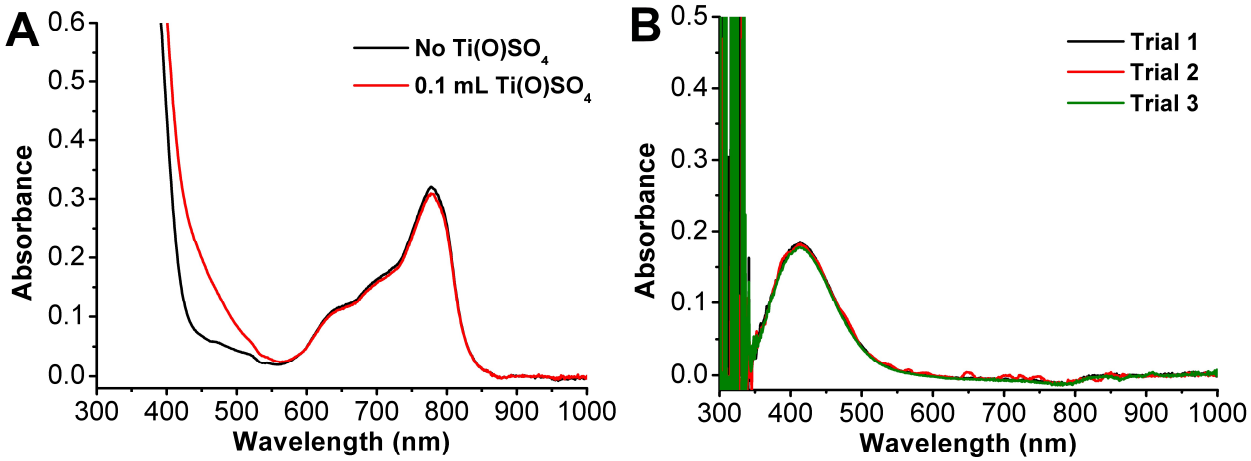

Figure S6.68. H_2O_2 product quantification of ORR by **Ph_2Phen^{2+}** with TFAH after 90 s. (A) UV-vis spectra of catalytic aliquot before (black) and after (red) 0.1 mL of 0.1 M $Ti(O)SO_4$ solution was added. (B) Corrected spectra (red – black trace from A). Conditions: 40 μM **Ph_2Phen^{2+}**, 25 mM TFAH, 1 mM Cp^*_2Fe, 4.05 mM O_2 in MeCN.

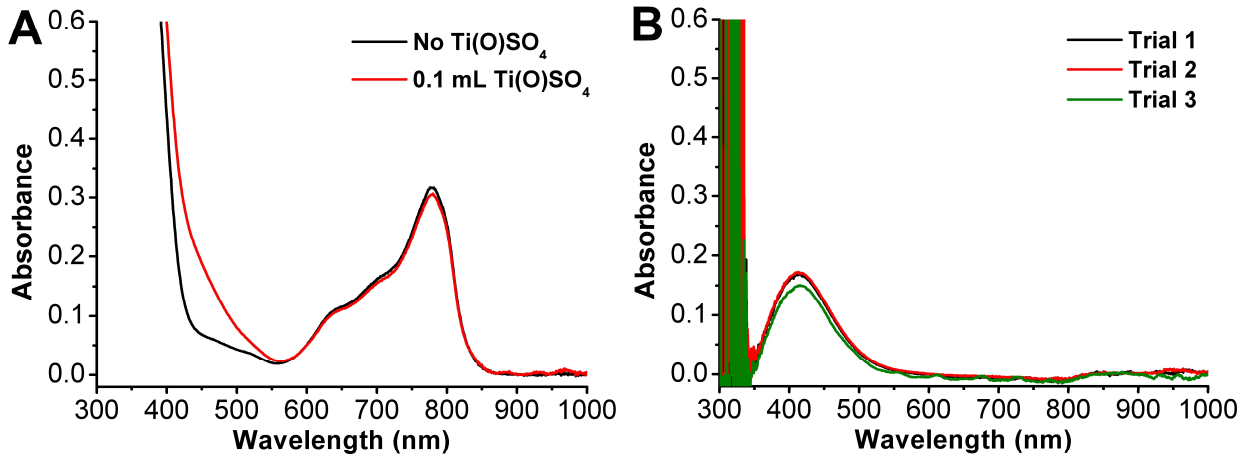

Figure S6.69. H_2O_2 product quantification of ORR by **Ph_2Phen^{2+}** with Cl_3AcOH after 90 s. (A) UV-vis spectra of catalytic aliquot before (black) and after (red) 0.1 mL of 0.1 M $Ti(O)SO_4$ solution was added. (B) Corrected spectra (red – black trace from A). Conditions: 40 μM **Ph_2Phen^{2+}**, 25 mM Cl_3AcOH, 1 mM Cp^*_2Fe, 4.05 mM O_2 in MeCN.

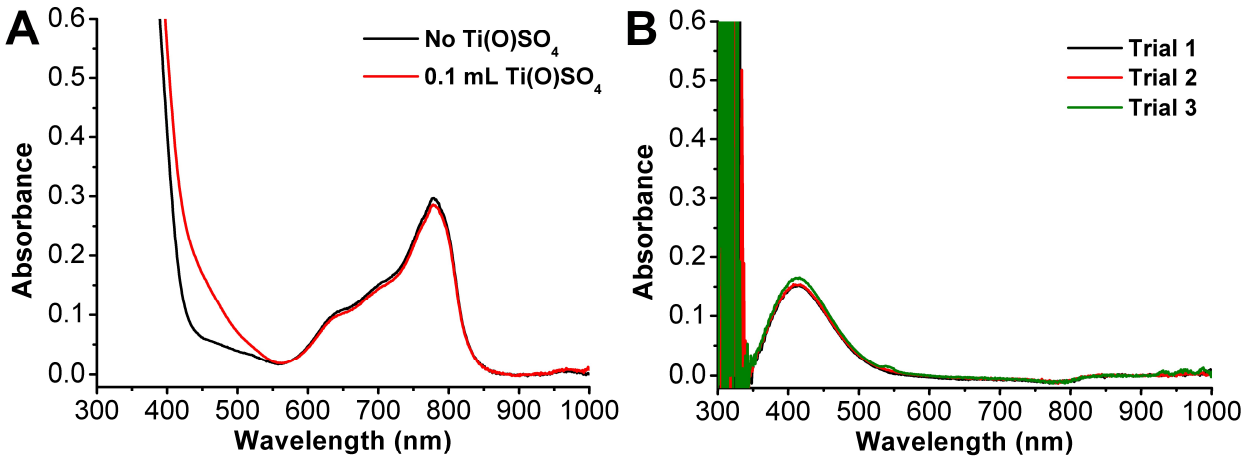

Figure S6.70. H_2O_2 product quantification of ORR by **Ph_2Phen^{2+}** with Cl_2AcOH after 2 min. (A) UV-vis spectra of catalytic aliquot before (black) and after (red) 0.1 mL of 0.1 M $Ti(O)SO_4$ solution was added. (B) Corrected spectra (red – black trace from A). Conditions: 40 μM **Ph_2Phen^{2+}**, 25 mM Cl_2AcOH, 1 mM Cp^*_2Fe, 4.05 mM O_2 in MeCN.

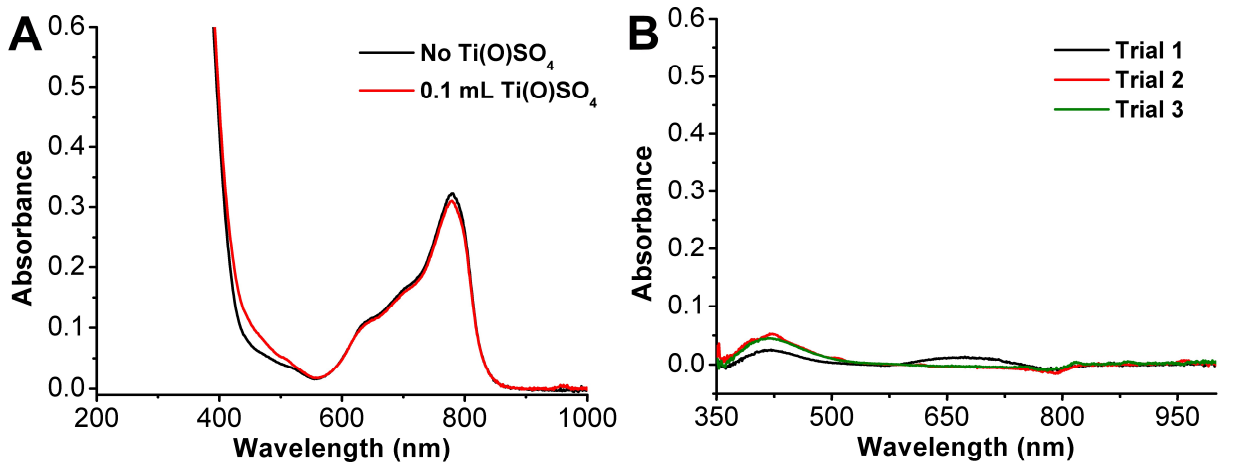

Figure S6.71. H_2O_2 product quantification of ORR by **Ph_2Phen^{2+}** with ClAcOH after 3 min. (A) UV-vis spectra of catalytic aliquot before (black) and after (red) 0.1 mL of 0.1 M $Ti(O)SO_4$ solution was added. (B) Corrected spectra (red – black trace from A). Conditions: 40 μM **Ph_2Phen^{2+}**, 25 mM ClAcOH, 1 mM Cp^*_2Fe, 4.05 mM O_2 in MeCN.

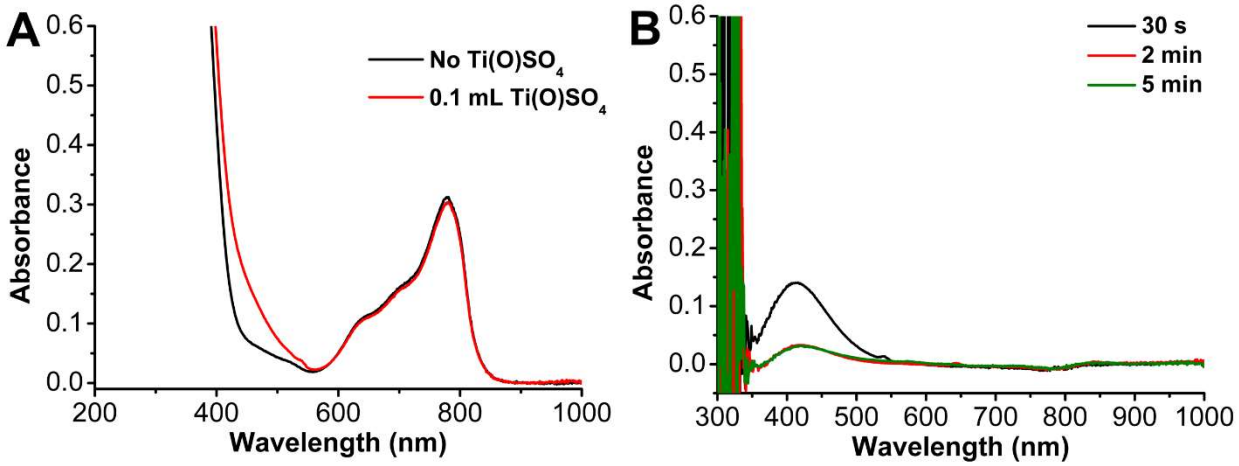

Figure S6.72. H_2O_2 product quantification of ORR by **Ph_2Phen^{2+}** with ClAcOH after 30 s, 2 min, and 5 min. (A) UV-vis spectra of catalytic aliquot before (black) and after (red) 0.1 mL of 0.1 M $Ti(O)SO_4$ solution was added after 30 s. (B) Corrected spectra (red – black trace from A) after 30 s, 2 min, and 5 min. Conditions: 40 μM **Ph_2Phen^{2+}**, 25 mM ClAcOH, 1 mM Cp^*_2Fe, 4.05 mM O_2 in MeCN.

Table S6.3. Summary of ORR selectivity of **Ph_2Phen^{2+}** with ClAcOH at various time points from **Figure S6.73**.[a]

Time (s)	% H_2O_2
30	67.4 ± 5.9
120	20.6 ± 2.8
300	22.0 ± 5.2

[a]40 μM [**Ph_2Phen^{2+}**], 25 mM [ClAcOH], 4.05 mM [O_2], 1 mM [Cp^*_2Fe]

H_2O_2 Stability Control Studies

To determine the stability of H_2O_2 in the presence of **Ph_2Phen^{2+}**, acid, and O_2, control studies were conducted. Generally, solutions containing 80 μM [**Ph_2Phen^{2+}** and 50 mM acid (TFAH, Cl_3AcOH, Cl_2AcOH, or ClAcOH) were sparged with O_2 gas and rapidly mixed in a 1:1 ratio with a N_2 saturated 1.76 mM urea•H_2O_2 solution to a final volume of 4 mL (final concentrations: 40 μM **Ph_2Phen^{2+},** 0.88 mM urea•H_2O_2, 25 mM acid, 4.05 mM O_2). The reactions were allowed to reach completion and 2 mL of the reaction solution was added to 2 mL of water. A UV-vis spectrum was taken before and after the addition of 0.1 mL of 0.1 M $Ti(O)SO_4$ solution and the difference at 408 nm was used to determine the amount of H_2O_2 present ($[H_2O_2]_{detected}$). The % recovery was determined according to **Eq S6.23** from measured $[H_2O_2]_{expected}$ of the H_2O_2 stock solution.

$$\frac{[H_2O_2]_{detected}}{[H_2O_2]_{expected}} \times 100 = \%\ H_2O_2\ recovery \qquad \textbf{(Eq S6.23)}$$

Table S6.4. Summary of H_2O_2 Recovery for Stability Control Studies by **Ph_2Phen^{2+}** with each acid.[a]

	% H_2O_2 Recovered
TFAH	97.6 ± 0.88
Cl_3AcOH	101 ± 5.0
Cl_2AcOH	95.5 ± 1.7
ClAcOH	94.3 ± 2.9

[a] 40 µM [**Ph_2Phen^{2+}**], 25 mM [AH], 4.05 mM [O_2], 0.88 mM [urea•H_2O_2]

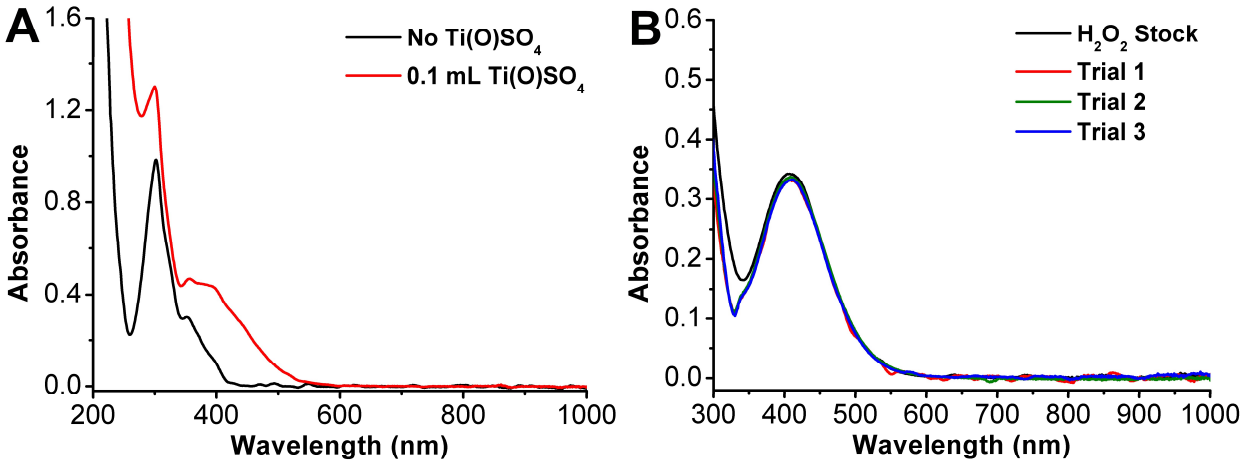

Figure S6.73. Stability test of urea•H_2O_2 in the presence of **Ph_2Phen^{2+}**, TFAH, and O_2 (A) before (black trace) and after (red trace) the addition of 0.1 mL of 0.1 M $Ti(O)SO_4$ to an aliquot. (B) Corrected UV-vis spectra (red – black from A) of each trial after 90 s with the H_2O_2 stock (black). Conditions: 40 µM Ph2Phen2+, 25 mM TFAH, 4.05 mM O2, 0.88 mM urea•H2O2 in MeCN.

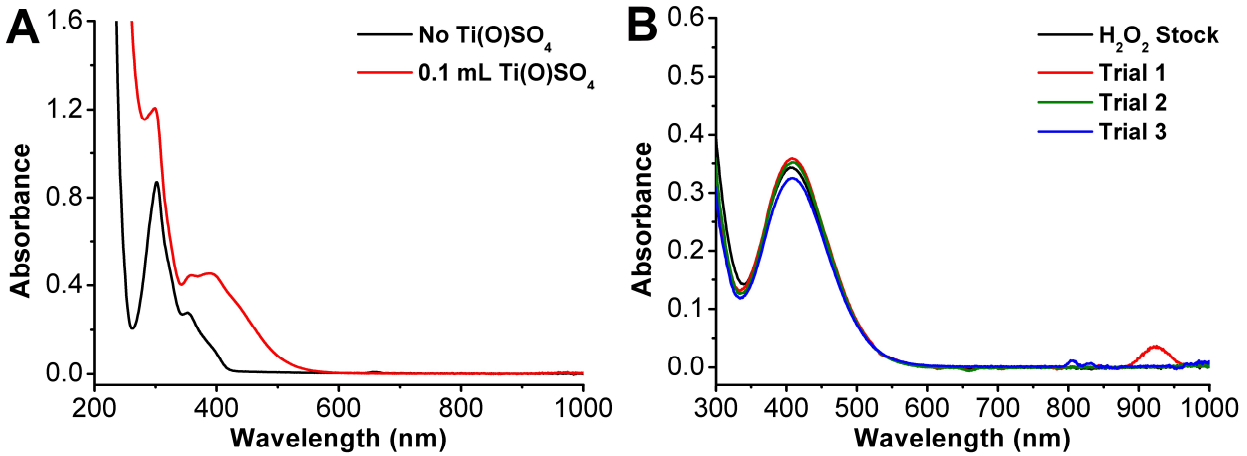

Figure S6.74. Stability test of urea•H_2O_2 in the presence of **Ph_2Phen^{2+}**, Cl_3AcOH, and O_2 (A) before (black trace) and after (red trace) the addition of 0.1 mL of 0.1 M Ti(O)SO4 to an aliquot. (B) Corrected UV-vis spectra (red – black from A) of each trial after 90 s with the H_2O_2 stock (black). Conditions: 40 μM **Ph_2Phen^{2+}**, 25 mM Cl_3AcOH, 4.05 mM O_2, 0.88 mM urea•H_2O_2 in MeCN.

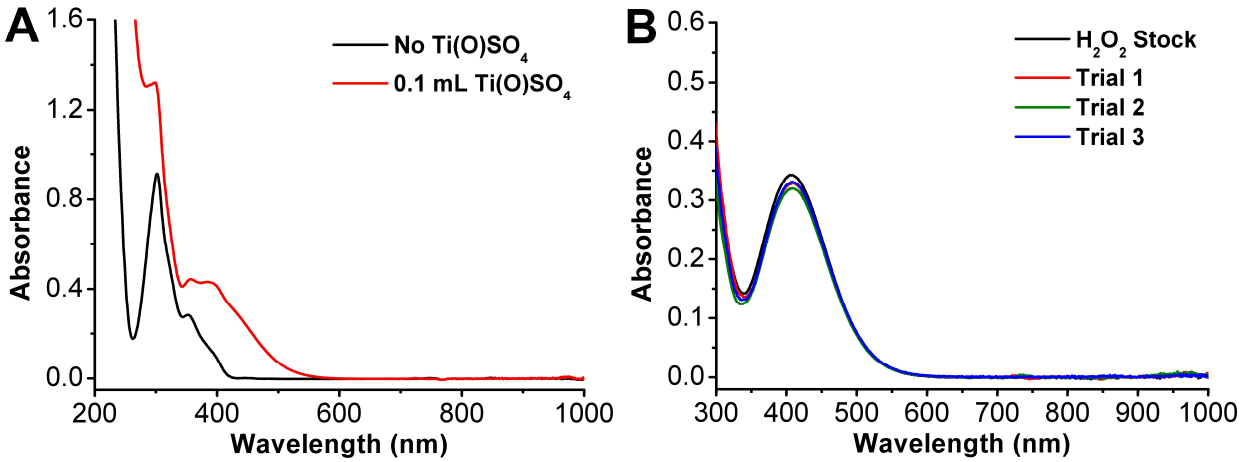

Figure S6.75. Stability test of urea•H_2O_2 in the presence of **Ph_2Phen^{2+}**, Cl_2AcOH, and O_2 (A) before (black trace) and after (red trace) the addition of 0.1 mL of 0.1 M $Ti(O)SO_4$ to an aliquot. (B) Corrected UV-vis spectra (red – black from A) of each trial after 2 min with the H_2O_2 stock (black). Conditions: 40 μM Ph_2Phen^{2+}, 25 mM Cl_2AcOH, 4.05 mM O_2, 0.88 mM urea•H_2O_2 in MeCN.

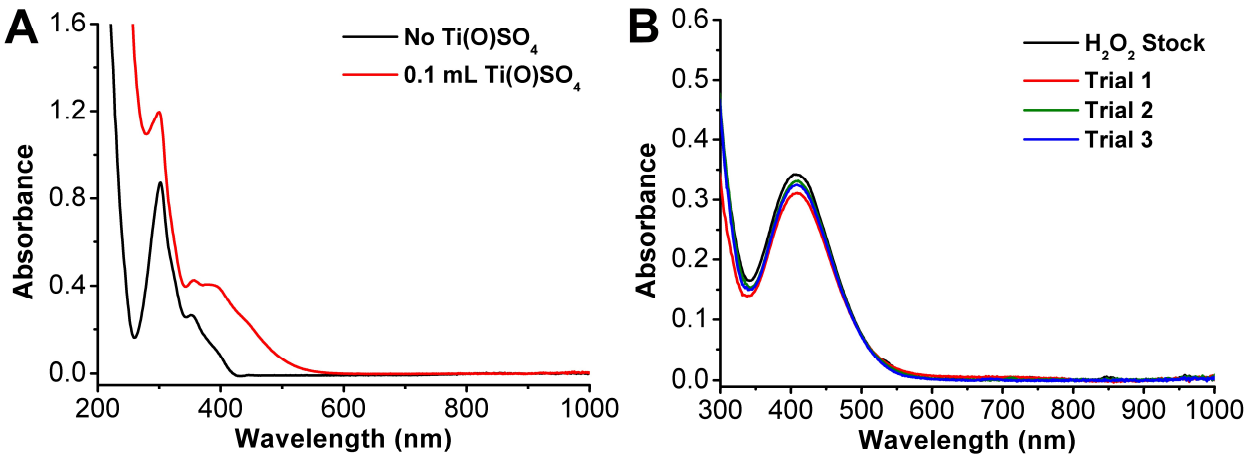

Figure S6.76. Stability test of urea•H_2O_2 in the presence of **Ph_2Phen^{2+}**, ClAcOH, and O2 (A) before (black trace) and after (red trace) the addition of 0.1 mL of 0.1 M $Ti(O)SO_4$ to an aliquot. (B) Corrected UV-vis spectra (red – black from A) of each trial after 3 min with the H_2O_2 stock (black). Conditions: 40 μM Ph_2Phen^{2+}, 25 mM ClAcOH, 4.05 mM O_2, 0.88 mM urea•H_2O_2 in MeCN.

^{1}H-NMR Studies

^{1}H-NMR studies were conducted in order to observe reactivity of reduced **Ph_2Phen^{2+}** with O_2. To increase solubility of Ph_2Phen^{2+}, the Br^- counterions were exchanged for PF_6^- (**$Ph_2Phen(PF_6)_2$**) as described above. Cp^*_2Fe was used as a chemical reductant in solution and added in a stoichiometric amount. NMR samples were made in a N_2-filled glovebox. Samples were exposed to air for ~1 h prior to spectra being taken.

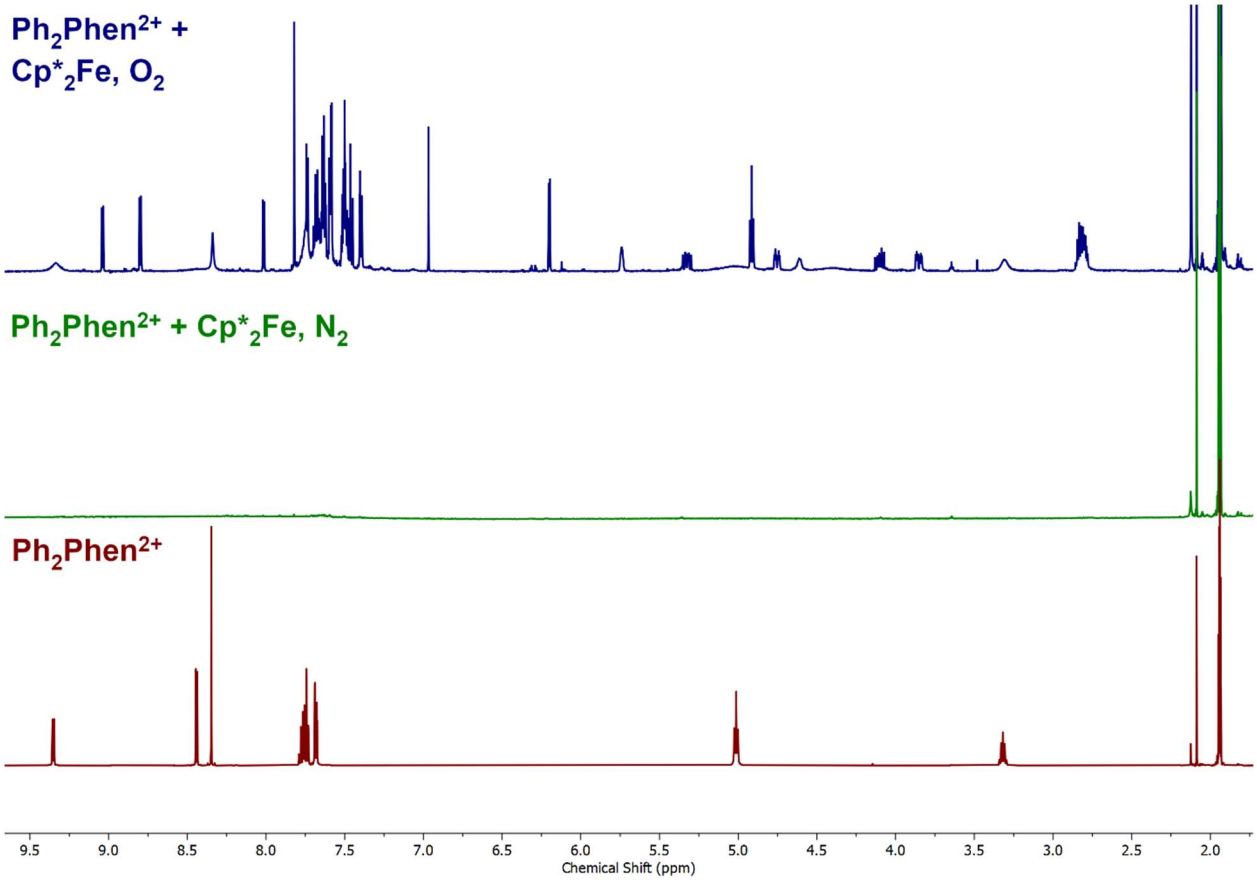

Figure S6.77. ^{1}H NMR spectra of **$Ph_2Phen(PF_6)_2$** (red) in the presence of Cp^*_2Fe under N_2 (green) and exposed to air (blue). Conditions: 3.2 mM [**$Ph_2Phen(PF_6)_2$**], 4 mM [Cp^*_2Fe]; MeCN-d_3; Varian 600 MHz.

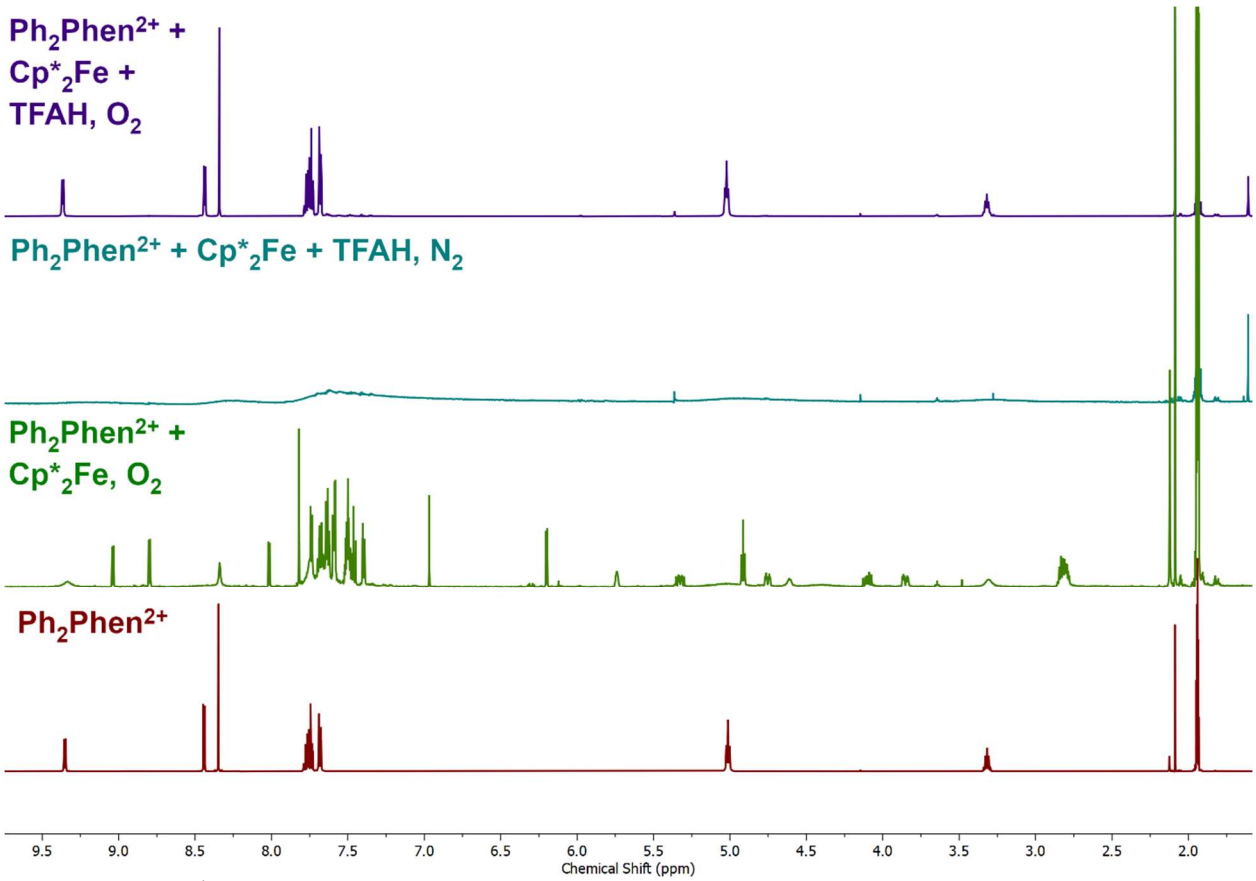

Figure S6.78. ^{1}H NMR spectra of **$Ph_2Phen(PF_6)_2$** (red) in the presence of Cp^*_2Fe exposed to air (green) and TFAH under N_2 (teal) and exposed to air (purple). Conditions: 3.2 mM [**$Ph_2Phen(PF_6)_2$**], 4 mM [Cp^*_2Fe], 4 mM [TFAH]; MeCN-d_3; Varian 600 MHz.

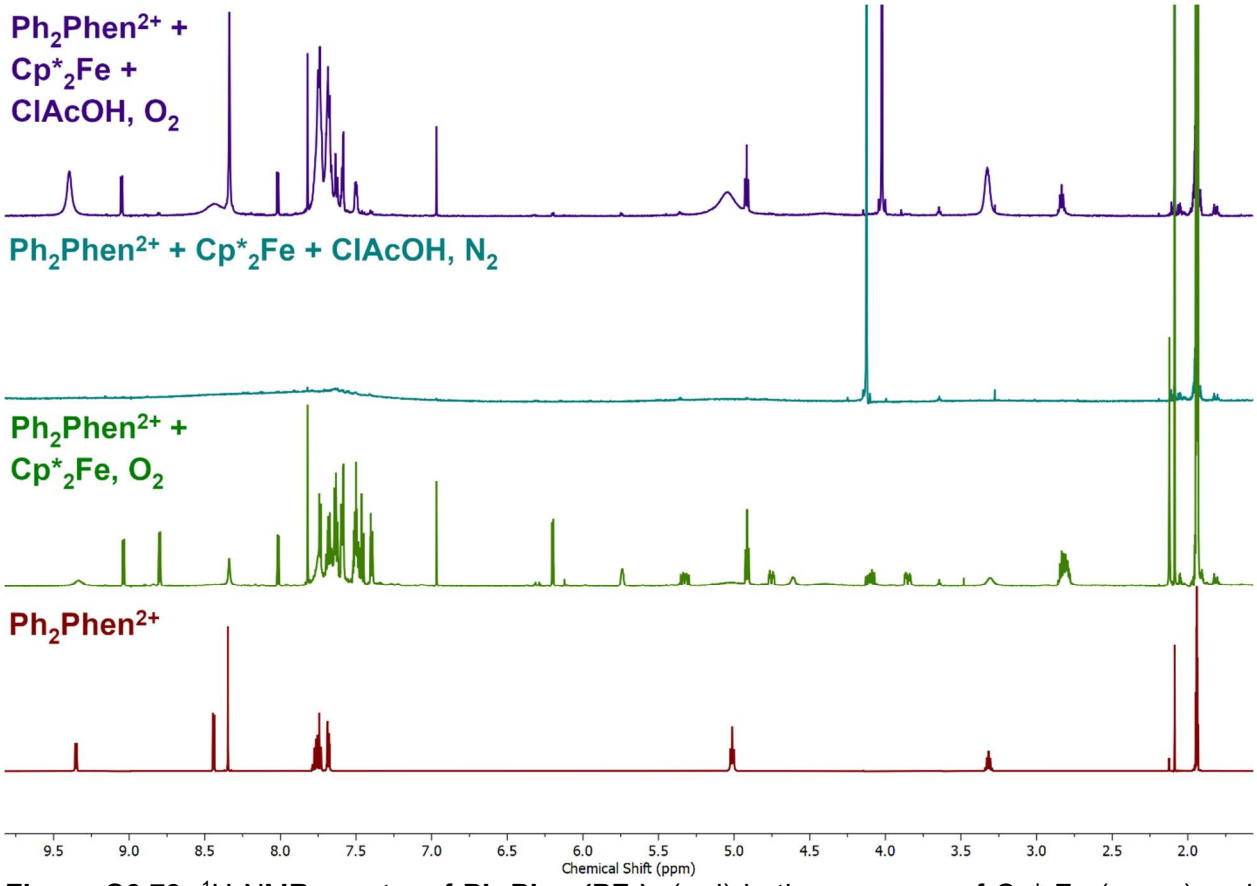

Figure S6.79. ^{1}H NMR spectra of **$Ph_2Phen(PF_6)_2$** (red) in the presence of Cp^*_2Fe (green) and ClAcOH under N_2 (teal) and exposed to air (purple). Conditions: 3.2 mM [**$Ph_2Phen(PF_6)_2$**], 4 mM [Cp^*_2Fe], 4 mM [ClAcOH]; MeCN-d_3; Varian 600 MHz.

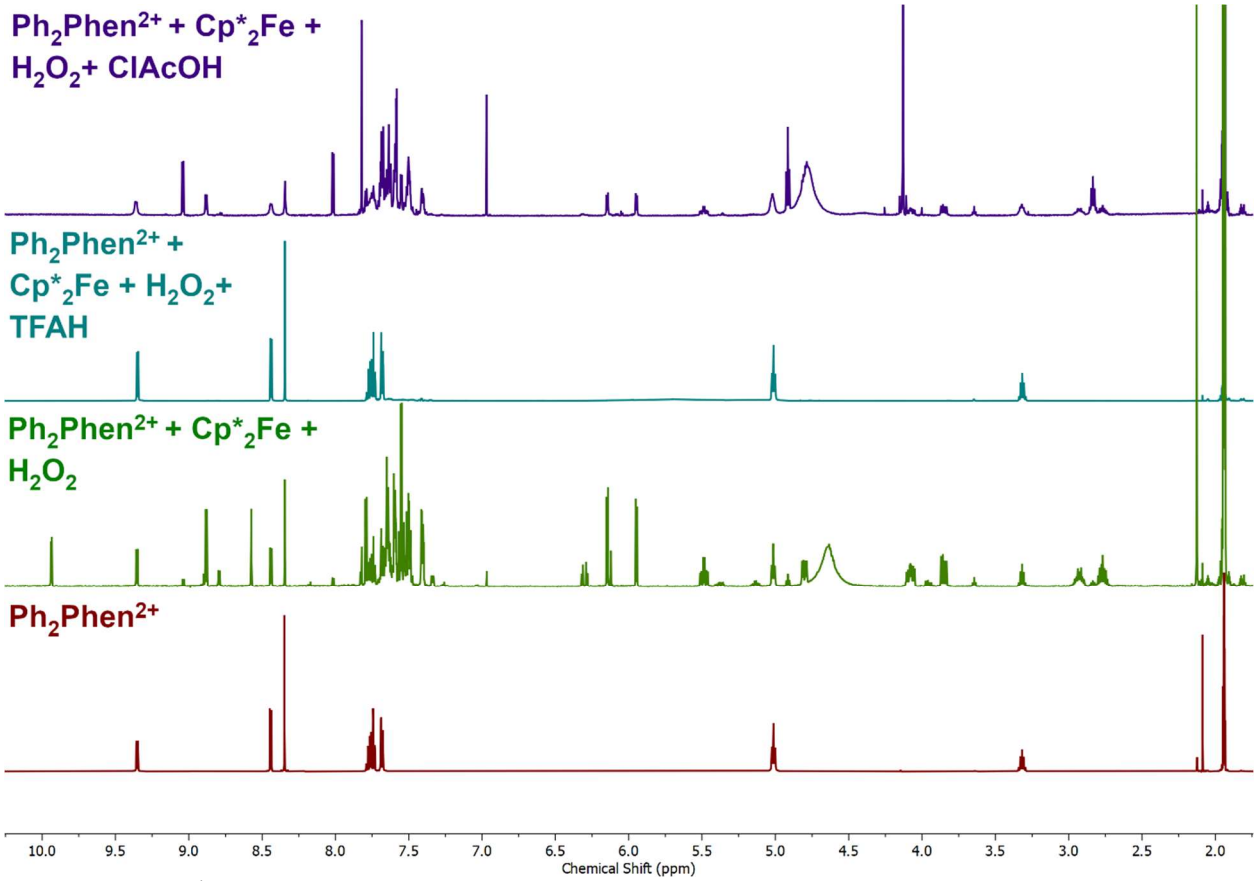

Figure S6.80. ^{1}H-NMR spectra of **$Ph_2Phen(PF_6)_2$** (red) in the presence of Cp^*_2Fe and urea•H_2O_2 (green) with TFAH (teal) and ClAcOH (purple) under N_2 atmosphere. Conditions: 3.7 mM [**$Ph_2Phen(PF_6)_2$**], 4 mM [Cp^*_2Fe] if present, 5.3 mM [urea•H_2O_2] if present, 4 mM [TFAH] if present, 5.3 mM [ClAcOH] if present; N_2 atmosphere; MeCN-d_3; Varian 600 MHz.

X-Ray Crystallographic Details

An orange, block shaped crystal of **Ph_2Phen^{2+}** measuring 0.035×0.045×0.079 mm was coated with Paratone oil and mounted on a MiTeGen micromount. Data for **Ph_2Phen^{2+}** were measured on a Bruker D8 VENTURE dual wavelength Mo/Cu Kappa four-circle diffractometer equipped with a PHOTON III detector and an Incoatec IμS 3.0 microfocus sealed X-ray tube (Mo K_α, λ=0.71073 Å) using a HELIOS double bounce multilayer mirror as monochromator. The crystal temperature was controlled with an Oxford Cryostream 800 low temperature device. Data collection and processing were done within the Bruker APEX5 software suite.[41] All data were integrated with the Bruker SAINT 8.40B software using a narrow-frame algorithm. Data were corrected for absorption effects using a Multi-Scan method (SADABS).The structure was solved by direct methods with SHELXT[42] and refined by full-matrix least-squares methods against F^2 using SHELXL[43] within OLEX2.[42] All non-hydrogen atoms were refined with anisotropically. Hydrogen atoms were placed in geometrically calculated positions with U_{iso} = 1.2U_{equiv} of the parent atom (1.5U_{equiv} for methyl). This report and the CIF file were generated using FinalCif.[44]

*Refinement details for **Ph_2Phen^{2+}***

The relative occupancy of the disordered atoms was freely refined. No constraints or restraints were used.

Table S6.5. Crystal data and structure refinement for **Ph_2Phen^{2+}**

CCDC number	2346924
Empirical formula	$C_{27}H_{22}Br_2N_2$
Formula weight	534.28
Temperature [K]	100.00
Wavelength [Å]	0.71073
Crystal size [mm^3]	0.035×0.045×0.079
Crystal habit	orange block
Crystal system	triclinic
Space group	$P\overline{1}$ (2)
a [Å]	8.1468(4)
b [Å]	11.9512(7)
c [Å]	13.4202(8)
α [°]	64.647(2)
β [°]	75.441(2)
γ [°]	73.068(2)
Volume [$Å^3$]	1117.42(11)
Z	2
ρ_{calc} [gcm^{-3}]	1.588
μ [mm^{-1}]	3.645
F(000)	536
2θ range [°]	4.05 to 54.95 (0.77 Å)
Index ranges	−10 ≤ h ≤ 9 −15 ≤ k ≤ 15 −17 ≤ l ≤ 17
Reflections collected	32293
Independent reflections	5129 [R_{int} = 0.0777]
Data / Restraints / Parameters	5129 / 0 / 293
Goodness-of-fit on F^2	1.032
Final *R* indexes [$I \geq 2\sigma(I)$]	R_1 = 0.0357 wR_2 = 0.0777
Final *R* indexes [all data]	R_1 = 0.0536 wR_2 = 0.0854
Largest peak/hole [$eÅ^{-3}$]	0.83/−0.49

Computational Methods

Geometry optimization was done with the Gaussian 16 package[45] at the B3LYP-D3(BJ)/def2-TZVP level[46-53] with a complete structural model. Dispersion and bulk solvent effects (acetonitrile = MeCN; ε = 35.688) were accounted for at the optimization stage, by using Grimme's D3 parameter set with Becke-Johnson (BJ) damping[52,53] and the SMD continuum model,[54] respectively. The stationary points and their nature as minima (no imaginary frequencies) were characterized by vibrational analysis using the IGRRHO approach as implemented by default in the software package, which also produced enthalpy (H), entropy (S) and Gibbs energy (G) data at 298.15 K. The minima connected by a given transition state were determined by perturbing the transition states along the TS coordinate and optimizing to the nearest minimum. Free energies were corrected (ΔG_{qh}) to account for concentration effects and for errors associated with the harmonic oscillator approximation. Thus, according to Truhlars's quasi-harmonic approximation for vibrational entropy and enthalpy, all vibrational frequencies below 100 cm^{-1} were set to this value.[55] These anharmonic and concentration corrections were calculated with the Goodvibes code.[56] Concentrations were set at 0.001 M for all species unless otherwise indicated, 0.004 M for O_2, 0.500 M for acid, and 18.9 M for MeCN. Single point calculations for refining energy differences were completed with Orca 5.0[57] at the DLPNO-CCSD(T1)/cc-pVTZ level.[51,58,59] Evaluation of spin density was done at the ωB97M-D4/def2-TZVPPD level.[50,51,60-64] The stability of the wavefunction and spin contamination were studied at the triple-zeta level of theory. Reduction potentials from computational data were obtained according to our previous methodology by using the calculated free energy of reduction of the species of interest by $[phenazine]^{-}$, corrected to the experimental potential of phenazine reduction vs Fc^{+}/Fc.[65]

6.7. References

(1) Pegis, M. L.; Wise, C. F.; Martin, D. J.; Mayer, J. M. Oxygen Reduction by Homogeneous Molecular Catalysts and Electrocatalysts. *Chem. Rev.* **2018**, *118* (5), 2340-2391. DOI: 10.1021/acs.chemrev.7b00542.

(2) Machan, C. W. Advances in the Molecular Catalysis of Dioxygen Reduction. *ACS Catal.* **2020**, *10* (4), 2640-2655. DOI: 10.1021/acscatal.9b04477.

(3) Cook, E. N.; Machan, C. W. Homogeneous catalysis of dioxygen reduction by molecular Mn complexes. *Chem. Commun.* **2022**, *58* (84), 11746-11761, 10.1039/D2CC04628H. DOI: 10.1039/D2CC04628H.

(4) Campos-Martin, J. M.; Blanco-Brieva, G.; Fierro, J. L. G. Hydrogen peroxide synthesis: An outlook beyond the anthraquinone process. *Angew. Chem. Int. Ed.* **2006**, *45* (42), 6962-6984. DOI: 10.1002/anie.200503779.

(5) Campbell, A. N.; Stahl, S. S. Overcoming the “Oxidant Problem”: Strategies to Use O2 as the Oxidant in Organometallic C–H Oxidation Reactions Catalyzed by Pd (and Cu). *Acc. Chem. Res.* **2012**, *45* (6), 851-863. DOI: 10.1021/ar2002045.

(6) Wang, X.; Li, Z.; Qu, Y.; Yuan, T.; Wang, W.; Wu, Y.; Li, Y. Review of Metal Catalysts for Oxygen Reduction Reaction: From Nanoscale Engineering to Atomic Design. *Chem* **2019**, *5* (6), 1486-1511. DOI: 10.1016/j.chempr.2019.03.002.

(7) Blomberg, M. R. A. Mechanism of Oxygen Reduction in Cytochrome c Oxidase and the Role of the Active Site Tyrosine. *Biochem.* **2016**, *55* (3), 489-500. DOI: 10.1021/acs.biochem.5b01205.

(8) Denisov, I. G.; Makris, T. M.; Sligar, S. G.; Schlichting, I. Structure and Chemistry of Cytochrome P450. *Chem. Rev.* **2005**, *105* (6), 2253-2278. DOI: 10.1021/cr0307143.

(9) Yee, G. M.; Tolman, W. B. Transition Metal Complexes and the Activation of Dioxygen. In *Sustaining Life on Planet Earth: Metalloenzymes Mastering Dioxygen and Other Chewy Gases*, Kroneck, P. M. H., Sosa Torres, M. E. Eds.; Springer International Publishing, 2015; pp 131-204.

(10) Nichols, A. W.; Cook, E. N.; Gan, Y. J.; Miedaner, P. R.; Dressel, J. M.; Dickie, D. A.; Shafaat, H. S.; Machan, C. W. Pendent Relay Enhances H_2O_2 Selectivity during Dioxygen Reduction Mediated by Bipyridine-Based Co–N_2O_2 Complexes. *J. Am. Chem. Soc.* **2021**, *143* (33), 13065-13073. DOI: 10.1021/jacs.1c03381.

(11) Cook, E. N.; Courter, I. M.; Dickie, D. A.; Machan, C. W. Controlling product selectivity during dioxygen reduction with Mn complexes using pendent proton donor relays and added base. *Chem. Sci.* **2024**, 10.1039/D3SC02611F. DOI: 10.1039/D3SC02611F.

(12) Carver, C. T.; Matson, B. D.; Mayer, J. M. Electrocatalytic Oxygen Reduction by Iron Tetra-arylporphyrins Bearing Pendant Proton Relays. *J. Am. Chem. Soc.* **2012**, *134* (12), 5444-5447. DOI: 10.1021/ja211987f.

(13) Bhunia, S.; Ghatak, A.; Rana, A.; Dey, A. Amine Groups in the Second Sphere of Iron Porphyrins Allow for Higher and Selective 4e–/4H+ Oxygen Reduction Rates at Lower Overpotentials. *J. Am. Chem. Soc.* **2023**, *145* (6), 3812-3825. DOI: 10.1021/jacs.2c13552.

(14) Pegis, M. L.; McKeown, B. A.; Kumar, N.; Lang, K.; Wasylenko, D. J.; Zhang, X. P.; Raugei, S.; Mayer, J. M. Homogenous electrocatalytic oxygen reduction rates correlate with reaction overpotential in acidic organic solutions. *ACS Cent. Sci.* **2016**, *2* (11), 850-856. DOI: 10.1021/acscentsci.6b00261.

(15) Andrieux, C. P.; Hapiot, P.; Sa Véant, J. M. Electron transfer coupling of diffusional pathways. Homogeneous redox catalysis of dioxygen reduction by the methylviologen cation radical in acidic dimethylsulfoxide. *J. Electroanal. Chem. Interf. Electrochem.* **1985**, *189* (1), 121-133. DOI: 10.1016/0368-1874(85)85630-6.

(16) Audebert, P.; Hapiot, P. Preparation and electrochemistry of several substituted 9-(4-R-phenyl)-N-methylacridinium salts.: Kinetic analysis of the O2 catalytic reduction in acidic dimethylsulfoxide and in hydrophobic Nafion® gels. *J. Electroanal. Chem.* **1993**, *361* (1), 177-183. DOI: 10.1016/0022-0728(93)87052-W.

(17) Karimi, M.; Borthakur, R.; Dorsey, C. L.; Chen, C.-H.; Lajeune, S.; Gabbaï, F. P. Bifunctional Carbenium Dications as Metal-Free Catalysts for the Reduction of Oxygen. *J. Am. Chem. Soc.* **2020**, *142* (32), 13651-13656. DOI: 10.1021/jacs.0c04841.

(18) Tanjedrew, N.; Thammanatpong, K.; Surawatanawong, P.; Chakthranont, P.; Chantarojsiri, T.; Unjarern, T.; Kiatisevi, S. Tunable Metal-free Imidazole-Benzimidazole Electrocatalysts for Oxygen Reduction in Aqueous Solutions. *Chem. Eur. J.* **2023**, *30* (5), e202302854. DOI: 10.1002/chem.202302854.

(19) Dai, L.; Xue, Y.; Qu, L.; Choi, H.-J.; Baek, J.-B. Metal-Free Catalysts for Oxygen Reduction Reaction. *Chem. Rev.* **2015**, *115* (11), 4823-4892. DOI: 10.1021/cr5003563.

(20) Zhai, Q.; Pan, Y.; Dai, L. Carbon-Based Metal-Free Electrocatalysts: Past, Present, and Future. *Acc. Mater. Res.* **2021**, *2* (12), 1239-1250. DOI: 10.1021/accountsmr.1c00190.

(21) Huang, X.; Shen, T.; Sun, S.; Hou, Y. Synergistic Modulation of Carbon-Based, Precious-Metal-Free Electrocatalysts for Oxygen Reduction Reaction. *ACS Appl. Mater. Interfaces* **2021**, *13* (6), 6989-7003. DOI: 10.1021/acsami.0c19922.

(22) Ma, R.; Lin, G.; Zhou, Y.; Liu, Q.; Zhang, T.; Shan, G.; Yang, M.; Wang, J. A review of oxygen reduction mechanisms for metal-free carbon-based electrocatalysts. *Npj Comput. Mater.* **2019**, *5* (1), 78. DOI: 10.1038/s41524-019-0210-3.

(23) Cook, E. N.; Davis, A. E.; Hilinski, M. K.; Machan, C. W. Metal-Free Homogeneous O2 Reduction by an Iminium-Based Electrocatalyst. *J. Am. Chem. Soc.* **2024**. DOI: 10.1021/jacs.3c14549.

(24) Marshall-Roth, T.; Libretto, N. J.; Wrobel, A. T.; Anderton, K. J.; Pegis, M. L.; Ricke, N. D.; Voorhis, T. V.; Miller, J. T.; Surendranath, Y. A pyridinic Fe-N4 macrocycle models the active sites in Fe/N-doped carbon electrocatalysts. *Nat. Commun.* **2020**, *11* (1), 5283. DOI: 10.1038/s41467-020-18969-6.

(25) Costentin, C.; Savéant, J.-M. Coupling of Electrode Electron Transfers with Homogeneous Chemical Reactions. In *Elements of Molecular and Biomolecular Electrochemistry*, 2019; pp 81-181.

(26) McCarthy, B. D.; Martin, D. J.; Rountree, E. S.; Ullman, A. C.; Dempsey, J. L. Electrochemical reduction of brønsted acids by glassy carbon in acetonitrile-implications for electrocatalytic hydrogen evolution. *Inorg. Chem.* **2014**, *53* (16), 8350-8361. DOI: 10.1021/ic500770k.

(27) Harraz, D. M.; Weng, S.; Surendranath, Y. Electrochemically Quantifying Oxygen Reduction Selectivity in Nonaqueous Electrolytes. *ACS Catal.* **2023**, *13* (2), 1462-1469. DOI: 10.1021/acscatal.2c04564.

(28) Matsubara, Y. Unified Benchmarking of Electrocatalysts in Noninnocent Second Coordination Spheres for CO2 Reduction. *ACS Energy Lett.* **2019**, *4* (8), 1999-2004. DOI: 10.1021/acsenergylett.9b01180.

(29) Kütt, A.; Tshepelevitsh, S.; Saame, J.; Lõkov, M.; Kaljurand, I.; Selberg, S.; Leito, I. Strengths of Acids in Acetonitrile. *Eur. J. Org. Chem.* **2021**, *2021* (9), 1407-1419. DOI: 10.1002/ejoc.202001649.

(30) Sathrum, A. J.; Kubiak, C. P. Kinetics and Limiting Current Densities of Homogeneous and Heterogeneous Electrocatalysts. *J. Phys. Chem. Lett.* **2011**, *2* (18), 2372-2379. DOI: 10.1021/jz2008227.

(31) Hooe, S. L.; Machan, C. W. Dioxygen Reduction to Hydrogen Peroxide by a Molecular Mn Complex: Mechanistic Divergence between Homogeneous and Heterogeneous Reductants. *J. Am. Chem. Soc.* **2019**, *141* (10), 4379-4387. DOI: 10.1021/jacs.8b13373.

(32) Cook, E. N.; Dickie, D. A.; Machan, C. W. Catalytic Reduction of Dioxygen to Water by a Bioinspired Non-Heme Iron Complex via a 2+2 Mechanism. *J. Am. Chem. Soc.* **2021**, *143* (40), 16411-16418. DOI: 10.1021/jacs.1c04572.

(33) Cook, E. N.; Hooe, S. L.; Dickie, D. A.; Machan, C. W. Homogeneous Catalytic Reduction of O2 to H2O by a Terpyridine-Based FeN3O Complex. *Inorg. Chem.* **2022**, *61* (22), 8387-8392. DOI: 10.1021/acs.inorgchem.2c00524.

(34) Cook, E. N.; Courter, I. M.; Dickie, D. A.; Machan, C. W. Controlling product selectivity during dioxygen reduction with Mn complexes using pendent proton donor relays and added base. *Chem. Sci.* **2024**, *15* (12), 4478-4488, 10.1039/D3SC02611F. DOI: 10.1039/D3SC02611F.

(35) Burés, J. A simple graphical method to determine the order in catalyst. *Angew. Chem. Int. Ed.* **2016**, *55* (6), 2028-2031. DOI: 10.1002/anie.201508983.

(36) F. van Strijdonck, G. P.; Boele, M. D. K.; Kamer, P. C. J.; de Vries, J. G.; van Leeuwen, P. W. N. M. Fast Palladium Catalyzed Arylation of Alkenes Using Bulky Monodentate Phosphorus Ligands. *Eur. J. Inorg. Chem.* **1999**, *1999* (7), 1073-1076. DOI: 10.1002/(sici)1099-0682(199907)1999:7<1073::aid-ejic1073>3.3.co;2-k.

(37) Li, Q.; Batchelor-McAuley, C.; Lawrence, N. S.; Hartshorne, R. S.; Compton, R. G. Anomalous solubility of oxygen in acetonitrile/water mixture containing tetra-n-butylammonium perchlorate supporting electrolyte; the solubility and diffusion coefficient of oxygen in anhydrous acetonitrile and aqueous mixtures. *J. Electroanal. Chem.* **2013**, *688*, 328-335. DOI: 10.1016/j.jelechem.2012.07.039.

(38) Hooe, S. L.; Rheingold, A. L.; Machan, C. W. Electrocatalytic Reduction of Dioxygen to Hydrogen Peroxide by a Molecular Manganese Complex with a Bipyridine-Containing Schiff Base Ligand. *J. Am. Chem. Soc.* **2018**, *140* (9), 3232-3241. DOI: 10.1021/jacs.7b09027.

(39) Zhou, R.; Zheng, Y.; Jaroniec, M.; Qiao, S. Z. Determination of the Electron Transfer Number for the Oxygen Reduction Reaction: From Theory to Experiment. *ACS Catal.* **2016**, *6* (7), 4720-4728. DOI: 10.1021/acscatal.6b01581.

(40) Wang, Y. H.; Pegis, M. L.; Mayer, J. M.; Stahl, S. S. Molecular Cobalt Catalysts for O2 Reduction: Low-Overpotential Production of H2O2 and Comparison with Iron-Based Catalysts. *J. Am. Chem. Soc.* **2017**, *139* (46), 16458-16461. DOI: 10.1021/jacs.7b09089.

(41) *Saint; APEX5*; Bruker AXS Inc.: Madison, Wisconsin, USA, 2019.

(42) Sheldrick, G. M. SHELXT - Integrated space-group and crystal-structure determination. *Acta Cryst.* **2015**, *71* (1), 3-8. DOI: 10.1107/S2053273314026370.

(43) Sheldrick, G. Crystal structure refinement with SHELXL. *Acta Cryst. C* **2015**, *71* (1), 3-8. DOI: doi:10.1107/S2053229614024218.

(44) Kratzert, D. *FinalCif*. https://dkratzert.de/finalcif.html

(45) *Gaussian 16, Revision B.01*; Gaussian, Inc.: Wallingford CT, 2016.

(46) Becke, A. D. Density-functional thermochemistry. III. The role of exact exchange. *J. Chem. Phys.* **1993**, *98* (7), 5648-5652. DOI: 10.1063/1.464913.

(47) Lee, C.; Yang, W.; Parr, R. G. Development of the Colle-Salvetti correlation-energy formula into a functional of the electron density. *Phys. Rev. B* **1988**, *37* (2), 785-789.

(48) Vosko, S. H.; Wilk, L.; Nusair, M. Accurate spin-dependent electron liquid correlation energies for local spin density calculations: a critical analysis. *Can. J. Phys.* **1980**, *58* (8), 1200-1211. DOI: 10.1139/p80-159.

(49) Stephen, P. J.; Devlin, F. J.; Chabalowski, C. F.; Frisch, M. J. Ab Initio Calculation of Vibrational Absorption and Circular Dichroism Spectra Using Density Functional Force Fields. *J. Phys. Chem.* **1994**, *98* (45), 11623-11627.

(50) Weigend, F.; Ahlrichs, R. Balanced basis sets of split valence, triple zeta valence and quadruple zeta valence quality for H to Rn: Design and assessment of accuracy. *Phys. Chem. Chem. Phys.* **2005**, *7* (18), 3297-3305. DOI: 10.1039/b508541a.

(51) Weigend, F. Accurate Coulomb-fitting basis sets for H to Rn. *Phys. Chem. Chem. Phys.* **2006**, *8* (9), 1057-1065. DOI: 10.1039/b515623h.

(52) Grimme, S.; Antony, J.; Ehrlich, S.; Krieg, H. A consistent and accurate ab initio parametrization of density functional dispersion correction (DFT-D) for the 94 elements H-Pu. *J. Chem. Phys.* **2010**, *132* (15), 154104-154104. DOI: 10.1063/1.3382344.

(53) Grimme, S.; Ehrlich, S.; Goerigk, L. Effect of the damping function in dispersion corrected density functional theory. *J. Comput. Chem.* **2011**, *32* (7), 1456-1465. DOI: 10.1002/jcc.21759.

(54) Marenich, A. V.; Cramer, C. J.; Truhlar, D. G. Universal solvation model based on solute electron density and on a continuum model of the solvent defined by the bulk dielectric constant and atomic surface tensions. *J. Phys. Chem. B* **2009**, *113* (18), 6378-6396. DOI: 10.1021/jp810292n.

(55) Ribeiro, R. F.; Marenich, A. V.; Cramer, C. J.; Truhlar, D. G. Use of solution-phase vibrational frequencies in continuum models for the free energy of solvation. *J. Phys. Chem. B* **2011**, *115* (49), 14556-14562. DOI: 10.1021/jp205508z.

(56) *Goodvibes v.3.0.1*; 2019.

(57) Neese, F. Software update: The ORCA program system—Version 5.0. *WIREs Computational Molecular Science* **2022**, *12* (5), e1606. DOI: 10.1002/wcms.1606.

(58) Dunning, T. H., Jr. Gaussian basis sets for use in correlated molecular calculations. I. The atoms boron through neon and hydrogen. *J. Chem. Phys.* **1989**, *90* (2), 1007-1023. DOI: 10.1063/1.456153.

(59) Weigend, F.; Köhn, A.; Hättig, C. Efficient use of the correlation consistent basis sets in resolution of the identity MP2 calculations. *J. Chem. Phys.* **2002**, *116* (8), 3175-3183. DOI: 10.1063/1.1445115.

(60) Mardirossian, N.; Head-Gordon, M. ωB97M-V: A combinatorially optimized, range-separated hybrid, meta-GGA density functional with VV10 nonlocal correlation. *J. Chem. Phys.* **2016**, *144* (21), 214110. DOI: 10.1063/1.4952647.

(61) Hellweg, A.; Hättig, C.; Höfener, S.; Klopper, W. Optimized accurate auxiliary basis sets for RI-MP2 and RI-CC2 calculations for the atoms Rb to Rn. *Theor. Chem. Acc.* **2007**, *117* (4), 587-597. DOI: 10.1007/s00214-007-0250-5.

(62) Caldeweyher, E.; Bannwarth, C.; Grimme, S. Extension of the D3 dispersion coefficient model. *J. Chem. Phys.* **2017**, *147* (3), 034112. DOI: 10.1063/1.4993215.

(63) Caldeweyher, E.; Ehlert, S.; Hansen, A.; Neugebauer, H.; Spicher, S.; Bannwarth, C.; Grimme, S. A generally applicable atomic-charge dependent London dispersion correction. *J. Chem. Phys.* **2019**, *150* (15), 154122. DOI: 10.1063/1.5090222

(64) Najibi, A.; Goerigk, L. DFT-D4 counterparts of leading meta-generalized-gradient approximation and hybrid density functionals for energetics and geometries. *J. Comput. Chem.* **2020**, *41* (30), 2562-2572. DOI: 10.1002/jcc.26411.

(65) Moreno, J. J.; Hooe, S. L.; Machan, C. W. DFT Study on the Electrocatalytic Reduction of CO2 to CO by a Molecular Chromium Complex. *Inorg. Chem.* **2021**, *60* (6), 3635-3650. DOI: 10.1021/acs.inorgchem.0c03136.

Chapter 7:

Summary and Outlook

7.1. Overview and Extensions of Completed Research

This thesis describes a number of studies that have investigated homogeneous catalytic ORR by varying supporting ligand framework, transition metal center, and utilizing metal-free organocatalysts. Both Fe-based systems with N_3O ligand frameworks reported were found to catalytically reduce O_2 to H_2O via a 2+2 mechanism, where H_2O_2 was a discrete intermediate during catalysis. In the Mn-based systems, the effect of incorporating a pendent proton relay was studied. It was found that the hydrogen-bonding network suppressed catalysis under certain conditions but shifted selectivity to produce higher amounts of H_2O_2 under all conditions. We also found that the pK_a of the Mn-H_2O_2 intermediate was crucial in determining accessible reaction pathway. Finally, using metal-free organic molecules was found to be an efficient strategy for reducing O_2 to either H_2O or H_2O_2. This work has provided a mechanistic understanding of understudied catalytic systems for the ORR, which will contribute to the ongoing work to develop sustainable and efficient catalysts for the reduction of O_2.

7.1.1. Non-Porphyrinic Iron-Based ORR

Non-heme Fe-based systems remain understudied relative to heme-based variants, providing a continuing opportunity for new fundamental understanding of how to make better ORR catalysts during the development of these systems. Synthetic systems that activate and reduce O_2 can also provide insight into the reactivity of non-heme cofactors found in nature. In the long-term, improved knowledge of the underlying structure-function relationships can be a pathway to the development optimized ORR systems for alternative energy and industrial processes.

We analyzed two Fe-based electrocatalysts for the ORR with N_3O ligand frameworks. $Fe(PMG)(Cl)_2$ was first studied, which contained an amine-based ligand framework with pyridine moieties and carboxylic acid group in the inner coordination sphere.[1] $Fe(tpy^{tbu}pho)Cl_2$ incorporated a terpyridine based framework with a phenolate moiety in the inner coordination sphere.[2] Under electrochemical and spectrochemical conditions with AcOH as a proton source in

acetonitrile solution, both of these systems were found to catalytically reduced O_2 to H_2O via a 2+2 mechanism. Interestingly, there were distinct differences in the observed mechanism, where $Fe(PMG)(Cl)_2$ operated through an off-cycle bridging peroxo dimer species, where its cleavage was the rate-determining step. Additionally, the anionic O group in the inner coordination sphere engaged in H-bonding with AcOH during catalysis. On the other hand, the rate-determining step for the $Fe(tpy^{tbu}pho)Cl_2$ complex was O_2 binding to the reduced metal center, and the O group did not participate in H-bonding during catalysis. Interestingly, these results show the nuances of the ORR through ligand modification, where a key factor in observed reactivity was the ligand in the axial position to the O_2 binding site.

There are a number of strategies that can be employed to expand upon this work. Ligand modification of both complexes could provide further optimization opportunities for non-heme Fe-based systems. Utilizing the PMG ligand framework, we can substitute the pyridine moieties in the *ortho* position to prevent off-cycle dimer formation. Additionally, incorporation of functional groups in the *ortho* position that can engage in H-bonding $Fe–O_2$ intermediates could stabilize reactive intermediates and possibly control product selectivity, as has been shown previously in O_2 activation studies.[3] This would enhance catalysis and provide a means to control accessible reaction pathways.

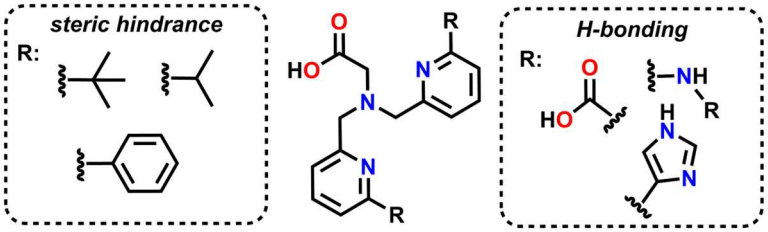

Figure 7.1. Ligand modification of PMG ligand framework to prevent dimer formation and accelerate catalysis, where R indicates functional group.

Another method to improve ORR in our studied Fe-based systems, specifically the terpyridine system, is enhancing the rate-limiting O_2 binding step. One strategy of interest is axial ligand modification to tune O_2 binding to the reduced metal center and stability of the $Fe–O_2$

intermediates. Because the axial ligand position *trans* to O_2 binding site is occupied by a solvent molecule during catalysis, incorporation of an electron-donating axial ligand, such as imidazole, could enhance O_2 binding and tune the pK_a of the peroxo intermediates, contributing to selectivity control (Figure 7.2.).[4-7] Additionally, synthesis of substituted imidazoles at the N and C-positions is known,[8-10] providing extensive ability to explore the axial ligand effects in tuning O_2 reactivity at Fe(tpy^{tbu}pho)Cl_2.

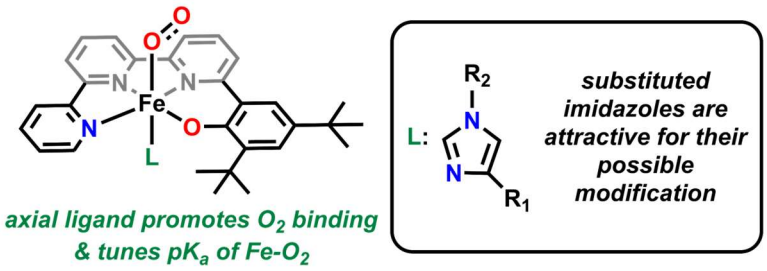

Figure 7.2. Tunable imidazole axial ligands *trans* to O_2 binding can affect the ORR by Fe(tpy-^{tbu}pho)Cl_2.

7.1.2. Manganese Based ORR

In comparison to Fe and Co, Mn is much less widely studied for ORR catalysis due to strong binding of O_2 to Mn metal centers, which over-stabilizes intermediates, slowing the reaction. Here, the synthesis and examination of two Mn complexes with N_2O_2 bipyridine based ligand frameworks for ORR was undertaken.[11] One complex incorporated pendent –OMe groups in the secondary coordination sphere to understand how pendent proton relays could affect catalysis. Using an ammonium-based proton source (DIEPEAHPF$_6$), catalysis was studied under electrochemical and spectrochemical conditions using both buffered and unbuffered proton sources. Under unbuffered conditions rate-limiting O_2 binding was observed with both the control complex and pendent relay complex. However, without presence of added base, incorporation of a pendent relay suppressed catalysis due to strong H-bonding interactions, but selectivity was shifted to exclusively produce H_2O_2 due to favorable proton transfer to the proximal oxygen in the Mn-hydroperoxo intermediate. Interestingly, in the presence of added base, there is a favorable dimerization pathway available, which results in the formation of H_2O as the primary product.

Further, added base mitigates the H-bonding induced suppression of the pendent relay complex. Taken together, these results showed the importance of secondary sphere effects in product selectivity during Mn-based ORR as well as the role of added based during catalysis.

Based on our results, there are several proposed approaches that could be used to better understand ORR by Mn systems. First, in order to prevent or tune dimer formation during catalysis, introduction of steric hindrance through substituting tertbutyl, mesityl, and phenyl groups onto the bpy backbone of the ligand framework could be employed. Additionally, tuning the basicity of the pendent proton groups could be used to take advantage of the acid activity to rapidly transfer protons to the active site while preventing the H-bonding induced suppression that was observed. This would require a pendent group that would not be substantially more basic than the proton source. Changing the position of the proton pendent relays to the backbone of the bpy moiety could also help to stabilize Mn–O_2 intermediates to direct protonation, further enhance catalysis, and control selectivity (**Figure 7.3.**). Previous work has shown that amine and carboxylic acid groups can act as pendent proton donor relays during ORR and could be suitable options to better enhance Mn-based reactivity.[12,13] Taken together, synthetic tunability of the bpy-based ligand framework provides a number of opportunities to further tune catalysis and establish structure-function relationships of the ORR by Mn.

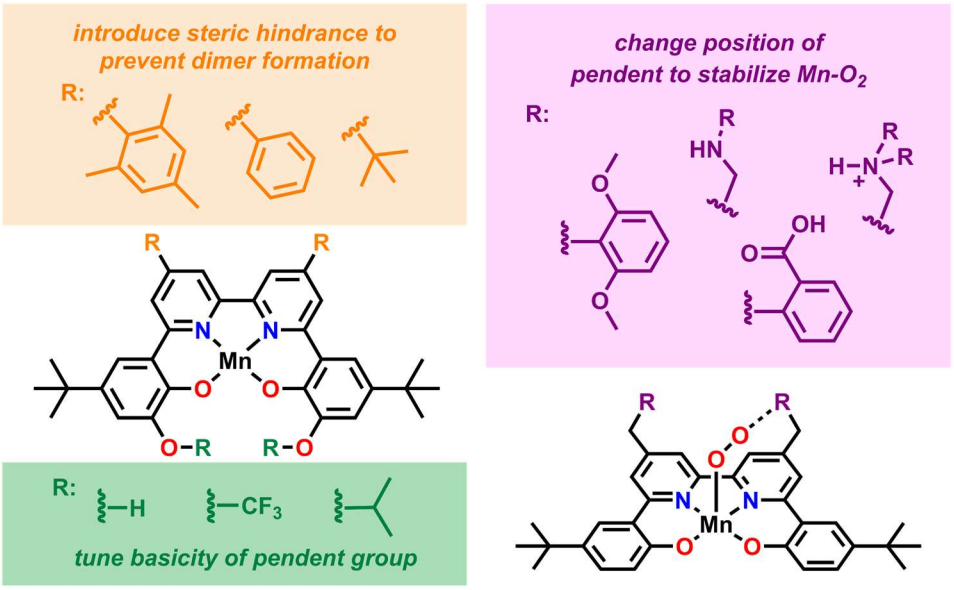

Figure 7.3. Proposed ligand modifications to enhance ORR by Mn-based N_2O_2 complexes.

7.1.3. Metal-Free Catalysts for the ORR

Redox-active organic molecules that are stable toward ROSs have drawn increasing attention in recent years for possible use as sustainable ORR catalysis. Here, two cationic organic molecules have been evaluated as ORR catalysts. First, an iminium-based compound was studied under both electrochemical and spectrochemical conditions with TFAH as a proton source and was shown to catalytically reduce O_2.[14] Interestingly, there was a divergence in mechanism, where under spectrochemical conditions, outer-sphere O_2 reduction occurred to produce H_2O_2. However, under electrochemical conditions in the presence of excess reduced catalyst, $O_2^{\bullet-}$ could bind and be further reduced to produce H_2O. Then, a substituted phenanthroline diium compound (Ph_2Phen^{2+}) was studied for its propensity to effectively reduce O_2. Acetic acid derivatives were used to understand the dependence of ORR by Ph_2Phen^{2+} on acid strength under both electrochemical and spectrochemical conditions. It was found that activity scaled with acid strength. Further, a change in rate-determining step was observed with weaker acids under spectrochemical conditions. For the strongest acids, the formation of a hydroperoxo intermediate was rate limiting, for the acids of intermediate strength protonation of the hydroperoxo

intermediate to facilitate product release was rate limiting, and exiting from an equilibrium involving an off-cycle bridging peroxo intermediate was rate-limiting with the weakest acid. However, under electrochemical conditions the off-cycle dimer species was observed to be kinetically relevant under all conditions due to the relative concentration of reduced catalyst in the reaction diffusion layer. Taken together, these results show the opportunity to further tune and understand catalytic O_2 reduction by metal-free catalysts.

There has been work shown that ORR in metal-free catalysts can be tuned by the electron-donating or -withdrawing character of the molecule.[15,16] Further, we have shown that metal-based ORR can be tuned by altering the acid pK_a and electron delivery.[14] Taken together, there is a vast opportunity for further understanding of metal-free systems for the ORR, and there are several synthetic possibilities of the phenanthroline derivative to explore. Such as substituent modifications to alter the electron donating/withdrawing character of the molecule, introduction of more sterically bulky groups would prevent off-cycle dimer formation, and incorporation of pendent groups that can act as proton relays during catalysis (**Figure 7.4.**). We have shown that ORR proceeds via an inner-sphere mechanism under certain conditions with $O_2^{\bullet-}$, suggesting that we are able to tune the binding, reactivity, and possibly selectivity during catalysis.

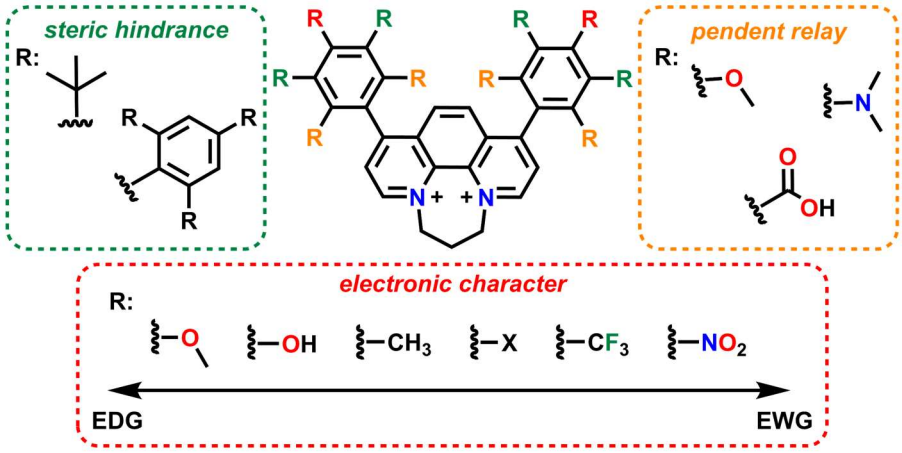

Figure 7.4. Proposed organic molecules for optimization of the ORR, where R = functional group modification sites.

7.2. Outlook and Perspectives

While the field of ORR is expansive, there are still numerous opportunities to further enhance and optimize catalytic O_2 reduction with earth abundant catalysts. Since our reports on non-porphyrinic Fe-based ORR catalysis, there have been additional studies that have focused on further understanding the systems.[17,18] Non-porphyrinic systems provide a unique opportunity to modify groups bound to the active metal center. Modification of the inner-coordination sphere will provide further insight into the electronic structure and tunability of catalytic activity. In addition, there is a lack of comparable non-porphyrinic systems between Fe and Mn. Being able to compare the metal center would allow for a new fundamental understanding of how to further tune and compare O_2 reduction as well as activation between these two active sites. This would contribute not only to catalytic ORR but also to the understanding of comparable biological metallocofactors and their structure-function relationships. Further, efficient catalytic ORR by metal-free organic molecules remains an extremely novel area in need of further development. There is extensive opportunity to expand upon this field through synthetic modification. The works described here have contributed to the fundamental understanding of effective ORR catalysts for the eventual development of alternative energy and industrial processes that will be crucial to the long-term sustainable growth of our population.

7.3. References

(1) Cook, E. N.; Machan, C. W. Bioinspired mononuclear Mn complexes for O2 activation and biologically relevant reactions. *Dalton Trans.* **2021**, *50* (46), 16871-16886, 10.1039/D1DT03178C. DOI: 10.1039/D1DT03178C.

(2) Cook, E. N.; Hooe, S. L.; Dickie, D. A.; Machan, C. W. Homogeneous Catalytic Reduction of O2 to H2O by a Terpyridine-Based FeN3O Complex. *Inorg. Chem.* **2022**, *61* (22), 8387-8392. DOI: 10.1021/acs.inorgchem.2c00524.

(3) Cook, S. A.; Borovik, A. S. Molecular Designs for Controlling the Local Environments around Metal Ions. *Acc. Chem. Res.* **2015**, *48* (8), 2407-2414. DOI: 10.1021/acs.accounts.5b00212.

(4) Pegis, M. L.; Wise, C. F.; Martin, D. J.; Mayer, J. M. Oxygen Reduction by Homogeneous Molecular Catalysts and Electrocatalysts. *Chem. Rev.* **2018**, *118* (5), 2340-2391. DOI: 10.1021/acs.chemrev.7b00542.

(5) Tsuda, M.; Kasai, H. Imidazole ligand effect on O2 interaction with metalloporphyrins. *Surface Science* **2007**, *601* (22), 5200-5206. DOI: https://doi.org/10.1016/j.susc.2007.04.229.

(6) Chlistunoff, J.; Sansiñena, J.-M. Effects of Axial Coordination of the Metal Center on the Activity of Iron Tetraphenylporphyrin as a Nonprecious Catalyst for Oxygen Reduction. *J. Phys. Chem. C* **2014**, *118* (33), 19139-19149. DOI: 10.1021/jp5044249.

(7) Ohta, T.; Nagaraju, P.; Liu, J.-G.; Ogura, T.; Naruta, Y. The secondary coordination sphere and axial ligand effects on oxygen reduction reaction by iron porphyrins: a DFT computational study. *JBIC Journal of Biological Inorg. Chem.* **2016**, *21* (5), 745-755. DOI: 10.1007/s00775-016-1380-9.

(8) Kadu, V. D.; Mali, G. A.; Khadul, S. P.; Kothe, G. J. Simple practical method for synthesis of trisubstituted imidazoles: an efficient copper catalyzed multicomponent reaction. *RSC Advances* **2021**, *11* (36), 21955-21963, 10.1039/D1RA01767E. DOI: 10.1039/D1RA01767E.

(9) Gupta, N.; Pathak, D. P. Synthesis and Evaluation of N-substituted Imidazole Derivatives for Antimicrobial Activity. *Indian Journal of Pharmaceutical Sciences* **2011**, *73* (6), 674-678. DOI: 10.4103/0250-474X.100246.

(10) Shabalin, D. A.; Camp, J. E. Recent advances in the synthesis of imidazoles. *Organic & Biomolecular Chemistry* **2020**, *18* (21), 3950-3964, 10.1039/D0OB00350F. DOI: 10.1039/D0OB00350F.

(11) Cook, E. N.; Courter, I. M.; Dickie, D. A.; Machan, C. W. Controlling product selectivity during dioxygen reduction with Mn complexes using pendent proton donor relays and added base. *Chemical Science* **2024**, 10.1039/D3SC02611F. DOI: 10.1039/D3SC02611F.

(12) Carver, C. T.; Matson, B. D.; Mayer, J. M. Electrocatalytic Oxygen Reduction by Iron Tetra-arylporphyrins Bearing Pendant Proton Relays. *J. Am. Chem. Soc.* **2012**, *134* (12), 5444-5447. DOI: 10.1021/ja211987f.

(13) Bhunia, S.; Ghatak, A.; Rana, A.; Dey, A. Amine Groups in the Second Sphere of Iron Porphyrins Allow for Higher and Selective 4e–/4H+ Oxygen Reduction Rates at Lower Overpotentials. *J. Am. Chem. Soc.* **2023**, *145* (6), 3812-3825. DOI: 10.1021/jacs.2c13552.

(14) Cook, E. N.; Davis, A. E.; Hilinski, M. K.; Machan, C. W. Metal-Free Homogeneous O2 Reduction by an Iminium-Based Electrocatalyst. *J. Am. Chem. Soc.* **2024**. DOI: 10.1021/jacs.3c14549.

(15) Tanjedrew, N.; Thammanatpong, K.; Surawatanawong, P.; Chakthranont, P.; Chantarojsiri, T.; Unjarern, T.; Kiatisevi, S. Tunable Metal-free Imidazole-Benzimidazole Electrocatalysts for Oxygen Reduction in Aqueous Solutions. *Chem. Eur. J.* **2023**, *30* (5), e202302854. DOI: 10.1002/chem.202302854.

(16) Audebert, P.; Hapiot, P. Preparation and electrochemistry of several substituted 9-(4-R-phenyl)-N-methylacridinium salts.: Kinetic analysis of the O2 catalytic reduction in acidic dimethylsulfoxide and in hydrophobic Nafion® gels. *J. Electroanal. Chem.* **1993**, *361* (1), 177-183. DOI: 10.1016/0022-0728(93)87052-W.

(17) Zhang, H.-T.; Xie, F.; Guo, Y.-H.; Xiao, Y.; Zhang, M.-T. Selective Four-Electron Reduction of Oxygen by a Nonheme Heterobimetallic CuFe Complex. *Angew. Chem. Int. Ed.* **2023**, *62* (48), e202310775. DOI: 10.1002/anie.202310775 (acccessed 2024/02/06).

(18) Santra, A.; Das, A.; Kaur, S.; Jain, P.; Ingole, P. P.; Paria, S. Catalytic reduction of oxygen to water by non-heme iron complexes: exploring the effect of the secondary coordination sphere proton exchanging site. *Chem. Sci.* **2024**, 10.1039/D3SC06753J. DOI: 10.1039/D3SC06753J.

EMMA N. COOK

EDUCATION

University of Virginia **August 2019 – Expected May 2024**
Ph.D. Inorganic Chemistry
University of North Carolina at Chapel Hill **August 2015 – May 2019**
B.S. Chemistry, Medical Anthropology Minor

RESEARCH EXPERIENCE

Graduate Research Assistant (UVA) **August 2019 – Present**
Advisor: Dr. Charles W. Machan
Development of earth-abundant transition metal based electrocatalysts for O_2 activation and reduction.

Undergraduate Research Assistant (UNC) **August 2017 – June 2019**
Advisor: Dr. Jillian L. Dempsey
Analyzing ligand exchange reactivity at CdSe and PbS quantum dot surfaces.

LEADERSHIP EXPERIENCE

Graduate Student Council Executive Board Officer **May 2022 – April 2024**
UVA Department of Chemistry
Vice President and Green Labs Representative April 2023 – April 2024
- Developed by-laws for the Graduate Student Council. Served as a chemistry representative with the Office of Sustainability at UVA including monthly meetings to develop sustainability programming within the department and beyond.

Social Co-Chair May 2022 – April 2023
- Organized community-building events for department graduate students, postdoctoral researchers, staff, and faculty. Financial budgeted for various events. Participated in decision-making and advocating for the graduate student body within the chemistry department.

Heritage University Collaboration Co-Lead **January 2022 – December 2023**
UVA Department of Chemistry & Heritage University (Toppenish, WA)
- Developed teaching laboratory experiment and teaching materials for introductory environmental science and chemistry courses. Presented lecture materials and facilitated in-person laboratory experiments with HU students.

Annual Retreat & Open House Planning Committee **July 2021 – October 2023**
UVA Department of Chemistry
- Worked in collaboration with chemistry department faculty and staff members to co-lead a group of graduate students in organizing a department-wide event.

ChemSciComm Mentorship Program **March 2021 – May 2024**
UVA Department of Chemistry
- Promote effective science communication within the department of chemistry by publishing written research summaries for a general scientific audience and the public, organized and leading fellowship application writing workshops, and organizing, leading and moderating a discussion-based career seminars.

Policy Education Chair **June 2020 – May 2024**
Science Policy Initiative at UVA
- Developed Journal Club curricula for science policy education and policy discussion.
- Led bi-weekly and monthly discussions on political literature.

- Moderated seminar series and professional development events focused on careers in science policy.
- Wrote and published science policy memo.

LatinX Communities Alternative Spring Break **March 2017**
UNC Assisting People in Planning Learning Experiences in Service
- Traveled around North Carolina learning about the migrant farmworker population.
- Volunteered with groups that provide health, legal and monetary assistance to migrant farmworkers.

MENTORSHIP EXPERIENCE

Graduate Peer Mentor **August 2021 – May 2023**
UVA Department of Chemistry
- Peer mentor for first-year graduate students to facilitate their transition into graduate school.

Undergraduate Researcher Mentor **August 2021 – Present**
UVA Department of Chemistry
- Train undergraduate UVA students in laboratory techniques, general chemistry concepts, conducting research, and communicating science.

Refugee Mentor **September 2016 – April 2017**
Chapel Hill Refugee Support Center
- Provided weekly mathematics tutoring and mentorship to a high school senior.

TEACHING EXPERIENCE

Graduate Teaching Assistant **August 2019 – May 2021**
UVA Department of Chemistry
Honors General Chemistry Laboratory (CHEM 1811)
Honors Organic Chemistry I Laboratory (CHEM 1821)
Organic Chemistry II Laboratory (CHEM 2321)

Undergraduate Teaching Assistant **August 2017 – May 2019**
UNC Department of Chemistry
Instrument TA
Honors Analytical Laboratory (245L)
Analytical Laboratory (CHEM 241L)

AWARDS AND HONORS

Lifetime Service Award March 2024
University of Virginia Department of Chemistry
Third Place, Best Poster October 2023
UVA Department of Chemistry Annual Department Retreat
Jefferson Arts and Sciences Dissertation Year Fellow Aug 2023 – May 2024
Jefferson Scholars Foundation
Adam Ritchie Award March 2023
University of Virginia Department of Chemistry
Raven Society March 2023
University of Virginia
Young Investigator Award March 2023
American Chemical Society Division of Inorganic Chemistry
First Place, Best Poster Award August 2022
VA Clean Energy and Catalysis Club Summit

ACS DIC Travel Award — August 2022
American Chemical Society Division of Inorganic Chemistry

Department Travel Award — August 2022
UVA Department of Chemistry

First Place, Best Poster Award — October 2021
UVA Department of Chemistry Annual Department Retreat

High Pass Candidacy — February 2021
UVA Department of Chemistry

Undergraduate Teaching Assistant Award — May 2019
UNC Department of Chemistry

Dean's List — May 2018, 2019
UNC

Summer Undergraduate Research Fellowship — May 2018
UNC Department of Undergraduate Research

PEER-REVIEWED PUBLICATIONS

1. **Cook, E. N.**; Davis, A. E.; Hilinski, M. K.; Machan, C. W. Metal-Free Homogeneous O_2 Reduction by an Iminium-Based Electrocatalyst *Journal of the American Chemical Society* **2024**, 146, 12, 7931-7935. doi: 10.1021/jacs.3c14549
2. **Cook, E. N.**; Courter, I. M.; Dickie, D. A.; Machan, C. W. Controlling product selectivity during dioxygen reduction with Mn complexes using pendent proton donor relays and added base *Chemical Science* **2024**, 15, 4478-4488. doi: 10.1039/D3SC02611F
3. Machost, H. R.[#]; Obi, A. D.[#]; Molino, A.; **Cook, E. N.**; Nichols, A. W.; Freeman, L. A.; Stegner, S. G.; Dickie, D. A.; Wilson, D. J. D.; Machan, C. W.; Gilliard Jr., R. J.; Chemical Reduction of Azolium-Thiocarboxylate: Isolation of Carbon Disulfide Radial Anions and Dianions. *Submitted.*
4. Dressel, J. M.; **Cook, E. N.**; Hooe, S. L.; Moreno, J. J.; Dickie, D. A.; Machan, C. W.; Electrocatalytic hydrogen evolution reaction by a Ni(N_2O_2) complex based on 2,2'-bipyridine *Inorganic Chemistry Frontiers* **2023**, 10, 972-978. doi: 10.1039/D2QI01928K
5. **Cook, E. N.** and Machan, C. W. Homogeneous catalysis of dioxygen reduction by molecular Mn complexes. *Chemical Communications* **2022**, 58, 11746-11761. doi: 10.1039/D2CC04628H
6. **Cook, E. N.[#]**; Hooe, S. L.[#]; Dickie, D. A.; Machan, C. W. Homogeneous Catalytic Reduction of O_2 to H_2O by a Terpyridine-Based FeN_3O Complex. *Inorganic Chemistry* **2022**, 61, 8387-8392. doi: 10.1021/acs.inorgchem.2c00524 Selected as Feature Article. Featured in *Early-Career Researchers in Organic and Inorganic Chemistry* Virtual Issue.
7. Kessler, M. L.; Kelm, J. E.; Starr, H. E.; **Cook, E. N.**; Miller, J. D.; Rivera, N. A.; Hsu-Kim, H.; Dempsey, J. L. Unraveling Changes to PbS Nanocrystal Surfaces Induced by Thiols. *Chemistry of Materials* **2022**, doi: 10.1021/acs.chemmater.1c03888.
8. **Cook, E. N.**; Machan, C. W. Bioinspired mononuclear Mn complexes for O_2 activation and biologically relevant reactions *Dalton Transactions* **2021**, 50, 16871-16886. doi: 10.1039/D1DT03178C. Selected as HOT article.
9. Hooe, S. L.; Moreno, J. J.; Reid, A. G.; **Cook, E. N.**; Machan, C. W. Mediated Inner-Sphere Electron Transfer Induces Homogeneous Reduction of CO_2 via Through-Space Electronic Conjugation *Angewandte Chemie, Int. Ed.* **2021**, 60, 1-6. doi: 10.1002/anie.292109645
10. **Cook, E. N.**; Dickie, D. A.; Machan, C. W. Catalytic Reduction of Dioxygen to Water by a Bioinspired Non-Heme Iron Complex via a 2+2 Mechanism *Journal of the American Chemical Society* **2021**, 143, 40, 16411-16418. doi: 10.1021/jacs.1c04572.

11. Nichols, A. W.; **Cook, E. N.**; Gan, Y. J.; Miedaner, P. R.; Dressel, J. M.; Dickie, D. A.; Shafaat, H. S.; Machan, C. W. Pendent Relay Enhances H_2O_2 Selectivity during Dioxygen Reduction Mediated by Bipyridine-Based Co-N_2O_2 Complexes *Journal of the American Chemical Society* **2021**, 143, 33, 13065-13073. doi: 10.1021/jacs.1c03381.
12. Hooe, S. L; **Cook, E. N.**; Reid, A. G.; Machan, C. W. Non-covalent Assembly of Proton Donors and *p*-benzoquinone Anions for Co-electrocatalytic Reduction of Dioxygen *Chemical Science* **2021**, 12, 9733-9741.doi: 10.10139/D1SC01271A.

PRESENTATIONS

1. "*Development of Earth Abundant Materials for Energy Relevant Oxygen Conversion*" Jefferson Foundation Fellows Symposium, Charlottesville, VA. January 25, 2024 (oral)
2. "*Controlling Product Selectivity during Dioxygen Reduction with Mn Complexes using Pendent Proton Donor Relays and Added Base*" SERMACS 2023, Durham, NC. October 28, 2023 (oral)
3. "*Pendent Relays Promote Dimerization During Catalytic Dioxygen Reduction Mediated by Mn-complexes*" SERMACS 2023, Durham, NC. October 25, 2023 (poster)
4. "*Pendent Relays Promote Dimerization During Catalytic Dioxygen Reduction Mediated by Mn-complexes*" UVA Department of Chemistry Annual Retreat, October 3, 2023. (poster, 3rd place Best Poster)
5. "*Pendent Relays Promote Dimerization During Catalytic Dioxygen Reduction Mediated by Mn-Complexes"* ACS Fall 2023, Young Investigator Awards Symposium, San Francisco, CA. August 13, 2023 (oral), *invited*
6. "*Pendent Relay Effects in Homogeneous Mn-Based Catalysts for Oxygen Reductio*n" ACS Fall 2023, San Francisco, CA. August 13, 2023 (poster)
7. "*Pendent Relay Effects in Homogeneous Mn-Based Catalysts for Oxygen Reductio*n" Virginia Clean Energy and Catalysis Club Summit. August 7, 2023 (poster)
8. "*Pendent Relays Promote Dimerization During Catalytic Dioxygen Reduction Mediated by Mn-Complexes"* Gordon Research Seminar – Inorganic Reaction Mechanisms. March 4, 2023 (poster)
9. "*Pendent Relays Promote Dimerization During Catalytic Dioxygen Reduction Mediated by Mn-Complexes"* Gordon Research Seminar – Inorganic Reaction Mechanisms. March 4, 2023 (oral), *invited*
10. "*Development of Earth Abundant Transition Metal Catalysts for Dioxygen Reduction*" UVA Dept. of Chemistry Fourth Year Seminar. January 23, 2023 (oral)
11. "*Electrocatalytic Reduction of Dioxygen by Non-Porphyrinic Fe Complexes"* ACS Fall 2022, Chicago, IL. August 23, 2022 (oral)
12. "*Development of Non-Porphyrinic Catalysts for Oxygen Reduction and Activation*" ACS Fall 2022, Chicago IL. August 21, 2022 (poster)
13. "*Development of Non-Porphyrinic Catalysts for Oxygen Reduction and Activation*" Virginia Clean Energy and Catalysis Club Summit. August 8, 2022 (poster, winner Best Poster).
14. "*Development of Fe and Mn Non-Porphyrinic Catalysts for Oxygen Reduction and Activation"* UVA Department of Chemistry 3rd Year Poster Session. April 14, 2022. (poster)
15. *"Catalytic Reduction of Dioxygen to Water by a Bioinspired Non-Heme Iron Complex via a 2+2 Mechanism"* UVA Department of Chemistry Annual Retreat. October 12, 2021 (poster, winner Best Poster).
16. *"Electrocatalytic Reduction of Dioxygen to Water by a Bioinspired Non-Heme Iron Complex via a 2+2 Mechanism"* ACS Fall 2021. August 23, 2021 (oral).

17. *Electrocatalytic Reduction of Dioxygen to Water by a Bioinspired Non-Heme Iron Complex via a 2+2 Mechanism"* Virginia Clean Energy and Catalysis Club Summit. August 2, 2021 (poster).
18. *"Electrocatalytic Reduction of Dioxygen to Water by a Bioinspired Non-Heme Iron Complex via a 2+2 Mechanism"* University of Virginia Environmental Resilience Institute Research for Action Symposium, March 31, 2021 (poster).
19. *"Analysis of Size-Dependent Thiol Binding on the Surfaces of CdSe Quantum Dots"* University of North Carolina at Chapel Hill Undergraduate Research Symposium, April 24, 2019 (poster).
20. "*Thermodynamic Analysis of Size-Dependent Ligand Exchange on CdSe Quantum Dots"* Triangle Student Research Competition, September 19, 2018 (poster).

OTHER PUBLICATIONS

1. Bushana, P. N.; **Cook, E. N.** NIDA's Funding Policies Contribute to Racial Biases in the Treatment of Drug Use *Journal of Science Policy and Governance* **2021**, 19, 1. doi: 10.38126/JSPG190102.

PROFESSIONAL ORGANIZATIONS

American Chemical Society, VA Chapter, Division of Inorganic Chemistry	April 2020 – Present
American Association for the Advancement of Science	April 2021 – Present